Spring 1-1-2013

Gravity Field Characterization around Small Bodies

Yu Takahashi
University of Colorado at Boulder, yu.takahashi.astro@gmail.com

Gravity Field Characterization around Small Bodies

by

Yu Takahashi

B.S., Embry-Riddle Aeronautical University, 2007

M.S., University of Colorado at Boulder, 2010

A thesis submitted to the

Faculty of the Graduate School of the

University of Colorado in partial fulfillment

of the requirements for the degree of

Doctor of Philosophy

Department of Aerospace Engineering Sciences

2013

This thesis entitled:
Gravity Field Characterization around Small Bodies
written by Yu Takahashi
has been approved for the Department of Aerospace Engineering Sciences

Daniel J. Scheeres

George H. Born

Shyam Bhaskaran

Steve Nerem

John Wahr

Date

The final copy of this thesis has been examined by the signatories, and we find that both the content and the form meet acceptable presentation standards of scholarly work in the above mentioned discipline.

Takahashi, Yu (Ph.D., Aerospace Engineering Sciences)

Gravity Field Characterization around Small Bodies

Thesis directed by Prof. Daniel J. Scheeres

A small body rendezvous mission requires accurate gravity field characterization for safe, accurate navigation purposes. However, the current techniques of gravity field modeling around small bodies are not achieved to the level of satisfaction. This thesis will address how the process of current gravity field characterization can be made more robust for future small body missions.

First we perform the covariance analysis around small bodies via multiple slow flybys. Flyby characterization requires less laborious scheduling than its orbit counterpart, simultaneously reducing the risk of impact into the asteroid's surface. It will be shown that the level of initial characterization that can occur with this approach is no less than the orbit approach. Next, we apply the same technique of gravity field characterization to estimate the spin state of 4179 Touatis, which is a near-Earth asteroid in close to 4:1 resonance with the Earth. The data accumulated from 1992-2008 are processed in a least-squares filter to predict Toutatis' orientation during the 2012 apparition. The center-of-mass offset and the moments of inertia estimated thereof can be used to constrain the internal density distribution within the body. Then, the spin state estimation is developed to a generalized method to estimate the internal density distribution within a small body. The density distribution is estimated from the orbit determination solution of the gravitational coefficients. It will be shown that the surface gravity field reconstructed from the estimated density distribution yields higher accuracy than the conventional gravity field models. Finally, we will investigate two types of relatively unknown gravity fields, namely the interior gravity field and interior spherical Bessel gravity field, in order to investigate how accurately the surface gravity field can be mapped out for proximity operations purposes. It will be shown that these formulations compute the surface gravity field with unprecedented accuracy for a well-chosen set of parametric settings, both regionally and globally.

Dedication

I would like to dedicate this dissertation to my parents, Michiaki and Eiko Takahashi. They condoned my stubborn attitude and allowed me to travel far when I insisted on going to a university in the U.S. Without their love and support, I could not have come this far. I also dedicate this dissertation to my grandparents, especially both my grandfathers who could not live long enough to see the day. I can only imagine how happy they would have been. Finally, I dedicate this dissertation to all my family members back in Japan. Thank you is not good enough. Domo arigato, everyone.

Acknowledgements

First and foremost, I would like to acknowledge and thank my advisor, Dan Scheeres. His guidance in research as well as his role as a life mentor was essential in my completing graduate school. My education motto is: "Education is like bottomless mimosa on Saturday morning." That is, the educator should never judge how big the student's glass is. He can only pour his knowledge until it overflows, and Dan did exactly that. I learned the joy of learning and my glass will never be full. Having Dan as my graduate advisor was the best decision I have ever made. I would also like to extend my appreciation for all the committee members, especially Dr. Born. Your statistical orbit determination class changed my views of astrodynamics.

From JPL, I would like to acknowledge Steve Broschart, Ryan Park, Lance Benner, David Wiese, Jill and Carl Seubert, Aurore Sibois, and Al Cangahuala for giving me countless advices in research and life. My sincere gratitude goes to Ted Sweetser and Shyam Bhaskaran, for funding the initial years of graduate school and offering me a position as a navigation engineer at JPL. The job offer from JPL in December 2012 was the best Christmas gift I have ever received. Regarding the funding, I'd like to acknowledge NASA/JPL and OSIRIS-REx New Frontiers mission.

In addition, I was lucky enough to meet great research collaborators, Michael Busch and Bob Werner. Michael provided me an opportunity to work on the spin state estimation of Toutatis. Also, a significant portion of my research is based on the past work by Bob. Thank you Bob, for being my inspiration.

Last but not least, I'd like to acknowledge all my lab mates at CU and all the friends, professors, and faculties who helped me throughout the years. I talked about mimosa earlier, but it is not my favorite drink. Let's drink beer when we see each other again.

Contents

Chapter

Tables

Table

Figures

Figure

Chapter 1

Introduction

The theory of gravitational potential has mesmerized human kind for centuries, with the advent of Newton marking the birth of such a mathematical field [40]. In spite of numerous, earnest efforts in the past, the accuracies of the solutions to the gravitational potential are still not achieved to the level of satisfaction after three centuries. While the potential expression has remained an enigma since its birth, its applications have changed significantly. In the early days, humans observed the celestial bodies to ponder what would reasonably explain their orbit, which is the act of gravitation that many are familiar with these days. On the other hand, now in the era of space age, humans wonder how they can accurately guide their objects (spacecrafts, or even humans) to one or more of these celestial bodies. Furthermore, the need for better gravitational potential expression has changed remarkably since the dawn of the space age. Humans are not only sending manmade objects to large planets, but also to small primitive bodies (i.e., asteroids and comets). This thesis will specifically address how to characterize the gravity field environment around these small bodies as described in the thesis statement below.

Thesis Statement:

> Initial gravity field characterization around small bodies can be achieved by implementing multiple slow flybys instead of orbits for a spacecraft rendezvous mission. Such a mission profile will reduce the time required for the initial survey phase and in some cases can be sufficient for the bulk of the scientific return. The gravitational coefficients estimated from such an orbit determination process constitute measurements that can be used to estimate the density distribution within the body, assuming the presence of a sufficiently accurate shape model. The estimated density distribution can be used to reconstruct the surface gravity field for proximity operations purposes. Furthermore, the interior spherical harmonic gravity

field and the interior spherical Bessel gravity field assist accurate regional and total mapping of the surface gravity field. The density estimation algorithm, together with the interior spherical harmonic and the interior spherical Bessel gravity fields, constitute new techniques that allow safe and robust trajectory designs down to the surface for future spacecraft missions. All of the surface gravity models by far exceed the accuracy of the exterior gravity field conventionally used for gravity field characterization.

1.1 Motivation for Small Body Explorations

Scientific interest in understanding asteroids and comets has been growing significantly during the last decade, with a number of mission studies, actual missions, and planned future missions in the works. Asteroid and comets are often referred to as primitive bodies or small bodies in the solar system, and they are regarded as valuable objects in space that are important for science, engineering, and even public communities. The reasons of high interest for small body missions include, but are not limited to, the scientific interest in tracing the history and evolution of the solar system, the exploration of deep space prior to a future manned mission to Mars, potential discovery and development of in-situ resource utilization (ISRU) to further the robotic/manned deep space missions, realization of a business model by asteroid mining/ISRU (e.g., Planetary Resources), and establishment of the planetary defense technologies to prevent potentially hazardous objects (PHOs) from causing catastrophic damage to the Earth.

Glassmeier et al. [18] mention that the small bodies are widely considered to contain the least processed material in the solar system, possibly for billions of years, since the condensation from the proto-solar nebula, and even pre-solar grains could be preserved in them. Thus, deeper understanding of these small bodies is the key to decoding evolutionary process of the solar system, and meaningful constraints can be levied by deciphering families of asteroids in detail. The sizes of these small bodies vary over orders of magnitude, with the smallest to largest ranging from a few meters to a few hundred kilometers in radius. Out of ~ 10000 asteroids that have been found and catalogued by the Near-Earth Objects Program, a majority ($> 80\%$) of them are singles while it is estimated that roughly 16% of the population are binary systems, with a few others that are ternaries [7, 37]. Figure 1.1 shows a montage of a small fraction of the asteroid population.

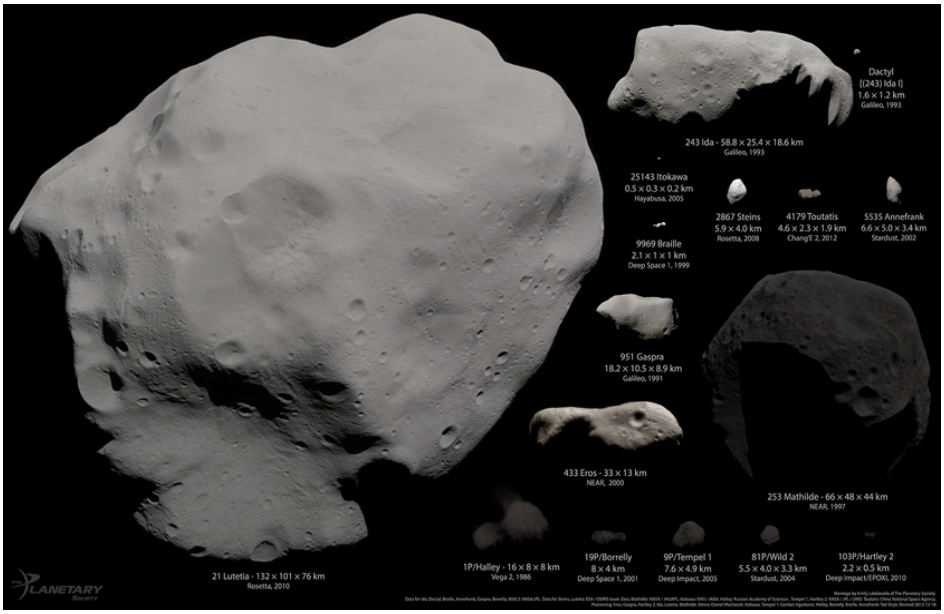

Figure 1.1: Asteroid montage (Source: Emily Lakdawalla/The Planetary Society).

As shown in Figure 1.1, there are a multitude of asteroid shapes and sizes. Their compositions also vary from C-type (carbonaceous) to S-type (stony) to M-type (metallic), and more specific categories exist based on their spectral and albedo measurements. Often these bodies are too small for their gravitation to construct a spherical shape, which complicates the mission design since the perturbations due to their non-spherical shape are significantly greater than those experienced around the large planets. The situation is made more complex due to the presence of the solar radiation pressure and other perturbation effects that can be as large as the gravitation itself, and small deviations in the spacecraft position/velocity can cause an impact to/escape from the system in a matter of hours to days. Moreover, these bodies have suffered many bombardment of/collisions with other asteroids, rendering a large number of craters and boulders on the surface that will require very accurate deep space navigation, for example, to perform a touch-and-go (TAG) sample collection maneuver. These irregular shapes, sizes, and surface morphology of small bodies provide unique challenges that have to be overcome for the future missions to asteroids. Our interest lies in contributing to this unique field in the space exploration by delivering more robust techniques to characterize the gravity field environment, which brings tremendous benefit to both robotic spacecraft missions and crewed missions to small bodies.

1.1.1 Current and Future Missions

The goals of a small body mission include, but are certainly not limited to, the determination of the shape of the body, determination of rotational dynamics, determination and evaluation of the gravity field, evaluation of stable/unstable orbits, estimation of internal density structure, and proximity operations. Such a mission can be highlighted by Near Earth Asteroid Rendezvous (NEAR) Shoemaker spacecraft that orbited 433 Eros for about a year to characterize the Eros' physical parameters [38]. In addition, the Hayabusa spacecraft of Japan Aerospace Exploration Agency (JAXA) became the first spacecraft to touch down on an asteroid (Itokawa) and collect samples from the surface for a safe return to Earth in 2010. Currently the Hayabusa 2 mission is being prepared for launch in 2014 to perform a sample return from the target body 1999 JU3. Unlike Itokawa's S-type composition, 1999 JU3 is a C-type asteroid which will help answer the existence of organic matters, which in turn relates to the existence of life on Earth.

As a current mission, DAWN spacecraft of National Aeronautics and Space Administration (NASA) is en route to a dwarf planet 1 Ceres for a rendezvous in February 2015 after it departed from the first target asteroid 4 Vesta in September 2012. Rosetta of European Space Agency (ESA) is expected to encounter the comet 67P/ChuryumovGerasimenko in 2014 with its lander Philae to study its surface. Also for ESA, M3-class mission proposal named MarcoPolo-R is under study among four other competitors, and it will also attempt to return a sample from a near-Earth asteroid (the target body is 2008 EV5 at the time of writing) in 2020's. Moreover, OSIRIS-REx is selected as the third New Frontiers Program in 2011 to make a sample return from Bennu (formerly known as 1999 RQ36) in 2023, and NASA apportioned $\sim$ \$US100 million for the initial study of a near-Earth asteroid capture plan to bring back an asteroid to the Earth-moon system. The above missions are only a fraction of the current/future planned missions, and more small body missions are expected to emerge in the future.

1.1.2 Notes on the Human Exploration

Manifested in the space policy speech of 2010 by the U.S. president, a manned mission to an Near-Earth asteroid (NEA) is regarded as one of the key stepping stones for achieving a manned mission to Mars in mid-2030s. While these primitive bodies possess very high scientific values and are attracting the interests of the science communities at increasing pace, some of their Earth-crossing characteristics promises to provide a new gateway for the future manned mission to deep space. In fact, NEAs prove to be the appropriate targets before Mars, because the manned missions to NEAs are expected to close the strategical knowledge gaps (SKGs) that need to be addressed prior to the first manned Mars mission.

The SKGs represent the gaps in required knowledge, data sets, and technology that are not fully developed with the status quo, and these gaps must be resolved before a human mission to Mars can commence. These SKGs are the primary drivers in pursuing a crewed mission to NEAs before one to Mars and beyond, and successful completion of the crewed NEA mission will serve as a gateway to further advance our technology and support future deep space missions. Significant benefits can be derived from a crewed NEA exploration that will facilitate the vital operational experience and development of the systems engineering/communications in deep space, which will also pave the way for future exploration of Phobos and Deimos, two moons of Mars.

Methods to deliver solutions to these SKGs vary widely from research and analysis (R&A), ground-based observations, space-based observations, and robotic precursor missions. Although this thesis does not specifically address the crewed mission to small bodies, it is not irrelevant from such a mission architecture. As a matter of fact, this thesis will be able to contribute to more robust mission design of robotic precursor missions. Specifically, the estimation technique of the physical characteristics of the target body such as its size, shape, and rotational dynamics is addressed in the thesis. These parameters can roughly be characterized by albedo and lightcurve measurements from ground-based/space-based observations, but it is necessary for a precursor spacecraft to perform accurate estimation of these parameters via orbit determination (OD). Careful consideration of

these parameters are important because the target bodies need to satisfy the criteria such as the minimum diameter to secure a sampling site that is accessible by the crew and the minimum rotation period to allow precise deep space navigation and assure crew's safety.

Regarding the crew's safety, accurate gravity field modeling plays a key role in surveying the surface property of the body. The surface property is one of the most puzzling unknowns when crew operate in close proximity to the surface of the target asteroid. For example, electrostatic dust environment, dust toxicity, small-sized (nano, micro-scale) particle interactions with spacesuit, propulsion-induced ejecta, and distribution of volatiles and regolith materials are still yet to be understood. Such parameters can be studied efficiently and effectively, for example, by deploying an explosive charge as envisioned for the BASiX mission proposal [51, 61].

Furthermore, accurate gravity field modeling is essential in maximizing the time that the crew can spend on scientific activities and in ensuring the safety of the crew members. That is, the crewed spacecraft can be immediately inserted in a stable home orbit upon rendezvousing with the target body to perform crew's duties, as the thorough gravity field characterization has been already performed by a precursor robotic spacecraft. It is crucial to perform this initial gravity field characterization prior to crew's arrival because it is often the case that the crew can spend only several days or a few weeks at most around these small bodies due to the ΔV and/or total travel time constraints.

1.1.3 Notes on the Potentially Hazardous Objects

A striking incident that exemplifies the risk of PHOs occurred on February 15, 2013, where an unmarked asteroid entered the Earth's atmosphere and flew over Chelyabinsk, Russia to inflict injuries to over hundreds of people. Interestingly enough, this event happened nearly simultaneously with the Earth flyby of 2012 DA14 (this asteroid was being tracked), which came only 16 hours after the superbolide's Earth entry. This event illustrated to the public that the hazardous outcome of a meteor strike is not just one's imagination, and some mitigation technique needs to be established to lower the risk of such an event occurring again.

One obvious countermeasure is to reinforce the surveillance network. With advanced ground-based and space-based asteroid survey systems, we are discovering more and more asteroids. NASA authorization act of 2005 states that the 90% of NEOs larger than 140 $[m]$ in diameter be catalogued within 15 years thereafter. The current number of cumulative NEAs reach over 10000, and roughly 850 of them are larger than 1 $[km]$. The NEA search/characterization programs such as Wide-field Infrared Survey Explorer (NEO/NEOWISE), Panoramic Survey Telescope and Rapid Response System (Pan-Starrs), Catalina Sky Survey (CSS), Lincoln Near-Earth Asteroid Research (LINEAR), and Goldstone/Arecibo/Very Large Array (VLA) radars all contribute to discovering/characterizing new asteroids. The aforementioned observation capabilities simultaneously allow us to diagnose the NEA orbits and the sources of NEA families to facilitate the selection process of the appropriate candidate targets that are scientifically rewarding for both a robotic mission and a crewed mission.

1.2 Gravitational Potential

Of all tasks performed upon spacecraft's arrival to the asteroid, the most important is the initial characterization of the gravity field. The gravity field of the target body is expressed in terms of its potential, and it is defined in a remarkably simple manner as follows:

$$U = G\int_V \frac{\rho(\vec{r}\,')dv}{|\vec{r}-\vec{r}\,'|} = G\int_M \frac{1}{\Delta}dm' \tag{1.1}$$

where U is the gravitational potential, G is the gravitational constant, $\vec{r}$ is the position vector of the field point, V is the total volume, v is its differential volume element, ρ is density of a mass element (m), M is the total mass, and $\vec{\Delta}$ is the relative position between the field point and the mass element (Figure 1.2). For convenience, we denote the quantities associated with the mass element with a prime.

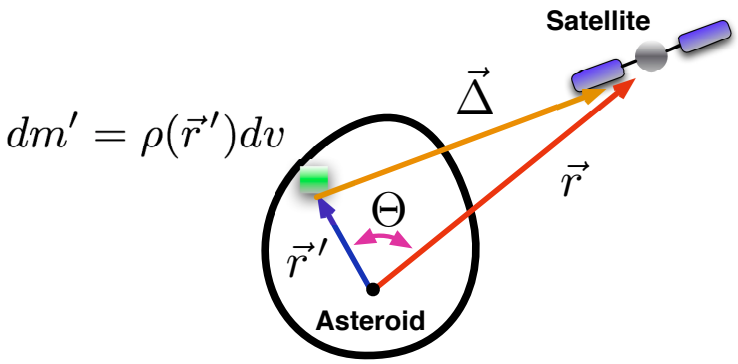

Figure 1.2: Potential definition.

In Figure 1.2, Θ is the angle between $\vec{r}$ and $\vec{r}\,'$. The properties of the trigonometric functions yield

$$\Delta^2 = r^2 + \left(r'\right)^2 - 2rr'\cos\Theta \tag{1.2}$$

$$\cos\Theta = \sin\phi\sin\phi' + \cos\phi\cos\phi'\cos(\lambda - \lambda') \tag{1.3}$$

where ϕ is the latitude and λ is the longitude. The potential expression in Equation 1.1 must satisfy either Laplace's or Poisson's equation. We will briefly summarize their derivations in the following.

1.2.1 Laplace's Equation

The potential expression in Equation 1.1 satisfies Laplace's equation outside the body. The details are summarized by, for example, MacRobert [36] (Chapter 8), and they are reviewed here.

From Equation 1.1, we have

$$\frac{\partial U}{\partial \vec{r}} = -G\int_M \frac{\vec{\Delta}}{\Delta^3}dm \tag{1.4}$$

which yields

$$\frac{\partial^2 U}{\partial \vec{r}^2} = -G \int_M \frac{1}{\Delta^3} \left[1_{[3\times 3]} - 3\frac{\vec{\Delta}\vec{\Delta}}{\Delta^2} \right] dm \tag{1.5}$$

where $1_{[3\times 3]}$ is the 3×3 identity matrix. Thus, Laplace's equation is given by computing the trace of the second-order partial of the potential.

$$\nabla^2 U = \frac{\partial^2 U}{\partial x^2} + \frac{\partial^2 U}{\partial y^2} + \frac{\partial^2 U}{\partial z^2} = tr\left(\frac{\partial^2 U}{\partial \vec{r}^2}\right) = 0 \tag{1.6}$$

Equation 1.6 is valid anywhere outside the body.

1.2.2 Poisson's Equation

Next, we derive Poisson's equation. Again, the detailed proof is given by MacRobert [36] (Chapter 2 and 8). We first start from the Gauss's theorem:

Theorem 1. ***(Gauss's Theorem)*** *Let $S_{\tilde{D}}$ be a closed surface surrounding a region $\tilde{D}$ containing attracting matter whose total mass is M; then if F_n is the normal component of the force ($\vec{F}$) at any point of $S_{\tilde{D}}$ due to the attraction of the mass within $S_{\tilde{D}}$ and also of any matter external to $S_{\tilde{D}}$.*

Then, we have

$$\iint F_n dS_{\tilde{D}} = -4\pi G M \tag{1.7}$$

where the integral is taken over the whole surface $S_{\tilde{D}}$, and F_n is regarded positive when the normal force acts away from $\tilde{D}$. F_n has the simple form

$$\begin{aligned} F_n &= \vec{F} \cdot \hat{n} = \frac{\partial U}{\partial \vec{r}} \cdot \hat{n} = \left(\frac{\partial U}{\partial x}\hat{i} + \frac{\partial U}{\partial y}\hat{j} + \frac{\partial U}{\partial z}\hat{k}\right) \cdot \left(\frac{\partial x}{\partial n_1}\hat{i} + \frac{\partial y}{\partial n_2}\hat{j} + \frac{\partial z}{\partial n_3}\hat{k}\right) \\ &= \sum_{i=1}^{3} \frac{\partial U}{\partial n_i} = \frac{\partial U}{\partial n} \end{aligned} \tag{1.8}$$

Then, Equation 1.7 becomes

$$\iint \frac{\partial U}{\partial n} dS_{\tilde{D}} \quad = \quad -4\pi M \quad = \quad -4\pi G \iiint \rho d\tilde{D} \tag{1.9}$$

In Equation 1.9, we rewrote the total mass in terms of the density distribution (ρ) over the volume $\tilde{D}$. In addition to Gauss's theorem, Green's theorem states that

Theorem 2. ***(Green's Theorem)*** *Let $\mathscr{Y}$ and U be two functions, which, with their first and second derivatives, are uniform and continuous at all points of a space $\tilde{D}$ bounded by a surface $S_{\tilde{D}}$: then, if $\hat{n}$ is the normal to the surface, measured outwards,*

$$\iint \mathscr{Y} \frac{\partial U}{\partial n} dS_{\tilde{D}} \quad = \quad \iiint \left(\frac{\partial \mathscr{Y}}{\partial x} \frac{\partial U}{\partial x} + \frac{\partial \mathscr{Y}}{\partial y} \frac{\partial U}{\partial y} + \frac{\partial \mathscr{Y}}{\partial z} \frac{\partial U}{\partial z} \right) + \iiint \mathscr{Y} \nabla^2 U d\tilde{D} \tag{1.10}$$

where ∇^2 is the Laplacian, and the surface and volume integrals are taken over $S_{\tilde{D}}$ and throughout $\tilde{D}$, respectively. Now, we let $\mathscr{Y} = 1$, change the order of the equation from right to left, substitute Equation 1.9, and get

$$\iiint \nabla^2 U d\tilde{D} \quad = \quad \iint \frac{\partial U}{\partial n} dS_{\tilde{D}} \quad = \quad -4\pi G \iiint \rho d\tilde{D} \quad = \quad \iiint -4\pi G \rho d\tilde{D} \tag{1.11}$$

For Equation 1.11 to hold at any location within $\tilde{D}$, we need

$$\nabla^2 U \quad = \quad -4\pi G \rho \tag{1.12}$$

which is Poisson's equation. Equation 1.12 is valid anywhere inside the body.

1.2.3 Gravity Field Models and Limitations

There are a great deal of mathematical models of the potential U that satisfy Laplace's equation. The most commonly used expression for the gravity field is the "exterior gravity field," or

spherical harmonic gravity field, which is derived from the orthogonal spherical harmonic coefficients paired with the associated Legendre functions of degree n and order m [30, 35].

$$U(r,\phi,\lambda) = \frac{GM}{r}\left[1+\sum_{n=1}^{\infty}\left(\frac{R^*}{r}\right)^n\sum_{m=0}^{n}P_{nm}(\sin\phi)\left[C_{nm}\cos(m\lambda)+S_{nm}\sin(m\lambda)\right]\right] \quad (1.13)$$

where R^* is the reference radius, P_{nm} is the associated Legendre function of degree n and order m, and C_{nm} and S_{nm} are the spherical harmonic coefficients defined as

$$\begin{cases} C_{nm} = \dfrac{(2-\delta_{0,m})}{M^*}\dfrac{(n-m)!}{(n+m)!}\displaystyle\int_M\left(\frac{r'}{R^*}\right)^n P_{nm}(\sin\phi')\cos(m\lambda')dm' \\ S_{nm} \overset{m\geq 0}{=} \dfrac{2}{M^*}\dfrac{(n-m)!}{(n+m)!}\displaystyle\int_M\left(\frac{r'}{R^*}\right)^n P_{nm}(\sin\phi')\sin(m\lambda')dm' \end{cases} \quad (1.14)$$

where M^* is the reference mass used to non-dimensionalize the spherical harmonic coefficients and δ is Kronecker delta function. Note that the spacecraft coordinates must be expressed in the body frame in Equation 1.13. This exterior gravity field satisfies Laplace's equation and is valid only outside the body. To be more accurate, as will be shown in Chapter 6, the exterior gravity field is only valid outside the Brillouin sphere of the asteroid (hence the name "exterior gravity field"). The Brillouin sphere can be equated with the circumscribing sphere of the asteroid, within which all mass elements of the asteroid reside [10]. Thus, the exterior gravity field cannot model the dynamical environment within the Brillouin sphere, which poses a problem when, for example, performing a TAG maneuver.

There are alternatives to the exterior gravity field, three most widely acquainted models of which are the ellipsoidal gravity field [17, 52], polyhedral gravity field [75], and mass concentration (mascon) model, all of which contain distinct problems inherent in their expressions. The ellipsoidal gravity field suffers a similar divergence problem as the exterior gravity field, and the gravity field within the Brillouin ellipsoid does not converge. The polyhedral gravity field converges anywhere around the body (even on the surface) and contains information of infinitely higher-degree and

higher-order expansion of the spherical harmonic gravity field. Although these are very attractive features for a gravity field expression, the polyhedral gravity field is computationally intensive (for mitigation measures, see Cangahuala [13]). Furthermore, the polyhedral gravity field assumes a ***known*** density distribution, and as will be discussed in Chapter 5, its estimation is convoluted. A useful application of the mascon model is to estimate the mass of a particular surface feature as discussed by Gottlieb [19], but the surface gravity field cannot be computed accurately by mascons for small body navigation purposes. In fact, estimation of each mass element renders a singularity as the number of particles is increased, as shown by Park et al. [49].

1.3 Dissertation Overview

This dissertation will address how the gravity field environment around small bodies can be characterized with better accuracy by overcoming the shortcomings of the aforementioned gravity field models. Chapter 2 and 3 are devoted to the initial characterization of the gravity field environment away from the surface, and Chapter 4 discusses the spin state of a near-Earth asteroid 4179 Toutatis as an application of the least-squares filter developed for the covariance analysis. Chapter 5 through 7 are devoted to the new techniques of accurate gravity field modeling near/on the surface of small bodies for the purpose of proximity operation. Comparisons between the exterior gravity field, reconstructed surface gravity field from the estimated density distribution, interior spherical harmonic gravity field, and interior spherical Bessel gravity field are made in order to evaluate how well each gravity field maps the surface gravity field around small bodies. The results show that the last three gravity field models exhibit unprecedented accuracy of the surface gravity field around small bodies compared to the most widely used exterior gravity field. We will give more specific descriptions of each chapter in the following:

Chapter 2 and 3 *Analytical and Numerical Approach to Orbit Determination*

In Chapter 2 and 3, we will address how the current techniques of initial orbit determination can be made more rapid and robust. Specifically, Chapter 2 will discuss the effective use

of ΔV to break the scale invariance associated with the optical-only measurements. This technique is referred to as the ΔV ranging. Then, an analytical estimation method of the gravitational parameter is proposed, which utilizes both the optical measurement and the ΔV ranging. Chapter 3 will perform numerical covariance analysis for a series of flybys. This covariance analysis is run for three asteroids (Itokawa, Didymos, and Eros) in order to evaluate the level of characterization that we can achieve with this type of mission design. The goal of Chapter 2 and 3 is to eliminate the initial survey orbit phase and replace it with multiple slow flybys. Such an approach to orbit determination is different from the past missions where the best possible model of the asteroid is estimated from the existing data [33, 38]. In addition, our goal is to evaluate the best possible performance of flybys by executing multiple maneuvers. Such an approach is also different from the past missions, for example, a flyby of 5535 Annefrank by Stardust where the spacecraft only had limited observation time. The resulting reduction in time necessary for the initial characterization of small bodies will allow mission operators to allocate more time for the main scientific analysis and will be useful for future small body missions.

Chapter 4 *Spin State and Moment of Inertia Characterization of 4179 Toutatis*

In Chapter 4, we will estimate the spin state of a near-Earth asteroid 4179 Toutatis by processing observations collected between 1992-2008. The observations are 3-1-3 Euler angles determined from the delay-Doppler images obtained at Arecibo and Goldstone. It is found that Toutatis' orientation during the 2012 apparition was predicted within the formal uncertainty of $\sim 30^\circ$ about each of Euler angles. The moment of inertia ratios (I_{xx}/I_{zz} and I_{yy}/I_{zz}) are estimated to fractional precision of 0.9% and 2.2%, which serve as the best constraint on the internal density distribution of any near-Earth asteroid not visited by a spacecraft. It is of particular importance to mention that the spin state estimation algorithm only processed the ground observations, and no space-based observations were processed. The same spin state estimation technique can be applied for any tumbling body

given sufficient data, and will prove particularly useful for analyzing the rotational dynamics of other tumbling near-Earth asteroids. All observations were provided by Michael Busch, and this work is a collaborative effort with the individual.

Chapter 5 *Internal Density Distribution Estimation*

Chapter 5 will detail the estimation technique for the internal density distribution. The goal is to provide a robust density estimation algorithm so that the polyhedral gravity field can be used to map out the surface gravity field. The density values are estimated via least-squares fit to the potential, where the exterior spherical harmonic coefficients and the shape model determined from OD are used as data. Such a formulation requires accurate knowledge of a density map prior to potential fitting in order to get accurate density distribution, but we will mitigate this constraint by dissecting the body into blocks of different sizes (i.e., block density algorithm). Then, the estimated density distribution is used to reconstruct the surface gravity field and its accuracy is evaluated. It is found that the accuracy of the reconstructed surface gravity field by far surpasses that of the exterior gravity field.

Chapter 6 *Interior Spherical Harmonic Gravity Field*

The interior spherical harmonic gravity field is derived, and its performance is evaluated for the purpose of regional mapping of the surface gravity field around small bodies. The interior spherical harmonic gravity filed is a solution type that appears after solving Laplace's equation by separation of variables. Although its existence has been known for many years, such a solution type has been ignored, and its useful application has not been proposed to date. Recent work by Werner [74] shed light on it and discovered its application to small body's surface gravity field mapping. We then fully developed the theory with his collaboration to enable the higher-order partial of the potential expression. Furthermore, the conversion between the exterior and interior spherical harmonic gravity fields and numerical approximation of the interior spherical harmonic coefficients for a homogeneous body

are discussed. The performance of the interior spherical harmonic gravity field is shown to be robust for asteroids with a highly non-spherical shape, such as Castalia.

Chapter 7 *Interior and Exterior Spherical Bessel Gravity Fields*

In Chapter 7, the interior and exterior spherical Bessel gravity fields are derived. These two spherical Bessel gravity fields exhibit strong contrasts with the exterior/interior spherical harmonic gravity fields that satisfy Laplace's equation. As a matter of fact, both the exterior and interior spherical Bessel gravity fields satisfy Poisson's equation and are obtained by solving Poisson's equation by separation of variables. The original work by Allen et al. [3] and Palmer [47] is focused on the dynamical propagation of celestial bodies, but we will apply the same gravity field model to achieve total mapping of the surface gravity field around small bodies. The computation of the interior spherical Bessel gravity field directly gives the surface gravity field around small bodies, and it is found that its accuracy is a few orders of magnitude better than the conventional exterior gravity field.

Finally, Chapter 8 presents the conclusions and future work for further development of accurate surface gravity models.

1.4 Contributions

We will list the contributions of this thesis to the field of astrodynamics in the following:

ΔV ranging: ΔV ranging is a technique to estimate the position and velocity of the spacecraft relative to the target body by breaking the singularity associated with the optical-only measurements. The singularity arises because the optical-only measurements do not contain the range information to the target boy. However, such a singularity can be resolved by executing and measuring a maneuver accurately by changing the scale of the geometry of the spacecraft trajectory before and after the maneuver, which results in rapid determination of the spacecraft state in the initial phase of the rendezvous with the target body.

Optimization of initial target body characterization via flybys: We analyze how the initial characterization of small bodies can be optimized by multiple slow flybys around the target body. The flyby characterization does not require stability analysis as the spacecraft is in a hyperbolic trajectory. Such a mission profile enables safe and rapid mission planning and characterization of the target body.

Estimation of an asteroid's moments of inertia based on ground-based measurements: We estimate the spin state of a near-Earth asteroid 4179 Toutatis solely from the ground-based radar measurements. The observations are 3-1-3 Euler angles extracted from the delay-Doppler images, and we fit these data in a least-squares sense by incorporating necessary dynamical models. Since 4179 Toutatis is in a tumbling rotation mode, the moments of inertia and the center-of-mass-center-of-figure offset can be estimated. It is the first time that the moments of inertia of a near-Earth asteroid was determined without any space-based measurements.

Precise estimation of a tumbling asteroid's rotation state and validated predictions: Aforementioned estimated spin state of 4179 Toutatis fit the 3-1-3 Euler angles within the 3σ bounds over a span of 16 years between 1992 and 2008. The dynamical model was then propagated forward in time, and the orientation of the body for the 2012 apparition was predicted within the formal uncertainty of $\sim 30^\circ$ around each of Euler angles.

Development of improved methods for internal density estimation: We develop a robust density distribution estimation technique for small bodies after the shape and the exterior spherical harmonic coefficients are estimated through the orbit determination process. Specifically, we propose the block density estimation algorithm where the shape is divided into a number of blocks, each homogeneous within itself, in order to remove the assumption about the known a priori density map. The estimated density distribution is then used to reconstruct the surface gravity field by using the polyhedral gravity field, which shows significant improvement from the exterior gravity field.

Development and application of the interior gravity field: The interior gravity field is derived and applied for robust evaluation of an asteroid's gravity field within the exterior Brillouin sphere. The interior gravity field converges around a point on the surface and proves particularly useful for the regional mapping of the surface gravity field. The interior gravity field realizes a safe and robust trajectory design for future sample return missions to small bodies.

Development of the interior/exterior spherical Bessel gravity fields: We rigorously derive and develop the interior/exterior spherical Bessel gravity fields for the purpose of surface gravity field mapping. The convergence region of the interior spherical Bessel gravity field resides within the exterior Brillouin sphere, and its computation directly gives the surface gravity field. While the interior gravity field only achieves regional mapping, the interior spherical Bessel gravity field achieves the total mapping of the surface gravity field. The performance of the interior spherical Bessel gravity field is evaluated for computation of an asteroid's gravity field within the exterior Brillouin sphere.

Chapter 2

Analytical Approach to Orbit Determination

Estimation of physical parameters of the target asteroid is often carried out by orbit determination (OD). Contrary to its literal connotation, orbit determination does not only determine the orbit of the spacecraft, but also the physical parameters of the target body that relate to the dynamics of the spacecraft through the dynamical/measurement equations. Similarly, other parameters that are not part of the body but affect the trajectory of the spacecraft, such as the solar radiation pressure, can be estimated as the observations that we obtain from the spacecraft are functions of their dynamics.

The OD technique is to say the least a form of art that enables us to navigate the spacecraft in deep space. Without it, it is impossible to know, for example, the size of the target body, or even, where the spacecraft is. Needless to say, it is not a long ruler that measures the position of the spacecraft relative to the Earth nor a large scale that measures the weight of the celestial bodies. We somehow know how to measure these parameters that are directly unobservable. For example, note this seemingly harmless equation below:

$$y \quad = \quad f(x) \quad = \quad ax^2 + bx + c \tag{2.1}$$

The essence is that we want to know y, but it cannot be directly measured. Fortunately, we know that x can be measured, and it is related to y via three coefficients a, b, and c. The construction of the functional form $f(x)$ in Equation 2.1 is called the forward modeling.

In the case of orbit determination, this procedure is reversed. That is, we measure y but we do not know x. For instance, we can measure the distance between the Earth and the spacecraft (y), and we want to extract the spacecraft position/velocity (x). This inverse problem is often harder than the forward modeling, and numerous techniques have been proposed to date. For spacecraft navigation purposes, we often use a batch or sequential filter that are both based on the least-squares formulation [29, 72]. While these filtering techniques usually resort to numerical computation, this chapter is devoted to some analytical aspects of the orbit determination technique.

2.1 Motivation for ΔV Ranging

When the spacecraft rendezvouses with the target body, it is crucial to determine the spacecraft state (i.e., position/velocity) precisely to ensure the safety of the spacecraft and perform appropriate orbit insertion maneuver. This maneuver is often aimed to insert the spacecraft in a high-altitude orbit (HAO) as was done for NEAR Shoemaker spacecraft [33, 38] and DAWN spacecraft [1, 31, 32, 48, 63]. Here, a new operational procedure named ΔV ranging is introduced, which can eliminate the need for spacecraft-target ranging data during the initial characterization phase. Specifically, ΔV ranging analyzes the effectiveness of performing a precise maneuver during a hyperbolic flyby in order to break the scale invariance associated with optical-only observations.

ΔV ranging also provides a new method to analytically estimate the precision of the estiamted gravitational parameter (μ) based on the geometry and time of flight around the asteroid. The conventional method derives the gravitational parameter by leveraging the property that the inbound and outbound hyperbolic velocities (V_∞) are equal in magnitude and separated by the hyperbolic turn angle (δ_H). This method renders the gravitational parameter as a function of the impact radius (b_∞), hyperbolic velocity, and change in hyperbolic velocity (ΔV_{flyby}). In contrast, our analytical estimate derives an expression of the gravitational parameter based on the measured time of flight. These two analytical expressions for the gravitational parameter are compared with the full least-squares covariance analysis in order to determine their accuracies.

2.1.1 Problem Settings of ΔV Ranging

In this section, we analyze the strength of optical measurements in the context of gravity field and spacecraft dynamics estimation. Optical measurement is classified into two types: centerfinding [9, 46] and landmark tracking [33]. Both types are angular measurements, and the range content is not available. We will model the centerfinding for its simplicity.

Assuming no errors in the model, the optical centerfinding provides a line-of-sight vector from the spacecraft to the center of mass of the target asteroid. Since a single optical measurement does not provide any information about the spacecraft's range relative to the asteroid, the geometry (i.e., scale) of the spacecraft trajectory cannot be determined uniquely. We call this singularity the scale invariance, and we will prove that the information matrix computed with the optical-only measurement is singular. In contrast, lidar measures the line-of-sight distance between the spacecraft and the asteroid, which breaks the scale invariance. However, the operational distance of lidar is limited to short range, and removing this measurement will drop the cost of overall mission. We show that it is possible to break the scale invariance by inserting a ΔV during a flyby even with optical-only observations, and we call this technique ΔV ranging.

This problem can be reduced to the idealized situation where we estimate two scalar quantities b_∞ (impact radius) and V_∞ (incoming hyperbolic velocity) for a massless asteroid during a flyby by taking optical measurements (θ). The impact radius can be considered as the radius of the closest approach as the spacecraft flies by the asteroid. This estimation problem contains a singularity, and it is not possible to analytically solve for b_∞ and V_∞ independently.

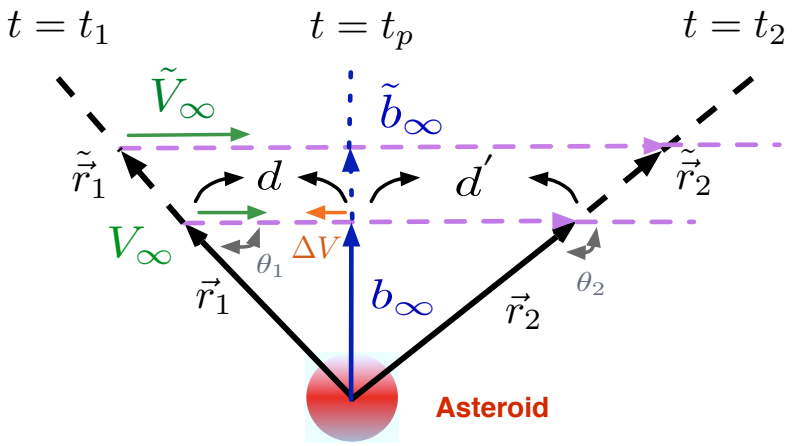

Figure 2.1: Scale invariance.

In Figure 2.1, θ measures the angle between the line-of-sight unit vector from the spacecraft to the asteroid's center of mass and $\vec{V}_\infty$, and there are three measurements at time $t = t_1$, t_p, and t_2. We define t_p as the time of periapsis passage with the p subscript, and $\theta_p = 90°$. For simplicity, we set $t_p = 0$ and specify that a ΔV occurs at the periapsis in the opposite direction to $\vec{V}_\infty$. The linear travel distance d has a simple expression $d = V_\infty(t_p - t_1)$. All quantities after the maneuver are denoted with a prime as

$$\begin{cases} V'_\infty &= V_\infty - \Delta V \\ d' &= (V_\infty - \Delta V)(t_2 - t_p) \end{cases} \tag{2.2}$$

and b'_∞ is identical to b_∞. The quantities with a tilde in Figure 2.1 are associated with the scale singularity and will be explained later.

2.1.2 Scale Invariance due to Optical-only Navigation

Before we proceed to solve for the analytical solution of b_∞ and V_∞, we discuss the singularity associated with the optical measurement by showing that the observation partials and information matrix are rank deficient. The mathematical formulation of least-squares estimation is deferred to Chapter 3 and is not discussed here. We relate the observation θ to impact radius b_∞ and linear travel distance d through geometry given in Figure 2.1.

$$\cos\theta = \begin{cases} \dfrac{d}{r} = \left[\left(\dfrac{b_\infty}{d}\right)^2 + 1\right]^{-1/2} & \text{for } t \le t_p \\ -\dfrac{d}{r} = -\left[\left(\dfrac{b_\infty}{d'}\right)^2 + 1\right]^{-1/2} & \text{for } t > t_p \end{cases} \tag{2.3}$$

$$\sin\theta = \frac{b_\infty}{r} = \begin{cases} \left[1 + \left(\dfrac{d}{b_\infty}\right)^2\right]^{-1/2} & \text{for } t \le t_p \\ \left[1 + \left(\dfrac{d'}{b_\infty}\right)^2\right]^{-1/2} & \text{for } t > t_p \end{cases} \tag{2.4}$$

where the cosine term changes its sign to take care of the quadrant issue as the spacecraft passes through the periapsis. The observation partials ($\tilde{H}$), also known as the sensitivity matrix, are defined as the partial derivative of the observables with respect to the state vector (i.e., $\tilde{H} = \partial Z/\partial X$). We define our state vector (X) as b_∞, V_∞, and ΔV and observables (Z) as θ and ΔV:

$$X = \begin{bmatrix} b_\infty & V_\infty & \Delta V \end{bmatrix}^T \tag{2.5}$$

$$Z = \begin{bmatrix} \theta & \Delta V \end{bmatrix}^T \tag{2.6}$$

where superscript T denotes the transpose. In order to measure the maneuver (ΔV), we assume that the spacecraft is equipped with an onboard accelerometer or the maneuver can be measured from Doppler tracking. Then, the observation partials are obtained as

$$\tilde{H}(t \le t_p) = \begin{bmatrix} \dfrac{d}{b_\infty^2 + d^2} & -\dfrac{b_\infty d}{V_\infty(b_\infty^2 + d^2)} & 0 \\ 0 & 0 & \delta(t - t_p) \end{bmatrix} \tag{2.7}$$

$$\tilde{H}(t > t_p) = \begin{bmatrix} -\dfrac{d'}{b_\infty^2 + d'^2} & \dfrac{b_\infty d'}{(V_\infty - \Delta V)(b_\infty^2 + d'^2)} & -\dfrac{b_\infty d'}{(V_\infty - \Delta V)(b_\infty^2 + d'^2)} \\ 0 & 0 & 0 \end{bmatrix} \tag{2.8}$$

In Equation 2.7, we introduced the Dirac delta function $\delta(t)$ which is equal to zero when $t \neq t_p$ and $\int_{-\infty}^{\infty} \delta(\tau) d\tau = 1$. In both Equation 2.7 and 2.8, V_∞ appears when we express the elapsed time as $(t_p - t_1) = d/V_\infty$ and $(t_2 - t_p) = d'/(V_\infty - \Delta V)$. From Equation 2.7, one can immediately realize that the observation partials are rank deficient without a maneuver, and even an infinite number of observations will not make the state vector observable. This result can be conceptually comprehended as follows: if we draw a line of infinite length that extends from the center of the asteroid to the spacecraft position at time t_1 and t_2, we can have infinitely many choices of b_∞ and V_∞ that satisfy the angular measurement θ_1 and θ_2 as shown in Figure 2.1 as $\tilde{V}_\infty$ and $\tilde{b}_\infty$.

Now we compare two cases to show how the ΔV measurement makes a full-rank system. We compute the information matrix $\Lambda = \sum \tilde{H}^T \tilde{H}$ with three measurements at $t = t_1$, t_p, and t_2 with and without maneuver. We artbitrary choose $b_\infty = 3$ $[km]$, $V_\infty = 10$ $[m/s]$, $t_1 = -500$ $[s]$, $t_p = 0$ $[s]$, $t_2 = 500$ $[s]$, and $\Delta V = 1$ $[m/s]$. Equations 2.9 and 2.10 show the information matrix without a maneuver (Λ) and with a maneuver ($\Lambda_{\Delta V}$):

$$\Lambda = \begin{bmatrix} 0.0432 & -12.9758 & 0 \\ -12.9758 & 3892.7336 & 0 \\ 0 & 0 & 0 \end{bmatrix} \tag{2.9}$$

$$\Lambda_{\Delta V} = \begin{bmatrix} 0.0453 & -14.3774 & 7.8895 \\ -14.3774 & 4576.2156 & -2629.8487 \\ 7.8895 & -2629.8487 & 2630.8487 \end{bmatrix} \tag{2.10}$$

It is shown that the information matrix is only rank one without a maneuver, whereas it becomes full rank with a maneuver, verifying the concept of ΔV ranging. Although we assumed a

massless asteroid in the problem, the quality of the assessment does not change for a flyby of an actual body with finite mass. That is, the spacecraft trajectory does not need to be linear, and bending of the spacecraft trajectory is allowed.

2.1.3 Ranging Accuracy

Having broken the scale invariance with a maneuver, we wish to analytically compute the uncertainties of the impact radius and hyperbolic velocity (i.e., σ_{b_∞} and σ_{V_∞}). In doing so, we need to analytically solve for b_∞ and V_∞ as follows:

$$b_\infty = \frac{|t_1|\tan\theta_1}{1+\frac{|t_1|\tan\theta_1}{|t_2|\tan\theta_2}}\Delta V \tag{2.11}$$

$$V_\infty = \frac{1}{1+\frac{|t_1|\tan\theta_1}{|t_2|\tan\theta_2}}\Delta V \tag{2.12}$$

Note that both Equation 2.11 and 2.12 are derived for a massless asteroid since they assume a linear trajectory of the spacecraft. Now we wish to compute $\sigma^2_{b_\infty} = E[\delta b^2_\infty]$ and $\sigma^2_{V_\infty} = E[\delta V^2_\infty]$, where E stands for the expected value. Since b_∞ and V_∞ are only functions of θ_1, θ_2, and ΔV, we compute the variation of b_∞ and V_∞ as

$$\delta b_\infty = \frac{\partial b_\infty}{\partial\theta_1}\delta\theta_1 + \frac{\partial b_\infty}{\partial\theta_2}\delta\theta_2 + \frac{\partial b_\infty}{\partial\Delta V}\delta\Delta V \tag{2.13}$$

$$\delta V_\infty = \frac{\partial V_\infty}{\partial\theta_1}\delta\theta_1 + \frac{\partial V_\infty}{\partial\theta_2}\delta\theta_2 + \frac{\partial V_\infty}{\partial\Delta V}\delta\Delta V \tag{2.14}$$

Then, assuming no correlation between θ_1, θ_2, and ΔV (i.e., each observation is independent of each other), the variance of b_∞ and V_∞ can be obtained as

$$\begin{aligned}\sigma_{b_\infty}^2 &= \left(\frac{\partial b_\infty}{\partial \theta_1}\right)^2 \sigma_{\theta_1}^2 + \left(\frac{\partial b_\infty}{\partial \theta_2}\right)^2 \sigma_{\theta_2}^2 + \left(\frac{\partial b_\infty}{\partial \Delta V}\right)^2 \sigma_{\Delta V}^2 \\ &= \left[|t_1|(1+\tan^2\theta_1)\frac{V_\infty^2}{\Delta V}\right]^2 \sigma_{\theta_1}^2 + \left(\frac{|t_1|^2}{|t_2|}\frac{V_\infty^2}{\Delta V}\frac{\tan^2\theta_1}{\sin^2\theta_2}\right)^2 \sigma_{\theta_2}^2 + \left(\frac{b_\infty}{\Delta V}\right)^2 \sigma_{\Delta V}^2\end{aligned} \tag{2.15}$$

$$\begin{aligned}\sigma_{V_\infty}^2 &= \left(\frac{\partial V_\infty}{\partial \theta_1}\right)^2 \sigma_{\theta_1}^2 + \left(\frac{\partial V_\infty}{\partial \theta_2}\right)^2 \sigma_{\theta_2}^2 + \left(\frac{\partial V_\infty}{\partial \Delta V}\right)^2 \sigma_{\Delta V}^2 \\ &= \left(\frac{|t_1|}{|t_2|}\frac{1+\tan^2\theta_1}{\tan\theta_2}\frac{V_\infty^2}{\Delta V}\right)^2 \sigma_{\theta_1}^2 + \left(\frac{|t_1|}{|t_2|}\frac{V_\infty^2}{\Delta V}\frac{\tan\theta_1}{\sin^2\theta_2}\right)^2 \sigma_{\theta_2}^2 + \left(\frac{V_\infty}{\Delta V}\right)^2 \sigma_{\Delta V}^2\end{aligned} \tag{2.16}$$

In Equation 2.15 and 2.16, notice that both σ_{b_∞} and σ_{V_∞} scale with ΔV. That is , $\sigma_{b_\infty}/b_\infty \propto 1/\Delta V$ and $\sigma_{V_\infty}/V_\infty \propto 1/\Delta V$. Thus, a larger ΔV yields smaller uncertainty of b_∞ and V_∞. Also, as $\sigma_{\Delta V}$ is an additive term in both equations, smaller uncertainty in ΔV also results in smaller uncertainty in b_∞ and V_∞. This result explicitly states the strength of the ΔV ranging where a large ΔV with small uncertainty allows the geometry to change more dramatically and make the estimation of the relative scale between the spacecraft and the asteroid more precise. Since the strength of the lidar measurement lies in reducing the relative position uncertainty of the spacecraft and the asteroid, we anticipate that the optical measurement becomes a good substitute for the lidar measurement as long as we can measure ΔV accurately. Table 2.1 is provided to show the rough idea of the performance of the ΔV ranging:

Table 2.1: Example parameters for ΔV ranging.

t_1 $[hr]$	t_2 $[hr]$	b_∞ $[km]$	V_∞ $[m/s]$	ΔV $[m/s]$	$\sigma_{\Delta V}$ $[mm/s]$	σ_{b_∞} $[m]$	σ_{V_∞} $[cm/s]$
2	2	3	10	1	1	5	2

In Table 2.1, both the impact radius and the hyperbolic incoming velocity are determined to fractional precision of $\sim 0.2\%$.

2.2 Analytical Gravitational Parameter Estimation

In this section, we investigate the manner in which tracking data provides an estimate of the gravitational parameter during a flyby. We will present two formulations, namely $\mu_\perp$ and $\mu_\parallel$.

2.2.1 Gravitational Parameter $\mu_\perp$

We first present the conventional analytical estimation method for the gravitational parameter, which we define as $\mu_\perp$. Suppose that we have Doppler tracking from Earth, which measures the line-of-sight velocity component of the spacecraft relative to the Earth. Then, when the angle between $\vec{V}_\infty$ and line-of-sight from the Earth to the spacecraft ($\hat{\rho}$) is perpendicular, the turn angle of the spacecraft is best determined from this data (hence the name $\mu_\perp$). The geometry of a hyperbolic flyby around an asteroid viewed from the Earth is given in Figure 2.2:

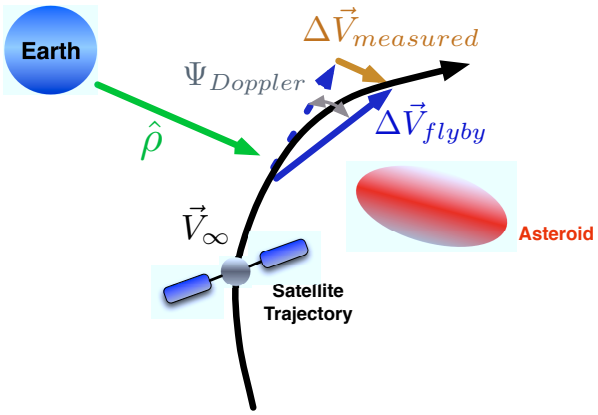

Figure 2.2: Spacecraft trajectory and Doppler measurements.

In Figure 2.2, the angle $\psi_{Doppler}$ is defined as the angle between $\Delta\vec{V}_{flyby}$ and the perpendicular component of $\Delta\vec{V}_{flyby}$ to $\hat{\rho}$, and $\Delta\vec{V}_{measured}$ is the cumulative velocity change measured by Doppler tracking. We add the subscript "flyby" to the change in velocity in order to differentiate it from the navigation maneuver discussed in the ΔV ranging. The computation of $\mu_\perp$ is purely based on the geometry of the hyperbolic flyby and a point mass approximation to the asteroid's gravity field. Other perturbations such as the solar radiation pressure and third body gravity field are absent.

The geometry we deal with is a hyperbola with an eccentricity $\gg 1$ assuming that the spacecraft has a high enough speed approaching the asteroid. Due to the conservation of energy, the inbound hyperbolic velocity (V_∞^-) and outbound hyperbolic velocity (V_∞^+) have the same speed relative to the asteroid. These assumptions yield the eccentricity and ΔV_{flyby} as follows:

$$e = \sqrt{1+\frac{2\epsilon h^2}{\mu^2}} = \left\{\sin\left(\frac{\delta_H}{2}\right)\right\}^{-1} \tag{2.17}$$

$$\Delta V_{flyby} = 2V_\infty \sin\left(\frac{\delta_H}{2}\right) = \frac{2V_\infty}{e} \tag{2.18}$$

where e is the eccentricity, δ_H is the hyperbolic turn angle, V_∞ is the magnitude of inbound/outbound hyperbolic velocity, ΔV_{flyby} is the change in the magnitude of the spacecraft velocity after the flyby, and ϵ is the specific energy which is equal to $V_\infty^2/2$ for a hyperbolic orbit. By substituting the expression for the specific angular momentum h and reorganizing Equation 2.17 and 2.18, the following expression for $\mu_\perp$ is obtained:

$$\mu_\perp = \frac{V_\infty^2 b_\infty \Delta V_{flyby}}{\sin\psi_{Doppler}\sqrt{4V_\infty^2 - \Delta V_{flyby}^2}} \tag{2.19}$$

As seen in Equation 2.19, $\mu_\perp$ is a function of only four parameters: b_∞, V_∞, ΔV_{flyby}, and $\psi_{Doppler}$. The factor of $(\sin\psi_{Dopper})^{-1}$ arises due to the fact that we do not directly measure ΔV_{flyby}. In fact, $\Delta V_{flyby} = \dfrac{\Delta V_{measured}}{\sin\psi_{Doppler}}$ as shown in Figure 2.2.

2.2.2 Uncertainty of $\mu_\perp$

We will analytically compute the uncertainty of the gravitational parameter given by Equation 2.19. By expressing the variation of $\mu_\perp$ as $\delta\mu_\perp = \dfrac{\partial\mu_\perp}{\partial b_\infty}\delta b_\infty + \dfrac{\partial\mu_\perp}{\partial V_\infty}\delta V_\infty + \dfrac{\partial\mu_\perp}{\partial\Delta V_{flyby}}\delta\Delta V_{flyby}$, its variance is computed as

$$\sigma_{\mu_\perp}^2 = \left(\frac{\partial \mu_\perp}{\partial b_\infty}\right)^2 \sigma_{b_\infty}^2 + \left(\frac{\partial \mu_\perp}{\partial V_\infty}\right)^2 \sigma_{V_\infty}^2 + \left(\frac{\partial \mu_\perp}{\partial \Delta V_{flyby}}\right)^2 \sigma_{\Delta V_{flyby}}^2 \tag{2.20}$$

$$= \frac{1}{\sin^2 \psi_{Dopper}} \left[\frac{V_\infty^4 \Delta V_{flyby}^2}{4V_\infty^2 - \Delta V_{flyby}^2} \sigma_{b_\infty}^2 + 4 \frac{b_\infty^2 \Delta V_{flyby}^2 V_\infty^2 (2V_\infty^2 - \Delta V_{flyby}^2)^2}{(4V_\infty^2 - \Delta V_{flyby}^2)^3} \sigma_{V_\infty}^2 \right.$$
$$\left. + 16 \frac{V_\infty^8 b_\infty^2}{(4V_\infty^2 - \Delta V_{flyby}^2)^3} \sigma_{\Delta V_{flyby}}^2 \right]$$

In order to simplify the expression given in Equation 2.20, we assume that $\sigma_{b_\infty}^2$ and $\sigma_{V_\infty}^2$ are small and $V_\infty \gg \Delta V_{flyby}$. These simplifications yield

$$\sigma_{\mu_\perp} = \frac{V_\infty b_\infty \sigma_{\Delta V_{flyby}}}{2 \sin \psi_{Doppler}} \tag{2.21}$$

where $\sigma_{\Delta V_{flyby}}$ corresponds to the uncertainty of ΔV_{flyby}. Equation 2.21 states that $\sigma_{\mu_\perp} \gg 1$ when $\sin \psi_{Doppler} \approx 0$. However, numerical analysis shows that this is not true and that good mass estimation is also possible even when the flyby is observed along the trajectory. Motivated by this result, we explore an alternate derivation for the mass estimate in the following sections.

2.2.3 Gravitational Parameter $\mu_\parallel$

In this section, an alternative expression for the gravitational parameter is derived. This alternative expression is robust when $\sin \psi_{Doppler} \approx 0$, and we define this quantity as $\mu_\parallel$. The computation of $\mu_\parallel$ is based on the time of flight difference between the hypothetical linear trajectory that the spacecraft would trace without the presence of the asteroid's gravity field and the "actual" spacecraft trajectory. The word "actual" is quoted as we still assume that the asteroid's gravity field is a point mass and other perturbations are ignored. Figure 2.3 shows three types of trajectories considered in the problem setting.

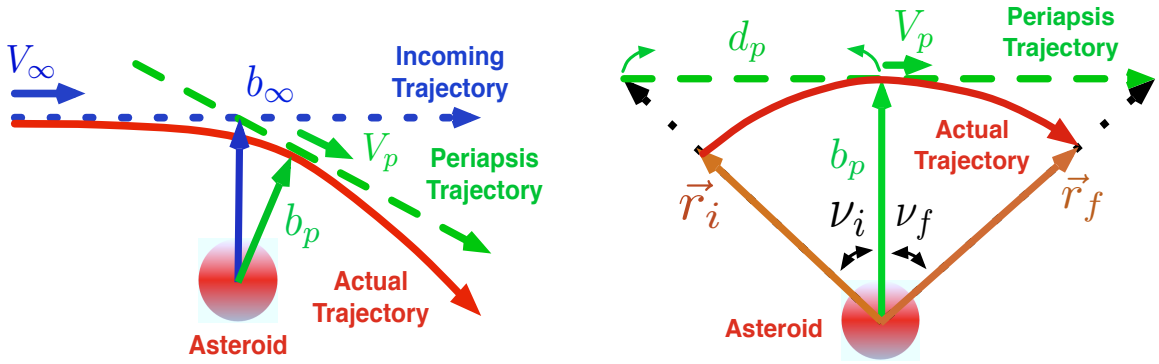

(a) Incoming, periapsis, and actual trajectories

(b) Periapsis and actual trajectories

Figure 2.3: Trajectories for $\mu_{\|}$ estimation.

The first is the incoming trajectory with the ∞ subscript, which is a hypothetical linear trajectory for a massless body with the constant approach speed of V_∞. The second is the periapsis trajectory with the p subscript, which is also a hypothetical linear, constant-speed flyby that is extrapolated with the periapsis radius of b_p and periapsis velocity of V_p. The third is the actual two-body trajectory. Then, assuming the two-body solution and comparing the times of flight of the periapsis and actual trajectories, we can find the expression for $\mu_{\|}$.

In the actual trajectory, the **i** and **f** subscript denote the initial and the final state of the spacecraft. The spacecraft approaches the asteroid at an incoming velocity of V_∞ directed toward the hyperbolic target point (i.e., $\vec{b}_\infty$). Without the asteroid, the spacecraft would traverse in a straight line that is referred to as the incoming trajectory in blue. However, the presence of the asteroid deflects the spacecraft into the actual trajectory in red. We assume that true anomalies ν_i and ν_f have the same magnitude but the opposite signs and can be measured with optical measurements.

Now that the flyby geometry is defined, the derivation of the gravitational parameter can commence. Equation 2.22 shows the relationship between the true anomaly and the hyperbolic anomaly (H):

$$\tanh\left(\frac{H}{2}\right) = \sqrt{\frac{e-1}{e+1}}\tan\left(\frac{\nu}{2}\right) \tag{2.22}$$

We let T_∞ denote the elapsed time for the spacecraft to move from ν_i to ν_f in the actual trajectory. Taking into account the symmetry of the spacecraft trajectory, T_∞ can be expressed as

$$T_\infty = 2\sqrt{\frac{-a^3}{\mu}}(e\sinh H_f - H_f) \tag{2.23}$$

where a is the semi-major axis. We substitute Equation 2.22 into Equation 2.23 and use the specific energy equation ($\epsilon = -\mu/2a = V_\infty^2/2$) to express T_∞ as a function of b_∞ and V_∞:

$$\begin{aligned} T_\infty = 2\frac{\mu}{V_\infty^3}\left\{\sqrt{1+\frac{b_\infty^2 V_\infty^4}{\mu^2}}\sinh\left[2\tanh^{-1}\left\{\sqrt{\frac{e-1}{e+1}}\tan\frac{\nu}{2}\right\}\right]\right. \\ \left. -2\tanh^{-1}\left\{\sqrt{\frac{e-1}{e+1}}\tan\frac{\nu}{2}\right\}\right\} \end{aligned} \tag{2.24}$$

Now, recall the geometry in Figure 2.3. The relationship between d_p, b_p, and ν is simply $\tan\nu = d_p/b_p$. A useful property of the trigonometric functions yields the half-angle tangent as

$$\tan\frac{\nu}{2} = \frac{\sin\nu}{1+\cos\nu} = \frac{\dfrac{d_p}{\sqrt{d_p^2+b_p^2}}}{1+\dfrac{b_p}{\sqrt{d_p^2+b_p^2}}} = \frac{d_p}{\sqrt{d_p^2+b_p^2}+b_p} \tag{2.25}$$

Also, note the following formula for $\tanh^{-1}$:

$$\tanh^{-1}\gamma = \frac{1}{2}\ln\frac{1+\gamma}{1-\gamma} \tag{2.26}$$

where γ is an arbitrary real number. Therefore, the argument of tanh in Equation 2.24 can be simplified, and we define a new parameter χ.

$$\begin{aligned}\chi &= 2\tanh^{-1}\left\{\sqrt{\frac{e-1}{e+1}}\tan\frac{\nu}{2}\right\} \\ &= \ln\left\{\frac{\sqrt{e+1}\left(\sqrt{d_p^2+b_p^2}+b_p\right)+\sqrt{e-1}d_p}{\sqrt{e+1}(\sqrt{d_p^2+b_p^2}+b_p)-\sqrt{e-1}d_p}\right\} \\ &= \ln\Upsilon\end{aligned} \tag{2.27}$$

Then, by definition, $\sinh\chi$ reduces to

$$\sinh\chi = \frac{1}{2}\left(exp(\chi)-exp(-\chi)\right) = \frac{1}{2}\left(\Upsilon-\Upsilon^{-1}\right) \tag{2.28}$$

which yields

$$\begin{aligned}T_\infty &= 2\frac{\mu}{V_\infty^3}\left\{\frac{1}{2}\sqrt{1+\frac{b_\infty^2V_\infty^4}{\mu^2}}\left(\Upsilon-\Upsilon^{-1}\right)-\ln\Upsilon\right\} \\ &\simeq 2\frac{\mu}{V_\infty^3}\left\{\frac{1}{2}\frac{b_\infty V_\infty^2}{\mu}\left(\Upsilon-\Upsilon^{-1}\right)-\ln\Upsilon\right\}\end{aligned} \tag{2.29}$$

where we assumed $e \gg 1$. Then, solving for μ, the following equation is obtained:

$$\mu_\parallel = \frac{1}{2}\frac{V_\infty^2 b_\infty}{\ln\Upsilon}\left\{\left(\Upsilon-\Upsilon^{-1}\right)-\frac{V_\infty T_\infty}{b_\infty}\right\} \tag{2.30}$$

This is the final expression for $\mu_\parallel$ derived from the time of flight difference between the actual spacecraft trajectory and the periapsis trajectory.

2.2.4 Uncertainty of $\mu_{\parallel}$

As with $\mu_{\perp}$, the uncertainty of $\mu_{\parallel}$ can be analytically derived. Equation 2.31 shows the variation of $\mu_{\parallel}$:

$$\delta\mu_{\parallel} = \frac{\partial\mu_{\parallel}}{\partial b_{\infty}}\delta b_{\infty} + \frac{\partial\mu_{\parallel}}{\partial V_{\infty}}\delta V_{\infty} + \cdots + \frac{\partial\mu_{\parallel}}{\partial T_{\infty}}\delta T_{\infty} \tag{2.31}$$

All uncertainties associated with the geometry and the initial condition of the flyby are assumed negligible, leveraging the results of ΔV ranging. Thus, we assume no variations in V_{∞}, b_{∞}, b_p, and d. Consequently, there is no uncertainty in Υ. Then, the only term that contributes to the uncertainty of $\mu_{\parallel}$ is $\sigma_{T_{\infty}}$, which yields the analytical covariance of $\mu_{\parallel}$ as

$$\sigma_{\mu_{\parallel}} = \frac{1}{2}\frac{V_{\infty}^3}{\ln\Upsilon}\sigma_{T_{\infty}} \tag{2.32}$$

In order to find $\sigma_{T_{\infty}}$ analytically, it is required to take the partial derivatives of Equation 2.29, from which $\sigma_{\mu_{\parallel}}$ was derived. Instead, the assumption is made that $\sigma_{T_p} = \sigma_{T_{\infty}}$, where T_p is the duration of the periapsis trajectory ($T_p = 2b_p \tan\nu / V_p$). This assumption bases the uncertainty of the time measurement solely on T_p.

$$\begin{aligned} \delta T_p &= \frac{\partial\delta T_p}{\partial b_p}\delta b_p + \frac{\partial\delta T_p}{\partial V_p}\delta V_p + \frac{\partial\delta T_p}{\partial\nu_f}\delta\nu_f \\ &= \frac{2\tan\nu_f}{V_p}\delta b_p - \frac{2b_p\tan\nu_f}{V_p^2}\delta V_p + \frac{2b_p}{V_p\cos^2\nu_f}\delta\nu_f \end{aligned} \tag{2.33}$$

In order to be consistent with the discussions made earlier (i.e., ΔV ranging), we set $\sigma_{b_p} = \sigma_{V_p} = 0$, which yields the following expression for σ_{T_p}:

$$\sigma_{T_p} = \frac{2b_p}{V_p\cos^2\nu_f}\sigma_{\nu_f} \tag{2.34}$$

Then, assuming $\sigma_{\nu_f} = 10^{-4}$ $[rad.]$ based on an optical measurement uncertainty of $25 \sim 100 \times 10^{-6}$ $[rad.]$, σ_{T_p} can be evaluated. The order of magnitude of σ_{T_p} for an asteroid flyby is a few seconds. This equation is validated later in Section 2.3.2.

2.3 Performance of ΔV Ranging and Analytical Gravitational Parameter Estimation

We present the results of ΔV ranging and analytical estimates of the gravitational parameter given by $\mu_\perp$ and $\mu_\parallel$.

2.3.1 b_∞ and V_∞ Estimation via ΔV Ranging

We wish to compare the analytical expressions of σ_{b_∞} and σ_{V_∞} with our full numerical covariance analysis. For the full covariance analysis, the state vector is a 10×1 vector of spacecraft position, velocity, gravitational parameter, and a maneuver. The asteroid model we use is 25143 Itokawa, the gravitational parameter of which is 2.36×10^{-9} $[km^3/s^2]$ [59]. In the simulation, $b_\infty = 3$ $[km]$ and $V_\infty = 10$ $[m/s]$ while ΔV is varied between 0.1 and 1.0 $[m/s]$. The high values of b_∞ and V_∞ are chosen so that the spacecraft dynamics approximate a linear trajectory. The measurements are taken at 60 $[s]$ intervals, and ΔV occurs at the closest approach to the asteroid. The total time of the flyby is 2 $[hr]$ (i.e., t_1 and t_2 are 1 $[hr]$ before and after the closest approach). For all analytical work, $\sigma_\theta = 25 \times 10^{-6}$ $[rad.]$ and $\sigma_{\Delta V} = 1$ $[mm/s]$ are assumed. Figure 2.4 shows the numerical results in the blue line, analytical results in the red line, and the fractional uncertainty of ΔV in the green line.

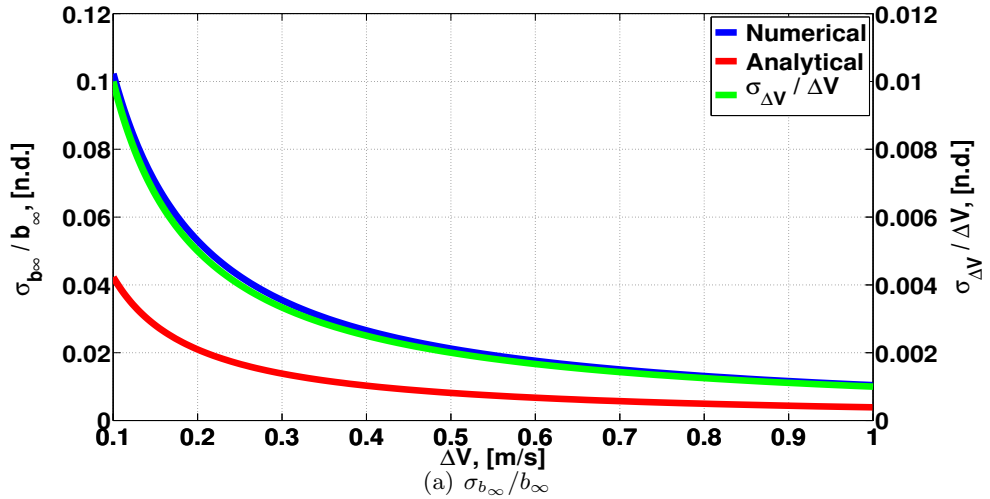

(a) $\sigma_{b_\infty}/b_\infty$

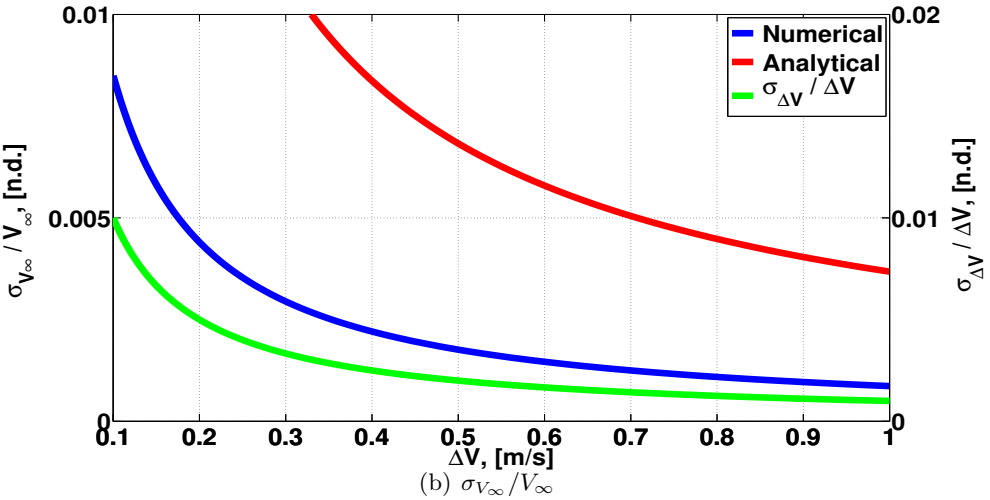

(b) $\sigma_{V_\infty}/V_\infty$

Figure 2.4: $\sigma_{b_\infty}/b_\infty$ and $\sigma_{V_\infty}/V_\infty$ as a function of ΔV. The numerical covariance (blue line) and analytical covariance (red line) are compared. In order to show the scalability of σ_{b_∞} and σ_{V_∞} as suggested in Section 2.1.3, $\sigma_{\Delta V}/\Delta V$ is also plotted in green line.

In Figure 2.4, it is shown that the ΔV ranging dramatically improved σ_{b_∞} and σ_{V_∞}, and their values are proportional to the magnitude of ΔV. Notice that both $\sigma_{b_\infty}/b_\infty$ and $\sigma_{V_\infty}/V_\infty$ decreased by more than an order of magnitude between the smallest and the largest ΔV, and the numerical and analytical results tend toward each other. This result suggests that our analytical expressions serve as a good first-cut approximation of the uncertainties associated with the flyby geometry.

2.3.2 $\sigma_{\mu_\perp}$ and $\sigma_{\mu_\parallel}$

In this section, we present the results of $\sigma_{\mu_\perp}$ and $\sigma_{\mu_\parallel}$. Three cases are investigated:

- Case 1 varies μ. The gravitational parameter is based on the uniform density of 2.0 $[g/cm^3]$ for a spherical body. The radius of the asteroid (R) is changed to compute the gravitational parameter. For all simulation, $b_\infty = 2R$ and $V_\infty = \sqrt{2}V_{escape}$, where V_{escape} is computed at the impact radius of $2R$. This value of V_∞ ensures a hyperbolic flyby.

- Case 2 varies V_∞. For all simulation, $b_\infty = 4\mu/V_\infty^2$ in order to ensure that a hyperbolic flyby is attained. The gravitational parameter is that of Itokawa's.

- Case 3 varies b_∞. For all simulation, $V_\infty = \sqrt{2}V_{escape}$. The gravitational parameter is that of Itokawa's.

For the numerical analysis, the observations are Doppler tracking, lidar, optical, and Earth ranging measured with the same frequency as in Table 3.4. Figure 2.5 shows the gravitational uncertainty in one standard deviation for all three cases on the next page.

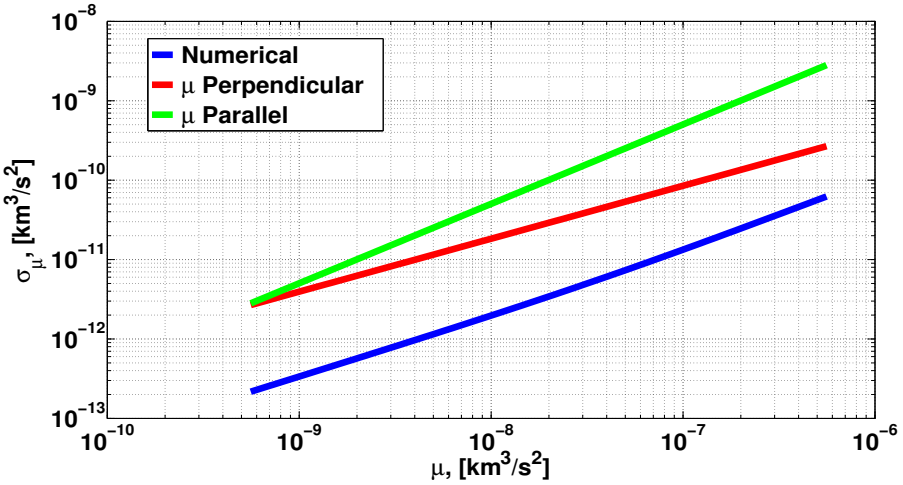

(a) Case 1: μ is varied

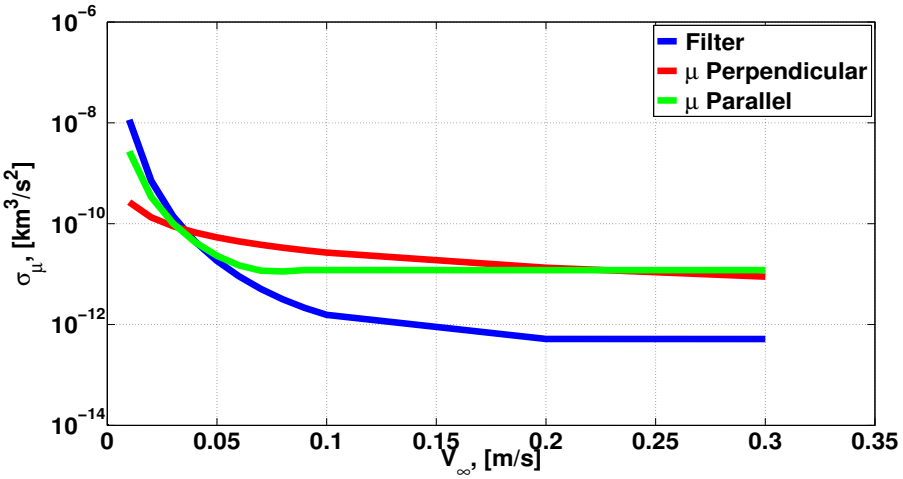

(b) Case 2: V_∞ is varied

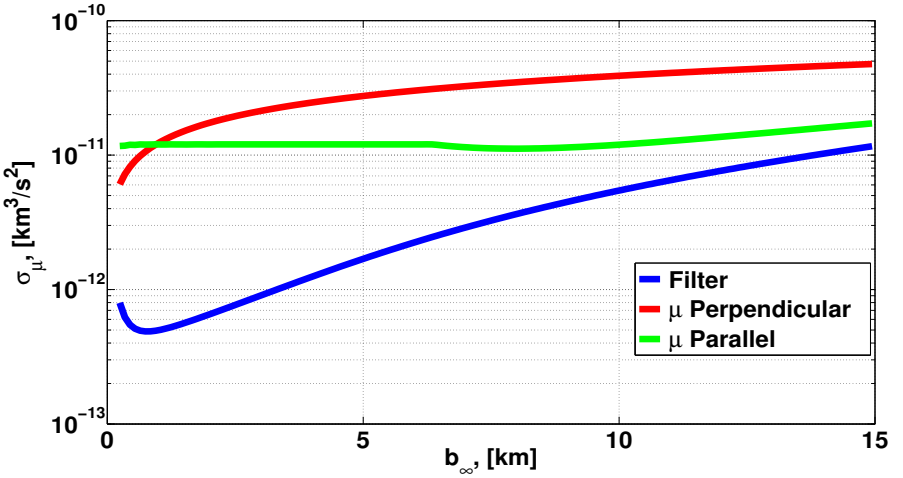

(c) Case 3: b_∞ is varied

Figure 2.5: σ_μ in one standard deviation for case 1, 2, and 3. The numerical covariance (blue line), $\sigma_{\mu_\perp}$ (red line), and $\sigma_{\mu_\parallel}$ (green line) are plotted for various asteroid sizes (case 1), for various V_∞ (case 2), and various b_∞ (case 3) with other values fixed.

In Figure 2.5, we see that the batch filter covariance yields the minimum μ uncertainty for most cases. For case 1, a larger μ value seems to invalidate assumptions for $\mu_{\parallel}$, but not for $\mu_{\perp}$. This result indicates that as the gravity field of the asteroid forces the spacecraft out of the linear trajectory, the comparison of the nominal trajectory and the deflected trajectory is no longer valid. For case 2 and 3, $\mu_{\parallel}$ and μ_{filter} follow each other closely, indicating that $\mu_{\parallel}$ may provide better accuracy for μ estimation as long as the linear trajectory approximation is valid.

2.4 Conclusions

This chapter investigated the use of ΔV in order to break the singularity associated with the optical-only measurements. This ΔV ranging yields analytical expressions for b_∞ and V_∞, and their uncertainties can also be analytically obtained. The resulting expressions for σ_{b_∞} and σ_{V_∞} shows that these quantities scale proportionally with the magnitude of ΔV, which is the expected outcome because a larger ΔV results in a more dramatic change in the flyby geometry. The accuracies of the analytical expressions for σ_{b_∞} and σ_{V_∞} are compared with the full covariance analysis to show that the order of magnitude of σ_{b_∞} and σ_{V_∞} from the filter match those from the analytical expressions, proving that the analytical orbit determination technique can be used as the first order approximation for the b_∞ and V_∞ uncertainties.

In concert with the studies of ΔV ranging, we investigated two ways to express σ_μ analytically. One is derived from the geometric argument (i.e., $\sigma_{\mu_\perp}$) while the other is from the travel time of the flyby trajectory (i.e., $\sigma_{\mu_\parallel}$). The only assumption made during the derivation of $\sigma_{\mu_\parallel}$ is that the flyby is highly eccentric, which is usually the case for this type of trajectory. These analytical expressions are again compared with the numerical covariance analysis and provide roughly the same magnitude of σ_μ as the filter's. Thus, these analytical expressions for σ_μ can also be used as the first order approximation for the uncertainty of the gravitational parameter that can be used as a priori uncertainty for the full numeral simulation.

Chapter 3

Numerical Approach to Orbit Determination

The previous chapter investigated the analytical approach to orbit determination. Specifically, ΔV ranging was introduced to break the scale invariance associated with the optical-only measurements, allowing us to determine the spacecraft position/velocity relative to the target body. An accurate estimation of the spacecraft state is only a fraction of what orbit determination can achieve, and other parameters, such as the asteroid's gravity field and rotational dynamics, can also be estimated numerically by processing the observations collected by the spacecraft. This estimation is often performed via a filter by minimizing a predefined cost function. Aside from the estimates of the parameters, it is also important to quantify their uncertainties, and this uncertainty quantification is called the covariance analysis. This chapter is dedicated to the numerical covariance analysis around small bodies.

In general, at an early stage of a small body rendezvous mission, it is important to accurately estimate the gravity field prior to entering an orbit or main mission phase. The gravity field is the major source of perturbation to the spacecraft dynamics, and failure to perform this task with desired precision in a timely manner results in a delay and shortening of the time frame dedicated for the planned scientific studies. This characterization proves particularly difficult for a highly non-spherical shape of a body represented by majority of NEOs. The irregular gravity field created by these irregularly-shaped bodies often become a hindrance to designing a safe/accurate sample return trajectory of a spacecraft onto the surface of an asteroid. The situation can potentially exacerbate to even cause the spacecraft to impact the surface of the body if the gravity field is not

characterized with sufficient accuracy. This chapter focuses on how this initial estimation process can be made robust and as rapid as possible, while not sacrificing precision in the estimated models. The goal is to determine whether an orbiting phase can be eliminated altogether and substituted with a series of flybys. Such an implementation would enable the development of a simpler mission plan that could be executed in a shorter time, thus maintaining scientific return while decreasing the costs of mission operations significantly.

The analysis discussed in this chapter represents a different focus than previous studies that described the application of traditional orbit determination techniques for the gravity field estimation of Eros during the NEAR mission [33, 38] and that of Itokawa during the Hayabusa mission [59]. Those studies were focused on processing all existing data to develop the best possible model. The current focus is to determine how rapidly an initial estimate of the gravity environment of a small body can be determined. In general, such a model is needed prior to embarking on the main mission phase, and thus the development of a systematic and rapid technique for performing the initial evaluation will be an important development for future missions. We perform the covariance analysis for three different small bodies: Itokawa, Didymos, and Eros in the order of increasing size. These asteroids represent over two orders of magnitude in size, and it is important to see whether consistent results can be found across all of these bodies.

3.1 Least-squares Filter

The gravity field of the body is a global parameter. The global parameters are time-independent and do not change over time. Thus, the same set of estimated parameters can be used for any data arc. Other types of parameters are called local parameters that exhibit time-dependent nature (e.g., spacecraft position and velocity). It is necessary to estimate them separately for different data arcs. In our analysis, the estimated parameters are the mixture of both. Specifically, the state vector consists of the spacecraft and asteroid dynamics ($\vec{R}$ and $\vec{V}$), the gravitational parameter (μ), the solar radiation pressure scaling factor (η_{SRP}), spin state (to be defined later), the higher-degree and higher-order spherical harmonic coefficients (C and S), impulsive maneuvers

(ΔV), and the times of the maneuvers (τ). We model the rotational dynamics of the asteroid as either a principal-axis rotator or a precessing rotator (Section 3.5).

This section briefly reviews the filter equations for the least-squares batch filter with a square-root information algorithm. Most of the equations in this section are well documented by Tapley et al. [72], and only the key steps are highlighted.

3.1.1 Dynamical Equations

For a state vector $\vec{X}$ that is an array of estimated parameters, we have the dynamical equation $\dot{\vec{X}}$ and observations $\vec{Y}$:

$$\dot{\vec{X}} = F(\vec{X}, t) \tag{3.1}$$

$$\vec{Y}_k = Z(\vec{X}_k, t_k) + \vec{\epsilon}_k \tag{3.2}$$

where F is the dynamical equation that computes the time derivative of the state vector, Z is the observation model, $\vec{\epsilon}$ is the observation error, and k is the time index. Assuming that the dynamics of the reference state stays sufficiently close to the true state over the period of data arc, Equation 3.1 and 3.2 can be expanded in a first-order Taylor series to yield

$$\dot{\vec{x}}(t) = A(t)\vec{x}(t) \tag{3.3}$$

$$\vec{y}_k = \tilde{H}_k\vec{x}_k + \vec{\epsilon}_k \tag{3.4}$$

This process is often called the "linearization" of the dynamical and observable equations. In Equation 3.3 and 3.4, lowercase letters are used to denote the deviations of the full state, A is the dynamics matrix, and $\tilde{H}$ is the observation partial given as

$$A(t) = \left.\frac{\partial F(t)}{\partial \vec{X}(t)}\right|_{\vec{X}=\vec{X}^*(t)} \tag{3.5}$$

$$\tilde{H}_k = \left.\frac{\partial Z}{\partial \vec{X}}\right|_{\vec{X}=\vec{X}^*(t_k)} \tag{3.6}$$

where $\vec{X}^*$ is the reference state. Thus, both the dynamics matrix and the observation partial are computed on the reference trajectory, and the state deviation follows the dynamics dictated by Equation 3.5. The assumption that the reference state is **close** to the true state is often supported due to the dense data that we typically obtain for deep space navigation purposes. Now, we realize that the linearized observation equation (Equation 3.4) only relates the state deviation at time t_k to the observation deviation at the same time. If we were to estimate all state deviations at different times, the number of observations is generally much smaller than the number of estimated parameters, yielding an underdetermined system. In order to avoid this rank-deficiency, the state deviation at $t = t_k$ is mapped back to epoch ($t = t_0$) so the observation made at time $t = t_k$ can be related to the state deviation at $t = t_0$. Such reformulation can be achieved by introducing the state transition matrix (STM), which is expressed as

$$\Phi(t_2, t_1) = \frac{\partial \vec{X}(t_2)}{\partial \vec{X}(t_1)} \tag{3.7}$$

That is, the STM is the partial of the state at time t_2 with respect to the state at time t_1. Or rather, it can be rephrased as the sensitivity of the state at $t = t_1$ to the state at $t = t_2$. Then, this STM can be used to map the state deviation from time t_1 to time t_2 as follows:

$$\vec{x}(t_2) = \Phi(t_2, t_1)\vec{x}(t_1) \tag{3.8}$$

This property of STM is of great importance, as it allows one to relate the observation deviation at time $t = t_k$ to the state deviation at epoch (Equation 3.9).

$$\vec{y}_k = \tilde{H}_k\vec{x}_k + \vec{\epsilon}_k = \tilde{H}_k\Phi(t_k, t_0)\vec{x}_0 + \vec{\epsilon}_k = H_k\vec{x}_0 + \vec{\epsilon}_k \tag{3.9}$$

where $H_k = \tilde{H}_k\Phi(t_k, t_0)$. The significance of Equation 3.9 is subtle but noteworthy. Equation 3.9 states that the state deviation at $t = t_k$ can be mapped back to epoch with use of STM. In so many words, the state deviation at epoch has sensitivity to the observation made at $t = t_k$. Thus, the information content present in the observations at future times can be mapped back and accumulated with respect to epoch, allowing one to solve for the epoch time state deviation.

For a system of non-linear dynamical equation, STM cannot be computed analytically and has to be numerically propagated together with the reference state. The time derivative of the STM is given as

$$\dot{\Phi}(t, t_0) = A(t)\Phi(t, t_0) \tag{3.10}$$

where $\Phi(t_0, t_0)$ is the identity matrix by definition. The computation of the STM is described in detail in Section 3.8.

3.1.2 Cost Function

The goal of a least-squares filter is to minimize the cost function J_{LSF} defined as

$$J_{LSF} = \frac{1}{2}(\vec{y} - H\vec{x}_0)^T W(\vec{y} - H\vec{x}_0) + \frac{1}{2}(\bar{\vec{x}}_0 - \vec{x}_0)^T \bar{P}_0^{-1}(\bar{\vec{x}}_0 - \vec{x}_0) \tag{3.11}$$

where W is the observation weighting matrix, P is the covariance matrix, and barred quantities are a priori values. Specifically, $\bar{P}_0$ is the a priori covariance matrix of the estimated parameters at $t = t_0$. Then, this cost function is differentiated with respect to $\vec{x}_0$ and set to zero to yield the normal equation as

$$\hat{x}_0 = \left(\sum \mathbf{H^T W H} + \bar{P}_0^{-1}\right)^{-1}\left(\sum \mathbf{H^T W y} + \bar{P}_0^{-1}\bar{\vec{x}}_0\right) \tag{3.12}$$

where $\hat{x}_0$ denotes the correction to the full state and bold quantities belong to the summation notation. The quantities in the first parenthesis is called the information matrix (Λ), and the quantities in the second parenthesis is called the normal matrix. The covariance matrix that define the uncertainty of the estimated parameters can be obtained by taking the inverse of the information matrix, as shown in Equation 3.12. Note that, the observations only contribute to the normal matrix, and the computation of the covariance matrix does not require any observation. That is, the covariance depends only on the dynamics of the spacecraft and the observable models. This illustrates the powerfulness of the covariance analysis, where we can characterize the uncertainties of the estimated parameters prior to obtaining the actual observations.

3.2 Square-root Information Filter

As mentioned earlier, we implement a batch filter with a square-root information algorithm. This formulation is commonly called a square-root information filter (SRIF), and it is recommended for its numerical stability. The SRIF algorithm is derived for a sequential filter by Tapley et al. [72], but we will reformulate this algorithm for a batch filter. A majority of theories discussed here are inherited from their work and are summarized as necessary.

3.2.1 Information Matrix and the Condition Number

When processing the observations in a least-squares filter, their information content is accumulated in the information matrix (Λ). This information matrix is the inverse of the covariance matrix (P), which is the direct measure of the uncertainties of the estimated parameters.

$$\Lambda = P^{-1} \tag{3.13}$$

In short, Equation 3.13 states that as more information is accumulated, the information matrix grows larger, yielding smaller uncertainty on the estimated parameters. We then define the matrix $\mathscr{G}$ as the upper triangular square root matrix of the information matrix as

$$\Lambda = \mathscr{G}^T\mathscr{G} \tag{3.14}$$

By defining $\mathscr{M}$ as the inverse of $\mathscr{G}$ (i.e., $\mathscr{M} = \mathscr{G}^{-1}$), we can express the information matrix and the covariance matrix as

$$\Lambda = P^{-1} = \mathscr{G}^T\mathscr{G} = (\mathscr{M}^{-1})^T\mathscr{M}^{-1} \tag{3.15}$$

$$P = \Lambda^{-1} = \mathscr{M}\mathscr{M}^T = \mathscr{G}^{-1}(\mathscr{G}^{-1})^T \tag{3.16}$$

When mapping the covariance from t_1 to t_2, we can simply map either $\mathscr{M}$ or $\mathscr{G}$ by the STM (Φ) to get

$$\mathscr{M}(t_2) = \Phi(t_2, t_1)\mathscr{M}(t_1) \tag{3.17}$$

$$\mathscr{G}(t_2) = \mathscr{G}(t_1)\Phi(t_1, t_2) \tag{3.18}$$

where $\Phi(t_1, t_2) = \Phi^{-1}(t_2, t_1)$. The reason that the SRIF is preferred over the regular batch filter is because the SRIF is more numerically stable. Let us define the condition number, $C(P)$ as the ratio of the maximum eigenvalue to the minimum eigenvalue of the covariance matrix P as follows:

$$C(P) = \frac{max(\lambda_P)}{min(\lambda_P)} \tag{3.19}$$

where λ_P is the vector of the eigenvalues of the covariance matrix P. In base 10 arithmetic with p significant digits, numerical difficulties with matrix inversion may be encountered as $C(P)$ $\rightarrow 10^p$. It can be shown that the condition number for $\mathscr{G}$ is the square root of $C(P)$. That is,

$$C(\mathscr{G}) = \sqrt{C(P)} \tag{3.20}$$

Thus, the numerical difficulty is less likely to be encountered if $\mathscr{G}$ and $\mathscr{M}$ are used to compute/propagate the covariance matrix.

3.2.2 SRIF Formulation

Now we introduce how we process observations in SRIF, as documented by Tapley et al [72]. Recall that the a priori estimate of the state deviation (x) is given as

$$\bar{x} = x + \eta \tag{3.21}$$

We multiply Equation 3.21 by a priori value of $\mathscr{G}$ ($\tilde{\bar{\mathscr{G}}}$) from the left-hand side to get

$$\tilde{\bar{\mathscr{G}}}\bar{x} = \tilde{\bar{\mathscr{G}}}x + \tilde{\bar{\mathscr{G}}}\eta \tag{3.22}$$

Also, we multiply the observable-state deviation equation by the square root of the weighting matrix (W) to get

$$W^{1/2}y = W^{1/2}\tilde{H}x + W^{1/2}\epsilon \tag{3.23}$$

Then, by defining $\bar{b} = \tilde{\bar{\mathscr{G}}}\bar{x}$, $\bar{\eta} = \tilde{\bar{\mathscr{G}}}\eta$, $y_w = W^{1/2}y$, $\tilde{H}_w = W^{1/2}\tilde{H}$, and $\epsilon_w = W^{1/2}\epsilon$, we get

$$\begin{aligned} \bar{b} &= \tilde{\bar{\mathscr{G}}}x + \bar{\eta} \\ y_w &= \tilde{H}_w x + \epsilon_w \end{aligned} \tag{3.24}$$

Recalling that η is the error in the a priori estimate and ϵ is the observation error residual, we define the performance index as

$$\begin{aligned} J_{LSF} &= \|\bar{\eta}\|^2 + \|\epsilon_w\|^2 \\ &= \left\|\tilde{\bar{\mathscr{G}}}x - \bar{b}\right\|^2 + \left\|\tilde{H}_w x - y_w\right\|^2 \\ &= \left\| \begin{bmatrix} \tilde{\bar{\mathscr{G}}} \\ \tilde{H}_w \end{bmatrix} x - \begin{bmatrix} \bar{b} \\ y_w \end{bmatrix} \right\|^2 \\ &= \left\{ \begin{bmatrix} \tilde{\bar{\mathscr{G}}} \\ \tilde{H}_w \end{bmatrix} x - \begin{bmatrix} \bar{b} \\ y_w \end{bmatrix} \right\}^T Q^T Q \left\{ \begin{bmatrix} \tilde{\bar{\mathscr{G}}} \\ \tilde{H}_w \end{bmatrix} x - \begin{bmatrix} \bar{b} \\ y_w \end{bmatrix} \right\} \end{aligned} \tag{3.25}$$

where Q is an orthogonal matrix with the following properties:

$$QQ^T = 1 \tag{3.26}$$

$$Q^{-1} = Q^T \tag{3.27}$$

$$\|Qx\| = \|x\| \tag{3.28}$$

Thus, the norm of the performance index, J_{LSF}, is left unchanged. We further constrain the matrix Q such that the following orthogonal transformations are satisfied.

$$Q \begin{bmatrix} \tilde{\bar{\mathscr{G}}} \\ \tilde{H}_w \end{bmatrix} = \begin{bmatrix} \mathscr{G} \\ 0 \end{bmatrix} \tag{3.29}$$

$$Q \begin{bmatrix} \bar{b} \\ y_w \end{bmatrix} = \begin{bmatrix} b \\ e \end{bmatrix} \tag{3.30}$$

By substituting Equation 3.29 and 3.30, Equation 3.25 can be rewritten as

$$J_{LSF} = \left\| \begin{bmatrix} \mathscr{G} \\ 0 \end{bmatrix} x - \begin{bmatrix} b \\ e \end{bmatrix} \right\|^2 = \|\mathscr{G}x - b\|^2 + \|e\|^2 \tag{3.31}$$

which yields the best estimate of x as

$$\hat{x} = \mathscr{G}^{-1} b \tag{3.32}$$

It is evident from Equation 3.32 that $\mathscr{G}$ is equivalent to the information matrix (Λ), and Equation 3.29 can be viewed as adding more observable information to $\mathscr{G}$. For the next iteration of the least-squares fit, the a priori state deviation is updated by

$$\bar{x}_i = \bar{x}_{i-1} - \hat{x}_{i-1} \tag{3.33}$$

where the subscript i indicates the number of iterations.

3.2.3 SRIF in Batch Filter

In a batch filter, the observations are processed with respect to the epoch state (i.e., $t = t_0$). Thus, the state deviation must be properly mapped from the epoch to the time of observation by the state transition matrix. We first rewrite equation 3.24 as

$$\begin{aligned} \bar{b} &= \tilde{\bar{\mathscr{G}}}\Phi(t,t_0)x_0 + \bar{\eta} \\ y_w &= \tilde{H}_w\Phi(t,t_0)x_0 + \epsilon_w \end{aligned} \tag{3.34}$$

and make the following substitutions:

$$H = \tilde{H}(t)\Phi(t,t_0) \tag{3.35}$$

$$\bar{\mathscr{G}} = \tilde{\bar{\mathscr{G}}}\Phi(t,t_0) \tag{3.36}$$

Then, by expressing $W^{1/2}H$ as H_w, we get

$$Q\begin{bmatrix} \bar{\mathscr{G}}_{t_n,t_0} \\ H_w \end{bmatrix} = \begin{bmatrix} \mathscr{G}_{t_n,t_0} \\ 0 \end{bmatrix} \tag{3.37}$$

$$Q\begin{bmatrix} \bar{b}_{t_n,t_0} \\ y_{w(X,t)} \end{bmatrix} = \begin{bmatrix} b_{t_n,t_0} \\ e_{t_n,t_0} \end{bmatrix} \tag{3.38}$$

In Equation 3.37 and 3.38, the subscript t_n, t_0 indicates the n_{th} epoch mapped back to time t_0. When the next observation is processed, the same SRIF algorithm can be performed by letting $\bar{\mathscr{G}}_{t_{n+1},t_0} = \mathscr{G}_{t_n,t_0}$ and $\bar{b}_{n+1,t_0} = b_{n,t_0}$.

3.3 Coordinate Frames

The coordinate frames and the asteroid models are defined in this section. The filter extensively uses two coordinate frames: the asteroid-centered inertial (ACI) and asteroid-centered asteroid-fixed (ACAF) coordinate frames. This is because the gravitational attraction by the asteroid is computed in the asteroid's body frame, while the final covariance output is desired in the

inertial frame. In addition to these two coordinate frames, the sun-centered inertial (SCI) frame is used to propagate the asteroid's heliocentric orbit. Figure 3.1 shows these three coordinate frames implemented in the filter:

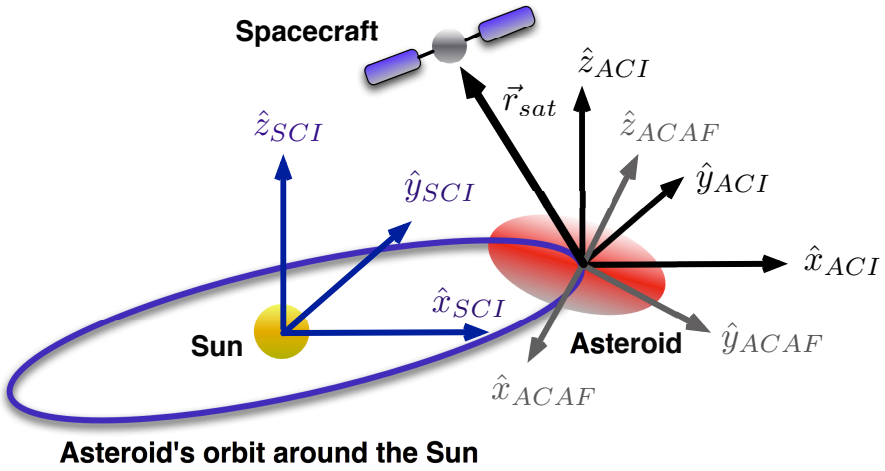

Figure 3.1: Relative orientations of the ACI, ACAF, and SCI frames.

In Figure 3.1, the origin of the ACI frame is incident on the asteroid's center of mass, and its orientation is fixed in the inertial frame. The offset between the ACAF frame and the ACI frame is specified by the 3-1-3 Euler angles (α, β, γ) or quaternions $\vec{q} = [q_0, q_1, q_2, q_3]$ which are explained in Section 3.5. These attitude coordinates compose the rotation matrix $[NB]$, which performs the coordinate transformation from the ACAF frame (B) to the ACI frame (N). The rotation matrix $[BN]$ performs the opposite coordinate transformation (i.e., N to B).

3.4 Asteroid's Orbit

The asteroid's orbit is propagated under the two-body dynamics around the sun in the SCI frame, which is shown in Figure 3.1. This SCI frame is simply the ACI frame translated to the center of mass of the Sun. Figure 3.2 shows the relative position vectors between the sun, asteroid, and spacecraft.

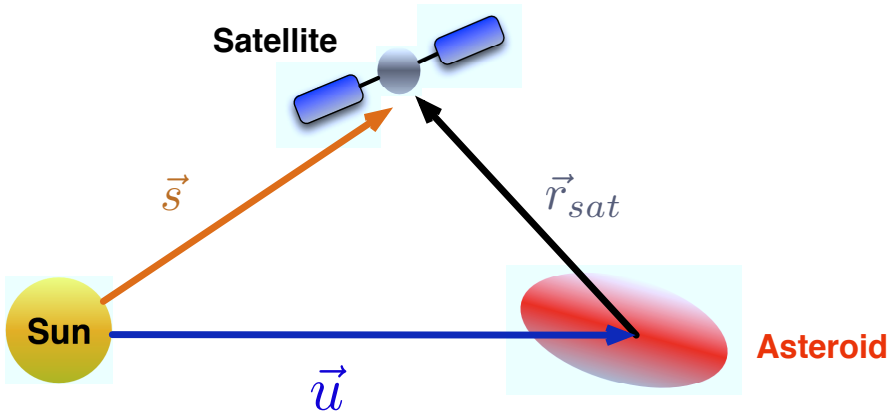

Figure 3.2: Definitions of $\vec{s}$, $\vec{r}$, and $\vec{u}$.

As shown in Figure 3.2, $\vec{s}$ is the relative position of the spacecraft with respect to the sun, $\vec{r}$ is that of the spacecraft with respect to the asteroid, and $\vec{u}$ is that of the asteroid with respect to the sun. These vectors satisfy a simple linear combination $\vec{s} = \vec{r} + \vec{u}$. Note that $\vec{r}$ can also be expressed by $\vec{r} = \vec{R}_{sat} - \vec{R}_{ast}$, where $\vec{R}$ is the position vector in an arbitrary inertial frame. Our filter estimates $\vec{R}_{sat}$ and $\vec{R}_{sat}$ centered at the center of mass of the asteroid. The initial condition of the asteroid is based on data from the Jet Propulsion Laboratory's (JPL) small body data browser (http://ssd.jpl.nasa.gov/sbdb.cgi).

3.5 Rotation Dynamics Models

We discuss two types of rotation modes in this section: a principal-axis rotator and a precessing rotator. For a spacecraft mission, it is desirable to explore a principal-axis rotator as a precessing rotator adds significant complexity to deep space navigation. Although many asteroids settle into this principal-axis rotation mode after dissipating its rotational energy, there are a class of asteroids that are tumbling such as Toutatis [44]. The motion of Toutatis is investigated in detail in Chapter 4.

3.5.1 A Principal-axis Rotator

The rotational dynamics of a principal-axis rotator are discussed. This spin configuration is stable with its spin axis pointed along the body z-axis. The body frame of the asteroid is oriented so that the moment of inertia around the z-axis (I_{zz}) has the largest moment of inertia. Therefore, this spin configuration corresponds to the minimum energy configuration assuming the conservation of angular momentum in which all asteroids would eventually settle after sufficiently long time has passed and the asteroid's rotational energy has been dissipated. Note that the only attitude coordinate that changes with respect to time is the angle around the body z-axis. Thus, we describe the rotational motion of the asteroid via 3-1-3 Euler angles α, β, and γ (Figure 3.3).

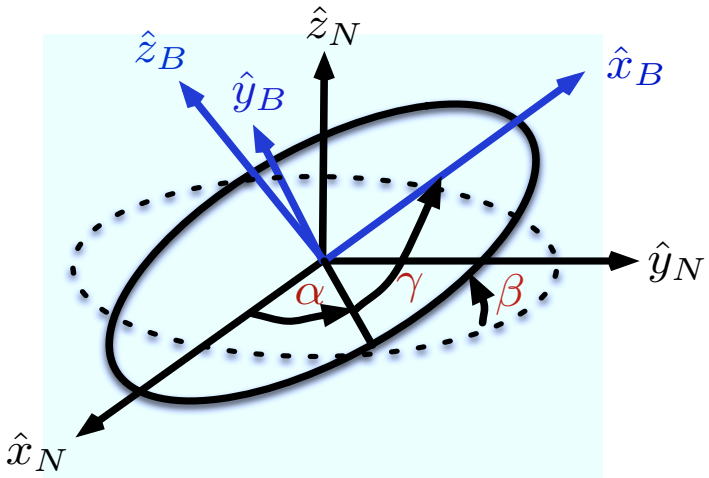

Figure 3.3: 3-1-3 Euler angles. The N subscript is used for the inertial coordinate frame and the B subscript for the body coordinate frame, both of which are defined by a set of three orthonormal, right-handed vectors $\hat{x}$, $\hat{y}$, and $\hat{z}$.

The body frame is obtained by rotating the body z-axis by α, then the body x-axis by β, and finally the body z-axis by γ, all measured positive in the counter-clockwise direction when looking down into the axis of rotation. Of all three attitude coordinates, only γ is the time dependent parameter. At $t = t_0$, $\gamma(t_0) = \gamma_0$, and $\gamma(t) = \gamma_0 + \dot{\gamma}(t - t_0)$. Thus, we define the attitude coordinates as α, β, γ_0, and $\dot{\gamma}$. Using these parameters, we can compute the rotation matrix $[BN]$ as

$$[BN] = \mathscr{R}_{3,\dot{\gamma}(t-t_0)} \cdot \mathscr{R}_{3,\gamma_0} \cdot \mathscr{R}_{1,\beta} \cdot \mathscr{R}_{3,\alpha} \tag{3.39}$$

where $\mathscr{R}$ is the rotation matrix with the subscript indicating the rotation axis (i.e., $1 \rightarrow x$, $2 \rightarrow y$, and $3 \rightarrow z$) and the angle of rotation (θ) as on the next page.

$$\mathscr{R}_{1,\theta} = \begin{bmatrix} 1 & 0 & 0 \\ 0 & \cos\theta & \sin\theta \\ 0 & -\sin\theta & \cos\theta \end{bmatrix} \tag{3.40}$$

$$\mathscr{R}_{2,\theta} = \begin{bmatrix} \cos\theta & 0 & -\sin\theta \\ 0 & 1 & 0 \\ \sin\theta & 0 & \cos\theta \end{bmatrix} \tag{3.41}$$

$$\mathscr{R}_{3,\theta} = \begin{bmatrix} \cos\theta & \sin\theta & 0 \\ -\sin\theta & \cos\theta & 0 \\ 0 & 0 & 1 \end{bmatrix} \tag{3.42}$$

In order to estimate the attitude coordinates, it is necessary to compute the partial of $[NB]$ with respect to themselves so the STM is computed. Such a formulation will be discussed in Section 3.7.2.

3.5.2 A Precessing Rotator

A precessing rotator exhibits a "wobble" like a spinning top. Most asteroids in this precessing rotation mode are assumed to have dissipated enough energy to precess around the body z-axis and be in a stable rotation mode. We can define our body frame as the principal coordinate frame placed at the center of mass of the asteroid, where all off-diagonal elements in the inertia tensor are zero. However, in order to align the body frame with the principal coordinate frame, we need to

have accurate knowledge of the internal density distribution, the estimation of which is a complex topic in itself. As a matter of fact, we often have the center of mass offset and misalignment of the coordinate frames resulting in non-zero off-diagonal terms in the inertia tensor. Thus, we consider a general case where all off-diagonal terms are non-zero. This assumption prohibits us from using analytical solution widely known for a torque-free precessing rotator, and we have to resort to numerical integration to compute the asteroid's orientation.

For a precessing rotator, we use the quaternions, body-frame angular velocity, and inertia tensor as the attitude coordinates. A great deal of theories discussed here are inherited from Schaub and Junkins [55]. The definition of the quaternions is

$$\vec{q} = \begin{bmatrix} q_0 \\ q_1 \\ q_2 \\ q_3 \end{bmatrix} = \begin{bmatrix} \cos\left(\frac{\vartheta}{2}\right) \\ e_1 \sin\left(\frac{\vartheta}{2}\right) \\ e_2 \sin\left(\frac{\vartheta}{2}\right) \\ e_3 \sin\left(\frac{\vartheta}{2}\right) \end{bmatrix} \tag{3.43}$$

where ϑ is the angle of rotation and $\vec{e} = (e_1, e_2, e_3)$ is the axis of rotation, which is invariant before and after the rotation. The angle ϑ is measured positive counter-clockwise looking down the axis of rotation. For a given set of quaternions, the corresponding rotation matrices, $[BN]$ and $[NB]$, are computed as

$$[BN] = \begin{bmatrix} q_0^2 + q_1^2 - q_2^2 - q_3^2 & 2(q_1q_2 + q_0q_3) & 2(q_1q_3 - q_0q_2) \\ 2(q_1q_2 - q_0q_3) & q_0^2 - q_1^2 + q_2^2 - q_3^2 & 2(q_2q_3 + q_0q_1) \\ 2(q_1q_3 + q_0q_2) & 2(q_2q_3 - q_0q_1) & q_0^2 - q_1^2 - q_2^2 + q_3^2 \end{bmatrix} \tag{3.44}$$

$$[NB] = \begin{bmatrix} q_0^2 + q_1^2 - q_2^2 - q_3^2 & 2(q_1q_2 - q_0q_3) & 2(q_1q_3 + q_0q_2) \\ 2(q_1q_2 + q_0q_3) & q_0^2 - q_1^2 + q_2^2 - q_3^2 & 2(q_2q_3 - q_0q_1) \\ 2(q_1q_3 - q_0q_2) & 2(q_2q_3 + q_0q_1) & q_0^2 - q_1^2 - q_2^2 + q_3^2 \end{bmatrix} \tag{3.45}$$

The benefits of working with quaternions as the attitude coordinates is that the quaternions are non-singular attitude descriptions, their equations of motion are linear, and they work well for both small and large rotations. The drawbacks are that the constraint equation must be satisfied at all times, and their visualization is not as simple as the Euler angles. Equation 3.46 shows the constraint equation for the quaternions:

$$q_0^2 + q_1^2 + q_2^2 + q_3^2 \quad = \quad 1 \tag{3.46}$$

That is, the quaternions are constrained to have the magnitude of unity at all times. This constraint equation must be enforced when numerically integrating the equation of motion given below:

$$\dot{\vec{q}} \quad = \quad \frac{1}{2}\left[\mathscr{K}(\vec{q})\right]\vec{\omega} \quad = \quad \frac{1}{2}\left[\mathscr{L}(\vec{\omega})\right]\vec{q} \tag{3.47}$$

where $[\mathscr{K}(\vec{q})]$ and $[\mathscr{L}(\vec{\omega})]$ are defined as

$$[\mathscr{K}(\vec{q})] \quad = \quad \begin{bmatrix} -q_1 & -q_2 & -q_3 \\ q_0 & -q_3 & q_2 \\ q_3 & q_0 & -q_1 \\ -q_2 & q_1 & q_0 \end{bmatrix} \tag{3.48}$$

$$[\mathscr{L}(\vec{\omega})] \quad = \quad \begin{bmatrix} 0 & -\omega_1 & -\omega_2 & -\omega_3 \\ \omega_1 & 0 & \omega_3 & -\omega_2 \\ \omega_2 & -\omega_3 & 0 & \omega_1 \\ \omega_3 & \omega_2 & -\omega_1 & 0 \end{bmatrix} \tag{3.49}$$

This concludes the discussion of a precessing rotator.

3.6 Trajectory Design

The flyby trajectories are determined by the flyby sequence and target points. The flyby sequence determines the temporal restrictions (i.e., schedule) and the target points determine the spatial restrictions (i.e., coordinates). Both of these factors must be appropriately defined for a successful spacecraft mission. Note that we only consider a continuous, single spacecraft mission in this analysis.

3.6.1 Flyby Sequence

An example of the flyby scenario is discussed to aid the visualization of the overall mission sequence. The flyby sequence is composed of three elements: a flyby, an impulsive maneuver, and a coasting. We define a flyby as the trajectory that crosses the B-plane of the asteroid, and a coasting is an intermediate trajectory that connects two flybys. A coasting is not necessary if the spacecraft crosses the B-plane consecutively, in which case an impulsive maneuver is sufficient. Figure 3.4 shows a nominal flyby scenario which consists of five flybys and two coastings:

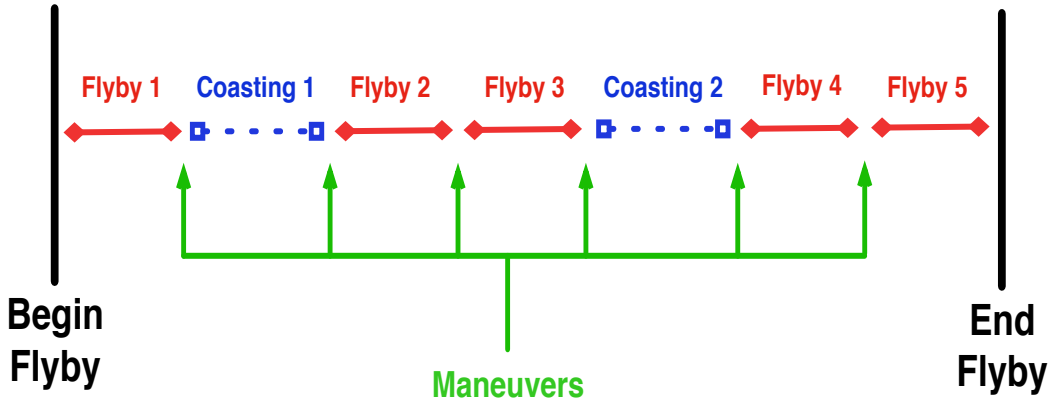

Figure 3.4: Nominal flyby sequence. The red lines correspond to flybys, and the blue dashed lines correspond to coastings. After each of flyby/coasting, a maneuver is executed to reach the target point.

In the scenario shown in Figure 3.4, the duration of the entire sequence is 14 days, with a total of six impulsive maneuvers occurring at two-day intervals. That is, each flyby and coasting is

two-day long. This two-day turn around may be too aggressive for the mission operators in some cases and can be relaxed for the real spacecraft mission.

The five segments in red lines are the flybys, and the closest approaches to the asteroid occur at 1, 5, 7, 11, 13 days into the sequence. During the coastings, the spacecraft does not reach its periapsis, meaning that the spacecraft is still en route to the asteroid. The coastings are implemented due to the reduction in the flyby speeds between two consecutive flybys. For example, we can consider the following target parameters:

Table 3.1: Examples of b_p and V_p.

Flyby Number	b_p $[km]$	V_p $[m/s]$
1	2	10
2	1.5	1
3	1	0.5
4	1	0.1
5	1	0.1

where b_p and V_p are the targeted periapsis radius and periapsis flyby speed. The first flyby speed is at 10 $[m/s]$, which, in a linear approximation, results in a travel distance of 1728 $[km]$ in two days. On the other hand, the second flyby is at 1 $[m/s]$, and its travel distance is merely 172.8 $[km]$. Therefore, we need to propagate the spacecraft at some intermediate speed to bring the spacecraft back into the regime where it is possible to perform the second flyby with a reduced speed. As with the first coasting phase, the second coasting phase is accompanied by the reduction of the flyby speed from 0.5 $[m/s]$ to 0.1 $[m/s]$.

In the above flyby sequence, note that not all the boundary conditions are constrained. Since a maneuver is a control over three parameters, we need at least two maneuvers to fully constrain the position and velocity. When only one maneuver is executed prior to targeting, we only constrain the target position and let the target velocity vary. More details are presented in Section 3.6.3.

3.6.2 Target Points

In addition to the flyby sequence, the target points must be specified. Recall that the covariance of the estimated states solely depends on the dynamics of the spacecraft and the measurement types. Thus, a judicious choice of target points is important. The periapsis radius is denoted as b_p, its longitude in the ACI frame as λ_p, and its latitude in the ACI frame as ϕ_p. For convenience, these target points are defined in the xz-plane of the ACI frame, and the target velocity (V_p) is always in the $\pm y$-direction which alternates for each flyby. Figure 3.5 shows the target points for the nominal sequence:

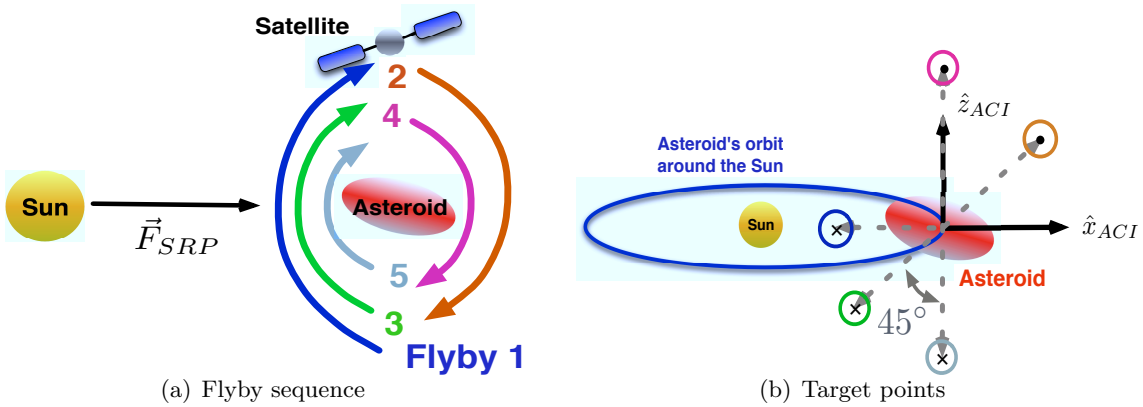

(a) Flyby sequence (b) Target points

Figure 3.5: Flyby sequence and target points.

In Figure 3.5, the target points are specified in the xz-plane, and the direction of the flyby velocity is specified by the conventional current flow notation. Note that the polar flyby in the ACI frame does not necessarily correspond to one in the ACAF frame because of the offset between the inertial and body z-axes. The first flyby trajectory is always designed to travel on the sunlit side in order to allow for the optical measurements of the asteroid to map out its surface. Table 3.2 and 3.3 show b_p, V_p, λ_p, and ϕ_p implemented for Itokawa, Didymos, and Eros flybys.

Table 3.2: b_p $[km]$ and V_p $[m/s]$ for five flybys around Itokawa, Didymos, and Eros.

(a) Itokawa		(b) Didymos		(c) Eros		(d) Itokawa		(e) Didymos		(f) Eros	
$b_{p,1}$	2	$b_{p,1}$	2.5	$b_{p,1}$	50	$V_{p,1}$	10	$V_{p,1}$	10	$V_{p,1}$	20
$b_{p,2}$	1.5	$b_{p,2}$	2.0	$b_{p,2}$	40	$V_{p,2}$	1	$V_{p,2}$	5	$V_{p,2}$	15
$b_{p,3}$	1	$b_{p,3}$	1.5	$b_{p,3}$	35	$V_{p,3}$	0.5	$V_{p,3}$	1	$V_{p,3}$	10
$b_{p,4}$	1	$b_{p,4}$	1.5	$b_{p,4}$	30	$V_{p,4}$	0.1	$V_{p,4}$	0.5	$V_{p,4}$	10
$b_{p,5}$	1	$b_{p,5}$	1.2	$b_{p,5}$	30	$V_{p,5}$	0.1	$V_{p,5}$	0.5	$V_{p,5}$	10

Table 3.3: λ_p $[deg.]$ and ϕ_p $[deg.]$ for five flybys around Itokawa, Didymos, and Eros.

(a) Latitude		(b) Longitude	
$\lambda_{p,1}$	180	$\phi_{p,1}$	0
$\lambda_{p,2}$	0	$\phi_{p,2}$	45
$\lambda_{p,3}$	180	$\phi_{p,3}$	-45
$\lambda_{p,4}$	0	$\phi_{p,4}$	90
$\lambda_{p,5}$	0	$\phi_{p,5}$	-90

For all target bodies, the first flyby has the largest b_p and V_p. This is a normal operational procedure as slow, close flyby is more likely to cause the spacecraft to impact the surface.

3.6.3 Targeting via Newton-Raphson Method

The Newton-Raphson method via the state transition matrix is implemented to target the flyby parameters. The computation of the state transition matrix is detailed in Section 3.8. We define the position of the spacecraft as a function of the initial conditions and time as follows:

$$\vec{r}(t) \quad = \quad \Gamma_r(t; \vec{r}_0, \vec{V}_0, t_0) \tag{3.50}$$

where Γ_r is the solution flow of the spacecraft position. In Equation 3.50, velocity is the only parameter that we can adjust in order to design an ideal trajectory. Thus, we seek to obtain the velocity at $t = t_0$ that will target the next target point, given the initial position of the spacecraft and the elapsed time. With a slight perturbation in the initial velocity, the spacecraft undergoes a slight position deviation at the final epoch. Letting $\vec{r}_f$ be the desired position at the final epoch,

the following equation is obtained by expanding Equation 3.50 to the first order about the reference trajectory.

$$\begin{aligned}
\vec{r}_f &= \Gamma_r(t_f; \vec{r}_0, \vec{V}_0^{(0)} + \delta\vec{V}, t_0) \\
&= \Gamma_r(t_f; \vec{r}_0, \vec{V}_0^{(0)}, t_0) + \left.\frac{\partial \Gamma_r}{\partial \vec{V}_0^{(0)}}\right|_{\Gamma_r(t_f;\vec{r}_0,\vec{V}_0^{(0)},t_0)} \delta\vec{V} + \cdots \qquad (3.51) \\
&= \vec{r}_f{}^{(0)} + \left.\frac{\partial \Gamma_r}{\partial \vec{V}_0^{(0)}}\right|_{\Gamma_r(t_f;\vec{r}_0,\vec{V}_0^{(0)},t_0)} \delta\vec{V} + \cdots
\end{aligned}$$

In Equation 3.51, the superscript in parenthesis denotes the iteration count. Then, neglecting the higher-order terms, we get

$$\delta\vec{V} = \left(\frac{\partial \Gamma_r}{\partial \vec{V}_0^{(0)}}\right)^{-1} (\vec{r}_f - \vec{r}_f{}^{(0)}) \qquad (3.52)$$

which is the correction to the initial velocity. For the next iteration, the initial velocity is updated to $\vec{V}_0^{(1)} = \vec{V}_0^{(0)} + \delta\vec{V}$, and we repeat this process until the solution converges (i.e., $|\delta\vec{V}| \simeq 0$). The initial estimate of the velocity vector, for instance, can be computed by Lambert's algorithm or simply by solving for the linear trajectory that connects the initial and final positions.

In Equation 3.52, notice that $\partial\Gamma_r/\partial\vec{V}_0^{(0)}$ is a subcomponent of the state transition matrix, and it naturally falls out of the integrator. Also, note here that we have not fully constrained the spacecraft dynamics at the target point. That is, the velocity at the target point is allowed to vary. As a maneuver is three control authorities (i.e., change of velocity in each component), it is necessary to perform exactly two maneuvers (i.e., position and velocity = six degrees of freedom) in order to match both the position and velocity at the target point. This argument is illustrated in Figure 3.6.

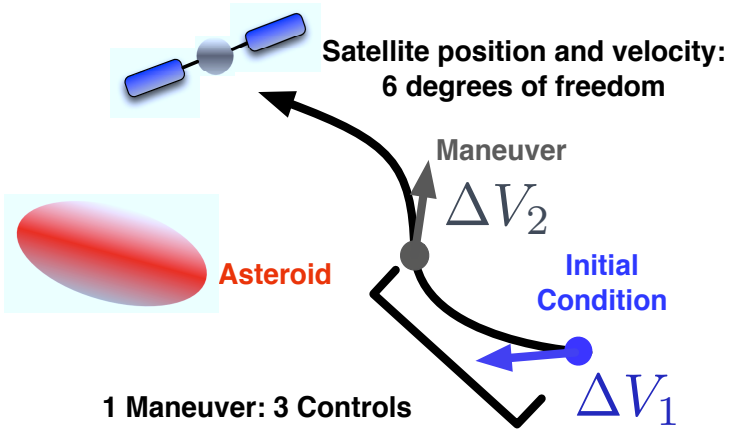

Figure 3.6: Maneuver constraints.

Thus, the position and velocity of the flyby subsequent to two consecutive maneuvers can be fully constrained. However, when two flybys are scheduled back to back with only one impulsive maneuver in between, only the target position can be constrained.

3.7 Measurements

The measurement types play a significant role in computing the covariance matrix. This section explores the measurement models and their sensitivities to the estimated parameters.

3.7.1 Measurement Models

We discuss the observation models and compute the measurement partials. The measurement types used in the simulation are Doppler tracking, Earth ranging, optical, and lidar. Figure 3.7 shows the schematic of all four measurement types.

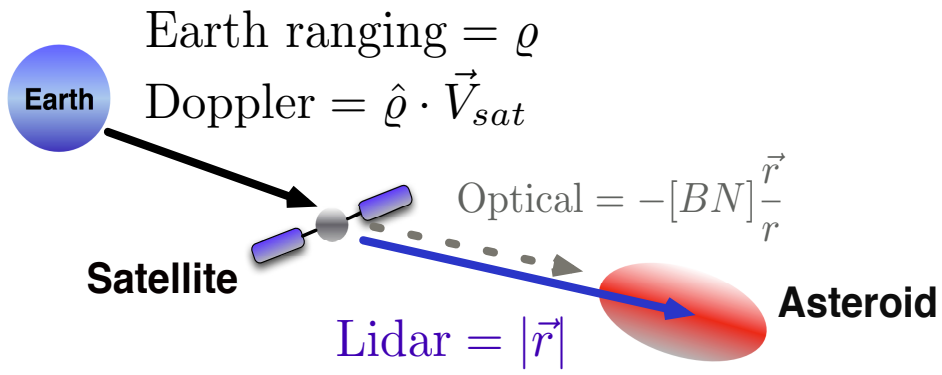

Figure 3.7: Observation types.

Doppler tracking measures the line-of-sight velocity of the spacecraft with respect to the Earth ground station, Earth ranging measures the distance between the Earth ground station and the spacecraft (ϱ with unit vector $\hat{\varrho}$), optical measures the line-of-sight vector from the spacecraft to the asteroid's center of mass by centerfinding, and lidar measures the distance between the spacecraft and the asteroid's surface. The Doppler tracking and Earth ranging assume precise station coordinates, Earth orientation, and atmospheric calibrations. For simplicity, the Earth ground station coordinates are equated to the Earth's coordinates in the inertial frame, and we ignore the atmospheric calibrations. The matrix $[BN]$ is used to rotate the optical measurement expressed in the inertial frame (N) into the body frame (B) to correlate the observation to the topography of the body. Likewise, the lidar measurements assume the existence of a shape model for precise processing, but we model them as the distance between the spacecraft and the center of mass of the body for simplicity. Equation 3.53 through 3.56 define our observable models:

$$Z_{Doppler} = \hat{\varrho} \cdot \vec{V}_{sat} = \left(\frac{\vec{R}_{sat} - \vec{R}_{earth}}{|\vec{R}_{sat} - \vec{R}_{earth}|} \right) \cdot \vec{V}_{sat} \tag{3.53}$$

$$Z_{ER} = |\vec{\varrho}| = |\vec{R}_{sat} - \vec{R}_{earth}| \tag{3.54}$$

$$Z_{optical} = -\hat{r}_B = -[BN]\left(\frac{\vec{R}_{sat} - \vec{R}_{ast}}{|\vec{R}_{sat} - \vec{R}_{ast}|}\right) = -[BN]\hat{r}_N \tag{3.55}$$

$$Z_{lidar} = r = |\vec{R}_{sat} - \vec{R}_{ast}| \tag{3.56}$$

These measurement data are collected at the frequency shown in Table 3.4.

Table 3.4: Measurement frequencies.

Measurement Type	Frequency	Uncertainty
Doppler	Continual at 60 $[s]$ intervals	0.1 $[mm/s]$
Earth Ranging	Continual at 4 $[hr]$ intervals	10 $[m]$
Optical	Continual at 4 $[hr]$ intervals	Equation 3.57
Lidar	Discrete at $[-1, 0, 1]$ $[hr]$ around the target point	10 $[m]$

During the coasting, the lidar measurement is turned off as this measurement requires close distance to the target object. Out of four measurements, only the optical measurement does not have the constant measurement uncertainty. We model its measurement uncertainty as a function of the distance from the asteroid to the spacecraft:

$$\sigma_{optical} = \sqrt{\sigma_{Angle}^2 + \left(\frac{\sigma_{Map}}{r}\right)^2} \tag{3.57}$$

where $\sigma_{Angle} = 25 \times 10^{-6}$ $[rad.]$ is the fixed uncertainty based on the resolution of the optical instrument itself, and $\sigma_{Map} = 100 \times 10^{-6}$ $[rad.]$ is its capability to relate an optical measurement to the surface topology. Thus, the uncertainty of the optical measurement is dictated by σ_{Angle} when the spacecraft is far from the body, and it is dictated by σ_{Map} when the spacecraft is close to the body.

3.7.2 Sensitivity Matrix

The computation of the sensitivity matrix (i.e., observation partials) reveals the strength of the observables with respect to the estimated parameters. For example, the sensitivity value of zero means that there is no direct information about the state parameter that can be extracted

from the measurement, and the state parameter must be related to the measurement via the STM. The observable equations (Equation 3.53 through 3.56) are used to compute the sensitivity matrix ($\tilde{H}$) for the position and velocity of the spacecraft as follows:

$$\tilde{H}_{Doppler} = \left[\left(\frac{1_{[3\times3]}}{\varrho} - \frac{\vec{\varrho}\vec{\varrho}}{\varrho^3} \right) \cdot \vec{V}_{sat[1\times3]}, \quad \hat{\varrho}_{[1\times3]} \right] \tag{3.58}$$

$$\tilde{H}_{ER} = \left[\hat{\varrho}_{[1\times3]}, \quad 0_{[1\times3]} \right] \tag{3.59}$$

$$\tilde{H}_{Optical} = \left[-[BN] \left(\frac{1_{[3\times3]}}{r} - \frac{\vec{r}\vec{r}}{r^3} \right)_{[3\times3]}, \quad 0_{[3\times3]} \right] \tag{3.60}$$

$$\tilde{H}_{Lidar} = \left[\hat{r}_{[1\times3]}, \quad 0_{[1\times3]} \right] \tag{3.61}$$

Equation 3.58 through 3.61 are used to accumulate the information matrix (Λ) after being mapped to epoch by the STM.

As mentioned above, the optical measurement is mapped into the body frame of the asteroid (Equation 3.60). This rotation allows us to relate an optical measurement to the terrain features of the asteroid. Realizing that the rotation matrix $[BN]$ is a function of the attitude parameters, we can relate an optical measurement to the Euler angles for a principal-axis rotator:

$$\frac{\partial[BN]}{\partial\alpha} = [\mathscr{R}_{3,\dot{\gamma}(t-t_0)}][\mathscr{R}_{3,\gamma_0}][\mathscr{R}_{1,\beta}]\frac{\partial[\mathscr{R}_{3,\alpha}]}{\partial\alpha} \tag{3.62}$$

$$\frac{\partial[BN]}{\partial\beta} = [\mathscr{R}_{3,\dot{\gamma}(t-t_0)}][\mathscr{R}_{3,\gamma_0}]\frac{\partial[\mathscr{R}_{1,\beta}]}{\partial\beta}[\mathscr{R}_{3,\alpha}] \tag{3.63}$$

$$\frac{\partial[BN]}{\partial\gamma_0} = [\mathscr{R}_{3,\dot{\gamma}(t-t_0)}]\frac{\partial[\mathscr{R}_{3,\gamma_0}]}{\partial\gamma_0}[\mathscr{R}_{1,\beta}][\mathscr{R}_{3,\alpha}] \tag{3.64}$$

$$\frac{\partial[BN]}{\partial\dot{\gamma}} = \frac{\partial\left[\mathscr{R}_{3,\dot{\gamma}(t-t_0)}\right]}{\partial\dot{\gamma}}[\mathscr{R}_{3,\gamma_0}][\mathscr{R}_{1,\beta}][\mathscr{R}_{3,\alpha}] \tag{3.65}$$

where each partial is given as

$$\frac{\partial[\mathscr{R}_{3,\alpha}]}{\partial\alpha} = \begin{bmatrix} -\sin\alpha & \cos\alpha & 0 \\ -\cos\alpha & -\sin\alpha & 0 \\ 0 & 0 & 0 \end{bmatrix} \tag{3.66}$$

$$\frac{\partial[\mathscr{R}_{1,\beta}]}{\partial\beta} = \begin{bmatrix} 0 & 0 & 0 \\ 0 & -\sin\beta & \cos\beta \\ 0 & -\cos\beta & -\sin\beta \end{bmatrix} \tag{3.67}$$

$$\frac{\partial[\mathscr{R}_{3,\gamma_0}]}{\partial\gamma_0} = \begin{bmatrix} -\sin\gamma_0 & \cos\gamma_0 & 0 \\ -\cos\gamma_0 & -\sin\gamma_0 & 0 \\ 0 & 0 & 0 \end{bmatrix} \tag{3.68}$$

$$\frac{\partial[\mathscr{R}_{3,\dot{\gamma}(t-t_0)}]}{\partial\dot{\gamma}} = (t-t_0)\begin{bmatrix} -\sin(\dot{\gamma}(t-t_0)) & \cos(\dot{\gamma}(t-t_0)) & 0 \\ -\cos(\dot{\gamma}(t-t_0)) & -\sin(\dot{\gamma}(t-t_0)) & 0 \\ 0 & 0 & 0 \end{bmatrix} \tag{3.69}$$

Then, the partial of the optical measurement with respect to the Euler angles is given as

$$\frac{\partial Z_{optical}}{\partial\mathscr{P}_i} = -\frac{\partial[BN]}{\partial\mathscr{P}_i}\hat{r} \tag{3.70}$$

where $\vec{\mathscr{P}} = [\alpha, \beta, \gamma_0, \dot{\gamma}]$ and i indicates the index of the parameter. For a precessing rotator, we get

$$\begin{aligned}
\frac{\partial[BN]}{\partial q_0} &= 2\begin{bmatrix} q_0 & q_3 & -q_2 \\ -q_3 & q_0 & q_1 \\ q_2 & -q_1 & q_0 \end{bmatrix} \qquad \frac{\partial[BN]}{\partial q_2} = 2\begin{bmatrix} -q_2 & q_1 & -q_0 \\ q_1 & q_2 & q_3 \\ q_0 & q_3 & -q_2 \end{bmatrix} \\
\frac{\partial[BN]}{\partial q_1} &= 2\begin{bmatrix} q_1 & q_2 & q_3 \\ q_2 & -q_1 & q_0 \\ q_3 & -q_0 & -q_1 \end{bmatrix} \qquad \frac{\partial[BN]}{\partial q_3} = 2\begin{bmatrix} -q_3 & q_0 & q_1 \\ -q_0 & -q_3 & q_2 \\ q_1 & q_2 & q_3 \end{bmatrix}
\end{aligned} \tag{3.71}$$

which yields

$$\frac{\partial Z_{optical}}{\partial q_i} = -\frac{\partial[BN]}{\partial q_i}\hat{r} \tag{3.72}$$

Other parameters, such as the solar radiation scaling factor, have zero sensitivity, and they are related to the observables via the dynamical equations.

3.8 Spacecraft Dynamics

In this section, we discuss the dynamics of the spacecraft subject to four perturbations: higher-degree and higher-order gravity field, solar tide, solar radiation pressure, and impulsive maneuvers. Equation 3.73 shows the acceleration of the spacecraft in the ACI frame.

$$\ddot{\vec{r}} = -\frac{\mu}{|\vec{r}|^3}\vec{r} + [NB]\frac{\partial U_{(n\geq 1)}}{\partial \vec{r}_B} - \frac{\mu_{sun}}{|\vec{r}+\vec{d}|^3}(\vec{r}+\vec{d}) + \frac{\mu_{sun}}{|\vec{d}|^3}\vec{d} + \vec{a}_{SRP} + \vec{a}_{\Delta V} \tag{3.73}$$

where μ_{sun} is the gravitational parameter of the sun. The first two terms arise from the gravitational field of the asteroid, the third and fourth terms from the solar tide, the fifth term from the solar radiation pressure, and the sixth term from a maneuver. Specifically, the first

term is the two-body acceleration due to the asteroid's total mass, and $U_{(n\geq 1)}$ is the potential of higher-degree and higher-order gravity field in Equation 1.13. For the computation of the higher-degree and higher-order acceleration and the dynamics matrix, a recursive method developed by Cunningham [15], also more concisely introduced by Montenbruck and Gill [39] and Werner [74], is implemented. The solar tide comes from the direct and indirect contributions of the sun's gravity field on the dynamics of the spacecraft and asteroid. The solar radiation pressure and the impulsive maneuver are discussed in Section 3.8.2 and 3.8.4.

When propagating the spacecraft dynamics under the force models in Equation 3.73, it is necessary to propagate the STM simultaneously in order to compute the covariance matrix. The computation of STM requires the dynamics matrix (A), and by definition of the dynamics matrix, it is necessary to compute the partials of the spacecraft acceleration with respect to the state vector. Since vector addition is a linear operator, the partials of the acceleration due to the gravity field, solar tide, SRP, and maneuver can be computed individually. The following sections discuss the force models and the dynamics matrix in detail [65, 67].

3.8.1 Gravity Field Force Model

The gravity field modeling is detailed in Chapter 6 and 7. However, we briefly discuss the computation of the partials that enter the dynamics matrix. The partial of the inertial acceleration with respect to the spacecraft position in the inertial frame is obtained by invoking a series of chain rule as follows:

$$\begin{aligned}\frac{\partial \vec{a}_{N,sat}}{\partial \vec{r}_{N,sat}} &= \frac{\partial([NB]\vec{a}_{B,sat})}{\partial \vec{r}_{N,sat}} = [NB]\frac{\partial \vec{a}_{B,sat}}{\partial \vec{r}_{N,sat}} = [NB]\frac{\partial \vec{a}_{B,sat}}{\partial \vec{r}_{B,sat}}\frac{\partial \vec{r}_{B,sat}}{\partial \vec{r}_{N,sat}} \\ &= [NB]\frac{\partial \vec{a}_{B,sat}}{\partial \vec{r}_{B,sat}}[NB]^{-1} = [NB]\frac{\partial^2 U}{\partial \vec{r}^{\,2}_{B,sat}}[BN]\end{aligned} \tag{3.74}$$

By the same token, $\partial\vec{a}_{N,sat}/\partial\mu$, $\partial\vec{a}_{N,sat}/\partial C$, and $\partial\vec{a}_{N,sat}/\partial S$ are obtained as

$$\frac{\partial\vec{a}_{N,sat}}{\partial\mu} = \frac{\partial([NB]\vec{a}_{B,sat})}{\partial\mu} = [NB]\frac{\partial\vec{a}_{B,sat}}{\partial\mu} = [NB]\frac{\partial^2 U}{\partial\mu\partial\vec{r}_{B,sat}} \tag{3.75}$$

$$\frac{\partial\vec{a}_{N,sat}}{\partial C} = \frac{\partial([NB]\vec{a}_{B,sat})}{\partial C} = [NB]\frac{\partial\vec{a}_{B,sat}}{\partial C} = [NB]\frac{\partial^2 U}{\partial C\partial\vec{r}_{B,sat}} \tag{3.76}$$

$$\frac{\partial\vec{a}_{N,sat}}{\partial S} = \frac{\partial([NB]\vec{a}_{B,sat})}{\partial S} = [NB]\frac{\partial\vec{a}_{B,sat}}{\partial S} = [NB]\frac{\partial^2 U}{\partial S\partial\vec{r}_{B,sat}} \tag{3.77}$$

Then, these equations above are used to fill the dynamics matrix. Specific forms of Equation 3.75 through 3.77 are discussed in Chapter 6. Other non-zero components of the dynamics matrix due to the solar radiation pressure, solar tide, and a maneuver are derived in the following sections.

3.8.2 Solar Tides Force Model

The acceleration due to the solar tide is given as

$$\vec{a}_{ST} = -\frac{\mu_{sun}}{|\vec{r}_{N,sat}+\vec{d}|^3}(\vec{r}_{N,sat}+\vec{d}) + \frac{\mu_{sun}}{|\vec{d}|^3}\vec{d} \tag{3.78}$$

Since the second term in Equation 3.78 is a function only of $\vec{d}$, only the first term remains when taking the partial with respect to the spacecraft position. This partial is given as

$$\begin{aligned}\frac{\partial\vec{a}_{ST}}{\partial\vec{R}_{sat}} &= \frac{\partial}{\partial\vec{R}_{sat}}\left\{-\frac{\mu_{sun}}{|\vec{r}_{N,sat}+\vec{d}|^3}(\vec{r}_{N,sat}+\vec{d})\right\} \\ &= -\frac{\mu_{sun}}{|\vec{r}_{N,sat}+\vec{d}|^3}1_{[3\times3]} + 3\mu_{sun}\frac{(\vec{r}_{N,sat}+\vec{d})(\vec{r}_{N,sat}+\vec{d})}{|\vec{r}_{N,sat}+\vec{d}|^5}\end{aligned} \tag{3.79}$$

This expression is already in the inertial frame, and no coordinate transformation is necessary.

3.8.3 Solar Radiation Pressure Force Model

We implement a simple cannon-ball model for the solar radiation pressure. This cannon-ball model computes the acceleration due to the solar radiation pressure as a linear function of $P_{SRP}C_RA_{sat}/m_{sat}$, where P_{SRP} is the solar pressure, C_R is the coefficient of reflectivity, A_{sat} is the cross-sectional area of the cannon ball, and m_{sat} is the spacecraft mass. Then, the SRP acceleration can be expressed as

$$\vec{a}_{SRP,ACI} = \eta_{SRP}\frac{P_{SRP}C_RA}{m_{sat}}\hat{s} \tag{3.80}$$

where $\hat{s}$ is the unit vector of sun-spacecraft vector as shown in Figure 3.2. In Equation 3.80, η_{SRP} is added to scale the magnitude of the SRP acceleration, and η_{SRP} is one of the estimated parameters in the batch filter. The reason to add this scaling factor is that P_{SRP}, C_R, A, and m_{sat} are dependent on each other and cannot be estimated separately. Thus, instead of estimating one of four coefficients, we estimate η_{SRP} to find the overall strength of the SRP acceleration.

In Equation 3.80, P_{SRP} is expressed as

$$P_{SRP} = \frac{R_s^2\sigma_{SB}T_s^4}{c|\vec{r}_{N,sat}+\vec{d}|^2} \tag{3.81}$$

where R_s is the radius of the sun, σ_{SB} is the Stefan-Boltzmann constant, T_s is the temperature of the sun, and c is the speed of light. After substituting the expression for the solar pressure, Equation 3.80 becomes

$$\vec{a}_{SRP,ACI} = \eta_{SRP}\frac{C_RAR_s^2\sigma_{SB}T^4}{m_{sat}c}\frac{\vec{r}_{N,sat}+\vec{d}}{|\vec{r}_{N,sat}+\vec{d}|^3} \tag{3.82}$$

This is the final form of the SRP acceleration. Since $\vec{a}_{SRP,ACI}$ is a function of the spacecraft position, it is necessary to take the derivative of $\vec{a}_{SRP,ACI}$ with respect to $\vec{r}_{N,sat}$ when computing the dynamics matrix (Equation 3.83).

$$\frac{\partial \vec{a}_{SRP,ACI}}{\partial \vec{R}_{sat}} = \eta_{SRP}\frac{C_R A R_s^2 \sigma_{SB} T^4}{m_{sat} c}\left[\frac{1_{[3\times 3]}}{|\vec{r}_{N,sat}+\vec{d}|^3} - 3\frac{(\vec{r}_{N,sat}+\vec{d})(\vec{r}_{N,sat}+\vec{d})}{|\vec{r}_{N,sat}+\vec{d}|^5}\right] \quad (3.83)$$

As with the solar tide, Equation 3.83 is already expressed in the inertial frame, and no coordinate transformation is necessary. Note the remarkable similarity between Equation 3.79 and 3.83. These two equations work in the opposite direction with different magnitudes.

3.8.4 Maneuver Force Model

The acceleration of the i_{th} impulsive maneuver is modeled as

$$\vec{a}_{\Delta V,i} = \Delta\vec{V}_i \delta(t-\tau_i) \quad (3.84)$$

where $\Delta\vec{V}_i$ is the change in velocity and τ_i is the time of maneuver. This equation captures the property of the acceleration by an impulsive maneuver as shown in Equation 3.85:

$$\int_{\tau_i - \frac{\epsilon_\tau}{2}}^{\tau_i + \frac{\epsilon_\tau}{2}} \Delta\vec{V}_i \delta(t-t_i)dt = \Delta\vec{V}_i \quad (3.85)$$

where ϵ_τ is an infinitesimal time variation. We will discuss the STM for maneuvers in the following sections.

3.8.4.1 Solution Form of STM

Before beginning the derivation of the STM for $\Delta\vec{V}$ and τ, the solution for a non-homogeneous linear differential equation is investigated. By defining the STM of position and velocity as ϕ, the time derivative of the STM with respect to any arbitrary constants takes on the form of Equation 3.86, and the solution to this equation is given by Equation 3.87.

$$\dot{\Psi} = A_{[\vec{R},\vec{V}]}\Psi + F_{\Xi}(t) \tag{3.86}$$

$$\Psi(t,t_0) = \varphi(t,t_0)\int_{t_0}^{t}\varphi(t_0,t')F_{\Xi_0}(t')dt' \tag{3.87}$$

where $\Psi(t,t_0) = \Phi_{\Xi_0}^{\vec{R}(t),\vec{V}(t)}$, $A_{[\vec{R},\vec{V}]} = \partial[\dot{\vec{R}},\dot{\vec{V}}]/\partial[\vec{R},\vec{V}]$, $\varphi(t,t_0) = \Phi_{\vec{R}_0,\vec{V}_0}^{\vec{R}(t),\vec{V}(t)}$, $\Phi_{\vec{X}_0}^{\vec{X}(t)}$ is the full STM that falls out of the integrator, Ξ is an array of constants, $F_{\Xi} = \partial[\dot{\vec{R}},\dot{\vec{V}}]/\partial\Xi$, and t' is the dummy variable for time. The notation of the STMs (Ψ, φ, and Φ) is defined as such; the deviations of the parameters in the subscript at time t_0 gives the deviations of the parameters in the superscript at time t. The superscript is assumed to be the spacecraft position ($\vec{R}_{sat}$) and velocity ($\vec{V}_{sat}$) unless specified otherwise.

3.8.4.2 Variation of Parameters

Equation 3.87 is proven via variation of parameters. $\dot{\Psi}_{\Xi} = A_{[\vec{R},\vec{V}]}\Psi_{\Xi}$ has a homogeneous solution

$$\Psi_{\Xi} = \varphi\Psi_{\Xi_0} \tag{3.88}$$

Then, by variation of parameters, the time derivative of Ψ_{Ξ} becomes

$$\frac{d\Psi_{\Xi}}{dt} = \dot{\varphi}\Psi_{\Xi_0} + \varphi\dot{\Psi}_{\Xi_0} \tag{3.89}$$

Also,by definition, the time derivative of Ψ_{Ξ} is computed as

$$\Psi_{\Xi}^{\vec{R},\vec{V}} = \frac{\partial[\vec{R},\vec{V}]}{\partial\Xi} \tag{3.90}$$

$$\dot{\Psi}_{\Xi_0}^{\vec{R},\vec{V}} = A_{[\vec{R},\vec{V}]}\Psi_{\Xi} + F_{\Xi_0} \tag{3.91}$$

Substituting $A_{[\vec{R},\vec{V}]}\Psi_{\Xi} = A_{[\vec{R},\vec{V}]}\varphi\Psi_{\Xi_0} = \dot{\varphi}\Psi_{\Xi_0}$ and equating Equation 3.89 and Equation 3.91 leaves $\varphi\dot{\Psi}_{\Xi_0} = F_{\Xi_0}$. Thus,

$$\dot{\Psi}_{\Xi} = \varphi^{-1}F_{\Xi_0} \tag{3.92}$$

Then, by integrating Equation 3.92, and applying Equation 3.88, we get

$$\Psi_{\Xi} = \varphi\Psi^*_{\Xi_0} + \varphi\int_{t_0}^{t}\varphi^{-1}(t',t_0)F_{\Xi_0}dt = \varphi(t,t_0)\int_{t_0}^{t}\varphi(t_0,t')F_{\Xi_0}dt' \tag{3.93}$$

where the condition $\Psi^*_{\Xi_0} = 0$ is substituted as the spacecraft dynamics have not been affected by the constants at $t = t_0$. Now that Equation 3.87 is proven, an analytical expressions for the $\Delta\vec{V}$ STM and τ STM can be derived.

3.8.4.3 ΔV STM

By definition, $F_{\Delta\vec{V}_i}$ is given as

$$F_{\Delta\vec{V}_i} = \frac{\partial\dot{X}}{\partial\Delta\vec{V}_i} = \begin{bmatrix} 0_{[3\times3]} \\ 1_{[3\times3]}\delta(t-\tau_i) \end{bmatrix} \tag{3.94}$$

Then, substitution of Equation 3.94 into Equation 3.93 yields

$$\Psi^{\vec{r},\vec{V}}_{\Delta\vec{V}_i}\Big|_{t\geq\tau_i} = \varphi(t,t_0)\int_{t_0}^{t}\varphi(t_0,t')\begin{bmatrix} 0_{[3\times3]} \\ 1_{[3\times3]}\delta(t-\tau_i) \end{bmatrix}dt' = \varphi(t,\tau_i)\begin{bmatrix} 0_{[3\times3]} \\ 1_{[3\times3]} \end{bmatrix} \tag{3.95}$$

This is the final form of the ΔV STM. Equation 3.95 makes sense not only mathematically but also intuitively because the STM must experience a "jump" in its state due to an impulsive maneuver. The ΔV STM can be computed analytically, or numerically by filling the appropriate rows and columns with $[0_{[3\times3]}, 1_{[3\times3]}]$ as shown in Equation 3.95 and let the propagator integrate their dynamics. The rows correspond to the position and velocity of the spacecraft, and the columns correspond to those of a maneuver.

3.8.4.4 τ STM

Next, we consider the STM for the maneuver execution time (τ_i). F_{τ_i} is given as

$$F_{\tau_i} = \frac{\partial \dot{X}}{\partial \tau_i} = \begin{bmatrix} 0_{[3\times1]} \\ \Delta\vec{V}_i \dfrac{\partial \delta(t-\tau_i)}{\partial \tau_i} \end{bmatrix} \tag{3.96}$$

One immediately finds that Equation 3.93 cannot be solved analytically due to the partial of Dirac delta function. For this reason, Equation 3.91 is revisited. Considering the spacecraft dynamics around $t = \tau_i$ and ignoring all the parameters other than the velocity (i.e., ignoring the spacecraft position), Equation 3.91 becomes

$$\begin{bmatrix} \dot{\Psi}^{\vec{r}}_{\tau_i} \\ \dot{\Psi}^{\vec{V}}_{\tau_i} \end{bmatrix} = \begin{bmatrix} 0_{[3\times3]} & 1_{[3\times3]} \\ 0_{[3\times3]} & 0_{[3\times3]} \end{bmatrix} \begin{bmatrix} \Psi^{\vec{r}}_{\tau_i} \\ \Psi^{\vec{V}}_{\tau_i} \end{bmatrix} + \begin{bmatrix} 0_{[3\times1]} \\ \Delta\vec{V}_i \end{bmatrix} \frac{\partial \delta(t-\tau_i)}{\partial \tau_i} \tag{3.97}$$

Then, expanding Equation 3.97 results in the following equations:

$$\dot{\Psi}^{\vec{r}}_{\tau_i} = \Psi^{\vec{V}}_{\tau_i} \tag{3.98}$$

$$\dot{\Psi}^{\vec{V}}_{\tau_i} = \Delta\vec{V}_i \frac{\partial \delta(t-\tau_i)}{\partial \tau_i} \tag{3.99}$$

Notice a close relationship between $\Psi^{\vec{r}}_{\tau_i}$ and $\Psi^{\vec{V}}_{\tau_i}$. Taking the time derivative of Equation 3.98, we get

$$\ddot{\Psi}^{\vec{r}}_{\tau_i} = \Delta\vec{V}_i \frac{\partial \delta(t-\tau_i)}{\partial \tau_i} \tag{3.100}$$

which yields

$$\Psi^{\vec{r}}_{\tau_i} = -\Delta\vec{V}_i \tag{3.101}$$

Then, comparison of Equation 3.98 and 3.101 reveals

$$\Psi_{\tau_i}^{\vec{V}} = \dot{\Psi}_{\tau_i}^{\vec{r}} = 0_{[3\times1]} \tag{3.102}$$

Therefore, by combining Equation 3.101 and 3.102, we get

$$\Psi_{\tau_i}^{\vec{r},\vec{V}}\Big|_{t=\tau_i} = \begin{bmatrix} -\Delta\vec{V}_i \\ 0_{[3\times1]} \end{bmatrix} \tag{3.103}$$

Note that $\Psi_{\tau_i}^{\vec{r},\vec{V}}\Big|_{t=\tau_i}$ corresponds to Ψ_{Ξ_0} in Equation 3.88. By mapping Equation 3.103 forward in time, we get

$$\Psi_{\tau_i}^{\vec{r},\vec{V}}\Big|_{t\geq\tau_i} = \varphi(t,\tau_i)\begin{bmatrix} -\Delta\vec{V}_i \\ 0_{[3\times1]} \end{bmatrix} \tag{3.104}$$

This is the final form of the τ STM. As with the ΔV STM, Equation 3.104 can be computed either analytically or numerically by inserting $[-\Delta\vec{V}_i, 0_{[3\times1]}]$ in the rows that correspond to the spacecraft position and velocity and in the columns that correspond to τ_i.

3.8.4.5 Geometric Derivation of ΔV and τ STM

The previous sections discussed algebraic derivation of the ΔV and τ STMs. Here, we derive the same result geometrically. First, we start from the definition of the ΔV and τ STMs and apply the chain rule as shown below:

$$\Psi_{\Delta\vec{V}_i}^{\vec{R},\vec{V}} = \frac{\partial[\vec{R}(t),\vec{V}(t)]}{\partial\Delta\vec{V}_i} = \frac{\partial[\vec{R}(t),\vec{V}(t)]}{\partial[\vec{R}(\tau_i),\vec{V}(\tau_i)]}\frac{\partial[\vec{R}(\tau_i),\vec{V}(\tau_i)]}{\partial\Delta\vec{V}_i} = \varphi(t,\tau_i)\frac{\partial[\vec{R}(\tau_i),\vec{V}(\tau_i)]}{\partial\Delta\vec{V}_i} \tag{3.105}$$

$$\Psi_{\tau_i}^{\vec{R},\vec{V}} = \frac{\partial[\vec{R}(t),\vec{V}(t)]}{\partial\tau_i} = \frac{\partial[\vec{R}(t),\vec{V}(t)]}{\partial[\vec{R}(\tau_i),\vec{V}(\tau_i)]}\frac{\partial[\vec{R}(\tau_i),\vec{V}(\tau_i)]}{\partial\tau_i} = \varphi(t,\tau_i)\frac{\partial[\vec{R}(\tau_i),\vec{V}(\tau_i)]}{\partial\tau_i} \tag{3.106}$$

In both Equation 3.105 and 3.106, the partials of the position and velocity with respect to ΔV and τ_i at the maneuver time are the only unknowns as the state transition matrix $\varphi(t, \tau_i)$ is computed simultaneously with the spacecraft dynamics. Equation 3.105 is simple to compute, and we get the expected outcome shown below:

$$\Psi^{\vec{r},\vec{V}}_{\Delta\vec{V}_i} = \varphi(t, \tau_i) \begin{bmatrix} 0_{[3\times3]} \\ 1_{[3\times3]} \end{bmatrix} \tag{3.107}$$

Now we turn to Equation 3.106 and solve for the partials of the position and velocity with respect to the maneuver time. We consider the spacecraft dynamics around the maneuver time τ_i (Figure 3.8).

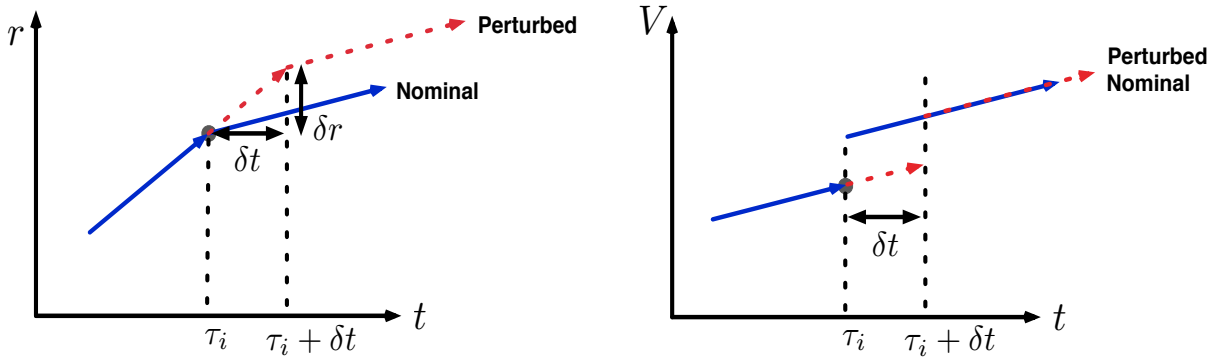

(a) Spacecraft position around τ_i

(b) Spacecraft velocity around τ_i

Figure 3.8: Spacecraft position and velocity around τ_i.

In Figure 3.8, the nominal trajectory is obtained without time variation, and the perturbed trajectory is obtained with the time variation (δt). In Figure 3.8(a), the velocity changes before and after τ_i due to the maneuver, which results in the position variation (δr) between the nominal and perturbed trajectories. This position variation can be expressed as

$$\delta\vec{r} = \vec{r}_{perturbed} - \vec{r}_{nominal} = -\Delta V \delta t \tag{3.108}$$

which results in

$$\frac{\partial \vec{r}(\tau_i)}{\partial \tau_i} = \lim_{\delta t \to 0} \frac{\delta \vec{r}}{\delta t} = -\Delta V_i \tag{3.109}$$

On the other hand, as shown in Figure 3.8(b), there is no velocity variation. Thus, we get

$$\Psi_{\tau_i}^{\vec{r},\vec{V}} = \varphi(t,\tau_i) \begin{bmatrix} -\Delta \vec{V}_i \\ 0_{[3\times 1]} \end{bmatrix} \tag{3.110}$$

Thus, the same ΔV and τ STMs are obtained geometrically.

3.9 Consider Covariance Analysis

The formulation of consider covariance is explained in detail by Scheeres [56] and Tapley et al [72]. The consider covariance analysis studies the effects of unestimated constant parameters on the overall performance of the covariance. The batch filter we have developed can consider the spin state of the asteroid and/or the higher-degree and higher-order spherical harmonic coefficients. Other constant parameters can be considered accordingly if their dynamics are known. In this section, we briefly review the concept of consider covariance analysis.

First, a new parameter Π is introduced, which relates the unestimated parameters to the dynamics of the spacecraft. This parameter Π is defined as

$$\Pi(t,t_k) = \frac{\partial X(t)}{\partial \mathscr{C}(t_k)} \tag{3.111}$$

where $\mathscr{C}$ is an array of consider parameters that are assumed constant but contain uncertainty. By definition, $\Pi(t_0,t_0)$ is the null-matrix. Given the above definition, Π is propagated as

$$\dot{\Pi} = A\Pi + F_{\mathscr{C}} \tag{3.112}$$

where A is the dynamics matrix used to propagate the STM, and $F_{\mathscr{C}} = \partial \dot{X}/\partial \mathscr{C}$. In addition to the spacecraft dynamics, consider parameters can have effects on the observable equation. The consider observation partial ($\tilde{H}_c$) is computed as

$$\tilde{H}_c = \frac{\partial Z}{\partial \mathscr{C}} \tag{3.113}$$

Since the batch filter processes the observables with respect to the epoch state, we have to map $\tilde{H}_c$ to the epoch as

$$H_c(t) = \tilde{H}_x(t)\Pi(t, t_0) + \tilde{H}_c \tag{3.114}$$

Now, recall that the observables are the Doppler tracking, Earth ranging, optical, and lidar measurements, and none of them contain the spin state or the gravitational coefficients in their mathematical formulation. Thus, $\tilde{H}_c$ is a null matrix for all observation types, and $H_c(t) = \tilde{H}_x(t)\Pi(t, t_0)$. After compiling all the equations presented above, the consider covariance is given as

$$P_c = P_x + \mathscr{S} P_{cc} \mathscr{S}^T \tag{3.115}$$

where P_c is the consider covariance, P_x is the covariance from the SRIF, P_{cc} is the covariance of the consider parameters, and $\mathscr{S}$ is the consider sensitivity matrix (i.e., $\mathscr{S} = \partial\hat{x}/\partial\hat{c}$ where $\hat{x}$ is the state deviation, and $\hat{c}$ is the deviation of the consider parameters). This consider sensitivity matrix ($\mathscr{S}$) is computed as

$$\mathscr{S} = -P_x(\mathbf{H_x^T W H_c}) \tag{3.116}$$

where both P_x and $(\mathbf{H_x^T W H_c})$ are accumulated values. This concludes the discussion of consider covariance.

3.10 Smoother

The estimates of the epoch state variables after processing the observables at the final epoch do not necessarily take full advantage of all the information contained in the observations. In particular, our knowledge of the state vector as a function of time along the trajectory has its lowest uncertainty at the initial epoch but has higher uncertainty at the final epoch. In order to properly account for all the observations for determining the uncertainty of the states, it is necessary to reprocess the observations, starting at the final epoch and moving backwards in time to the initial epoch. This process is called smoothing and is performed by running the batch filter in reverse, essentially. First we map the covariance matrix from the initial epoch to the final epoch. Then, we run the dynamics backwards and develop improved estimates of the final epoch based on all available information. As we carry out this process the uncertainty of all other state variables will also decrease, and will now represent the totality of observation information from the entire sequence.

As discussed above, we are interested in refining the covariance at the final epoch by running a smoother; thus, we need to map $\mathscr{G}(t_0)$ (i.e., square root of the information matrix) forward in time to acquire the a priori covariance at the final epoch. This a priori covariance can be computed easily by $\mathscr{G}(t_f) = \mathscr{G}(t_0)\Phi(t_0, t_f)$. Using this a priori covariance, the spacecraft dynamics are run backwards in time to process the same observables. Alternatively, the spacecraft dynamics can be stored in memory during the forward processing and requested as necessary. Note that we need $\Phi(t, t_f)$ to compute $H = \tilde{H}\Phi(t, t_f)$ in the smoother, which can be obtained by a simple relationship $\Phi(t, t_f) = \Phi(t, t_0) \cdot \Phi(t_0, t_f) = \Phi(t, t_0) \cdot \Phi^{-1}(t_f, t_0)$.

3.11 Results

In this section, we present results on full numerical covariance analysis. Two cases are tested for each asteroid: case 1 with lidar measurements and case 2 without them. We assume a principal-axis rotator for all target bodies. The nominal SRIF estimates the 2×2 gravity field under the 4×4

gravity field perturbations, and this result is compared to the consider covariance of 4×4 gravity field and smoother. The flyby trajectories are constructed from parameters shown in Table 3.2 and 3.3. As mentioned earlier, when only one maneuver is executed prior to targeting, we fix the target coordinates and let the flyby speed vary. Thus, the third and fifth flybys have some in-plane velocity components as the spacecraft crosses the xz-plane.

We will present the covariance outputs in the order of Itokawa, Didymos, and Eros. Their physical characteristics are documented in Appendix A. Figure 3.9 shows the time history of the uncertainties of μ and η_{SRP} in one standard deviation for case 1 for Itokawa.

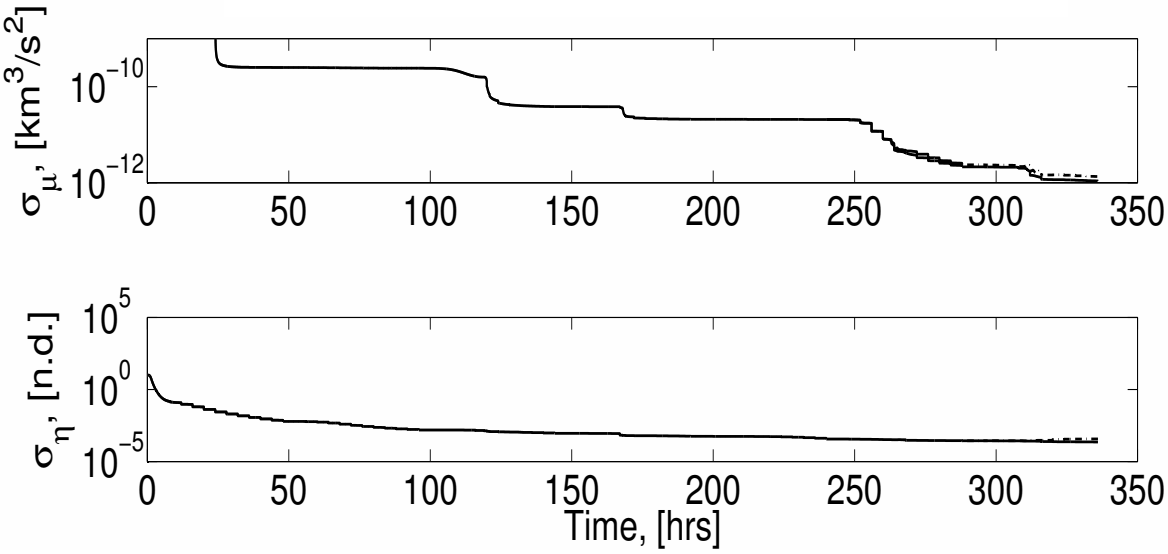

Figure 3.9: μ and η uncertainties for case 1 around Itokawa.

In Figure 3.9, a steady decrease in μ and η uncertainties are observed. The dashes lines indicate the consider covariance which does not deviate far from the SRIF covariance. We see that both σ_μ and σ_η drop significantly during the first flyby followed by a gradual decrease over time. The largest decrease occurs around 24 $[hrs]$ into the first flyby, indicating the strength of the gravity field as well as lidar measurement. Figure 3.10 shows the time history of the uncertainties of the second-degree spherical harmonic coefficients in one standard deviation for case 1 for Itokawa.

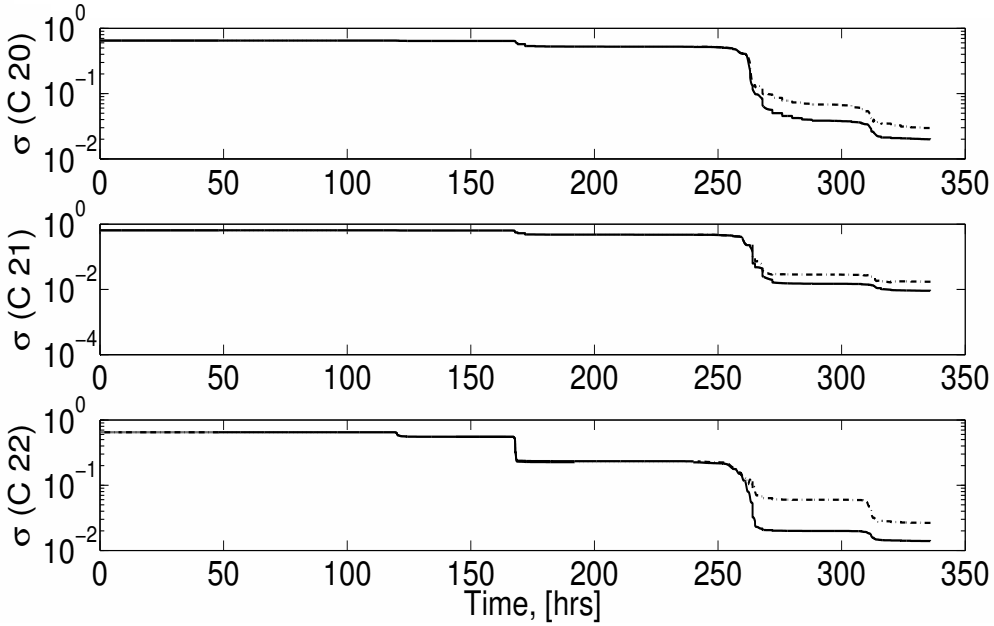

Figure 3.10: Uncertainties of the second-degree spherical harmonic coefficients for case 1 around Itokawa.

In Figure 3.10, the consider covariance picks up in the last flyby, meaning that the effects of the third and the fourth order gravity field are significant enough to affect the spacecraft dynamics; in other words, the third and the fourth-degree gravity fields can be estimated. An alternative explanation of this covariance pick-up is as follows: when the uncertainty reduces to a certain level, even a small uncertainty in the unestimated parameters causes large deviations in the covariance of the estimated parameters, again indicating that there is sufficient information to estimate the consider parameters. The reason that we did not include the third and fourth-degree and order gravity field in the state vector is that multiple slow, close flybys are necessary in order to reduce the uncertainty of those higher-degree and higher-order gravity field coefficients to a meaningful level. This behavior is manifested in Figure 3.10, where the uncertainties of the second-degree gravity field do not decrease until we perform the last two flybys. In general, estimation of too many parameters prior to the acquisition of accurate global parameters results in divergence of the filter and should be avoided.

Note that the total number of spherical harmonic coefficients, including the C_{00} term, is equal to $(n_{max}+1)^2$ where n_{max} is the degree of the gravity field. Thus, as n_{max} becomes large, it quickly becomes difficult to compare the uncertainty of each spherical harmonic coefficient. Thus, before we look at the actual uncertainties of the covariance output, we define the n-th degree spherical harmonic variance as

$$\sigma_n^2 = \sum_{m=0}^{n} (\sigma_{C_{nm}}^2 + \sigma_{S_{nm}}^2) \tag{3.117}$$

In Equation 3.117, σ_n^2 is the unnormalized n-th degree spherical harmonic variance. The normalized spherical harmonic variance is simply $\sigma_n^2 / \sum_{m=0}^{n} (C_{nm}^2 + S_{nm}^2)$, where the denominator is equivalent to the degree variance defined by Kaula [30]. We use "ratio" to denote the units of the normalized spherical harmonic variance. This method is a convenient way of assessing the precision to which we can determine the spherical harmonic coefficients for each degree.

Table 3.5 shows the uncertainties of μ, spin state, and the first and second-degree spherical harmonic coefficients for case 1 and 2 for Itokawa, all in one standard deviation.

Table 3.5: Uncertainty results of Itokawa after five flybys with/without lidar measurements.

	Case 1 (Lidar On)			Case 2 (Lidar Off)		
	Nominal	**Consider**	**Smoother**	**Nominal**	**Consider**	**Smoother**
μ **[ratio]**	4.578717×10^{-4}	5.633964×10^{-4}	3.239329×10^{-4}	4.962439×10^{-4}	6.314587×10^{-4}	3.514977×10^{-4}
η_{SRP} **[n.d.]**	2.263708×10^{-4}	3.702789×10^{-4}	1.605640×10^{-4}	2.327557×10^{-4}	3.493386×10^{-4}	1.654869×10^{-4}
α **[rad.]**	2.1441×10^{-4}	2.5631×10^{-4}	1.5160×10^{-4}	2.2380×10^{-4}	2.8111×10^{-4}	1.5823×10^{-4}
β **[rad.]**	4.3738×10^{-4}	6.1846×10^{-4}	3.0945×10^{-4}	4.6192×10^{-4}	6.3303×10^{-4}	3.2690×10^{-4}
γ_0 **[rad.]**	1.1378×10^{-3}	1.8198×10^{-3}	8.0847×10^{-4}	1.2242×10^{-3}	2.0683×10^{-3}	8.6855×10^{-4}
$\dot{\gamma}$ **[rad./s]**	1.1048×10^{-9}	1.7735×10^{-9}	7.8423×10^{-10}	1.1820×10^{-9}	2.0060×10^{-9}	8.3810×10^{-10}
$\mathbf{C_{1,0}}$ **[n.d.]**	5.147×10^{-4}	3.562×10^{-3}	3.658×10^{-4}	8.641×10^{-4}	3.327×10^{-3}	6.116×10^{-4}
$\mathbf{C_{1,1}}$ **[n.d.]**	2.393×10^{-3}	9.910×10^{-3}	1.703×10^{-3}	4.295×10^{-3}	1.007×10^{-2}	3.044×10^{-3}
$\mathbf{C_{2,0}}$ **[n.d.]**	1.987×10^{-2}	2.940×10^{-2}	1.406×10^{-2}	2.085×10^{-2}	3.025×10^{-2}	1.475×10^{-2}
[ratio]	0.0612	0.0905	0.0433	0.0642	0.0931	0.0454
$\mathbf{C_{2,1}}$ **[n.d.]**	8.996×10^{-3}	1.698×10^{-2}	6.363×10^{-3}	9.713×10^{-3}	1.724×10^{-2}	6.870×10^{-3}
$\mathbf{C_{2,2}}$ **[n.d.]**	1.390×10^{-2}	2.643×10^{-2}	9.832×10^{-3}	1.511×10^{-2}	2.752×10^{-2}	1.069×10^{-2}
[ratio]	0.0981	0.1866	0.0694	0.1067	0.1943	0.0754
$\mathbf{S_{1,1}}$ **[n.d.]**	3.202×10^{-3}	1.011×10^{-2}	2.261×10^{-3}	3.982×10^{-3}	1.114×10^{-2}	2.810×10^{-3}
$\mathbf{S_{2,1}}$ **[n.d.]**	8.301×10^{-3}	1.400×10^{-2}	5.857×10^{-3}	1.016×10^{-2}	1.766×10^{-2}	7.167×10^{-3}
$\mathbf{S_{2,2}}$ **[n.d.]**	1.237×10^{-2}	2.061×10^{-2}	8.753×10^{-3}	1.449×10^{-2}	2.523×10^{-2}	1.025×10^{-2}
σ_1 **[n.d.]**	4.03085×10^{-3}	1.45998×10^{-2}	2.85391×10^{-3}	5.92016×10^{-3}	1.53771×10^{-2}	4.18813×10^{-3}
σ_2 **[n.d.]**	2.98489×10^{-2}	4.97190×10^{-2}	2.11103×10^{-2}	3.27213×10^{-2}	5.40144×10^{-2}	2.31405×10^{-2}
[ratio]	0.08426	0.14035	0.05959	0.09237	0.15247	0.06532

In Table 3.5, the ratio of the gravitational parameter is given by the standard deviation divided by the value. As shown in both tables, the gravitational parameter is determined to less than 0.1% uncertainty together with the 2×2 gravitational coefficients of approximately $5 \sim 10\%$ uncertainty. Note that all uncertainties decrease as the observations are reprocessed backwards in time (i.e., smoothing), and the largest uncertainty in the gravitational coefficient is approximately 7.5% even if the lidar measurements are not available. For this particular flyby mission sequence, the uncertainties reduce by approximately 30% after smoothing, demonstrating its effectiveness. This result is expected since the initial a priori covariance do not represent the accurate description of parameter uncertainties, and reprocessing the observations backwards in time elegantly takes care of this problem.

Table 3.6 and 3.7 show the uncertainties of μ, spin state, and the first and second-degree spherical harmonic coefficients for case 1 and 2 for Didymos and Eros, all in one standard deviation.

Table 3.6: Uncertainty results of Didymos after five flybys with/without lidar measurements.

	Case1 (Lidar On)			**Case 2 (Lidar Off)**		
	Nominal	**Consider**	**Smoother**	**Nominal**	**Consider**	**Smoother**
μ **[ratio]**	3.197259×10^{-4}	5.324993×10^{-3}	2.262714×10^{-4}	3.819699×10^{-4}	6.811407×10^{-4}	2.703229×10^{-4}
η_{SRP} **[n.d.]**	1.910322×10^{-4}	3.816721×10^{-3}	1.353463×10^{-4}	1.950423×10^{-4}	3.024037×10^{-3}	1.381413×10^{-4}
α **[rad.]**	7.2485×10^{-4}	1.5702×10^{-2}	5.1292×10^{-4}	8.1855×10^{-5}	1.7895×10^{-2}	5.7949×10^{-4}
β **[rad.]**	2.4632×10^{-4}	2.7130×10^{-3}	1.7420×10^{-4}	2.7171×10^{-4}	3.0412×10^{-3}	1.9218×10^{-4}
γ_0 **[rad.]**	1.3130×10^{-3}	3.6344×10^{-8}	9.2928×10^{-4}	1.4629×10^{-3}	2.6804×10^{-2}	1.0357×10^{-3}
$\dot{\gamma}$ **[rad./s]**	1.2679×10^{-9}	5.585×10^{-7}	8.9734×10^{-10}	1.4202×10^{-9}	3.2603×10^{-8}	1.0054×10^{-9}
$\mathbf{C_{1,0}}$ **[n.d.]**	6.934×10^{-4}	1.517×10^{-2}	4.911×10^{-4}	1.397×10^{-3}	1.658×10^{-2}	9.905×10^{-4}
$\mathbf{C_{1,1}}$ **[n.d.]**	1.657×10^{-3}	6.232×10^{-2}	1.172×10^{-3}	1.773×10^{-3}	6.476×10^{-2}	1.255×10^{-3}
$\mathbf{C_{2,0}}$ **[n.d.]**	5.627×10^{-3}	8.412×10^{-2}	3.983×10^{-3}	6.923×10^{-3}	9.479×10^{-2}	4.901×10^{-3}
[ratio]	0.0887	1.3264	0.0628	0.1092	1.4946	0.0773
$\mathbf{C_{2,1}}$ **[n.d.]**	2.963×10^{-3}	6.627×10^{-2}	2.096×10^{-3}	3.181×10^{-3}	6.565×10^{-2}	2.251×10^{-3}
$\mathbf{C_{2,2}}$ **[n.d.]**	3.892×10^{-3}	1.365×10^{-1}	2.754×10^{-3}	4.298×10^{-3}	1.517×10^{-1}	3.042×10^{-3}
[ratio]	0.9505	33.3424	0.6725	1.0496	37.0527	0.7430
$\mathbf{S_{1,1}}$ **[n.d.]**	2.002×10^{-3}	8.437×10^{-2}	1.417×10^{-3}	2.214×10^{-3}	8.467×10^{-2}	1.567×10^{-3}
$\mathbf{S_{2,1}}$ **[n.d.]**	2.883×10^{-3}	6.055×10^{-2}	2.040×10^{-3}	3.209×10^{-3}	6.709×10^{-2}	2.271×10^{-3}
$\mathbf{S_{2,2}}$ **[n.d.]**	5.116×10^{-3}	2.408×10^{-1}	3.622×10^{-3}	5.455×10^{-3}	2.383×10^{-1}	3.861×10^{-3}
σ_1 **[n.d.]**	2.69014×10^{-3}	1.05982×10^{-1}	1.90348×10^{-3}	3.16192×10^{-3}	1.07878×10^{-1}	2.23817×10^{-3}
σ_2 **[n.d.]**	9.49122×10^{-3}	3.02921×10^{-1}	6.71729×10^{-3}	1.07975×10^{-2}	3.12411×10^{-1}	7.64268×10^{-3}
[ratio]	0.14934	4.76632	0.10569	0.16989	4.91564	0.12025

Table 3.7: Uncertainty results of Eros after five flybys with/without lidar measurements.

	Case 1 (Lidar On)			Case 2 (Lidar Off)		
	Nominal	**Consider**	**Smoother**	**Nominal**	**Consider**	**Smoother**
μ **[ratio]**	8.164935×10^{-6}	5.1618×10^{-2}	5.783082×10^{-6}	2.973216×10^{-5}	4.806984×10^{-2}	2.102136×10^{-5}
η_{SRP} **[n.d.]**	3.711550×10^{-4}	4.078417×10^{-1}	2.711491×10^{-4}	4.279977×10^{-4}	3.260102×10^{-1}	3.181783×10^{-4}
α **[rad.]**	4.3721×10^{-5}	2.2745×10^{-1}	3.0992×10^{-5}	5.2297×10^{-5}	1.8233×10^{-1}	4.7064×10^{-5}
β **[rad.]**	2.8594×10^{-5}	8.8568×10^{-2}	2.0420×10^{-5}	4.599×10^{-5}	1.0781×10^{-1}	3.7392×10^{-5}
γ_0 **[rad.]**	4.9308×10^{-5}	2.4100×10^{-1}	3.4965×10^{-5}	7.7360×10^{-5}	1.9150×10^{-1}	5.4903×10^{-5}
$\dot{\gamma}$ **[rad./s]**	1.7456×10^{-11}	7.0725×10^{-8}	1.2351×10^{-11}	2.5210×10^{-11}	6.2950×10^{-8}	1.7863×10^{-11}
$\mathbf{C_{1,0}}$ **[n.d.]**	2.675×10^{-5}	7.058×10^{-2}	1.894×10^{-5}	6.501×10^{-5}	1.847×10^{-1}	4.603×10^{-5}
$\mathbf{C_{1,1}}$ **[n.d.]**	2.571×10^{-5}	3.763×10^{-1}	1.819×10^{-5}	3.055×10^{-5}	3.835×10^{-1}	2.161×10^{-5}
$\mathbf{C_{2,0}}$ **[n.d.]**	5.148×10^{-5}	2.856×10^{-1}	3.655×10^{-5}	1.151×10^{-4}	3.202×10^{-1}	8.158×10^{-4}
[ratio]	0.0004	2.4350	0.0003	0.0010	2.7298	0.0007
$\mathbf{C_{2,1}}$ **[n.d.]**	4.320×10^{-5}	3.212×10^{-1}	3.055×10^{-5}	5.249×10^{-5}	3.290×10^{-1}	3.715×10^{-5}
$\mathbf{C_{2,2}}$ **[n.d.]**	3.538×10^{-5}	5.420×10^{-1}	2.502×10^{-5}	3.918×10^{-5}	5.082×10^{-1}	2.772×10^{-5}
[ratio]	0.0007	10.1897	0.0005	0.0007	489.4125	0.0005
$\mathbf{S_{1,1}}$ **[n.d.]**	2.985×10^{-5}	2.106×10^{-1}	2.111×10^{-5}	3.415×10^{-5}	2.147×10^{-1}	2.417×10^{-5}
$\mathbf{S_{2,1}}$ **[n.d.]**	3.001×10^{-5}	2.450×10^{-1}	2.123×10^{-5}	3.521×10^{-5}	2.566×10^{-1}	2.494×10^{-5}
$\mathbf{S_{2,2}}$ **[n.d.]**	3.391×10^{-5}	5.243×10^{-1}	2.398×10^{-5}	3.778×10^{-5}	5.429×10^{-1}	2.673×10^{-5}
[ratio]	0.0019	28.8942	0.0013	0.0021	29.9223	0.0015
σ_1 **[n.d.]**	4.76166×10^{-5}	4.36990×10^{-1}	3.36964×10^{-5}	7.95297×10^{-5}	4.76770×10^{-1}	5.63009×10^{-5}
σ_2 **[n.d.]**	8.84263×10^{-5}	9.01868×10^{-1}	6.26192×10^{-5}	1.42168×10^{-4}	9.10886×10^{-1}	1.00703×10^{-4}
[ratio]	0.00068	6.93346	0.00048	0.00109	7.00278	0.00077

As we compare Table 3.5 through 3.7, it is observed that larger asteroids yield smaller fractional uncertainty in μ as well as higher-degree and higher-order spherical harmonic coefficients except for the C_{22} term of Didymos. The spin state is better determined for Didymos and Eros than that of Itokawa by one order of magnitude. This can be attributed to the spin rate of the system, with Itokawa having the slowest spin rate of 12.1 $[hrs]$, Eros 5.27 $[hrs]$, and Didymos 2.25 $[hrs]$. It is important to note that, for a faster spinning body, small errors in the reference values may throw the spacecraft dynamics out of the linear regime to lend the filter to diverge. Thus, it is desired to have denser data and obtain the filtering solution more rapidly and frequently in the case of faster spinning asteroids. Although we modeled all three asteroids as principal-axis rotators, the same analysis can be performed for a precessing body. Such an analysis is omitted for space purposes.

3.12 Conclusion

In this chapter, we discussed the framework in which the spacecraft dynamics, solar radiation pressure, gravitational parameter, spin state, higher-degree and higher-order gravity fields, and maneuvers can be estimated from Doppler tracking, Earth ranging, optical, and lidar measurements. The spacecraft dynamics are subject to the perturbations from the higher-degree and higher-order gravity fields, solar radiation pressure (SRP), solar tide, and maneuvers. The flyby parameters were targeted via Newton-Raphson method via STM.

The results show that the lidar measurement is shown to be effective in reducing the μ uncertainty in the first flyby. However, after multiple flybys are performed, the benefit of having lidar measurement is small. The current flyby sequence provides approximately $5 \sim 10\%$ uncertainty for the second-degree gravitational coefficients. The consider covariance grows during the last flyby, indicating the significance of the effects of the higher-degree and higher-order gravity fields on the spacecraft dynamics. This result implies that the third and fourth gravity fields can be estimated. In addition to the consider covariance analysis, smoother uniformly reduced the uncertainties of the estimated states by approximately 30%.

The overall performance of the flyby covariance analysis shows that a series of multiple slow flybys is sufficient for the initial phase of the spacecraft rendezvous mission and the orbit phase may be eliminated for some mission architecture, aiding a rapid and robust characterization of small body parameters.

Chapter 4

Spin State and Moment of Inertia Characterization of 4179 Toutatis

The previous two chapters analyzed the performance of the covariance analysis around small bodies. These analyses were carried out without processing the actual observations, determining the level of characterization that we can achieve for the asteroid parameters by performing a series of flybys. In this chapter, we estimate the spin state of a near-Earth asteroid 4179 Toutatis by processing the actual observations. This analysis is an application of the least-squares filter that we have discussed so far and shall be considered in the same context.

The 4.5 km-long near-Earth asteroid 4179 Toutatis (hereafter Toutatis) is close to a $4:1$ orbital resonance with the Earth, and has made six close Earth flybys since its discovery in 1989 [44]. The first radar imaging campaigns of Toutatis in 1992 and 1996 were led by Ostro and Hudson at Arecibo Planetary Radar and Goldstone Solar System Radar, and their results revealed a tumbling, non-principal axis (NPA) rotator in a two-lobe configuration [23, 25, 26, 43, 44, 64], as shown in Figure 4.1 (provided by courtesy of Michael Busch). Its recent flyby around Earth in December 2012 was observed extensively at the Goldstone and Very Large Array (VLA) radar telescopes.

Hudson and Ostro [25] discussed that Toutatis' tumbling rotation could be described as a 5.41-day spin period around its long axis with the precession period of 7.35 days around the asteroid's angular momentum vector. Scheeres et al. [62] showed that the current Toutatis' NPA spin state is consistent with having close flybys between the asteroid and the Earth. This NPA rotation mode becomes an advantage when estimating, or at least constraining, the mass distribution of the body. The NPA rotation mode is a complex function of the initial spin state (i.e., orientation and angular

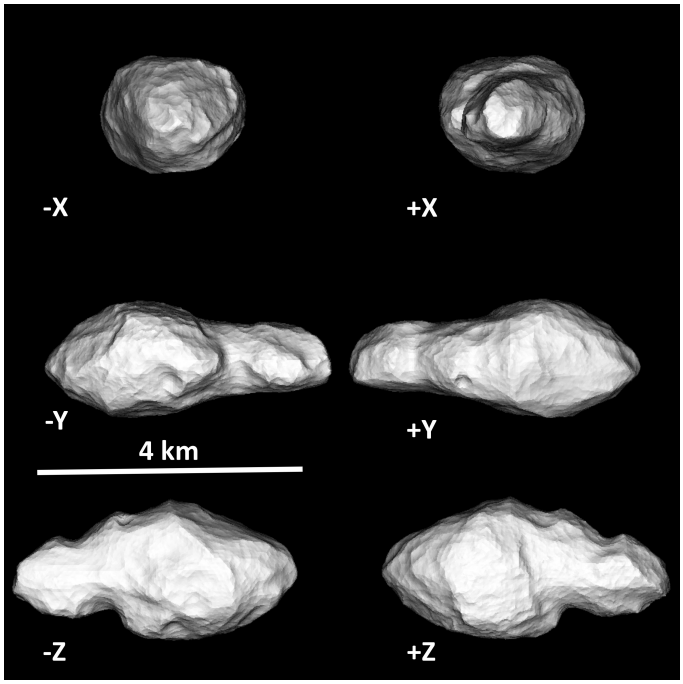

Figure 4.1: Toutatis shape model, refined from that of Hudson et al. [23], and viewed from along its principal axes (provided by courtesy of Michael Busch). The x-, y-, and z-axes are the long, intermediate, and short principal axes respectively. The model is based on the 1992-2008 images only.

velocity), moments of inertia, and center-of-mass-center-of-figure (COM-COF) offset. All of these parameters are estimated in a least-squares sense by processing the radar images captured with the Arecibo Planetary Radar and the Goldstone Solar System Radar from 1992 to 2008. As the moments of inertia and COM-COF offset are functions of the mass distribution of the body, they allow one to put a strong constraint on the mass and density distribution of the body. Such a constraint cannot be enforced on a principal-axis rotator simply by looking at its rotation mode, as its spin state only depends on the rotation axis and the rotation period. That is, its rotational dynamics do not depend on the mass distribution.

The estimation of the aforementioned parameters was performed prior to the December 2012 apparition. The spin state dynamics as well as the uncertainties of the Euler angles and angular velocity of the converged solution are then propagated to December 2012 in order to compare the dynamical model to the most recent Toutatis observations. The results show that the moment

of inertia ratios are estimated within a few percent of the values, and the predicted Toutatis' orientation fit the actual observation in 2012 within the formal uncertainty of 20°-30° for each of the 3-1-3 Euler angles. It is the first time that an Earth-crossing asteroid's spin state has been estimated to this precision from ground observations. With the reconstruction of the Toutatis shape model in progress with the most recent radar images, the estimated moment of inertia ratios and the COM-COF offset will be used to constrain the internal density distribution of the body in the future. The same technique of rotational dynamics estimation can be applied to any other tumbling body, given sufficiently accurate observations.

This work has been carried out in collaboration with Michael Busch, and the author would like to acknowledge his contribution.

4.1 Rotational Dynamics

The motion of a rotating rigid body is reviewed in this section. The formulation that we develop for Toutatis is different from the one presented in Chapter 3 (Section 3.5). As the image data recorded by the radar telescopes is converted into the instantaneous Euler angles and angular velocity of the body, we develop an algorithm to express the rotational dynamics of Toutatis by these parameters. Most of the equations are discussed in detail by Schaub and Junkins [55], and only the key equations are presented here.

4.1.1 Euler Angles

An inertial frame and a body-fixed frame can be related via the rotation matrix composed of the 3-1-3 Euler angles, as was discussed in Section 3.5 (Figure 3.3). As Toutatis exhibits a tumbling motion, α and β are no longer constant, and γ cannot be expressed as a linear function. Thus, the attitude coordinates $\vec{\alpha} = (\alpha, \beta, \gamma)$ must be numerically propagated. Using the Euler angles, the rotation matrix $[BN]$ that maps a vector from the inertial frame to the body frame is given in a similar manner to Equation 3.39 as

$$[BN] \quad = \quad \mathscr{R}_{3,\gamma} \cdot \mathscr{R}_{1,\beta} \cdot \mathscr{R}_{3,\alpha} \tag{4.1}$$

where $\mathscr{R}$ is the rotation matrix defined in Equation 3.40 through 3.42. These Euler angles are the direct measures of the orientation of a rigid body in the inertial frame, which motivates to express their dynamical equations in order to relate a set of Euler angles at one epoch to that at another. Without proof, the time derivative of the 3-1-3 Euler angles ($\vec{\alpha}$) is given by the following equation:

$$\dot{\vec{\alpha}} \quad = \quad \frac{1}{\sin\beta} \begin{bmatrix} \sin\gamma & \cos\gamma & 0 \\ \cos\gamma\sin\beta & -\sin\gamma\sin\beta & 0 \\ -\sin\gamma\cos\beta & -\cos\gamma\cos\beta & \sin\beta \end{bmatrix} \vec{\omega}_B \quad = \quad [C(\vec{\alpha})]\vec{\omega}_B \tag{4.2}$$

where $\vec{\omega}$ is the angular velocity. Note that the angular velocity must be expressed in the body frame, as indicated by the B subscript. Equation 4.2 suffers a singularity when $\beta = 0°$ or $180°$ because the first and third rotation axes are aligned in these two cases. These conditions were never encountered for the whole duration of Toutatis' rotational dynamics propagation.

The rotation matrix $[BN]$ becomes useful when computing the torques due to the Earth and sun, as the orbit of a planet is generally expressed in the inertial frame but the torque computation must be performed in the body frame. The torque computation and orbit propagation methods are discussed in Section 4.1.3 and Section 4.2, respectively.

4.1.2 Angular Velocity

The time derivative of the angular velocity is computed by Euler's equation. In order to derive the equation, we define the angular momentum around the center of mass as

$$\vec{H}_{CM} \quad = \quad I_{CM}\vec{\omega}_{CM} \tag{4.3}$$

where the inertia tensor I_{CM} is a constant, symmetric 3×3 tensor in the body frame. Then, the rate of change of the angular momentum around the center of mass in the body frame is related to the torque ($\vec{L}_{B,CM}$) acting on the system as

$$\dot{\vec{H}}_{B,CM} = I_{B,CM}\dot{\vec{\omega}}_{B,CM} + [\tilde{\omega}_{B,CM}]I_{B,CM}\vec{\omega}_{B,CM} = \vec{L}_{B,CM} \tag{4.4}$$

where the tilde denotes the cross-product operator defined as

$$[\tilde{\omega}] = \begin{bmatrix} 0 & -\omega_3 & \omega_2 \\ \omega_3 & 0 & -\omega_1 \\ -\omega_2 & \omega_1 & 0 \end{bmatrix} \tag{4.5}$$

By rearranging Eq. 4.4, Euler's equation is obtained as

$$\dot{\vec{\omega}}_{B,CM} = I_{B,CM}^{-1}\left(-[\tilde{\omega}_{B,CM}]I_{B,CM}\vec{\omega}_{B,CM} + \vec{L}_{B,CM}\right) \tag{4.6}$$

The computation of the external torque is discussed in the next section.

4.1.3 External Torque

The external torque $\vec{L}_{B,CM}$ in the body frame about the center of mass of the rigid body due to an external spherical mass can be modeled as

$$\vec{L}_{B,CM} = -M_s\vec{r} \times \frac{\partial U}{\partial \vec{r}} \tag{4.7}$$

as discussed by Scheeres [57]. In Equation 4.7, U is the gravitational potential due to the rigid body, M_s is the mass of the external spherical body, and $\vec{r}$ is the position of the spherical body relative to the rigid body. Thus, in order to compute the external torque properly, it is necessary to know the gravity field of the rigid body (i.e., density distribution) and the relative position between

the rigid body and the sphere. The computation of the relative position is deferred to Section 4.2, and the potential expression is studied in this section.

The gravitational potential and the spherical harmonic coefficients are defined in Equation 1.13 and 1.14. By direct expansion, the first and second-degree spherical harmonic coefficients are shown to be functions of the COM-COF offset and the moments of inertia as follows:

$$\begin{cases} R^* C_{11} &= x_{CM} \\ R^* S_{11} &= y_{CM} \\ R^* C_{10} &= z_{CM} \end{cases} \tag{4.8}$$

$$\begin{cases} C_{20} &= \dfrac{1}{2M^*(R^*)^2}(I_{xx} + I_{yy} - 2I_{zz}) \\ C_{21} &= -\dfrac{1}{M^*(R^*)^2} I_{xz} \\ C_{22} &= \dfrac{1}{4M^*(R^*)^2}(I_{yy} - I_{xx}) \\ S_{21} &= -\dfrac{1}{M^*(R^*)^2} I_{yz} \\ S_{22} &= -\dfrac{1}{2M^*(R^*)^2} I_{xy} \end{cases} \tag{4.9}$$

Thus, as shown in Eq. 4.7, the COM-COF offset and the moment of inertia ratios give rise to the perturbations by the external torques through the first and second-degree gravity coefficients. In so many words, the observations (i.e., Euler angles discussed in Section 4.3) are related to the rotational dynamics in Eq. 4.6, enabling one to process their information to estimate the COM-COF offset and the moment of inertia ratios. Only a 2×2 gravity field is used to compute the

terrestrial and solar tidal torques, as the third-degree gravitational perturbations are proven to be negligible in the preliminary analysis.

Now that the general torque computation is discussed, the gravitational potential and acceleration of the first and second-degree spherical harmonic coefficients can be solved explicitly. The first-degree potential is expressed as

$$U_1 = \frac{GM^*}{r^3}\vec{r}\cdot\vec{r}_{CM} \tag{4.10}$$

which yields

$$\frac{\partial U_1}{\partial \vec{r}} = \frac{GM^*}{r^3}\left[1_{[3\times 3]} - 3\hat{r}\hat{r}\right]\cdot\vec{r}_{CM} = \frac{GM^*R^*}{r^3}\left[1_{[3\times 3]} - 3\hat{r}\hat{r}\right]\cdot\begin{bmatrix} C_{11} \\ S_{11} \\ C_{10} \end{bmatrix} \tag{4.11}$$

Thus, the acceleration due to the COM-COF offset is a linear function of itself. Substitution of Eq. 4.11 into Eq. 4.7 yields the torque due to the first-degree spherical harmonic coefficients as

$$\vec{L}_1 = -M_s\vec{r}\times\frac{\partial U_1}{\partial \vec{r}} = -\frac{GM^*M_s}{r^3}[\tilde{r}]\cdot\vec{r}_{CM} = -\frac{GM^*M_sR^*}{r^3}[\tilde{r}]\cdot\begin{bmatrix} C_{11} \\ S_{11} \\ C_{10} \end{bmatrix} \tag{4.12}$$

In addition, the second-degree potential is defined as

$$U_2 = \frac{G}{2r^3}I_T - \frac{3G}{2r^5}\vec{r}\cdot[I]\cdot\vec{r} \tag{4.13}$$

where I_T is the trace of the inertia tensor. Note that $\vec{r}\cdot[I]\cdot\vec{r}$ is the tensorial notation which yields a scalar and shall not be confused with the dot product of vectors. Then, the acceleration due to the second-degree potential becomes

$$\frac{\partial U_2}{\partial \vec{r}} = -\frac{3G}{2r^5} I_T \vec{r} + \frac{15G}{2r^7} \left(\vec{r} \cdot [I] \cdot \vec{r}\right) \vec{r} - \frac{3G}{r^5} [I] \vec{r} \tag{4.14}$$

which yields

$$\vec{L}_2 = \frac{3GM_s}{r^5} [\tilde{r}][I]\vec{r} \tag{4.15}$$

The external torque is exerted from both Earth and sun, so their contributions must be summed together.

4.2 Toutatis' Orbit

Toutatis is in an approximately 4:1 resonance with the Earth's orbit, in an eccentric, low-inclination orbit. Figure 4.2 shows the heliocentric orbit of Toutatis (blue) and Earth (red) in the inertial J2000 frame:

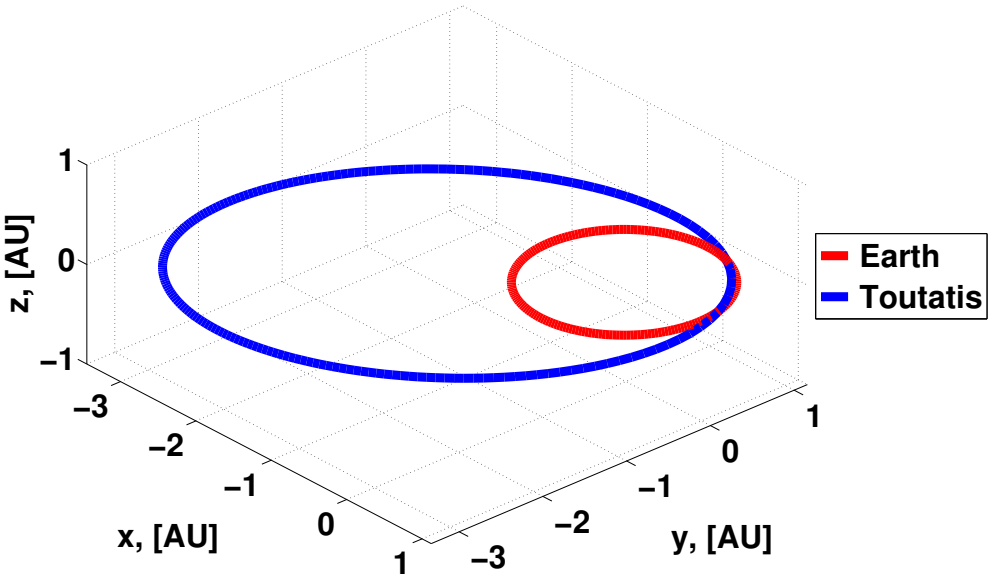

Figure 4.2: Toutatis' orbit in J2000 frame. The semi-major axis is $a = 2.53$ $[AU]$, the eccentricity is $e = 0.629$ $[n.d.]$, and the inclination is $\iota = 0.446$ $[deg.]$.

The observations, to be discussed in the next section, were taken between 1992 and 2012 during either the inbound or outbound leg of the Earth-crossings. Table 4.1 shows the observation epochs and the minimum distance from the Earth to Toutatis during these periods:

Table 4.1: Observation epochs and Earth-Toutatis distance.

Year	Month	D_{min} (Lunar Distance)
1992	November	9.40
1996	November	13.79
2000	October	28.75
2004	September	4.03
2008	November	19.56
2012	December	18.03

Toutatis' closest approach to Earth since its discovery occurred during the 2004 flyby, at a distance of four lunar distances, and the recent flyby in December 2012 was the closest Earth encounter until 2069. During the outbound leg of the December 2012 flyby, Toutatis was imaged by the Chinese Chang'e 2 spacecraft, a lunar probe that departed from Earth-Moon L2 Lagrange point to fly by Toutatis as an extended mission. This was the first time that an near-Earth asteroid was flown by a spacecraft while making a flyby of Earth.

As shown in Figure 4.2, the Earth apparition nearly coincides with the perihelion passage when the torque due to the solar tide becomes the greatest. In order to illustrate the significance of the Earth flybys and solar tidal torque on the change in the rotation dynamics of the asteroid, Figure 4.3 shows the signed change in the magnitude of the angular momentum, normalized by initial angular momentum magnitude at epoch in 1992, on the next page.

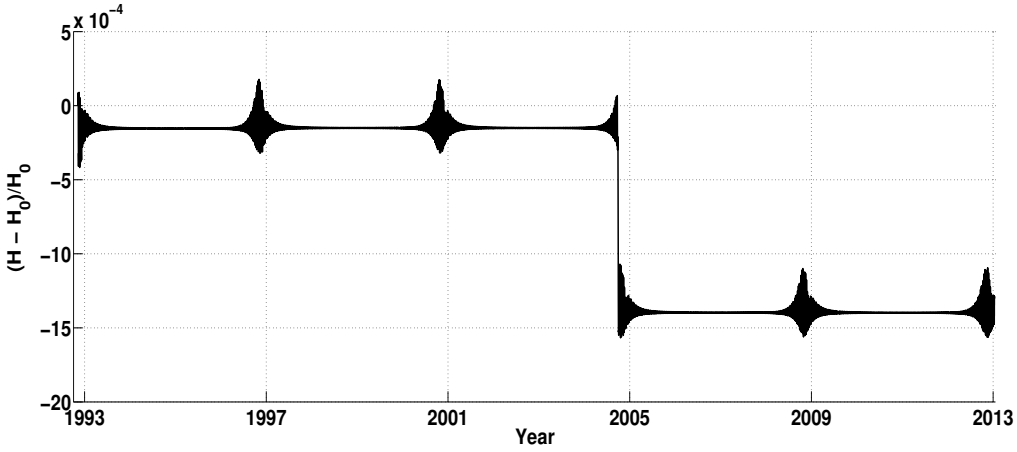

Figure 4.3: Change in the angular momentum magnitude over time.

Figure 4.3 shows that the solar tide exerts a strong torque around the perihelion passage, and the terrestrial torque reinforce to further change the rotation dynamics of Toutatis (0.1% change in the magnitude of the angular momentum in 20 years). The terrestrial tide is significant only during each Earth flyby, so the dynamical model only includes it from one month before until one month after each flyby epoch. The solar tide is active at all times, and the lunar tide is proven to be negligible in the preliminary analysis. Although the magnitude of the angular momentum is relatively constant in between each Earth flyby, there are small oscillations due to the solar tide that lead to significant orientation offsets. The 2004 apparition is by far the strongest perturbation from the terrestrial torque, as indicated by a large change in the magnitude of the angular momentum.

Not only the rotational dynamics, but Toutatis' orbit also changes due to perturbations after every Earth flyby and during the course of its heliocentric orbit, which prohibits one from using simple two-body dynamics in the heliocentric frame. Therefore, Toutatis' orbit is retrieved from the JPL Horizons system (http://ssd.jpl.nasa.gov/?horizons). The relative position of Toutatis with respect to Earth was obtained in 30-minute increments, and that of Toutatis with respect to the sun was obtained in one-day increments. The terrestrial torques were computed by linearly interpolating Toutatis' position in the inertial frame. When the solar tidal torque is computed, a more advanced interpolation method, referred to as the f-g series [16], is employed due to the large time interval in order to lower the orbit error to less than decameters. Assuming two-body

dynamics during each one-day interval, an approximation can be made with regard to the position of Toutatis in the heliocentric frame as follows:

$$\vec{r}(t) = f\vec{r}_0 + g\vec{V}_0 \tag{4.16}$$

where f, g, υ, and ζ are defined as

$$f = 1 - \frac{1}{2}\upsilon(t-t_0)^2 + \frac{1}{2}\upsilon\zeta(t-t_0)^3 + \cdots \tag{4.17}$$

$$g = (t-t_0) - \frac{1}{6}\upsilon(t-t_0)^3 + \cdots \tag{4.18}$$

$$\upsilon = \frac{\mu_{sun}}{r_0^3} \tag{4.19}$$

$$\zeta = \frac{\vec{r}_0 \cdot \vec{V}_0}{r_0^2} \tag{4.20}$$

which is the Taylor series expansion of the two-body dynamics with an assumption that $(t-t_0)$ is sufficiently small. Then, the orbit of Toutatis computed by the equations above are fed into the torque computation algorithm (Section 4.1.3).

4.3 Observation Data

The fundamental observation data used in our estimation was obtained by correlating radar images of Toutatis to the existing shape model. For example, Figure 4.4 shows the delay-Doppler radar images of Toutatis from Goldstone in 2000, and Arecibo in 2004 and 2008. Both Figure 4.4 and 4.5 are provided by courtesy of Michael Busch. Within each image in Figure 4.4, time delay, equivalent to distance from Earth, increases from top to bottom, and Doppler frequency, equivalent

to line-of-sight velocity, increases from left to right. These images have a total range extent of 5 $[km]$, and range resolution of 18.75 $[m/pixel]$ at Goldstone and 15 $[m/pixel]$ at Arecibo. The Doppler extents of the images vary; Doppler resolution was 0.033 $[Hz]$ at Goldstone, 0.011 $[Hz]$ at Arecibo in 2004, and 0.019 $[Hz]$ at Arecibo in 2008. In this projection, Toutatis appears to rotate counter-clockwise, but because of the asteroid's slow rotation, there is little rotation smear during the imaging during each day. The Goldstone images have low signal to noise ratios because of the greater distance to the asteroid in 2000 and the relatively low sensitivity of the telescope as compared to Arecibo.

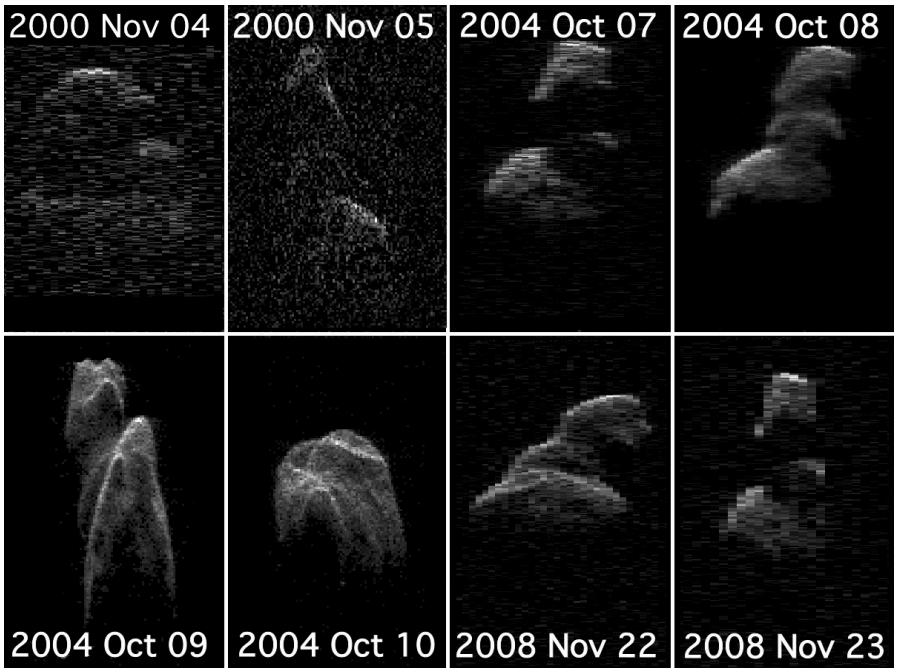

Figure 4.4: Delay-Doppler radar images of Toutatis from Goldstone in 2000, and Arecibo in 2004 and 2008.

Using these radar images, the 3-1-3 Euler angles, along with the body frame angular velocity, were recorded at each observation epoch. All observations are listed in Appendix B (Table B.1). There are varying numbers of observations for each apparition, totaling to 17 observations in 1992, 8 observations in 1996, 2 observations in 2000, 4 observations in 2004, and 2 observations in 2008. Uncertainties have been omitted for brevity, but range between 3° and 15° for Euler angles and

between 2 [deg./day] and 10 [deg./day] for components of the instantaneous spin vectors. These observations are processed by the filter (Section 4.4) to estimate the rotational dynamics and relevant physical parameters of Toutatis. Another example of the radar images are presented in Figure 4.5. These figures show comparisons between the radar observations and the predicted rotational dynamics with and without the terrestrial and solar torques.

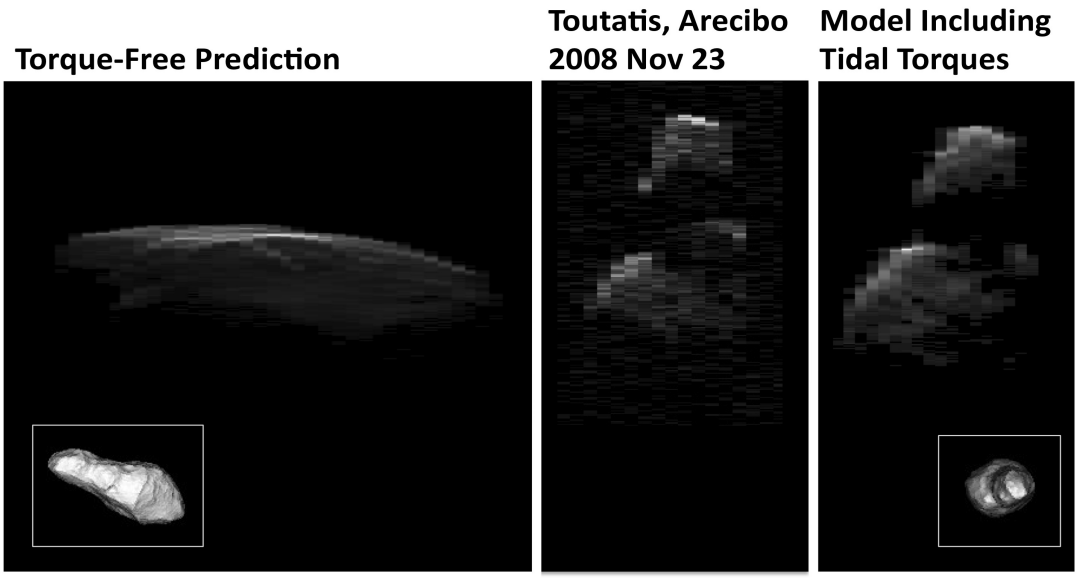

Figure 4.5: Predicted orientation of Toutatis on 2008 Nov 23.

Figure 4.5 shows the predicted orientation of Toutatis on 2008 Nov 23 using the best-fit torque-free spin state for the 2000-2004 images (left) compared to the observed orientation (center). The $\sim 100^\circ$ offset in the asteroid's orientation is due to tidal torques, primarily from the Earth during the 2004 flyby. Including the terrestrial torque resolves the discrepancy (right). Insets show the orientation of the Toutatis shape model projected onto the plane of the sky for the two spin state models. Arecibo viewed Toutatis nearly end-on, with the smaller lobe closer to Earth. The observed and modeled radar images are oriented as in Figure 4.4.

4.4 Filter Formulation

All of the 1992-2008 Euler angle observations are fit in a least-squares sense incorporating both terrestrial and solar tidal torques. For this purpose, a SRIF batch filter is implemented (Chapter 3), and observations are processed with respect to the epoch (i.e., t_0) to get the best estimates of the epoch state. The estimated quantities are the initial Euler angles, angular velocity, moment of inertia ratios, and a potential COM-COF offset shown below.

$$\vec{X} = \left[\begin{array}{cccc} \vec{\alpha} & \vec{\omega}_B & \bar{I} & \vec{r}_{CM} \end{array} \right] \tag{4.21}$$

The initial Euler angles and angular velocity were obtained by backward propagation of one of the observations during the 1992 flyby. The epoch is defined as 17:49:47 UTC on November 9, 1992 since it is one month prior to Toutatis' closest approach to the Earth during the 1992 apparition, and it coincides with the onset of the terrestrial torque for this data arc. As mentioned earlier, the moments of inertia are all normalized by I_{zz}. For qualitative analysis, it is only necessary to know the ratios of the moments of inertia to infer the internal structure of the body. The reference values of the moment of inertia ratios (Table 4.2) were estimated by Busch starting from the solution of Ostro et al. [44]. Note that the uncertainty of I_{zz} is tightened so the filter practically leaves this parameter out of the state vector (i.e., I_{zz} is not a free parameter as only the ratios are estimated).

Now, recall that the observables are the 3-1-3 Euler angles. Thus, the observation partial yields a simple form

$$\tilde{H}_k = \left[1_{[3\times3]} \quad 0_{[3\times11]} \right] \tag{4.22}$$

This observation partial is related to the epoch state deviation by the STM to process observations (Equation 3.9). The computation of the dynamics matrix (A) required to obtain the STM is described in Appendix B. There are only five non-zero components, and we list them individually in Appendix B.0.1.

Once the SRIF is implemented, the entire data arcs from 1992 through 2008 were fit simultaneously instead of fitting two consecutive apparitions and adding more data for the next observation arc. Although the angular velocity data is available, only the Euler angles are processed. The angular velocity data is used to validate that the filter solution models the spin state of Toutatis accurately. One difficulty encountered during the estimation process is that when the actual observation uncertainties were used to weight the data, the filter did not converge. Thus, the observation uncertainties were artificially inflated to ensure convergence. The observation uncertainties were uniformly increased to 15 deg. for 1992 through 2000 apparitions and 20 deg. for 2004 through 2008 apparitions.

4.5 Results

In this section, the solution from the least-squares filter is discussed. The initial conditions (i.e., reference state), one sigma a priori uncertainties, the converged solution, and estimated one sigma uncertainties of Toutatis' spin state at 17:49:47 UTC on November 9, 1992 are presented in Table 4.2.

Table 4.2: Initial condition and converged solution of the state vector and their uncertainties at 17:49:47 UTC on November 9, 1992.

Parameter	Initial Value	A priori 1-σ Uncertainty	Estimated Value	Estimated 1-σ Uncertainty
α $[deg.]$	144.863	15	145.498	3.762
β $[deg.]$	65.467	15	65.865	2.388
γ $[deg.]$	241.785	15	241.524	2.586
ω_1 $[^\circ/day]$	14.514	0.1	14.510	0.0994
ω_2 $[^\circ/day]$	33.532	0.1	33.529	0.0971
ω_3 $[^\circ/day]$	-98.713	0.1	-98.709	0.0957
$\bar{I}_{xx}$ $[n.d.]$	3.091	1×10^{-1}	3.0836	0.02822
$\bar{I}_{yy}$ $[n.d.]$	3.2178	1×10^{-1}	3.235	0.0714
$\bar{I}_{zz}$ $[n.d.]$	1	1×10^{-9}	1	1×10^{-9}
$\bar{I}_{xy}$ $[n.d.]$	0	1×10^{-2}	-7.1082×10^{-4}	0.00994
$\bar{I}_{yz}$ $[n.d.]$	0	1×10^{-2}	1.1707×10^{-3}	0.00939
$\bar{I}_{xz}$ $[n.d.]$	0	1×10^{-2}	1.3252×10^{-3}	0.00753
$\bar{r}_x$ $[km]$	0	1×10^{-3}	5.126×10^{-7}	1.6789×10^{-5}
$\bar{r}_y$ $[km]$	0	1×10^{-3}	-1.720×10^{-7}	3.3489×10^{-5}
$\bar{r}_z$ $[km]$	0	1×10^{-3}	-3.6732×10^{-7}	4.2864×10^{-5}

The converged solution shows that the off-diagonal terms in the inertia tensor and the COM-COF offset are indistinguishable from zero. Figure 4.6 show the Euler angle post-fit residuals normalized by the observation uncertainties.

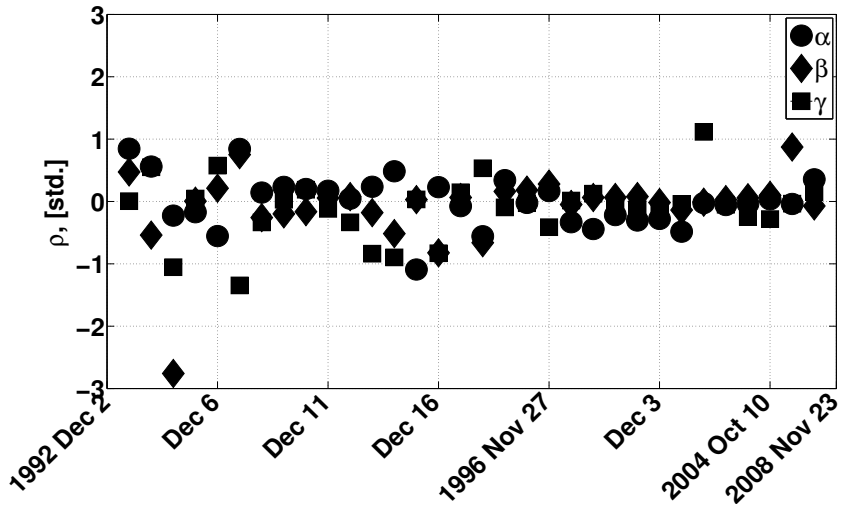

Figure 4.6: Euler angles post-fit residuals normalized by observation uncertainties. The circle markers are the first Euler angle, the diamond markers are the second, and the square markers are the third.

In Figure 4.6, all post-fit residuals lie within the 3 sigma bounds. One observation during 1992 apparition was recorded when Toutatis was observed near end-on, and it corresponds to the largest post-fit residual near -3 sigma bounds (i.e., a diamond marker). Figure 4.7 shows the normalized angular velocity residuals for the converged solution.

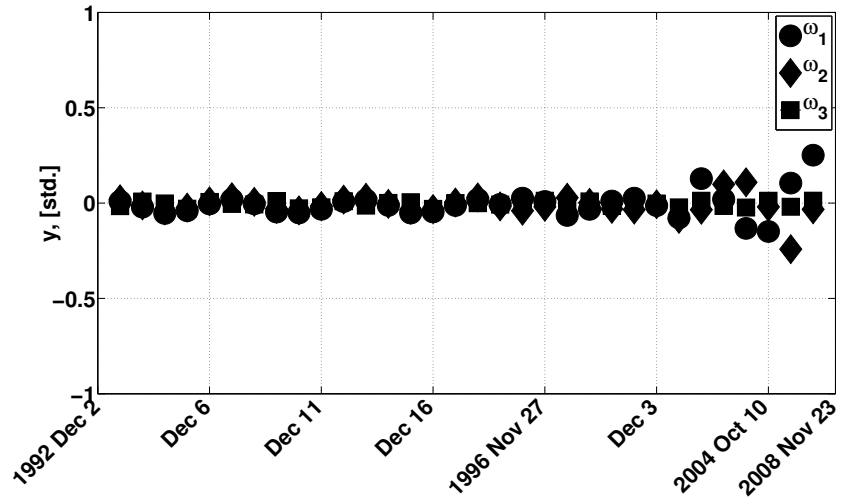

Figure 4.7: Angular velocity post-fit residuals normalized by observation uncertainties. The circle markers are the first components, the diamond markers are the second components, and the square markers are the third components of the angular velocity.

As shown in Figure 4.7, none of the observations exceed the 3 sigma bounds, or even 1 sigma bounds, and the angular velocity is well modeled by the converged solution.

4.6 Discussions and Future Observation Opportunities

The moment of inertia ratios I_{xx}/I_{zz} and I_{yy}/I_{zz} are estimated to fractional precision of 0.9% and 2.2% respectively. These measurements are unprecedented for any near-Earth asteroid, and will provide stringent constraints on Toutatis' internal density distribution. However, it is still impetuous to make any claims to the absence or presence of internal density variations at this time, because the current Toutatis shape model is not sufficiently accurate to distinguish mass anomalies $< 3\%$ of the asteroid's total mass from shape differences. The radar and Chang'e 2 images from 2012 show that the shape model of Hudson et al. [23] only corresponds to Toutatis' actual shape over $\sim 97\%$ of its volume. When a more accurate shape model of Toutatis is available, the moment ratio measurements will be sensitive to smaller mass anomalies.

Using the converged solution provided in Table 4.2, we extrapolated our model of Toutatis' spin state forward in time from 2008 to Toutatis' next Earth flybys in 2012 December and 2016 December/2017 January. The uncertainties in Toutatis' orientation grow with time; during the 2012 flyby they were $\sim 25^\circ$ (3σ). With that caveat, we predicted what we would see during future radar imaging campaigns (Figure 4.8).

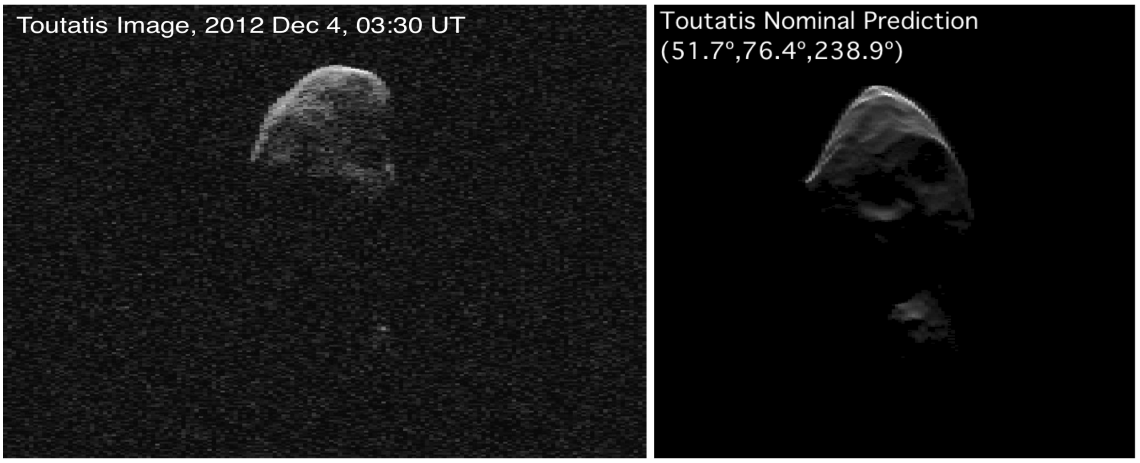

Figure 4.8: Actual observation (left) and predicted Toutatis' orientation (right) at 3:30 UT on December 4, 2012.

During the 2012 flyby, over Dec 3 - Dec 22, Goldstone obtained delay-Doppler resolution as fine as 0.025 $[\mu s]$ delay / 3.75 $[m]$ range resolution (closest approach was 0.04633 $[AU]$ on 2012 Dec 12). As viewed from Earth, Toutatis was seen from both broadsides (sub-Earth point near the $\pm z$ directions) and both ends (sub-Earth near the $\pm x$ directions), viewing nearly the entire surface. The asteroid's orientations matched our predictions to within their uncertainties. Following the radar campaign, we have begun to refine our spin state model to specify Toutatis' orientation in 2012 to within a few degrees and to match the spin vector measurements from radar speckle tracking [12]. We will then be able to make a better comparison between our model and images from the Chang'e 2 flyby. The final results of the 2012 radar campaign will be the subject of a future research.

At the end of 2016 and the beginning of 2017, Toutatis will be much further from Earth than in 2012 (0.2512 $[AU]$ on 2016 Dec 29). Radar observations would be limited to Arecibo only, with delay resolution of ~ 1 $[\mu s]$ or 300 $[m]$ in range; which would still be sufficient to improve the spin state model, measuring the spin state change from the 2012 flyby. There will be no significant tidal torques from the Earth due to the 2016 flyby, because of the greater distance. After 2016, Toutatis will not approach within 0.5 AU of Earth until 2065, when it begins the next set of once-per-four-years flybys, and there will be no additional radar opportunities until then. There will be

frequent opportunities for optical lightcurve observations, which could in principle lead to a YORP measurement.

4.7 Conclusions

In this chapter, a method to estimate the rotational dynamics of a tumbling body was described. Specifically, this method is applied to estimate the rotational dynamics of 4179 Toutatis, which is a near-Earth asteroid that has been making an Earth flyby approximately every four years. The spin state estimation is realized by directly relating the center-of-mass-center-of-figure (COM-COF) offset and the moment of inertia ratios to the spherical harmonic coefficients of the first and second-degree gravity potential, which are the driving forces of the external torque due to an external spherical body. The dynamical model included the solar and terrestrial torques as perturbations. The Euler angles data between 1992 and 2008 obtained at Goldstone and Arecibo were processed to show that the asteroid has negligible COM-COF offset, and that the estimated moment of inertia ratios predicted Toutatis' December 2012 orientation within the formal uncertainties of 20°-30°. In the future, the 2012 observations will be used to refine the spin state model and compare it to an improved Toutatis shape model to constrain the asteroid's internal structure.

Chapter 5

Internal Density Distribution Estimation

The previous chapter touched on how we can constrain the internal density distribution within a body by estimating the inertia tensor and the COM-COF offset. In this chapter, we explore methods to detect and characterize the internal density distribution of small bodies using the gravity field and shape of the body as data. Both data sets are determined from orbit determination process, which re-emphasizes the importance of the numerical covariance analysis in Chapter 3. The estimated internal density distribution can be used to reconstruct the gravity field environment near the surface of the body where the conventional spherical harmonic gravity field breaks down. Such a technique can be particularly useful for proximity operations. The previous chapters (Chapter 2 through 4) addressed the remote characterization of small bodies, while the next three chapters are dedicated to the interior characterization of and proximity operations around small bodies.

As more and more small body missions are planned, the demand for studying the internal structure of small bodies is increasing. Understanding the internal structure of small bodies holds the key to their formation process, and it is believed that it will ultimately help humans decipher the evolutionary process of the entire solar system. Such demand motivates performing proximity operations in order to collect specimen from the surface, which puts stringent constraints on the internal density distribution within a body. In order to support the close proximity operations of the mission, it is necessary to develop an accurate gravity field valid to the surface.

One way to construct an accurate gravity field model is via the polyhedral gravity field [75]. The polyhedral gravity field is the most robust technique to express the gravity field environment,

as it contains information equivalent to infinitely many degree and order expansion of the exterior gravity field. Moreover, the convergence of the potential is guaranteed anywhere on the surface and outside of the body, which is an attractive feature to leverage for proximity operations. However, the accuracy of the polyhedral gravity field depends on the resolution of the shape model and the accuracy of the prescribed density distribution. In general, the shape model can be determined accurately through optical/ranging measurements, but the density distribution cannot be uniquely determined. An assumption is often made that the body density is homogeneous, but, for a majority of asteroid, this homogeneous density assumption may not be suitable. As the gravitation of a body can be modeled error-free had we obtained the error-free shape model and internal density distribution, it is worthwhile to attempt to achieve such a model for accurate trajectory design/safe navigation purposes. We will focus on the estimation of the density distribution as the shape model is usually determined with sufficient accuracy in the early phase of spacecraft rendezvous, as mentioned above.

Many researchers attempted to tackle the density estimation problem in the past, and our effort should be considered in the same context. Takahashi and Scheeres [68] addressed how to identify the heterogeneity in the density distribution by comparing the discrepancies in the spherical harmonic coefficients between a homogeneous body and OD solution. Also, they discussed the density estimation technique in an informal conference report [71] by leveraging the results of Scheeres et al. [60], where the density distribution was estimated from the spherical harmonic coefficients determined from OD. Zuber et al. [77] showed that the COM-COF offset of 433 Eros can be explained by small variations in Eros's internal mechanical structure, given the global homogeneity in surface composition. Park et al. [49] discussed the density estimation algorithm for mason models with spheres and cubes. The density values of the sphere/cubes were estimated by processing the range and range-rate observations. Their results revealed inherent difficulty of the density estimation for a mascon model. That is, particles close to each other become indistinguishable from one particle of the same total mass depending on the trajectory of the spacecraft, yielding higher uncertainties for the particles placed inward (i.e., farther from the spacecraft) and smaller uncertainties for those

placed near the surface of the body (i.e., closer to the spacecraft). In addition, recent effort by Russell et al. [53] and Asmar [6] discussed the detection of an iron core of Vesta by comparing the measured second-degree spherical harmonic coefficients to the prescribed core-mantle-crust model.

In this chapter, a generalized density estimation algorithm is investigated in order to produce an accurate gravity field model near the surface of the body. As the preliminary analysis, the discrepancies in the spherical harmonic coefficients are compared between the gravity fields generated by the heterogeneous and homogeneous density distributions. The following heterogeneous density distributions are modeled for 1999 KW4 and Castalia: the planar division, surface layer, a single core at the coordinate center, double core placed along the x-axis, a torus around the equator, a cylinder with rings, and blocks. Using the differences in the spherical harmonic coefficients, a constraint is enforced on the internal density distribution of an asteroid, creating an archive of characteristics associated with each degree spherical harmonic coefficients.

After the preliminary analysis, a generalized density estimation method is presented. We propose this method as the block density estimation, which dissects the entire body into small slivers and blocks, each homogeneous within itself, to estimate their density values. Remarkable similarities are observed between the block model and mascon model. However, the block estimation has significant advantage over the mascons, as it alleviates us from choosing a specific density map and the number of blocks can be controlled with ease to yield a unique solution to the density distribution. The results show that an accurate and consistent density distribution map is achieved by increasing the number of blocks, converging on the true density distribution as the resolution of the density map is increased. The estimated density distribution also computes the surface potential and acceleration within 10%, the accuracy that is not achievable with the conventional gravity field modeling technique. The block density estimation can be a useful tool to map out the gravity field environment in close proximity to small body's surface for accurate trajectory/safe navigation purposes.

5.1 Density Maps

If the density distribution is known a priori, the polyhedral gravity field can be used to compute the gravitation around the body. However, the inversion process of estimating the density distribution from a given gravity field is not trivial. This can be illustrated in a simple example where there are multiple concentric spheres and shells of the same mass.

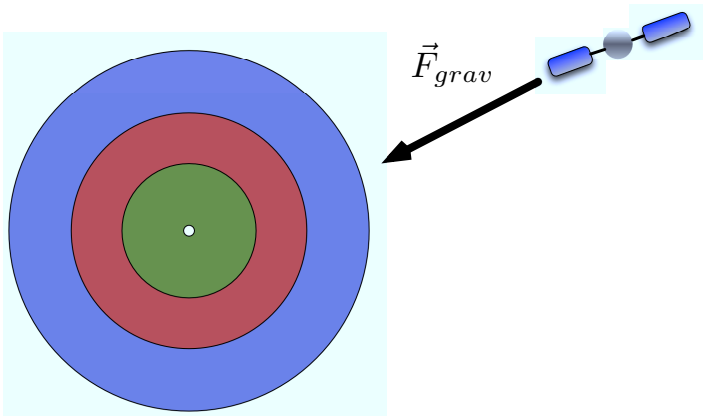

Figure 5.1: Concentric spheres and shells.

In Figure 5.1, as long as each sphere and shell have the same mass, the gravitation sensed by the spacecraft is identical ($\vec{F}_{grav}$), and there are infinitely many other choices of equal mass spheres/shells that satisfy this condition. This simple example illustrates that the inversion process is not unique, and infinitely many solutions of density distribution exist for a given gravity field.

It is worthwhile to pause for a moment and clarify a couple of terminologies. The density distribution contains two connotations: density map and density value. The density map refers to the distribution of different density regions within the body, and the density value is the value of density associated with each density region.

In Figure 5.2(a), the body has a density map with two different density regions ($\tilde{R}_{A,1}$ and $\tilde{R}_{A,2}$) with two different density values associated with them ($\rho_{A,1}$ and $\rho_{A,2}$). On the other hand, in Figure 5.2(b), the body has a density map with three different density regions ($\tilde{R}_{B,1}$, $\tilde{R}_{B,2}$, and $\tilde{R}_{B,3}$) with three different density values associated with them ($\rho_{B,1}$, $\rho_{B,2}$, and $\rho_{B,3}$). If the density

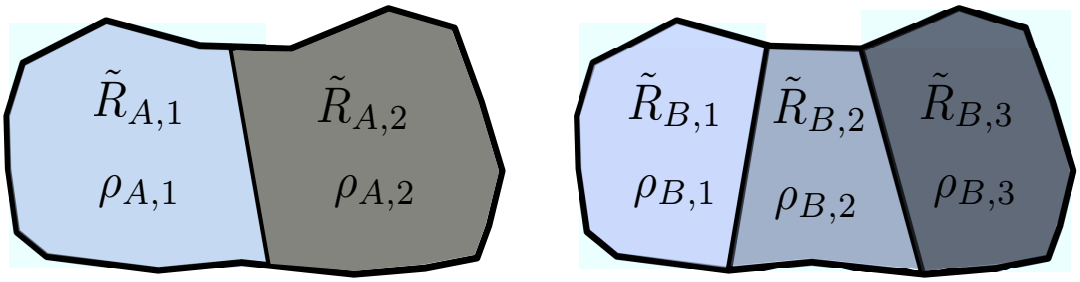

(a) Two-part density map (b) Three-part density map

Figure 5.2: Density maps and density values.

map is known, groups of different density regions can be constructed from the shape model, and the spherical harmonic coefficients can be computed by assigning artificial density values [76]. Scheeres et al. [60] discussed the estimation of the density values by fitting the spherical harmonic coefficients to the solution from orbit determination. Although the density values can be fitted to approximate the spherical harmonic coefficients in a least-squares sense, it is necessary to have an accurate density map prior to estimating the density values. That is, if there is a modeling mismatch in the density distribution map, the exact gravity field of the body cannot be extracted. Such a case is encountered, for instance, when estimating the density distribution shown in Figure 5.2(a), while using the density map in Figure 5.2(b). The given solution of $\rho_{B,1}$ and $\rho_{B,3}$ may not correspond to the true density values of $\rho_{A,1}$ and $\rho_{A,2}$. Furthermore, $\rho_{B,2}$ may not be the average of $\rho_{A,1}$ and $\rho_{A,2}$.

In this thesis, we model seven types of density maps: the planar division, surface layer, a single core at the coordinate center, two cores along x-axis, a torus around the equator, a cylinder with rings, and blocks. All the density maps are discussed in detail in Appendix C.

5.2 Density Value Estimation

The density values associated with the density map can be estimated in a least-squares sense. We will discuss such a formulation in this section.

5.2.1 Algorithm

The goal of the density value estimation algorithm is to match the potential of the heterogeneous density distribution to that of the measured gravity field (i.e., orbit determination solution). The measured gravity field is given as

$$U_{OD} = \frac{GM_{OD}}{r} + \frac{GM_{OD}}{R^*}\sum_{n=1}^{\infty}\sum_{m=0}^{n}\left(\frac{R^*}{r}\right)^{n+1} P_{nm}(\sin\phi)\begin{bmatrix}\cos(m\lambda)\\ \sin(m\lambda)\end{bmatrix}\cdot\begin{bmatrix}C_{nm}^{OD}\\ S_{nm}^{OD}\end{bmatrix} \tag{5.1}$$

where OD denotes the orbit determination solution. The two-body term is written separately from the higher-degree and higher-order perturbations. On the other hand, the potential of a heterogeneous body can be expressed as

$$U_{HT} = \sum_{p=1}^{N_p}\frac{G\rho_p V_p}{R^*}\sum_{n=0}^{\infty}\sum_{m=0}^{n}\left(\frac{R^*}{r}\right)^{n+1} P_{nm}(\sin\phi)\begin{bmatrix}\cos(m\lambda)\\ \sin(m\lambda)\end{bmatrix}\cdot\begin{bmatrix}C_{nm,p}^{HT}\\ S_{nm,p}^{HT}\end{bmatrix} \tag{5.2}$$

where HT stands for the heterogeneous distribution, p is the index for each density region, and N_p is the total number of the heterogeneous density regions. In so many words, Equation 5.2 states that the total potential is the summation of the potential contribution from each density region. In the next step, Equation 5.2 is transformed into the same form as Equation 5.1 by changing the order of summation, separating out the two-body terms from each density region, and scaling each term by the total mass determined from orbit determination.

$$\begin{aligned} U_{HT} &= \frac{GM_{OD}}{r}\left\{\frac{1}{M_{OD}}\sum_{p=1}^{N_p}\rho_p V_p\right\} \\ &+\frac{GM_{OD}}{R^*}\sum_{n=1}^{\infty}\sum_{m=0}^{n}\left(\frac{R^*}{r}\right)^{n+1} P_{nm}(\sin\phi)\begin{bmatrix}\cos(m\lambda)\\ \sin(m\lambda)\end{bmatrix}\cdot\left\{\frac{1}{M_{OD}}\sum_{p=1}^{N_p}\rho_p V_p\begin{bmatrix}C_{nm,p}^{HT}\\ S_{nm,p}^{HT}\end{bmatrix}\right\} \end{aligned} \tag{5.3}$$

Then, for the two potentials U_{OD} and U_{HT} to be identical, it is necessary to have

$$1 = \frac{1}{M_{OD}} \sum_{p=1}^{N_p} \rho_p V_p \tag{5.4}$$

$$\begin{bmatrix} C_{nm}^{OD} \\ S_{nm}^{OD} \end{bmatrix} = \frac{1}{M_{OD}} \sum_{p=1}^{N_p} \rho_p V_p \begin{bmatrix} C_{nm,p}^{HT} \\ S_{nm,p}^{HT} \end{bmatrix} \tag{5.5}$$

Equation 5.4 is the constraint on the total mass (i.e., $C_{00} = 1$), and Equation 5.5 is the constraint on the higher-degree and higher-order spherical harmonics. By defining an array of volume $[V] = [V_1, V_2, \dots]$ ($[1 \times N_p]$ array) and an array of density values $[\rho] = [\rho_1, \rho_2, \dots]$ ($[N_p \times 1]$ array), the total mass constraint can be written as

$$\frac{M_{OD} - [V][\rho]}{M_{OD}} = 0 \tag{5.6}$$

which is a linear function of $[\rho]$. In addition, Equation 5.5 can also be expressed as a linear function of $[\rho]$. For this purpose, a vector $[\tilde{C}_{nml}^{HT}]$ is defined, which is an array of the spherical harmonic coefficients ordered in the following manner:

$$[\tilde{C}_{nml}^{HT}] = [\ C_{10}^{HT},\ C_{11}^{HT},\ S_{11}^{HT},\ \dots,\ C_{NN}^{HT},\ S_{NN}^{HT}\ ] \tag{5.7}$$

where $\tilde{C}_{nm0}^{HT} = C_{nm}^{HT}$ and $\tilde{C}_{nm1}^{HT} = S_{nm}^{HT}$. For a $[n_{max} \times n_{max}]$ gravity field, there are $(n_{max}+1)^2$ spherical harmonic coefficients including C_{00}. Thus, the dimension of $[\tilde{C}_{nml}^{HT}]$ is a $[\{(n_{max}+1)^2 - 1\} \times 1]$ array because C_{00} is already constrained by Equation 5.6. Then, Equation 5.5 is rewritten in the matrix form as

$$\frac{1}{M_{OD}} \left[V_p \tilde{C}_{nml,p}^{HT} \right] [\rho] = [\tilde{C}_{nml}^{OD}] \tag{5.8}$$

where $\left[V_p \tilde{C}_{nml,p}^{HT} \right]$ indicates that the spherical harmonic coefficients of the p-th region are multiplied by the volume of the p-th region. Specifically, $\left[V_p \tilde{C}_{nml,p}^{HT} \right]$ ($[\{(n_{max}+1)^2 - 1\} \times N_p]$ array) is organized in the following manner.

$$\left[V_p \tilde{C}^{HT}_{nml,p}\right] = \begin{bmatrix} V_1 C_{10,1} & V_2 C_{10,2} & \dots & V_{N_p} C_{10,N_p} \\ V_1 C_{11,1} & V_2 C_{11,2} & \dots & V_{N_p} C_{11,N_p} \\ V_1 S_{11,1} & V_2 S_{11,2} & \dots & V_{N_p} S_{11,N_p} \\ \vdots & \vdots & \vdots & \vdots \\ V_1 S_{NN,1} & V_2 S_{NN,2} & \dots & V_{N_p} S_{NN,N_p} \end{bmatrix} \tag{5.9}$$

The computation of the nominal spherical harmonic coefficients ($\tilde{C}^{HT}_{nml,p}$) from the polyhedral model is detailed by Werner [76]. Then, a cost function J_ρ is constructed in order to minimize the difference between the nominal spherical harmonic coefficients and the measured gravity field:

$$\begin{aligned} J_\rho = & \frac{1}{2}\left(\frac{1}{M_{OD}}\left[V_p \tilde{C}^{HT}_{nml,p}\right][\rho] - [\tilde{C}^{OD}_{nml}]\right)^T W_{\tilde{C}} \left(\frac{1}{M_{OD}}\left[V_p \tilde{C}^{HT}_{nml,p}\right][\rho] - [\tilde{C}^{OD}_{nml}]\right) \\ & + \lambda_\rho \left(\frac{M_{OD} - [V][\rho]}{M_{OD}}\right) \end{aligned} \tag{5.10}$$

where $W_{\tilde{C}}$ is the weight matrix, and the Lagrange multiplier (λ_ρ) is utilized to ensure that the total mass constraint is enforced with no error. Note that the methodology discussed by Scheeres et al. [60] only constrains $C_{00} = 1$ in a least-squares sense. The weight matrix can be inherited from the covariance of the OD solution. In Equation 5.10, the cost function J_ρ is minimized with respect to the density vector $[\rho]$ by setting its partial to zero, yielding the least-squares solution.

$$[\rho] = \Lambda^{-1}[N_\rho + \mathscr{C}_\rho] \tag{5.11}$$

where the information matrix Λ, the normal matrix N_ρ, the constraint matrix $\mathscr{C}_\rho$, the Lagrange multiplier (λ_ρ), the constant ς, and the unconstrained density vector $[\tilde{\rho}]$ are given as

$$\Lambda = \left(\frac{1}{M_{OD}}\left[V_p\tilde{C}^{HT}_{nml,p}\right]^T\right) W_{\tilde{C}} \left(\frac{1}{M_{OD}}\left[V_p\tilde{C}^{HT}_{nml,p}\right]\right) \tag{5.12}$$

$$N_\rho = \frac{1}{M_{OD}}\left[V_p\tilde{C}^{HT}_{nml,p}\right]^T W_{\tilde{C}}[\tilde{C}^{OD}_{nml}] \tag{5.13}$$

$$\mathscr{C}_\rho = \frac{1}{M_{OD}}\lambda_\rho[V]^T \tag{5.14}$$

$$\lambda_\rho = \frac{1}{\varsigma}\left(M_{OD} - [V][\tilde{\rho}]\right) \tag{5.15}$$

$$\varsigma = [V]\Lambda^{-1}M_{OD}^{-1}[V]^T \tag{5.16}$$

$$[\tilde{\rho}] = \Lambda^{-1}N \tag{5.17}$$

Note that $[\tilde{\rho}]$ is the least-squares solution of the density vector without the total mass constraint. Then, the direct substitutions yield

$$[\rho] = \Lambda^{-1}\left\{\frac{1}{M_{OD}}\left[V_p\tilde{C}^{HT}_{nml,p}\right]^T W_{\tilde{C}}[\tilde{C}^{OD}_{nml}] + \frac{1}{\varsigma M_{OD}}\left(M_{OD} - [V][\tilde{\rho}]\right)[V]^T\right\} \tag{5.18}$$

5.2.2 Accuracy and Precision of the Estimated Density Distribution

The solution of the least-squares fit yields a unique solution for an over-determined system. However, the accuracy and precision of the solution are not easily quantifiable. As such, a couple of tools to check the accuracy and precision of the solution are introduced, namely the error variance and root-mean-square (RMS) error.

5.2.2.1 Error Variance

One of the tools that can be used to check the accuracy of the least-squares fit is the error variance. The n-th degree error variance ($\Delta\sigma_n$) is defined as

$$\Delta\sigma_n^2 = \sum_{m=0}^{n}(\Delta\bar{C}_{nm}^2 + \Delta\bar{S}_{nm}^2) / \sum_{m=0}^{n}(\bar{C}_{nm,OD}^2 + \bar{S}_{nm,OD}^2) \tag{5.19}$$

where

$$\begin{bmatrix}\Delta\bar{C}_{nm}\\ \Delta\bar{S}_{nm}\end{bmatrix} = \begin{bmatrix}\bar{C}_{nm,Estimated}\\ \bar{S}_{nm,Estimated}\end{bmatrix} - \begin{bmatrix}\bar{C}_{nm,OD}\\ \bar{S}_{nm,OD}\end{bmatrix} \tag{5.20}$$

The bar over the spherical harmonic coefficients denotes the normalized quantity defined by Kaula [30] and is summarized in Appendix D.1. The error variance represents the percentage error of the spherical harmonic coefficients between the least-square fit solution and the OD solution. As the first-degree coefficients are usually set to zero for the OD solutions (i.e., COM-COF offset is zero), the first-degree error variance is simply the sum of squares of the estimated spherical harmonic coefficients. By replacing the estimated quantities by those of a heterogeneous body and OD quantities by those of a homogeneous body, an archive of error variances can be compiled in order to detect inhomogeneity in the density distribution, which in turn can be used to constrain the possible density distributions for a given OD solution.

5.2.2.2 Root-mean-square Errors

In the real spacecraft missions, the true density distribution is unknown. Thus, the accuracy of the estimated density distribution cannot be directly evaluated. However, precision can be measured, which is the repetitiveness of the solution for different parametric settings. One way to check the precision of the solution is to see if a convergence is reached on a certain density distribution as the resolution of the density map is increased (see Section 5.3). The data points are scattered within the body to compute the root-mean-square (RMS) errors of the estimated density values.

$$RMS(x) = \sqrt{\frac{1}{N_{Data}} \sum_{i=1}^{N_{data}} (x_i - x_i^*)^2} \tag{5.21}$$

where N_{Data} is the number of the data points, x_i is the data value, and x_i^* is the density estimated from the highest-resolution density map (i.e., reference value). The RMS values can be computed for the spherical harmonic coefficients as well. The accuracy of the solution can be evaluated by replacing the reference value with the truth.

5.3 Density Map Estimation

Thus far, the least-squares formulation of the density **value** estimation has been discussed. However, retrieval of the true density **map** still remains to be solved. To address this problem, a generalized approach to the density estimation method is proposed, namely the block density estimation.

5.3.1 Algorithm

The block density estimation is similar to the work by Park et al. [49], where the entire body is filled with either cubes or spheres to recover the true density distribution of the body. In fact, block density estimation is motivated by their analysis. As the name implies, the block model (Appendix C.7) is used as the basis model of the density map. Therefore, when estimating the density values of the blocks, the resolution of the block segmentation directly maps into the accuracy of the estimated density values. The upside is that it is unnecessary to pick the "correct" density map in order to approximate the spherical harmonic coefficients from OD. As the number of blocks is increased, a more complicated density map can be estimated.

Although the block density estimation is similar to the estimation of the mascon model, there are slight, yet significant differences. Firstly, the morphology of the asteroid can be modeled without error (i.e., no concavity/extrusions/gaps between the blocks). The flawed shape model is a major source of error that gives rise to incorrect gravity field by mascons, but the block model is free from

such an error. Secondarily, the management of each block is more tractable than a sphere/cube, meaning that the size of each block can be controlled concisely. Furthermore, the total number of blocks can be controlled so the least-squares solution is unique (i.e., $N_{Blocks} < (n_{max}+1)^2$). This condition is hard to satisfy for a mascon model since the number of mass elements needed to simulate a continuous mass distribution grows rapidly, which motivated Park et al. to estimate the density values of each sphere/cube via navigation data. Although we treat each block individually in our analysis, the block density estimation method can be modified to connect adjacent blocks in order to form a chain of blocks that have the same density value.

5.3.2 Reconstruction of the Gravity Field from Estimated Density Distribution

After the density values of each block (and therefore those of each sliver) are estimated, the obtained density distribution can be used to compute the gravitation of the whole body via the polyhedral gravity field [75]. The accuracy of the reconstructed surface gravity field is of high importance as the exterior gravity field in Equation 1.13 is only valid outside the Brillouin sphere and does not converge near the surface of the body (see Chapter 6 for details).

In order to compute the gravity field of a body with a heterogeneous density distribution, the gravitation of each sliver is evaluated and summed over the whole body. This process requires subtracting the mass contribution of the smaller tetrahedron from the larger one for each sliver, as shown in Figure 5.3.

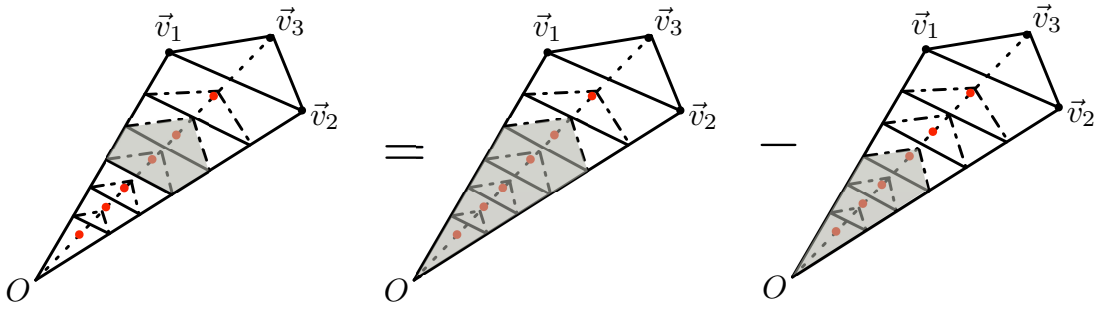

Figure 5.3: Gravitation of a sliver.

The same operation is iteratively performed for all slivers that make a shape model. The potential and acceleration errors between the estimated solution and the truth model will be plotted on the surface of the body in Section 5.6 and 5.8.2.

5.4 Comparison of the Error Variances for Different Density Maps

Comparison is made between the spherical harmonic coefficients generated from the heterogeneous density distributions and those generated from the homogeneous density distribution. We will investigate two asteroids, namely Castalia [24, 42] and 1999 KW4 [45] (Figure 5.4).

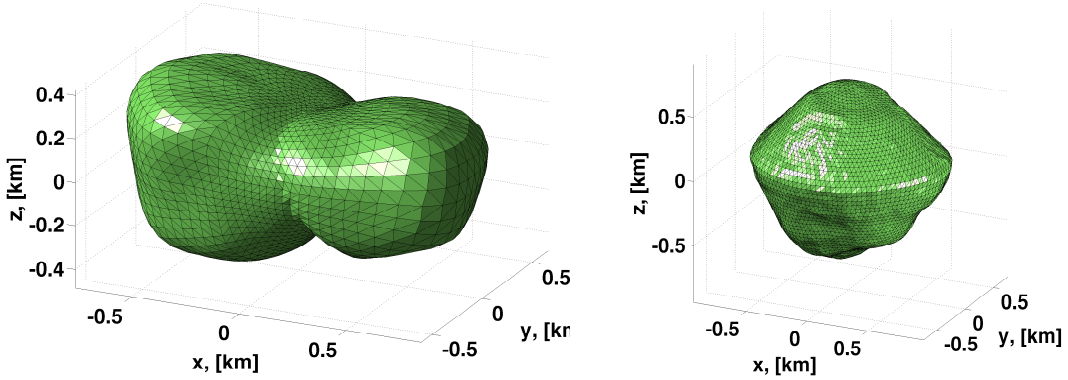

(a) Castalia (b) KW4

Figure 5.4: Shape models of Castalia and KW4.

As shown in Figure 5.4(a), Castalia is a contact-binary, which could possess two different density values associated with each lobe or two cores in each lobe. Thus, the planar division and double core models are investigated. We will also analyze the surface layer model and single core model. For KW4, it has been shown that loose material preferentially migrates towards the equatorial ridge of the body [58]. Therefore, the torus and cylinder models are used to separate the equatorial ridges from the central part of the body.

5.4.1 Castalia - Planar Division, Surface Layer, Single core, and Double core Models -

The shape model of Castalia is used to show how the spherical harmonic coefficients computed from the planar division, surface layer, single core, and double core models differ from those computed from the homogeneous density distribution model. For this purpose, the error variance is evaluated for different density maps. The total mass of the body is constrained by the uniform density of 2.1 $[g/cm^3]$. The surface layer is 50 $[m]$, and all cores have a radius of 200 $[m]$. Figure 5.5 shows the first through fourth-degree error variances for Castalia:

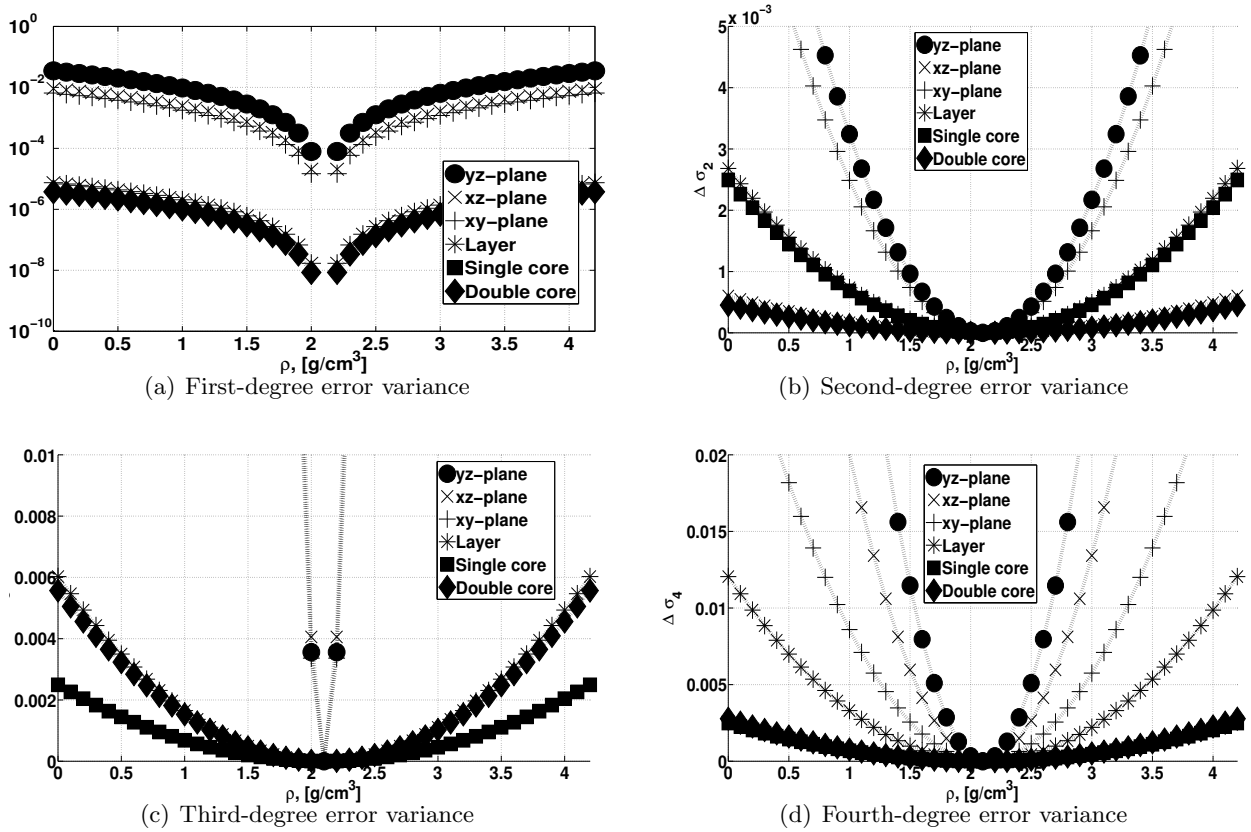

(a) First-degree error variance

(b) Second-degree error variance

(c) Third-degree error variance

(d) Fourth-degree error variance

Figure 5.5: First through fourth-degree error variances for Castalia.

In Figure 5.5, x-axis denotes the density value for a) the portion of the volume that lies in the positive-axis region for the planar division models, b) the surface layer, and c) the cores for both the single and double core models. For the double core model, the same density value is used

for both cores. As shown above, each density distribution model has a different signature, and its behavior varies from degree to degree. The concave shape is a common feature of all density maps. It is because the entire body is approaching toward/deviating away from the homogeneous density of 2.1 $[g/cm^3]$, at which point there are no errors in the spherical harmonic coefficients. In Figure 5.5(a), the first-degree error variance of the single core model is indistinguishable from zero and smaller than the scale of the plot.

5.4.2 Detection of a Core within the Body

Of all the heterogeneous density distributions plotted in Figure 5.5, it is particularly worthwhile to discuss the behavior of the single core model. The right-hand side of Equation 5.5 are the spherical harmonic coefficients from the heterogeneous density distribution. These spherical harmonic coefficients exhibits deviations from those of the homogeneous body. For a spherical core placed at the center of mass, the contributions to the higher-degree and higher-order coefficients vanish, and the spherical harmonic coefficients become only functions of the shape model. That is, the measured spherical harmonic coefficients (C_{nm}^{OD}, S_{nm}^{OD}) and constant-density spherical harmonic coefficients (C_{nm}^{CD}, S_{nm}^{CD}) are **identical** (except for the scaling factor, as discussed below). Similarly, a body with a spherical hollow/shell has the same spherical harmonic coefficients.

Now it seems that it is impossible to detect the core's presence by looking at the spherical harmonic coefficients. However, the total mass constraint can be used to detect the core. To verify this, Equation 5.5 is expanded to give

$$\begin{bmatrix} C_{nm}^{OD} \\ S_{nm}^{OD} \end{bmatrix} = \begin{bmatrix} C_{nm}^{Core} \\ S_{nm}^{Core} \end{bmatrix} = \frac{1}{M_{OD}} \rho V_{total} \begin{bmatrix} C_{nm}^{CD} \\ S_{nm}^{CD} \end{bmatrix} \tag{5.22}$$

Thus, for the spherical core model, each spherical coefficient obtained from the orbit determination solution (C_{nm}^{OD}, S_{nm}^{OD}) is the scaled value of the constant-density spherical harmonic coefficient (C_{nm}^{CD}, S_{nm}^{CD}). It is particularly important to note that this scaling factor $\rho V_{total}/M_{OD}$ is not a function of degree and order; the same scaling factor is used for all coefficients. This result

shows that the single core model is the easiest model to detect. That is, it is only necessary to show that all coefficients are scaled uniformly to detect the core's existence. In order to compute the core density, we take the difference of the spherical harmonic coefficients between the single core model and the homogeneous body to get

$$\begin{bmatrix} \Delta C_{nm} \\ \Delta S_{nm} \end{bmatrix} = \begin{bmatrix} C_{nm}^{Core} \\ S_{nm}^{Core} \end{bmatrix} - \begin{bmatrix} C_{nm}^{CD} \\ S_{nm}^{CD} \end{bmatrix} = -\frac{\Delta\rho V_{Core}}{M_{OD}} \begin{bmatrix} C_{nm}^{CD} \\ S_{nm}^{CD} \end{bmatrix} \tag{5.23}$$

from which the additional density in the core ($\Delta\rho$) can be obtained as

$$\Delta\rho = -\frac{M_{OD}}{V_{Core}} \frac{\Delta C_{nm}}{C_{nm}^{CD}} \tag{5.24}$$

Therefore, by assuming the size of the core (V_{Core}), the core density can be easily computed. One drawback is that it is impossible to constrain both the size of the core and the density value simultaneously, as they are multiplied by each other in the total mass constraint and are not independent from each other.

As an alternative approach, the same result can be obtained by comparing the potential of the homogeneous body with that of the spherical core model:

$$U_{CD} = \frac{GM_{CD}}{r} + \frac{GM_{CD}}{R^*} \sum_{n=1}^{\infty} \sum_{m=0}^{n} \left(\frac{R^*}{r}\right)^{n+1} P_{nm}(\sin\phi) \begin{bmatrix} \cos(m\lambda) \\ \sin(m\lambda) \end{bmatrix} \cdot \begin{bmatrix} C_{nm}^{CD} \\ S_{nm}^{CD} \end{bmatrix} \tag{5.25}$$

$$U_{Core}^{e} = \frac{GM_1}{r} + \frac{GM_1}{R^*} \sum_{n=1}^{\infty} \sum_{m=0}^{n} \left(\frac{R^*}{r}\right)^{n+1} P_{nm}(\sin\phi) \begin{bmatrix} \cos(m\lambda) \\ \sin(m\lambda) \end{bmatrix} \cdot \begin{bmatrix} C_{nm}^{CD} \\ S_{nm}^{CD} \end{bmatrix} + \frac{GM_2}{r} \tag{5.26}$$

where $M_1 = \rho V_{total}$, $M_2 = \Delta\rho V_{Core}$, and $M_{CD} = M_1 + M_2$. Then, the difference of the potentials is found to be

$$\Delta U = U_{Core} - U_{CD} = -\frac{G\Delta\rho V_{Core}}{R^*} \sum_{n=1}^{\infty} \sum_{m=0}^{n} \left(\frac{R^*}{r}\right)^{n+1} P_{nm}(\sin\phi) \begin{bmatrix} \cos(m\lambda) \\ \sin(m\lambda) \end{bmatrix} \cdot \begin{bmatrix} C_{nm}^{CD} \\ S_{nm}^{CD} \end{bmatrix} \tag{5.27}$$

Thus, for a given core size, the additional density in the core is obtained as

$$\Delta\rho = -\frac{R^*\Delta U}{GV_{Core}}\left(\sum_{n=1}^{\infty}\sum_{m=0}^{n}\left(\frac{R^*}{r}\right)^{n+1}P_{nm}(\sin\phi)\begin{bmatrix}\cos(m\lambda)\\ \sin(m\lambda)\end{bmatrix}\cdot\begin{bmatrix}C_{nm}^{CD}\\ S_{nm}^{CD}\end{bmatrix}\right)^{-1} \tag{5.28}$$

5.4.3 1999 KW4 - Torus and Cylinder Models -

The shape model of 1999 KW4 is used to study the deviations of the spherical harmonic coefficients from the homogeneous body, this time to test the torus and cylinder models. The total mass is again constrained by the uniform density of 2.1 $[g/cm^3]$. The torus has a radius of 800 $[m]$ and cross-sectional radius of 200 $[m]$. The cylinder has a radius of 400 $[m]$. The volume outside the cylinder is given a homogeneous density value. Figure 5.6 shows the first through fourth-degree error variances for KW4:

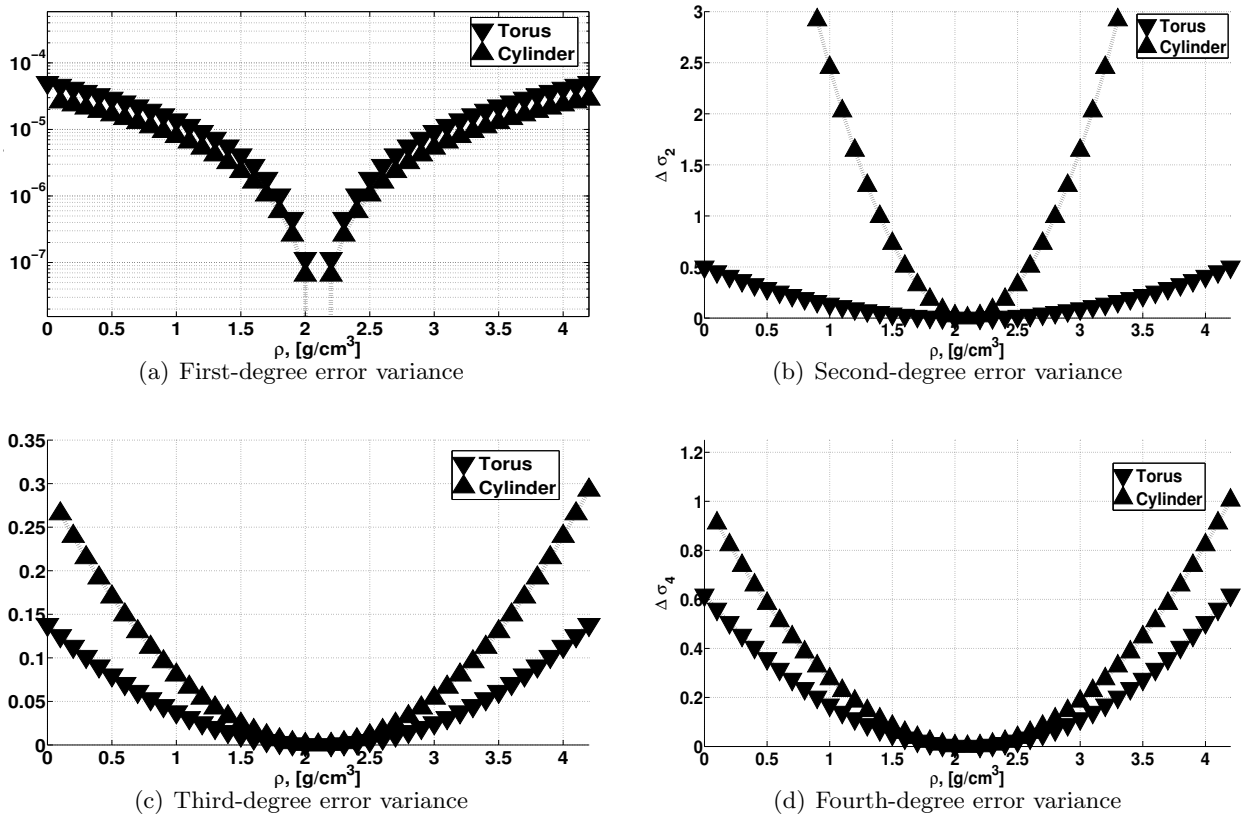

(a) First-degree error variance

(b) Second-degree error variance

(c) Third-degree error variance

(d) Fourth-degree error variance

Figure 5.6: First through fourth-degree error variances for KW4.

In Figure 5.6, x-axis denotes the density values for a) the torus and b) outer rings of the cylinder model. In Figure 5.6(b), both the torus and cylinder models yield noticeable deviations in the second-degree spherical harmonic coefficients. These deviations are caused by changing the mass distribution around the z-axis by the torus and rings. The moment of inertia around z-axis (I_{zz}) is related to the unnormalized second-degree spherical harmonic coefficients by

$$C_{20} = \frac{1}{2M_{OD}(R^*)^2}(I_{xx} + I_{yy} - 2I_{zz}) \tag{5.29}$$

By making an archive of deviations of the spherical harmonic coefficients for each density map, the types of possible density maps can be catalogued and compared with a set of spherical harmonic coefficients determined from orbit determination.

5.5 Density Estimation of Castalia

In this section, the density distribution of Castalia is estimated by the block density map. The true density distribution is the yz-planar division (i.e., the body is dissected along the x-axis). The tetrahedra on the positive x-axis are given the density of 2.5 $[g/cm^3]$, and those on the negative x-axis are given the density of 1.5 $[g/cm^3]$. The tetrahedra that cross the yz-plane are included in the positive axis region. This density map is chosen because of Castalia's distinguished two-lobe structure which could potentially possess two different density values. The data is the normalized 10×10 gravity field. It is recommended to use the normalized coefficients as the magnitude of higher-degree and higher-order coefficients diminishes rapidly for the unnormalized ones.

We will analyze the accuracy of the solution obtained for three different block segmentation types. The shape model of Castalia is divided evenly into the number of blocks specified by (N_S, N_V, N_H) (Table 5.1). As defined in Appendix C.7, N_S is the number of blocks along the x-axis, N_V is that along the y-axis, and N_H is that along the z-axis.

Table 5.1: Parameters of block segmentation for Castalia.

Case	(N_S, N_V, N_H)
1	$(2, 1, 1)$
2	$(10, 1, 1)$
3	$(10, 3, 3)$

As shown, the whole body is mainly sliced up along the x-axis, and only case 3 dissects the body along the y and z-axis. For both the truth and estimated models, each tetrahedron is dissected into ten slivers ($\kappa = 10$) along the radial direction.

5.5.1 Block Estimation with $(\mathbf{N_S}, \mathbf{N_V}, \mathbf{N_H}) = (\mathbf{2}, \mathbf{1}, \mathbf{1})$

First, the density distribution is estimated with $(N_S, N_V, N_H) = (2, 1, 1)$ (Case 1). Figure 5.7 shows the percentage error of the estimated density relative to the true density:

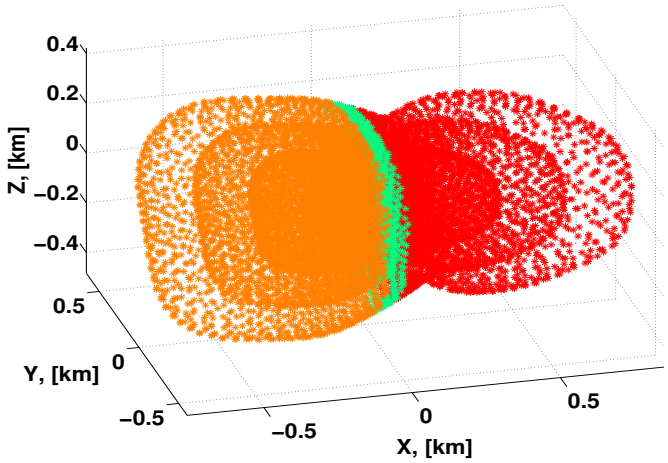

Figure 5.7: Percentage density error for yz-plane division with $(N_S, N_V, N_H) = (2, 1, 1)$.

In Figure 5.7, The red dots are less than 1% error, the orange dots less than 5% error, and the light green dots less than 40% error compared to the true density values. The 40% errors result from the facets that cross the zero along the x-axis and are systematic errors. The estimated density of the volume on the positive axis is 2.50518 $[g/cm^3]$, and that of the volume on the negative axis is 1.56171 $[g/cm^3]$.

5.5.2 Block Estimation with $(\mathbf{N_S}, \mathbf{N_V}, \mathbf{N_H}) = (\mathbf{10}, \mathbf{1}, \mathbf{1})$ and $(\mathbf{10}, \mathbf{3}, \mathbf{3})$

Next, the number of blocks is increased, and two cases where $(N_S, N_V, N_H) = (10, 1, 1)$ (Case 2) and $(N_S, N_V, N_H) = (10, 3, 3)$ (Case 3) are studied. Figure 5.8 shows the percentage error of the estimated density relative to the true density for both cases:

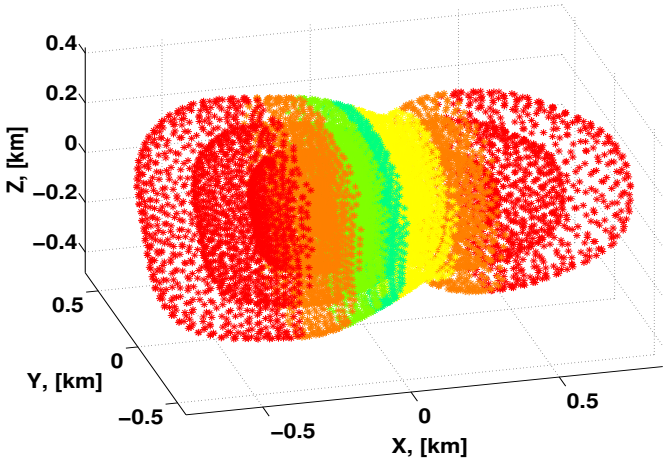

(a) $(N_S, N_V, N_H) = (10, 1, 1)$

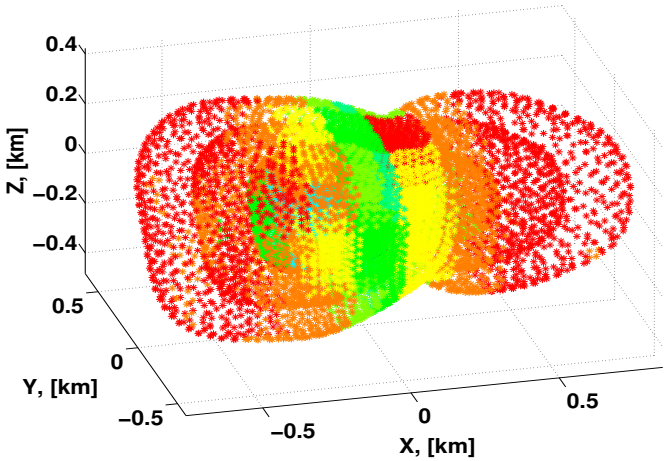

(b) $(N_S, N_V, N_H) = (10, 3, 3)$

Figure 5.8: Percentage density error for yz-plane division with $(N_S, N_V, N_H) = (10, 1, 1)$ and $(10, 3, 3)$.

In Figure 5.8, bands of density errors, representative of the block segmentation, are clearly shown. Again, the red dots are less than 1% error, the orange dots less than 5% error, the yellow dots less than 10% error, and the light green dots less than 40% error compared to the true density

values. In both Figure 5.8(a) and 5.8(b), those facets crossing the zero along the x-axis are adjusted by the green and yellow bands that run along the z-axis. It is shown that as the block moves farther from the yz-plane, the block density approaches the true density of 2.5 $[g/cm^3]$ on the positive axis and 1.5 $[g/cm^3]$ on the negative axis.

Table 5.2 shows the true values (fifth column) and errors of the spherical harmonic coefficients up to the second degree between the truth and the estimated density distribution models for case 1 through 3:

Table 5.2: True values and errors of the estimated spherical harmonic coefficients for yz-plane division of Castalia.

(N_S, N_V, N_H)	$(2,1,1)$	$(10,1,1)$	$(10,3,3)$	Truth
$\Delta\bar{C}_{10}$ $[n.d.]$	-1.6575×10^{-4}	-5.0336×10^{-5}	-1.2542×10^{-6}	4.0225×10^{-4}
$\Delta\bar{C}_{11}$ $[n.d.]$	5.6401×10^{-3}	-1.5447×10^{-4}	3.8855×10^{-6}	9.4653×10^{-2}
$\Delta\bar{C}_{11}$ $[n.d.]$	2.8096×10^{-4}	1.7100×10^{-4}	-1.0961×10^{-5}	-5.6233×10^{-4}
$\Delta\bar{C}_{20}$ $[n.d.]$	1.5495×10^{-3}	-5.8233×10^{-5}	-3.3112×10^{-6}	-0.11759
$\Delta\bar{C}_{21}$ $[n.d.]$	1.0195×10^{-4}	-5.0624×10^{-5}	7.9649×10^{-7}	1.9194×10^{-3}
$\Delta\bar{C}_{21}$ $[n.d.]$	1.6579×10^{-4}	8.9391×10^{-5}	2.0369×10^{-7}	6.1612×10^{-5}
$\Delta\bar{C}_{22}$ $[n.d.]$	-3.6104×10^{-3}	-9.1782×10^{-5}	9.8106×10^{-6}	0.16407
$\Delta\bar{C}_{22}$ $[n.d.]$	-9.0068×10^{-5}	8.6613×10^{-5}	-4.6480×10^{-6}	-1.7033×10^{-3}

As shown in Table 5.2, it is shown that the errors in the spherical harmonic coefficients have decreased about an order of magnitude each time the number of blocks is increased. This result supports the hypothesis that the spherical harmonic coefficients are better approximated as the total number of blocks is increased, simultaneously recovering the density distribution more accurately. In fact, when the higher-degree and higher-order spherical harmonic coefficients are compared, it is clearly observed that a better solution is obtained with more blocks (Figure 5.9).

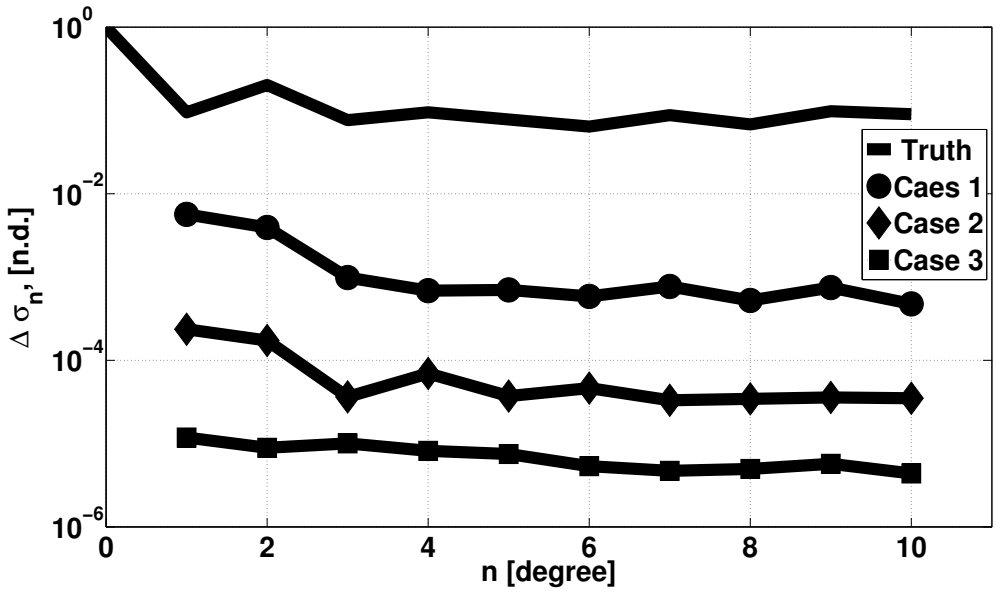

Figure 5.9: Error variances of the density distributions estimated via block segmentation for Castalia.

In Figure 5.9, the solid line without a marker is the degree variance (i.e., the square root of the sum of squares of the spherical harmonic coefficients of the same degree). This degree variance establishes the baseline of the magnitude of each degree spherical harmonic coefficient. The circle markers are the error variances of case 1, the diamond markers are those of case 2, and the square markers are those of case 3. As shown, all three cases yield good approximation of the higher-degree and higher-order spherical harmonic coefficients, and a better solution is achieved as more blocks are used to estimate the density distribution.

5.6 Surface Gravity Field Error Analysis

With the estimated density distribution available, it is of interest to compute the potential and acceleration errors in close proximity to the body surface. The acceleration errors between the true gravity field and the estimated heterogeneous density distribution are computed within the Brillouin sphere, as shown in Figure 5.10.

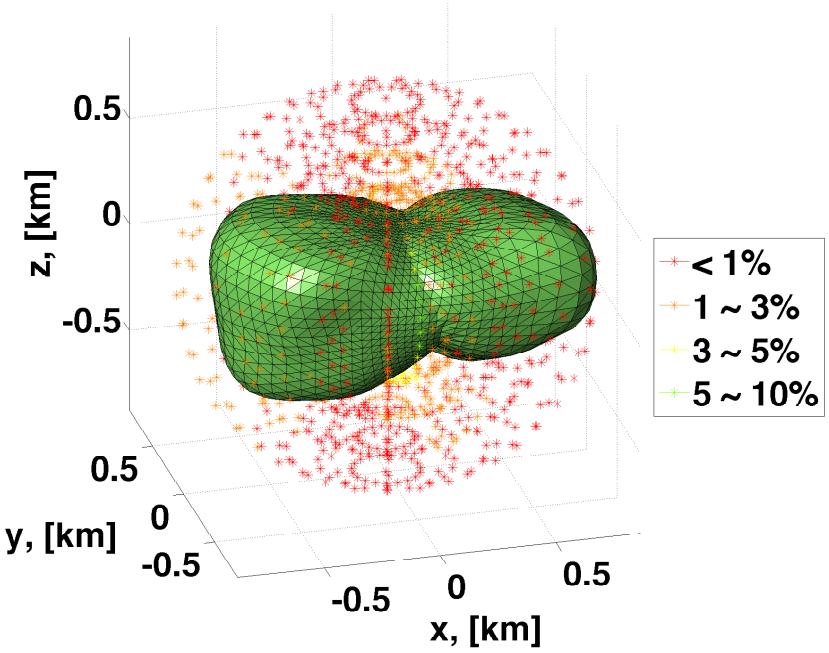

(a) Case 1

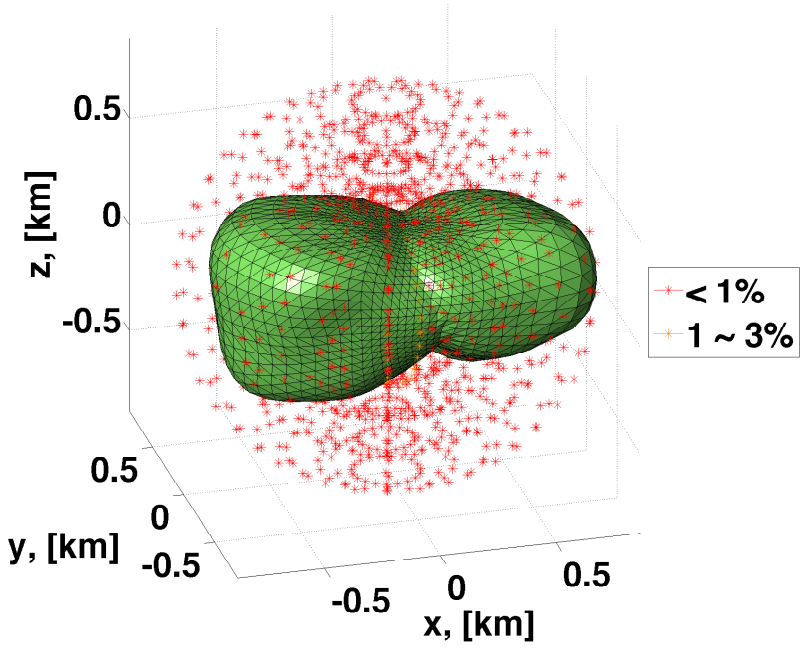

(b) Case 3

Figure 5.10: Radial distribution of acceleration errors between the truth and estimated solutions for case 1 (top) and case 3 (bottom).

As shown in Figure 5.10, the acceleration errors reduce as more blocks are used to estimate the density distribution. Similarly, the potential errors also reduce as more blocks are used. All acceleration errors are less than 10%, an order of accuracy that is not achievable with the exterior spherical harmonic gravity field, especially around the neck region of the body. For a sample return mission to an asteroid, it is necessary to perform a touch-and-go maneuver [14], and the computation of the surface gravity fields are particularly important. Figure 5.11 and 5.12 show the surface potential/acceleration errors for case 1 and 3.

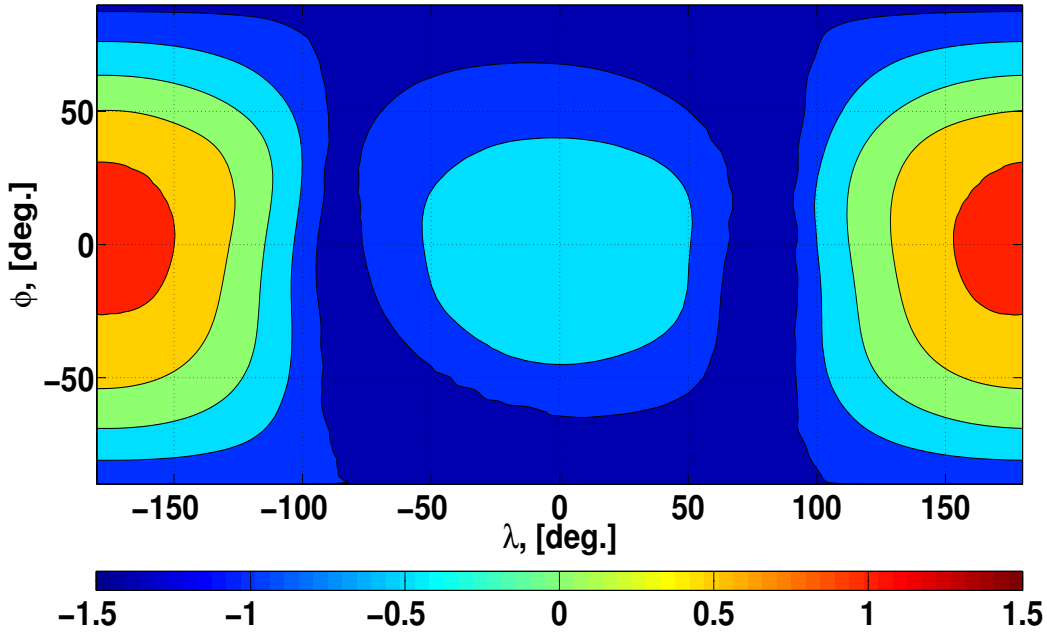

(a) Surface potential error for case 1

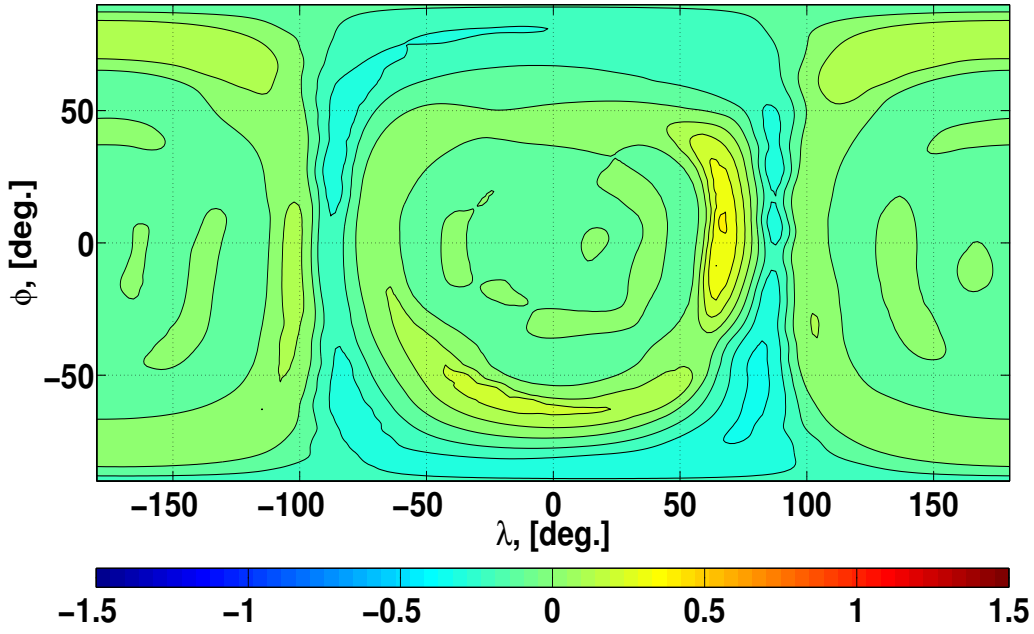

(b) Surface potential error for case 2

Figure 5.11: Surface potential error between the truth and estimated solutions for case 1 (top) and case 3 (bottom).

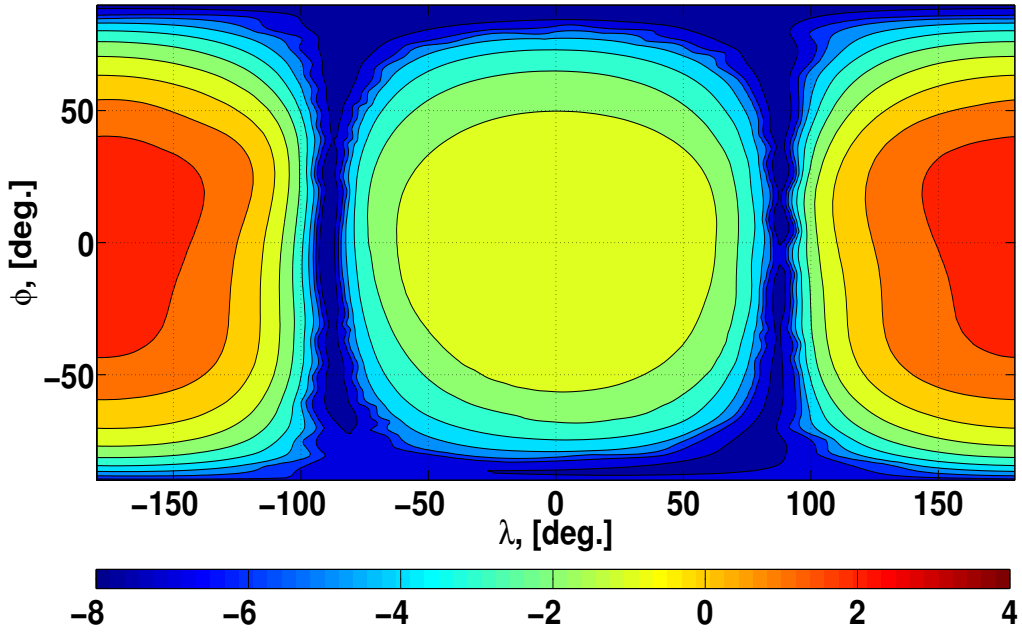

(a) Surface acceleration error for case 1

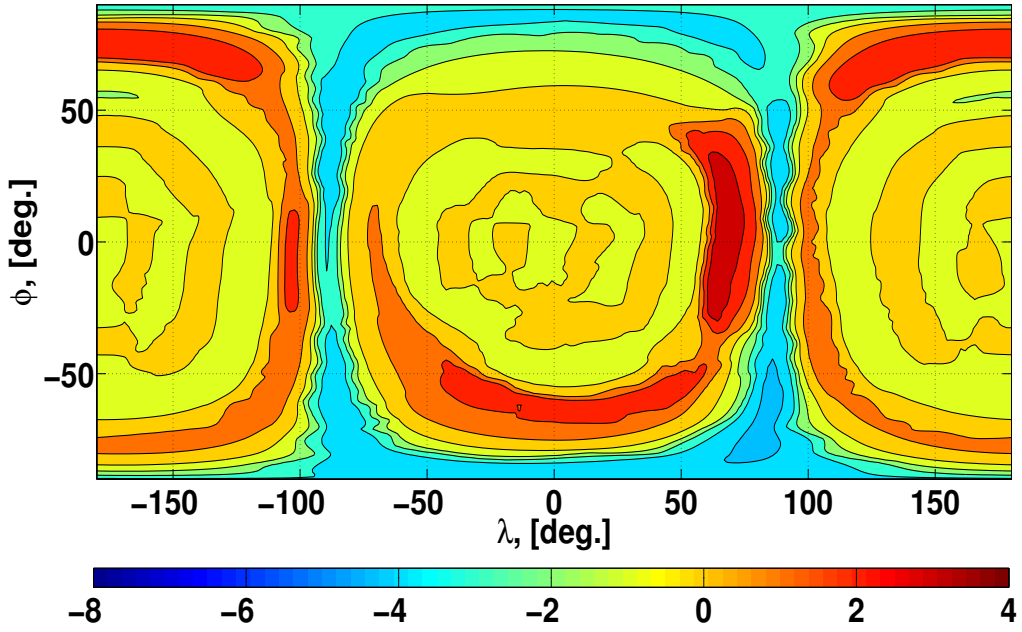

(b) Surface acceleration error for case 3

Figure 5.12: Surface acceleration error between the truth and estimated solutions for case 1 (top) and case 3 (bottom).

As shown in Figure 5.11 and 5.12, the potential errors are less than 1.5% and the acceleration errors are less than 10% for both case 1 and case 3. This result shows the remarkable improve-

ment from the conventional spherical harmonic gravity field model (Equation 1.13), as the surface potential/acceleration errors grow $> 100\%$ on the surface of Castalia with this formulation as will be shown in Chapter 7. It is worth mentioning that the computation of the polyhedral gravity field for a heterogeneous body is intensive. Thus, the interpolation methods such as cubed-sphere model [28], MRQSphere model [27], and Fetch model [5] are recommended for fast computation.

5.7 Consistency Analysis

It has been shown that increasing the number of blocks enables accurate estimation of the spherical harmonic coefficients and surface gravity fields. In this section, the consistency of the solution is investigated for different types of block segmentation. That is, the RMS errors are computed for the density values and the spherical harmonic coefficients with respect to the solutions of the highest-resolution block model. These RMS values are referred to as the consistency RMS errors. To this end, vectors $\vec{N}_S$, $\vec{N}_V$, and $\vec{N}_H$ are defined, which are arrays defining N_S, N_V, and N_H. For the analysis below, $\vec{N}_S = [1, 2, 4, 8, 10]$, $\vec{N}_V = [1]$, and $\vec{N}_H = [1]$. The true density distribution model is the yz-plane division model of Castalia with 2.5 $[g/cm^3]$ on the positive x-axis and 1.5 $[g/cm^3]$ on the negative x-axis. When the density RMS errors are computed, the data points are placed at the center of mass of each sliver. Figure 5.13 shows the RMS errors between the truth and the estimated (top), and the consistency RMS values (bottom).

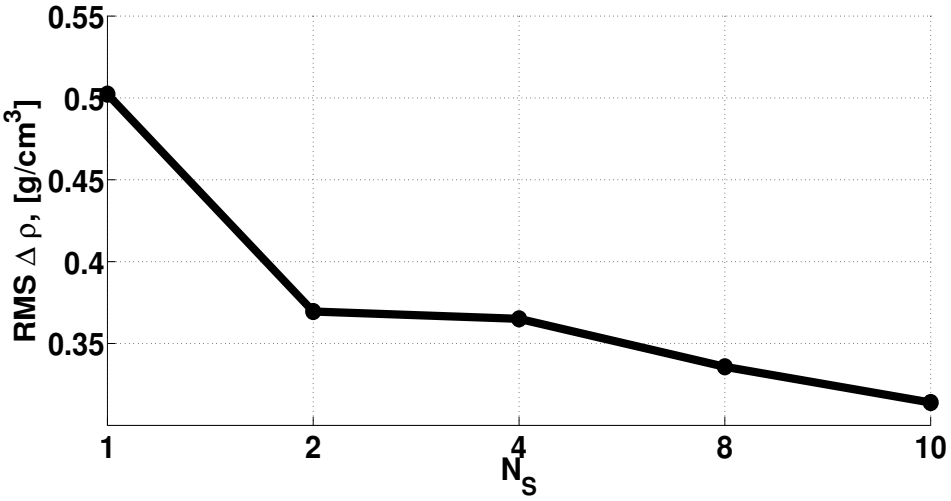

(a) $\Delta\rho$ RMS from the truth

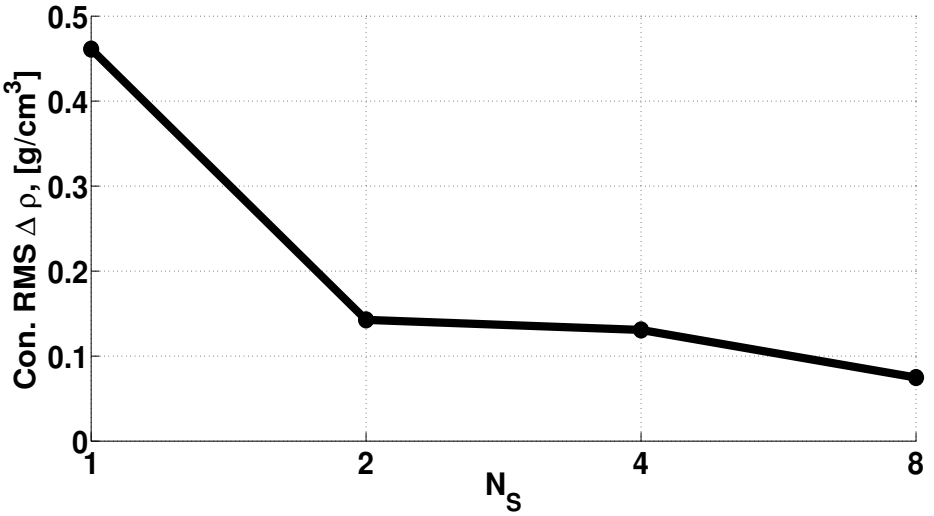

(b) $\Delta\rho$ consistency RMS

Figure 5.13: RMS error from the truth (top) and consistency RMS (bottom) of density for yz-plane division of Castalia.

As shown above, the RMS errors diminish and flatten out as the number of blocks is increased. This result indicates that the density distribution converges as more blocks are used to dissect the body. Figures 5.14 shows the RMS errors between the truth and the estimated (top) and consistency RMS (bottom) for the third-degree spherical harmonic coefficients.

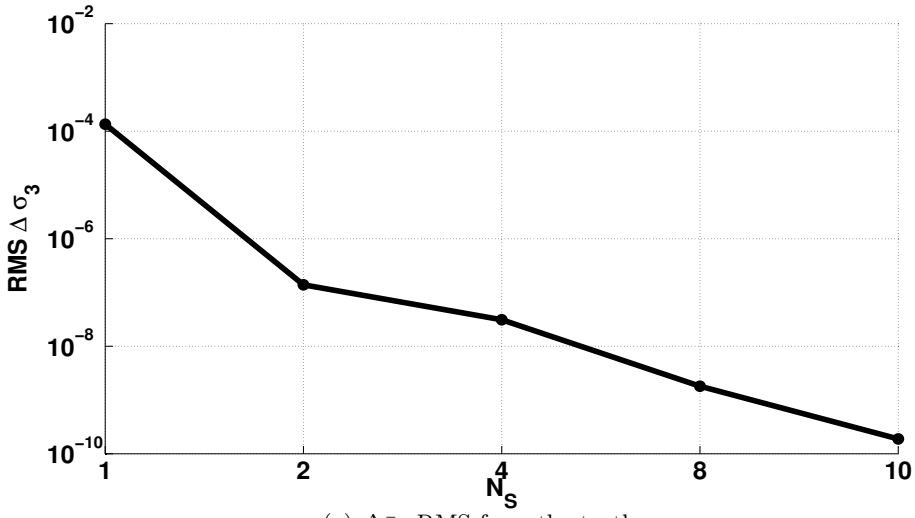

(a) $\Delta\bar{\sigma}_3$ RMS from the truth

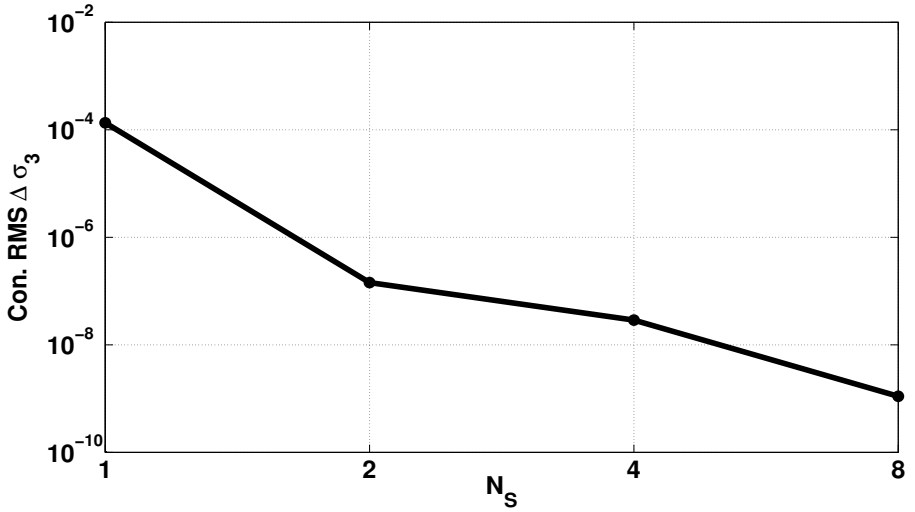

(b) $\Delta\bar{\sigma}_3$ consistency RMS

Figure 5.14: RMS error from the truth (top) and consistency RMS (left) of the third-degree spherical harmonics for yz-plane division of Castalia.

Again, the errors decrease as more blocks are used. Thus, both the density and spherical harmonic coefficients approach the true density distribution as the number of blocks used for the estimation is increased.

5.8 Density Estimation of 1999 KW4

In this section, the density distribution of 1999 KW is estimated for two density maps: a single core model and a torus model. For the single core model, the radius of the core is varied to evaluate the accuracy of the estimated density distribution. Similarly, the cross-sectional radius of the torus (r_{torus}) is varied for the torus model, keeping the same ring radius.

5.8.1 Single Core Density Estimation of 1999 KW4

The single core model is investigated to measure the accuracy of the estimated density distribution for different core sizes. The modeled core radius varies from 0.05 to 0.50 $[km]$ at 0.05 $[km]$ increments. The truth model has the core radius of 0.3 $[km]$ with the core density of 7.5 $[g/cm^3]$ and the mantle density of 2.5 $[g/cm^3]$. The core density is retrieved from the iron core density of Vesta, which is thought to be consistent with the density of iron meteorites [6, 53]. The scaling factor is obtained by comparing the value of C_{20} between the single core model and the constant density body (Equation 5.24). Figure 5.15 shows the density errors of the mantle and the core.

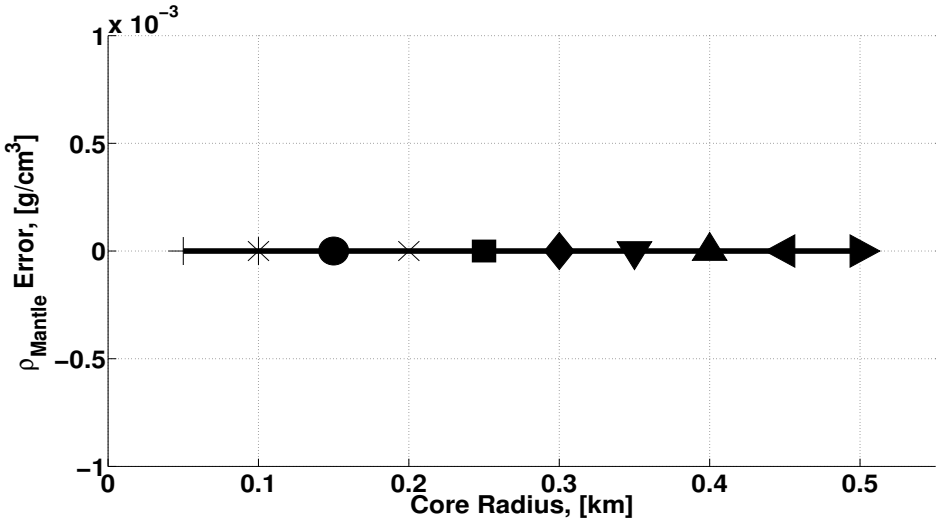

(a) Mantle density error

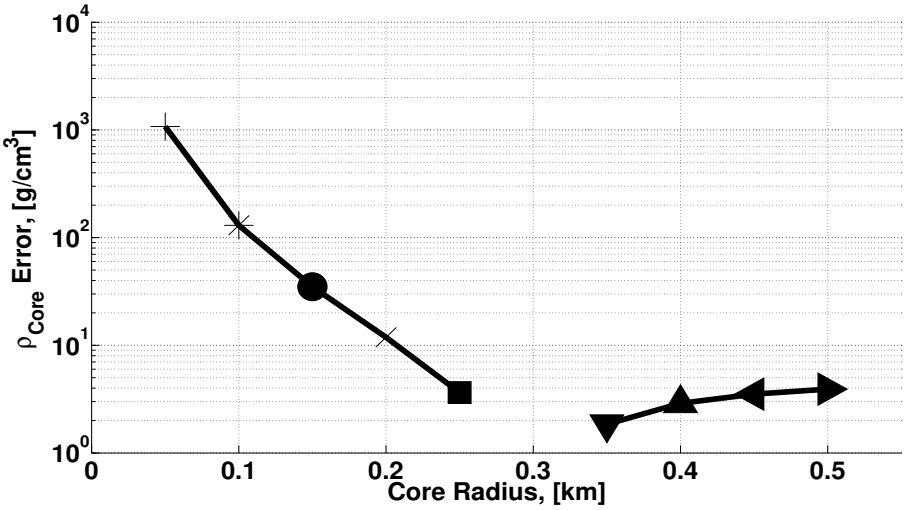

(b) Core density error

Figure 5.15: Mantle and core density errors.

In Figure 5.15, it is shown that the mantle density is well estimated for all core sizes, and the core density approaches the true value when the correct core radius is used for the density map. Note that in Figure 5.15(b), the value of zero does not appear in the log plot ($r_{Core} = 300$ $[m]$). The errors in the spherical harmonic coefficients are virtually zero, so are the potential/acceleration errors within the Brillouin sphere/on the surface. Thus, although the size of the core is not strictly constrained, the surface gravity fields can still be computed very accurately for the single core model.

5.8.2 Torus Density Estimation of 1999 KW4

The torus model is investigated to measure the accuracy of the estimated density distribution for different torus sizes. The modeled torus radius (r_{torus}) varies from 0.150 to 0.300 [km] at 0.025 [km] increments. For all cases, the ring radius (R_{ring}) is maintained at 0.8 [km]. The truth model has the torus radius of 0.225 [km], the ring radius of 0.8 [km], the torus density of 5.0 [g/cm^3], and the main body density of 2.5 [g/cm^3]. Figure 5.16 shows the density errors of the main body and the torus:

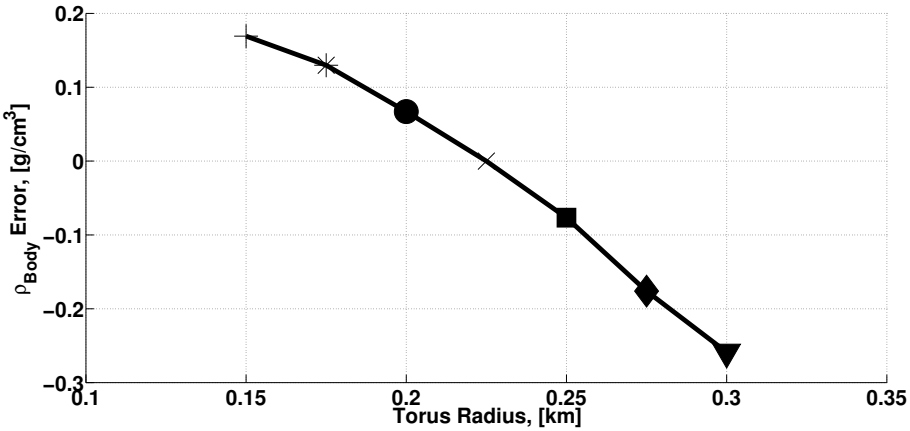

(a) Main body density error

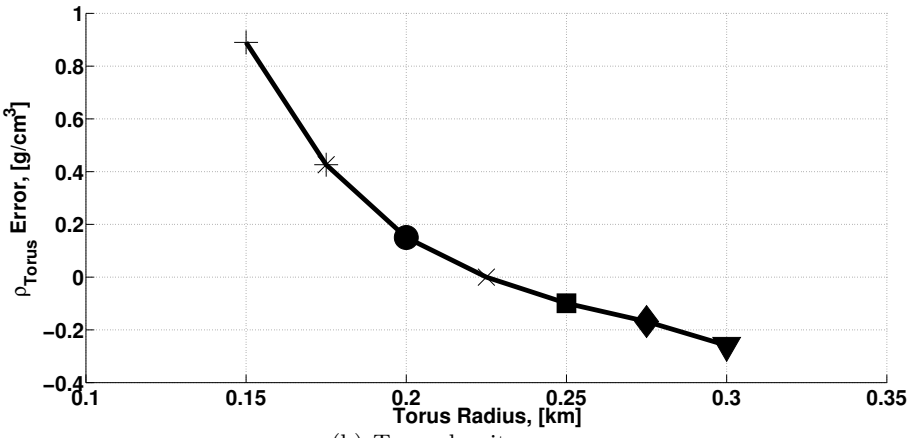

(b) Torus density error

Figure 5.16: Main body and torus density errors.

In Figure 5.16, it is shown that the density distribution is estimated more accurately as the geometry of the torus approaches the true density map, yielding nearly zero density errors for both main body and the torus. Figure 5.17 shows the error variances up to the 10-th degree:

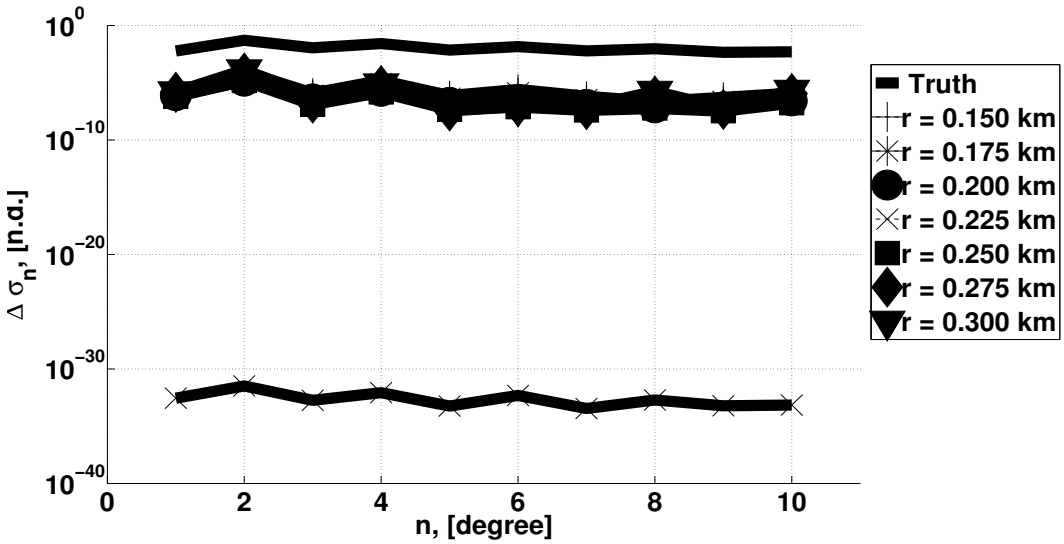

Figure 5.17: Error variances for the torus model.

As shown, the resulting spherical harmonic coefficient errors are on the same order of magnitude for all cases but the one with the true torus radius. When the estimated density map is identical to the truth model, the estimated spherical harmonic coefficients produce much lower error variances. Figure 5.18 and 5.19 show the percentage potential/acceleration errors on the surface between the true gravity field and the estimated torus model for $r_{torus} = 0.150$ $[km]$ and 0.200 $[km]$.

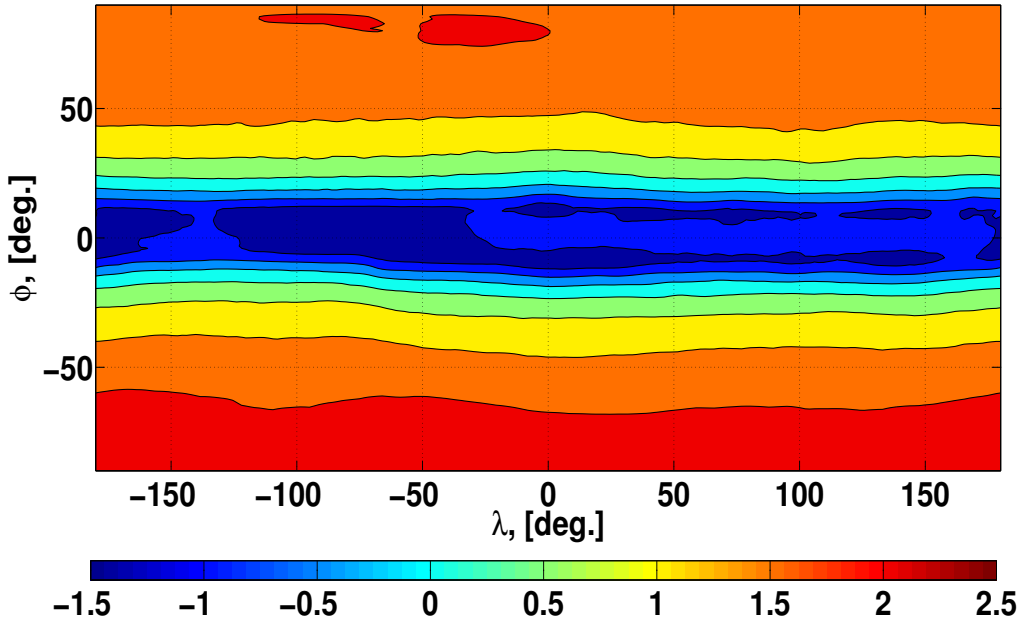

(a) Surface potential error with $r_{torus} = 0.150\ km$

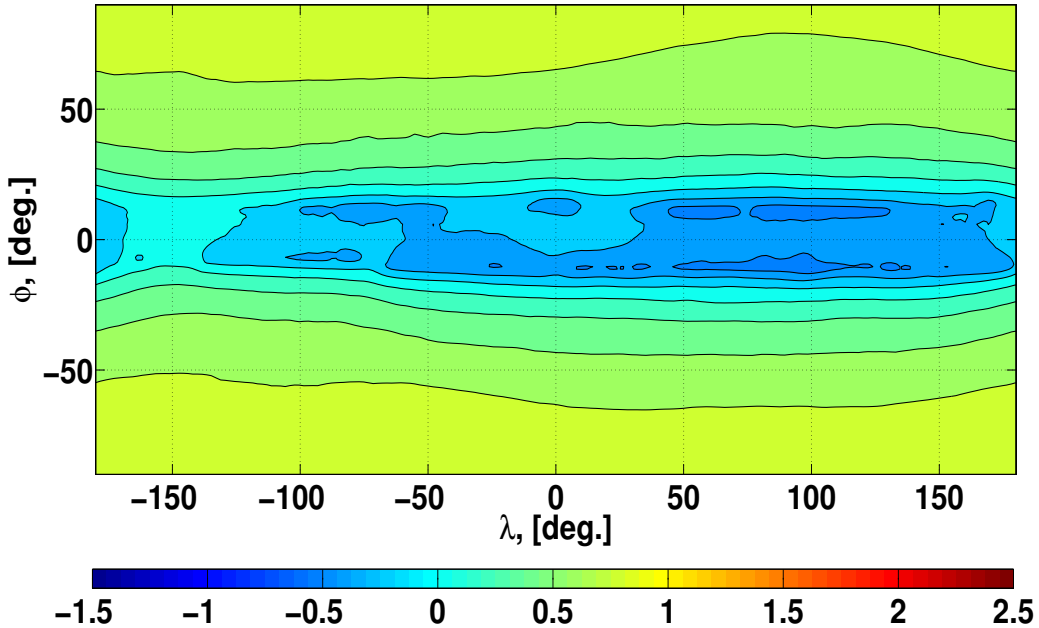

(b) Surface potential error with $r_{torus} = 0.200\ km$

Figure 5.18: Surface potential error ([%]) between the truth and estimated torus models for $r_{torus} = 0.150\ [km]$ (top) and $0.200\ [km]$ (bottom) for KW4.

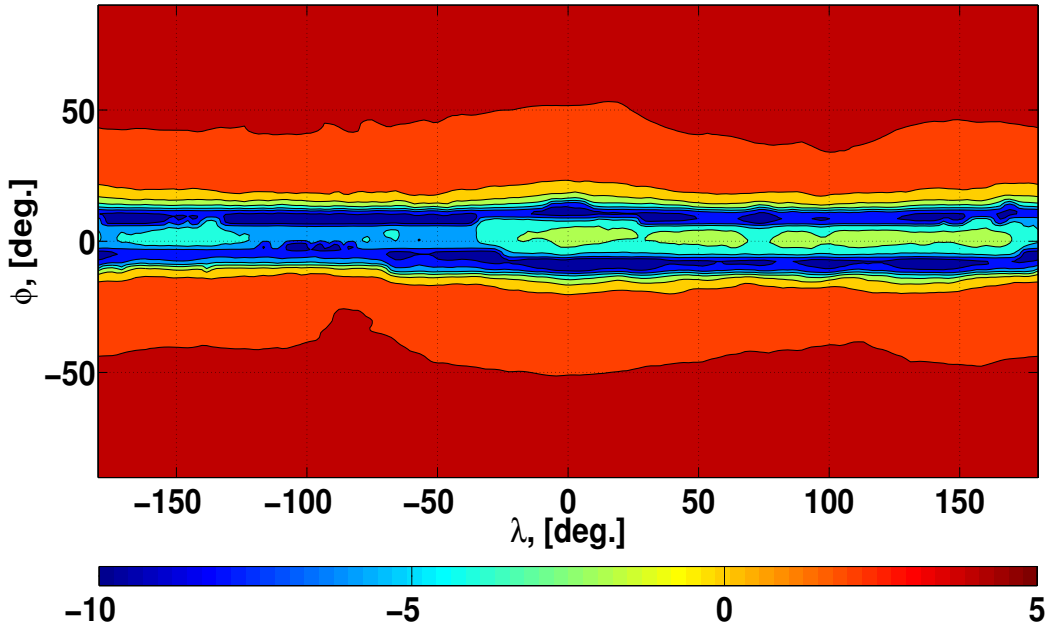

(a) Surface acceleration error with $r_{torus} = 0.150\ km$

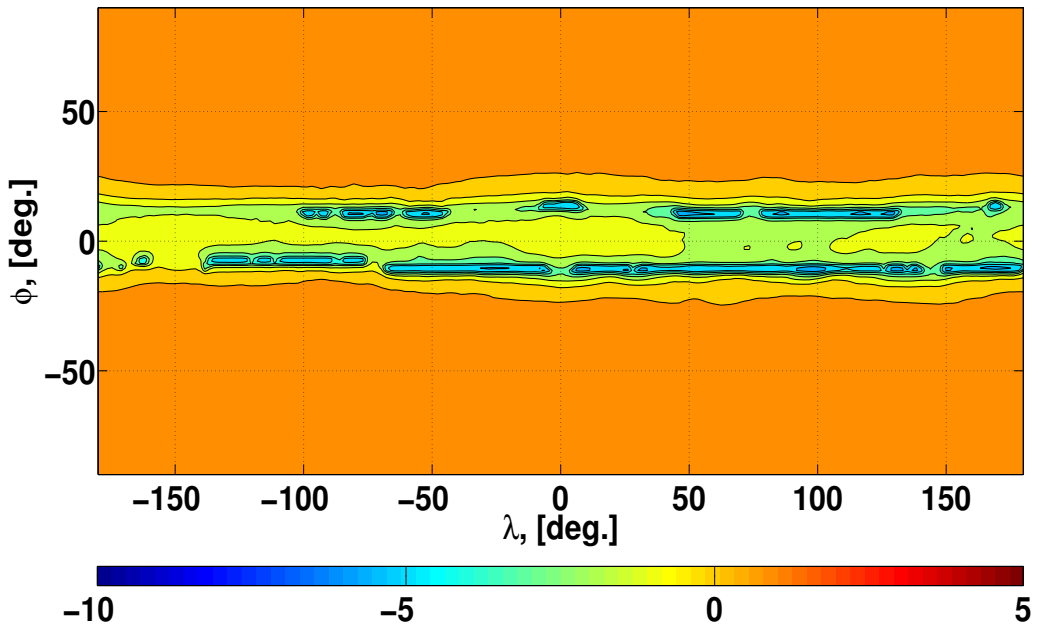

(b) Surface acceleration error with $r_{torus} = 0.200\ km$

Figure 5.19: Surface acceleration error ([%]) between the truth and estimated torus models for $r_{torus} = 0.150\ [km]$ (top) and $0.200\ [km]$ (bottom) for KW4.

As shown above, both potential and acceleration errors exhibit a band structure in the east-west direction representative of the torus. It is of interest to note that the width of each band is

not proportional to the radius of the torus. For all cases simulated, the potential error is $< 3\%$, and the acceleration error is $< 10\%$. Smaller potential/acceleration errors are achieved as the torus radius approaches the true value. The radial distribution of the potential/acceleration errors within the Brillouin sphere are on the same order of magnitude as the surface potential/acceleration errors. Table 5.3 summarizes the maximum, minimum, mean, and standard deviation of the surface potential/acceleration errors for the torus models.

Table 5.3: Statistics of the surface potential/acceleration errors ([%]) between the true gravity field and reconstructed gravity field for the torus models.

r_{torus} $[km]$	Maximum	Minimum	Mean	Standard Deviation
Potential				
0.150	2.093	-1.389	1.099	1.048
0.200	0.8747	-0.5392	0.5001	0.3867
Acceleration				
0.150	4.347	-9.532	2.468	3.362
0.200	1.725	-5.578	0.9758	1.286

5.9 Conclusions

In this chapter, methods to detect a heterogeneous density distribution within a body were studied. The density distribution was estimated from the shape model and spherical harmonic coefficients determined from orbit determination. At the heart of the algorithm is that the potentials between the orbit determination solution and the heterogeneous density distribution must be equal to each other, yielding a least-squares formulation. The results show that the heterogeneity in the density distribution provides certain signatures in the spherical harmonic coefficients, and comparing them with those generated by a homogeneous body proves to be a useful tool to constrain the density maps. Particularly, it was found that the spherical harmonic coefficients of the single core model differ from those of the homogeneous body only by a scaling factor, making the single core model the easiest model to identify.

In order to estimate the density distribution of a heterogeneous body, the block estimation method was proposed. Block estimation divides the shape model into a certain number of blocks and estimates the density value within each block. This approach has the benefit that one needs not know the density map a priori, and the accuracy of the estimated density values is controlled by the number of blocks used in the estimation. In the example shown, Castalia is used to identify that as the number of blocks in the estimation is increased, the estimated solution approaches the true density distribution, fitting the spherical harmonic coefficients more accurately.

One crucial result obtained from this analysis is that the gravity field in close proximity to the body surface (and on the surface) can be reconstructed from the estimated heterogeneous density distribution, yielding the potential and acceleration errors that are not achievable by the conventional spherical harmonic gravity field (i.e., $< 5\%$). Furthermore, it has been shown that as the number of the blocks is increased, the density distribution converges, indicating that the solution becomes more precise.

In addition to the block estimation technique, a single core and torus models were constructed for 1999 KW4 to study the accuracy of the fitting algorithm. The results showed that the estimated single core density distributions yielded potential/acceleration errors indistinguishable from zero within the Brillouin sphere. The torus model yielded $< 3\%$ error for potential and $< 10\%$ error for acceleration on the surface of the body, showing a band of high concentrated errors along the torus. For both analyses, the errors in the density distribution approach zero as the geometry of the density map approaches the truth model. The density estimation techniques discussed in this chapter are useful tools that can be leveraged to reveal the internal structure of small primitive bodies.

Chapter 6

Interior Spherical Harmonic Gravity Field

The previous chapter investigated how to estimate the internal density distribution of a body from the gravity field solution obtained via orbit determination, and how accurately the surface gravity fields can be reconstructed from the estimated density distribution. In this chapter, we investigate another method to map out the surface gravity fields of a body, namely the interior spherical harmonic gravity field.

The initial estimate of the total mass of an asteroid is determined from the Doppler measurements taken during the first encounters with the asteroid. It is customary for a spacecraft to lower its orbit to better characterize the asteroid's environment, as performed by the Near Earth Asteroid Rendezvous (NEAR) Shoemaker spacecraft [38]. After this characterization phase is over, there exists a measured gravity field and a precise shape model featuring the surface morphology of the asteroid. For a small body robotic mission, its ultimate goal is to accomplish a sample return from the asteroid, and the retrieval of actual specimens from the asteroid requires contact of the spacecraft with the asteroid's surface. Much research has been performed in support of such mission goals: the rapid characterization of environment via OD around asteroids [66, 67], OD techniques and characterization of an actual body [17, 33, 38, 59, 77], modeling of the gravity field by various mathematical formulations [19, 52, 75], efficient gravity field modeling [5, 8, 13, 27, 54], and proximity operations including a TAG sample return sequence [11, 14].

In order to characterize the gravity field of a body, the exterior gravity field (Equation 1.13) is widely in use, and it is particularly suitable for a body with a nearly spherical shape. However,

the exterior gravity field expression breaks down when computing the potential and its gradients within the Brillouin sphere, meaning that spacecraft dynamics cannot be modeled accurately in close proximity to the body's surface. On the other hand, the convergence of the potential and its gradients are guaranteed within the Brillouin sphere of the interior gravity field, a feature that makes it a good candidate for modeling the gravity field environment near the surface of the body. The original work has been published by Werner [74], and the application of the theory is discussed by Takahashi and Scheeres [69] and Takahashi et al [70]. The interior gravity field model is a variant of the spherical harmonic gravity field and has comparative computational load to the conventional exterior gravity field. As will be discussed later, the convergence of the interior gravity field is guaranteed up to a particular point on the surface of the asteroid. Leveraging this property, this analysis will particularly focus on a TAG mission, where a gravity expansion is only needed about one point on a body. That is, we perform the regional mapping, and the discussion of the total mapping is deferred to Chapter 7 where we introduce the interior spherical Bessel gravity field.

This chapter is devoted to the discussion of the interior gravity field with detailed descriptions of its derivations, characteristics, and evaluation near the surface of an asteroid for the purpose of small body proximity operations. The rest of the chapter discusses the following materials: the derivation of the exterior and interior gravity fields, a conversion method between two gravity fields (e.g., from an exterior gravity field into an interior gravity field), a numerical approximation method to the interior spherical harmonic coefficients via shape model integration, and finally the comparisons between the spacecraft dynamics propagated by the interior and polyhedral gravity fields to assess their relative accuracy. A detailed derivation of the higher-order partials of the interior potential are given in Appendix D.

This work has been carried out in collaboration with Robert A. Werner, and the author would like to acknowledge his contribution.

6.1 Derivation of the Exterior and Interior Gravity Fields

In this section, both the exterior and interior gravity fields are derived from the potential definition. Note that only the key steps are highlighted since Werner [74] provides a complete set.

6.1.1 Exterior Gravity Field Derived

We first derive the exterior gravity field from the potential definition in Equation 1.1. By substituting Equation 1.2, Equation 1.1 is expressed as

$$U(r,\phi,\lambda) \;=\; G\int_M \frac{1}{\Delta}dm \;=\; G\int_M \frac{1}{\sqrt{r^2+(r\,')^2-2rr\,'\cos\Theta}}dm' \tag{6.1}$$

The difference between the exterior and interior gravity fields arises from solving for the quantity in the square root in the integrand differently. First, the exterior gravity field is derived by factoring out r in Equation 6.1:

$$U^e(r,\phi,\lambda) \;=\; G\int_M \frac{1}{r}\frac{1}{\sqrt{1-2\left(\frac{r\,'}{r}\right)\cos\Theta+\left(\frac{r\,'}{r}\right)^2}}dm' \tag{6.2}$$

where the superscript e denotes the exterior quantity. The reason to factor out r is related to the convergence of the Legendre polynomial, which is defined as

$$P_n(\mathscr{U}) \;=\; \frac{1}{2^n n!}\frac{d^n}{d\mathscr{U}^n}(\mathscr{U}^2-1)^n \tag{6.3}$$

Here, $P_n(\mathscr{U})$ is the Legendre polynomial of degree n. This Legendre polynomial has the following property presented without proof:

$$\frac{1}{\sqrt{1-2\hbar\mathscr{U}+\hbar^2}} \;=\; \sum_{n=0}^{\infty}\hbar^n P_n(\mathscr{U}) \tag{6.4}$$

which converges absolutely and uniformly when $|\hbar| < 1$. By comparing this expression with Equation 6.2, it is immediately found that $\mathscr{U} = \cos\Theta$ and $\hbar = r'/r$ for the exterior gravity field. Then, substitution of Equation 6.4 into Equation 6.2 yields

$$U^e(r, \phi, \lambda) = G \int_M \sum_{n=0}^{\infty} \frac{(r')^n}{r^{n+1}} P_n(\cos\Theta) dm' \tag{6.5}$$

The sphere dictated by $|\hbar| < 1$ is called the Brillouin sphere. Thus, Equation 6.5 converges when the field point is outside the Brillouin sphere, the reason U^e is called the exterior gravity field. Note that the convergence region of the exterior gravity field is dictated by the farthest mass element of the asteroid away from the coordinate center, as shown in Figure 6.1:

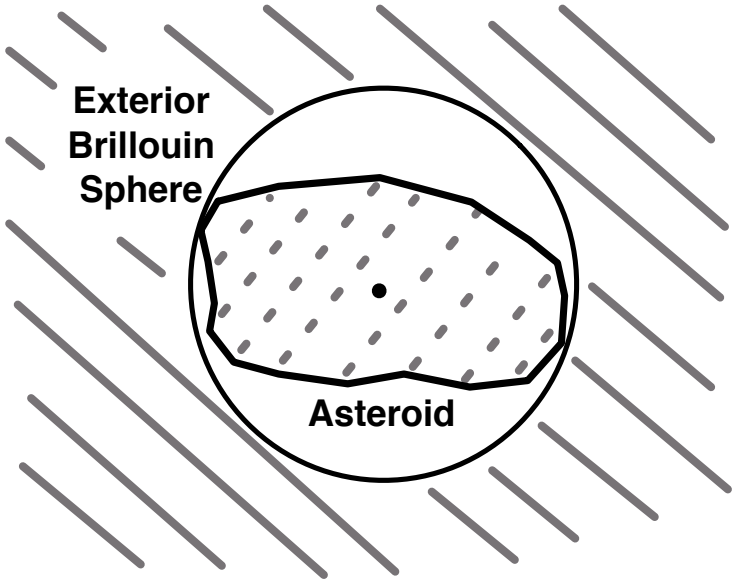

Figure 6.1: Convergence region of the exterior gravity field.

In Figure 6.1, the exterior Brillouin sphere is placed at the center of mass of the asteroid. The solid lines correspond to the region of convergence, and the dotted lines correspond to the mass elements that contribute to this exterior gravity field. This one-to-one correspondence seems obvious, but an example will be given in which it is not after the derivation of the interior gravity field.

6.1.2 Interior Gravity Field Derived

Now that the exterior gravity field is derived, a similar approach is taken to derive the interior gravity field. For the interior gravity field, Equation 6.1 is revisited to factor out r':

$$U^i(r,\phi,\lambda) = G\int_M \frac{1}{r'}\frac{1}{\sqrt{1-2\left(\frac{r}{r'}\right)\cos\Theta+\left(\frac{r}{r'}\right)^2}}dm' \tag{6.6}$$

By observation, $\mathscr{U} = \cos\Theta$ and $\hbar = r/r'$ for the interior gravity field. Thus, Equation 6.6 converges when the field point is closer than the mass element. That is, the interior potential converges inside a different Brillouin sphere associated with the interior expansion. By substituting Equation 6.4, Equation 6.6 becomes

$$U^i(r,\phi,\lambda) = G\int_M \sum_{n=0}^{\infty}\frac{r^n}{(r')^{n+1}}P_n(\cos\Theta)dm' \tag{6.7}$$

Note that, due to the condition of convergence dictated by $|\hbar| < 1$, the coordinate center of the interior gravity field does not lie within the asteroid, whereas the exterior gravity field is well defined by placing the coordinate center at the center of mass of the asteroid. Figure 6.2 shows the convergence region of the interior gravity field.

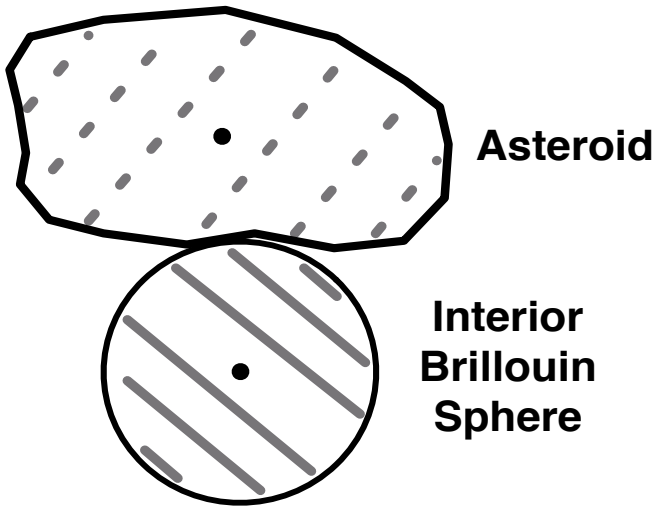

Figure 6.2: Convergence region of the interior gravity field.

As with Figure 6.1, the solid lines correspond to the region of convergence, and the dotted lines correspond to the mass elements that contribute to the interior gravity field. Again, there is one-to-one correspondence between the mass distribution and the convergence region. The only difference is that the convergence region of the interior gravity field is dictated by the closest mass element of the asteroid from the interior coordinate center. That is, the convergence of the interior gravity field is guaranteed up to a point on the surface, which, for practical purposes, is the TAG point. If a different TAG point is chosen, a different interior Brillouin sphere must be constructed.

Note that the exact coordinates of the interior coordinate center are not specified during the formulation of the interior gravity field. In fact, the only constraint is that the interior coordinate center must be placed so that the interior Brillouin sphere is tangent on the surface at the TAG point. Thus, the interior coordinate center can be placed anywhere along the the surface normal $\hat{n}$ that extends from the TAG point, as shown in Figure 6.3.

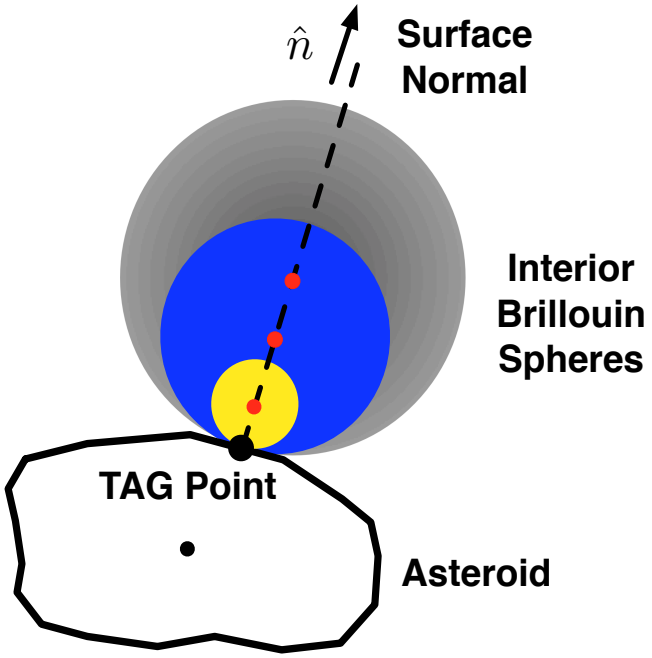

Figure 6.3: Different size interior Brillouin spheres for a TAG point. The red dots signify the centers of the yellow, blue, and gray interior Brillouin spheres.

The performance of the interior gravity field depends on the placement of its coordinate center, and it is one of the parameters that can be optimized. In contrast, the exterior gravity field does not enjoy the same liberty, and its Brillouin sphere is identical to the circumscribing sphere. More details are provided in Chapter 7 when we perform comparative study of the exterior/interior/interior Bessel gravity fields.

6.1.3 Convergence Region of the Exterior and Interior Gravity Fields

It has been shown that the convergence region is dictated by the farthest mass element for the exterior gravity field and by the closest one for the interior gravity field. For both gravity fields, the underlying idea is that the region of convergence should exclude any mass distribution. Now a hypothetical situation is considered where the two expansions are centered at the same point inside the asteroid (Figure 6.4).

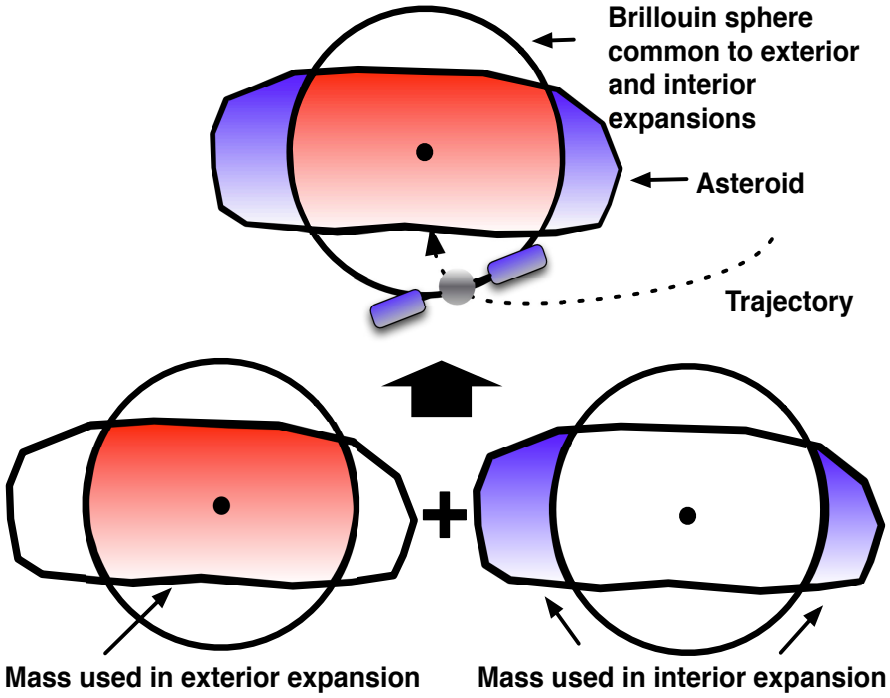

Figure 6.4: Time-varying/position-dependent Brillouin sphere.

As the spacecraft descends, its radial distance from the center can define a spherical boundary. Some asteroid mass is entirely outside this boundary, and the rest is inside. The sphere can be taken as the Brillouin sphere for both an exterior and interior expansion centered at the same point. Mass that is inside the sphere is used in the exterior expansion, and mass that is outside is used in the interior expansion. By superimposing the two expansions, it is possible to evaluate gravitation anywhere on the surface of the sphere. And by using a different sphere for every point on the trajectory, it is also possible to evaluate gravitation along the entire trajectory.

There are two obvious drawbacks. One is that the sphere size and the mass distribution outside and inside the sphere vary with spacecraft radial distance. In so many words, the spherical harmonic coefficients C_{nm} and S_{nm} of the two expansions are no longer constant and become position dependent; thus, the gravity coefficients become time-varying when motion of the spacecraft occurs. An unpublished experiment shows coefficients behave oddly with radius, defying simple polynomial representations. The other drawback is that gravity will always be evaluated on the surface of the sphere, right on the boundary between convergence/divergence regions for the two

expansions. It might take high-degree expansions to evaluate gravity accurately on these boundaries. While interesting, this approach of coincident centers and radially varying coefficients does not seem viable and will not be considered in our analysis.

6.1.4 Common Convergence Region

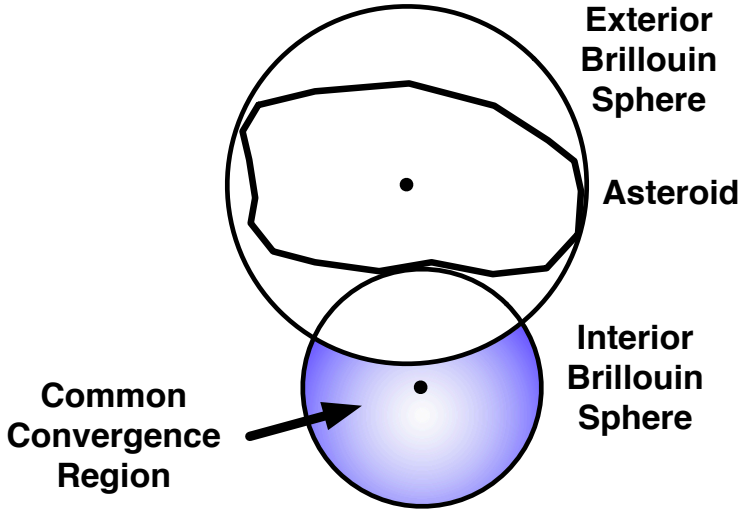

Figure 6.5: Common convergence region of the exterior and interior gravity fields.

In Figure 6.5, the faded blue region indicates the common convergence region of both the exterior and interior gravity fields. In this region, the acceleration of a field point, which is the gradient of the potential, given by the two formulae must be identical, if not the potentials themselves. Moreover, the second partial of the potential with respect to the field point position must be identical in both frames. If the second partials were not equal to each other, the two coordinate frames would have to observe different accelerations at the same location. Thus, the acceleration ($\ddot{\vec{r}}$) and the dynamics matrix ($A = \partial\ddot{\vec{r}}/\partial\vec{r}$) are identical in both frames. This property serves as an important tool when converting an exterior gravity field into an interior gravity field, the methodology of which will be discussed later.

6.1.5 Placement and Orientation of the Exterior and Interior Coordinates

In this section, the placement and orientation of the exterior and interior coordinate frames are discussed. In general, two vectors in different coordinate frames can be related by translation and rotation. For example, a position vector in the interior coordinate ($\vec{r}_i$) can be defined in terms of a position vector in the exterior coordinate ($\vec{r}_e$) as

$$\vec{r}_i = [IE](\vec{r}_e - \vec{r}_{e\to i}) \tag{6.8}$$

where $\vec{r}_{e\to i}$ is the vector that offsets the interior coordinate center from the exterior coordinate center, and $[IE]$ is the rotation matrix that maps the position vector in the exterior coordinate frame (E) into that in the interior coordinate frame (I). One of the most convenient ways to perform transformation is to set $[IE]$ to the identity matrix as shown in Figure 6.6:

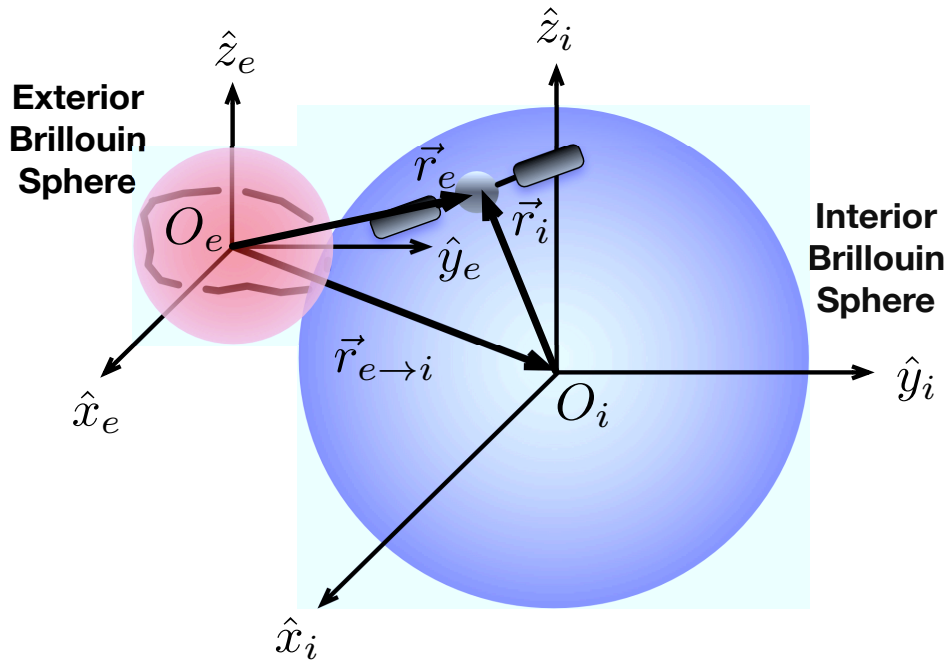

Figure 6.6: Exterior and interior coordinate frames without rotation.

In Figure 6.6, the red sphere is the exterior Brillouin sphere, and the blue sphere is the interior Brillouin sphere just touching the asteroid's surface at the touchdown site. If so desired,

one can define the interior coordinate frame relative to the touchdown site to match the surface normal so the spacecraft descends along the z-axis (i.e., local surface frame). This method requires the rotation matrix $[IE]$ be a non-identity matrix but can be useful when designing a landing trajectory. In our analysis, $[IE]$ is the identity matrix.

As shown in Figure 6.3, $\vec{r}_{e\to i}$ lies along the surface normal. The higher-degree and higher-order terms become important for the interior gravity field near the boundary of the Brillouin sphere (see Section 6.1.6); therefore, placing the interior coordinate center far from the exterior coordinate center requires accurate estimation of the higher-degree and higher-order spherical harmonic coefficients. Although not many spherical harmonic coefficients are needed to express the acceleration near the interior coordinate center, the higher-degree and higher-order coefficients become quickly important as the spacecraft dynamics are propagated along the landing trajectory.

6.1.6 Potential as a Double Summation Expression

Equation 6.5 and 6.7 are rewritten in a double summation notation using the property of the Legendre polynomial. First, we invoke the following expression for $P_n(\cos\Theta)$:

$$P_n(\cos\Theta) = \sum_{m=0}^{n}(2-\delta_{0,m})\frac{(n-m)!}{(n+m)!}\begin{bmatrix} P_{nm}(\sin\phi)\cos(m\lambda)P_{nm}(\sin\phi')\cos(m\lambda') \\ +P_{nm}(\sin\phi)\sin(m\lambda)P_{nm}(\sin\phi')\sin(m\lambda')\end{bmatrix} \tag{6.9}$$

That is, the Legendre polynomial of degree n is a function of the associated Legendre functions of degree n and order m. The dimensionless spherical harmonic coefficients (C_{nm} and S_{nm}) for the exterior and interior gravity fields are defined as

$$\begin{cases} C^e_{nm} = \dfrac{(2-\delta_{0,m})}{M^*}\dfrac{(n-m)!}{(n+m)!}\displaystyle\int_M\left(\frac{r'}{R^*_e}\right)^n P_{nm}(\sin\phi')\cos(m\lambda')dm' \\ \\ S^e_{nm} \overset{m\geq 0}{=} \dfrac{2}{M^*}\dfrac{(n-m)!}{(n+m)!}\displaystyle\int_M\left(\frac{r'}{R^*_e}\right)^n P_{nm}(\sin\phi')\sin(m\lambda')dm' \end{cases} \tag{6.10}$$

$$\begin{cases} C^i_{nm} &= \dfrac{(2-\delta_{0,m})}{M^*}\dfrac{(n-m)!}{(n+m)!}\displaystyle\int_M \left(\frac{R^*_i}{r'}\right)^{n+1} P_{nm}(\sin\phi')\cos(m\lambda')dm' \\ \\ S^i_{nm} &\overset{m\geq 0}{=} \dfrac{2}{M^*}\dfrac{(n-m)!}{(n+m)!}\displaystyle\int_M \left(\frac{R^*_i}{r'}\right)^{n+1} P_{nm}(\sin\phi')\sin(m\lambda')dm' \end{cases} \tag{6.11}$$

where Equation 6.10 is identical to Equation 1.14; we only clarified that the reference radius is that of the exterior gravity field. The reference quantities (i.e., the reference mass and the reference radius) are used only to non-dimensionalize the spherical harmonic coefficients, and their values do not affect the condition of convergence dictated by the ratio of r and r' mentioned earlier. For practical purposes, it is convenient to set the reference mass as the total mass of the asteroid and the reference radius as the radius of the Brillouin sphere (note that this quantity is different for the exterior and interior gravity fields). However, this is not necessary, and one can arbitrarily assign the values of M^* and R^*.

The direct substitution of Equation 6.9 into Equation 6.5 and 6.7 yields the double summation expressions of the exterior/interior gravity fields as

$$U^e = \frac{GM^*}{R^*_e}\sum_{n=0}^{\infty}\sum_{m=0}^{n}\left(\frac{R^*_e}{r}\right)^{n+1} P_{nm}(\sin\phi)\begin{bmatrix}\cos(m\lambda)\\ \sin(m\lambda)\end{bmatrix}\cdot\begin{bmatrix}C^e_{nm}\\ S^e_{nm}\end{bmatrix} \tag{6.12}$$

$$U^i = \frac{GM^*}{R^*_i}\sum_{n=0}^{\infty}\sum_{m=0}^{n}\left(\frac{r}{R^*_i}\right)^{n} P_{nm}(\sin\phi)\begin{bmatrix}\cos(m\lambda)\\ \sin(m\lambda)\end{bmatrix}\cdot\begin{bmatrix}C^i_{nm}\\ S^i_{nm}\end{bmatrix} \tag{6.13}$$

where the dot product multiplies the cosine term with C_{nm} and the sine term with S_{nm}. The normalized spherical harmonic coefficients can also be defined, and they are documented in Appendix D.

It is a well-known fact that C^e_{00} is unity when the reference mass is set to the total mass of the asteroid (i.e., $C^e_{00} = M/M^*$), the first-degree exterior spherical harmonic coefficients vanish when the coordinate center is placed at the center of mass (Equation 4.8), and the differences of the

second-degree exterior spherical harmonic coefficients are linearly related to the moments of inertia of the asteroid (Equation 4.9). On the other hand, the interior spherical harmonic coefficients do not directly represent a physical parameter. For example, C_{00}^{i} is defined as

$$C_{00}^{i} = \frac{R_i^*}{M^*} \int_M \frac{1}{r'} dm' \tag{6.14}$$

which is a function of the location of the interior coordinate center. Interestingly enough, this C_{00}^{i} term does not contribute to the field point acceleration since the zeroth-degree potential is only a bias term in Equation 6.13. In other words, the zeroth-degree interior gravity field does not depend on the field point position r. Unlike the exterior gravity field, the "point mass approximation" does not exist for the interior gravity field.

Even more interesting about the interior gravity field is the way that the field point acceleration interacts with the gravity field. A careful look at Equation 6.12 reveals that when the field point is placed far from the exterior coordinate center, the exterior potential is zero, and the field point acceleration can be approximated by a point mass. As the field point approaches closer to the asteroid, the field point is more susceptible to the higher-degree and higher-order terms, and the point mass assumption breaks down. On the other hand, the interior potential is identically zero when the spacecraft is placed at the interior coordinate center, and the acceleration at the interior coordinate center is constant and strictly due to the first-degree spherical harmonic coefficients. The behavior of the field point acceleration around the interior coordinate center is analogous to the field point placed far in the exterior gravity field. When the field point is placed near the boundary of the interior Brillouin sphere, the field point acceleration is more susceptible to the higher-degree and higher-order terms (analogous to the field point in close proximity to the asteroid in the exterior gravity field). Thus, errors in the interior gravity field grow as the spacecraft approaches the touchdown site.

6.2 Acceleration within the Interior Gravity Field

As a parameter of interest, the acceleration of a spacecraft due to the interior gravity field is presented in this section. The acceleration of the spacecraft is obtained by computing the gradient of the interior potential, an elegant method of which is explained in detail by Werner [74]. Supplemental equations are listed in Appendix D.5 through D.6.

Equation 6.15 through 6.17 provide the acceleration of a field point in the unnormalized/normalized interior gravity fields:

$$\begin{aligned}
\frac{\partial U^i}{\partial x} &= \frac{GM^*}{(R_i^*)^2}\sum_{n=1}^{\infty}\sum_{m=0}^{n}\begin{bmatrix} C_{nm}^i \\ S_{nm}^i \end{bmatrix}\cdot\left[-\frac{1}{2}(1+\delta_{0,m})b_{n-1,m+1}^i + \frac{1}{2}\frac{(n+m)!}{(n+m-2)!}b_{n-1,m-1}^i\right] \\
&= \frac{GM^*}{(R_i^*)^2}\sum_{n=1}^{\infty}\sum_{m=0}^{n}\begin{bmatrix} \bar{C}_{nm}^i \\ \bar{S}_{nm}^i \end{bmatrix}\cdot\left[-\frac{1}{2}(1+\delta_{0,m})\sqrt{\frac{(2-\delta_{0,m})}{2}\frac{(2n+1)}{(2n-1)}\frac{(n-m)!}{(n-m-2)!}}\bar{b}_{n-1,m+1}^i\right. \\
&\quad \left. +\frac{1}{2}\sqrt{\frac{(2-\delta_{0,m})}{(2-\delta_{1,m})}\frac{(2n+1)}{(2n-1)}\frac{(n+m)!}{(n+m-2)!}}\bar{b}_{n-1,m-1}^i\right]
\end{aligned} \tag{6.15}$$

$$\begin{aligned}
\frac{\partial U^i}{\partial y} &= \frac{GM^*}{(R_i^*)^2}\sum_{n=1}^{\infty}\sum_{m=0}^{n}\begin{bmatrix} S_{nm}^i \\ -C_{nm}^i \end{bmatrix}\cdot\left[\frac{1}{2}(1+\delta_{0,m})b_{n-1,m+1}^i + \frac{1}{2}\frac{(n+m)!}{(n+m-2)!}b_{n-1,m-1}^i\right] \\
&= \frac{GM^*}{(R_i^*)^2}\sum_{n=1}^{\infty}\sum_{m=0}^{n}\begin{bmatrix} \bar{S}_{nm}^i \\ -\bar{C}_{nm}^i \end{bmatrix}\cdot\left[\frac{1}{2}(1+\delta_{0,m})\sqrt{\frac{(2-\delta_{0,m})}{2}\frac{(2n+1)}{(2n-1)}\frac{(n-m)!}{(n-m-2)!}}\bar{b}_{n-1,m+1}^i\right. \\
&\quad \left. +\frac{1}{2}\sqrt{\frac{(2-\delta_{0,m})}{(2-\delta_{1,m})}\frac{(2n+1)}{(2n-1)}\frac{(n+m)!}{(n+m-2)!}}\bar{b}_{n-1,m-1}^i\right]
\end{aligned} \tag{6.16}$$

$$\begin{aligned}\frac{\partial U^i}{\partial z} &= \frac{GM^*}{(R_i^*)^2}\sum_{n=1}^{\infty}\sum_{m=0}^{n}\begin{bmatrix}C_{nm}^i\\ S_{nm}^i\end{bmatrix}\cdot\left[(n+m)b_{n-1,m}^i\right] \\ &= \frac{GM^*}{(R_i^*)^2}\sum_{n=1}^{\infty}\sum_{m=0}^{n}\begin{bmatrix}\bar{C}_{nm}^i\\ \bar{S}_{nm}^i\end{bmatrix}\cdot\left[\sqrt{\frac{(2n+1)}{(2n-1)}}(n+m)(n-m)\bar{b}_{n-1,m}^i\right]\end{aligned} \tag{6.17}$$

where the basis functions, b_{nm}^i and $\bar{b}_{nm}^i$, are defined in Appendix D.3 together with the derivation of the higher-order partials of the interior potential. Equations above are anchored to each degree and order interior spherical harmonic coefficient. Another type of expression anchored to the basis function is presented in Appendix D.6.

6.3 Computation of the Interior Spherical Harmonic Coefficients

In this section, the computation of the interior spherical harmonic coefficients from a shape model and an exterior gravity field is discussed.

6.3.1 Interior Spherical Harmonic Coefficients from an Existing Shape Model

A method to approximate the interior spherical harmonic coefficients through shape model integration is derived. It is assumed that the shape model is precise and high resolution, and the density is uniformly distributed. The last assumption allows for the density to be pulled out of the integrand in Equation 6.11 to yield

$$\begin{bmatrix}C_{nm}^i\\ S_{nm}^i\end{bmatrix} = \frac{1}{M^*}\int_M c_{nm}^i dm' = \frac{\rho_0}{M^*}\iiint_V c_{nm}^i dv \tag{6.18}$$

where ρ_0 is the constant density of the body and c_{nm}^i is the integrand of the interior spherical harmonic coefficients. In Equation 6.18, V is the total volume of the body and shall not be confused with the volume of the interior Brillouin sphere (i.e., each spherical harmonic coefficient

is a function of the mass distribution). Then, the divergence theorem is applied to Equation 6.18. The divergence theorem states that

$$\iiint_V div(\vec{F})dv \quad = \quad \iiint_V \nabla \cdot \vec{F} dv \quad = \quad \iint_{S_A} \vec{F} \cdot \hat{n} dA \tag{6.19}$$

where $\hat{n}$ is the surface normal and A is the differential area of the surface S_A. Note that the divergence of a vector is a scalar, and its value is identical irrespective of the coordinate frame chosen. In order to simplify Equation 6.18, it is desired to find a vector $\vec{F}$ such that $c^i_{nm} = div(\vec{F})$ ($\vec{F}$ shall not be confused with the force acting on the spacecraft). To make the computation tractable, the divergence is taken in the spherical coordinates (r, θ, λ), which is defined as

$$\nabla \cdot \vec{F} \quad = \quad \frac{1}{r^2}\frac{\partial}{\partial r}(r^2 F_r) + \frac{1}{r\sin\theta}\frac{\partial}{\partial \theta}(\sin\theta F_\theta) + \frac{1}{r\sin\theta}\frac{\partial F_\lambda}{\partial \lambda} \tag{6.20}$$

Note that the prime is omitted to avoid the clutter. Then, Equation 6.19 is satisfied when $\vec{F}$ is chosen to be

$$\vec{F} \quad = \quad F_r \hat{u}_r \quad = \quad -\frac{1}{n-2} r c^i_{nm} \hat{u}_r \quad = \quad -\frac{1}{n-2} c^i_{nm} \vec{r} \tag{6.21}$$

where $n \neq 2$ and $\hat{u}_r$ is the unit vector in the radial direction. Thus, we get

$$c^i_{nm} \quad = \quad -\frac{1}{n-2} \nabla \cdot (c^i_{nm} \vec{r}) \tag{6.22}$$

When $n = 2$,

$$c^i_{2m} \quad = \quad \nabla \cdot (\ln r c^i_{2m} \vec{r}) \tag{6.23}$$

Therefore, the integral in Equation 6.18 becomes

$$\iiint_V \nabla \cdot \vec{F} dv = \begin{cases} -\frac{1}{n-2} \iint_{S_A} r c^i_{nm} \hat{u}_r \cdot \hat{n} dA & \text{for } n \neq 2 \\ \iint_{S_A} r \ln r c^i_{nm} \hat{u}_r \cdot \hat{n} dA & \text{for } n = 2 \end{cases} \tag{6.24}$$

where $r\hat{u}_r \cdot \hat{n}$ is a constant and equal to the shortest distance from the field point to the plane of the facet. The identical expression can be obtained for the normalized spherical harmonic coefficients, and replacing c^i_{nm} with $\bar{c}^i_{nm}$ suffices. For the sake of visualization, Figure 6.7 shows two tetrahedra adjacent to each other (V_1 and V_2), which are enclosed by vertices O_e, v_1, v_2, v_3, and v_4.

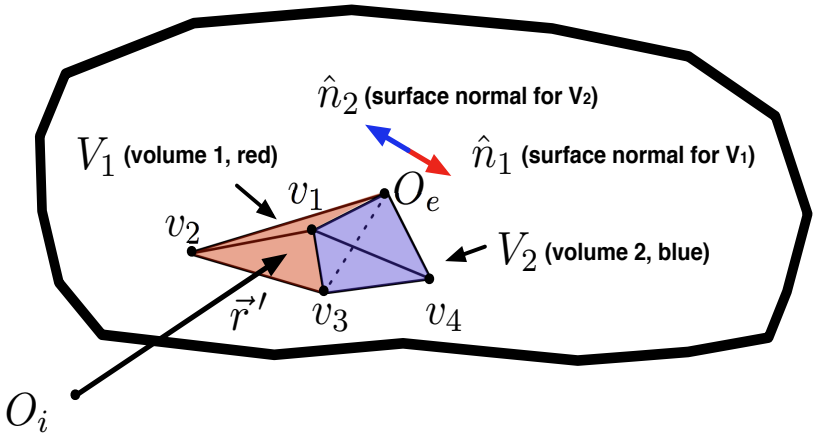

Figure 6.7: Two adjacent tetrahedra in the interior coordinate frame.

Equation 6.24 is hard to reduce to a simpler form. Thus, a numerical method is sought where the integrand is approximated by the value at the center of each facet. Note that the side facet adjacent to another tetrahedron (i.e., facet $v_1 v_3 O_e$) does not contribute to the overall spherical harmonic coefficients when the density is homogeneously distributed due to the alternating signs of $\hat{n}$. In case each tetrahedron has a different density value, all side facets need to be considered separately. One identity that might prove useful in reducing Equation 6.24 is that the interior spherical harmonic coefficients are a homogeneous function of degree $-(n+1)$. That is,

$$\vec{r}\cdot\frac{\partial c^i_{nm}}{\partial \vec{r}} = x\frac{\partial c^i_{nm}}{\partial x}+y\frac{\partial c^i_{nm}}{\partial y}+z\frac{\partial c^i_{nm}}{\partial z} = -(n+1)c^i_{nm} \tag{6.25}$$

Werner [76] leverages the property of the exterior spherical harmonic coefficients being homogeneous functions of degree n and carries out the volume integral for a unit tetrahedron after the change of coordinates. However, this approach is not suitable for the interior spherical harmonic coefficients since the integrand tends to infinity at the coordinate center.

6.3.2 Conversion between an Exterior Gravity Field and an Interior Gravity Field

Approximation of the interior spherical harmonic coefficients via shape model integration is valid only when the density is homogeneously distributed, and this may not be the case for NEOs. After the spacecraft rendezvouses with an asteroid, the exterior gravity field is estimated through OD. Here, a technique to convert an exterior gravity field into an interior gravity field is outlined.

6.3.2.1 Interior Spherical Harmonics via a Least-squares Fit

The idea of the conversion method is to estimate the interior spherical harmonic coefficients that best fit the potential, acceleration, and/or dynamics matrix computed by the exterior gravity field in a least-squares sense for a collection of data points in the common convergence region. As an example, a conversion method for the acceleration fitting is presented.

The state vector is the interior spherical harmonic coefficients ordered in the following manner:

$$[\tilde{C}^i_{nm}] = \left[C^i_{10}, C^i_{11}, S^i_{11}, C^i_{20}, C^i_{21}, S^i_{21}, C^i_{22}, S^i_{22}, C^i_{30}, \cdots\right] \tag{6.26}$$

which consists of n^2+2n coefficients. Note that C^i_{00} does not contribute to the field point acceleration. The objective here is to match the acceleration given by the exterior and interior gravity fields; therefore, the cost function is defined as

$$J_i = \frac{1}{2}\left([Q^i_{nm}][\tilde{C}^i_{nm}]-\frac{\partial U^e}{\partial \vec{r}_e}\right)^T W_i \left([Q^i_{nm}][\tilde{C}^i_{nm}]-\frac{\partial U^e}{\partial \vec{r}_e}\right) \tag{6.27}$$

where W_i is the weighting matrix, and $[Q^i_{nm}]$ is the partial of acceleration with respect to each interior spherical harmonic coefficient (Equation D.55 through D.60). W_i is chosen as the identity matrix with a scaling factor as there is no justification to weigh one component of the acceleration more than the others. The dimension of $[Q^i_{nm}]$ is $[3 \times (n^2 + 2n)]$. The cost function is minimized with respect to the spherical harmonic coefficients $[\tilde{C}^i_{nm}]$ to yield the normal equation as follows:

$$[\tilde{C}^i_{nm}] = \left([Q^i_{nm}]^T W_i [Q^i_{nm}]\right)^{-1} \left\{ [Q^i_{nm}]^T W_i \left(\frac{\partial U_e}{\partial \vec{r}_e} \right) \right\} \tag{6.28}$$

Thus, the scaling factor for W_i does not change the solution. It only changes the value of the uncertainty in each estimated coefficient. As the acceleration at each data point gives three components, the number of the data points (N_{Data}) has to satisfy the condition $3N_{Data} \geq n^2 + 2n$ in order to construct a full rank system.

The same approach can be used to estimate the normalized interior spherical harmonic coefficients by substituting the normalized components for $[\tilde{C}^i_{nm}]$ and $[Q^i_{nm}]$. Moreover, a similar least-squares fit to the potential and the dynamics matrix is also possible. For the potential fitting, the bias term plus the constant offset of the potential (treated as one parameter) needs to be estimated. For the dynamics matrix fitting, the state vector starts from the second-degree coefficients. The source gravity field model needs not be the exterior spherical harmonic gravity field; the source gravity field can be the polyhedral gravity field, mascon model, or any other gravity field model.

One caveat to the above conversion method is that there may be cases where the common convergence region is small, or even non-existent. For instance, if a TAG point is chosen to be at the neck of a contact binary, a good portion of the region above the surface is outside the convergence region of the exterior gravity field (i.e., inside the exterior Brillouin sphere). In such cases, one may construct initial guess of the interior spherical harmonics via shape model integration and estimate the interior spherical harmonic coefficients via OD. The study of this OD process for the interior gravity field is not treated in this thesis; however, it is expected that the estimation of

these parameters is difficult, as the spacecraft position is confined in the interior Brillouin sphere and does not get the full coverage of the dynamics.

6.3.2.2 Search for the Optimal Interior Gravity Field

The accuracy of the estimated interior spherical harmonic coefficients depends on the parameter settings of the least-squares fit. Here, we explore how these parameters can be adjusted to optimize the estimated solution.

The location of the landing site and the radius of the interior Brillouin sphere uniquely fix the location of the interior coordinate center. As shown in Figure 6.3, the interior coordinate center lies along the surface normal distanced by R_i^* from the landing site. Then, for a given Brillouin sphere, we have the freedom to choose the size of the data sphere. The data sphere is the sphere placed concentric with the interior Brillouin sphere within which the source data (i.e., potential/acceleration/dynamics matrix) is computed. For example, Figure 6.8 shows three data spheres within an interior Brillouin sphere:

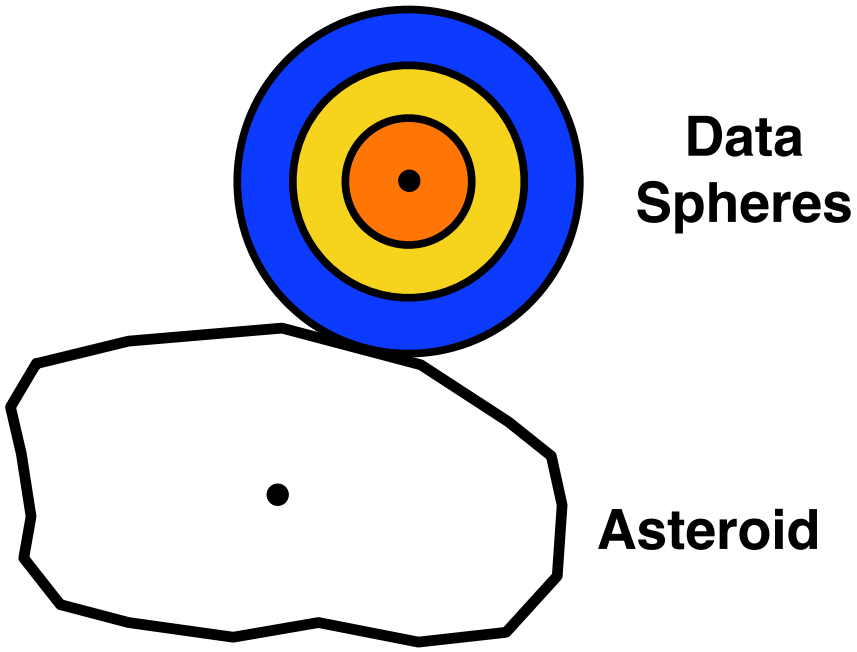

Figure 6.8: Data spheres for the interior gravity field estimation.

The size of the data sphere relative to the interior Brillouin sphere is denoted in ratios (i.e., R_{Data}/R_i^*), and its largest value is unity as the interior gravity field does not converge outside the interior Brillouin sphere. The data sphere size plays a key role in obtaining the desired accuracy of the least-squares estimation. For example, when only the lower-degree interior spherical harmonic coefficients are required, a small data sphere will give sufficient accuracy. On the other hand, a large data sphere is necessary to capture the information of the higher-degree and higher-order interior spherical harmonic coefficients. Thus, in order to construct an interior gravity field that is accurate out to the boundary of the interior Brillouin sphere, it is often judicious to combine solutions obtained from different parameter settings. We will refer to each solution as a **subset**. Each subset can be estimated with different source data types (i.e., potential/acceleration/dynamics matrix) and source gravity fields. As the OD solution is only obtained for the exterior gravity field, and the polyhedral gravity field can be reconstructed using the density estimation techniques discussed in Chapter 5, either the exterior or polyhedral gravity field can be used as the source gravity field.

For convenience, we denote the data types numerically and use 1 for the potential data, 2 for the acceleration data, and 3 for the dynamics matrix data. Note that not all the coefficients estimated for a subset needs to be assigned to the final solution. For example, one subset can be estimated up to the 10th-degree gravity field but only 5×5 gravity field can be assigned to the final solution.

In summary, each interior gravity field can be estimated via least-squares fit to the potential/acceleration/dynamics matrix (i.e., three source data type) computed inside the data sphere. These source data can be computed either from the exterior gravity field or polyhedral gravity field (i.e., two source gravity fields). This method yields an interior gravity field as a complex function of the degree and order of the potential expansion, the location of the interior coordinate center, source data type, size of the data sphere, and source gravity field. Furthermore, it is also possible to combine solutions from different least-squares fit to produce another set of interior gravity field coefficients.

With as many variables as there are, exhaust search for the optimal interior gravity field is prohibitively time-consuming. Therefore, an interior gravity field is estimated by exploring the parameter space manually. Automated search algorithm is possible in a powerful enough computing environment.

6.4 Performance of the Interior Gravity Field

In this section, we evaluate the performance of the interior gravity field. Specifically, the error distribution analysis and the landing trajectory analysis are presented.

6.4.1 Error Distribution Analysis

The error distribution analysis is conducted in order to evaluate how well the interior gravity field models the acceleration and the dynamics matrix within the common convergence region of the exterior/interior gravity fields. The base gravity field of a 15×15 exterior gravity field is numerically computed for 4769 Castalia from point masses placed at each vertex (i.e., mascon shell model). Each mass is equal, and the sum of all masses equals the total mass of Castalia. The interior coordinate center is placed at $[0.5, 0.1, 2.5]$ $[km]$ from the exterior coordinate center, which gives the interior Brillouin radius of 2.20 $[km]$. The errors are computed with respect to 15×15 and 50×50 interior gravity fields. The benefit of working with the mascon shell model is that the spherical harmonic coefficients can be computed without error both for exterior and interior gravity fields, allowing for direct one-to-one comparisons between the two gravity fields.

The acceleration error is computed by the difference in magnitude, and the dynamics matrix error is computed by the difference in determinant, which is the volume of the dyad:

$$\epsilon_{acce} = abs\left(\frac{|\vec{U}^i_{\vec{r}_i}| - |\vec{U}^e_{\vec{r}_e}|}{|\vec{U}^e_{\vec{r}_e}|}\right) \tag{6.29}$$

$$\epsilon_{DM} = abs\left(\frac{|\vec{U}^i_{\vec{r}_i\vec{r}_i}| - |\vec{U}^e_{\vec{r}_e\vec{r}_e}|}{|\vec{U}^e_{\vec{r}_e\vec{r}_e}|}\right) \tag{6.30}$$

Figure 6.9 and 6.10 show the error distributions of the acceleration and the dynamics matrix for $n_i = 15$ and 50. The errors are computed throughout the volume of the interior Brillouin sphere in an evenly spaced $[5 \times 20 \times 20]$ grid in the radial, longitudinal, and latitudinal directions. It is shown that the errors grow radially outward as manifested in Equation 6.13.

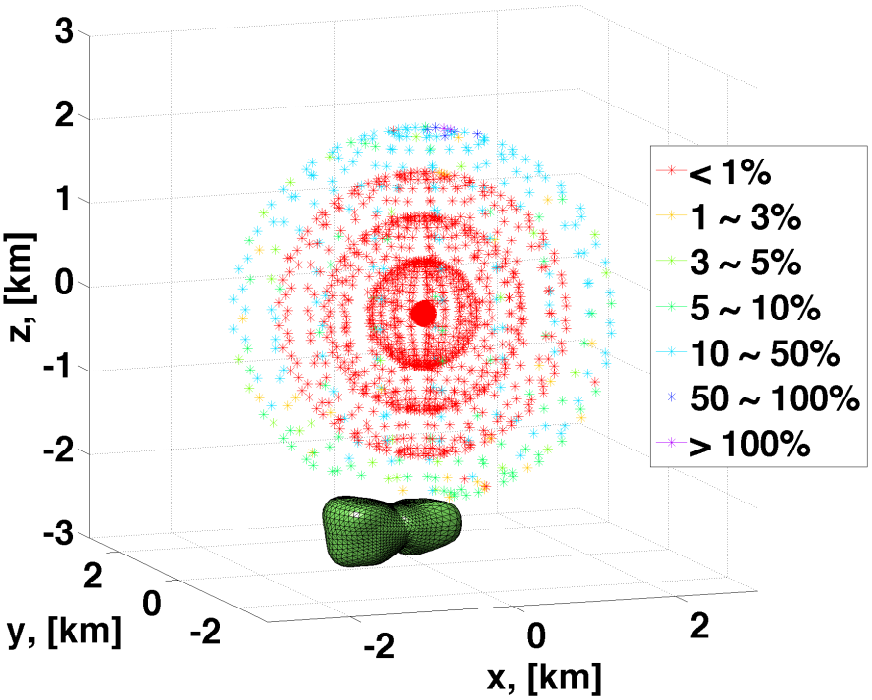

(a) Acceleration error with $n_i = 15$

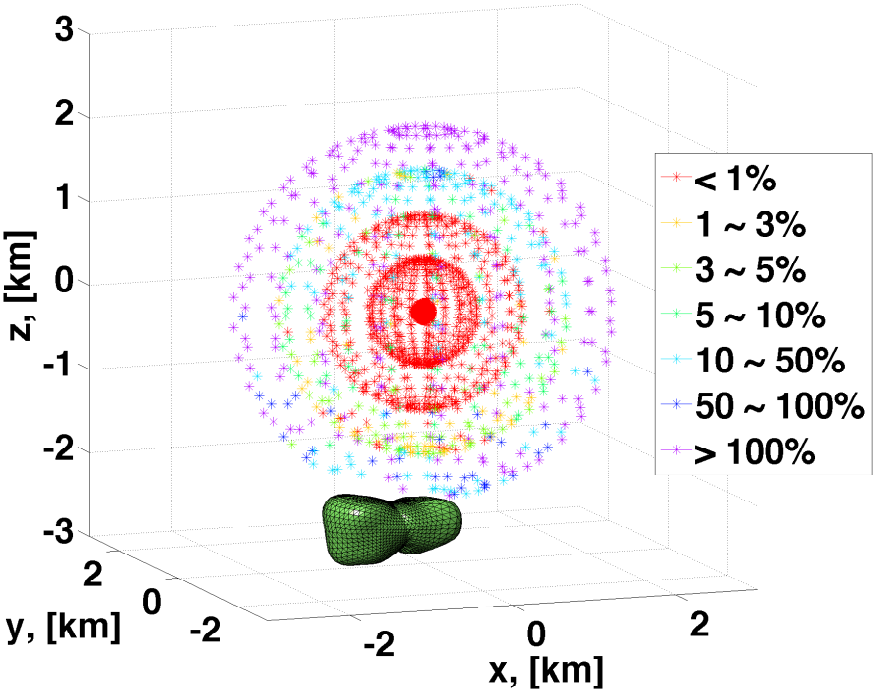

(b) Dynamics matrix error with $n_i = 15$

Figure 6.9: Acceleration and dynamics matrix errors between the exterior and interior gravity fields with $n_e = 15$ and $n_i = 15$.

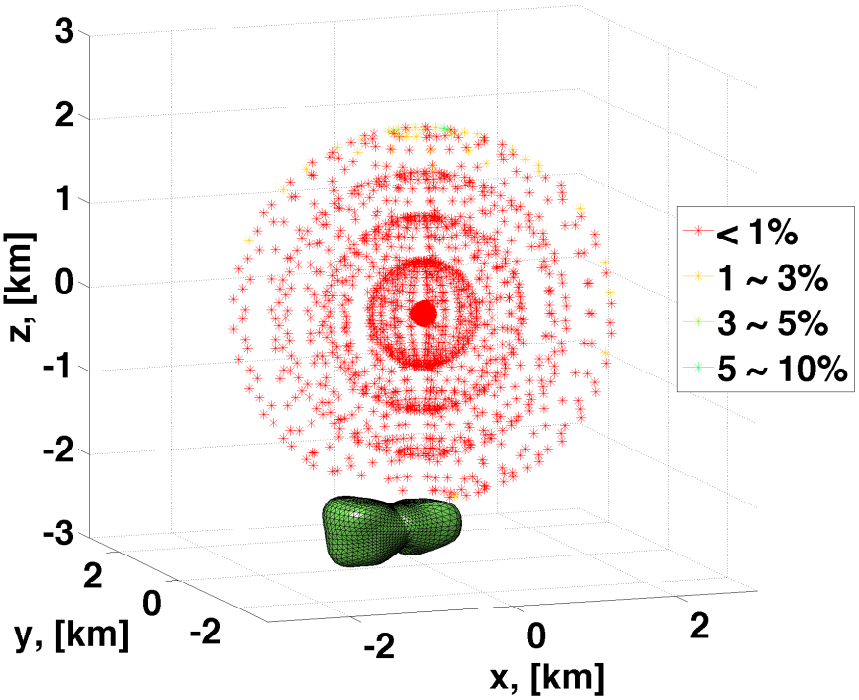

(a) Acceleration error with $n_i = 50$

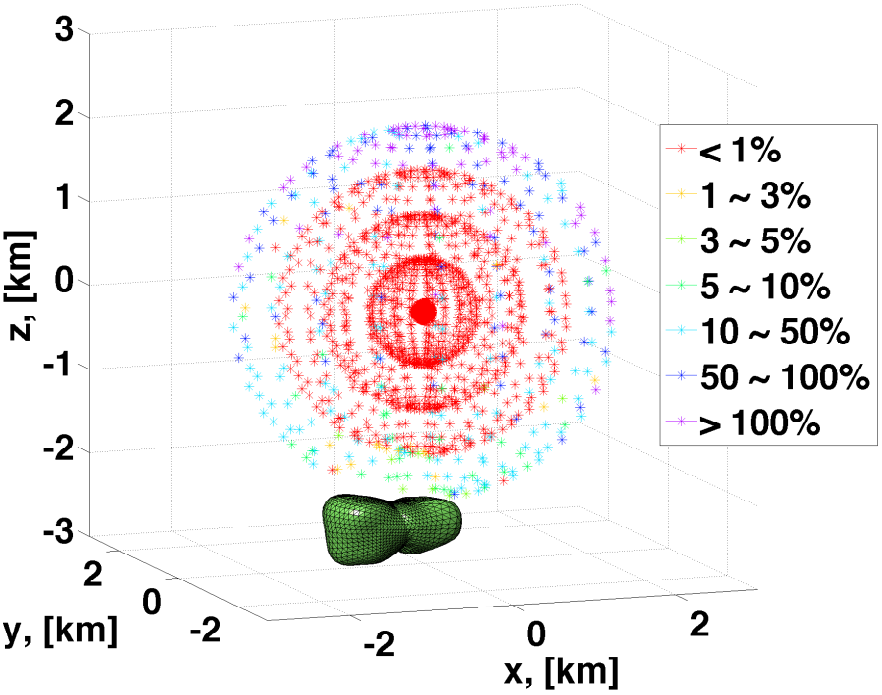

(b) Dynamics matrix error with $n_i = 50$

Figure 6.10: Acceleration and dynamics matrix errors between the exterior and interior gravity fields with $n_e = 15$ and $n_i = 50$.

Notice the significant reduction in errors for both the acceleration and the dynamics matrix as n_i is increased from 15 to 50. However, this result reveals that the interior gravity field requires considerably more terms than the exterior gravity field in order to accurately model the acceleration and the dynamics matrix, which is one drawback of using the interior gravity field.

6.4.2 Landing Trajectory Analysis

The landing trajectory analysis compares the accuracy of the interior spherical harmonic coefficients estimated via a least-squares fit and those obtained via shape model integration (i.e., numerically approximated coefficients). The truth model is the polyhedral gravity field, and the source data is computed by a 15×15 exterior gravity field, both of which are generated with a homogeneous density of 2.1 $[g/cm^3]$ [75, 76]. This setting yields the gravitational parameter of 9.4×10^{-8} $[km^3/s^2]$. The exterior gravity field is used to compute the source data as it is generally the only gravity field information about the body in the real mission scenario. It is important to note that the 15×15 exterior gravity field represents a rather optimistic scenario where the OD solution is obtained with high fidelity. The actual OD solution may not contain as many higher-degree and higher-order coefficients. However, this scenario will allow one to see the intrinsic powerfulness of the interior gravity field. Table 6.1 shows the parameters used for the least-squares fit:

Table 6.1: Parameters of the estimated interior gravity field around Castalia.

R_i^* $[km]$	Degree (n)	Data Type	Estimated Degree (n) for Each Subset	Assigned Degree (n) from Each Subset	Data Sphere Size w.r.t. R_i^*
2.5	40	$(1, 2, 3)$	$(30, 40, 40)$	$(1 \to 5, 6 \to 25, 26 \to 40)$	$(0.3, 0.8, 0.999)$

The spacecraft is initially placed at the TAG point of $[-0.344, -0.0677, 0.374]$ $[km]$ in the exterior coordinates, which lies on the flat plateau of the main lobe of Castalia. Then, the interior Brillouin radius of $R_i^* = 2.5$ $[km]$ yields the interior coordinate center of $[-0.0615, -0.154, 2.85]$ $[km]$. The initial velocities of the spacecraft, which are identical both in the exterior and interior coordinates, are shown on the next page.

Table 6.2: Initial velocity at the TAG point.

Case	V_x $[cm/s]$	V_y $[cm/s]$	V_z $[cm/s]$
1	0	0	-70
2	0	20	-70
3	0	-20	-70
4	20	20	-70
5	-20	-20	-70

The escape velocity at the initial spacecraft position is approximately 60 $[cm/s]$. Thus, the resulting trajectories are hyperbolic. These initial conditions are propagated backward in time for one hour to compare how well the interior gravity field models the polyhedral gravity field.

Figure 6.11 shows the spacecraft trajectories sprouting from the TAG point and the spacecraft distance from the interior coordinate center.

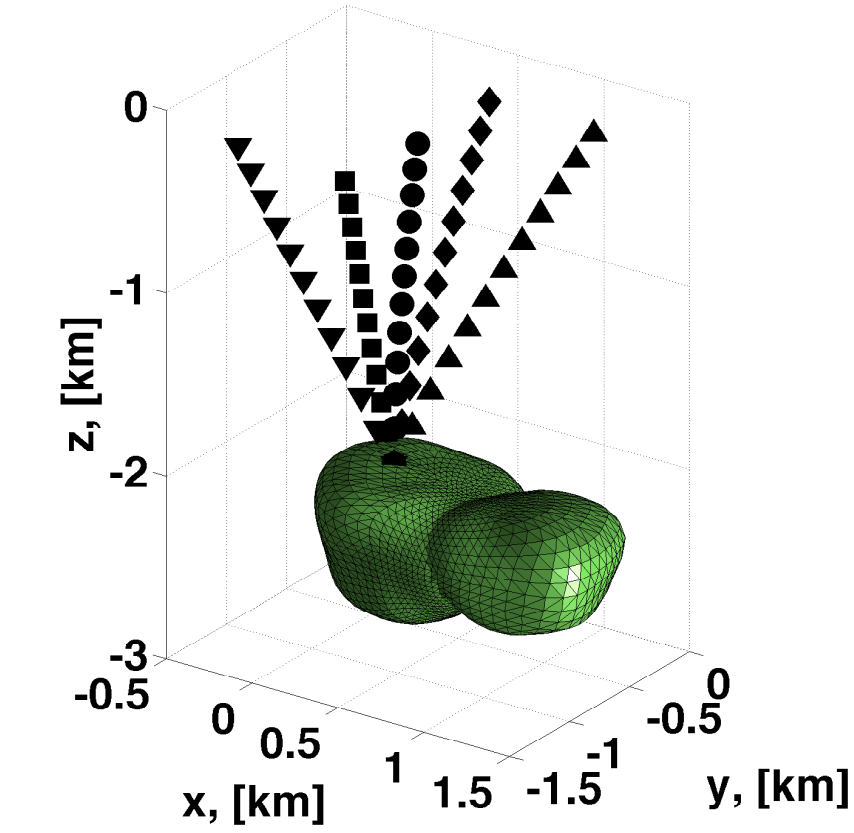

(a) Spacecraft trajectories

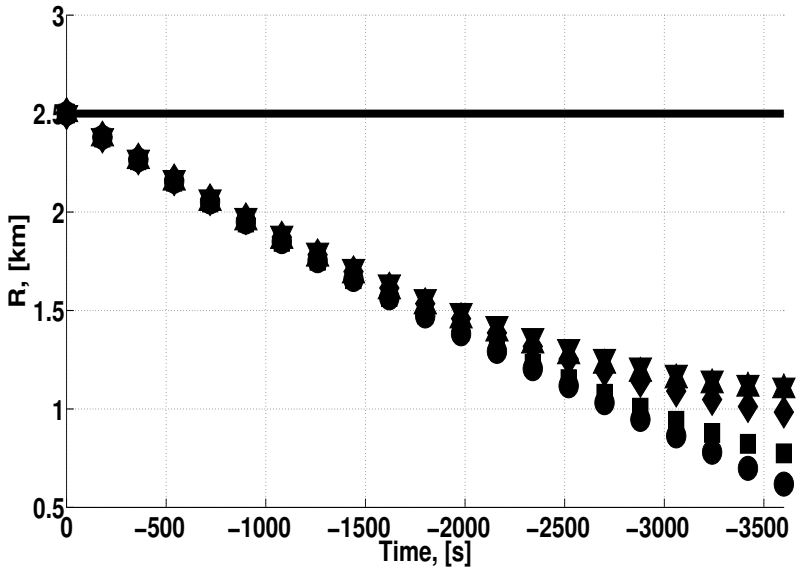

(b) Spacecraft distance from the interior coordinate center

Figure 6.11: Spacecraft trajectories in the interior coordinates (case 1 in circles, case 2 in squares, case 3 in diamonds, case 4 in down-triangles, and case 5 in up-triangles) and spacecraft distance from the interior coordinate center. The radius of the interior Brillouin sphere is the solid black line at 2.5 $[km]$.

As shown in Figure 6.11(b), the spacecraft stays within the convergence region of the interior gravity field at all times. The total travel distances range between 1.9 $[km]$ (case 1) and 2.0 $[km]$ (case 5). Figure 6.12 shows the L_2-norm position errors between the interior gravity fields (both estimated and numerically approximated) and the polyhedral gravity field:

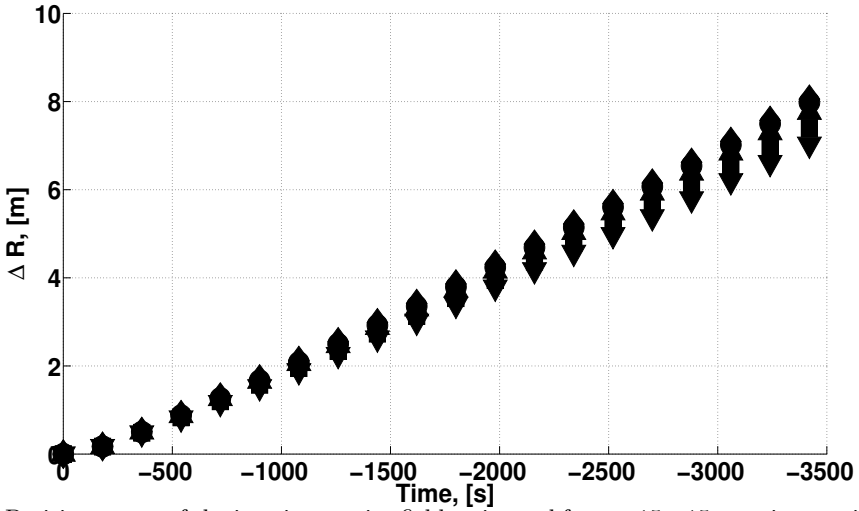

(a) Position errors of the interior gravity field estimated from a 15×15 exterior gravity field

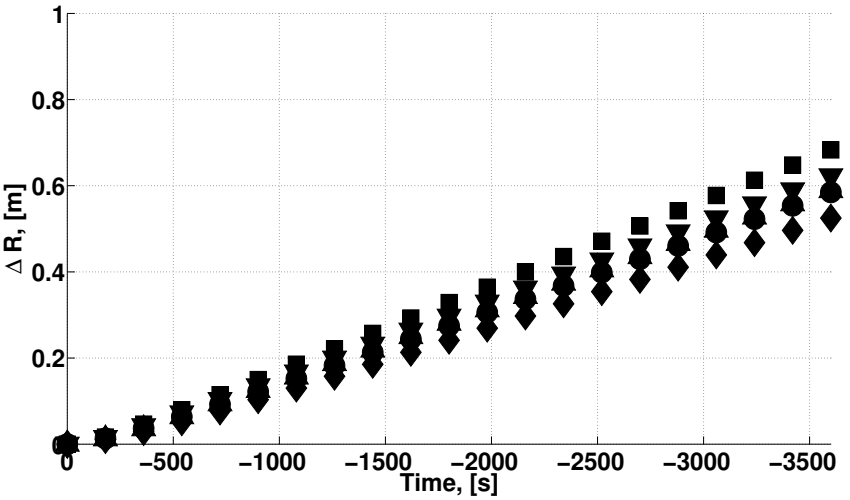

(b) Position errors of the numerically approximated interior gravity field

Figure 6.12: 3D position errors between the polyhedral gravity field and a) interior gravity field estimated from a 15×15 exterior gravity field and b) numerically approximated interior gravity field.

Both the estimated and numerically approximated interior gravity fields closely match the true polyhedral gravity field near the surface of the body. The position errors are < 10 $[m]$ for the estimated coefficients and < 1 $[m]$ for the numerically approximated coefficients after one hour of backward propagation.

Now, we investigate the sensitivity of the accuracy of the estimated solution to the source gravity field. To this end, the polyhedral gravity field is used as the source gravity field to estimate the interior spherical harmonic coefficients, keeping all other parameters unchanged. Note that the data can be computed anywhere around the body, providing information about the surface gravity field. Figure 6.13 shows the position errors of the interior gravity field estimated from the polyhedral gravity field:

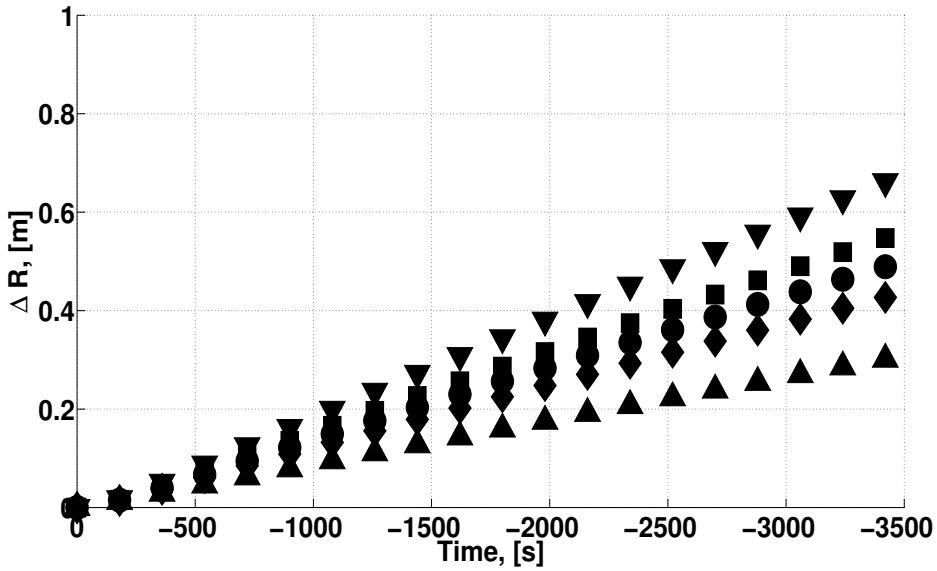

Figure 6.13: Position errors of the interior gravity field estimated from the polyhedral gravity field.

The accuracy of the estimated interior spherical harmonic coefficients greatly increases when the polyhedral gravity field is used as data. In Figure 6.13, the position error has decreased to < 1 $[m]$ and is comparable to the numerically approximated gravity field (Figure 6.12(b)). The advantage of the polyhedral gravity field is that it contains information of infinite degree and order terms. In addition, the convergence of the polyhedral gravity field is guaranteed anywhere around

the body as mentioned above. On the other hand, the exterior gravity field does not provide any information about the gravitation near the surface of the body and sufferes truncation errors. In general, it is a tremendously challenging task to constrain the higher-degree and higher-order spherical harmonic coefficients for small bodies. The degree of the spherical harmonic coefficients that can be estimated depends on the size/shape of the asteroid, and it is most likely that only the lower-degree coefficients can be determined. For reference, the lower-degree interior spherical harmonic coefficients are listed in Appendix D.7.

6.5 Conclusions

In this chapter, the interior gravity field was derived, and its characteristics were discussed and applied to the proximity operation around 4769 Castalia. The interior gravity field has the convergence region within the Brillouin sphere in contrast to the exterior gravity field, whose convergence region lies exterior to the Brillouin sphere. These two gravity fields are the mirror images of each other, and they share much commonality in their expressions.

It is shown that it is possible to convert an exterior gravity field, or any base model gravity field, into an interior gravity field through a least-squares fit. The necessary condition is that the base gravity field and the interior gravity field have the common convergence region. Moreover, the interior spherical harmonic coefficients can be numerically approximated by shape model integration for a homogeneous body. By comparing the spacecraft trajectories computed by the polyhedral gravity field, estimated interior gravity field (least-squares fit), and numerically approximated interior gravity field (shape model integration), it is shown that both estimated and numerically approximated interior gravity fields closely model the true polyhedral gravity field. This result indicates that the interior gravity field performs well to model the gravity field environment in close proximity to the asteroid's surface.

Chapter 7

Interior and Exterior Spherical Bessel Gravity Fields

The previous chapter investigated how the surface gravity field can be mapped via the interior gravity field, which is of the same type as the exterior gravity field. The interior gravity field resulted from directly solving the potential equation in Equation 1.1. The interior gravity field does not allow the total mapping of the surface gravity field, and its capability is limited around the TAG point on the surface. As manifested in Figure 6.2, many interior gravity fields are required to map out the entire surface gravity field around the body. This shortcoming becomes more critical, for example, when the gravity field is required in a severely concave region.

In this chapter, we will discuss other types of spherical harmonic gravity fields that bridge the null space of the exterior/interior gravity field expressions by solving Poisson's equation. These two gravity fields are obtained by assuming the form of Helmholtz's equation to Poisson's equation and exhibit strong contrast with the exterior/interior gravity fields that satisfy Laplace's equation. Specifically, we will solve Poisson's equation within the Brillouin sphere of the asteroid after re-distribution of mass within it. This approach renders the gravitational potentials as functions of spherical Bessel functions and spherical harmonic coefficients. We refer to these gravity fields as the interior/exterior spherical Bessel gravity fields and study their characteristics.

The original work of the interior spherical Bessel gravity field is discussed by Allen et al. [3] and Palmer [47], and its application to asteroid gravity fields by Herrera-Sucarrat et al [21]. In fact, the solution form of the interior spherical Bessel gravity field is hinted by Pinsky [50] when solving the heat equation in spherical coordinates and also by MacRobert when solving Laplace's equation

in the cylindrical coordinates. However, we believe that Allen et al. and Palmer first discussed its derivation with applications to the dynamic propagation of the celestial bodies in mind. Then, Herrera-Sucarrat et al. applied the theory to study the solutions to the equilibrium points and zero-velocity curves near the surface of small bodies, which gave qualitative insight into the performance of the interior spherical Bessel gravity field. In this chapter, we will also derive the interior spherical Bessel gravity field with slightly different motivation and quantify its performance. Specifically, we will leverage the properties of the interior spherical Bessel gravity field for the proximity operation around small bodies. That is, the performance of the interior spherical Bessel gravity field is studied in the context of accurate trajectory design and safe navigation of a spacecraft down to the surface of a small body in order to aid proximity operation strategies for future missions.

The following sections will entail the derivation of the interior spherical Bessel gravity field and its performance around asteroids (101955) Bennu (hereafter Bennu) and Castalia. Bennu is formerly known as 1999 RQ36, and it is the target body of the OSIRIS-REx mission. As the goal of the OSIRIS-REx mission is to collect samples from the asteroid's surface, thorough analysis of proximity operation is crucial. We will use the shape model determined by Nolan et al. [41] to evaluate the gravity field environment around Bennu. We will also study Castalia in order to evaluate the performance of the interior spherical Bessel gravity field around an irregularly shaped body. For both asteroids, we compare the performance of the exterior gravity field, interior gravity field, interior spherical Bessel gravity field, and polyhedral gravity field. Their accuracies are compared in context of total mapping vs. regional mapping. Finally, recommendations are given for mapping out the gravity field environment in close proximity to small body's surface for future mission planning.

7.1 Solution Space of Laplace's and Poisson's Equations

Both the exterior and interior gravity fields are solutions to Laplace's equation (Equation 1.6). These gravity fields only map the gravity field outside the body because Laplace's equation is only valid outside the body. In contrast to Laplace's equation, there exists Poisson's equation (Equa-

tion 1.12) that converges within the body. As we have two equations that are valid inside/outside the body, it seems natural to solve Poisson's/Laplace's equations directly and attempt to map out the gravity field within/outside the body in its entirety. However, there is subtle difficulty that we immediately notice when we graphically show their solution space. Figure 7.1 shows the regions where the Laplace's and Poisson's equations are satisfied along with the convergence regions of the exterior and interior gravity fields.

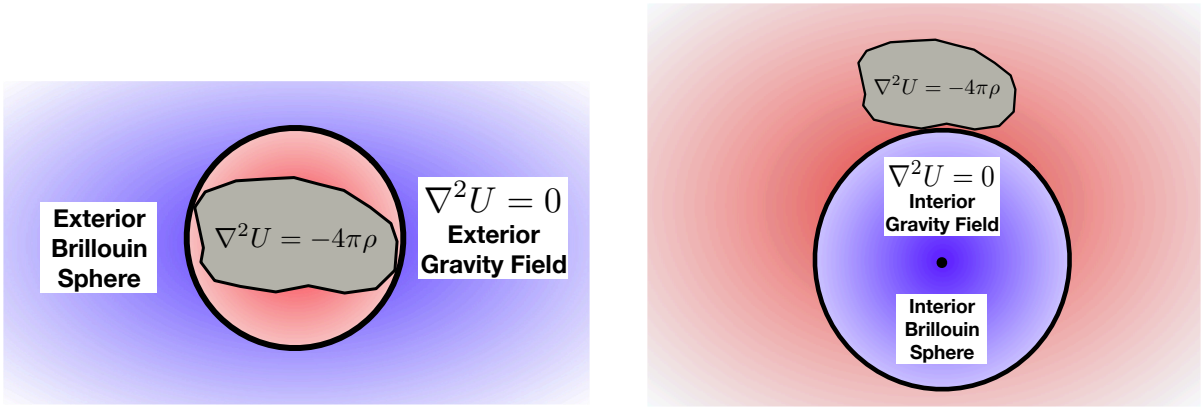

(a) Exterior gravity field (b) Interior gravity field

Figure 7.1: Solution space of Laplace's and Poisson's equations.

In Figure 7.1, the light gray body is the asteroid, within which the Poisson's equation must be satisfied. The blue regions are the convergence regions of the exterior and interior gravity fields which satisfy the Laplace's equation, and the red regions exist without a corresponding gravity field expression. Thus, even if the solutions are obtained for both Laplace's and Poisson's equations, the empty space without a corresponding gravity field is present, and directly solving Poisson's equation seems rather fruitless effort.

7.2 Redistribution of the Mass within the Circumscribing Sphere

Based on the discussion in the previous section, it appears that we are still facing the same problem as before even after solving Poisson's equation; that is, the proximity region to the surface does not have a well-defined gravity field expression. Before we further proceed, we make a few

notes about the relation between the gravity field and the mass distribution. From the potential definition in Equation 1.1, the gravitational potential is clearly a function of the mass distribution, and forward modeling of the potential, given a particular set of mass distribution, is straightforward. For example, the polyhedral gravity field by Werner and Scheeres [75] is particularly useful for this purpose (see Section 5.3.2). However, estimation of the mass distribution for a given gravity field is not trivial, as discussed in Chapter 5.

Now, recall Figure 5.1, where the spacecraft feels the identical gravitation due to the concentric spheres and shells of the same mass. These spheres and shells exert the same force on the spacecraft, and it is impossible to distinguish one model from another purely by the gravity field measurement unless constraints can be put on the mass distribution through the shape model and surface/internal composition. That is, infinitely many solutions of density distribution exist for a given gravity field.

On the other hand, if we change our point of view, the same example shows that we need not have the exact mass distribution in order to accurately model the sensed gravity field. That is, the disadvantage of not being able to constrain the mass distribution can be turned into our advantage. Therefore, it becomes viable again to solve Poisson's equation and obtain the solution, with the condition that the solution space terminates at the boundary of the exterior/interior Brillouin spheres, merging smoothly into the exterior/interior gravity fields. Figure 7.2 graphically shows the redistribution of mass of the asteroid within the exterior Brillouin sphere. As will be shown in Section 7.4, such a mass redistribution corresponds to the solution of the ***interior*** spherical Bessel gravity field. When the asteroid's mass is redistributed outside the interior Brillouin sphere, the corresponding gravity field expression is the ***exterior*** spherical Bessel gravity field.

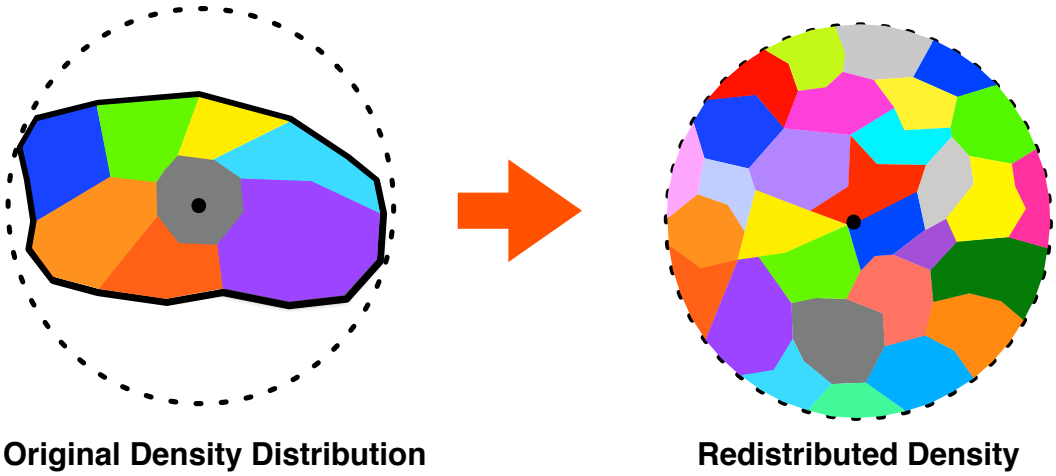

Figure 7.2: Redistribution of mass within the exterior Brillouin sphere. The original density distribution on the left is redistributed throughout the exterior Brillouin sphere to model the sensed gravity field.

7.3 Types of Partial Differential Equations

Before we depart to solve Poisson's equation, we briefly discuss different types of partial differential equations (PDEs). The details are discussed by Pinsky [50] (Chapter 0 and 3) and Arfken [4] (Chapter 2) and are summarized here. In a two-dimensional system, a linear second-order partial differential equation $u = u(x, y)$ takes on the form

$$Au_{xx} + 2Bu_{xy} + Cu_{yy} + Du_x + Eu_y + Fu \quad = \quad G \tag{7.1}$$

where the subscript denotes the parameter with respect to which the partial derivative is computed, and A, B, C, D, E, F, and G are all functions of x and y. The equation is called homogeneous if $G = 0$, which is the case for Laplace's equation. In general, Equation 7.1 is classified into three types, depending on the values of the coefficients A, B, and C.

- If $AC - B^2 > 0$, the equation is elliptic.
- If $AC - B^2 = 0$, the equation is parabolic.
- If $AC - B^2 < 0$, the equation is hyperbolic.

Furthermore, we can categorize Equation 7.1 into specific types of equations.

- Laplace's equation:

$$u_{xx} + u_{yy} = 0 \tag{7.2}$$

- The wave equation:

$$u_{tt} - c^2 u_{xx} = 0 \tag{7.3}$$

- The heat equation:

$$u_t - K u_{xx} = 0 \tag{7.4}$$

- The telegraph equation:

$$u_{tt} - c^2 u_{xx} + 2\beta u_t + \alpha u = 0 \tag{7.5}$$

- Poisson's equation:

$$u_{xx} + u_{yy} = G \tag{7.6}$$

where t is time. Thus, Laplace's and Poisson's equations are elliptic, the heat equation is parabolic, and the wave and telegraph equations are hyperbolic. A common boundary condition of an elliptic PDE is that the value of $u(x, y)$ is specified, which is called the Dirichlet problem. Similarly, we can also solve the equation with Neumann boundary conditions where the gradient of u is given. In this case, the solution is not unique, and any constant offset of the solution is also a solution (Pinsky [50], Chapter 3).

Now, we consider the solution to the equation of generic form

$$\nabla^2\psi + k^2\psi = 0 \tag{7.7}$$

for which we have four cases:

- $k^2 = 0$. Laplace's equation.
- $k^2 > 0$, constant. Helmholtz's equation.
- $k^2 < 0$, constant. Diffusion equation.
- k^2 = constant $\times$ kinetic energy. Schrödinger wave equation.

There are 11 coordinate systems in which Equation 7.7 is separable, all of which can be considered particular cases of the confocal ellipsoidal system [4]. In the list above, we observe remarkable similarities between Poisson's equation and Helmholtz's equation. In Equation 1.12, none of the variables on the right-hand side are negative. Thus, when the whole term is moved to the left-hand side of the equation, we have $k^2 > 0$, only missing the factor of ψ. As a matter of fact, Poisson's equation can be solved by assuming the form of Helmholtz's equation, and we perform such an analysis in the next section.

7.4 Solution to Poisson's Equation via Spherical Bessel Function

In this section, we solve Poisson's equation. Poisson's equation is solved by combining the work by Allen et al. [3], Palmer [47], and separation of variables [20, 36, 50].

7.4.1 Poisson's Equation as Helmholtz's Equation

Poisson's equation (Equation 1.12), assuming the form of the Helmholtz's equation, is written as

$$\nabla^2 V = -4\pi G\rho = -k^2 V \tag{7.8}$$

where V is used for potential and shall not be confused with the volume of the asteroid. From now on, the potential U is used for the solutions to Laplace's equation, and V is used for the solutions to Poisson's equation. Equation 7.8 is equivalent to expressing the density as a function of the potential.

$$\rho = \frac{k^2 V}{4\pi G} \tag{7.9}$$

It is worthwhile to pause for a moment and ponder the meaning of Equation 7.9. The equation states that the density distribution conforms to the potential distribution, scaled by the coefficient k ($k = 0$ yields Laplace's equation). That is, Equation 7.9 translates to artificially redistributing the mass in the solution space to obtain the desired gravity field. As shown in Figure 7.1, the solution space that is missing the gravity field expression is inside the exterior Brillouin sphere and outside the interior Brillouin sphere. Therefore, we redistribute the mass of the asteroid inside the exterior Brillouin sphere and outside the interior Brillouin sphere to obtain two types of solutions to Poisson's equation. As these boundaries form a sphere, it is natural to solve Equation 7.8 in the spherical coordinates (r, λ, ϕ).

7.4.2 Radial Potential Expression

In spherical coordinates, $\nabla^2 V$ is expressed as

$$\nabla^2 V = \left(\frac{\partial^2 V}{\partial r^2} + \frac{2}{r}\frac{\partial V}{\partial r}\right) + \frac{1}{r^2}\left(\frac{\partial^2 V}{\partial \phi^2} - \tan\phi \frac{\partial V}{\partial \phi}\right) + \frac{1}{r^2 \cos^2\phi}\frac{\partial^2 V}{\partial \lambda^2} \tag{7.10}$$

Now, we set $V = R(r)\Phi(\phi)\Lambda(\lambda)$ to apply separation of variables and find

$$\begin{aligned}\frac{r^2\nabla^2 V}{V} &= \frac{1}{R(r)}\left(r^2\frac{\partial^2 R(r)}{\partial r^2}+2r\frac{\partial R(r)}{\partial r}\right)\\ &+\frac{1}{\Phi(\phi)}\left(\frac{\partial^2\Phi(\phi)}{\partial\phi^2}-\tan\phi\frac{\partial\Phi(\phi)}{\partial\phi}\right)+\frac{1}{\cos^2\phi\Lambda(\lambda)}\frac{\partial^2\Lambda(\lambda)}{\partial\lambda^2} = -k^2r^2\end{aligned} \tag{7.11}$$

where $R(r)$ is the radial potential, $\Phi(\phi)$ is the latitudinal potential, and $\Lambda(\lambda)$ is the longitudinal potential. Then, moving $-k^2r^2$ to the left-hand side of the equation, we get

$$\begin{aligned}&\left[\frac{1}{R(r)}\left(r^2\frac{\partial^2 R(r)}{\partial r^2}+2r\frac{\partial R(r)}{\partial r}\right)+k^2r^2\right]\\ &+\left[\frac{1}{\Phi(\phi)}\left(\frac{\partial^2\Phi(\phi)}{\partial\phi^2}-\tan\phi\frac{\partial\Phi(\phi)}{\partial\phi}\right)\right]+\left[\frac{1}{\cos^2\phi\Lambda(\lambda)}\frac{\partial^2\Lambda(\lambda)}{\partial\lambda^2}\right] = 0\end{aligned} \tag{7.12}$$

Notice that the expressions in the second and the third brackets are independent of r, and therefore, so is the first. As the sum of three terms yields zero, the first term and the sum of the second and the third terms must be a constant with opposite signs. We set the constant value of the first term to $n(n+1)$ to get

$$\frac{1}{R(r)}\left(r^2\frac{\partial^2 R(r)}{\partial r^2}+2r\frac{\partial R(r)}{\partial r}\right)+k^2r^2 = n(n+1) \tag{7.13}$$

which yields

$$\frac{\partial^2 R(r)}{\partial r^2}+\frac{2}{r}\frac{\partial R(r)}{\partial r}+\left[k^2-\frac{n(n+1)}{r^2}\right]R(r) = 0 \tag{7.14}$$

The solution of $R(r)$ is the spherical bessel function of the first kind $j_n(k_{ln}r)$ and second kind $\mathcal{Y}_n(k_{ln}r)$, which are defined as

$$j_n(x) = \sqrt{\frac{\pi}{2x}}J_{n+\frac{1}{2}}(x) \tag{7.15}$$

$$\mathcal{Y}_n(x) \;=\; \sqrt{\frac{\pi}{2x}}Y_{n+1/2}(x) \;=\; (-1)^{n+1}\sqrt{\frac{\pi}{2x}}J_{-(n+1/2)}(x) \;=\; (-1)^{n+1}j_{-(n+1)}(x) \qquad (7.16)$$

where J_n and Y_n are the Bessel functions of first and second kind, respectively. The subscript n is referred to as the order of the Bessel function by convention, but we use the term "degree" instead. The meaning of the l subscript for constant k will be clarified later. The Bessel and spherical Bessel functions of second kind are also known as Weber's function and spherical Neumann function, respectively. For the rest of the paper, $j_n(x)$ is referred to as the spherical Bessel function and $\mathcal{Y}_n(x)$ the spherical Neumann function. The spherical Neumann function of degree n is conventionally denoted as $n_n(x)$, but we will adopt $\mathcal{Y}_n(x)$ to avoid confusion with the degree n. Note that $j_n(x)$ is defined everywhere for $x \geq 0$, but $\mathcal{Y}_n(x)$ tends to negative infinity as $x \to 0$ (Figure 7.3). Thus, the solution by j_n is used to describe the gravity field inside the exterior Brillouin sphere, and $\mathcal{Y}_n$ to describe the gravity field outside the interior Brillouin sphere.

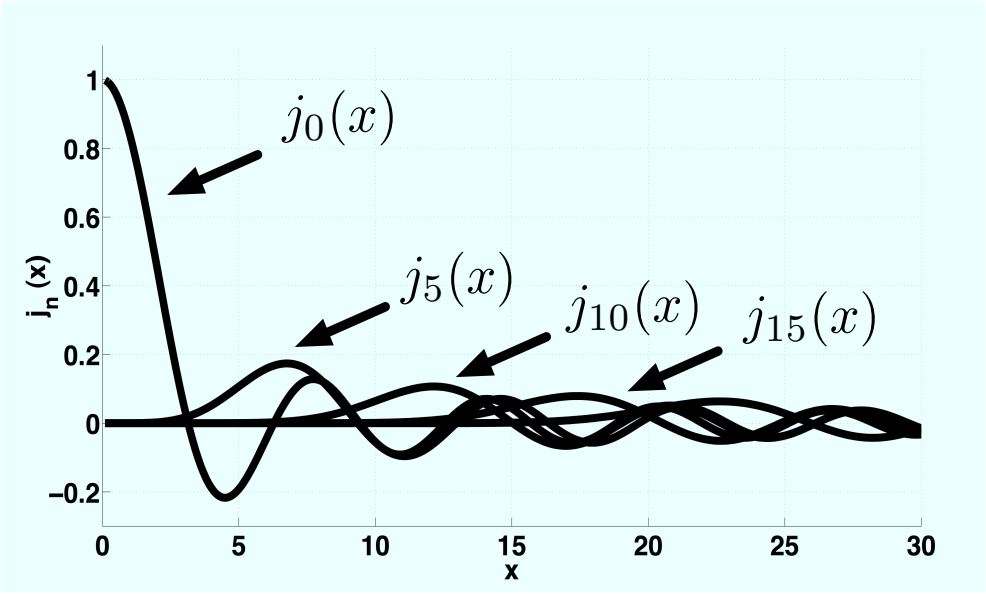

(a) $j_n(x)$

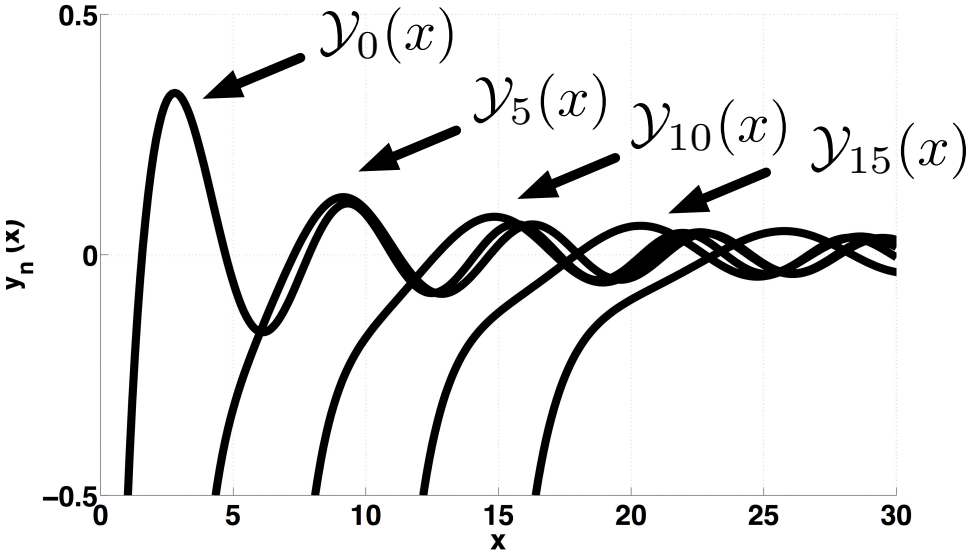

(b) $\mathcal{Y}_n(x)$

Figure 7.3: Spherical Bessel/Neumann functions.

7.4.3 Longitudinal Potential Expression

Now that the radial potential $R(r)$ is obtained, $\Lambda(\lambda)$ and $\Phi(\phi)$ remain to be solved. We first find the solutions to $\Lambda(\lambda)$. After multiplying both sides of Equation 7.12 by $\cos^2\phi$, we obtain

$$\frac{\cos^2\phi}{\Phi(\phi)}\frac{\partial^2\Phi(\phi)}{\partial\phi^2} - \frac{\sin\phi\cos\phi}{\Phi(\phi)}\frac{\partial\Phi(\phi)}{\partial\phi} + n(n+1)\cos^2\phi = -\frac{1}{\Lambda(\lambda)}\frac{\partial^2\Lambda(\lambda)}{\partial\lambda^2} \tag{7.17}$$

Now we have separated the terms to those dependent only on ϕ and λ. Thus, the terms on either side of the equation must be a constant. We set the term on the right-hand side of the equation to m^2 and get

$$\frac{\partial^2\Lambda(\lambda)}{\partial\lambda^2} + m^2\Lambda(\lambda) = 0 \tag{7.18}$$

which is a simple harmonic oscillator. Therefore, we get

$$\Lambda(\lambda) = \mathscr{A}_{lnm}\cos m\lambda + \mathscr{B}_{lnm}\sin m\lambda \tag{7.19}$$

The coefficients $\mathscr{A}_{lnm}$ and $\mathscr{B}_{lnm}$ define the amplitude of the function $\Lambda(\lambda)$. The subscript l and m are defined later as we discuss the final form of the potential expression.

7.4.4 Latitudinal Potential Expression

Now, for $\Phi(\phi)$, we find

$$\frac{\partial^2\Phi(\phi)}{\partial\phi^2} - \tan\phi\frac{\partial\Phi(\phi)}{\partial\phi} + \left[n(n+1) - \frac{m^2}{\cos^2\phi}\right]\Phi(\phi) = 0 \tag{7.20}$$

Then, we substitute $\xi = \sin\phi$ and express Equation 7.20 as a function of ξ. The first and second-order partials of Φ with respect to ξ are computed as

$$\frac{\partial\Phi}{\partial\phi} = \frac{\partial\Phi}{\partial\xi}\frac{\partial\xi}{\partial\phi} = \cos\phi\frac{\partial\Phi}{\partial\xi} \tag{7.21}$$

$$\frac{\partial^2\Phi}{\partial\phi^2} = \frac{\partial}{\partial\phi}\left(\frac{\partial\Phi}{\partial\phi}\right) = -\sin\phi\frac{\partial\Phi}{\partial\xi} + \cos\phi\frac{\partial}{\partial\phi}\left(\frac{\partial\Phi}{\partial\xi}\right) = -\sin\phi\frac{\partial\Phi}{\partial\xi} + \cos^2\phi\frac{\partial^2\Phi}{\partial\xi^2} \quad (7.22)$$

Then, direct substitution of Equations 7.21 and 7.22 into Equation 7.20 yields

$$\begin{aligned} 0 &= \cos^2\phi\frac{\partial^2\Phi}{\partial\xi^2} - 2\sin\phi\frac{\partial\Phi}{\partial\xi} + \left[n(n+1) - \frac{m^2}{1-\sin^2\phi}\right]\Phi \\ &= (1-\xi^2)\frac{\partial^2\Phi}{\partial\xi^2} - 2\xi\frac{\partial\Phi}{\partial\xi} + \left[n(n+1) - \frac{m^2}{1-\xi^2}\right]\Phi \quad (7.23) \\ &= \frac{\partial}{\partial\xi}\left\{(1-\xi^2)\frac{\partial\Phi}{\partial\xi}\right\} + \left[n(n+1) - \frac{m^2}{1-\xi^2}\right]\Phi \end{aligned}$$

Equation 7.23 is referred to as the Legendre's associated equation, and its solution is given by, for example, MacRobert [36] (Chapter 4) as

$$\Phi(\phi) = P_{nm}(\sin\phi) \quad (7.24)$$

which is the associated Legendre function of degree n and order m.

7.4.5 Interior and Exterior Spherical Bessel Gravity Fields

Finally, we combine the solutions for $R(r)$, $\Lambda(\lambda)$, and $\Phi(\phi)$ to obtain

$$V^i = \sum_{l=0}^{\infty}\sum_{n=0}^{\infty}\sum_{m=0}^{n} j_n(k_{ln}^i r)P_{nm}(\sin\phi)\left(\mathscr{A}_{lnm}^i\cos m\lambda + \mathscr{B}_{lnm}^i\sin m\lambda\right) \quad (7.25)$$

$$V^e = \sum_{l=0}^{\infty}\sum_{n=0}^{\infty}\sum_{m=0}^{n} \mathcal{Y}_n(k_{ln}^e r)P_{nm}(\sin\phi)\left(\mathscr{A}_{lnm}^e\cos m\lambda + \mathscr{B}_{lnm}^e\sin m\lambda\right) \quad (7.26)$$

where V^i is the interior spherical Bessel gravity field, and V^e is the exterior spherical Bessel gravity field. Accordingly, $\mathscr{A}_{lnm}^i$ and $\mathscr{B}_{lnm}^i$ are referred to as the interior spherical Bessel coefficients,

and $\mathscr{A}^e_{lnm}$ and $\mathscr{B}^e_{lnm}$ as the exterior spherical Bessel coefficients. These two Bessel gravity fields complement the solution space of the exterior/interior spherical harmonic gravity fields (Figure 7.4). Note that both V^i and V^e are other solution forms of the spherical harmonic potential expression as they contain the surface spherical harmonic potential $\mathscr{H}_{nm}$ (see Equation 7.61).

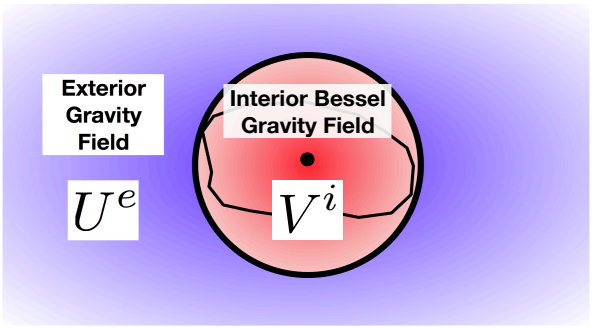

(a) Exterior gravity field and interior spherical Bessel gravity field

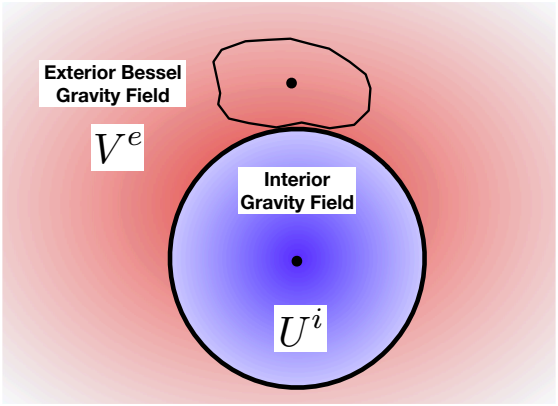

(b) Interior gravity field and exterior spherical Bessel gravity field

Figure 7.4: Solution space of the exterior/interior spherical harmonic gravity fields and interior/exterior spherical Bessel gravity fields. The blue regions are the solution space of the exterior/interior gravity fields obtained from Laplace's equation. The red regions are the solution space of the interior/exterior spherical Bessel gravity fields obtained from Poisson's equation. Note that the entire asteroid is within the solution space of the interior/exterior spherical Bessel gravity fields.

In Equation 7.25 and 7.26, both the interior and exterior spherical Bessel gravity fields are summed over l, n, and m, as each different value of k, n, and m satisfy the Poisson's equation, and a linear combination of solutions is also a solution. In our analysis, the l subscript is referred to as the "power" of the spherical Bessel function. Thus, we have degree n, order m, and power l for the Bessel gravity fields. Particular values of k_{ln}, which are different for the interior and exterior expansions, are discussed later when the boundary conditions are applied. The following discussions will focus on the interior spherical Bessel gravity field, as its computation directly gives the gravitation within the exterior Brillouin sphere. Detailed descriptions of the exterior spherical Bessel gravity field are given in Appendix E.7.

7.5 Structure of the Interior Spherical Bessel Coefficients

In this section, we derive the explicit expressions for the interior spherical Bessel coefficients. To do so, we first rewrite Equation 7.25 as

$$V^i = \frac{GM^*}{R_e^*} \sum_{l=0}^{\infty} \sum_{n=0}^{\infty} \sum_{m=0}^{n} j_n \left(\frac{\alpha_{ln}^i r}{R_e^*} \right) P_{nm}(\sin\phi) \begin{bmatrix} \cos(m\lambda) \\ \sin(m\lambda) \end{bmatrix} \cdot \begin{bmatrix} \mathscr{A}_{lnm}^i \\ \mathscr{B}_{lnm}^i \end{bmatrix} \tag{7.27}$$

where the coefficients $\mathscr{A}_{lnm}^i$ and $\mathscr{B}_{lnm}^i$ were scaled by a factor of R_e^*/M^*G (the same notation of $\mathscr{A}_{lnm}^i$ and $\mathscr{B}_{lnm}^i$ is maintained). In addition, we introduced the non-dimensionalized parameter

$$\alpha_{ln}^i = R_e^* k_{ln}^i \tag{7.28}$$

which is the eigenvalue of the spherical Bessel function [34, 73]. Note that the ***exterior*** reference radius (R_e^*) is used to non-dimensionalize the ***interior*** spherical Bessel coefficients ($\mathscr{A}_{lnm}^i$ and $\mathscr{B}_{lnm}^i$). This is not a misprint, and the reason will become clear in Section 7.6.

7.5.1 Density Distribution due to the Interior Spherical Bessel Gravity Field

Before we discuss the structure of the interior spherical Bessel coefficients, we seek the expression for the density distribution. The direct substitution of Equation 7.27 into Equation 7.9 renders the density distribution as

$$\rho_i = \frac{M^*}{4\pi R_e^{*3}} \sum_{l=0}^{\infty} \sum_{n=0}^{\infty} \sum_{m=0}^{n} \alpha_{ln}^{i2} j_n \left(\frac{\alpha_{ln}^i r}{R_e^*} \right) P_{nm} \begin{bmatrix} \cos(m\lambda) \\ \sin(m\lambda) \end{bmatrix} \cdot \begin{bmatrix} \mathscr{A}_{lnm}^i \\ \mathscr{B}_{lnm}^i \end{bmatrix} \tag{7.29}$$

It turns out that we can express $\mathscr{A}_{lnm}^i$ and $\mathscr{B}_{lnm}^i$ via the volume integral of density over the Brillouin sphere, and we will perform such an analysis in the following.

7.5.2 Unnormalized Interior Spherical Bessel Coefficients

The interior spherical Bessel coefficients are obtained by leveraging the orthogonal properties of the associated Legendre function and the spherical Bessel function. The orthogonality of the associated Legendre function is given in Appendix D.1. The orthogonality of the spherical Bessel function is given as

$$\int_0^{R^*} j_n\left(\alpha_{\mu n}\frac{r}{R^*}\right) j_n\left(\alpha_{\nu n}\frac{r}{R^*}\right) r^2 dr \;=\; \frac{R^{*3}}{2}\left[j_{n+1}(\alpha_{\mu n})\right]^2 \delta_{\mu\nu} \quad \text{for} \quad \begin{cases} j_n(\alpha_{\mu n}) &= 0 \\ j_n(\alpha_{\nu n}) &= 0 \end{cases} \tag{7.30}$$

where both $\alpha_{\mu n}$ and $\alpha_{\nu n}$ are the roots of j_n (Arfken [4], Chapter 11.7). However, in our case, $\alpha_{\mu n}$ and $\alpha_{\nu n}$ are both the roots of j_{n-1}. This condition arises due to the boundary conditions that we enforce on the exterior Brillouin sphere and is explained in Section 7.7. The orthogonality of j_n for such a case is derived in Appendix E.3.2 (Equation E.24) and given as

$$\int_0^{R^*} j_n\left(\alpha_{\mu n}\frac{r}{R^*}\right) j_n\left(\alpha_{\nu n}\frac{r}{R^*}\right) r^2 dr \;=\; \frac{R^{*3}}{2}\left[j_n(\alpha_{\mu n})\right]^2 \delta_{\mu\nu} \quad \text{for} \quad \begin{cases} j_{n-1}(\alpha_{\mu n}) &= 0 \\ j_{n-1}(\alpha_{\nu n}) &= 0 \end{cases} \tag{7.31}$$

Therefore, by taking the integral of the cosine term of the density over the whole Brillouin sphere, with appropriate multiplication factor, we get

$$\int_V j_n\left(\frac{\alpha_{ln}^i r'}{R_e^*}\right) P_{nm}(\sin\phi')\cos(m\lambda')\rho_i dv \;=\; \frac{\mathscr{A}_{lnm}^i M^* \mathscr{E}_n^i(\alpha_{ln}^i)(n+m)!}{2(2-\delta_{0m})(2n+1)(n-m)!} \tag{7.32}$$

where $\mathscr{E}_q^i(\alpha_{ln}^i) = \alpha_{ln}^{i2}\left[j_q(\alpha_{ln}^i)\right]^2$, $dv = r^2\sin\theta dr d\phi d\lambda$, and $\theta = \pi/2 - \phi$ (i.e., the colatitude). We can perform similar operation for the sine term of the density to get

$$\begin{cases} \mathscr{A}_{lnm}^i &= \dfrac{2(2-\delta_{0m})(2n+1)(n-m)!}{M^*\mathscr{E}_n^i(\alpha_{ln}^i)(n+m)!}\displaystyle\int_M j_n\left(\frac{\alpha_{ln}^i r'}{R_e^*}\right) P_{nm}(\sin\phi')\cos(m\lambda')dm' \\ \mathscr{B}_{lnm}^i &\overset{m\geq 0}{=} \dfrac{4(2n+1)(n-m)!}{M^*\mathscr{E}_n^i(\alpha_{ln}^i)(n+m)!}\displaystyle\int_M j_n\left(\frac{\alpha_{ln}^i r'}{R_e^*}\right) P_{nm}(\sin\phi')\sin(m\lambda')dm' \end{cases} \tag{7.33}$$

where $dm' = \rho_i dv$ is substituted. Notice the remarkable similarities between the interior spherical Bessel coefficients and the exterior spherical harmonic coefficients (Equation 6.10).

7.5.3 Normalized Interior Spherical Bessel Coefficients

The normalized coefficients are given as

$$\begin{cases} \bar{\mathscr{A}}^i_{lnm} = \dfrac{2}{M^* \mathscr{E}^i_n(\alpha^i_{ln})} \sqrt{\dfrac{(2-\delta_{0m})(2n+1)(n-m)!}{(n+m)!}} \displaystyle\int_M j_n \left(\frac{\alpha^i_{ln} r'}{R^*_e} \right) P_{nm}(\sin\phi') \cos(m\lambda') dm' \\ \bar{\mathscr{B}}^i_{lnm} \overset{m\geq 0}{=} \dfrac{2}{M^* \mathscr{E}^i_n(\alpha^i_{ln})} \sqrt{\dfrac{2(2n+1)(n-m)!}{(n+m)!}} \displaystyle\int_M j_n \left(\frac{\alpha^i_{ln} r'}{R^*_e} \right) P_{nm}(\sin\phi') \sin(m\lambda') dm' \end{cases} \tag{7.34}$$

7.6 Exterior Gravity Field Expressed via Spherical Bessel Function

The relationship between the exterior gravity field (U^e) and the interior spherical Bessel gravity field (V^i) becomes clear when we express the exterior gravity field via spherical Bessel function, as was done by Allen et al. [3], Palmer [47], and Herrera-Sucarrat et al. [21]. As they only provide the final expression, we will clarify its origin and motivation of such mathematical reformulation.

The two potential expressions U^e and V^i (Equation 6.12 and 7.27) are derived by solving Laplace's and Poisson's equations, respectively. As we saw in Section 7.4, they complement the solution space of each other, sharing their common boundary which is the exterior Brillouin sphere. As the gravitational potential is a continuous function, these potential expressions cannot have discontinuity on the boundary of the exterior Brillouin sphere. Therefore, we impose a constraint that the potentials given by U^e and V^i match on the boundary of the exterior Brillouin sphere.

From Equation 6.12, the exterior potential on the boundary of the exterior Brillouin sphere is given as

$$U^e|_{r=R_e^*} = \frac{GM^*}{R_e^*}\sum_{n=0}^{\infty}\sum_{m=0}^{n} P_{nm}(\sin\phi)\begin{bmatrix}\cos(m\lambda)\\ \sin(m\lambda)\end{bmatrix}\cdot\begin{bmatrix}C_{nm}^e\\ S_{nm}^e\end{bmatrix} \tag{7.35}$$

Similarly, from Equation 7.27, the interior spherical Bessel potential on the boundary of the exterior Brillouin sphere is given as

$$V^i|_{r=R_e^*} = \frac{GM^*}{R_e^*}\sum_{l=0}^{\infty}\sum_{n=0}^{\infty}\sum_{m=0}^{n} j_n\left(\alpha_{ln}^i\right) P_{nm}(\sin\phi)\begin{bmatrix}\cos(m\lambda)\\ \sin(m\lambda)\end{bmatrix}\cdot\begin{bmatrix}\mathscr{A}_{lnm}^i\\ \mathscr{B}_{lnm}^i\end{bmatrix} \tag{7.36}$$

As we must have the condition $U^e|_{r=R_e^*} = V^i|_{r=R_e^*}$, comparison of the two equations immediately yields

$$\begin{cases} C_{nm}^e = \sum_{l=0}^{\infty} j_n(\alpha_{ln}^i)\mathscr{A}_{lnm}^i \\ \\ S_{nm}^e = \sum_{l=0}^{\infty} j_n(\alpha_{ln}^i)\mathscr{B}_{lnm}^i \end{cases} \tag{7.37}$$

Equation 7.37 puts a constrain on the possible values of the interior spherical Bessel coefficients. In so many words, the exterior spherical harmonic coefficients are weighted sum of the interior spherical Bessel coefficients, the weight function being the spherical Bessel function evaluated with the eigenvalue of the same degree and power. Given this result, the exterior gravity field can be expressed in terms of the interior spherical Bessel coefficients as

$$U^e = \frac{GM^*}{R_e^*}\sum_{l=0}^{\infty}\sum_{n=0}^{\infty}\sum_{m=0}^{n} j_n(\alpha_{ln}^i)\left(\frac{R_e^*}{r}\right)^{n+1} P_{nm}(\sin\phi)\begin{bmatrix}\cos(m\lambda)\\ \sin(m\lambda)\end{bmatrix}\cdot\begin{bmatrix}\mathscr{A}_{lnm}^i\\ \mathscr{B}_{lnm}^i\end{bmatrix} \tag{7.38}$$

The specific values of the eigenvalue α_{ln}^i are sought after in the next section.

7.7 Boundary Conditions and Eigenvalues of the Interior Spherical Bessel Gravity Field

In this section, we wish to obtain the necessary conditions for the eigenvalues α_{ln}^i from the boundary conditions. On the boundary of the exterior Brillouin sphere, the acceleration of the field point must match between the exterior gravity field and the interior spherical Bessel gravity field. That is,

$$\begin{aligned} \ddot{\vec{r}}\Big|_{r=R_e^*} &= \frac{\partial U^e}{\partial r}\hat{r} + \frac{1}{r}\frac{\partial U^e}{\partial \phi}\hat{\phi} + \frac{1}{r\cos\phi}\frac{\partial U^e}{\partial \lambda}\hat{\lambda}\Big|_{r=R_e^*} \\ &= \frac{\partial V^i}{\partial r}\hat{r} + \frac{1}{r}\frac{\partial V^i}{\partial \phi}\hat{\phi} + \frac{1}{r\cos\phi}\frac{\partial V^i}{\partial \lambda}\hat{\lambda}\Big|_{r=R_e^*} \end{aligned} \tag{7.39}$$

We already know that the longitudinal and latitudinal components of the acceleration are matched as we have the equivalent radial component $j_n(\alpha_{ln}^i)$ at $r = R_e^*$ (Equation 7.35 and 7.36). Consequently, the necessary condition for α_{ln}^i falls out by matching the radial component of the acceleration. This boundary condition is conveniently expressed by working with Equation 7.38. As with the interior spherical Bessel potentail, the potential expression in Equation 7.38 can be obtained via separation of variables. That is, $U_{lmm}^e = R_{ln}^e(r)\Phi_{nm}^e(\phi)\Lambda_m^e(\lambda)$, where the exterior radial potential is given as

$$R_{ln}^e(r) = \frac{GM^*}{R_e^*} j_n(\alpha_{ln}^i)\left(\frac{R_e^*}{r}\right)^{n+1} \tag{7.40}$$

Then, the radial component of the acceleration $\ddot{r}_{lnm}$ due to the exterior gravity field, expressed via the interior spherical Bessel coefficients of degree n, order m, and power l is computed as

$$\ddot{r}_{lnm}|_{r=R_e^*} = \frac{\partial R_{ln}^e(r)}{\partial r}\Big|_{r=R_e^*} = -(n+1)\frac{GM^*}{R_e^{*2}} j_n(\alpha_{ln}^i) \tag{7.41}$$

In Equation 7.41, we dropped $\Phi_{nm}^e(\phi)$ and $\Lambda_m^e(\lambda)$ (i.e., exterior latitudinal and longitudinal potentials) as neither of them is a function of r. Similarly, we compute $\ddot{r}_{lnm}$ from V^i, which

requires the partial derivative of $j_n(\alpha^i_{ln} r/R^*_e)$. Arfken [4] (Section 11.7) gives useful expressions of the recurrence theorem and the derivative of $j_n(x)$:

$$j_{n+1}(x) = \frac{2n+1}{x} j_n(x) - j_{n-1}(x) \tag{7.42}$$

$$(2n+1)\frac{\partial\left[j_n(x)\right]}{\partial x} = n j_{n-1}(x) - (n+1) j_{n+1}(x) \tag{7.43}$$

We substitute Equation 7.42 into Equation 7.43 and replace x with $\alpha^i_{ln} r/R^*_e$ to get

$$\frac{\partial}{\partial r}\left[j_n\left(\frac{\alpha^i_{ln} r}{R^*_e}\right)\right] = \frac{\alpha^i_{ln}}{R^*_e} j_{n-1}\left(\frac{\alpha^i_{ln} r}{R^*_e}\right) - \frac{(n+1)}{r} j_n\left(\frac{\alpha^i_{ln} r}{R^*_e}\right) \tag{7.44}$$

which yields

$$\ddot{r}_{lnm}|_{r=R^*_e} = \frac{GM^*\alpha^i_{ln}}{R^{*2}_e} j_{n-1}(\alpha^i_{ln}) - (n+1)\frac{GM^*}{R^{*2}_e} j_n\left(\alpha^i_{ln}\right) \tag{7.45}$$

The second component is identical to Equation 7.41. Thus, the first term needs to vanish. Accordingly, the eigenvalues are given by the condition

$$j_{n-1}(\alpha^i_{ln}) = 0 \tag{7.46}$$

The eigenvalues satisfying Equation 7.46 can be obtained by, for example, the Newton-Raphson method and are given in Appendix E.4. From the properties of the spherical Bessel function, there are no repeated roots for different degree n, except at zero, and all other eigenvalues are real and positive. Careful inspection of the behavior of j_n reveals that, for the zeroth-power interior spherical Bessel coefficients, only α^i_{00} and α^i_{01} are non-zero, and all other α^i_{0n} for $n > 1$ are zero. Thus, by the definition of the interior spherical Bessel coefficients (Equation 7.33 and 7.34),

there are only the zeroth and first-degree interior spherical Bessel coefficients for the zeroth power (i.e., $\mathscr{A}^i_{000}$, $\mathscr{A}^i_{010}$, $\mathscr{A}^i_{011}$, and $\mathscr{B}^i_{011}$ only).

Abramowitz and Stegun [2] list the lower-degree spherical Bessel functions, and analytical solutions are obtained up to the second degree by Allen et al. [3]. We also summarize these quantities in Appendix E.5.1.

7.8 Analytical Conversion between the Exterior Spherical Harmonic Coefficients and Interior Spherical Bessel Coefficients

In this section, we investigate the conversion method between the exterior spherical harmonic coefficients and the interior spherical Bessel coefficients. The same method is discussed by Herrera-Sucarrat et al. [21], but we will provide more intermediate steps to indicate how the process can be generalized in future research. Recall that as we matched the potentials of both expansions on the boundary of the exterior Brillouin sphere, we obtained Equation 7.37, which showed that the exterior spherical harmonic coefficients are weighted sum of the interior spherical Bessel coefficients. Here, we further put a constraint on the possible values of the interior spherical Bessel coefficients from the density distribution.

In order for the solutions to Poisson's equation to make a smooth transition to Laplace's equation, the density distribution evaluated on the boundary of the exterior Brillouin sphere has to reach the limit

$$\lim_{r \to R_e^*} \rho_i(r, \phi, \lambda) \quad = \quad 0 \quad \text{for } \forall\phi, \forall\lambda \tag{7.47}$$

For Equation 7.47 to hold for any point on the spherical boundary (i.e., for any ϕ and λ), we have to satisfy

$$\begin{cases} \sum_{l=0}^{\infty} \alpha_{ln}^{i2} j_n(\alpha_{ln}^i) \mathscr{A}_{lnm}^i &= 0 \\ \\ \sum_{l=0}^{\infty} \alpha_{ln}^{i2} j_n(\alpha_{ln}^i) \mathscr{B}_{lnm}^i &= 0 \end{cases} \tag{7.48}$$

according to Equation 7.29. Now, we wish to combine Equations 7.37 and 7.48 into one equation. Before we proceed, we make a remark that α_{0n}^i is non-zero only for $n = 0$ and 1 as mentioned earlier. We denote the first non-zero α_{ln}^i as $\alpha_{l^*n}^i$:

$$l^* = \begin{cases} 0 \quad , \quad \text{if} \quad n = 0, 1 \\ \\ 1 \quad , \quad \text{if} \quad n > 1 \end{cases} \tag{7.49}$$

Then, we can expand Equation 7.37 as

$$j_n(\alpha_{l^*n}^i) \mathscr{A}_{l^*nm}^i = C_{nm}^e - \sum_{l=l^*+1}^{\infty} j_n(\alpha_{ln}^i) \mathscr{A}_{lnm}^i \tag{7.50}$$

Also, Equation 7.48 can be expanded as

$$\alpha_{l^*n}^{i2} \left[C_{nm}^e - \sum_{l=l^*+1}^{\infty} j_n(\alpha_{ln}^i) \mathscr{A}_{lnm}^i \right] + \sum_{l=l^*+1}^{\infty} \alpha_{ln}^{i2} j_n(\alpha_{ln}^i) \mathscr{A}_{lnm}^i = 0 \tag{7.51}$$

where we separated the term due to $l = l^*$ and substituted Equation 7.50. By rearranging Equation 7.51, we get

$$\begin{cases} C_{nm}^e &= \sum_{l=l^*+1}^{\infty} \left(1 - \frac{\alpha_{ln}^{i2}}{\alpha_{l^*n}^{i2}} \right) j_n(\alpha_{ln}^i) \mathscr{A}_{lnm}^i \\ \\ S_{nm}^e &= \sum_{l=l^*+1}^{\infty} \left(1 - \frac{\alpha_{ln}^{i2}}{\alpha_{l^*n}^{i2}} \right) j_n(\alpha_{ln}^i) \mathscr{B}_{lnm}^i \end{cases} \tag{7.52}$$

Again, Equation 7.52 states that the weighted sum of the interior spherical Bessel coefficients must converge to the exterior spherical harmonic coefficients. However, the exact values of the interior spherical Bessel coefficients cannot be determined uniquely from C^e_{nm} and S^e_{nm}. Moreover, orbit determination process does not estimate the interior spherical Bessel coefficients. Thus, we devise a mathematical reformulation and consider a series $g(\gamma)$ such that

$$\left(1 - \frac{\alpha^{i2}_{ln}}{\alpha^{i2}_{l^*n}}\right) j_n(\alpha^i_{ln}) \mathscr{A}^i_{lnm} = \left(\frac{g(s)}{\sum_{\gamma=1}^{\infty} g(\gamma)}\right) C^e_{nm} \tag{7.53}$$

where

$$s = \begin{cases} l \quad , \text{ if } \quad l^* = 0 \\ \\ l-1 \quad , \text{ if } \quad l^* = 1 \end{cases} \tag{7.54}$$

Then, the summation of Equation 7.53 over l, from $l = l^* + 1$, yields Equation 7.52. We can consider the series $g(\gamma)$ as the weight function of the spherical harmonic coefficient C^e_{nm}; that is, a predetermined fraction of the exterior spherical harmonic coefficient is accounted for by each interior spherical Bessel coefficient. Thus, naturally, we require a convergent series for $g(\gamma)$. We can define a similar expression for $\mathscr{B}^i_{lnm}$ and get

$$\begin{cases} \mathscr{A}^i_{lnm} = \dfrac{\alpha^{i2}_{l^*n}}{(\alpha^{i2}_{l^*n} - \alpha^{i2}_{ln}) j_n(\alpha^i_{ln})} \dfrac{g(s)}{\sum_{\gamma=1}^{\infty} g(\gamma)} C^e_{nm} \\ \\ \mathscr{B}^i_{lnm} = \dfrac{\alpha^{i2}_{l^*n}}{(\alpha^{i2}_{l^*n} - \alpha^{i2}_{ln}) j_n(\alpha^i_{ln})} \dfrac{g(s)}{\sum_{\gamma=1}^{\infty} g(\gamma)} S^e_{nm} \end{cases} \tag{7.55}$$

for $l \geq l^* + 1$. The only coefficients that are not included in Equation 7.55 are $A^i_{l^*nm}$ and

$B^i_{l^*nm}$, both of which are obtained from the density constraint on the boundary of the exterior Brillouin sphere (Equation 7.48) as shown below:

$$\begin{cases} \mathscr{A}^i_{l^*nm} &= -\dfrac{1}{\alpha^{i2}_{l^*n} j_n(\alpha^i_{l^*n})} \displaystyle\sum_{l=l^*+1}^{\infty} \alpha^{i2}_{ln} j_n(\alpha^i_{ln}) \mathscr{A}^i_{lnm} \\ \\ \mathscr{B}^i_{l^*nm} &= -\dfrac{1}{\alpha^{i2}_{l^*n} j_n(\alpha^i_{l^*n})} \displaystyle\sum_{l=l^*+1}^{\infty} \alpha^{i2}_{ln} j_n(\alpha^i_{ln}) \mathscr{B}^i_{lnm} \end{cases} \tag{7.56}$$

Explicit expressions of Equation 7.55 for $n = 0$, $n = 1$, and $n > 1$ are given as

$$\mathscr{A}^i_{l00} = \frac{\alpha^{i2}_{00}}{(\alpha^{i2}_{00} - \alpha^{i2}_{l0}) j_0(\alpha^i_{l0})} \frac{g(l)}{\displaystyle\sum_{\gamma=1}^{\infty} g(\gamma)} C^e_{00} \tag{7.57}$$

$$\begin{cases} \mathscr{A}^i_{l1m} &= \dfrac{\alpha^{i2}_{01}}{(\alpha^{i2}_{01} - \alpha^{i2}_{l1}) j_1(\alpha^i_{l1})} \dfrac{g(l)}{\displaystyle\sum_{\gamma=1}^{\infty} g(\gamma)} C^e_{1m} \\ \\ \mathscr{B}^i_{l11} &= \dfrac{\alpha^{i2}_{01}}{(\alpha^{i2}_{01} - \alpha^{i2}_{l1}) j_1(\alpha^i_{l1})} \dfrac{g(l)}{\displaystyle\sum_{\gamma=1}^{\infty} g(\gamma)} S^e_{11} \end{cases} \tag{7.58}$$

$$\begin{cases} \mathscr{A}^i_{lnm} &\overset{n\geq 1}{=} \dfrac{\alpha^{i2}_{1n}}{(\alpha^{i2}_{1n} - \alpha^{i2}_{ln}) j_n(\alpha^i_{ln})} \dfrac{g(l-1)}{\displaystyle\sum_{\gamma=1}^{\infty} g(\gamma)} C^e_{nm} \\ \\ \mathscr{B}^i_{lnm} &\overset{n\geq 1}{=} \dfrac{\alpha^{i2}_{1n}}{(\alpha^{i2}_{1n} - \alpha^{i2}_{ln}) j_n(\alpha^i_{ln})} \dfrac{g(l-1)}{\displaystyle\sum_{\gamma=1}^{\infty} g(\gamma)} S^e_{nm} \end{cases} \tag{7.59}$$

We refer to this conversion between the exterior spherical harmonic coefficients and interior spherical Bessel coefficients as the analytical conversion method. The choice of the function $g(\gamma)$ is arbitrary, and Herrera-Sucarrat et al. [21] compares the accuracy of the trajectories resulting from different weight functions. In our analysis, the weight function $g(\gamma)$ is defined as

$$g(\gamma) = \frac{1}{\gamma^{10}} \tag{7.60}$$

which is one of the weight functions used by Herrera-Sucarrat et al. Note that the same conversion method between the interior gravity field and exterior spherical Bessel gravity field is possible. This is of theoretical interest but has no practical usage for the spacecraft navigation purposes. Details of the analytical conversion method for the exterior spherical Bessel coefficients are given in Appendix E.7.4.

7.9 First and Second-order Partials of the Interior Spherical Bessel Gravity Field

In this section, we derive the first and second-order partials of the interior spherical Bessel gravity field. To do so, we define the basis function $\beta^i_{nm}(\alpha^i_{ln})$ and the surface spherical harmonic potential $\mathscr{H}_{nm}$ (in the complex number notation, as defined by Werner [74] and also summarized in Appendix D.4):

$$\begin{cases} \beta^i_{nm}(\alpha^i_{ln}) = j_n\left(\dfrac{\alpha^i_{ln} r}{R^*_e}\right)\mathscr{H}_{nm} \\ \\ \mathscr{H}_{nm} = P_{nm}(\sin\phi)e^{im\lambda} \end{cases} \tag{7.61}$$

such that

$$V^i = \frac{GM^*}{R^*_e}\sum_{l=0}^{\infty}\sum_{n=0}^{\infty}\sum_{m=0}^{n}\beta^i_{nm}(\alpha^i_{ln})\cdot\begin{bmatrix}\mathscr{A}^i_{lnm}\\ \mathscr{B}^i_{lnm}\end{bmatrix} \tag{7.62}$$

where i in the exponent of the exponential function e is the imaginary unit that satisfies $i^2 = -1$ and shall not be confused with the superscript for the interior quantities.

7.9.1 Acceleration due to the Interior Spherical Bessel Gravity Field

The acceleration is given by the first-order partial of the basis function, with appropriate multipliers. The partial derivative of the spherical harmonic functions is thoroughly discussed by Werner [74] and Takahashi et al. [70], and the key equations are summarized in Appendix D. We only present the final expression of the acceleration for the unnormalized/normalized interior spherical Bessel coefficients.

7.9.1.1 Unnormalized Interior Spherical Bessel Gravity Field

Equation 7.63 through 7.64 give the acceleration due to the unnormalized interior spherical Bessel gravity field.

$$
\begin{aligned}
\frac{\partial}{\partial x}\beta^i_{nm}(\alpha^i_{ln}) &\overset{m\geq 0}{=} -\frac{\alpha^i_{ln}x}{R^*_e r} j_{n+1}\left(\frac{\alpha^i_{ln}r}{R^*_e}\right)\mathscr{H}_{nm} - \frac{1}{2}\frac{1}{r} j_n\left(\frac{\alpha^i_{ln}r}{R^*_e}\right)\mathscr{H}_{n-1,m+1} \\
&\quad + \frac{(n+m)(n+m-1)}{2}\frac{1}{r} j_n\left(\frac{\alpha^i_{ln}r}{R^*_e}\right)\mathscr{H}_{n-1,m-1} \\
&\overset{m=0}{=} -\frac{\alpha^i_{ln}x}{R^*_e r} j_{n+1}\left(\frac{\alpha^i_{ln}r}{R^*_e}\right)\mathscr{H}_{n0} - \frac{1}{r} j_n\left(\frac{\alpha^i_{ln}r}{R^*_e}\right) P_{n-1,1}\begin{bmatrix}\cos\lambda \\ 0\end{bmatrix} \\
\frac{\partial}{\partial y}\beta^i_{nm}(\alpha^i_{ln}) &\overset{m\geq 0}{=} -\frac{\alpha^i_{ln}y}{R^*_e r} j_{n+1}\left(\frac{\alpha^i_{ln}r}{R^*_e}\right)\mathscr{H}_{nm} + \frac{1}{2}\frac{1}{r} j_n\left(\frac{\alpha^i_{ln}r}{R^*_e}\right) i\mathscr{H}_{n-1,m+1} \\
&\quad + \frac{(n+m)(n+m-1)}{2}\frac{1}{r} j_n\left(\frac{\alpha^i_{ln}r}{R^*_e}\right) i\mathscr{H}_{n-1,m-1} \\
&\overset{m=0}{=} -\frac{\alpha^i_{ln}y}{R^*_e r} j_{n+1}\left(\frac{\alpha^i_{ln}r}{R^*_e}\right)\mathscr{H}_{n0} - \frac{1}{r} j_n\left(\frac{\alpha^i_{ln}r}{R^*_e}\right) P_{n-1,1}\begin{bmatrix}\sin\lambda \\ 0\end{bmatrix}
\end{aligned}
\tag{7.63}
$$

$$
\frac{\partial}{\partial z}\beta^i_{nm}(\alpha^i_{ln}) = -\frac{\alpha^i_{ln}z}{R^*_e r} j_{n+1}\left(\frac{\alpha^i_{ln}r}{R^*_e}\right)\mathscr{H}_{nm} + (n+m)\frac{1}{r} j_n\left(\frac{\alpha^i_{ln}r}{R^*_e}\right)\mathscr{H}_{n-1,m} \tag{7.64}
$$

7.9.1.2 Normalized Interior Spherical Bessel Gravity Field

Equation 7.65 through 7.67 give the acceleration due to the normalized interior spherical Bessel gravity field.

$$\begin{aligned}\frac{\partial}{\partial x}\bar{\beta}^i_{nm}(\alpha^i_{ln}) &\overset{m\geq 0}{=} -\frac{\alpha^i_{ln}x}{R^*_e r}j_{n+1}\left(\frac{\alpha^i_{ln}r}{R^*_e}\right)\bar{\mathscr{H}}_{nm} - \bar{\mathscr{F}}_1(n,m)\frac{1}{r}j_n\left(\frac{\alpha^i_{ln}r}{R^*_e}\right)\bar{\mathscr{H}}_{n-1,m+1} \\ &\quad +\bar{\mathscr{F}}_2(n,m)\frac{1}{r}j_n\left(\frac{\alpha^i_{ln}r}{R^*_e}\right)\bar{\mathscr{H}}_{n-1,m-1} \\ &\overset{m=0}{=} -\frac{\alpha^i_{ln}x}{R^*_e r}j_{n+1}\left(\frac{\alpha^i_{ln}r}{R^*_e}\right)\bar{\mathscr{H}}_{n0} - 2\bar{\mathscr{F}}_1(n,m)\frac{1}{r}j_n\left(\frac{\alpha^i_{ln}r}{R^*_e}\right)\bar{P}_{n-1,1}\begin{bmatrix}\cos\lambda\\0\end{bmatrix}\end{aligned} \tag{7.65}$$

$$\begin{aligned}\frac{\partial}{\partial y}\bar{\beta}^i_{nm}(\alpha^i_{ln}) &\overset{m\geq 0}{=} -\frac{\alpha^i_{ln}y}{R^*_e r}j_{n+1}\left(\frac{\alpha^i_{ln}r}{R^*_e}\right)\bar{\mathscr{H}}_{nm} + \bar{\mathscr{F}}_1(n,m)\frac{1}{r}j_n\left(\frac{\alpha^i_{ln}r}{R^*_e}\right)i\bar{\mathscr{H}}_{n-1,m+1} \\ &\quad +\bar{\mathscr{F}}_2(n,m)\frac{1}{r}j_n\left(\frac{\alpha^i_{ln}r}{R^*_e}\right)i\bar{\mathscr{H}}_{n-1,m-1} \\ &\overset{m=0}{=} -\frac{\alpha^i_{ln}y}{R^*_e r}j_{n+1}\left(\frac{\alpha^i_{ln}r}{R^*_e}\right)\bar{\mathscr{H}}_{n0} - 2\bar{\mathscr{F}}_1(n,m)\frac{1}{r}j_n\left(\frac{\alpha^i_{ln}r}{R^*_e}\right)\bar{P}_{n-1,1}\begin{bmatrix}\sin\lambda\\0\end{bmatrix}\end{aligned} \tag{7.66}$$

$$\frac{\partial}{\partial z}\bar{\beta}^i_{nm}(\alpha^i_{ln}) = -\frac{\alpha^i_{ln}z}{R^*_e r}j_{n+1}\left(\frac{\alpha^i_{ln}r}{R^*_e}\right)\bar{\mathscr{H}}_{nm} + \bar{\mathscr{F}}_3(n,m)\frac{1}{r}j_n\left(\frac{\alpha^i_{ln}r}{R^*_e}\right)\bar{\mathscr{H}}_{n-1,m}$$

where

$$\begin{cases} \bar{\mathscr{F}}_1(n,m) &= \dfrac{1}{2}\sqrt{\dfrac{(2-\delta_{0m})(2n+1)(n-m)!}{2(2n-1)(n-m-2)!}} \\ \\ \bar{\mathscr{F}}_2(n,m) &= \dfrac{1}{2}\sqrt{\dfrac{(2-\delta_{0m})(2n+1)(n+m)!}{(2-\delta_{1,m})(2n-1)(n+m-2)!}} \\ \\ \bar{\mathscr{F}}_3(n,m) &= \sqrt{\dfrac{(2n+1)}{(2n-1)}(n+m)(n-m)} \end{cases} \tag{7.67}$$

7.9.2 Dynamics Matrix due to the Interior Spherical Bessel Gravity Field

The second-order partials, also referred to as the dynamics matrix, can be directly computed to show that

$$\nabla^2 \beta^i_{nm}(\alpha^i_{ln}) = -\frac{\alpha^{i2}_{ln}}{R^{*2}_e}\beta^i_{nm}(\alpha^i_{ln}) \tag{7.68}$$

Thus, Poisson's equation is satisfied. The explicit expressions of the second-order partials are given in Appendix E.5.3.2. Although the form of Equation 7.68 is expected, it presents itself with a confounding property. Specifically, the dynamics matrix of the interior spherical Bessel gravity field cannot be used to propagate the state transition matrix as it does not satisfy Laplace's equation. In fact, each element of the dynamics matrix computed by the interior spherical Bessel gravity field completely differs from the actual environment between the surface of the body and the exterior Brillouin sphere (i.e., the red region in Figure 7.1(a)). The only exception is the set of interior spherical Bessel coefficients obtained via the analytical conversion method that are evaluated on the boundary of the exterior Brillouin sphere, in which case the dynamics matrix conforms to Laplace's equation as the density is constrained to be zero (Equation 7.47).

This result reveals a paradoxical nature of the interior spherical Bessel gravity field, where both the potential and acceleration can be modeled properly but not the dynamics matrix. One would expect to see that the second-order partial of the potential is modeled well when the potential

and its first-order partials are, but this is not the case. We have yet to give a clear explanation of why there is a disconnect between the first-order and second-order partials.

The following sections entail the quantitative analysis of the performance of different types of gravity field expressions for proximity operations purposes. The exterior gravity field, interior gravity field, and interior spherical Bessel gravity field are compared with the truth model of homogeneous-density polyhedral gravity field.

7.10 Performance of the Exterior Gravity Field

In this section, we look at the performance of the exterior gravity field in the vicinity of the body surface. We will look at two types of error distribution: cross-sectional errors and surface errors. Both error types are compared with the homogeneous-density polyhedral gravity field [75], which is regarded as the truth model for the rest of the analysis. For the cross-sectional errors, the data points are scattered in the xy, yz, and xz-planes. For the surface errors, the data points are on the surface of the body. The errors obtained here set the benchmark of the accuracy of the current small body navigation performance. The test bodies are Bennu (Figure 7.5), which is close to a spherical configuration, and Castalia [24] (Figuer 5.4(a)), which has a distinct two-lobe configuration.

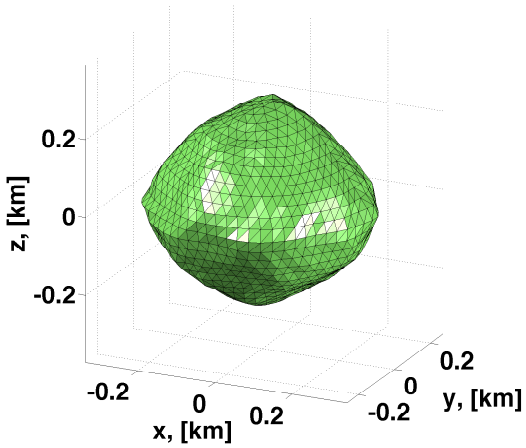

Figure 7.5: Shape model of Bennu.

The radius of the exterior Brillouin sphere (i.e., circumscribing sphere) is 0.287 $[km]$ for Bennu and 0.879 $[km]$ for Castalia. The closest point on the surface from the origin is 0.224 $[km]$ for Bennu and 0.274 $[km]$ for Castalia. The homogeneous density of the body is 0.98 $[g/cm^3]$ for Bennu and 2.1 $[g/cm^3]$ for Castalia.

7.10.1 Exterior Gravity Field around Bennu

We first look at Bennu and map the potential/acceleration errors for 0, 4, and 10-th degree exterior gravity field constructed from a homogeneous body [76]. Figure 7.6 and 7.7 shows the cross-sectional distributions of the potential/acceleration errors. In both figures, the innermost black line is the cross-section of Bennu. The dotted black lines represent the exterior Brillouin sphere, within which the exterior gravity field does not converge. Each row is the degree of the exterior gravity field, and each column is the plane. The percentage errors are plotted in the log scale with base 10. That is, the plotted values ($\epsilon_{_U}$) are expressed by

$$\epsilon_{_U} \quad = \quad \log_{10}\left[abs\left(\frac{U^e - U_{poly}}{U_{poly}}\right) \times 100\right] \tag{7.69}$$

As shown in Figure 7.6, the magnitude of the potential errors decreases as higher-degree and higher-order terms are included, yielding a fan-like structure that protrude radially outward. This is related to the wavelength of the gravity field [30]. The maximum potential error is on the order of several percent. Similarly, the fan-like structure is observed for the acceleration errors in Figure 7.7. The maximum acceleration error reaches $\sim 20\%$ for the zeroth-degree and $\sim 10\%$ for the 10th-degree exterior gravity field. In general, the potential is better approximated than the acceleration.

Next, we show the potential/acceleration errors between the polyhedral gravity field and exterior gravity field on the surface of the body (Figure 7.8 and 7.9). The values are plotted in percentage. As with the cross-sectional error distributions, the potential is better modeled than the acceleration. Higher-degree and higher-order gravity fields yield a large number of small-scale, concentrated errors, which correspond to the fan-like structures shown in Figure 7.6 and 7.7.

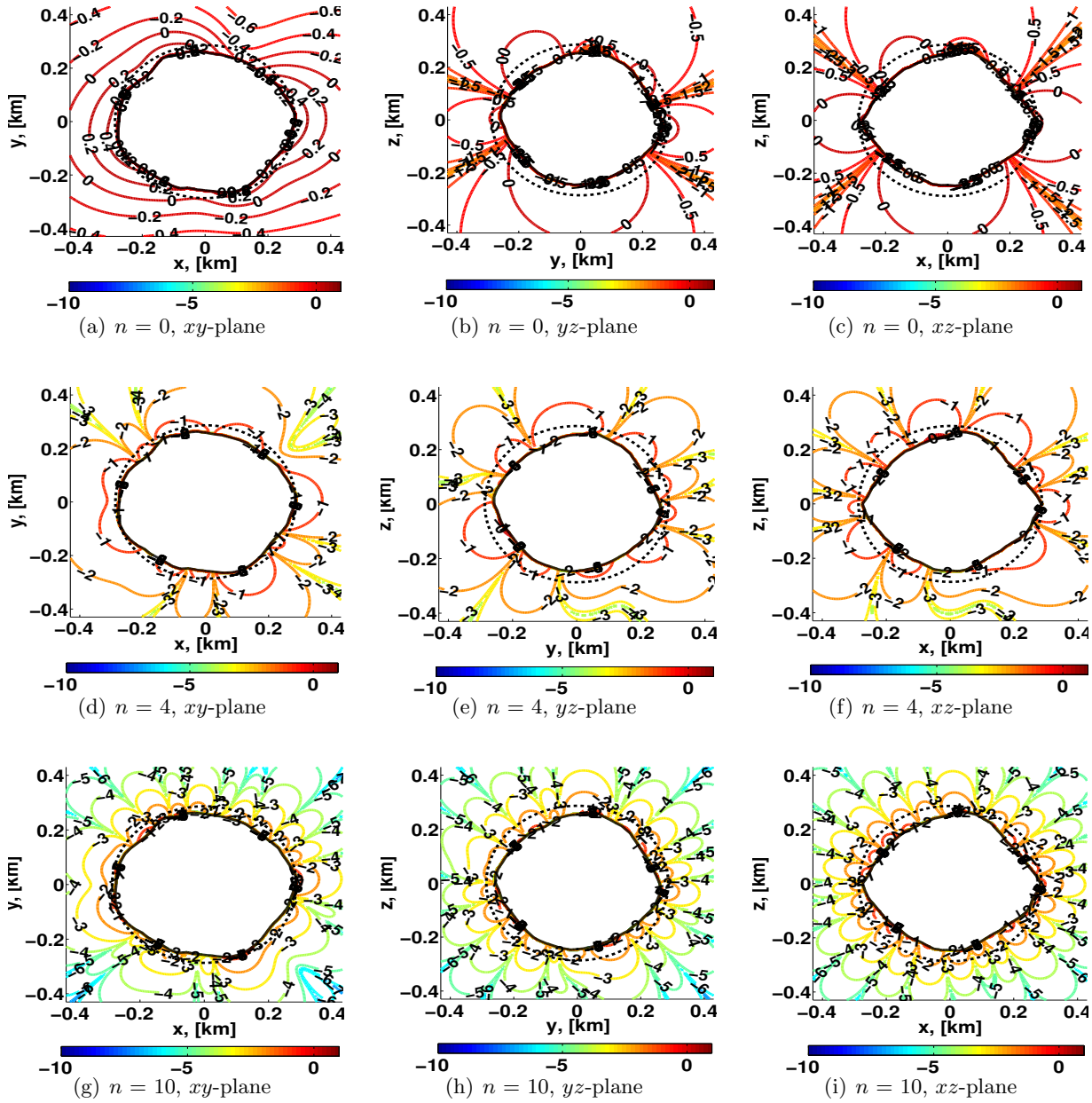

(a) $n = 0$, xy-plane (b) $n = 0$, yz-plane (c) $n = 0$, xz-plane

(d) $n = 4$, xy-plane (e) $n = 4$, yz-plane (f) $n = 4$, xz-plane

(g) $n = 10$, xy-plane (h) $n = 10$, yz-plane (i) $n = 10$, xz-plane

Figure 7.6: Cross-sectional distribution of potential error ($[\log 10(\%)]$) between the polyhedral gravity field and exterior gravity field of degree 0, 4, and 10 for Bennu.

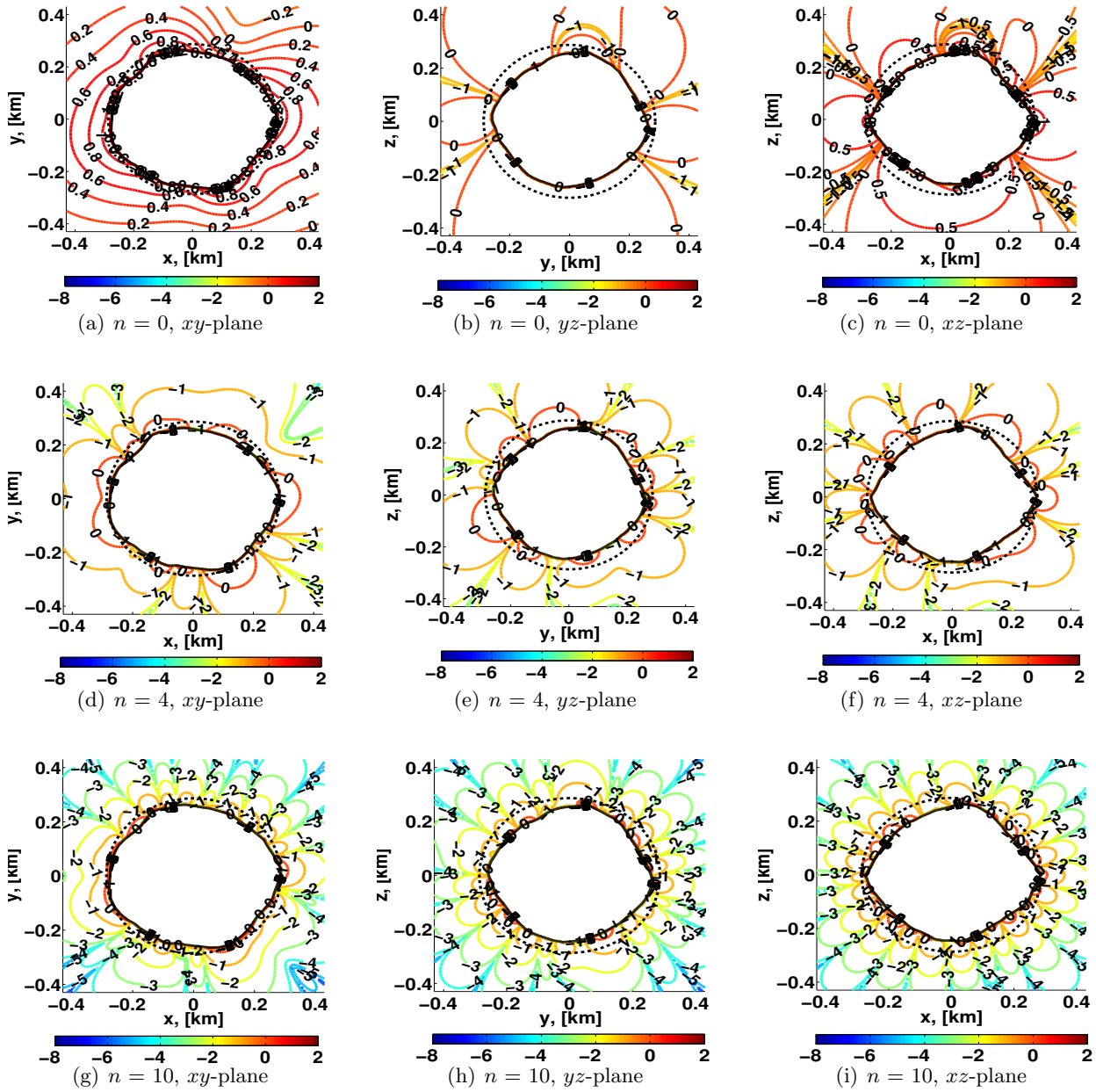

(a) $n = 0$, xy-plane (b) $n = 0$, yz-plane (c) $n = 0$, xz-plane

(d) $n = 4$, xy-plane (e) $n = 4$, yz-plane (f) $n = 4$, xz-plane

(g) $n = 10$, xy-plane (h) $n = 10$, yz-plane (i) $n = 10$, xz-plane

Figure 7.7: Cross-sectional distribution of acceleration error ($[\log 10(\%)]$) between the polyhedral gravity field and exterior gravity field of degree 0, 4, and 10 for Bennu.

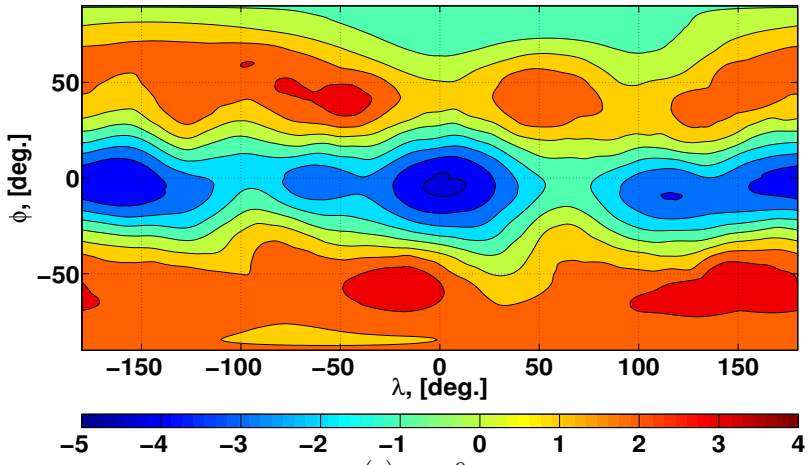

(a) $n = 0$

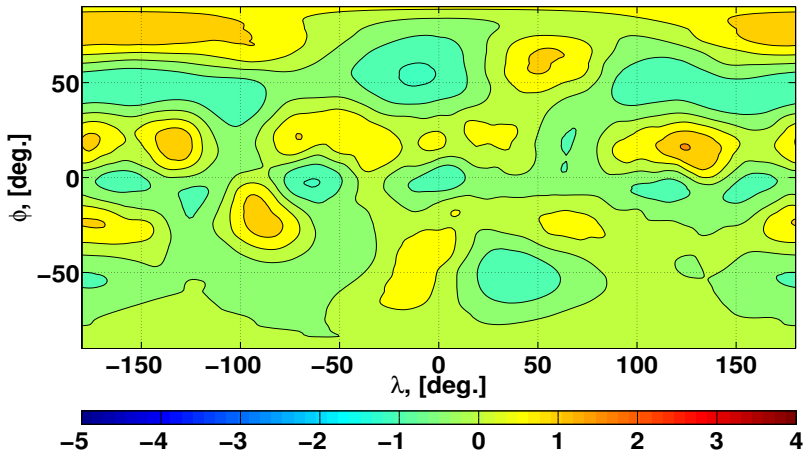

(b) $n = 4$

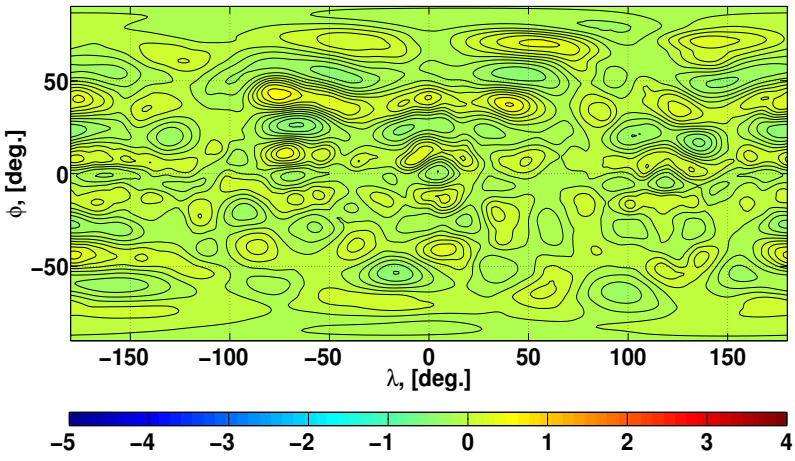

(c) $n = 10$

Figure 7.8: Surface potential error ([%]) between the polyhedral gravity field and exterior gravity field for Bennu.

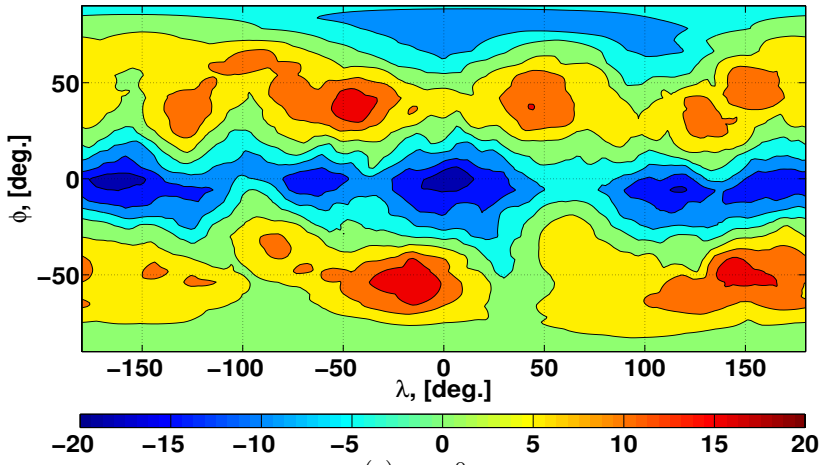

(a) $n = 0$

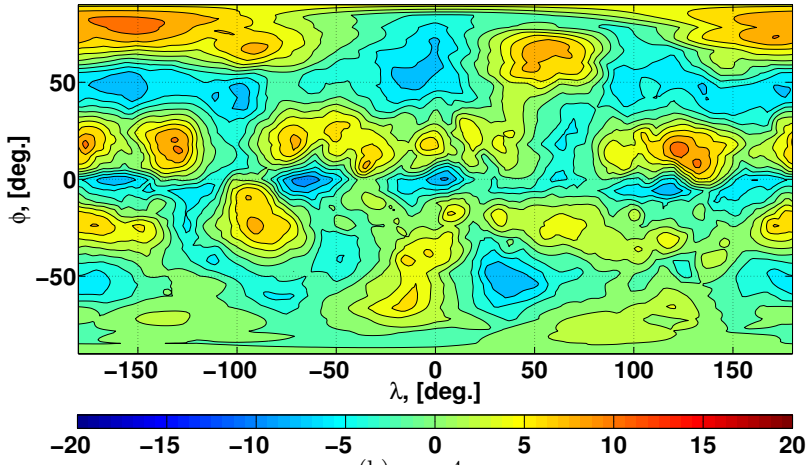

(b) $n = 4$

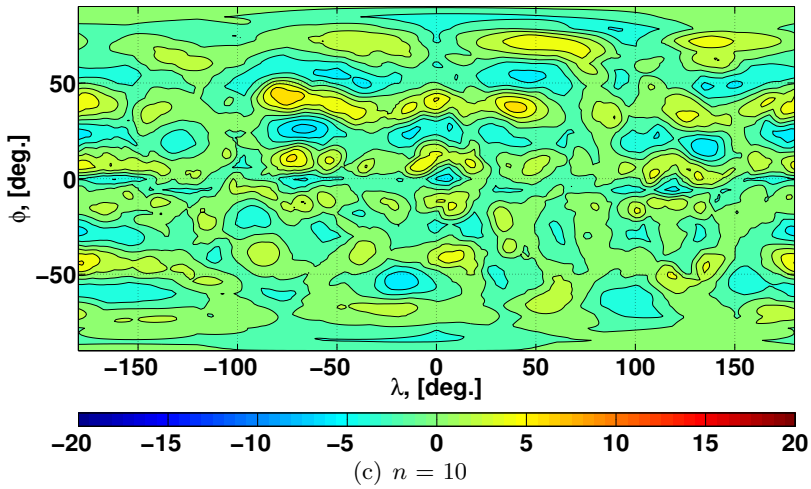

(c) $n = 10$

Figure 7.9: Surface acceleration error ([%]) between the polyhedral gravity field and exterior gravity field for Bennu.

Table 7.1 summarizes the maximum, minimum, mean, and standard deviation of the potential/acceleration errors of the exterior gravity field on the surface of Bennu.

Table 7.1: Statistics of the surface potential/acceleration errors ([%]) between the polyhedral gravity field and exterior gravity field for Bennu.

Degree (n)	Maximum	Minimum	Mean	Standard Deviation
Potential				
0	3.80464	-4.23787	0.768874	1.81990
4	1.52346	-1.07433	0.0865826	0.501408
10	0.549317	-0.513510	2.30166×10^{-3}	0.139242
Acceleration				
0	19.2068	-18.4192	2.35658	6.96270
4	10.9592	-9.41072	0.747961	3.68576
10	7.03440	-6.67813	0.114995	1.87574

7.10.2 Exterior Gravity Field around Castalia

Figure 7.10 and 7.11 show the cross-sectional distributions of the potential/acceleration errors around Castalia.

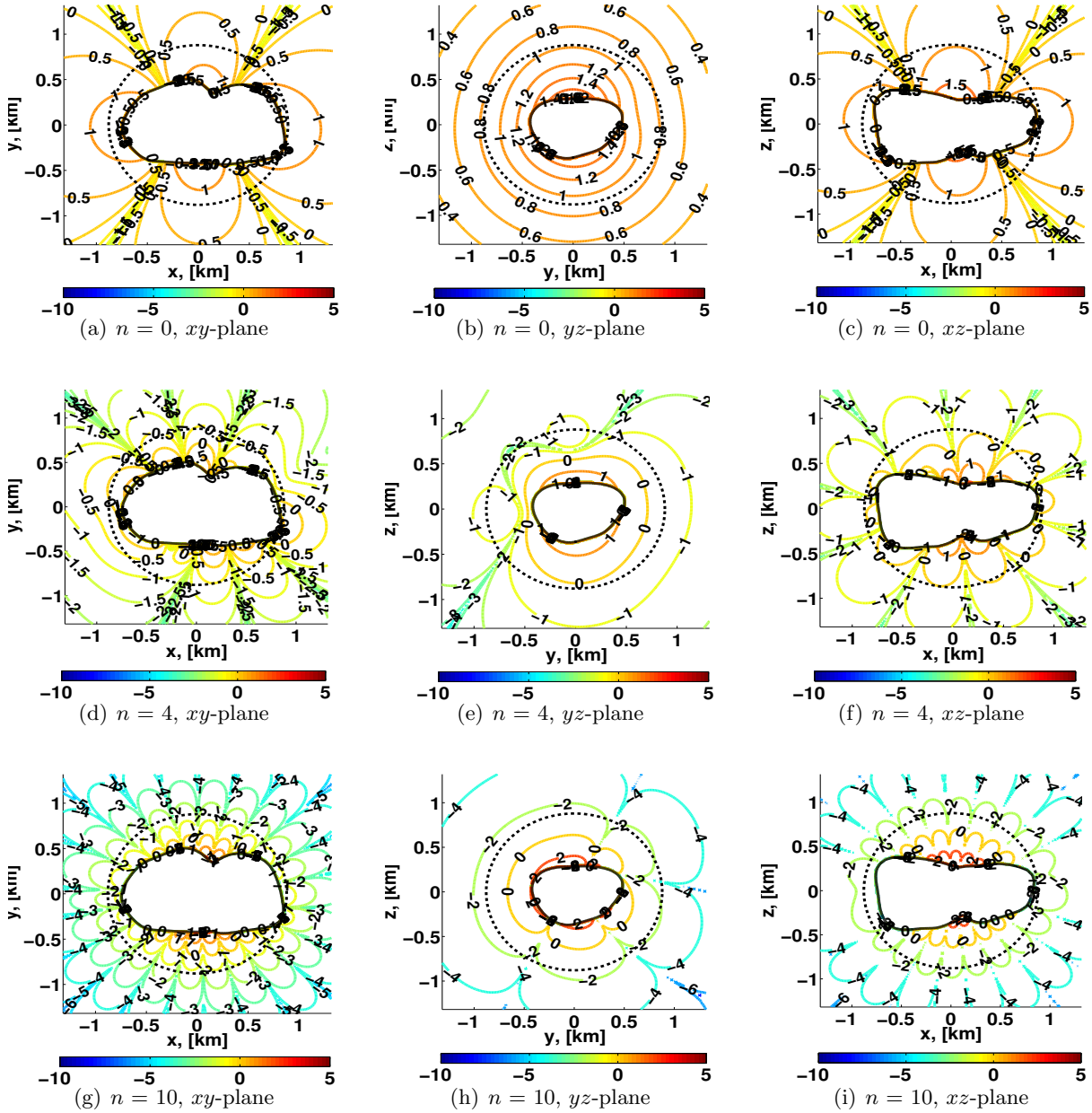

(a) $n = 0$, xy-plane (b) $n = 0$, yz-plane (c) $n = 0$, xz-plane

(d) $n = 4$, xy-plane (e) $n = 4$, yz-plane (f) $n = 4$, xz-plane

(g) $n = 10$, xy-plane (h) $n = 10$, yz-plane (i) $n = 10$, xz-plane

Figure 7.10: Cross-sectional distribution of potential error ([log 10(%)]) between the polyhedral gravity field and exterior gravity field of degree 0, 4, and 10 for Castalia.

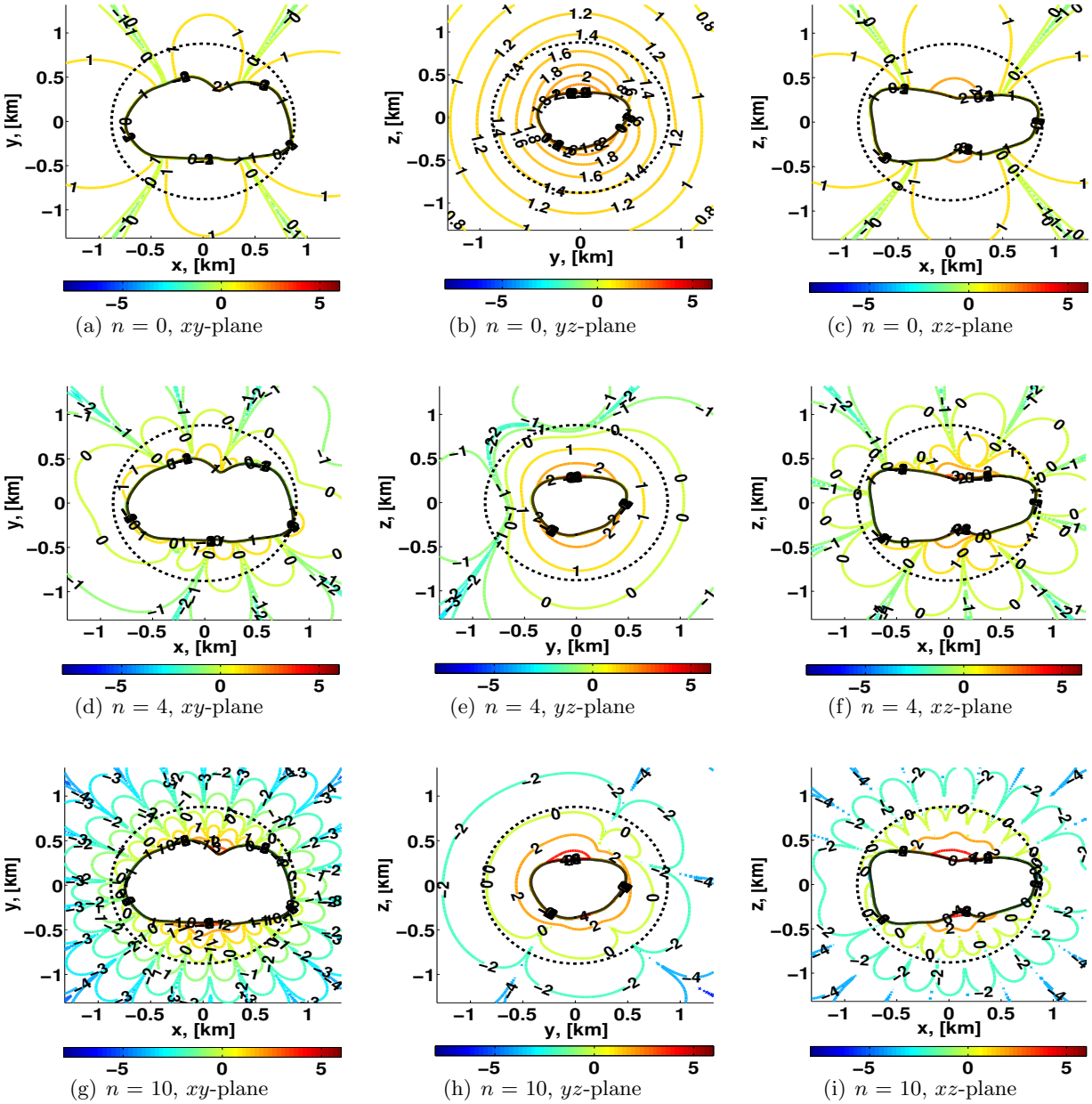

(a) $n = 0$, xy-plane (b) $n = 0$, yz-plane (c) $n = 0$, xz-plane

(d) $n = 4$, xy-plane (e) $n = 4$, yz-plane (f) $n = 4$, xz-plane

(g) $n = 10$, xy-plane (h) $n = 10$, yz-plane (i) $n = 10$, xz-plane

Figure 7.11: Cross-sectional distribution of acceleration error ([$\log 10(\%)$]) between the polyhedral gravity field and exterior gravity field of degree 0, 4, and 10 for Castalia.

The potential errors are significantly larger for Castalia than for Bennu due to its highly non-spherical shape. It is seen that the neck region is especially hard to characterize the gravity field environment. Near the surface of the body, $> 100\%$ errors are not uncommon. The same trend is seen for the acceleration errors, and the non-spherical shape of the body degrades the accuracy of

the exterior gravity field rapidly. The surface errors are simply too big, and it is meaningless to plot them. This analysis reports the exterior gravity field's vulnerability within the exterior Brillouin sphere, and it can yield tremendously large errors ($> 100\%$) for a body with a non-spherical shape.

7.11 Performance of the Interior Gravity Field

In this section, we study the performance of the interior gravity field in close proximity to the asteroid's surface. Recall that the total mapping within the exterior Brillouin sphere, including the surface, requires countless interior gravity fields as their convergence is only guaranteed up to a point on the surface (Figure 7.12).

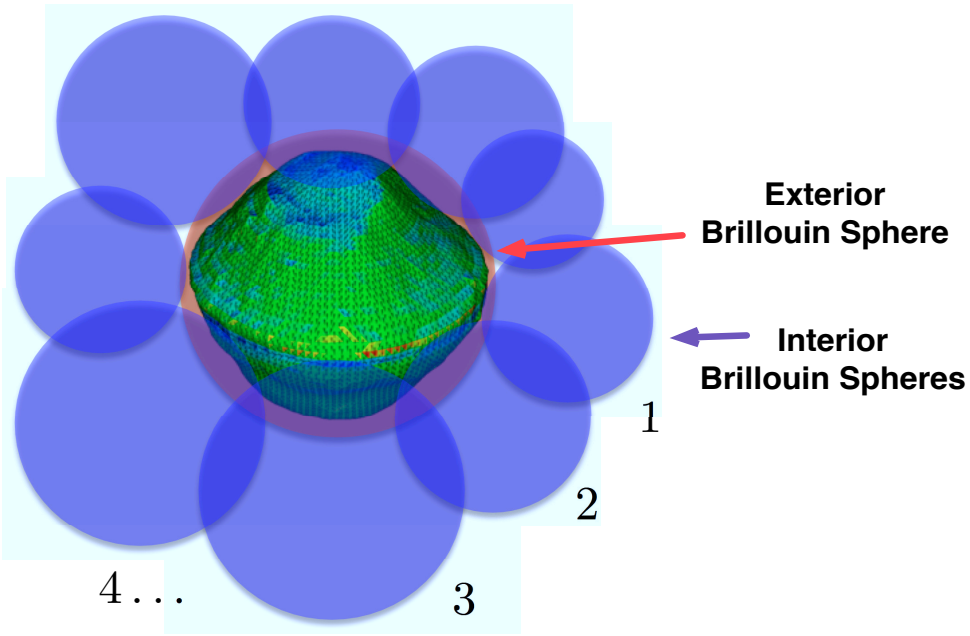

Figure 7.12: Total mapping by the interior gravity fields. The red sphere in the middle is the exterior Brillouin sphere, and the blue spheres surrounding the body are the interior Brillouin spheres.

Discussions in Section 6.3.2 showed that the parameter space of the optimal interior gravity field for one TAG point is extensive and requires much computational power. Thus, we will perform regional mapping of the surface gravity fields.

Three landing sites are chosen for both Bennu and Castalia, and an interior gravity field is computed for each landing site (Table 7.2). These landing sites are arbitrarily chosen in regions

where the surface is smooth so the interior Brilloin sphere can be drawn without making contacts with other parts of the body. Also, regions close to the tip of the body are avoided, as it is of our interest to quantify the performance of the interior gravity field in regions where the exterior gravity field does not perform well.

Table 7.2: TAG point coordinates for Bennu and Castalia.

Site #	Facet #	(x, y, z) $[km]$	(r, λ, ϕ) $[km, deg., deg.]$
Bennu			
1	525	$(-0.200, -0.0376, 0.127)$	$(0.240, -169.347, 32.076)$
2	929	$(0.104, 0.221, 0.0430)$	$(0.248, 64.78, 9.978)$
3	1907	$(0.157, -0.101, -0.146)$	$(0.237, -32.697, -38.051)$
Castalia			
1	574	$(-0.345, -0.067, 0.370)$	$(0.510, -168.931, 46.44)$
2	629	$(0.459, 0.0235, 0.302)$	$(0.550, 2.937, 33.314)$
3	2363	$(0.0418, -0.348, -0.168)$	$(0.389, -83.153, -25.635)$

The following sections discuss the results of the regional mapping for Bennu and Castalia.

7.11.1 Regional Mapping by Interior Gravity Fields around Bennu

Three interior gravity fields are constructed around Bennu to perform regional mapping of the surface gravity field. Table 7.3 shows the parameters used for the least-squares fit.

Table 7.3: Parameters of the optimal interior gravity fields around Bennu.

Site #	R_i^* $[km]$	Degree (n)	Data Type
1	1.0	30	$(2, 2, 2)$
2	1.0	35	$(2, 2, 2)$
3	1.0	30	$(2, 2, 2)$

Site #	Estimated Degree (n) for Each Subset	Assigned Degree (n) from Each Subset	Data Sphere Size w.r.t $.R_i^*$
1	$(10, 25, 30)$	$(1 \to 5, 6 \to 20, 21 \to 30)$	$(0.3, 0.8, 0.99999)$
2	$(10, 25, 35)$	$(1 \to 5, 6 \to 20, 21 \to 35)$	$(0.3, 0.8, 0.99999)$
3	$(10, 25, 30)$	$(1 \to 5, 6 \to 20, 21 \to 30)$	$(0.3, 0.8, 0.99999)$

As shown in Table 7.3, each solution consists of three subsets of solutions. These parameter settings yield the 3D error distribution within the interior Brillouin spheres in Figure 7.13.

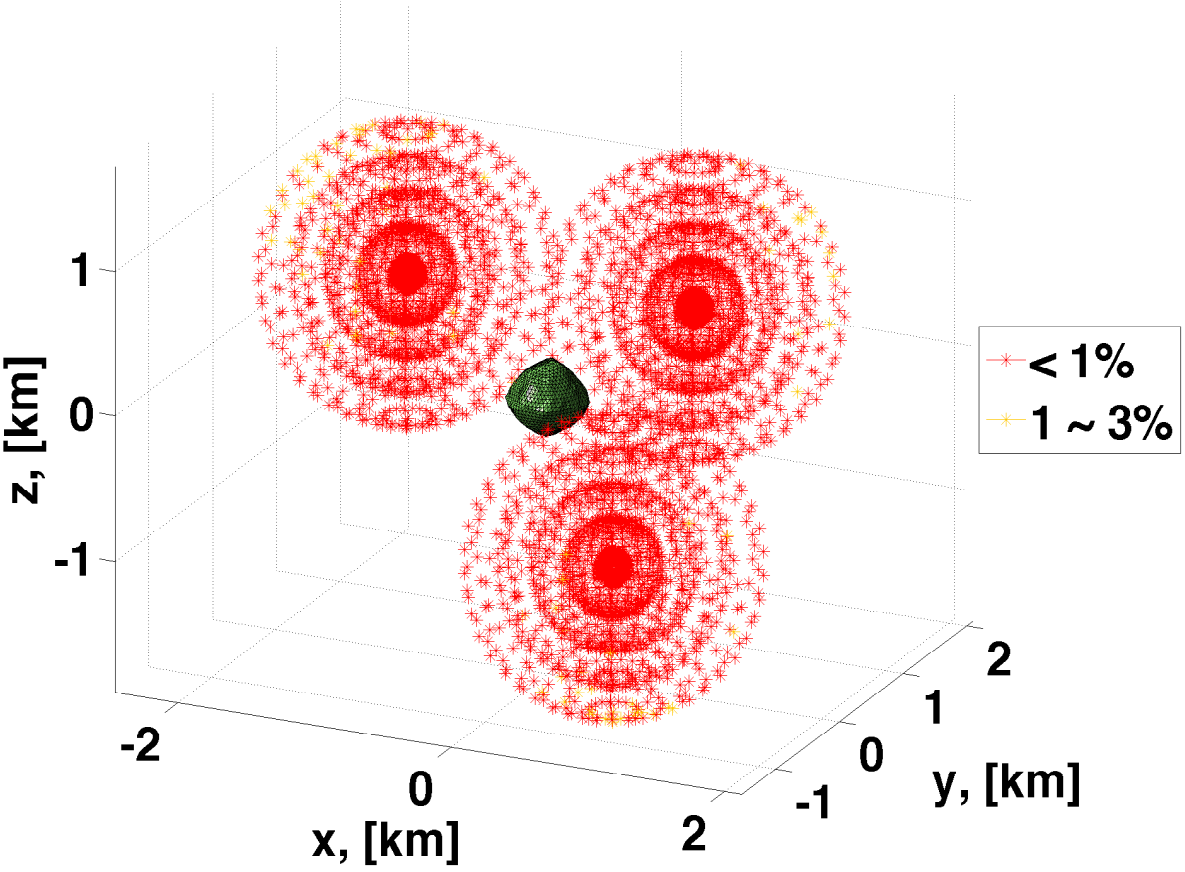

Figure 7.13: Acceleration errors by the regional mapping of interior gravity fields around Bennu.

In Figure 7.13, it is shown that all acceleration errors are less than 3%. In order to quantify the accuracy of these interior gravity fields, the acceleration error is computed at the landing site (i.e., TAG point) with respect to the polyhedral model (i.e., the truth model). In addition, the data points are scattered on the boundary of the interior Brillouin sphere (i.e., interior Brillouin shell) in evenly spaced $[20 \times 20]$ grid of latitude and longitude to evaluate the maximum, minimum, mean, and standard deviation of the acceleration errors (Table 7.4).

Table 7.4: Statistics of the acceleration errors by interior gravity fields around Bennu.

Site #	1	2	3
TAG Point [%]	1.123	-2.211	0.1598
Maximum [%]	2.606	2.183	1.736
Minimum [%]	-2.159	-2.211	-1.931
Mean [%]	3.846×10^{-2}	5.437×10^{-4}	-6.430×10^{-2}
Standard Deviation [%]	0.676	0.429	0.615

As shown in Table 7.4, the TAG point acceleration errors are less than a few percent for all three cases, and so are the maximum/minimum errors. Note that the mean is indistinguishable from zero, and the standard deviations are less than one percent. Thus, the maximum and minimum values are outside the 3σ bounds and represent only a small fraction of all data points. This result indicates that the interior gravity field outperform the exterior gravity field by approximately an order of magnitude for Bennu.

7.11.2 Regional Mapping by Interior Gravity Fields around Castalita

The regional mapping is also carried out for Castalia around three TAG points. Table 7.5 shows the parameter settings for the least-squares fit:

Table 7.5: Parameters of the optimal interior gravity fields around Castalia.

Site #	R_i^* $[km]$	Degree (n)	Data Type
1	2.5	30	$(2, 2, 2)$
2	2.0	35	2
3	2.5	35	2

Site #	Estimated Degree (n) for Each Subset	Assigned Degree (n) from Each Subset	Data Sphere Size w.r.t. R_i^*
1	$(10, 20, 30)$	$(1 \to 5, 6 \to 15, 16 \to 30)$	$(0.3, 0.8, 0.99999)$
2	35	$1 \to 35$	1
3	35	$1 \to 35$	1

These settings in Table 7.5 yield the 3D error distribution shown in Figure 7.14.

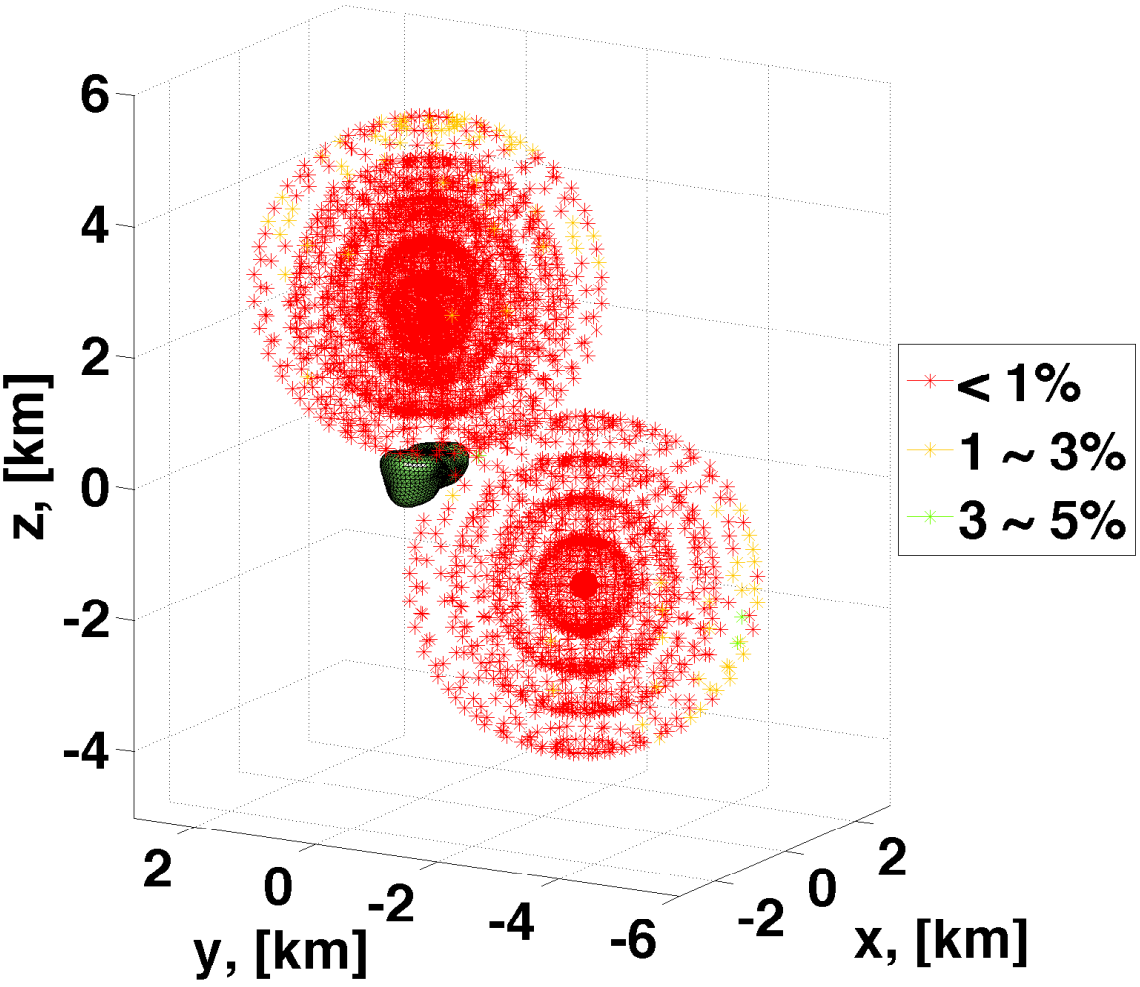

Figure 7.14: Acceleration errors by the regional mapping of interior gravity fields around Castalia.

It appears that there are only two interior gravity fields plotted in Figure 7.14, but it is an artifact of two landing sites being close to each other (i.e., site 1 and 2). The acceleration errors have increased slightly, up from $\sim 3\%$ for Bennu to $\sim 5\%$ for Castalia. This is the result of highly non-spherical shape of Castalia which makes the interior spherical harmonic coefficients estimation more difficult. The quantitative performance of the regional mapping around Castalia is given in Table 7.6.

Table 7.6: Statistics of the acceleration errors by interior gravity fields around Castalia.

Site #	1	2	3
TAG Point [%]	4.706	2.905	−4.075
Maximum [%]	4.706	2.905	3.078
Minimum [%]	−3.463	−2.903	−4.075
Mean [%]	2.352×10^{-2}	8.911×10^{-2}	-6.946×10^{-3}
Standard Deviation [%]	0.917	0.537	0.679

Table 7.6 shows that the maximum/minimum acceleration errors are obtained at the TAG sites. However, the acceleration errors are still on the order of several percent, which is the accuracy never achievable with the exterior gravity field (Section 7.10.2). Thus, it is shown that the interior gravity field outperforms the exterior gravity field even for a highly non-spherical body.

7.12 Performance of the Interior Spherical Bessel Gravity Field

In this section, we investigate the performance of the interior spherical Bessel gravity field. We will test two cases where the interior spherical Bessel coefficients are analytically converted from the exterior gravity field by matching the boundary conditions (Section 7.8), and they are estimated via least-squares fit as was done for the interior gravity field (Section 6.3.2)

7.12.1 Analytical Conversion Method

First, we convert the exterior spherical harmonic coefficients into the interior spherical Bessel coefficients by matching the boundary conditions as shown in Equation 7.57 through 7.59. The only parameters we change are the degree and power of the interior spherical Bessel gravity field. We will test six cases shown in Table 7.7.

Table 7.7: Degree (n) and power (l) of interior spherical Bessel gravity fields analytically converted from the exterior gravity field.

Case	Degree (n)	Power (l)
1	4	2
2	4	5
3	10	2
4	10	5
5	15	2
6	15	5

Note that, in the actual spacecraft mission, the higher-degree ($n \geq 10$) exterior gravity field may not be determined. Nonetheless, the parameters in Table 7.7 are explored to study the intrinsic capabilities of the analytically converted interior spherical Bessel gravity field.

7.12.1.1 Performance of the Analytically Converted Interior Spherical Bessel Gravity Field around Bennu

Figure 7.15 and 7.16 show the surface potential/acceleration errors for Bennu between the polyhedral gravity field and analytically converted interior spherical Bessel gravity field. As shown in both figures, the higher-degree interior spherical Bessel gravity field yields smaller potential/acceleration errors, but there is no significant change for different powers. All acceleration errors are within 10% on the surface of Bennu (Table 7.8).

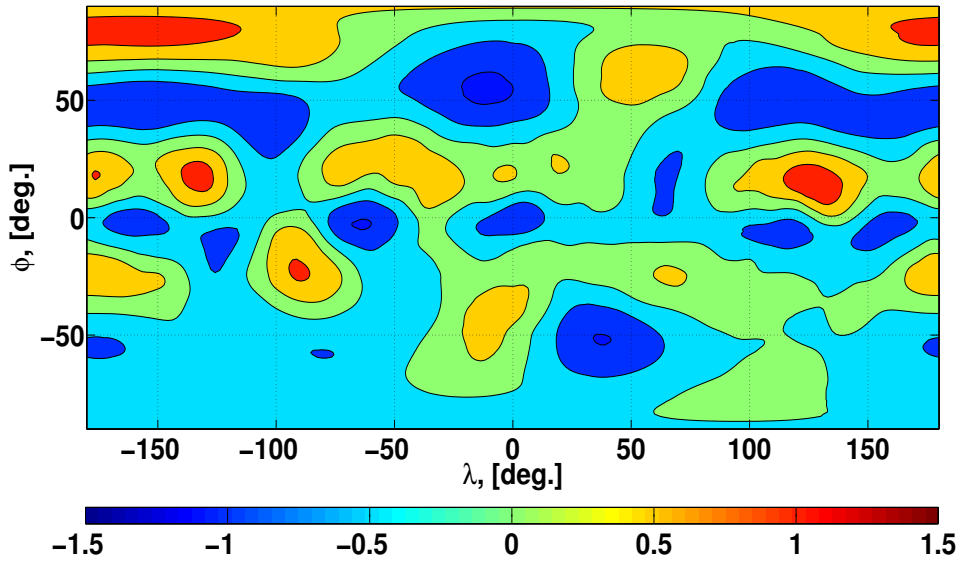

(a) Surface potential error for case 1 ($n = 4$, $l = 2$)

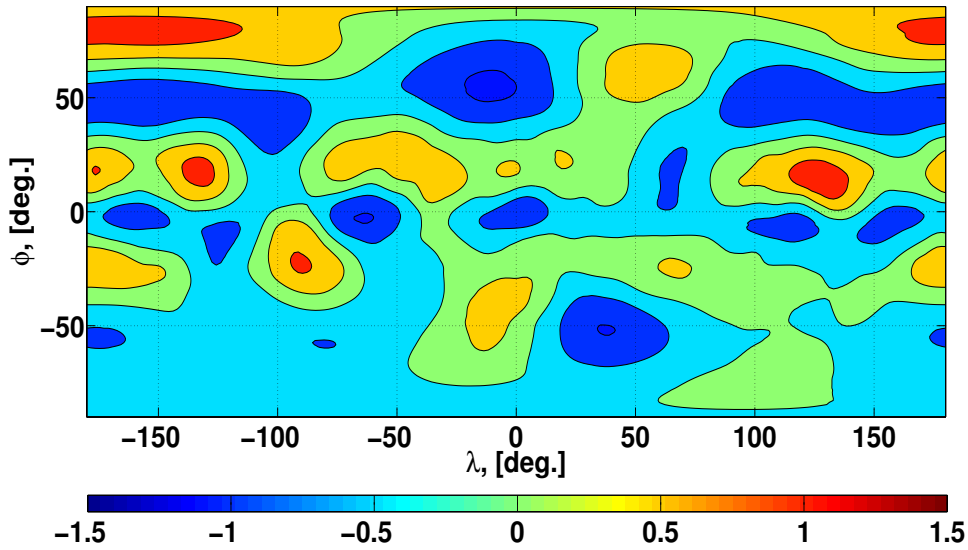

(b) Surface potential error for case 2 ($n = 4$, $l = 5$)

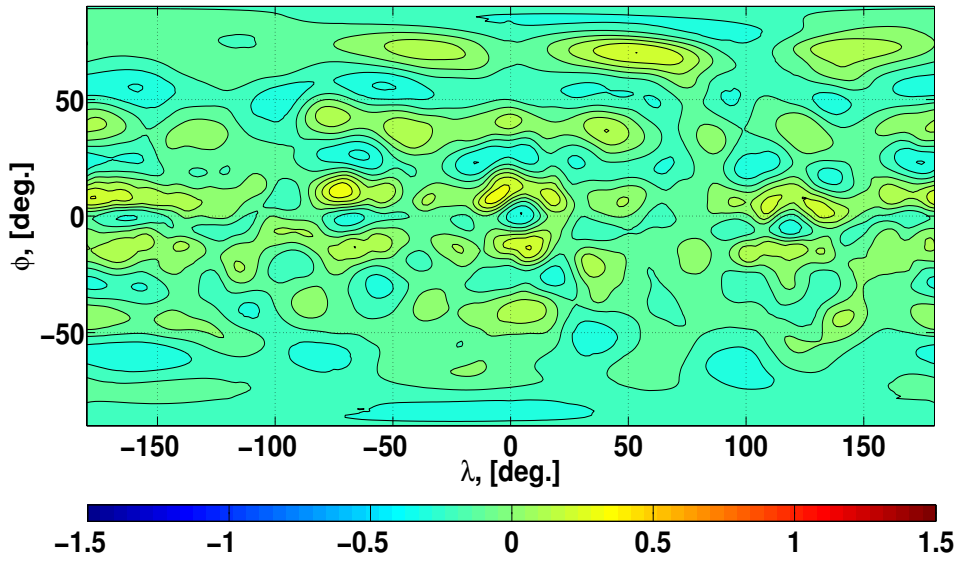

(c) Surface potential error for case 3 ($n = 10$, $l = 2$)

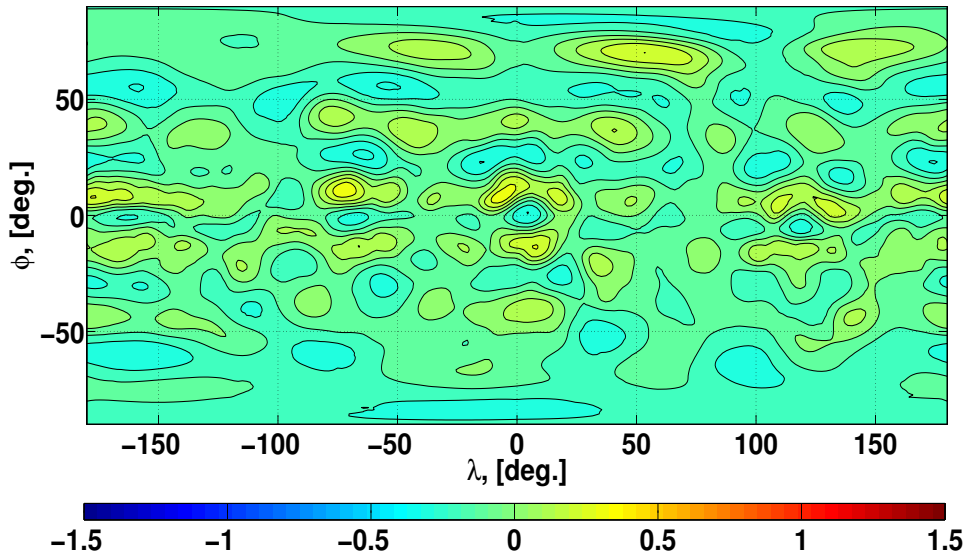

(d) Surface potential error for case 4 ($n = 10$, $l = 5$)

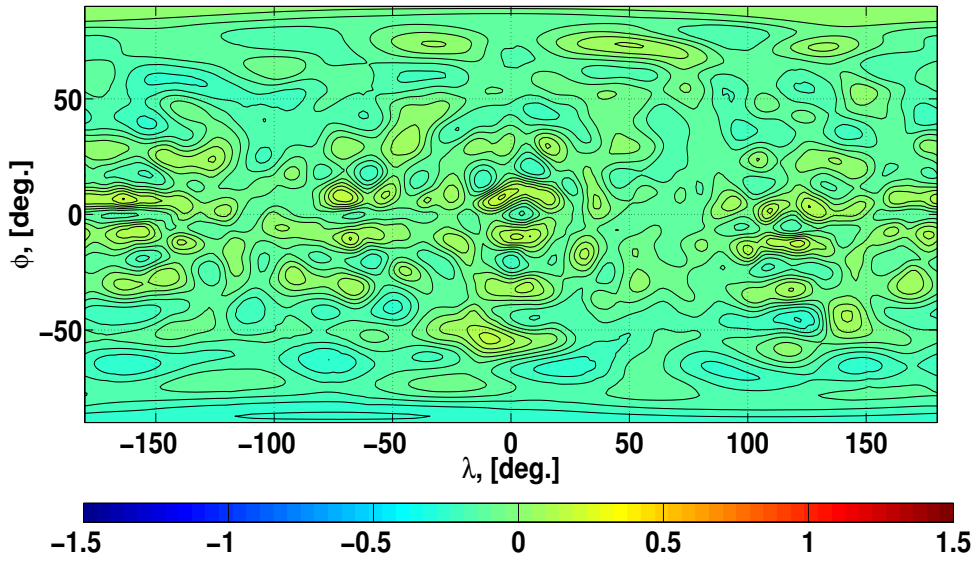

(e) Surface potential error for case 5 ($n = 15$, $l = 2$)

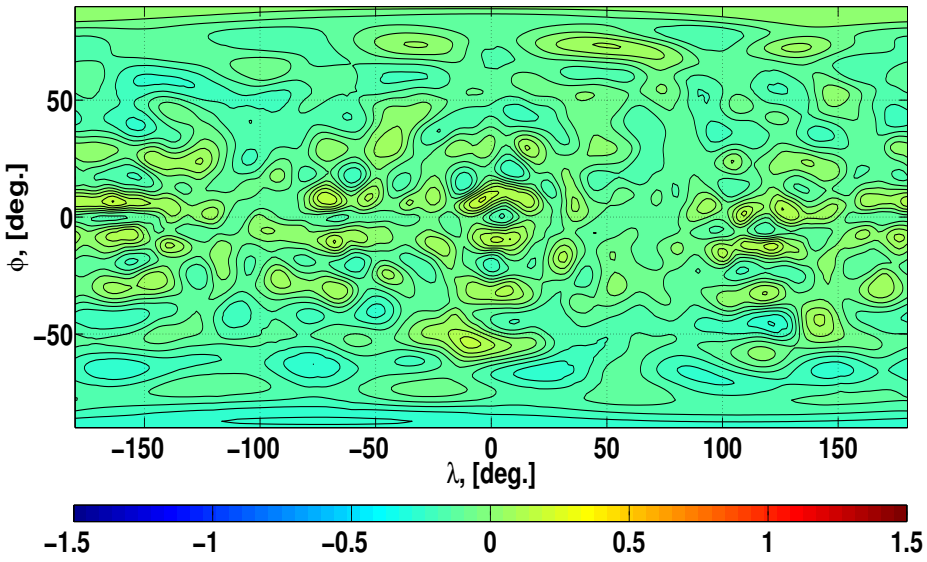

(f) Surface potential error for case 6 ($n = 15$, $l = 5$)

Figure 7.15: Surface potential error ([%]) between the polyhedral gravity field and analytically converted interior spherical Bessel gravity field: case 1 through case 6 for Bennu.

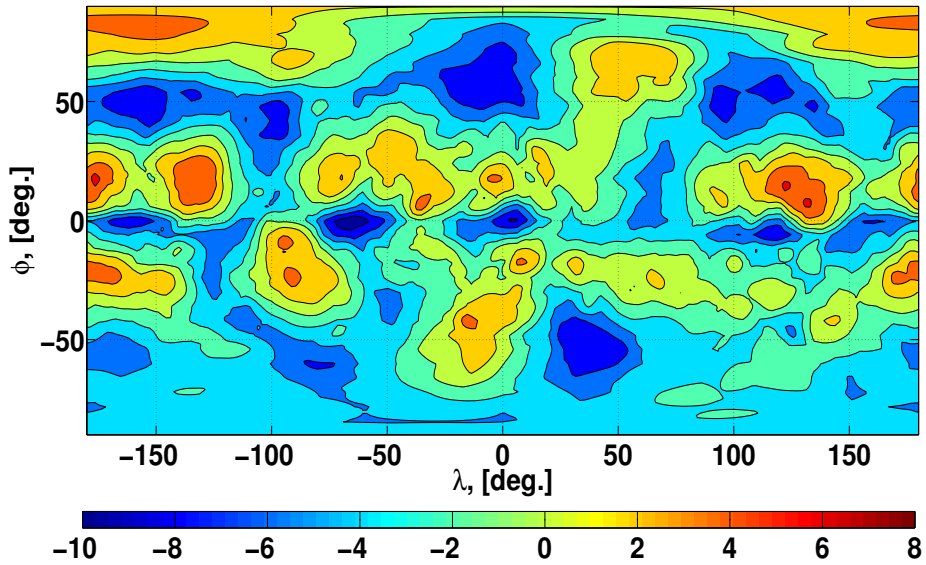

(a) Surface acceleration error for case 1 ($n = 4$, $l = 2$)

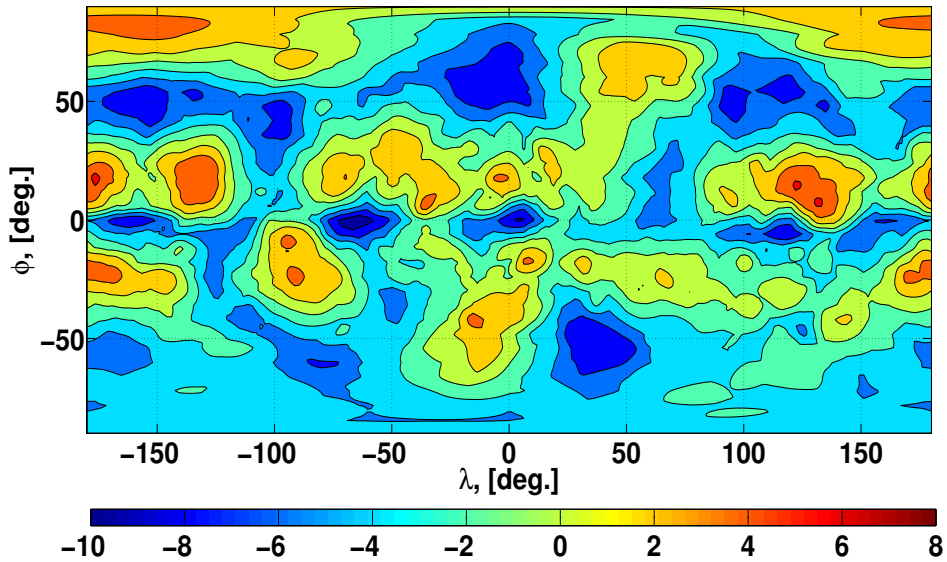

(b) Surface acceleration error for case 2 ($n = 4$, $l = 5$)

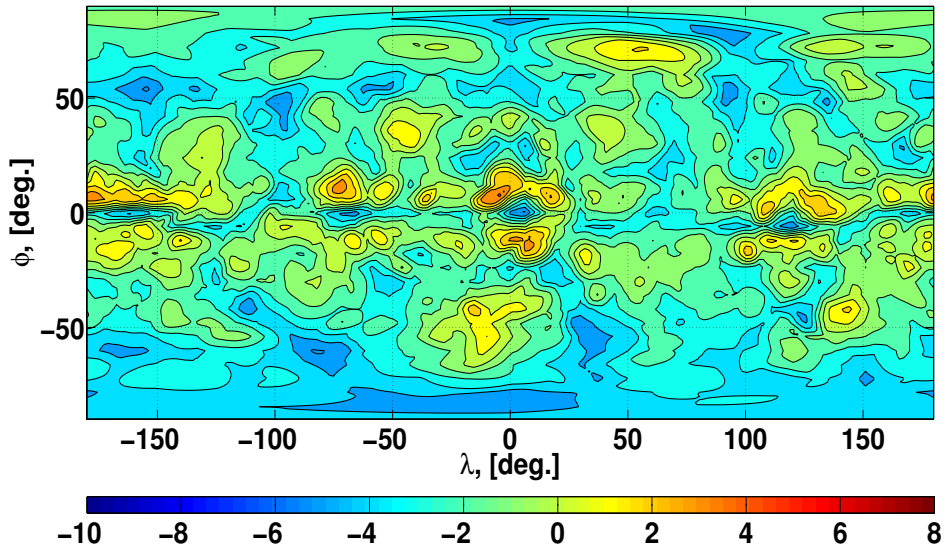

(c) Surface acceleration error for case 3 ($n = 10$, $l = 2$)

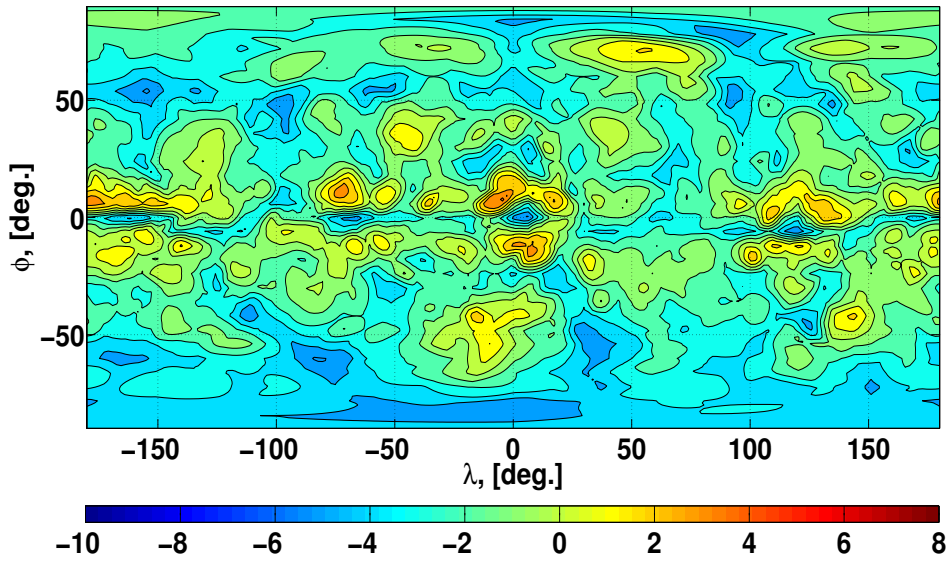

(d) Surface acceleration error for case 4 ($n = 10$, $l = 5$)

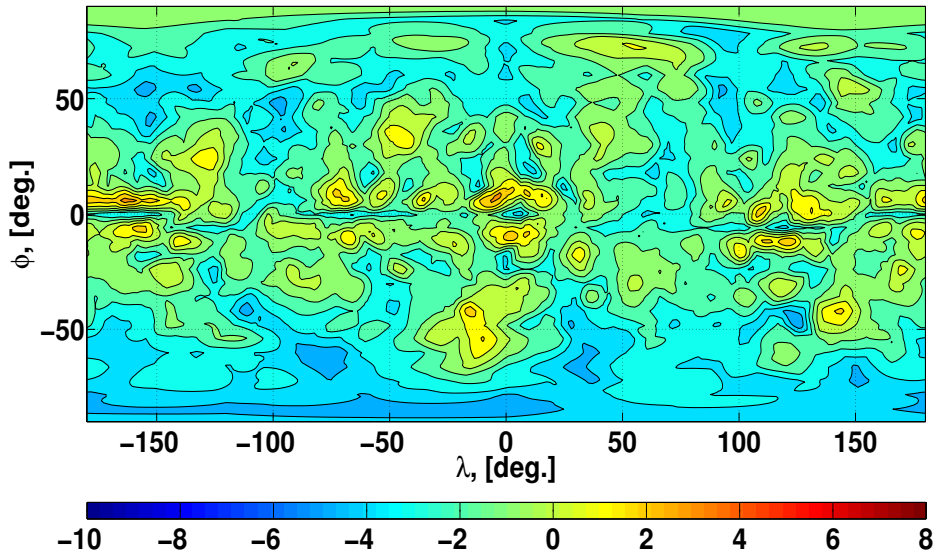

(e) Surface acceleration error for case 5 ($n = 15$, $l = 2$)

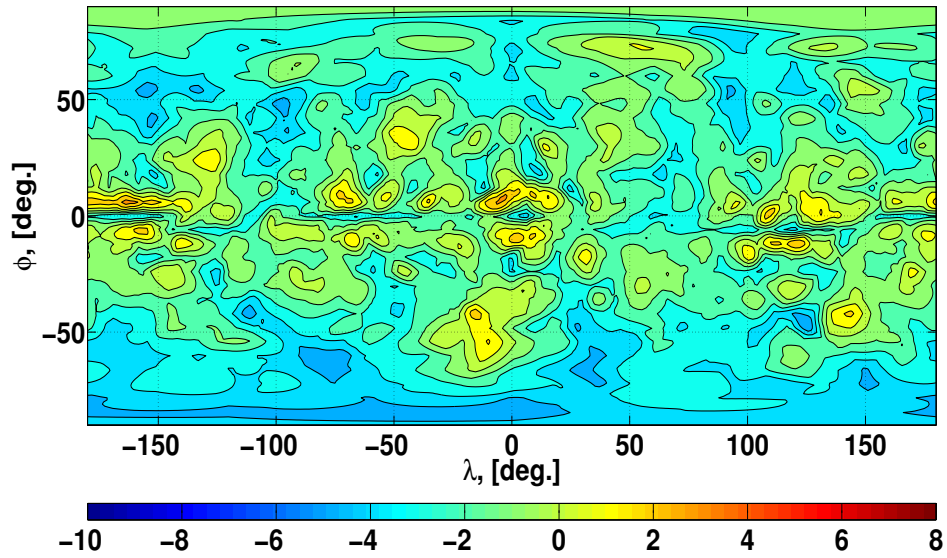

(f) Surface acceleration error for case 6 ($n = 15$, $l = 5$)

Figure 7.16: Surface acceleration error ([%]) between the polyhedral gravity field and analytically converted interior spherical Bessel gravity field: case 1 through case 6 for Bennu.

Table 7.8: Statistics of the surface potential/acceleration errors ([%]) between the polyhedral gravity field and analytically converted interior spherical Bessel gravity field: case 1 through case 6 for Bennu.

Degree (n)	Power (l)	Maximum	Minimum	Mean	Standard Deviation
Potential					
4	2	1.30730	−1.10122	-8.09664×10^{-4}	0.458908
4	5	1.30726	−1.10119	-7.84872×10^{-4}	0.458883
10	2	0.384995	−0.319545	−0.0708242	0.104228
10	5	0.384959	−0.319398	−0.0707926	0.104222
15	2	0.210780	−0.256909	−0.0698102	0.0747787
15	5	0.210769	−0.256911	−0.0697783	0.0747769
Acceleration					
4	2	6.60441	−9.44079	−1.37583	2.76404
4	5	6.60303	−9.44080	−1.37548	2.76361
10	2	4.21681	−5.15143	−1.65999	1.43883
10	5	4.21610	−5.15071	−1.65949	1.43890
15	2	3.35731	−4.91601	−1.64271	1.32577
15	5	3.35682	−4.91594	−1.64220	1.32589

7.12.1.2 Performance of the Analytically Converted Interior Spherical Bessel Gravity Field around Castalia

Figure 7.17 and 7.18 show the surface potential/acceleration errors of Castalia between the polyhedral gravity field and analytically converted interior spherical Bessel gravity field. Both plots show significantly larger errors for Castalia than for Bennu. However, the errors are still contained under 10% for potential and 30% for acceleration. It is a significant improvement from using the exterior gravity field, which frequently yields $> 100\%$ errors on the surface of the body. Notice that, compared to Figure 7.15 and 7.16, larger errors are spread out more widely in Figure 7.17 and 7.18. Table 7.9 summarizes the maximum, minimum, mean, and standard deviation of the potential/acceleration errors of the analytically converted interior spherical Bessel gravity field on the surface of Castalia.

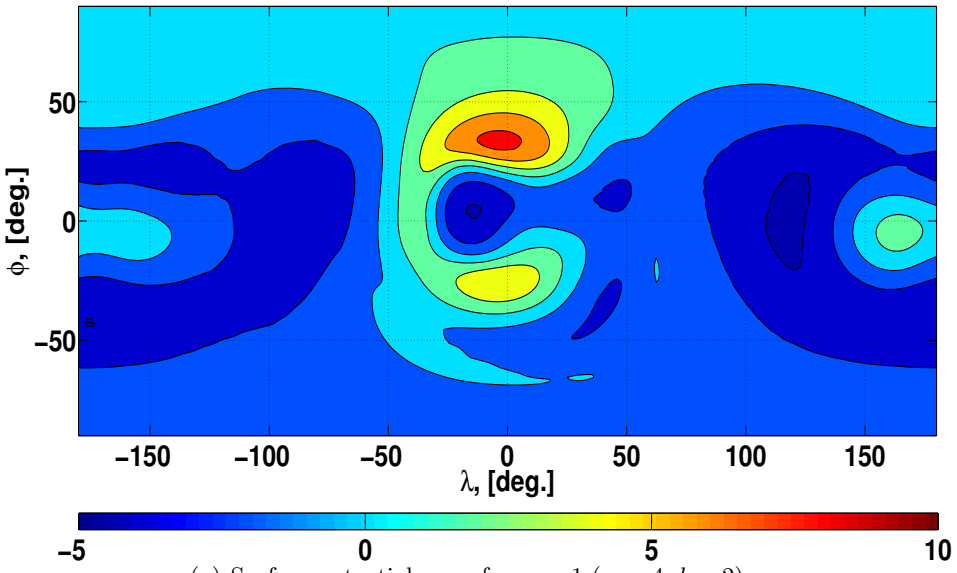

(a) Surface potential error for case 1 ($n = 4$, $l = 2$)

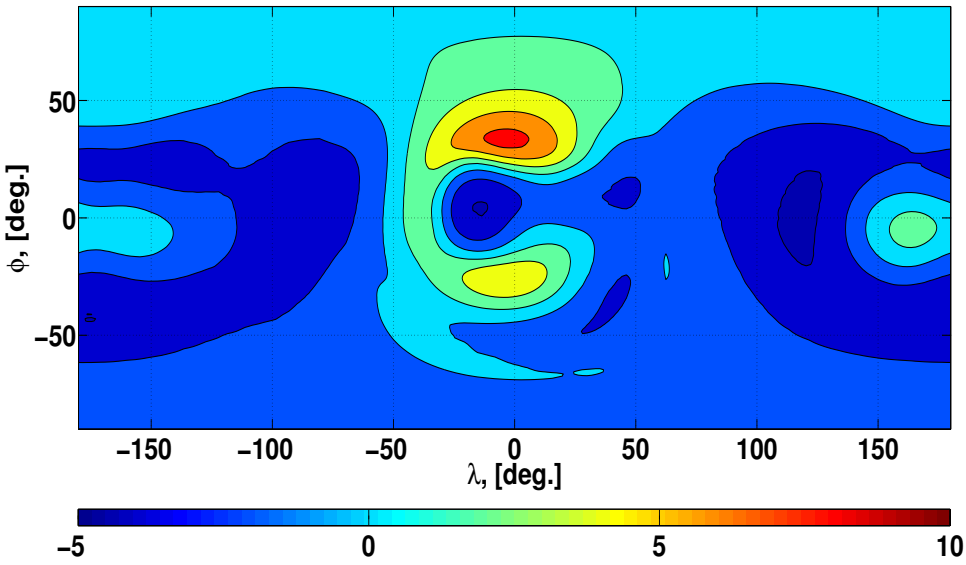

(b) Surface potential error for case 2 ($n = 4$, $l = 5$)

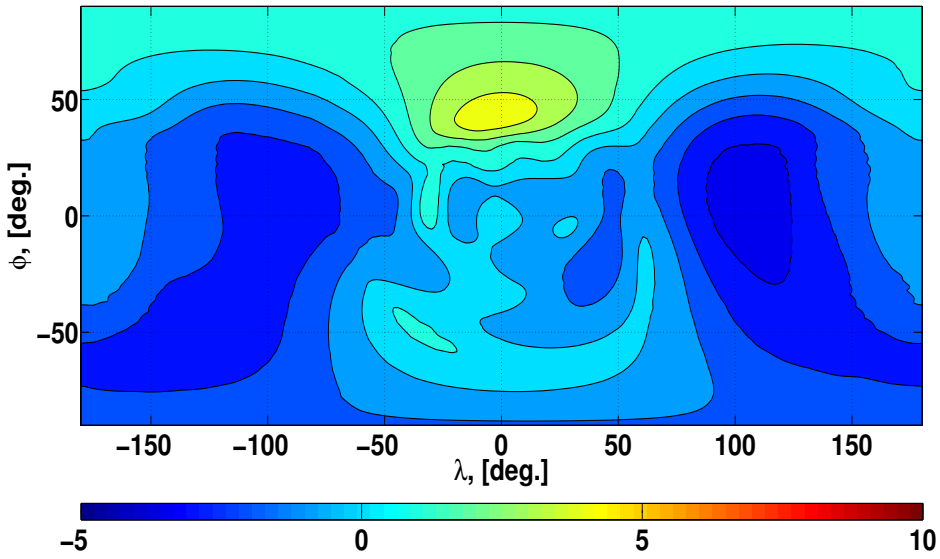

(c) Surface potential error for case 3 ($n = 10$, $l = 2$)

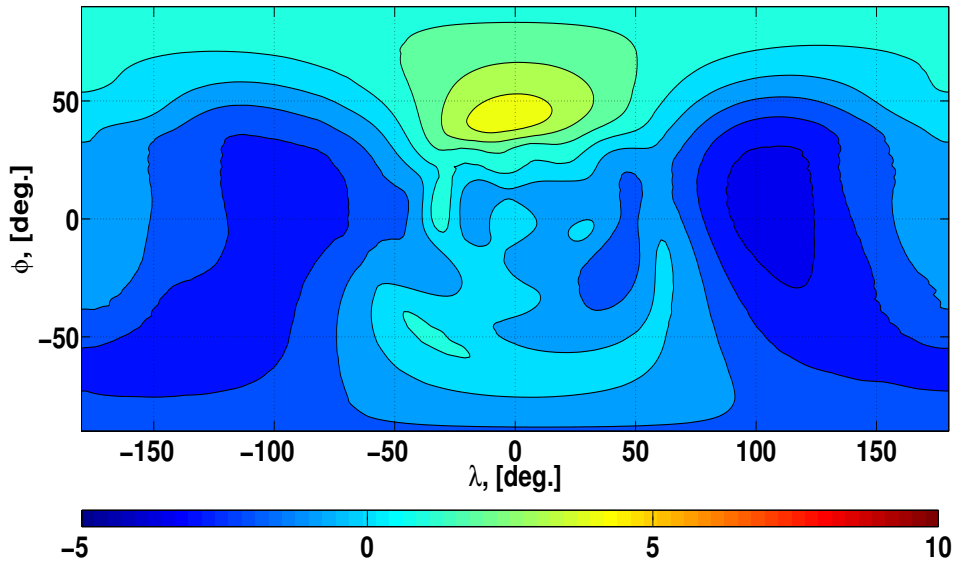

(d) Surface potential error for case 4 ($n = 10$, $l = 5$)

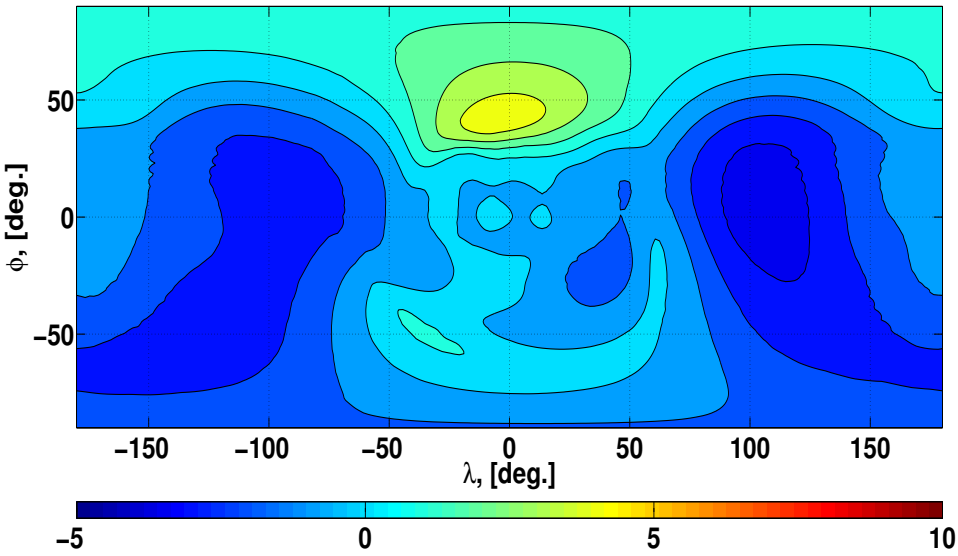

(e) Surface potential error for case 5 ($n = 15$, $l = 2$)

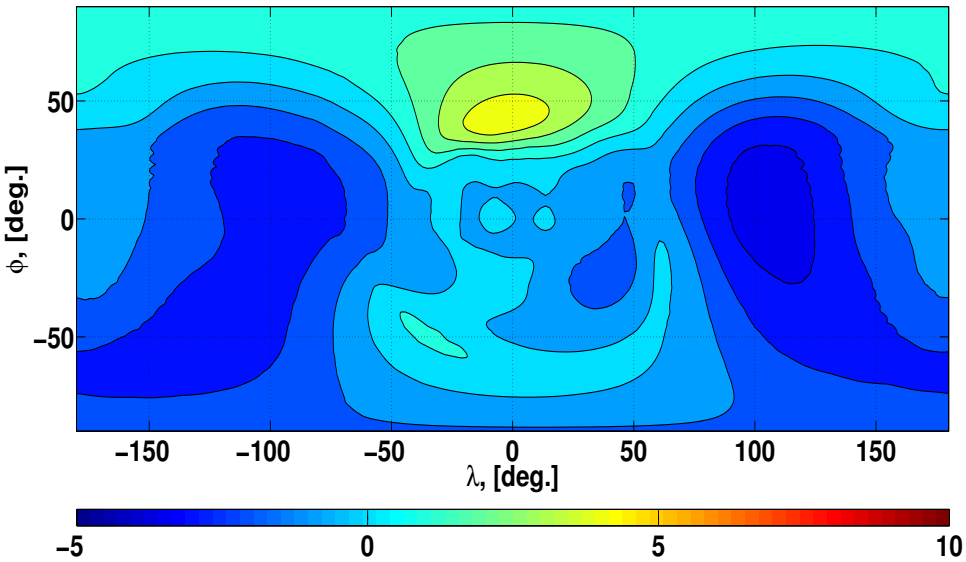

(f) Surface potential error for case 6 ($n = 15$, $l = 5$)

Figure 7.17: Surface potential error ([%]) between the polyhedral gravity field and analytically converted interior spherical Bessel gravity field: case 1 through case 6 for Castalia.

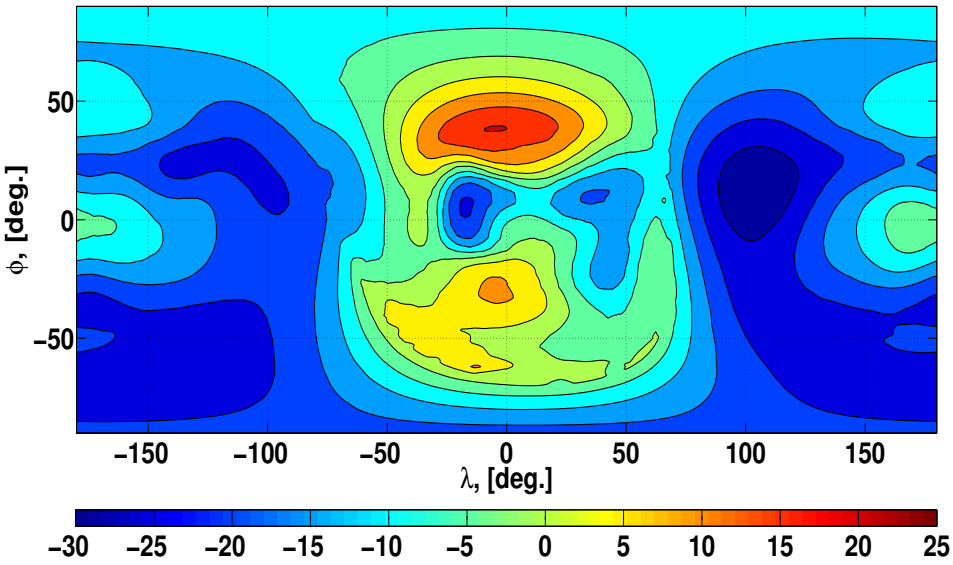

(a) Surface acceleration error for case 1 ($n = 4$, $l = 2$)

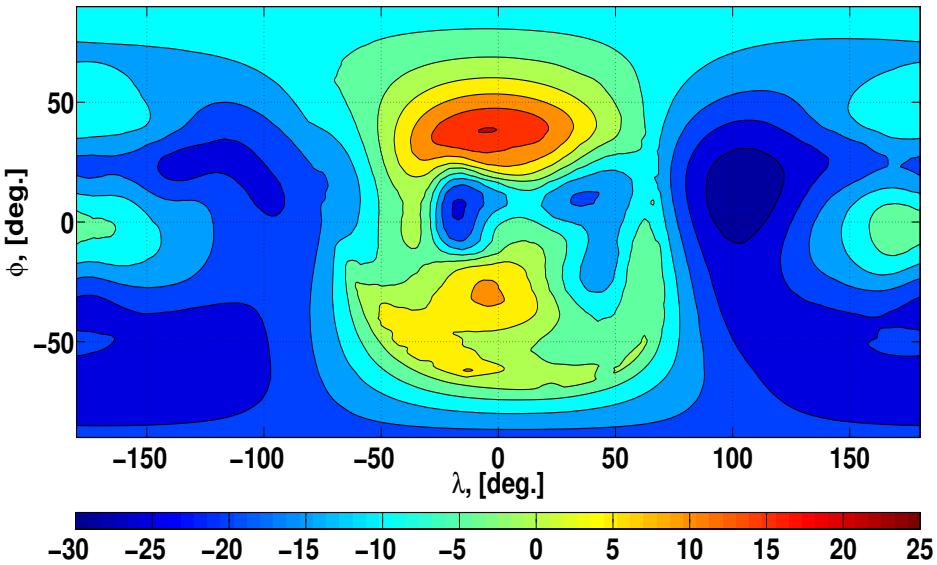

(b) Surface acceleration error for case 2 ($n = 4$, $l = 5$)

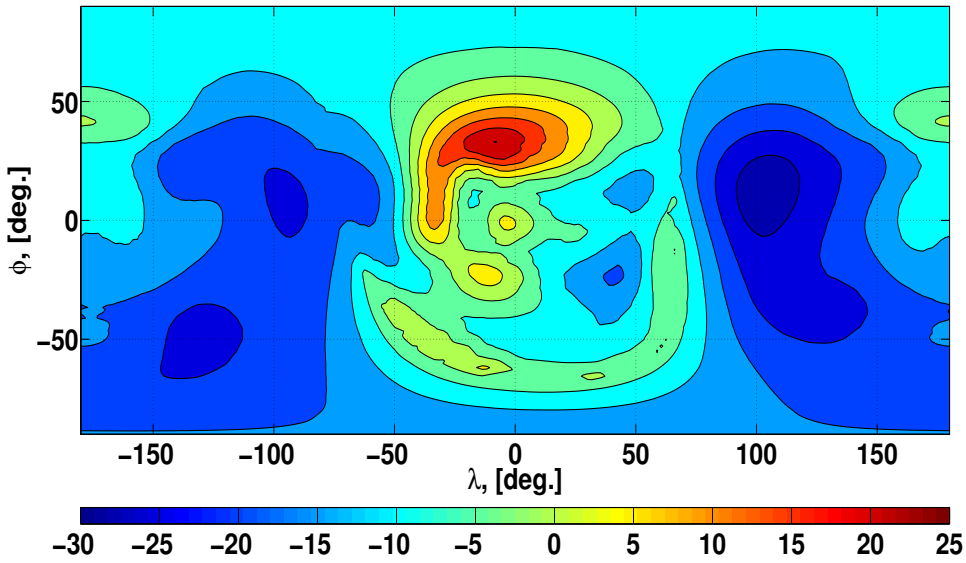

(c) Surface acceleration error for case 3 ($n = 10$, $l = 2$)

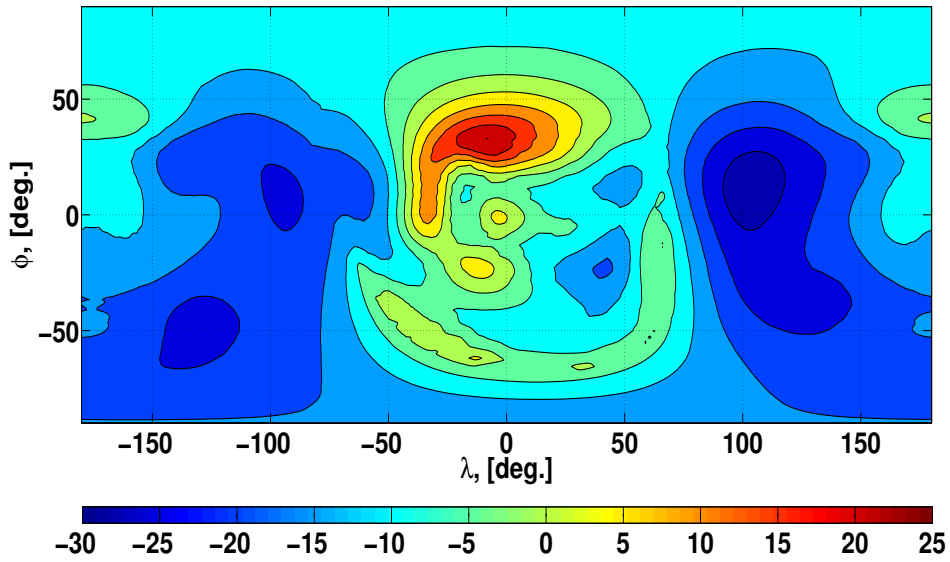

(d) Surface acceleration error for case 4 ($n = 10$, $l = 5$)

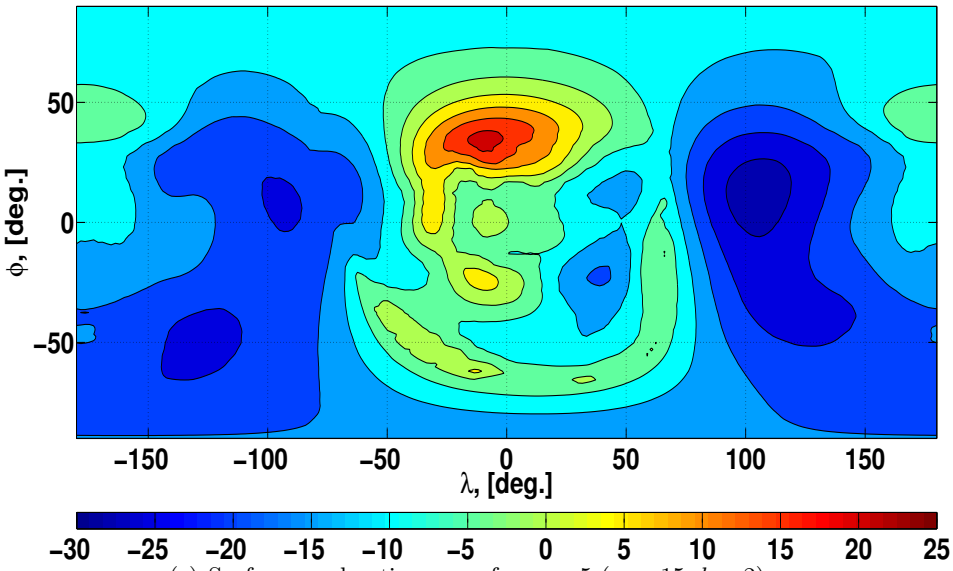

(e) Surface acceleration error for case 5 ($n = 15$, $l = 2$)

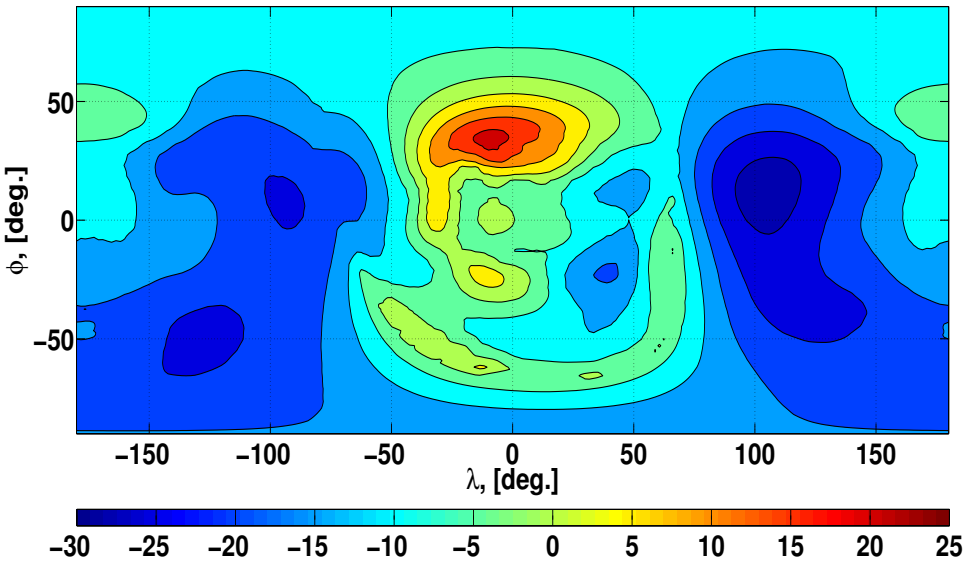

(f) Surface acceleration error for case 6 ($n = 15$, $l = 5$)

Figure 7.18: Surface acceleration error ([%]) between the polyhedral gravity field and analytically converted interior spherical Bessel gravity field: case 1 through case 6 for Castalia.

Table 7.9: Statistics of the surface potential/acceleration errors ([%]) between the polyhedral gravity field and analytically converted interior spherical Bessel gravity field: case 1 through case 6 for Castalia.

Degree (n)	Power (l)	Maximum	Minimum	Mean	Standard Deviation
Potential					
4	2	8.55932	−4.38073	−0.304808	2.01725
4	5	8.55508	−4.37939	−0.301064	2.01755
10	2	4.59364	−3.53261	−0.462649	1.59061
10	5	4.59430	−3.53079	−0.458757	1.59152
15	2	4.62814	−3.47930	−0.464882	1.58656
15	5	4.62866	−3.47724	$-0.460992e$	1.58748
Acceleration					
4	2	20.1551	−28.3260	−10.5150	9.18088
4	5	20.1077	−28.3173	−10.5188	9.17073
10	2	25.0558	−27.9169	−10.4564	7.71477
10	5	25.0286	−27.9085	−10.4591	7.70785
15	2	21.8928	−27.6136	−10.5238	7.51102
15	5	21.8671	−27.6063	−10.5264	7.50418

7.12.2 Fitting to the Polyhedral Gravity Field Acceleration

In this section, we estimate the interior spherical Bessel coefficients via a least-squares fit instead of analytically converting them from the exterior spherical harmonic coefficients. Such a conversion represents the ideal scenario where we know the density distribution of the body and have the true gravity field available. The estimated interior spherical Bessel gravity field greatly facilitates the potential/acceleration computation and reduce the overall computation time compared to the polyhedral integration.

The interior spherical Bessel coefficients ($\mathscr{A}^i_{lnm}$, $\mathscr{B}^i_{lnm}$) are estimated the same way the interior spherical harmonic coefficients (C^i_{nm}, S^i_{nm}) are estimated from the exterior gravity field (C^e_{nm}, S^e_{nm}) (see Section 6.3.2). Recall that the interior gravity field is fit to the potential/acceleration/dynamics matrix of the exterior gravity field in a least-squares sense. For the interior spherical Bessel gravity field, as the dynamics matrix does not satisfy Laplace's equation, the potential and acceleration are the only source data. In the following, the methodology of the least-squares fit and the performance

of the estimated interior spherical Bessel gravity fields are discussed. We will first show the general trend of the least-squares fit solution and commence the search for the optimal interior spherical Bessel gravity field.

7.12.2.1 Least-squares Conversion of the Interior Spherical Bessel Gravity Field

The least-squares estimation of the interior spherical Bessel coefficients is carried out in the same manner as that of the interior spherical harmonic coefficients. The state vector consists of the interior spherical Bessel coefficients ordered in the following manner:

$$
\begin{aligned}
[\tilde{\mathscr{A}}^i_{lnm}] \;=\; & [\mathscr{A}^i_{000}, \mathscr{A}^i_{010}, \mathscr{A}^i_{011}, \mathscr{B}^i_{011}, && l=0 \\
& \mathscr{A}^i_{100}, \mathscr{A}^i_{110}, \mathscr{A}^i_{111}, \mathscr{B}^i_{111}, \mathscr{A}^i_{120}, \mathscr{A}^i_{121}, \mathscr{B}^i_{121}, \mathscr{A}^i_{122}, \mathscr{B}^i_{122}, \mathscr{A}^i_{130}, \cdots && l=1 \\
& \mathscr{A}^i_{200}, \mathscr{A}^i_{210}, \mathscr{A}^i_{211}, \mathscr{B}^i_{211}, \mathscr{A}^i_{220}, \mathscr{A}^i_{221}, \mathscr{B}^i_{221}, \mathscr{A}^i_{222}, \mathscr{B}^i_{222}, \mathscr{A}^i_{230}, \cdots && l=2 \\
& \cdots, && \vdots \\
& \mathscr{A}^i_{l00}, \mathscr{A}^i_{l10}, \mathscr{A}^i_{l11}, \mathscr{B}^i_{l11}, \mathscr{A}^i_{l20}, , \mathscr{A}^i_{l21}, \mathscr{B}^i_{l21}, \cdots\cdots, \mathscr{B}^i_{lnn}] && l=l_{max}
\end{aligned}
\tag{7.70}
$$

which consists of $l(n+1)^2+4$ coefficients. Notice that only the zeroth and the first-degree coefficients are estimated when $l=0$. This is because the higher-degree and higher-order terms are all zero by definition for the zeroth power, as mentioned in Section 7.7.

The objective here is to match the potential/acceleration given by the polyhedral gravity field and interior spherical Bessel gravity field. We only derive equations for the acceleration fitting, but the potential fitting can be achieved by simple substitution. The cost function is defined as

$$
J_{\mathscr{B}} \;=\; \frac{1}{2}\left([\mathscr{Q}^i_{lnm}][\tilde{\mathscr{A}}^i_{lnm}] - \frac{\partial U}{\partial \vec{r}}\right)^T W_{\mathscr{B}} \left([\mathscr{Q}^i_{lnm}][\tilde{\mathscr{A}}^i_{lnm}] - \frac{\partial U}{\partial \vec{r}}\right) \tag{7.71}
$$

where $W_{\mathscr{B}}$ is the weighting matrix, and $[\mathscr{Q}^i_{lnm}]$ is the partial of acceleration with respect to each interior spherical Bessel coefficient. Therefore, the dimension of $[\mathscr{Q}^i_{lnm}]$ is $[3\times\{l(n+1)^2+4\}]$. The components of $[\mathscr{Q}^i_{lnm}]$ are listed in Appendix E.5.4. $\partial U/\partial\vec{r}$ is the acceleration due to the source gravity field, which, in our case, is the polyhedral gravity field. The cost function is minimized with respect to the interior spherical Bessel coefficients $[\tilde{\mathscr{A}}^i_{lnm}]$ to yield the normal equation

$$[\tilde{\mathscr{A}}^i_{lnm}] = \left([\mathscr{Q}^i_{lnm}]^T W_{\mathscr{B}}[\mathscr{Q}^i_{lnm}]\right)^{-1}\left\{[\mathscr{Q}^i_{lnm}]^T W_{\mathscr{B}}\left(\frac{\partial U}{\partial\vec{r}}\right)\right\} \tag{7.72}$$

The variance-covariance matrix is accumulated with a square-root information algorithm [72] because it ensures that we can invert this matrix even if the number of the estimated parameters is large, or there is only small sensitivity to the data. Small sensitivity is usually observed for the higher-degree, higher-order, and higher-power interior spherical Bessel coefficients. As a baseline, the square-root information algorithm is encouraged when $l \geq 5$.

In Equation 7.72, the acceleration at each data point gives three components. That is, the number of the data points N_{Data} has to satisfy the condition $3N_{Data} \geq l(n+1)^2+4$ in order to construct a full rank system. We can also use Equation 7.72 to estimate the normalized interior spherical Bessel coefficients by substituting the normalized components for $[\tilde{\mathscr{A}}^i_{lnm}]$ and $[\mathscr{Q}^i_{lnm}]$.

Table 7.10 shows the parameters of the interior spherical Bessel gravity field estimation:

Table 7.10: Parameters of the polyhedral - interior spherical Bessel gravity field conversion.

Case	Degree (n)	Power (l)	Data Type
1	5	2	Acceleration
2	5	5	Acceleration
3	10	2	Acceleration
4	10	5	Acceleration
5	15	2	Acceleration
6	15	5	Acceleration

In Table 7.10, only the acceleration is used as data because the preliminary analysis showed that the estimated interior spherical Bessel gravity field is more accurate when fit to the acceleration

than to the potential. For all cases, we scatter the data points in evenly spaced $[30 \times 30 \times 10]$ grids in the order of latitude, longitude, and radial distance, outward from the surface of the body to the boundary of the exterior Brillouin sphere. That is, the data points reside outside the body, within the exterior Brillouin sphere. The ratio of the size of the data sphere to that of the exterior Brillouin sphere is 0.999.

7.12.2.2 General Performance of the Fitted Interior Spherical Bessel Gravity Field around Bennu

Figure 7.19 and 7.20 show the surface potential/acceleration errors between the polyhedral and estimated (least-squares fit) interior spherical Bessel gravity fields for Bennu. In general, the potential is better estimated than the acceleration. Also, a higher-degree gravity field produces smaller errors. However, inspection of Table 7.11 indicates that there exists an optimal power l for the least-squares solution, and a large l does not necessarily produce smaller errors. For Bennu, the performance of the least-squares fit is comparable to the analytical conversion method.

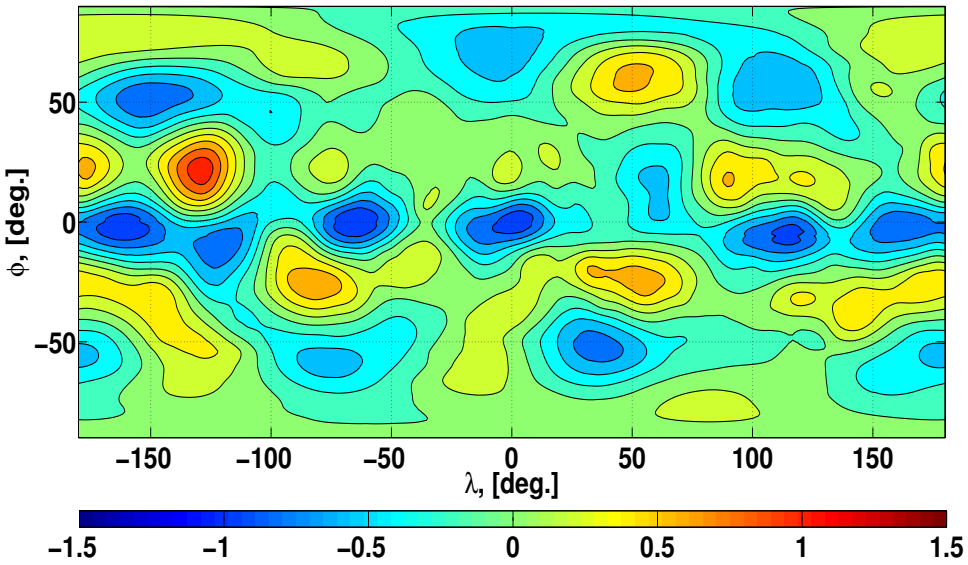

(a) Surface potential error for case 1 ($n = 5$, $l = 2$)

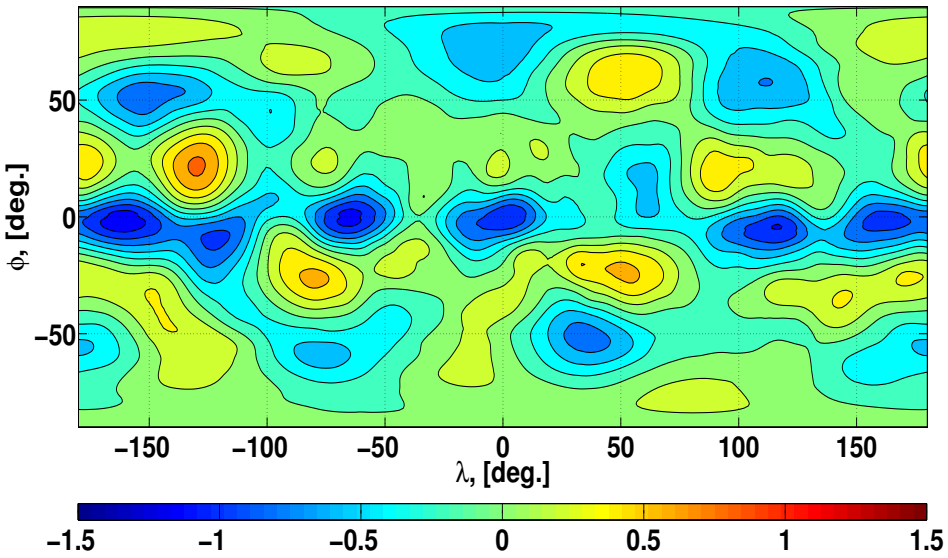

(b) Surface potential error for case 2 ($n = 5$, $l = 5$)

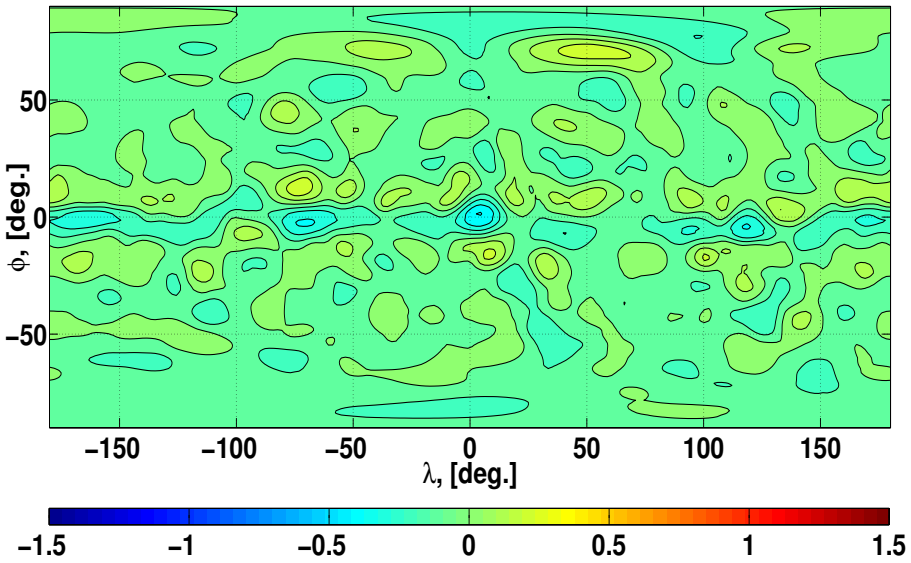

(c) Surface potential error for case 3 ($n = 10$, $l = 2$)

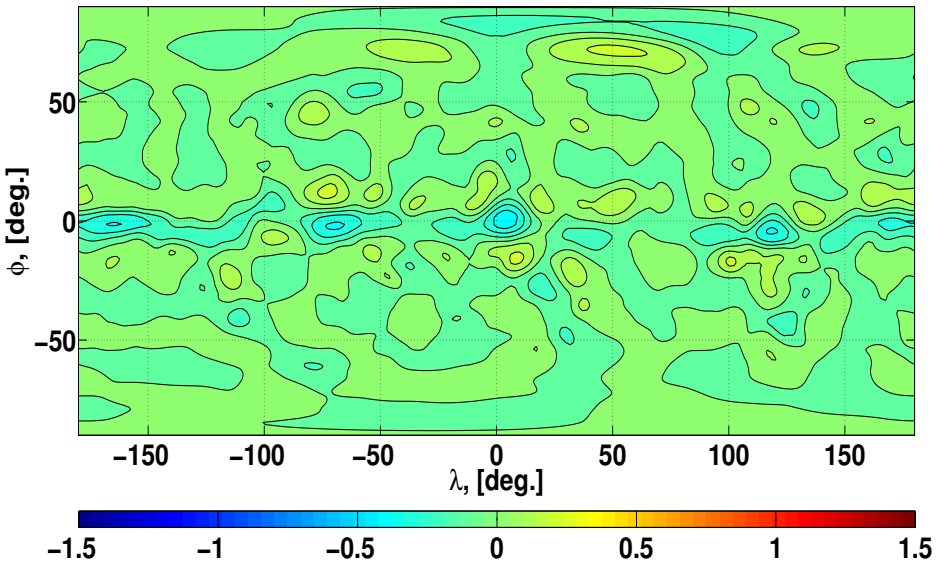

(d) Surface potential error for case 4 ($n = 10$, $l = 5$)

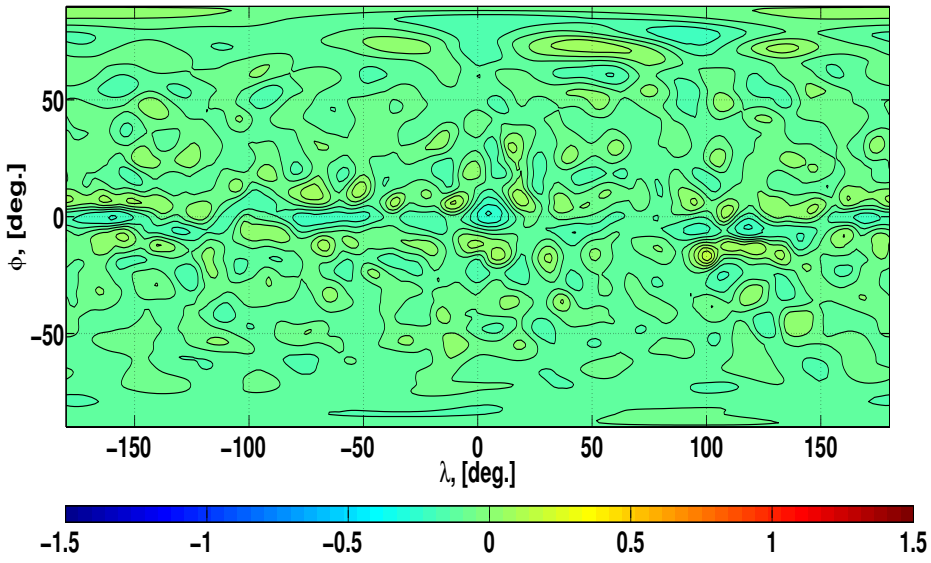

(e) Surface potential error for case 5 ($n = 15$, $l = 2$)

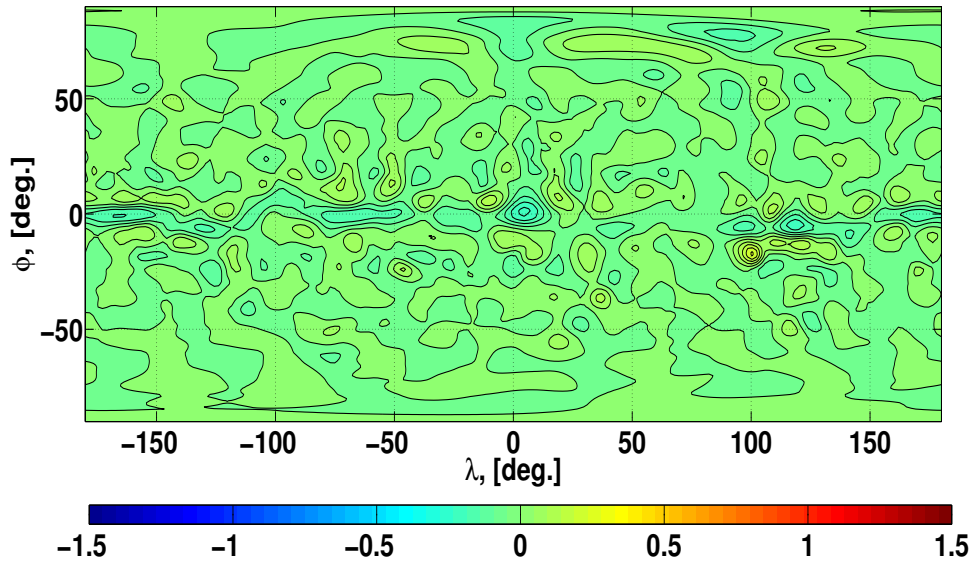

(f) Surface potential error for case 6 ($n = 15$, $l = 5$)

Figure 7.19: Surface potential error ([%]) between the polyhedral gravity field and estimated (least-squares fit) interior spherical Bessel gravity field: case 1 through case 6 for Bennu.

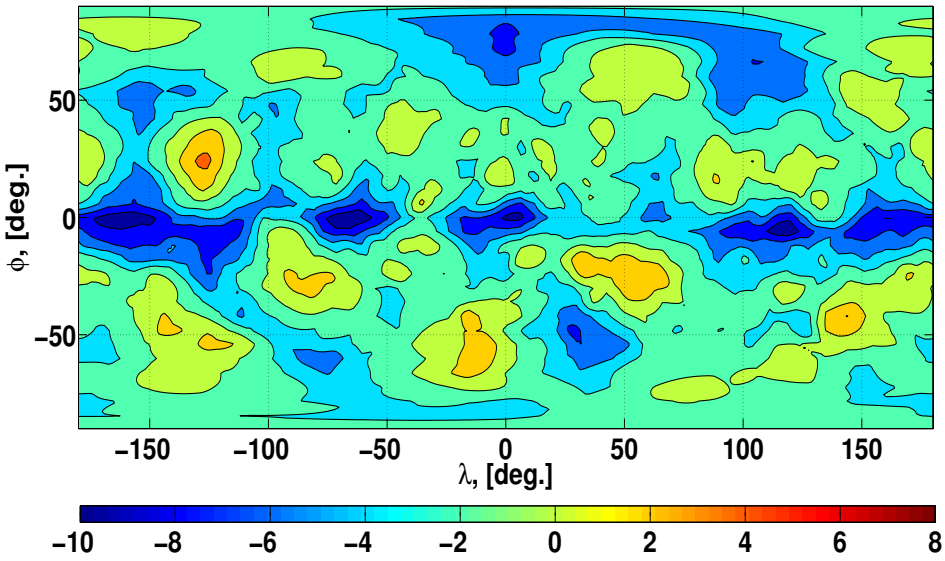

(a) Surface acceleration error for case 1 ($n = 5$, $l = 2$)

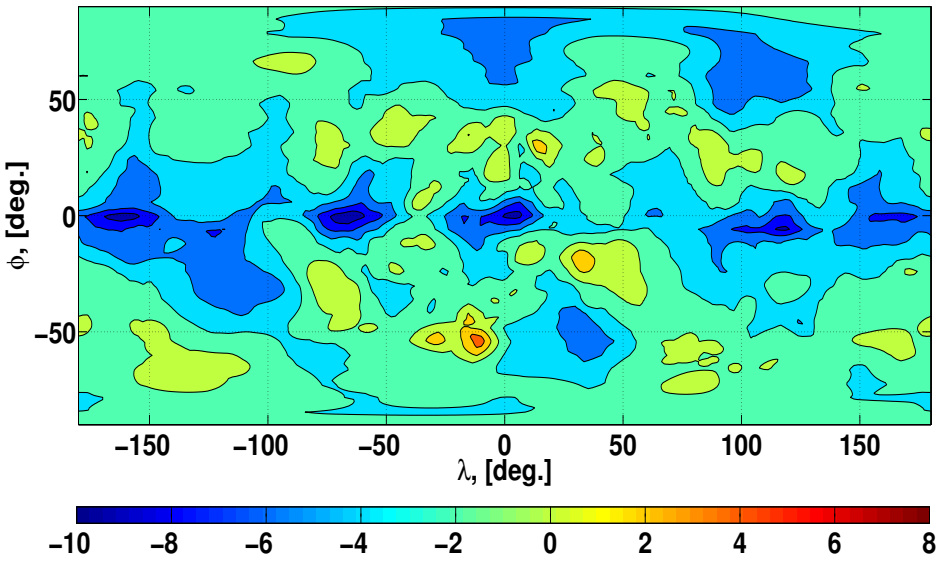

(b) Surface acceleration error for case 2 ($n = 5$, $l = 5$)

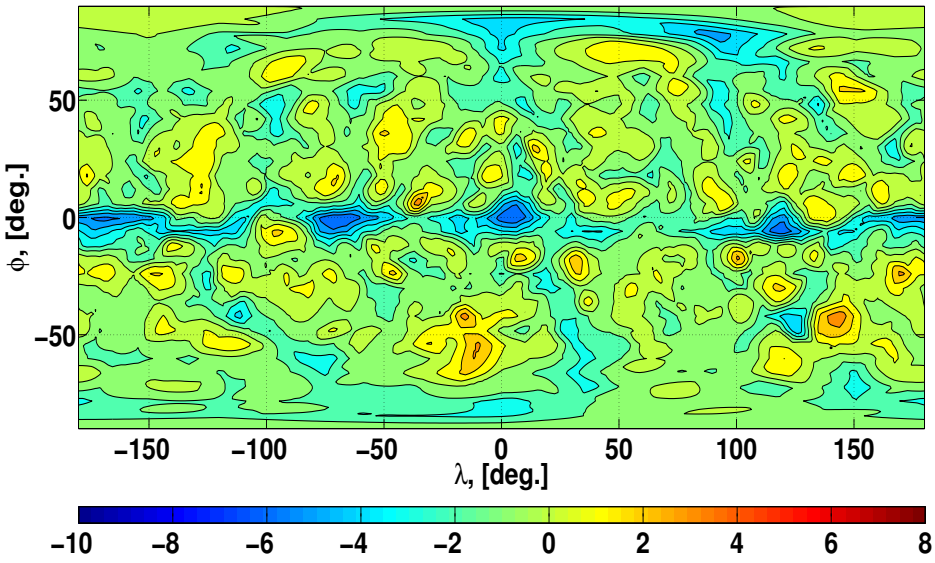

(c) Surface acceleration error for case 3 ($n = 10$, $l = 2$)

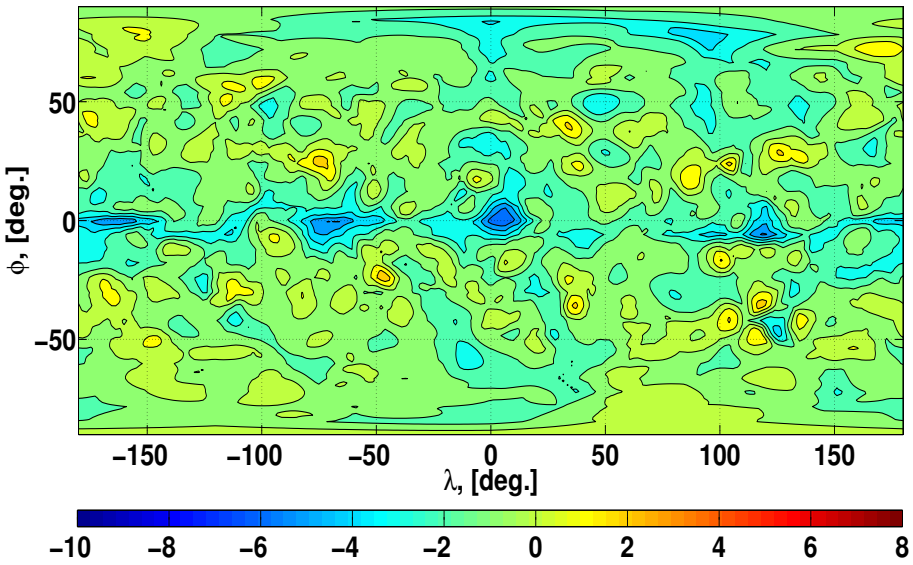

(d) Surface acceleration error for case 4 ($n = 10$, $l = 5$)

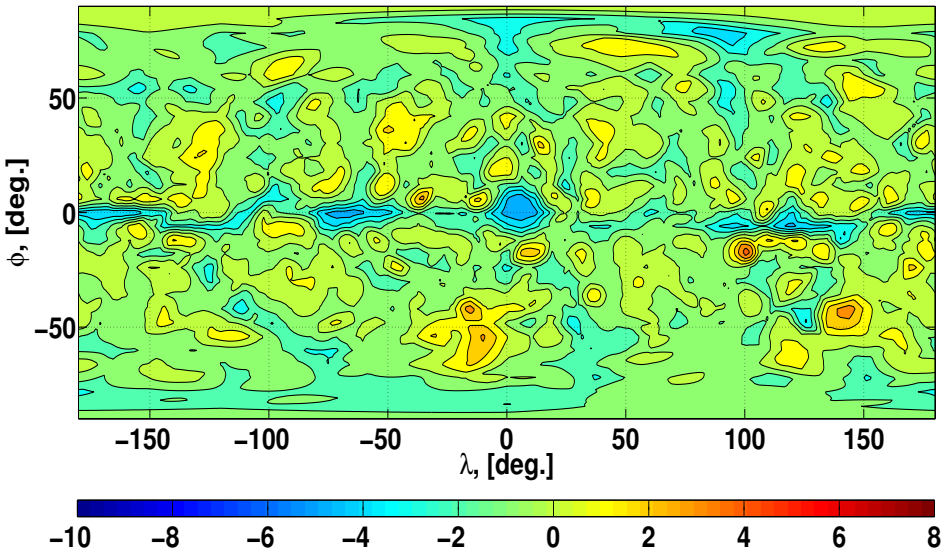

(e) Surface acceleration error for case 5 ($n = 15$, $l = 2$)

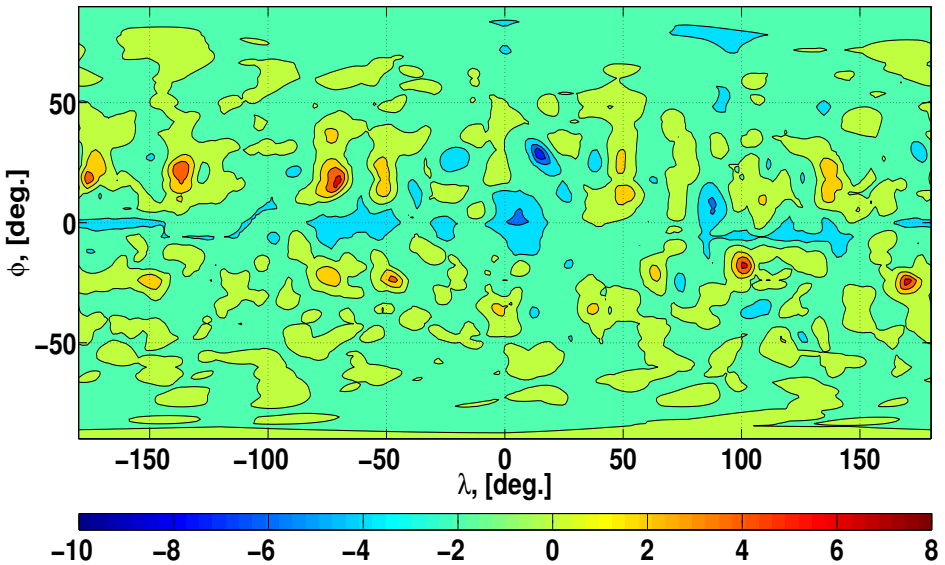

(f) Surface acceleration error for case 6 ($n = 15$, $l = 5$)

Figure 7.20: Surface acceleration error ([%]) between the polyhedral gravity field and estimated (least-squares fit) interior spherical Bessel gravity field: case 1 through case 6 for Bennu.

Table 7.11: Statistics of the surface potential/acceleration errors ([%]) between the polyhedral gravity field and estimated (least-squares fit) interior spherical Bessel gravity field: case 1 through case 6 for Bennu.

Degree (n)	Power (l)	Maximum	Minimum	Mean	Standard Deviation
Potential					
5	2	1.12686	−0.976124	−0.0203532	0.303438
5	5	0.838613	−1.14662	−0.0523238	0.295245
10	2	0.278297	−0.407028	−0.0268360	0.0714052
10	5	0.240126	−0.375800	6.68248×10^{-4}	0.0637953
15	2	0.192670	−0.258007	−0.0541950	0.0400404
15	5	0.260357	−0.219223	-5.08978×10^{-5}	0.0330392
Acceleration					
5	2	4.15387	−9.68197	−1.57927	2.04220
5	5	5.01853	−9.30806	−1.83312	1.62047
10	2	3.77595	−5.98568	−0.490040	1.13909
10	5	2.77834	−5.88321	−0.705962	0.906725
15	2	4.47100	−4.89808	−0.335766	0.948939
15	5	6.75528	−7.44448	−0.352836	0.958916

7.12.2.3 General Performance of the Fitted Interior Spherical Bessel Gravity Field around Castalia

Figure 7.21 and 7.22 show the surface potential/acceleration errors between the polyhedral and estimated (least-squares fit) interior spherical Bessel gravity fields for Castalia. Notice the large variations in the accuracies of the solutions between each case. This phenomenon is attributed the highly non-spherical shape of Castalia. Its irregular shape necessitates accurate estimation of the higher-degree, higher-order, and higher-power coefficients, whose information resides in the close proximity to the surface, or rather, the concave neck region closest to the origin. As with Bennu, it is evident that there exists an optimal interior spherical Bessel gravity field. Thus, we will search for such a solution in the next section.

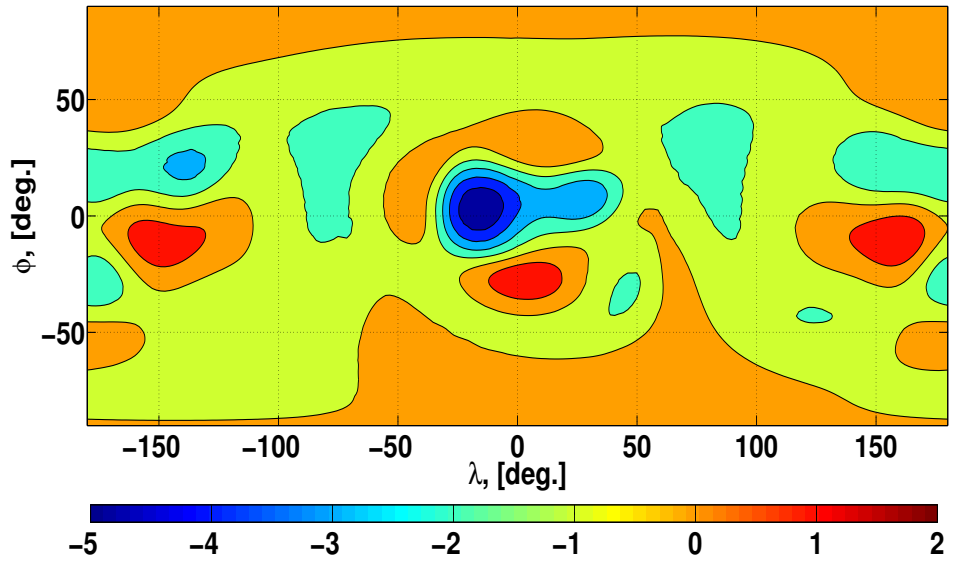

(a) Surface potential error for case 1 ($n = 5$, $l = 2$)

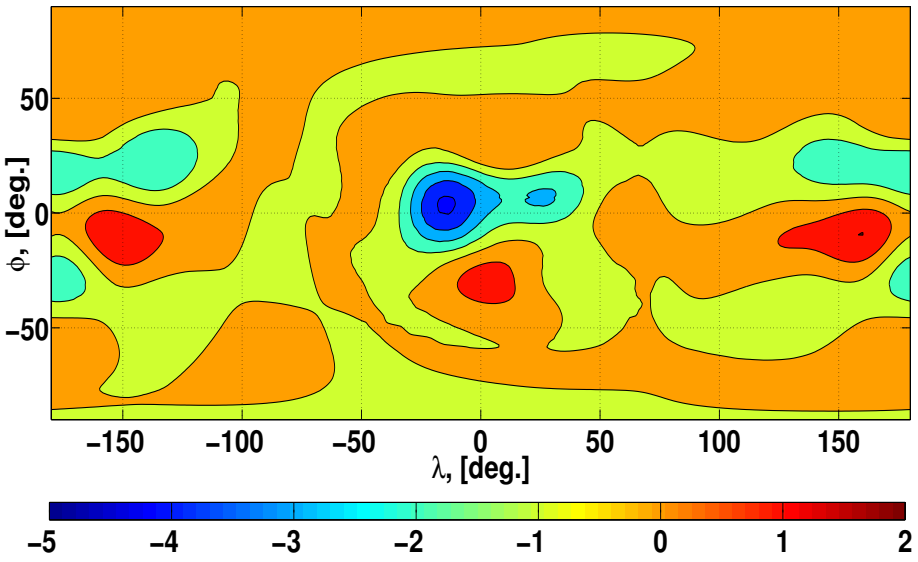

(b) Surface potential error for case 2 ($n = 5$, $l = 5$)

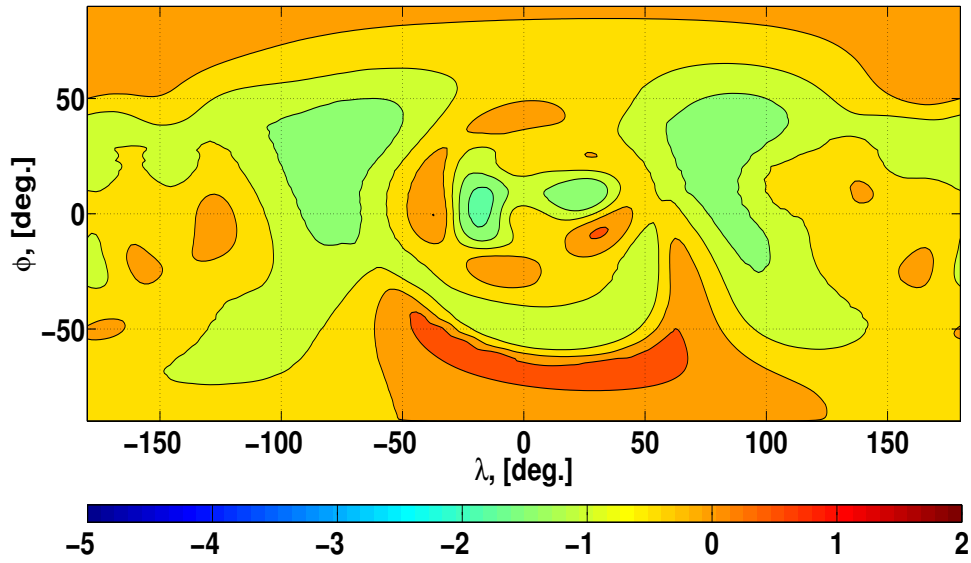

(c) Surface potential error for case 3 ($n = 10$, $l = 2$)

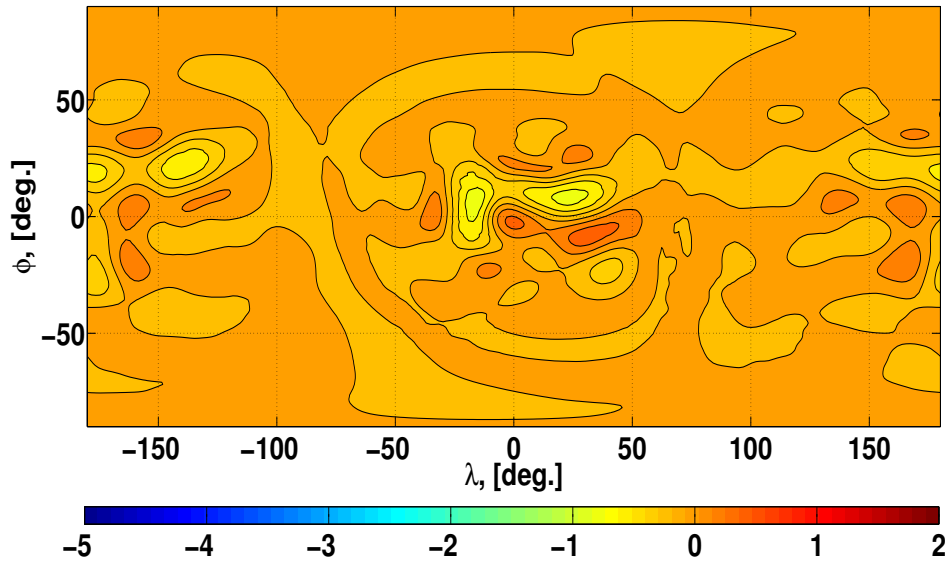

(d) Surface potential error for case 4 ($n = 10$, $l = 5$)

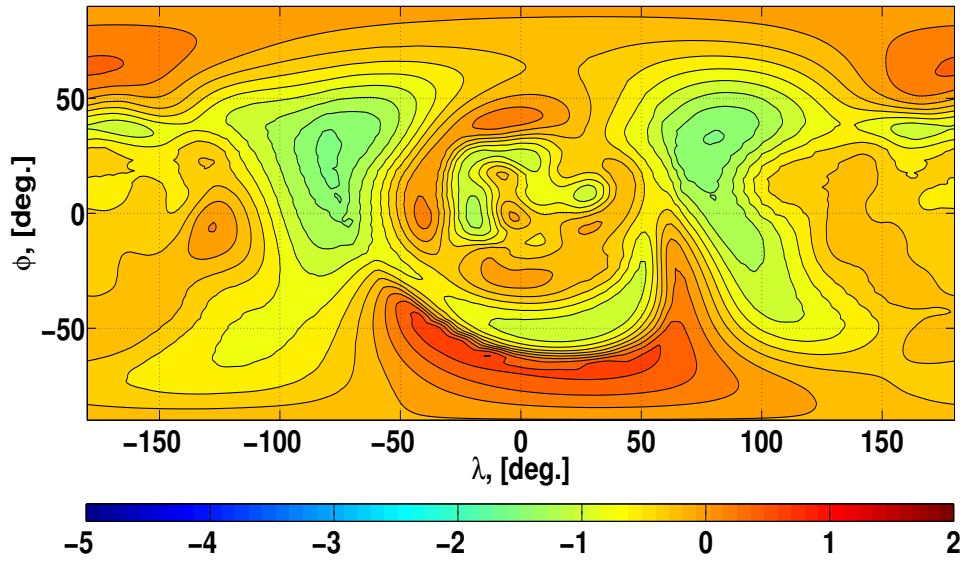

(e) Surface potential error for case 5 ($n = 15$, $l = 2$)

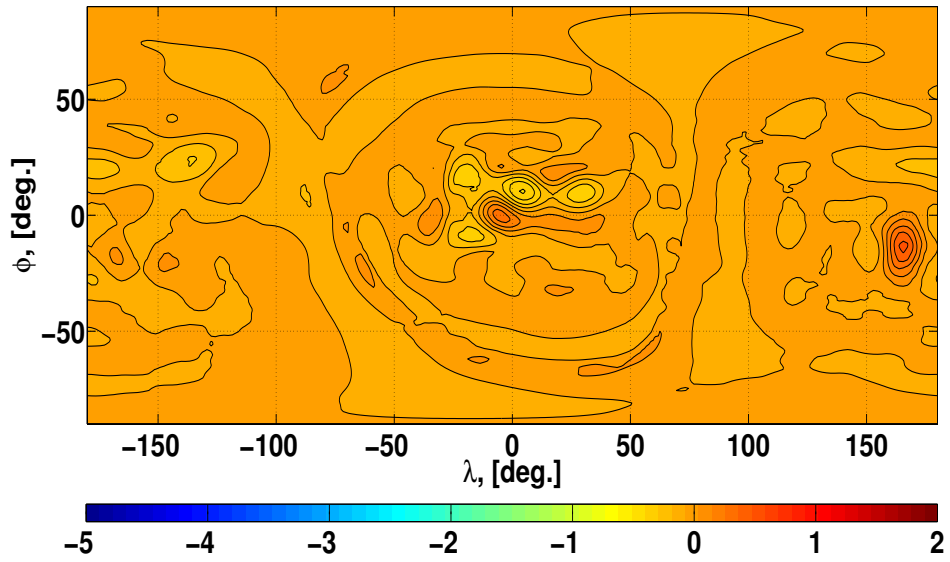

(f) Surface potential error for case 6 ($n = 15$, $l = 5$)

Figure 7.21: Surface potential error ([%]) between the polyhedral gravity field and estimated (least-squares fit) interior spherical Bessel gravity field: case 1 through case 6 for Castalia.

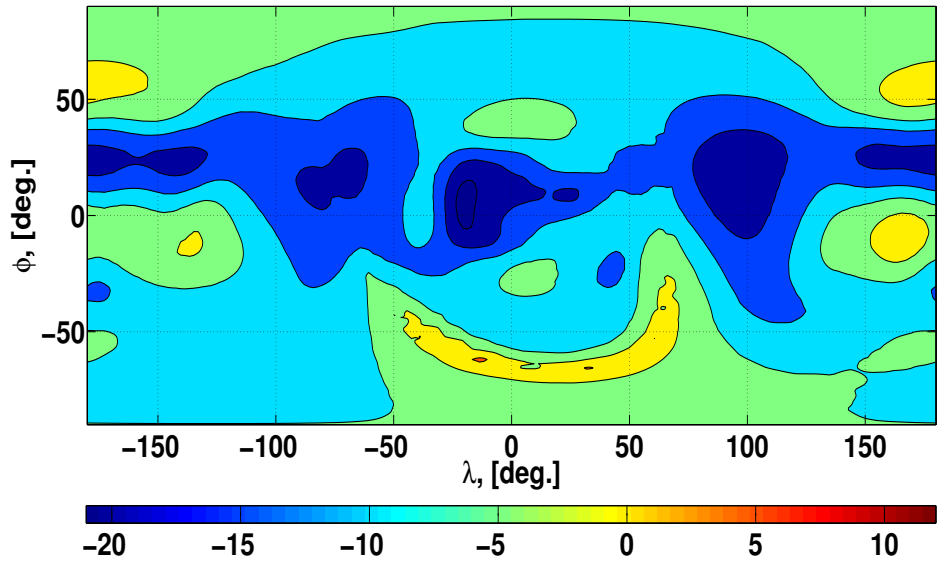

(a) Surface acceleration error for case 1 ($n = 5$, $l = 2$)

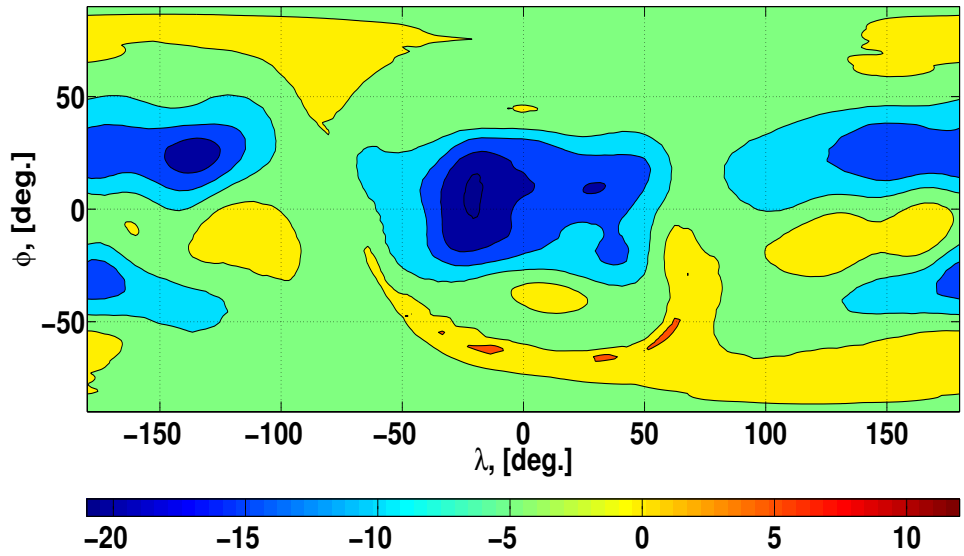

(b) Surface acceleration error for case 2 ($n = 5$, $l = 5$)

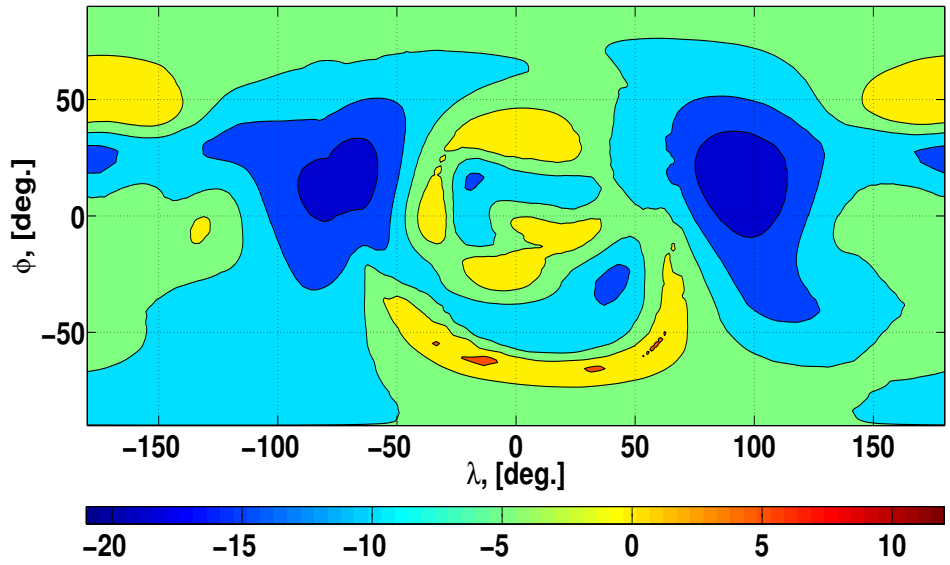

(c) Surface acceleration error for case 3 ($n = 10$, $l = 2$)

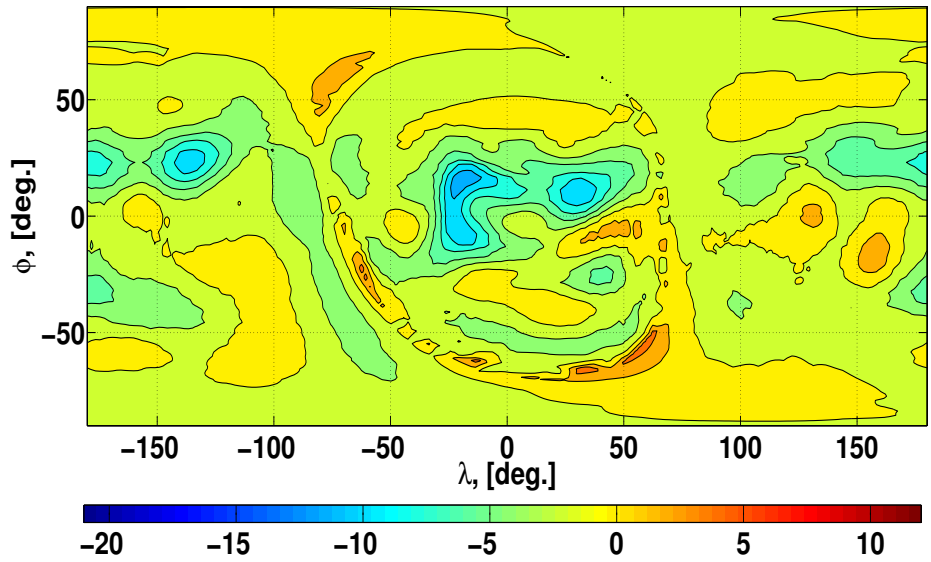

(d) Surface acceleration error for case 4 ($n = 10$, $l = 5$)

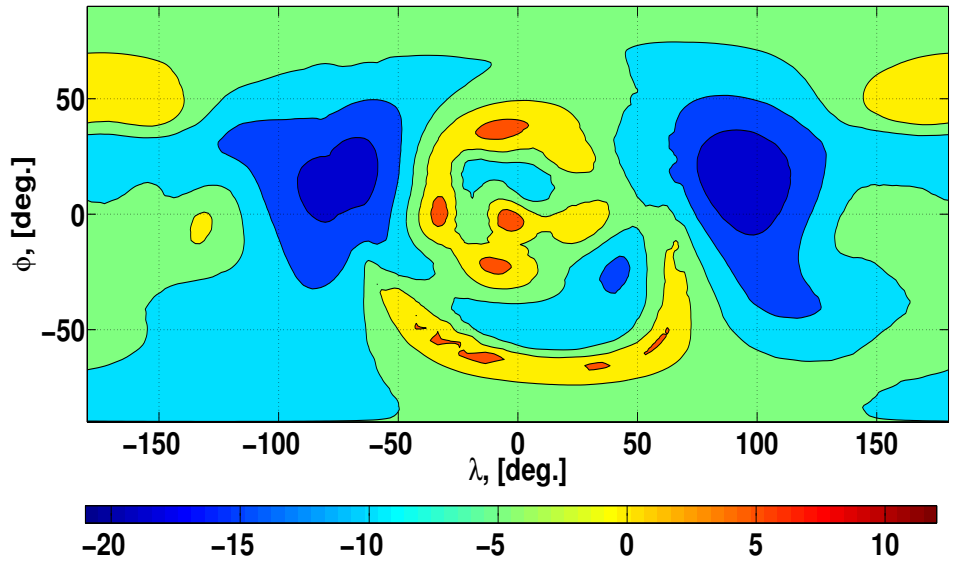

(e) Surface acceleration error for case 5 ($n = 15$, $l = 2$)

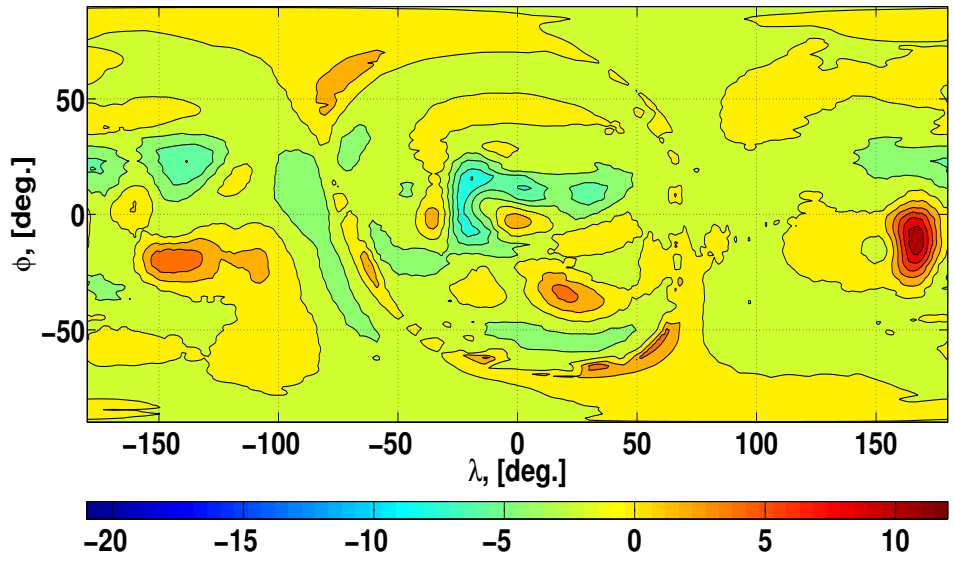

(f) Surface acceleration error for case 6 ($n = 15$, $l = 5$)

Figure 7.22: Surface acceleration error ([%]) between the polyhedral gravity field and estimated (least-squares fit) interior spherical Bessel gravity field: case 1 through case 6 for Castalia.

Table 7.12: Statistics of the surface potential/acceleration errors ([%]) between the polyhedral gravity field and estimated (least-squares fit) interior spherical Bessel gravity field: case 1 through case 6 for Castalia.

Degree (n)	Power (l)	Maximum	Minimum	Mean	Standard Deviation
Potential					
5	2	1.86773	−4.84572	−0.295941	0.747621
5	5	2.00176	−4.17350	−0.0664875	0.596186
10	2	0.776255	−1.74959	−0.317971	0.430355
10	5	0.5.28400	−0.738369	5.55394×10^{-3}	0.106925
15	2	0.814651	−1.51113	−0.314963	0.415563
15	5	0.525769	−0.410197	4.96216×10^{-3}	0.0499295
Acceleration					
5	2	6.72306	−20.9619	−7.16324	4.33379
5	5	9.03643	−20.5132	−3.20296	4.47056
10	2	8.69943	−18.6340	−5.50982	4.30593
10	5	5.98371	−11.5945	−0.902768	1.82682
15	2	9.63535	−18.7409	−5.17161	4.48272
15	5	11.5996	−8.06015	−0.327993	1.46124

7.12.3 Optimal Interior Spherical Bessel Gravity Field via Least-squares Fit

Now that the general performance of the interior spherical Bessel gravity field is discussed, it is of interest to search for an optimal interior spherical Bessel gravity field. We search for such a gravity field iteratively for a particular set of degree, power, source data, and combination of subsets. Our algorithm works as follows. First we estimate the interior spherical Bessel gravity fields from only one source data type for a given degree and power. The source data type is either potential (1) or acceleration (2). The source gravity field is the polyhedral gravity field with a homogeneous density. These solutions are referred to as the direct solutions. Then, after all direct solutions are obtained, these solutions are combined to check whether the combined solutions yield better accuracy than the direct ones. Note that the solutions from the same source data are not combined. The combined solutions are formulated either degree-wise or power-wise. The degree-wise combination yields an interior spherical Bessel gravity field assigning certain degree gravity fields from one solution and the rest from another, both for the full power. The power-wise

combination yields an interior spherical Bessel gravity field assigning certain power gravity fields from one solution and the rest from another, both for the full degree. The search space of the parameters is shown in Table 7.13:

Table 7.13: Search space for the optimal interior spherical Bessel gravity field. The source data is denoted by 1 for potential and 2 for acceleration.

Degree (n)	Power (l)	Source Data	Combination Type
5, 8, 10	2, 5	1, 2	Degree-wise
12, 15, 18, 20	8, 10	$1 \rightarrow 2$, $2 \rightarrow 1$	Power-wise

The parameter space in Table 7.13 yields 28 direct solutions and 9660 combined solutions. For each solution, the potential, acceleration, and acceleration gradient errors (angle between the accelerations given by the polyhedral and estimated interior spherical Bessel gravity fields) are computed on the surface of the body in $[20 \times 20]$ grid in latitude and longitude. Then, the maximum, minimum, mean, and standard deviation of the potential/acceleration/acceleration gradient errors are computed for each solution.

7.12.3.1 Performance of the Optimally Fitted Interior Spherical Bessel Gravity Field around Bennu

We present the performance of the optimal interior spherical Bessel gravity field for Bennu. When the parameter space is explored, the minimum value of the absolute value (i.e., $min(abs(value))$) is output for each solution type, which yields the following table.

Table 7.14: Search results for the optimal interior spherical Bessel gravity field for Bennu.

Solution Type	Maximum	Minimum	Mean	Standard Deviation
Potential Errors (%)				
1	1.19384e-01	2.43402e-01	1.00365e-02	5.18963e-02
2	2.89987e-02	7.96367e-02	1.68716e-03	2.16761e-02
$1 \rightarrow 2$, Degree-wise	8.64134e-02	8.80883e-02	2.02419e-05	3.28350e-02
$1 \rightarrow 2$, Power-wise	8.91628e-02	7.96367e-02	5.28855e-04	2.16761e-02
$2 \rightarrow 1$, Degree-wise	1.39828e-01	1.94247e-01	7.63359e-04	5.89729e-02
$2 \rightarrow 1$, Power-wise	1.45387e-01	2.74382e-01	5.60008e-03	5.76799e-02
Acceleration Errors (%)				
1	1.94184e+00	6.58638e+00	1.58734e-02	1.33255e+00
2	2.31592e+00	2.42479e+00	1.97550e-01	7.97654e-01
$1 \rightarrow 2$, Degree-wise	7.48083e-02	6.06490e-01	9.50240e-03	9.30130e-01
$1 \rightarrow 2$, Power-wise	2.31592e+00	3.59089e+00	2.21346e-02	8.72401e-01
$2 \rightarrow 1$, Degree-wise	1.94414e+00	3.36187e-02	1.52033e-04	1.01990e+00
$2 \rightarrow 1$, Power-wise	7.69208e+00	1.14874e+01	3.07032e-01	3.05316e+00
Acceleration Gradient Errors (deg.)				
1	2.07197e+00	8.72756e-03	5.18788e-01	3.58804e-01
2	1.02556e+00	7.22915e-03	2.46312e-01	1.83237e-01
$1 \rightarrow 2$, Degree-wise	1.02696e+00	1.03248e-03	2.88262e-01	1.84794e-01
$1 \rightarrow 2$, Power-wise	1.02556e+00	7.22918e-03	2.46312e-01	1.88764e-01
$2 \rightarrow 1$, Degree-wise	1.85724e+00	2.26463e-03	5.26049e-01	3.22479e-01
$2 \rightarrow 1$, Power-wise	2.35684e+00	6.72147e-03	6.01131e-01	4.15580e-01

Table 7.14 gives one a pointer to the optimal interior spherical Bessel gravity field. Each value corresponds to different solution type and degree/power of the interior spherical Bessel gravity field. The degree and power are omitted to avoid the clutter. Of all four error types shown in Table 7.14, the maximum and minimum values do not constitute reliable criteria as these values come from one particular data point on the surface. In fact, the corresponding solutions tend to have large errors for other data points as well. On the contrary, the mean is representative of all data points, but large errors in opposite signs can average out. We observed many such cases as well. Thus, we select the solution with the smallest standard deviation in order to find a solution that yields consistently small errors. Specifically, we choose the solution with the minimum standard deviation

in the acceleration errors, as the preliminary analysis (Section 7.12.2) showed that the acceleration is harder to fit than the potential. The optimal solution for Bennu is given by the $20 \times 20 \times 2$ (degree, order, power) interior spherical Bessel gravity field obtained directly from the acceleration data. Figure 7.23 shows the surface potential/acceleration errors between the polyhedral gravity field and optimal interior spherical Bessel gravity field for Bennu.

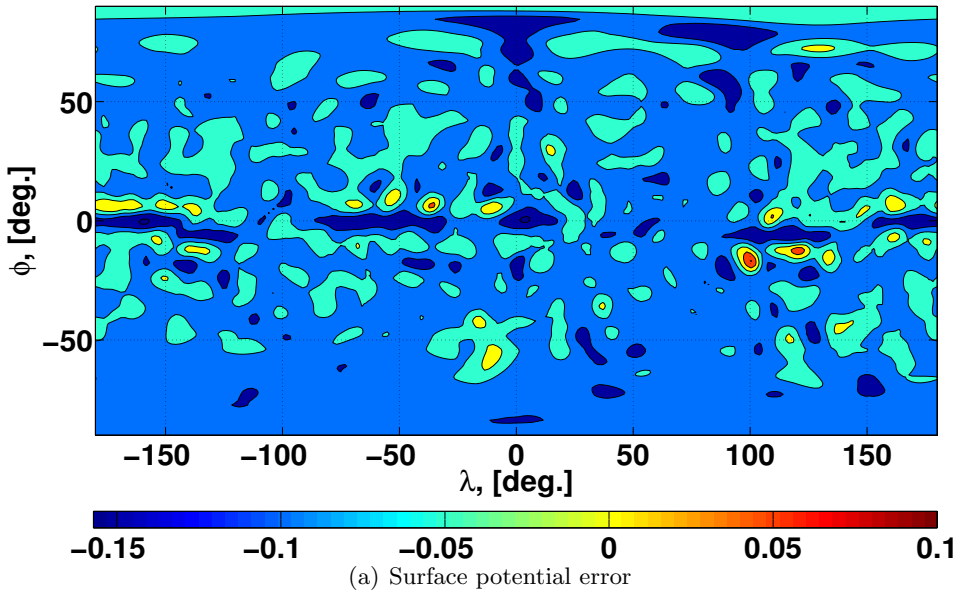

(a) Surface potential error

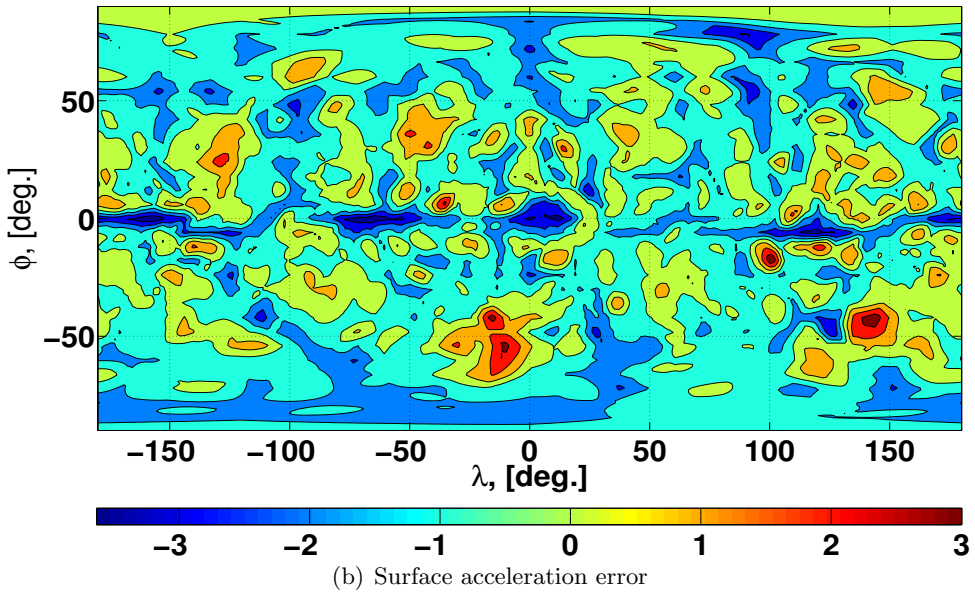

(b) Surface acceleration error

Figure 7.23: Surface potential/acceleration errors ([%]) between the polyhedral gravity field and optimal interior spherical Bessel gravity field for Bennu.

The magnitude of the resulting maximum/minimum surface errors is not much different from those generated by the analytically converted interior spherical Bessel gravity field (Section 7.12.1.1). Thus, for a body as spherical as Bennu, the analytical conversion method works sufficiently well.

Figure 7.24 shows the cross-sectional distribution of the potential/acceleration errors between the polyhedral gravity field and the combination of the exterior and optimal interior spherical Bessel gravity fields, produced in a similar manner to Figure 7.6 through 7.11. The errors are computed with respect to the exterior gravity field outside the exterior Brillouin sphere and with respect to the optimal interior gravity field inside it. Each column is a cross-section and rows are potential/acceleration. As shown, both the potential and acceleration are modeled accurately.

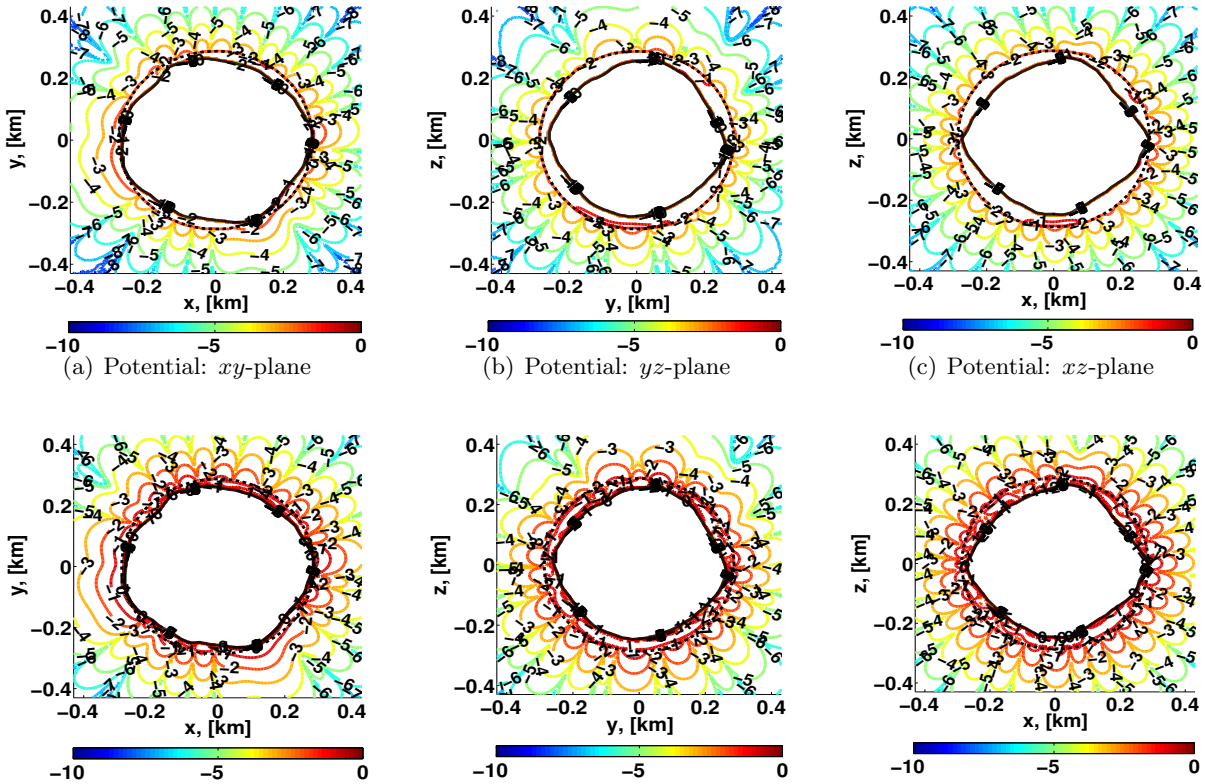

(a) Potential: xy-plane (b) Potential: yz-plane (c) Potential: xz-plane

(d) Acceleration: xy-plane (e) Acceleration: yz-plane (f) Acceleration: xz-plane

Figure 7.24: Cross-sectional distribution of potential/acceleration errors ([$\log 10(\%)$]) between the polyhedral gravity field and optimal interior spherical Bessel gravity field for Bennu.

7.12.3.2 Performance of the Optimally Fitted Interior Spherical Bessel Gravity Field around Castalia

We explore the same parameter space in Table 7.13 in order to find the optimal interior spherical Bessel gravity field for Castalia. Table 7.15 is obtained when we compute the poten-

tial/acceleration/acceleration gradient errors in [20 × 20] grid in latitude and longitude on the surface of the body.

Table 7.15: Search results for the optimal interior spherical Bessel gravity field for Castalia.

Solution Type	Maximum	Minimum	Mean	Standard Deviation
Potential Errors (%)				
1	2.68023e-01	4.63081e-01	1.90473e-03	1.12030e-01
2	1.87689e-01	1.26295e-01	2.59914e-03	3.02350e-02
1 → 2, Degree-wise	2.53351e-01	4.85438e-01	4.90898e-04	1.20796e-01
1 → 2, Power-wise	1.87689e-01	1.26295e-01	2.61616e-04	3.02350e-02
2 → 1, Degree-wise	3.01624e-01	3.57605e-01	4.73147e-04	8.02895e-02
2 → 1, Power-wise	4.37317e-01	4.63081e-01	1.90473e-03	1.12030e-01
Acceleration Errors (%)				
1	7.25948e-01	1.06465e+01	3.45349e-01	2.74251e+00
2	2.81395e+00	5.04134e+00	1.70893e-01	1.17291e+00
1 → 2, Degree-wise	1.78024e-02	5.85643e-01	4.88040e-03	2.73543e+00
1 → 2, Power-wise	2.81395e+00	5.04134e+00	2.51816e-02	1.17291e+00
2 → 1, Degree-wise	3.05756e+00	2.80896e+00	3.86657e-02	1.43766e+00
2 → 1, Power-wise	4.20644e+00	5.55305e+00	2.86288e-01	2.74251e+00
Acceleration Gradient Errors (deg.)				
1	4.08312e+00	6.08356e-03	5.43863e-01	5.64596e-01
2	1.39947e+00	1.84591e-03	2.03320e-01	2.45588e-01
1 → 2, Degree-wise	3.30978e+00	1.58088e-03	5.91717e-01	5.55263e-01
1 → 2, Power-wise	1.39947e+00	1.84591e-03	2.03320e-01	2.45588e-01
2 → 1, Degree-wise	2.46718e+00	8.14447e-03	4.89220e-01	4.32567e-01
2 → 1, Power-wise	4.06904e+00	6.08356e-03	5.43863e-01	5.64596e-01

The optimal solution is given by the $18 \times 18 \times 5$ interior spherical Bessel gravity field obtained by the direct solution from the acceleration data or by the power-wise combination of the potential/acceleration data (0-2nd power from the potential data and 3-5th power from the acceleration data). For convenience, we use the direct acceleration solution to generate the error plots. Figure 7.25 shows the surface potential/acceleration errors between the polyhedral gravity field and optimal interior spherical Bessel gravity field for Castalia.

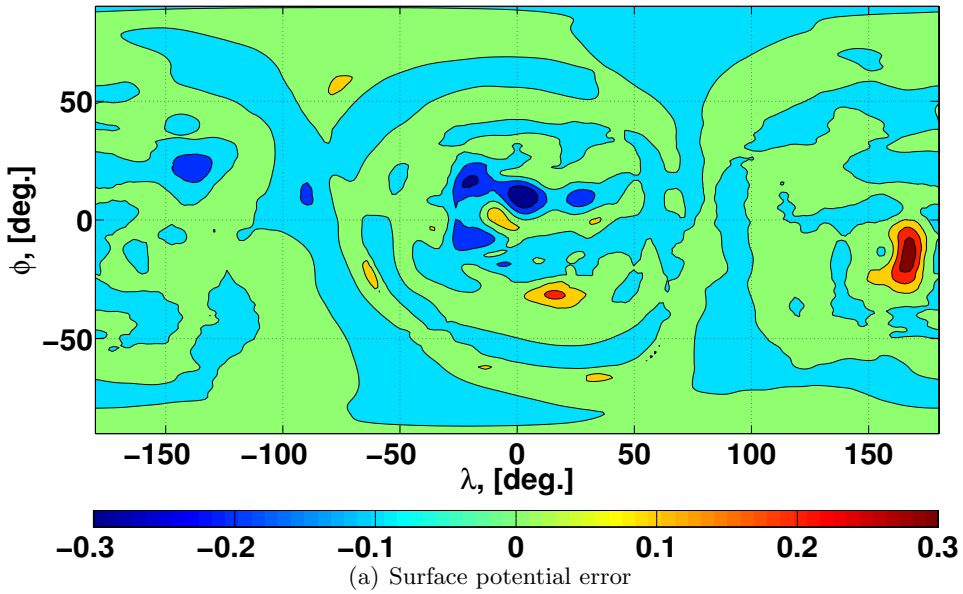

(a) Surface potential error

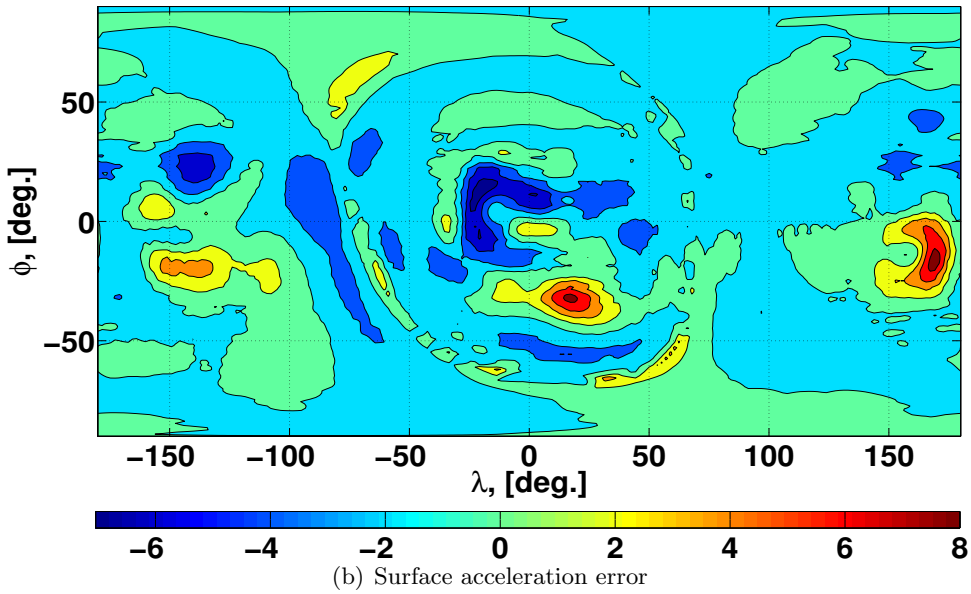

(b) Surface acceleration error

Figure 7.25: Surface potential/acceleration errors ([%]) between the polyhedral gravity field and optimal interior spherical Bessel gravity field for Castalia.

Notice the significant reduction in surface potential/acceleration errors from the exterior gravity field or analytically converted interior spherical Bessel gravity field. Often the potential and acceleration errors are several tens of percent or even larger than 100% for the exterior gravity field. However, the potential error is reduced to less than 1%, and the acceleration error is less

than 8% for the optimal interior spherical Bessel potential. The same order of accuracy cannot be achieved by the analytical conversion method. It is important to note that the largest errors are contained in small regions on the surface, and we do not see widespread, large error distribution shown in the analytically converted solutions (Figure 7.17 and 7.18). This result shows the inherent powerfulness of the interior spherical Bessel gravity field.

It is worthwhile to note that the errors of the optimal solutions are on the same order for both Bennu and Castalia, showing no clear evidence of modeling difficulty for both spheroidal and highly non-spherical bodies. Figure 7.26 shows the cross-sectional distribution of the potential/acceleration errors between the polyhedral gravity field and combination of the exterior and optimal interior spherical Bessel gravity fields for Castalia. As with Bennu, the surface gravity field is well modeled with the optimal interior spherical Bessel gravity field.

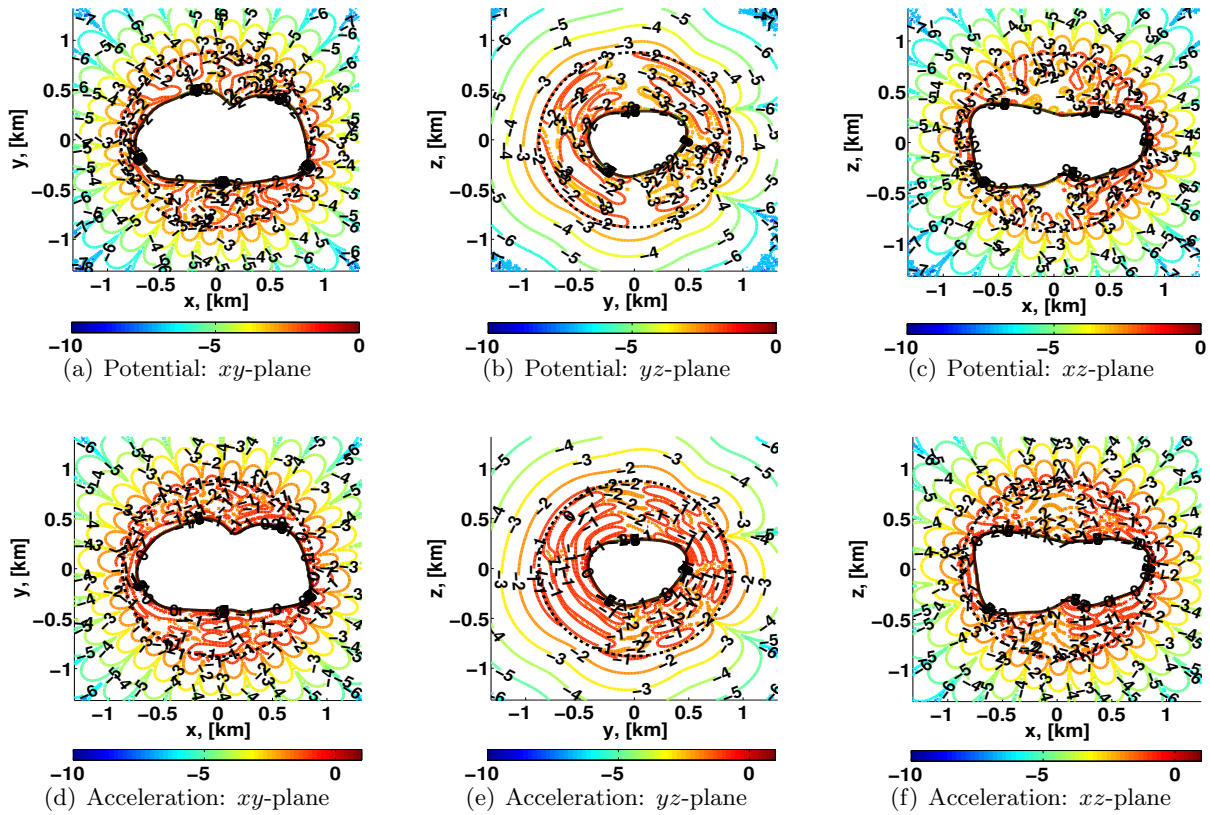

(a) Potential: xy-plane (b) Potential: yz-plane (c) Potential: xz-plane

(d) Acceleration: xy-plane (e) Acceleration: yz-plane (f) Acceleration: xz-plane

Figure 7.26: Cross-sectional distribution of potential/acceleration errors ([$\log 10(\%)$]) between the polyhedral gravity field and optimal interior spherical Bessel gravity field for Castalia.

7.13 Discussions and Recommendations

We have evaluated the gravity field environment near the surface of Bennu and Castalia using the exterior spherical harmonic gravity field, interior spherical harmonic gravity field, and interior spherical Bessel gravity field. One body is nearly spherical and the other a two-lobe configuration, representing extremes of the shapes that exist for small bodies. The three types of gravity field expansions are compared against the polyhedral gravity field model constructed from a homogeneous body.

The exterior gravity field performs with moderate accuracy around Bennu yielding a few percent error in potential and $< 10\%$ error in acceleration for a 4×4 expansion on the surface. It is shown that the higher-degree and higher-order terms further reduce the surface gravity errors. However, the accuracy of the exterior gravity field rapidly deteriorates as the body deviates farther and farther from a spherical shape. For Castalia, the potential and acceleration errors exceed well over 100% even for a 10×10 expansion. As the exterior gravity field does not converge within the exterior Brillouin sphere and there is no guarantee that it approximates the surface gravity field well for other nearly spherical body than Bennu, the exterior gravity field should never be used to model the gravitation near the surface of the body.

The interior gravity field performs well, on the order of a few percent acceleration error, to map out the regional space of the surface gravity field for both Bennu and Castalia. One drawback is that the total mapping requires considerable amount of time to optimize the solution. However, this does not pose a problem when designing a trajectory/navigating a spacecraft for a particular TAG point on the surface. Although much more higher-degree and higher-order terms are generally needed for the interior gravity field than the exterior gravity field and adds to the computation time, the benefit of improved accuracy is tremendous. In fact, the interior gravity field is the most computationally efficient method to characterize the surface gravity field.

The interior spherical Bessel gravity field is obtained either by matching the boundary conditions with the exterior gravity field or by fitting to the potential/acceleration data given from the

polyhedral/interior gravity fields. As the interior gravity field fitting requires the total mapping, we only performed the polyhedral gravity field fitting in this analysis. The general performance of the analytically converted solutions and the fitted solutions are presented, and the optimally fitted solutions are also given. The results show that the analytical conversion method and the fitting algorithm perform similarly for Bennu, yielding $< 0.3\%$ potential error and $< 5\%$ acceleration error. Both methods are slightly less accurate than the interior gravity field. The analytical conversion method for Castalia yields $< 5\%$ potential error and $< 20\%$ acceleration error. This is a significant improvement from the exterior gravity field for which $> 100\%$ potential/acceleration errors are not uncommon.

It is worthwhile to note that the analytical conversion method does not require rigorous tuning of the degree/power of the interior spherical Bessel gravity field. As a baseline, 5th-power gravity field produces moderate accuracy for any degree n. The fitted solution yields $< 0.5\%$ potential errors and $< 8\%$ acceleration errors on the surface of Castalia, with majority of the large errors concentrated in small regions scattered around the body. Comparison of Figure 7.18 and Figure 7.26 reveals that the regions with large errors are scattered in small patches when the least-squares fit is performed, while the analytical conversion method distributes large errors on a large scale. Thus, if the surface gravity field is available (e.g., the density distribution is known for the polyhedral gravity field), the least-squares fit yields accurate interior spherical Bessel gravity field. For both the analytical conversion method and the least-squares fit solution, one advantage of the interior spherical Bessel gravity field is that its convergence is guaranteed anywhere inside the exterior Brillouin sphere, and the total mapping is attained from its formulation. In addition, its computation time is much faster than the polyhedral gravity field. Thus, the interior spherical Bessel gravity field can be a useful tool, for example, when analyzing the gravity anomaly for scientific purposes.

The overall performance of the exterior, interior, and interior spherical Bessel gravity fields show that the interior gravity field is most suitable for regional mapping purposes and the interior spherical Bessel gravity field for total mapping purposes. One caveat here is that both gravity fields

do not perform well when the source gravity field is not determined with sufficient accuracy, which heavily depends on the accuracy of the OD solution that varies from one body to another. Thus, a case by case analysis is needed to evaluate which method performs with desired accuracy. If only the lower-degree exterior spherical harmonic coefficients ($n < 10$) are obtained, it is recommended that the analytically converted interior spherical Bessel gravity field be used as it is likely that the fitted interior gravity field is not accurate enough for either regional mapping or total mapping.

7.14 Conclusions

In this chapter, we investigated Poisson's equation in the form of Helmholtz's equation to seek a solution to the null space of the exterior/interior gravity fields. The outcome is that there exist two solutions that are mirror images of each other, just as the exterior and interior gravity fields are the mirror images of each other, that are named the interior/exterior spherical Bessel gravity fields. These gravity fields are derived from similar sets of spherical harmonic coefficients with the basis function expressed via the spherical Bessel function. The interior spherical Bessel gravity field complements the solution space of the exterior gravity field, and the exterior spherical Bessel gravity field complements the solution space of the interior gravity field.

We have discussed the analytical conversion method between the exterior gravity field and interior spherical Bessel gravity field by matching the boundary conditions. In addition, we estimated the interior spherical Bessel coefficients via least-squares fit to the polyhedral gravity field. Comparisons are made among four types of gravity field solutions: exterior gravity field, interior gravity field, interior spherical Bessel gravity field converted from the exterior gravity field, and that estimated via least-squares fit to the polyhedral gravity field. All errors are computed with respect to the polyhedral gravity field of homogeneous density.

The results show that the exterior gravity field performs with $< 20\%$ acceleration error on the surface of Bennu, but as the body takes on more concavity, the errors grow exponentially ($> 100\%$ for Castalia). The interior gravity fields were constructed for three landing sites for Bennu and Castalia and yielded $< 5\%$ acceleration errors around the TAG points. The analytically

converted interior spherical Bessel gravity field performed with $< 10\%$ acceleration error for Bennu and $< 30\%$ error for Castalia. The optimally fitted interior spherical Bessel gravity field yielded the acceleration errors on the order of $< 5\%$ for Bennu and $< 10\%$ for Castalia.

Recommendations are given based on the performance of the gravity fields analyzed in this chapter. It is concluded that the interior gravity field is most suitable for regional mapping purposes. The interior gravity field enables a safe trajectory design around a TAG point, although it is necessary to have sufficiently accurate source gravity field. If the OD solution yields only the lower-degree exterior gravity field, it is recommended to perform the total mapping via analytical conversion of the interior spherical Bessel gravity field, irrespective of the body's shape.

Chapter 8

Conclusions and Future Work

In this thesis, we investigated new techniques to characterize the gravity field environment around small bodies. The estimation of the gravity field is the key to designing a successful mission both in terms of the safety of the spacecraft and the quality of data. The estimated gravity field serves as an indicator to the interior structure of the body, which motivates a more robust and reliable technique for its estimation process. Furthermore, in light of growing numbers in sample return missions, more robust and accurate techniques for surface gravity field characterization are needed. We specifically proposed three techniques in order to outperform the exterior spherical harmonic gravity field conventionally used for gravity field characterization: reconstruction of the surface gravity field from the estimated density distribution, interior spherical harmonic gravity field, and interior spherical Bessel gravity field.

In Chapter 2, an analytical orbit determination technique called the ΔV ranging was studied. This method breaks the scale invariance associated with the optical-only measurements and allows the estimation of the position and velocity of the spacecraft by executing a maneuver during a flyby. The optical-only measurements do not contain the range information to the asteroid, and such a disadvantage can be overcome by the accurate measurement of the ΔV maneuver. It was shown that the flyby geometry (b_∞ and V_∞) are better computed for a large ΔV with a small uncertainty. In addition to the ΔV ranging, we derived two analytical expressions of the gravitational parameter, namely $\mu_\perp$ and $\mu_\parallel$. The conventional method of $\mu_\perp$ computes the gravitational parameter by measuring the change in velocity through the Doppler measurement,

while $\mu_{\|}$ utilizes the optical measurements. It was found that both formulations yield comparable accuracies, and the uncertainties of the gravitational parameter given by the two formulations can be used as a good a priori value.

In Chapter 3, numerical covariance analysis was performed around three small bodies: Itokawa, Didymos, and Eros in the order of increasing size. This numerical covariance analysis was carried out to assess whether the initial orbit phase could be eliminated altogether and replaced by multiple flybys. Such a flyby sequence can be more easily implemented than the orbit, and rigorous orbit stability analysis is unnecessary. Our analysis showed that the lower-degree gravity field coefficients can be determined to approximately 10% uncertainty in two weeks, realizing rapid characterization of the gravity field that can be sufficient for some mission profiles.

In Chapter 4, we estimated the spin state of a near-Earth asteroid 4179 Toutatis by processing the delay-Doppler radar images collected between 1992-2008. The converged solution was then propagated forward in time to predict Toutatis' orientation during the December 2012 apparition. The obtained images showed that the predicted spin state matched the actual orientation of Toutatis within the formal uncertainty of 20°-30° for each of 3-1-3 Euler angles. The estimated solution indicated that the center-of-mass-center-of-figure offset and the off-diagonal terms of the inertia tensor are indistinguishable from zero. The diagonal terms of the moments of inertia ratios (I_{xx}/I_{zz} and I_{yy}/I_{zz}) are determined to less than a few percent, which is the best density distribution constraint of any near-Earth asteroid.

In Chapter 5, we investigated how the internal density distribution can be estimated from the gravity field measurement. We first compared the spherical harmonic coefficients between various density maps and the homogeneous body. It was shown that all density maps exhibit different signatures, and the deviation of the spherical harmonic coefficients can be used to constrain the density map by making an archive of these characteristics. It is particularly interesting to note that the core detection is trivial. In order to prove core's existence, one only needs to show that the difference of the spherical harmonic coefficients between the homogeneous body and the core model is dictated by the scaling factor that is invariable for all degree and order.

We also proposed and analyzed the performance of the generalized density estimation approach, namely the block estimation. The block estimation is motivated by the mascon model, which models the body with a number of spheres/cubes. Instead of spheres/cubes, the block estimation divides the body into a number of blocks to estimate the density value of each block. As each block consists of slivers that are radially partitioned within each tetrahedron, there is no gap between each block and the shape of the body can be modeled with no error. Furthermore, the number of blocks can be controlled with ease so that the estimated density distribution is unique in a least-squares sense (i.e., the number of observations is larger than that of the blocks). We applied this method to estimate the density of Castalia whose hypothetical true density distribution is the planar division. That is, one lobe of the body has a different density value than the other. It was shown that the accuracy of the estimated density distribution increased as more blocks are used to construct the body. In addition, the reconstructed surface gravity field yielded $< 10\%$ acceleration errors. Such an accuracy is never achievable with the conventional spherical harmonic gravity field, for which $> 100\%$ acceleration errors are ubiquitous on the surface of the body as shown in Chapter 7. This block estimation is a useful technique to map out the surface gravity field around small bodies for proximity operation purposes.

In Chapter 6, we derived and investigated the performance of the interior gravity field in order to map the regional space of the surface gravity field. The study of the interior gravity field was carried out in contrast to the widely known exterior gravity field. The exterior gravity field only converges outside the exterior Brillouin sphere that is identical to the circumscribing sphere of the body, and the surface gravity field cannot be mapped by this model. On the other hand, the interior gravity field converges within the interior Brillouin sphere that is different from the exterior Brillouin sphere. As the interior Brillouin sphere must be placed outside the body, the convergence of the interior gravity field is guaranteed up to a point on the surface and only allows regional mapping of the surface gravity field. We introduced a method to approximate the interior spherical harmonic coefficients for a homogeneous body and discussed how the exterior gravity field can be converted into the interior gravity field. Then, we compared the accuracy of the landing

trajectories for Castalia. The true trajectory was computed for a homogeneous body using the polyhedral gravity field, and the interior gravity field was estimated from a 15×15 exterior gravity field. The resulting trajectory errors are < 10 $[m]$ after one hour of propagation time in a hyperbolic orbit. Thus, it was confirmed that the interior gravity field maps the regional space of the surface gravity field with sufficient accuracy.

In Chapter 7, we derived and investigated the performance of the interior spherical Bessel gravity field. Although this gravity field model is not widely known, we applied the theory to realize the total mapping of the surface gravity field around small bodies. This interior spherical Bessel gravity field is one of the solutions to Poisson's equation and its convergence region lies within the exterior Brillouin sphere. Thus, the total mapping of the surface gravity field is possible with this gravity field model. This formulation displays clear contrasts with the exterior/interior gravity fields that satisfy Laplce's equation. As with the relationship between the exterior and interior spherical harmonic gravity fields, there exists the exterior spherical Bessel gravity field. These four exterior/interior spherical harmonic/spherical Bessel gravity fields are all classified as the spherical harmonic gravity fields and complement the solution space of each other. As the solution space of Laplace's equation and Poisson's equation must transition smoothly, the boundary conditions can be applied to analytically convert an exterior gravity field into an interior spherical Bessel gravity field. In addition, the interior spherical Bessel coefficients can be estimated via a least-squares fit had the surface gravity field been already available. An example is when the density distribution is estimated via the block estimation method, and the surface gravity field is reconstructed using the polyhedral gravity field.

After the derivation, we thoroughly investigated the characteristics and the performance of the interior spherical Bessel gravity field. Specifically, the accuracies of the surface gravity fields are compared between the exterior gravity field, interior gravity field, and interior spherical Bessel gravity field for Bennu and Castalia. It was shown that the exterior gravity field quickly diverges within the exterior Brillouin sphere and should never be used to model the surface gravity field of small bodies. The interior gravity field performs the regional mapping accurately. However, its

accuracy is dependent on the source gravity field, and severely concave regions of the body may not be modeled with sufficient accuracy. Thus, a case-by-case analysis is required for the interior gravity field. The analytically converted interior spherical Bessel gravity field performed with remarkable improvement from the exterior gravity field, decreasing the surface acceleration errors from $> 100\%$ to $< 20\%$ for Castalia. Furthermore, the surface acceleration errors of the fitted solution yielded $< 10\%$ for Castalia and showed the inherent powerfulness of the interior spherical Bessel gravity field.

Future work is to study how the surface gravity field characterization can be generalized to different shape/density distribution of the body. It is of particularly interest to study how the regional mapping via the interior gravity field and the total mapping via the interior spherical Bessel gravity field can be generalized to a heterogeneous body. In addition, it is very intriguing to analyze the accuracies of the landing trajectories (i.e., error ellipse around the landing site) using the techniques described in this thesis. The theories discussed in this thesis can be further studied to make useful applications for the binary/ternary asteroids.

Bibliography

[1] Matt Abrahamson, Alessandro Ardito, Dongsuk Han, Robert Haw, Brian Kennedy, Nicholas Mastrodemos, Sumita Nandi, Ryan Park, Brian Rush, and Andrew Vaughan. Dawn orbit determination team: Trajectory modeling and reconstruction processes at vesta. AAS/AIAA Space Flight Mechanics Meeting, Kauai, pages 13–479, 2013.

[2] Milton Abramowitz and Irene A. Stegun, editors. Handbook of Mathematical Functions with Formulas, Graphs, and Mathematical Tables, chapter 9, 10. U.S. Department of Commerce and Knovel Library (online), 10 edition, 1972.

[3] A. J. Allen, P. L. Palmer, and J. Papaloizou. A conservative numerical technique for collisionless dynamical systems: Comparision of the radial and circular orbit instabilities. Mon. Not. Royal Astronomical Society, 242:576 – 594, 1992.

[4] George Arfken. Mathematical Methods for Physicists, chapter 9, 11, 12. Academic Press, Inc., 3rd edition, 1985.

[5] Nitin Arora and Ryan P. Russell. High-fidelty geopotential interpolation: Application to the grace ggm03c gravity model. AAS/AIAA Space Flight Mechanics Meeting, (13-321), 2013.

[6] Sami Asmar, Alex Konopoliv, Ryan Park, and Carol Raymond. Recovering the gravity field of vesta from dawn. AAS/AIAA Space Flight Mechanics Meeting, Kauai, (13-348), 2013.

[7] Julie Bellerose, James Chartres, Thomas Jones, Pascal Lee, Frank Marchis, and Keaton Burns. Missions operations at near-earth asteroids. 34th Annual AAS Guidance and Control Conference, (11-052), 2011.

[8] Gregory Beylkin and Robert Cramer. Toward multiresolution estimation and efficient representation of gravitational fields. Celestial Mechanics and Dynamical Astronomy, 84:87–104, 2002.

[9] Shyam Bhaskaran and Brian Kennedy. Terminal guidance navigation for an asteroid impactor spacecraft. AAS/AIAA Space Flight Mechanics Meeting, Kauai, (13-413), 2013.

[10] Marcel Brillouin. Equations aux dériveées partielles du 2e ordre. domaines à connexion multiple. fonctions sphériques non antipodes. Annales De L'Institut H. Poincaré, 4(2):173–206, 1933.

[11] Stephen B. Broschart. Close Proximity Spacecraft Maneuvers Near Irregularly Shaped Small-bodies: Hovering, Translation, and Descent. PhD thesis, The University of Michigan, 2006.

[12] Michael W. Busch, Shrinivas R. Kulkarni, Walter Brisken, Steven J. Ostro, Lance A. M. Benner, Jon D. Giorgini, and Michael C. Nolan. Determining asteroid spin states using radar speckles. Icarus, 209:535 – 541, 2009.

[13] L. Alberto Cangahuala. Augmentations to the polyhedral gravity model to facilitate small body navigation. American Astronomical Society, (05-4185), 2005.

[14] L. Alberto Cangahuala, Stephen B. Broschart, Behcet Acikmese, Milan Mandic, Lars Blackmore, Ed Riedel, David Bayard, and Mark Wallace. Gnc trades for touch-and-go sampling at small bodies. 34th Annual AAS Guidance and Control Conference, (11-057), 2011.

[15] Leland E. Cunningham. On the computation of the spherical harmonic terms needed during the numerical integration of the orbital motion of an artificial satellite. Celestial Mechanics, 2:207–216, 1970.

[16] J.M.A. Danby. Fundamentals of Celestial Mechanics, volume Chapter 6.7. Willman-Bell, Inc., 2nd edition, 1962.

[17] Romain Garmier, Jean-Pierre Barriot, Alexander S. Konopliv, and Donald K. Yeomans. Modeling of the eros gravity field as an ellipsoidal harmonic expansion from the near doppler tracking data. Geophysical Research Letters, 29(8), 2002.

[18] Karl-Heinz Glassmeier, Hermann Boehnhardt, Detlef Koschny, Ekkehard Kührt, and Ingo Richter. The rosetta mission: Flying towards the origin of the solar system. Space Science Reviews, 128:1 – 21, 2007.

[19] Peter Gottlieb. Estimation of local lunar gravity features. Radio Science, 5(2):301–312, 1970.

[20] J. Ray Hanna and John H. Rowland. Fourier Series, Transforms, and Boundary Value Problems, chapter 1, 2, 5, 6. A Wiley-Interscience Publication, 2nd edition, 1990.

[21] E. Herrera-Sucarrat, P.L. Palmer, and R.M. Roberts. Modeling the gravitational potential of a nonspherical asteroid. Journal of Guidance Control and Dynamics, 36(3):790 – 798, 2013.

[22] M. Hotine. Mathematical Geodesy, ESSA Monograph 2, chapter 21. Environmental Science Services Administration, U.S. Department of Commerce, 1969.

[23] R. S. Hudson, Steven J. Ostro, and D. J. Scheeres. High-resolution model of asteroid 4179 toutatis. Icarus, 161:346–355, 2003.

[24] R. Scott Hudson and Steven J. Ostro. Shape of asteroid 4769 castalia (1989 pb) from inversion of radar images. Science, 263:940–943, 1994.

[25] R. Scott Hudson and Steven J. Ostro. Shape and non-principal axis spin state of asteroid 4179 toutatis. Science, 270:84–86, 1995.

[26] R. Scott Hudson and Steven J. Ostro. Photometric properties of asteroid 4179 toutatis from lightcurves and a radar-derived physical model. Icarus, 135:451–457, 1998.

[27] Brandon A. Jones. Efficient Models for the Evaluation and Estimation of the Gravity Field. PhD thesis, The University of Colorado at Boulder, 2010.

[28] Brandon A. Jones, George H. Born, and Gregory Beylkin. A cubed sphere gravity model for fast orbit propagation. American Astronomical Society, (09-137), 2009.

[29] Rudolf Kalman. Discovery and invention: The newtonian revolution in systems technology. Journal of Guidance Control and Dynamics, 26(6), 2003.

[30] William M. Kaula. Theory of Satellite Geodesy, chapter 1. Blaisdell Publishing Company, Waltham, Massachusetts, 1966.

[31] Brian Kennedy, Matt Abrahamson, Alessandro Ardito, Dongsuk Han, Robert Haw, Nicholas Mastrodemos, Sumita Nandi, Ryan Park, Brian Rush, and Andrew Vaughan. Dawn orbit determination team: Trajectory and gravity prediction performance during vesta science phases. AAS/AIAA Space Flight Mechanics Meeting, Kauai, pages 13–345, 2013.

[32] Brian Kennedy, Matt Abrahamson, Alessandro Ardito, Robert Haw, Nicholas Mastrodemos, Sumita Nandi, Ryan Park, Brian Rush, and Andrew Vaughan. Dawn orbit determination team: Modeling and fitting of optical data at vesta. AAS/AIAA Space Flight Mechanics Meeting, Kauai, pages 13–347, 2013.

[33] Alexander S. Konopliv, James K. Miller, William M. Owen, Donald K. Yeomans, Jon D. Giorgini, Romain Garmier, and Jean-Pierre Barriot. A global solution for the gravity field, rotation, landmarks, and ephemeris of eros. Icarus, 160(2):289 – 299, 2002.

[34] Hongyu Liu and Jun Zou. Zeros of the bessel and spherical bessel functions and their applications for uniqueness in inverse acoustic obstacle scattering. Journal of Applied Mathematics, (72):817 – 831, 2007.

[35] J. B. Lundberg and B. E. Schutz. Recursion formulas of Legendre functions for use with nonsingular geopotential models. Journal of Guidance Control Dynamics, 11:31–38, February 1988.

[36] T. M. MacRobert. Spherical Harmonics: An Elementary Treatise on Harmonic Functions with Applications, chapter 2, 4, 6, 8, 14. Dover Publications, Inc., second edition, 1948.

[37] J. L. Margot, M. C. Nolan, L. A. M. Benner, S. J. Ostro ad R. F. Jurgens, J. D. Giorgini, M. A. Slade, and D. B. Campbell. Binary asteroids in the near-earth object population. Science, 296:1445 – 1448, 2002.

[38] J. K. Miller, A. S. Konopliv, P. G. Antreasian, J. J. Bordi, S. Chesley, C. E. Helfrich, W. M. Owen, T. C. Wang, B. G. Williams, D. K. Yeomans, and D. J. Scheeres. Determination of shape, gravity, and rotational state of asteroid 433 eros. Icarus, 155(1):3 – 17, 2002.

[39] Oliver Montenbruck and Eberhard Gill. Satellite Orbits: Models, Methods and Applications. Springer, 3 edition, September 2005.

[40] Isaac Newton. Philosophiae naturalis principia mathematica, trans. A. Motte (rev. F. Cajori)(Berkeley), 1962.

[41] M.C. Nolan, C. Magri, E.S. Howell, L. A. M. Benner, J. D. Giorgini, C.W. Hergenrother, R.S. Hudson, D.S. Lauretta, J.-L. Margot, S.J. Ostro, and D.J. Scheeres. Shape model and surface properties of the osiris-rex target asteroid (101955) bennu from radar and lightcurve observations. Icarus (Submitted), February 2013.

[42] Steven J. Ostro, John F. Chandler, Alice A. Hine, Keith D. Rosema, Irwin I. Shapiro, and Donald K. Yeomans. Radar images of asteroid 1989 pb. Science, 248:1523–1528, 1990.

[43] Steven J. Ostro and 13 colleagues. Radar images of asteroid 4179 toutatis. Science, 270:80 – 83, 1995.

[44] Steven J. Ostro, R. Scott Hudson, and 14 colleagues. Asteroid 4179 toutatis: 1996 radar observations. Icarus, 137:122–139, 1999.

[45] Steven. J. Ostro, Jean-Luc Margot, Lance A. M. Benner, Jon D. Giorgini, D. J. Scheeres, Eugene G. Fahnestock, Stephen B. Broschart, Julie Bellerose, Michael C. Nolan, Christopher Magri, Peter Pravec, Petr Scheirich, Randy Rose, Raymond F. Jurgens, Eric M. De Jong, and Shigeru Suzuki. Radar imaging of binary near-earth asteroid (66391) 1999 kw4. Science 314 (5803), 1276, 314:1276 – 1280, 2006.

[46] William M. Owen. Methods of optical navigation. AAS/AIAA Space Flight Mechanics Meeting, New Orleans, Louisiana, (11-215), February 2011.

[47] P. L. Palmer. Stability of Collisionless Stellar Systems - Mechanisms for the Dynamical Structure of Galaxies -, chapter 10, pages 181 – 190. Kluwer Academic Publishers, 1994.

[48] D. W. Parcher, M. Abrahamson, A. Ardito, D. Han, R.J. Haw, B.M. Kennedy, N. Mastrodemos, S. Nandi, R. S. Park, B.P. Rush, B.A. Smith, J.C. Smith, A.T. Vaughan, and G.J. Whiffen. Dawn maneuver design performance at vesta. AAS/AIAA Space Flight Mechanics Meeting, Kauai, (13-344), 2013.

[49] Ryan S. Park, Robert A. Werner, and Shyam Bhaskaran. Estimating small-body gravity field from shape model and navigation data. Journal of Guidance Control Dynamics, 33:212–221, 2010.

[50] Mark A. Pinsky. Introduction to Partial Differential Equations with Applications, chapter 0, 2, 3, 4. MacGraw-Hill Book Company, 1984.

[51] S. Roark, C. Cottingham, Richard Dissly, D. J. Scheeres, V. Petr, and K. Housen. Explosive surface pods for cratering experiments on small bodies. In 41st Lunar and Planetary Science Conference, The Woodlands, TX, 2010.

[52] Garmier Romain and Barriot Jean-Pierre. Ellipsoidal harmonic expansions of the gravitational potential: Theory and application. Celestial Mechanics and Dynamical Astronomy, 79:235–275, 2001.

[53] C.T. Russell, C. A. Raymond, A. Coradini, H.Y. McSween, M. T. Zuber, A. Nathues, M. C. De Sanctis, R. Jaumann, A. S. Konopliv, F. Preusker, S. W. Asmar, R. S. Park, R. Gaskell, H. U. Keller, S. Mottola, T. Roastsch, J. E. C. Scully, D. E. Smith, P. Tricarico, M. J. Toplis, U. R. Christensen, W. C. Feldman, D. J. Lawrence, T. J. McCoy, T. H. Prettyman, R. C. Reedy, M. E. Sykes, and T. N. Titus. Dawn at vesta: Testing the protoplanetary paradigm. Science, 336:684 – 686, 2012.

[54] Ryan P. Russell and Nitin Arora. Global point mascon models for simple, accurate and parallel geopotential computation. AAS/AIAA Space Flight Mechanics Meeting, (11-158), 2011.

[55] Hanspeter Schaub and John L. Junkins. Anaytical Mechanics of Space Systems. American Institute of Aeronautics and Astronautics, Inc., second edition, 2009.

[56] D. J. Scheeres. Failure modes of reduced-order orbit determination filters and their remedies. Technical report, Jet Propulsion Laboratory, 1993.

[57] D. J. Scheeres. Relative equilibria for general gravity fields in the sphere-restricted full 2-body problem. Celestial Mechanics and Dynamical Astronomy, 94:317 – 349, 2006.

[58] D. J. Scheeres, E. G. Fahnestock, S. J. Ostro, J.-L. Margot, L. A. M. Benner, S. B. Broschart, J. Bellerose, J. D. Giorgini, M. C. Nolan, C. Magri, P. Pravec, P. Scheirich, R. Rose, R. F. Jurgens, E. M. De Jong, and S. Suzuki. Dynamical configuration of binary near-earth asteroid (66391) 1999 kw4. Science, 314:1280–1283, 2006.

[59] D. J. Scheeres, R. Gaskell, S. Abe, O. Barnouin-Jha, T. Hashimoto, J. Kawaguchi, T. Kubota, J. Saito, M. Yoshikawa, N. Hirata, T. Mukai, M. Ishiguro, T. Kominato, K. Shirakawa, and M. Uo. The actual dynamical environment about itokawa. AIAA/AAS Astrodynamics Specialist Meeting, August 2006.

[60] D. J. Scheeres, B. Khushalani, and Robert A. Werner. Estimating asteroid density distributions from shape and gravity information. Planetary and Space Science, 48(10):965 – 971, 2000.

[61] Daniel Jay Scheeres, Richard Dissly, E. Nilsen, S. Roark, W. Frazier, T. Bank, D. Rosing, and E. Jordan. The binary asteroid in-situ explorer (basix) mission. In 2010 DPS meeting, Pasadena, CA, 2010. DPS 49.28L.

[62] D.J. Scheeres, S. J. Ostro, R. A. Werner, E. Asphaug, and R. S. Hudson. Effects of gravitational interactions on asteroid spin states. Icarus, 147:106 – 118, 2000.

[63] John C. Smith, Daniel W. Parcher, and Gregory J. Whiffen. Spiraling away from vesta: Design of the transfer from the low to high altitude dawn mapping orbits. AAS/AIAA Space Flight Mechanics Meeting, Kauai, pages 13–350, 2013.

[64] John R Spencer, Leonid A Akimov, Claudia Angeli, Paolo Angelini, M Antonietta Barucci, Peter Birch, Carlo Blanco, Marc W Buie, Anna Caruso, Vasilij G Chiornij, et al. The lightcurve of 4179 toutatis: Evidence for complex rotation. Icarus, 117(1):71–89, 1995.

[65] Yu Takahashi and D.J.Scheeres. Small-body postrendezvous characterization via slow hyperbolic flybys. Journal of Guidance, Control, and Dynamics, 34(6):1815 – 1827, 2011.

[66] Yu Takahashi and D. J. Scheeres. Analytical estimates of gravity field via flybys. AAS/AIAA Space Flight Mechanics Meeting, Toronto, 2010.

[67] Yu Takahashi and D. J. Scheeres. Rapid characterization of a small body via slow flybys. 20th AAS/AIAA Space Flight Mechanics Meeting, 2010.

[68] Yu Takahashi and D. J. Scheeres. Small body surface gravity field estimation from orbit determination. 34th Annual AAS Guidance and Control Conference, (11-053), 2011.

[69] Yu Takahashi and D.J. Scheeres. Surface gravity fields for asteroids and comets. 22nd AAS/AIAA Space Flight Mechanics Meeting, 2012.

[70] Yu Takahashi, D.J. Scheeres, and Robert A. Werner. Surface gravity fields for asteroids and comets. Journal of Guidance Control and Dynamics, 36(2):362 – 374, March - April 2013.

[71] Yu Takahsahi and D.J. Scheeres. Generalized density distribution estimation for small bodies. 23rd AAS/AIAA Space Flight Mechanics Meeting, (13-265), 2013.

[72] Byron D. Tapley, Bob E. Schutz, and George H. Born. Statistical Orbit Determination. Elsevier Academic Press, 2004.

[73] G.N. Watson. A Treatise on the Theory of Bessel Functions, chapter 2, 3, 15. Camridge University Press, 2nd edition, 1944.

[74] R. A. Werner. Evaluating descent and ascent trajectories near non-spherical bodies. Technical Report http://www.techbriefs.com/component/content/article/8726, Jet Propulsion Laboratory, 2010.

[75] R. A. Werner and D. J. Scheeres. Exterior gravitation of a polyhedron derived and compared with harmonic and mascon gravitation representations of asteroid 4769 castalia. Celestial Mechanics and Dynamical Astronomy, 65:314–344, 1997.

[76] Robert A. Werner. Spherical harmonic coefficients for the potential of a constant-density polyhedron. Computers and Geosciences, 23(10):1071 – 1077, 1997.

[77] Maria T. Zuber, David E. Smith, Andrew F. Cheng, James B. Garvin, Oded Aharonson, Timothy D. Cole, Peter J. Dunn, Yanping Guo, Grank G. Lemoine, Gregory A. Neumann, David Rowlands, and Mark H. Torrence. The shape of 433 eros from the near-shoemaker laser rangefinder. Science, 289:2097 – 2101, 2000.

Appendix A

Numerical Covariance Analysis

A.1 Asteroid and Orbit Parameters

Table A.1 shows the physical parameters of Itokawa, Didymos, and Eros:

Table A.1: Body parameters of Itokawa, Didymos, and Eros.

(a) Itokawa	
R^* $[km]$	0.161915
μ $[km^3/s^2]$	2.36×10^{-9}
V $[km^3]$	1.78×10^{-2}
ρ $[g/cm^3]$	1.98
T_p $[hr]$	12.132
$\lambda_{pole,lon}$ [deg.]	90.53
$\delta_{pole,dec}$ $[deg.]$	-66.30

(b) Didymos	
R^* $[km]$	0.380444
μ $[km^3/s^2]$	3.320×10^{-8}
ρ $[g/cm^3]$	2.157
T_p $[hr]$	2.2593
$\lambda_{pole,lon}$ [deg.]	329
$\delta_{pole,dec}$ [deg.]	-70

(c) Eros	
R^* $[km]$	16
μ $[km^3/s^2]$	4.46275×10^{-4}
V $[km^3]$	5293.471
ρ $[g/cm^3]$	2.67
T_p $[hr]$	5.2702
$\lambda_{pole,lon}$	11.363
$\delta_{pole,dec}$	17.232

In Table A.1, R^* is the reference radius that is used to non-dimensionalize the spherical harmonic coefficients, V is the total volume, ρ is the uniform density, T_p is the rotation period, and λ_{pole} and δ_{pole} are the right ascension and declination of the spin axis.

Table A.2: Orbital elements of Itokawa, Didymos, and Eros around the sun.

(a) Itokawa	
a $[AU]$	1.324056488316851
e $[n.d.]$	0.2801084071153689
ι $[deg.]$	1.621919453857606
Ω $[deg.]$	69.08550443441868
ω $[deg.]$	162.768624007089
$M[deg.]$	249.6404632373529

(b) Didymos	
a $[AU]$	1.644518330101378
e $[n.d.]$	0.3838262939391459
ι $[deg.]$	3.407768990565939
Ω $[deg.]$	73.24781297772449
ω $[deg.]$	319.1898847947696
M $[deg.]$	335.5803016226873

(c) Eros	
a $[AU]$	1.458104555173167
e $[n.d.]$	0.2227892846477366
ι $[deg.]$	10.82931668462072
Ω $[deg.]$	304.3716090460168
ω $[deg.]$	178.7591190760191
M $[deg.]$	303.6777989160755

A.2 Spherical Harmonic Coefficients

Table A.3 through A.5 present the unnormalized exterior spherical harmonic coefficients for Itokawa, Didymos, and Eros:

Table A.3: Unnormalized exterior spherical harmonic coefficients of Itokawa.

Order l	**Degree m**	**C coefficients C_{lm}**	**S coefficients S_{lm}**
0	0	1.0	-
1	0	0.0	-
1	1	0.0	0.0
2	0	−0.324712	-
2	1	0.0	0.0
2	2	0.141635	0.0
3	0	0.095551	-
3	1	−0.0303935	−0.006628
3	2	−0.016017	−0.016017
3	3	0.0096246	0.004737
4	0	0.263556	-
4	1	0.032320	0.004620
4	2	−0.027562	0.0000219
4	3	−0.001833	−0.0008979
4	4	0.003175	0.0002456

Table A.4: Unnormalized exterior spherical harmonic coefficients of Didymos.

Order l	**Degree m**	**C coefficients C_{lm}**	**S coefficients S_{lm}**
0	0	1.0	-
1	0	0.0	-
1	1	0.0	0.0
2	0	-0.063422	-
2	1	0	0
2	2	0.0040949	0
3	0	-0.0015154	-
3	1	0.00028455	0.00011578
3	2	2.89891×10^{-5}	-1.89599×10^{-5}
3	3	0.0003995	-0.0001293
4	0	0.0466049	-
4	1	-2.65537×10^{-5}	3.352119×10^{-5}
4	2	-9.588539×10^{-5}	-1.28121×10^{-6}
4	3	-8.305724×10^{-6}	-4.819896×10^{-6}
4	4	3.544874×10^{-5}	-7.124178×10^{-6}

Table A.5: Unnormalized exterior spherical harmonic coefficients of Eros.

Order l	**Degree m**	**C coefficients C_{lm}**	**S coefficients S_{lm}**
0	0	1.0	-
1	0	0.0	-
1	1	0.0	0.0
2	0	-0.117308	-
2	1	-2.11453×10^{-6}	-1.807441×10^{-7}
2	2	0.0531885	-0.018144
3	0	-0.0037423	-
3	1	0.0043854	0.00363836
3	2	0.00060659	-0.0002403
3	3	-0.001452	-0.0016832
4	0	0.0387944	-
4	1	-9.520125×10^{-5}	0.0001299
4	2	-0.0039061	0.00103509
4	3	-1.794045×10^{-5}	-7.123990×10^{-6}
4	4	0.0003688	-0.00019238

Appendix B

Spin State Estimation of 4179 Toutatis

The dynamics matrix and the observation log used to estimate the spin state of 4179 Toutatis are presented.

B.0.1 Dynamics Matrix

In order to compute the STM, it is necessary to compute the dynamics matrix A (Equation 3.10). There are only five components that are non-zero in the dynamics matrix, which are $\partial\dot{\vec{\alpha}}/\partial\vec{\alpha}$, $\partial\dot{\vec{\alpha}}/\partial\vec{\omega}$, $\partial\dot{\vec{\omega}}/\partial\vec{\omega}$, $\partial\dot{\vec{\omega}}/\partial I_{ij}$, and $\partial\dot{\vec{\omega}}/\partial\vec{r}_{CM}$. These five quantities are solved below.

B.0.1.1 $\partial\dot{\vec{\alpha}}/\partial\vec{\alpha}$

From Eq. 4.2, $\partial\dot{\vec{\alpha}}/\partial\vec{\alpha}$ is computed as

$$\frac{\partial\dot{\vec{\alpha}}}{\partial\alpha} = \frac{\partial[C(\vec{\alpha})]}{\partial\alpha}\vec{\omega}_B = 0 \tag{B.1}$$

$$\frac{\partial\dot{\vec{\alpha}}}{\partial\beta} = \frac{\partial[C(\vec{\alpha})]}{\partial\beta}\vec{\omega}_B = \frac{1}{\sin^2\beta}\begin{bmatrix} -\sin\gamma\cos\beta & -\cos\gamma\cos\beta & 0 \\ 0 & 0 & 0 \\ \sin\gamma & \cos\gamma & 0 \end{bmatrix}\vec{\omega}_B \tag{B.2}$$

$$\frac{\partial\dot{\vec{\alpha}}}{\partial\gamma} = \frac{\partial[C(\vec{\alpha})]}{\partial\gamma}\vec{\omega}_B = \begin{bmatrix} \frac{\cos\gamma}{\sin\beta} & -\frac{\sin\gamma}{\sin\beta} & 0 \\ -\sin\gamma & -\cos\gamma & 0 \\ -\frac{\cos\gamma}{\tan\beta} & \frac{\sin\gamma}{\tan\beta} & 0 \end{bmatrix}\vec{\omega}_B \tag{B.3}$$

B.0.1.2 $\partial\dot{\vec{\alpha}}/\partial\vec{\omega}$

Also from Eq. 4.2, $\partial\dot{\alpha}/\partial\vec{\omega}$ is computed as

$$\frac{\partial\dot{\vec{\alpha}}}{\partial\omega} = [C(\vec{\alpha})] \tag{B.4}$$

B.0.1.3 $\partial\dot{\vec{\omega}}/\partial\vec{\omega}$

First, note the following identity:

$$\frac{\partial(\tilde{\omega}\vec{a})}{\partial\vec{\omega}} = \frac{\partial(\vec{\omega}\times\vec{a})}{\partial\vec{\omega}} = -\frac{\partial(\vec{a}\times\vec{\omega})}{\partial\vec{\omega}} = -\frac{\partial(\tilde{a}\vec{\omega})}{\partial\vec{\omega}} = -\tilde{a} \tag{B.5}$$

Then, from Eq. 4.6, $\partial\dot{\vec{\omega}}/\partial\vec{\omega}$ becomes:

$$\frac{\partial\dot{\vec{\omega}}_{B,CM}}{\partial\vec{\omega}_{B,CM}} = I_{B,CM}^{-1}\left([\tilde{I\vec{\omega}}]_{B,CM} - \tilde{\omega}_{B,CM}I_{B,CM} + \frac{\partial\vec{L}_{B,CM}}{\partial\vec{\omega}_{B,CM}}\right) \tag{B.6}$$

where $\partial\vec{L}_{B,CM}/\partial\vec{\omega}_{B,CM}$ is nominally a zero matrix.

B.0.1.4 $\partial\dot{\vec{\omega}}/\partial I_{ij}$

In Eq. 4.6, the partial of $\dot{\vec{\omega}}$ with respect to I_{ij} is computed:

$$\frac{\partial\dot{\vec{\omega}}}{\partial I_{ij}} = \frac{\partial(I^{-1})}{\partial I_{ij}}(-\tilde{\omega}I\vec{\omega}+\vec{L}) + I^{-1}\left(-\tilde{\omega}\frac{\partial I}{\partial I_{ij}}\vec{\omega} + \frac{\partial\vec{L}}{\partial I_{ij}}\right) \tag{B.7}$$

In order to compute $\partial(I^{-1})/\partial I_{ij}$, we make use of the familiar identity $I^{-1}I = 1_{[3\times3]}$. That is,

$$\frac{\partial(I^{-1}I)}{\partial I_{ij}} = \frac{\partial(I^{-1})}{\partial I_{ij}}I + I^{-1}\frac{\partial I}{\partial I_{ij}} = \mathbf{0} \tag{B.8}$$

which yields

$$\frac{\partial(I^{-1})}{\partial I_{ij}} = -I^{-1}\frac{\partial I}{\partial I_{ij}}I^{-1} \tag{B.9}$$

Thus, Equation B.7 becomes

$$\frac{\partial\dot{\vec{\omega}}}{\partial I_{ij}} = -I^{-1}\frac{\partial I}{\partial I_{ij}}I^{-1}\left(-\tilde{\omega}I\vec{\omega} + \vec{L}\right) + I^{-1}\left(-\tilde{\omega}\frac{\partial I}{\partial I_{ij}}\vec{\omega} + \frac{\partial\vec{L}}{\partial I_{ij}}\right) \tag{B.10}$$

Note that $\vec{L}$ is expressed as a function of the spherical harmonics. These spherical harmonics are linearly related to the inertia tensor, so the chain rule can be used to compute $\partial\vec{L}/\partial I_{ij}$. The acceleration due to U_2 (Eq. 4.14) can be expressed as:

$$\frac{\partial U_2}{\partial\vec{r}} = \vec{a}_{C_{20}}C_{20} + \vec{a}_{C_{21}}C_{21} + \vec{a}_{C_{22}}C_{22} + \vec{a}_{S_{21}}S_{21} + \vec{a}_{S_{22}}S_{22} = \sum\vec{a}_{C_{2ml}}C_{2ml} \tag{B.11}$$

where each $\vec{a}_{2ml}$ is the partial of the total acceleration with respect to the parameter in the subscript, and C_{2ml} denotes all second-degree spherical harmonics ordered in the following manner:

$$C_{2ml} = \begin{bmatrix} C_{20} & C_{21} & C_{22} & S_{21} & S_{22} \end{bmatrix} \tag{B.12}$$

where $l = 0$ is used for C_{2m} and $l = 1$ for S_{2m}. Then, the torque due to the second-degree potential is expressed as

$$\vec{L}_2 = -M_s\vec{r}\times\frac{\partial U_2}{\partial\vec{r}} = -M_s[\tilde{r}]\left(\sum\vec{a}_{C_{2ml}}C_{2ml}\right) \tag{B.13}$$

Thus, the partial of the torque due to the second-degree spherical harmonics is given as

$$\frac{\partial \vec{L}_2}{\partial C_{2ml}} = -M_s[\tilde{r}]\vec{a}_{C_{2ml}} \tag{B.14}$$

Applying the chain rule, we get

$$\frac{\partial \vec{L}}{\partial I_{xx}} = \frac{\partial \vec{L}}{\partial C_{20}}\frac{\partial C_{20}}{\partial I_{xx}} + \frac{\partial \vec{L}}{\partial C_{22}}\frac{\partial C_{22}}{\partial I_{xx}} = -\frac{GM_s}{M^*(R^*)^2}[\tilde{r}]\left(\frac{1}{2}\vec{a}_{C_{20}} - \frac{1}{4}\vec{a}_{C_{22}}\right) \tag{B.15}$$

$$\frac{\partial \vec{L}}{\partial I_{yy}} = \frac{\partial \vec{L}}{\partial C_{20}}\frac{\partial C_{20}}{\partial I_{yy}} + \frac{\partial \vec{L}}{\partial C_{22}}\frac{\partial C_{22}}{\partial I_{yy}} = -\frac{GM_s}{M^*(R^*)^2}[\tilde{r}]\left(\frac{1}{2}\vec{a}_{C_{20}} + \frac{1}{4}\vec{a}_{C_{22}}\right) \tag{B.16}$$

$$\frac{\partial \vec{L}}{\partial I_{zz}} = \frac{\partial \vec{L}}{\partial C_{20}}\frac{\partial C_{20}}{\partial I_{zz}} = \frac{GM_s}{M^*(R^*)^2}[\tilde{r}]\vec{a}_{C_{20}} \tag{B.17}$$

$$\frac{\partial \vec{L}}{\partial I_{xy}} = \frac{\partial \vec{L}}{\partial S_{22}}\frac{\partial S_{22}}{\partial I_{xy}} = \frac{GM_s}{2M^*(R^*)^2}[\tilde{r}]\vec{a}_{S_{22}} \tag{B.18}$$

$$\frac{\partial \vec{L}}{\partial I_{yz}} = \frac{\partial \vec{L}}{\partial S_{21}}\frac{\partial S_{21}}{\partial I_{yz}} = \frac{GM_s}{M^*(R^*)^2}[\tilde{r}]\vec{a}_{S_{21}} \tag{B.19}$$

$$\frac{\partial \vec{L}}{\partial I_{xz}} = \frac{\partial \vec{L}}{\partial C_{21}}\frac{\partial C_{21}}{\partial I_{xz}} = \frac{GM_s}{M^*(R^*)^2}[\tilde{r}]\vec{a}_{C_{21}} \tag{B.20}$$

B.0.1.5 $\partial\dot{\vec{\omega}}/\partial\vec{r}_{CM}$

From Eq. 4.6, the partial of $\dot{\vec{\omega}}$ with respect to $\vec{r}_{CM}$ is computed as

$$\frac{\partial\dot{\vec{\omega}}}{\partial\vec{r}_{CM}} = I^{-1}\left(\sum_{Earth,Sun}\frac{\partial\vec{L}_1}{\partial\vec{r}_{CM}}\right) \tag{B.21}$$

where the following equation is substituted:

$$\frac{\partial\vec{L}_1}{\partial\vec{r}_{CM}} = -\frac{GM^*M_s}{r^3}[\tilde{r}] \tag{B.22}$$

B.0.2 Observation Log of Delay-Doppler Images

Table B.1 lists the observations of Toutatis used in the least-squares filter, which were recorded at Goldstone between 1992 and 2000, and at Arecibo between 2004 and 2008. Additional radar images were obtained at Arecibo in 1992 [25, 43], but these overlapped the time span of the Goldstone observations and do not provide more information on the spin state. Times are given at the mid-epoch of each observation, image resolution is given in time delay and Doppler shift.

Table B.1: Observation log of delay-Doppler images.

Date	Mid-Epoch (UTC)	Resolution ($\mu s \times Hz$)	Euler Angles $[deg.]$	Angular Velocity $[deg./day]$
Goldstone				
1992 Dec 02	21:40	0.500 x 0.1000	(122.2, 86.5,107.0)	(-35.6, 7.2, -97.0)
1992 Dec 03	19:30	0.500 x 0.1000	(86.3, 81.8, 24.5)	(-16.4,-29.1, -91.9)
1992 Dec 04	18:10	0.500 x 0.1000	(47.8, 60.7,284.0)	(29.1,-23.2, -97.8)
1992 Dec 05	18:50	0.125 x 0.0833	(14.6, 39.4,207.1)	(33.3, 8.2, -92.2)
1992 Dec 06	17:30	0.125 x 0.0833	(331.3, 23.7,151.6)	(6.6, 34.5, -95.8)
1992 Dec 07	17:20	0.500 x 0.1000	(222.5, 25.4,143.9)	(12.8, 25.4,-104.1)
1992 Dec 08	16:40	0.125 x 0.0330	(169.8, 45.5,106.9)	(-31.1,-21.9, -97.7)
1992 Dec 09	17:50	0.125 x 0.0330	(137.3, 71.3, 22.3)	(11.8,-36.9, -94.9)
1992 Dec 10	17:20	0.125 x 0.0330	(103.1, 85.2,292.6)	(35.8, -8.9, -97.9)
1992 Dec 11	09:40	0.500 x 0.1000	(77.0, 85.7,225.5)	(31.0, 17.0, -96.3)
1992 Dec 12	09:20	0.500 x 0.1000	(42.8, 70.2,133.2)	(-1.3, 37.0, -95.9)
1992 Dec 13	08:10	0.500 x 0.1000	(13.7, 44.4, 51.9)	(-38.3, 17.9, -97.3)
1992 Dec 14	07:50	0.500 x 0.1000	(323.7, 14.0, 0.0)	(-70.5,-30.6, -91.1)
1992 Dec 15	07:50	0.500 x 0.1000	(193.2, 24.4, 21.4)	(22.1,-26.6, -96.6)
1992 Dec 16	07:10	0.500 x 0.1000	(165.1, 46.4,310.6)	(33.4, -3.4, -93.7)
1992 Dec 17	06:49	0.500 x 0.1000	(130.6, 76.1,234.9)	(12.6, 33.9, -94.0)
1992 Dec 18	07:09	0.500 x 0.1000	(91.6, 81.6,142.4)	(-24.3, 29.6,-102.0)
Goldstone				
1996 Nov 25	19:48	0.125 x 0.0331	(130.5, 78.9,143.2)	(-32.0, 16.4, -98.2)
1996 Nov 26	17:51	0.125 x 0.0331	(94.2, 88.1, 57.7)	(-30.6,-18.7, -91.5)
1996 Nov 27	17:34	0.125 x 0.0331	(60.4, 81.2,320.9)	(10.7,-36.8, -94.7)
1996 Nov 29	15:37	0.125 x 0.0331	(349.3, 30.0,168.0)	(23.1, 28.9, -98.3)
1996 Nov 30	15:47	0.125 x 0.0331	(250.3, 14.2,166.9)	(-18.6, 32.1, -94.9)
1996 Dec 01	14:23	0.125 x 0.0331	(180.4, 37.6,139.3)	(-38.7, -0.5, -98.1)
1996 Dec 02	13:43	0.125 x 0.0331	(146.7, 64.0, 64.9)	(-12.6,-34.8, -97.9)
1996 Dec 03	12:20	0.125 x 0.0331	(116.7, 81.4,340.4)	(24.3,-28.2, -98.1)
Goldstone				
2000 Nov 04	17:06	0.125 x 0.0331	(110.0, 88.5, 30.0)	(0.0,-32.5, -98.9)
2000 Nov 05	18:01	0.125 x 0.0331	(70.6, 84.0,281.0)	(34.5,-17.2, -97.9)
Arecibo				
2004 Oct 07	13:56	0.100 x 0.0114	(79.9, 85.3,365.2)	(-2.5,-35.4,-109.0)
2004 Oct 08	14:04	0.100 x 0.0114	(44.9, 72.5,263.1)	(32.4,-18.1, -97.9)
2004 Oct 09	13:57	0.100 x 0.0114	(12.8, 47.3,181.4)	(29.7, 22.8, -98.1)
2004 Oct 10	13:17	0.100 x 0.0114	(327.7, 20.4,124.1)	(-10.7, 34.7, -97.3)
Arecibo				
2008 Nov 22	10:54	0.100 x 0.0186	(119.5, 90.7, 92.0)	(118.1, 90.4, 93.6)
2008 Nov 23	10:45	0.100 x 0.0186	(86.2, 85.0, 0.3)	(-0.4,-36.2, -98.9)

Appendix C

Internal Density Distribution Estimation

Details of the density maps analyzed in Chapter 5 are presented here.

C.1 Planar Division Model

The planar division model is the simplest of all density distribution models. The body is divided by the yz ($\pm x$-axis), xz ($\pm y$-axis), or xy-plane ($\pm z$-axis), and each region is given a different density value, which offsets the center of mass of the body. Figure C.1 shows an asteroid split into region 1 (positive axis) and 2 (negative axis) by the yz-plane (i.e., along the x-axis):

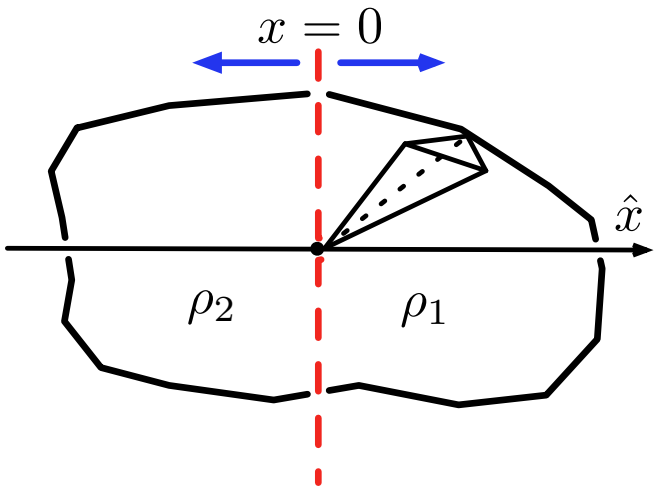

Figure C.1: Planar division model.

As shown in Figure C.1, the region 1 is assigned the density value ρ_1 and the region 2 the density value ρ_2, satisfying the mass constraint

$$M = \rho_1 V_1 + \rho_2 V_2 \tag{C.1}$$

In order to estimate the density values, it is necessary to compute the nominal spherical harmonic coefficients from a given density map (Section 5.2.1). The nominal spherical harmonic coefficients for a planar division model are computed for each tetrahedron and summed over the whole volume. Note that the contribution of each tetrahedron must be weighted by its mass. The tetrahedra that cross the plane are included in the positive axis region.

C.2 Surface Layer Model

The surface layer model is divided into two regions: entire body with homogeneous density ρ and the layer with a given depth with the density deviation $\Delta\rho$ (Figure C.2).

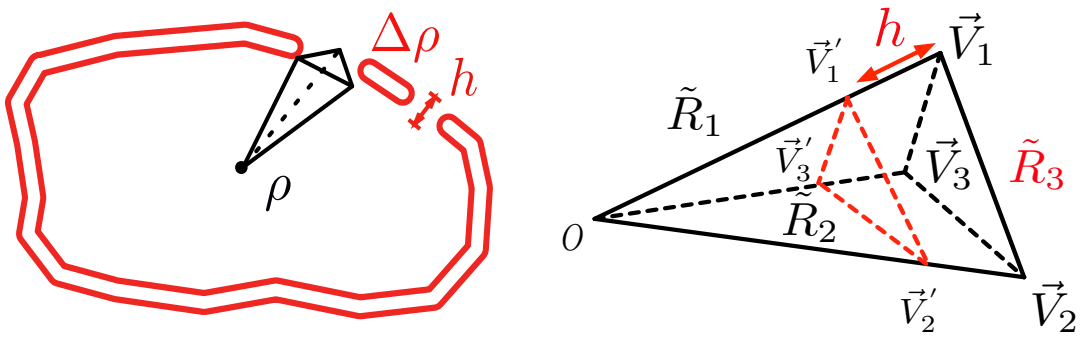

(a) Surface layer model (b) Tetrahedron for the surface layer

Figure C.2: Surface layer model and its tetrahedron.

In Figure C.2(a), the surface layer has the depth h with the absolute density value of $\rho + \Delta\rho$. The total mass is constrained by

$$M = \rho V_{total} + \Delta\rho V_{layer} \tag{C.2}$$

For this model, all tetrahedrons have contributions to the overall spherical harmonic coefficients due to the surface layer (Figure C.2(b)). Each vertex is specified by $\vec{V}_i$ extending from the

center of mass of the asteroid, and $\vec{V}_i'$ are the vertices which are equal distance apart by h from the corresponding parent vertex. $\vec{V}_i'$ is computed by a simple equation $\vec{V}_i' = \vec{V}_i - h\hat{V}_i$, where $\hat{V}_i$ is the unit vector of $\vec{V}_i$. Now let region 1 ($\tilde{R}_1$) be the whole volume enclosed by $\vec{V}_i$ and the origin, region 2 ($\tilde{R}_2$) be the volume enclosed by $\vec{V}_i'$ and the origin, and region 3 ($\tilde{R}_3$) be the volume enclosed by $\vec{V}_i$ and $\vec{V}_i'$. Then, the spherical harmonic coefficients of the surface layer is the contribution from the region 3. Since both region 1 and 2 contain the origin as a common point, a linear operation is allowed to subtract the mass contribution given by region 2 from from that given by region 1. Note that the contribution of each region to the spherical harmonic coefficients must be weighted by corresponding mass of the region. Thus, the spherical harmonic coefficients from the region 3 is computed as

$$\begin{bmatrix} C_{nm} \\ S_{nm} \end{bmatrix}_{\tilde{R}_3} M_3 = \begin{bmatrix} C_{nm} \\ S_{nm} \end{bmatrix}_{\tilde{R}_1} M_1 - \begin{bmatrix} C_{nm} \\ S_{nm} \end{bmatrix}_{\tilde{R}_2} M_2 \tag{C.3}$$

For the surface layer model, it is most convenient to compute the spherical harmonic coefficients from the entire volume with a constant density ρ and add the contribution from the surface layer with additional density $\Delta\rho$.

C.3 Single Core Model

The single core model is divided into two regions: whole body with homogeneous density ρ and the spherical core with the density deviation $\Delta\rho$ (Figure C.3).

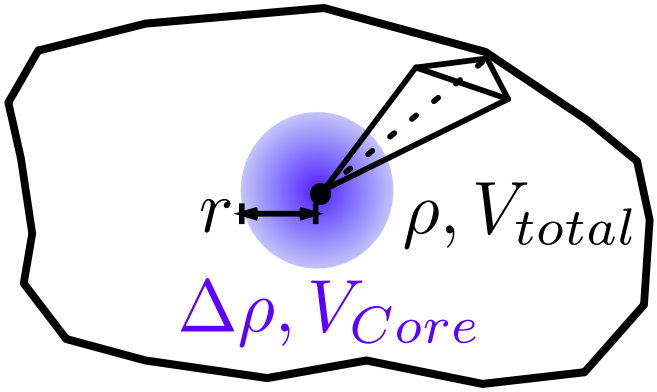

Figure C.3: Single-core model.

In Figure C.3, the core is placed at the center of figure of the asteroid, and the total mass is constrained by

$$M = \rho V_{total} + \Delta\rho V_{core} = \rho_{core} V_{core} + \rho_{mantle} V_{mantle} \tag{C.4}$$

The center of figure is defined by assuming a homogeneous density distribution and finding the location where the first-degree spherical harmonic coefficients disappear after integration. For the single core model, it is not necessary to dissect the tetrahedra, and superposition of the core onto the homogeneous body is sufficient. That is, there are no contributions to the higher-degree and higher-order spherical harmonic coefficients from the core, and only the total mass is altered. The region between the core and the surface is referred to as the mantle, and it is differentiated from the core.

C.4 Double Core Model

The double core model is divided into three regions: whole body with homogeneous density ρ and the two spherical cores in the positive and negative-axis region with the density deviations $\Delta\rho_1$ and $\Delta\rho_2$ (Figure C.4).

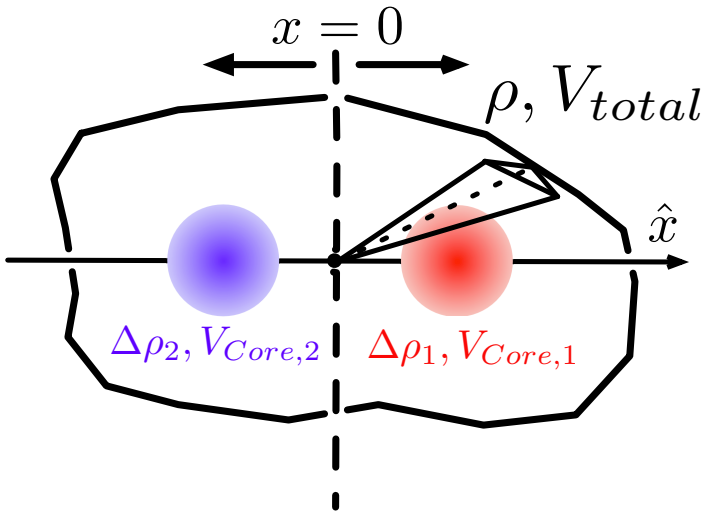

Figure C.4: Double-core model.

In Figure C.4, the two cores are placed at the centers of mass of the positive and negative-axis regions that are computed from the homogeneous density assumption. The total mass is constrained by

$$M = \rho V_{total} + \Delta\rho_1 V_{Core,1} + \Delta\rho_2 V_{Core,2} \tag{C.5}$$

The spherical harmonic coefficients due to the spherical cores reduce to two point masses placed at their centers. The analytical expressions of the exterior spherical harmonic coefficients are given in Equation 1.14. Note that the mass integral can be replaced with the total mass of each sphere.

C.5 Torus Model

The torus model is divided into two regions: whole body with homogeneous density ρ and the torus with the density deviation $\Delta\rho$ (Figure C.5).

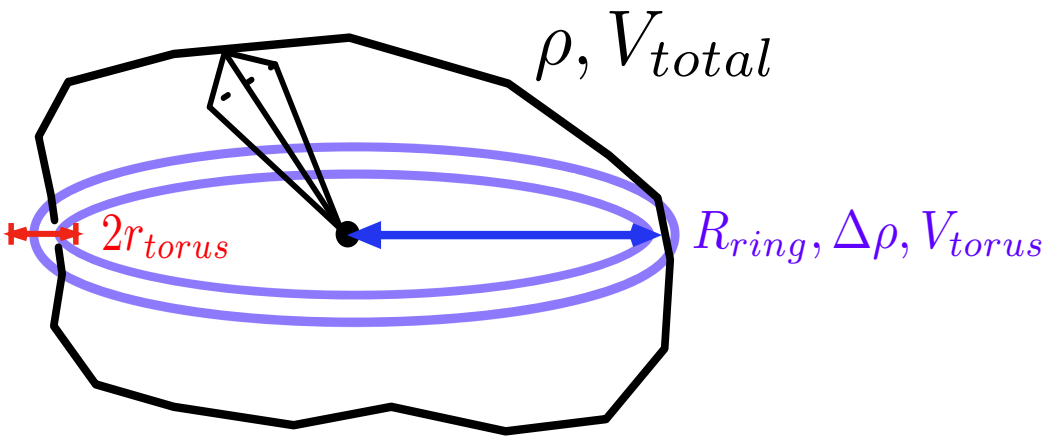

(a) Torus model

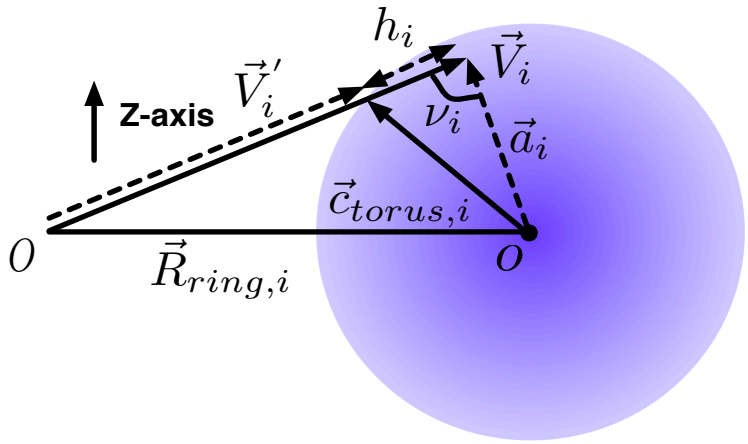

(b) Tetrahedron for the torus model

Figure C.5: Torus model and its tetrahedron.

The total mass is constrained by

$$M = \rho V_{total} + \Delta\rho V_{torus} \tag{C.6}$$

In Figure C.5(a), the torus is centered at the center of mass of the body and has a ring radius R_{ring} on the xy-plane. The cross-section of the torus has the radius r_{torus}. Figure C.5(b) shows the schematic of a tetrahedron and the torus intersecting each other. In Figure C.5(b), the torus is cut in $\hat{r}\hat{\theta}$-plane in the spherical coordinates (r, θ, ϕ) with respect to the i-th vertex of the facet. $\vec{R}_{ring,i}$ is the vector from the center of mass of the body to the center of the torus o, $\vec{c}_{torus,i}$ $(i = 1 \rightarrow 3)$ is the vector from o to the intersection of the edge $\vec{V_iO}$ with the torus, $\vec{a}_i$ is the vector from point

o to $\vec{V}_i$, and ν_i is the angle between $\vec{a}_i$ and $\vec{V}_i$. Then, $\vec{V}_i$ lies inside the torus' cross-section if the norm of $\vec{a}_i$ is less than the radius of the torus. The torus is constructed only when all three vertices satisfy this condition. The distance between $\vec{V}_i$ and $\vec{V}_i'$ can be computed by the law of cosine as

$$h_i = a_i \cos\nu_i + \sqrt{c_{torus,i}^2 - a_i^2 \sin^2\nu_i} \tag{C.7}$$

where the positive sign is chosen from the geometry. Then, the intersection of the cross-section and the edge $\vec{V}_i$ is computed by $\vec{V}_i' = \vec{V}_i - h_i\hat{V}_i$.

C.6 Cylinder Model

The cylinder model is specified by the radius of the cylinder (r_{cyl}) and the number of rings in the z-direction (Figure C.6):

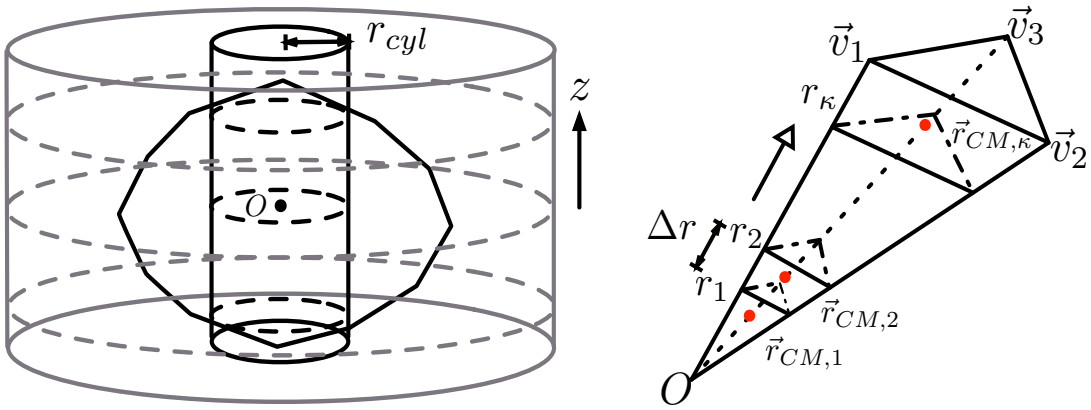

(a) Cylinder model

(b) Tetrahedron dissected into slivers

Figure C.6: Cylinder model and the tetrahedron dissected into slivers.

The total mass is constrained by

$$M = \rho_{cyl}V_{cyl} + \sum_{i=1}^{N_{ring}} \rho_i V_i \tag{C.8}$$

In Figure C.6(a), the volume inside the cylinder is given the density ρ_{cyl}, and the rest of the volume is sliced in the z-direction into the rings with a density value ρ_i (gray dashed lines). The

curvature of the cylinder adds complexity to the computation of the spherical harmonic coefficients, as the polyhedral integration is only applicable to polygons with straight edges [76]. In order to make the computation tractable, each tetrahedron is partitioned into slivers along the radial direction. In Figure C.6(b), the tetrahedron is dissected into κ many slivers in the radial direction with interval Δr along $O\vec{v}_1$, with each edge of the facet parallel to that of the parent facet. Each red dot signifies the center of mass of the sliver ($\vec{r}_{CM,q}$, $q = 1, 2, \ldots, \kappa$). Then, the coordinates of the center of mass are used to specify which sliver belongs to which ring (Figure C.7).

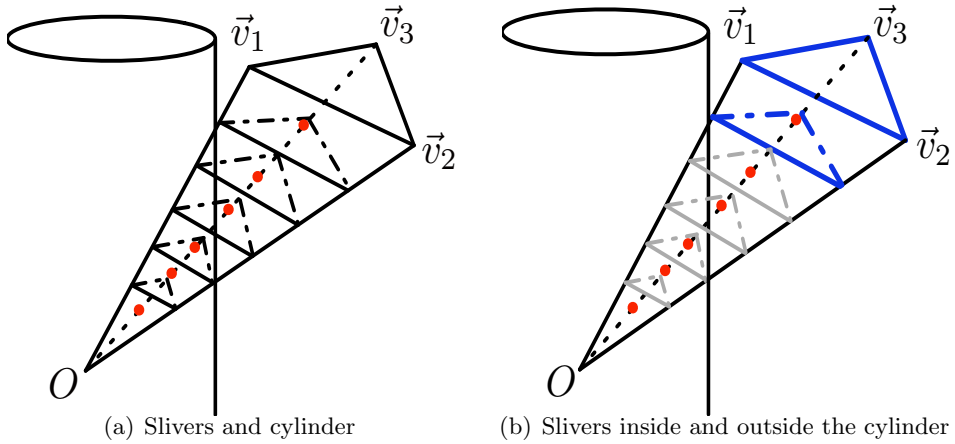

(a) Slivers and cylinder (b) Slivers inside and outside the cylinder

Figure C.7: Tetrahedron inside/outside the cylinder.

In Figure C.7(b), all slivers that completely lie outside the cylinder is included in the rings (blue). If any part of sliver lies within the cylinder, it is included in the cylinder (light gray). Based on the z-coordinates of the center of mass, each sliver that lies outside the cylinder is assigned to the corresponding ring. More complex division scheme may be implemented, but it is important to not count the same portion of the volume twice or discard a certain portion of the volume. When writing a routine in a script, it is advised to define κ and compute Δr for each edge to make the cuts smooth between two adjacent tetrahedra.

C.7 Block Model

The block model is composed of a number of square blocks that encompass the entire volume of the body. Three new parameters are defined: Δl_s (side cut), Δl_v (vertical cut), and Δl_h (horizontal cut), which are the lengths of the block in the x, y, and z-directions. The number of blocks in respective directions is represented as an ordered triplet (N_S, N_V, N_H), with the total number of blocks being $N_{Block} = N_S N_V N_H$. Each block is assigned an identifier computed by $i_{Block} = (i_x - 1)N_V N_H + (i_y - 1)N_V + i_z$, where i_x is the index of the side cut, i_y is that of the vertical cut, and i_z is that of the horizontal cut. Figure C.8 shows the body dissected into blocks.

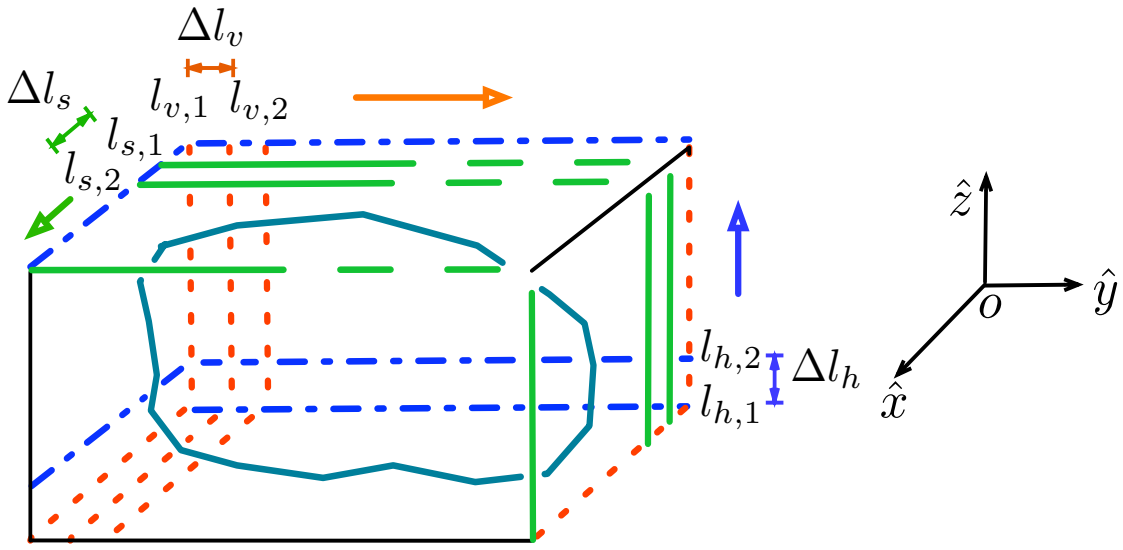

Figure C.8: Block model.

Each block has a homogeneous density distribution within itself, and the total mass is constrained by

$$M = \sum_{i=1}^{N_{Block}} \rho_i V_i \tag{C.9}$$

After the body is dissected into blocks, the problem becomes quickly complex due to the representation of the body via tetrahedra. When dissecting a tetrahedron to the specifications of

the block segmentation, it is required to rewire the vertices when a cut is made through a facet. Thus, as with the cylinder model, each tetrahedron is dissected into slivers and they are assigned to the appropriate block based on their center of mass locations. The discriminant is such that if the center of mass of a sliver $\vec{r}_{CM,q}$ lies within the block i_{Block}, the density value of $\rho_{i_{Block}}$ is assigned. The portions of the blocks that lie outside the body are discarded.

Appendix D

Interior Spherical Harmonic Gravity Field

Supplemental equations used to derive the interior gravity field are presented.

D.1 Normalization Factor

Both Equation 6.12 and 6.13 are referred to as the unnormalized exterior/interior gravity fields. In order to derive the normalized counterparts, we introduce the normalization factor N_{nm}. This normalization factor arises from the orthogonality relationship of the associated Legendre function (Kaula [30], Pinsky [50], and Werner [74]) given below:

$$\iint_{\sigma} S_{nmi} S_{rst} d\sigma = \begin{cases} 0 & \text{for} \quad n \neq r \text{ or } m \neq s \text{ or } i \neq t \\ \\ 4\pi \dfrac{(n+m)!}{(n-m)!(2n+1)(2-\delta_{0m})} & \text{for} \quad n = r \text{ and } m = s \text{ and } i = t \end{cases} \tag{D.1}$$

where σ is a unit-radius sphere (i.e., $d\sigma = \sin\theta d\phi d\lambda$ as defined in Equation 7.32), δ is Kronecker delta function, and S_{nmi} is defined as

$$S_{nmi} = \begin{cases} P_{nm}(\sin\phi)\cos m\lambda & , \quad i = 0 \\ P_{nm}(\sin\phi)\sin m\lambda & , \quad i = 1 \end{cases} \tag{D.2}$$

Note that the same notation as Werner [74] is used above in order to be consistent with the derivation of the interior gravity field. Then, the normalization factor N_{nm} is commonly defined for both the exterior and interior gravity fields as

$$N_{nm} = \sqrt{(2-\delta_{0,m})(2n+1)\frac{(n-m)!}{(n+m)!}} \tag{D.3}$$

which is the reciprocal of the quantity on the right-hand side of Equation D.1 without 4π. This normalization factor N_{nm} is introduced to alleviate the machine overflow and underflow by reducing the spherical harmonic coefficients to about the same comparable size as their root-mean-square value over a sphere [22]. The normalization factor is applied to both the spherical harmonics and the associated Legendre function so that the product of the two quantities yields the same value in the potential expression. That is,

$$\begin{bmatrix} C_{nm}P_{nm} \\ S_{nm}P_{nm} \end{bmatrix} = \begin{bmatrix} (C_{nm}/N_{nm})(N_{nm}P_{nm}) \\ (S_{nm}/N_{nm})(N_{nm}P_{nm}) \end{bmatrix} = \begin{bmatrix} \bar{C}_{nm}\bar{P}_{nm} \\ \bar{S}_{nm}\bar{P}_{nm} \end{bmatrix} \tag{D.4}$$

Note that this normalization does not make an orthonormal system, although one could add a factor of $\sqrt{1/4\pi}$ to Equation D.3 to make one.

D.2 Exterior Gravity Field Basis Functions

In this section, we define the basis functions and their recursive formulae for the exterior gravity field. Werner [74] rewrites Equation 6.12 such that the exterior potential is expressed by b^e_{nm}, c^e_{nm}, and their normalized counterparts:

$$\begin{aligned} U^e &= \frac{GM^*}{R^*_e}\sum_{n=0}^{\infty}\sum_{m=0}^{n} b^e_{nm}\cdot\frac{1}{M^*}\int_M c^e_{nm}dm' \\ &= \frac{GM^*}{R^*_e}\sum_{n=0}^{\infty}\sum_{m=0}^{n} \bar{b}^e_{nm}\cdot\frac{1}{M^*}\int_M \bar{c}^e_{nm}dm' \end{aligned} \tag{D.5}$$

where b_{nm} and c_{nm} are multiplied by the dot product. b^e_{nm}, c^e_{nm}, and their normalized counterparts are expressed as follows:

$$\begin{cases} b^e_{nm} &= \left(\dfrac{R^*_e}{r}\right)^{n+1} P_{nm}(\sin\phi) \begin{bmatrix}\cos(m\lambda)\\ \sin(m\lambda)\end{bmatrix} \\ c^e_{nm} &= (2-\delta_{0,m})\dfrac{(n-m)!}{(n+m)!}\left(\dfrac{r'}{R^*_e}\right)^n P_{nm}(\sin\phi') \begin{bmatrix}\cos(m\lambda')\\ \sin(m\lambda')\end{bmatrix} \end{cases} \tag{D.6}$$

$$\begin{cases} \bar{b}^e_{nm} &= \sqrt{(2-\delta_{0,m})(2n+1)\dfrac{(n-m)!}{(n+m)!}}\left(\dfrac{R^*_e}{r}\right)^{n+1} P_{nm}(\sin\phi) \begin{bmatrix}\cos(m\lambda)\\ \sin(m\lambda)\end{bmatrix} \\ \bar{c}^e_{nm} &= \sqrt{\dfrac{(2-\delta_{0,m})}{(2n+1)}\dfrac{(n-m)!}{(n+m)!}}\left(\dfrac{r'}{R^*_e}\right)^n P_{nm}(\sin\phi') \begin{bmatrix}\cos(m\lambda')\\ \sin(m\lambda')\end{bmatrix} \end{cases} \tag{D.7}$$

Then, simple recursion formulae exist for each quantity in Equation D.6 and D.7. The derivation, again, is given by Werner [74], and we only present the results below.

D.2.1 Recursive Formulae for the Unnormalized Exterior Gravity Field Basis Functions

The recursion formulae for b^e_{nm} and c^e_{nm} are given as

$$\begin{cases} b^e_{00} &= \dfrac{R^*_e}{r}\begin{bmatrix}1\\ 0\end{bmatrix} \\ b^e_{nn} &= (2n-1)\dfrac{R^*_e}{r}\begin{bmatrix}x/r & -y/r\\ y/r & x/r\end{bmatrix} b^e_{n-1,n-1} \\ b^e_{nm} &= \dfrac{(2n-1)}{(n-m)}\left(\dfrac{R^*_e}{r}\right)\left(\dfrac{z}{r}\right) b^e_{n-1,m} - \dfrac{(n+m-1)}{(n-m)}\left(\dfrac{R^*_e}{r}\right)^2 b^e_{n-2,m} \end{cases} \tag{D.8}$$

$$\begin{cases} c^e_{00} &= \begin{bmatrix} 1 \\ 0 \end{bmatrix} \\ c^e_{nn} &= \dfrac{(1+\delta_{1,n})}{(2n)} \begin{bmatrix} x'/R^*_e & -y'/R^*_e \\ y'/R^*_e & x'/R^*_e \end{bmatrix} c^e_{n-1,n-1} \\ c^e_{nm} &= \dfrac{(2n-1)}{(n+m)} \left(\dfrac{z'}{R^*_e}\right) c^e_{n-1,m} - \dfrac{(n-m-1)}{(n+m)} \left(\dfrac{r'}{R^*_e}\right)^2 c^e_{n-2,m} \end{cases} \tag{D.9}$$

D.2.2 Recursive Formulae for the Normalized Exterior Gravity Field Basis Functions

Also, the recursion formulae for $\bar{b}^e_{nm}$ and $\bar{c}^e_{nm}$ are given as

$$\begin{cases} \bar{b}^e_{00} &= \dfrac{R^*_e}{r} \begin{bmatrix} 1 \\ 0 \end{bmatrix} \\ \bar{b}^e_{nn} &= \sqrt{(1+\delta_{1,n})\dfrac{(2n+1)}{(2n)}} \dfrac{R^*_e}{r} \begin{bmatrix} x/r & -y/r \\ y/r & x/r \end{bmatrix} \bar{b}^e_{n-1,n-1} \\ \bar{b}^e_{nm} &= \sqrt{\dfrac{(2n+1)(2n-1)}{(n+m)(n-m)}} \left(\dfrac{R^*_e}{r}\right) \left(\dfrac{z}{r}\right) \bar{b}^e_{n-1,m} \\ & \quad -\sqrt{\dfrac{(2n+1)(n+m-1)(n-m-1)}{(2n-3)(n+m)(n-m)}} \left(\dfrac{R^*_e}{r}\right)^2 \bar{b}^e_{n-2,m} \end{cases} \tag{D.10}$$

$$\begin{cases} \bar{c}^e_{00} &= \begin{bmatrix} 1 \\ 0 \end{bmatrix} \\ \\ \bar{c}^e_{nn} &= (2n-1)\sqrt{\dfrac{(1+\delta_{1,n})}{(2n)(2n+1)}} \begin{bmatrix} x'/R^*_e & -y'/R^*_e \\ y'/R^*_e & x'/R^*_e \end{bmatrix} \bar{c}^e_{n-1,n-1} \\ \\ \bar{c}^e_{nm} &= (2n-1)\sqrt{\dfrac{(2n-1)}{(2n+1)(n+m)(n-m)}} \left(\dfrac{z'}{R^*_e}\right) \bar{c}^e_{n-1,m} \\ \\ & \quad -\sqrt{\dfrac{(2n-3)(n+m-1)(n-m-1)}{(2n+1)(n+m)(n-m)}} \left(\dfrac{r'}{R^*_e}\right)^2 \bar{c}^e_{n-2,m} \end{cases} \tag{D.11}$$

D.3 Interior Gravity Field Basis Functions

As with the exterior gravity field, we express U^i in terms of b^i_{nm}, c^i_{nm}, and their normalized counterparts:

$$\begin{aligned} U^i &= \frac{GM^*}{R^*_i} \sum_{n=0}^{\infty} \sum_{m=0}^{n} b^i_{nm} \cdot \frac{1}{M^*} \int_M c^i_{nm} dm' \\ &= \frac{GM^*}{R^*_i} \sum_{n=0}^{\infty} \sum_{m=0}^{n} \bar{b}^i_{nm} \cdot \frac{1}{M^*} \int_M \bar{c}^i_{nm} dm' \end{aligned} \tag{D.12}$$

where each quantity in the summation is defined by

$$\begin{cases} b^i_{nm} &= \left(\dfrac{r}{R^*_i}\right)^n P_{nm}(\sin\phi) \begin{bmatrix} \cos(m\lambda) \\ \sin(m\lambda) \end{bmatrix} \\ \\ c^i_{nm} &= (2-\delta_{0,m}) \dfrac{(n-m)!}{(n+m)!} \left(\dfrac{R^*_i}{r'}\right)^{n+1} P_{nm}(\sin\phi') \begin{bmatrix} \cos(m\lambda') \\ \sin(m\lambda') \end{bmatrix} \end{cases} \tag{D.13}$$

$$\begin{cases} \bar{b}^i_{nm} &= \sqrt{(2-\delta_{0,m})(2n+1)\dfrac{(n-m)!}{(n+m)!}}\left(\dfrac{r}{R^*_i}\right)^n P_{nm}(\sin\phi)\begin{bmatrix}\cos(m\lambda)\\ \sin(m\lambda)\end{bmatrix} \\ \bar{c}^i_{nm} &= \sqrt{\dfrac{(2-\delta_{0,m})}{(2n+1)}\dfrac{(n-m)!}{(n+m)!}}\left(\dfrac{R^*_i}{r'}\right)^{n+1} P_{nm}(\sin\phi')\begin{bmatrix}\cos(m\lambda')\\ \sin(m\lambda')\end{bmatrix} \end{cases} \tag{D.14}$$

D.3.1 Recursive Formulae for the Unnormalized Interior Gravity Field Basis Functions

The recursion formulae for b^i_{nm} and c^i_{nm} are given as

$$\begin{cases} b^i_{00} &= \begin{bmatrix}1\\ 0\end{bmatrix} \\ b^i_{nn} &= (2n-1)\begin{bmatrix}x/R^*_i & -y/R^*_i\\ y/R^*_i & x/R^*_i\end{bmatrix} b^i_{n-1,n-1} \\ b^i_{nm} &= \dfrac{(2n-1)}{(n-m)}\left(\dfrac{z}{R^*_i}\right) b^i_{n-1,m} - \dfrac{(n+m-1)}{(n-m)}\left(\dfrac{r}{R^*_i}\right)^2 b^i_{n-2,m} \end{cases} \tag{D.15}$$

$$\begin{cases} c^i_{00} &= \dfrac{R^*_i}{r'}\begin{bmatrix}1\\ 0\end{bmatrix} \\ c^i_{nn} &= \dfrac{(1+\delta_{1,n})}{(2n)}\left(\dfrac{R^*_i}{r'}\right)\begin{bmatrix}x'/r' & -y'/r'\\ y'/r' & x'/r'\end{bmatrix} c^i_{n-1,n-1} \\ c^i_{nm} &= \dfrac{(2n-1)}{(n+m)}\left(\dfrac{R^*_i}{r'}\right)\left(\dfrac{z'}{r'}\right) c^i_{n-1,m} - \dfrac{(n-m-1)}{(n+m)}\left(\dfrac{R^*_i}{r'}\right)^2 c^i_{n-2,m} \end{cases} \tag{D.16}$$

D.3.2 Recursive Formulae for the Normalized Interior Gravity Field Basis Functions

The recursion formulae for $\bar{b}^i_{nm}$ and $\bar{c}^i_{nm}$ are given as

$$\begin{cases} \bar{b}^i_{00} &= \begin{bmatrix} 1 \\ 0 \end{bmatrix} \\ \bar{b}^i_{nn} &= \sqrt{(1+\delta_{1,n})\dfrac{(2n+1)}{(2n)}} \begin{bmatrix} x/R^*_i & -y/R^*_i \\ y/R^*_i & x/R^*_i \end{bmatrix} \bar{b}^i_{n-1,n-1} \\ \bar{b}^i_{nm} &= \sqrt{\dfrac{(2n+1)(2n-1)}{(n+m)(n-m)}} \left(\dfrac{z}{R^*_i}\right) \bar{b}^i_{n-1,m} \\ & \quad -\sqrt{\dfrac{(2n+1)(n+m-1)(n-m-1)}{(2n-3)(n+m)(n-m)}} \left(\dfrac{r}{R^*_i}\right)^2 \bar{b}^i_{n-2,m} \end{cases} \tag{D.17}$$

$$\begin{cases} \bar{c}^i_{00} &= \dfrac{R^*_i}{r'} \begin{bmatrix} 1 \\ 0 \end{bmatrix} \\ \bar{c}^i_{nn} &= (2n-1)\sqrt{\dfrac{(1+\delta_{1,n})}{(2n)(2n+1)}} \left(\dfrac{R^*_i}{r'}\right) \begin{bmatrix} x'/r' & -y'/r' \\ y'/r' & x'/r' \end{bmatrix} \bar{c}^i_{n-1,n-1} \\ \bar{c}^i_{nm} &= (2n-1)\sqrt{\dfrac{(2n-1)}{(2n+1)(n+m)(n-m)}} \left(\dfrac{R^*_i}{r'}\right) \left(\dfrac{z'}{r'}\right) \bar{c}^i_{n-1,m} \\ & \quad -\sqrt{\dfrac{(2n-3)(n+m-1)(n-m-1)}{(2n+1)(n+m)(n-m)}} \left(\dfrac{R^*_i}{r'}\right)^2 \bar{c}^i_{n-2,m} \end{cases} \tag{D.18}$$

These are the all recursive formulae necessary to compute the potential at a field point. For both exterior and interior gravity fields, $(n-2)$-degree terms can be ignored when $n = 1$.

D.4 Potential as a Complex Number

It is desired to obtain the field point acceleration and the dynamics matrix for orbit determination purposes. Specifically, the acceleration is the first-order partial of the interior potential, and the dynamics matrix is the second-order partial of the interior potential. Although the connection between the gravitational field and the complex number is subtle, the partial derivatives of the exterior and interior potentials can be conveniently computed in the complex plane.

We first revert to Equation D.5. The multiplication of b^e_{nm} and c^e_{nm} can be considered as the dot product of the two vector quantities; or more conveniently, the same operation can be accomplished by expressing b^e_{nm} as a complex number:

$$b^e_{nm} \equiv \left(\frac{R^*_e}{r}\right)^{n+1} P_{nm}(\sin\phi)\left[\cos(m\lambda) + i\sin(m\lambda)\right] = \left(\frac{R^*_e}{r}\right)^{n+1} P_{nm}(\sin\phi)e^{im\lambda} \quad \text{(D.19)}$$

where i is the imaginary number that satisfies $i^2 = -1$, and $e = 2.7182\ldots$ is the Euler's number. By the same token, b^i_{nm} can be written as

$$b^i_{nm} = \left(\frac{r}{R^*_i}\right)^{n} P_{nm}(\sin\phi)e^{im\lambda} \quad \text{(D.20)}$$

Then, the dot products in Equation D.5 and D.12 are expressed as

$$b_{nm} \cdot \frac{1}{M^*}\int_M c_{nm}dm = \begin{bmatrix}\Re\{b_{nm}\}\\ \Im\{b_{nm}\}\end{bmatrix} \cdot \begin{bmatrix}C_{nm}\\ S_{nm}\end{bmatrix} = C_{nm}\Re\{b_{nm}\} + S_{nm}\Im\{b_{nm}\} \quad \text{(D.21)}$$

This result motivates to express $1/M^*\int_M c_{nm}dm$ as a complex number by defining K_{nm} as

$$K_{nm} = C_{nm} - iS_{nm} \quad \text{(D.22)}$$

such that

$$b_{nm}K_{nm} = (C_{nm}\Re\{b_{nm}\} + S_{nm}\Im\{b_{nm}\}) + i(-S_{nm}\Re\{b_{nm}\} + C_{nm}\Im\{b_{nm}\}) \quad \text{(D.23)}$$

Consequently, the exterior and interior potentials are given as the sum of the real part of the above expression. Note that the real part is extracted at the very end of the operation, and the whole potential shall be deemed complete only when combined with the imaginary part. Using this alternative expression, Equation D.5 and D.12 are expressed as

$$U^e = \frac{GM^*}{R_e^*}\sum_{n=0}^{\infty}\sum_{m=0}^{n}\Re\{K_{nm}^e b_{nm}^e\} \quad \text{(D.24)}$$

$$U^i = \frac{GM^*}{R_i^*}\sum_{n=0}^{\infty}\sum_{m=0}^{n}\Re\{K_{nm}^i b_{nm}^i\} \quad \text{(D.25)}$$

Now we return to Section D.2 and D.3 to discuss the recursive formulae of the basis functions. With the basis function b_{nm} expressed as a complex number, the recursive formulae derived by Werner [74] can be considered as the vector, or rather, complex number operation. That is, b_{nm} is most easily computed by independently defining the real part of b_{nm} and the imaginary part of b_{nm}. This statement is true of c_{nm} when the spherical harmonic coefficients of a particular point mass is required. For a system of multiple point masses (i.e., mascon model), a contribution of c_{nm} from each mass can be summed to compute the spherical harmonic coefficients of the total system:

$$C_{nm} = \frac{1}{M^*}\sum_{\kappa=1}^{\kappa_{max}} c_{nm,\kappa}m_\kappa \quad \text{(D.26)}$$

where κ is the index of each particle.

D.5 Partial Derivatives of the Interior Gravity Field

In this section, the partial derivatives of the interior potential in the Cartesian body frame, as discussed by Hotine [22] and Werner [74], are derived. Note that only the body-frame partials are

computed, and the transformation between the inertial frame and the body frame must be carried out via the rotation matrix as necessary.

D.5.1 First-order Partials in the Complex Plane

We leverage the results from Section D.4 and take the partials of the interior potential in the complex plane. The partials of the potential are computed in the complex plane by defining two complex-conjugate variables ξ and η:

$$\begin{cases} \xi &= x + iy \\ \eta &= x - iy \end{cases} \tag{D.27}$$

Then, $\partial/\partial x$ and $\partial/\partial y$ are given in terms of the linear combination of $\partial/\partial\xi$ and $\partial/\partial\eta$ as follows:

$$\frac{\partial}{\partial x} = \left(\frac{1}{2}\frac{\partial}{\partial x} + \frac{i}{2}\frac{\partial}{\partial y}\right) + \left(\frac{1}{2}\frac{\partial}{\partial x} - \frac{i}{2}\frac{\partial}{\partial y}\right) = \frac{\partial}{\partial \eta} + \frac{\partial}{\partial \xi} \tag{D.28}$$

$$\frac{\partial}{\partial y} = \Im\left\{\left(\frac{1}{2}\frac{\partial}{\partial x} + \frac{i}{2}\frac{\partial}{\partial y}\right) - \left(\frac{1}{2}\frac{\partial}{\partial x} - \frac{i}{2}\frac{\partial}{\partial y}\right)\right\} = (-i)\left(\frac{\partial}{\partial \eta} - \frac{\partial}{\partial \xi}\right) \tag{D.29}$$

The partial with respect to z is straightforward, and no complex-number operation is necessary. Equation D.29 has significance in itself that is easy to overlook. Equation D.29 can be interpreted not only arithmetically but also geometrically. On the complex plane, the multiplication by i corresponds to 90° rotation. That is, $i = (\cos 90° + i \sin 90°)$, and

$$\begin{aligned} r(\cos\theta + i\sin\theta) &\overset{i}{\rightarrow} r(-\sin\theta + i\cos\theta) \overset{i}{\rightarrow} r(-\cos\theta - i\sin\theta) \\ &\overset{i}{\rightarrow} r(\sin\theta - i\cos\theta) \overset{i}{\rightarrow} r(\cos\theta + i\sin\theta) \overset{i}{\rightarrow} \cdots \end{aligned} \tag{D.30}$$

which is geometrically shown in Figure D.1.

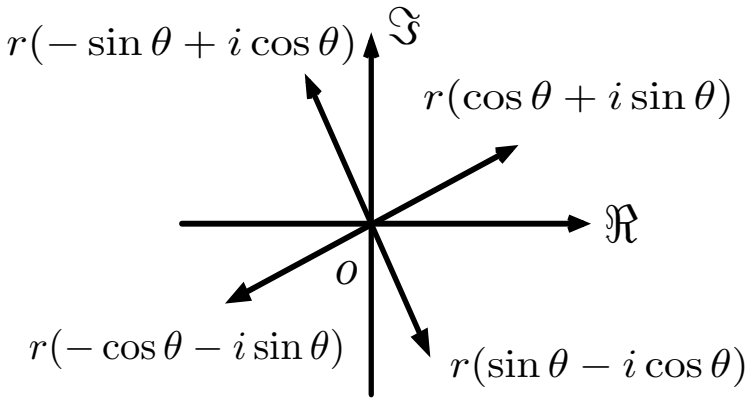

Figure D.1: 90° rotation in the complex plane.

By de Moivre's theorem, $(-i)$ corresponds to 270° rotation in the complex plane; $(-i) = (\cos 90° + i\sin 90°)^3$. Note that the y-component of the vector is now in the real part of the rotated vector. Thus, multiplying through $(-i)$ and taking the real part is identical to retrieving the y-component of the original vector. Now, for two complex numbers A and B, AB yields

$$AB = (\Re\{A\}\Re\{B\} - \Im\{A\}\Im\{B\}) + i(\Im\{A\}\Re\{B\} + \Re\{A\}\Im\{B\}) \quad \text{(D.31)}$$

and multiplying through $(-i)$ gives

$$(-i)AB = (\Im\{A\}\Re\{B\} + \Re\{A\}\Im\{B\}) + i(-\Re\{A\}\Re\{B\} + \Im\{A\}\Im\{B\}) \quad \text{(D.32)}$$

Thus, the operation by $(-i)$ can be considered as not only switching from x-component to y-component, but also switching the paring of $\Re\{A\}$, $\Im\{A\}$, $\Re\{B\}$, and $\Im\{B\}$. In the potential expression, C_{nm} is tied with the real part of b_{nm}, and S_{nm} is tied with the imaginary part of b_{nm}. However, multiplication by $(-i)$ disbands this relationship and pairs C_{nm} with the imaginary part of b_{nm} and S_{nm} with the real part of b_{nm}.

D.5.2 Second-order Partials in the Complex Plane

Successive applications of Equation D.28 and D.29 yields

$$\begin{bmatrix} \dfrac{\partial^2}{\partial x^2} & \dfrac{\partial^2}{\partial y \partial x} \\ \dfrac{\partial^2}{\partial x \partial y} & \dfrac{\partial^2}{\partial y^2} \end{bmatrix} = \begin{bmatrix} \left(\dfrac{\partial^2}{\partial \eta^2} + 2\dfrac{\partial^2}{\partial \eta \partial \xi} + \dfrac{\partial^2}{\partial \xi^2} \right) & (-i)\left(\dfrac{\partial^2}{\partial \eta^2} - \dfrac{\partial^2}{\partial \xi^2} \right) \\ (-i)\left(\dfrac{\partial^2}{\partial \eta^2} - \dfrac{\partial^2}{\partial \xi^2} \right) & -\left(\dfrac{\partial^2}{\partial \eta^2} - 2\dfrac{\partial^2}{\partial \eta \partial \xi} + \dfrac{\partial^2}{\partial \xi^2} \right) \end{bmatrix} \tag{D.33}$$

$$\begin{bmatrix} \dfrac{\partial^2}{\partial x \partial z} \\ \dfrac{\partial^2}{\partial y \partial z} \end{bmatrix} = \begin{bmatrix} \dfrac{\partial^2}{\partial \eta \partial z} + \dfrac{\partial^2}{\partial \xi \partial z} \\ (-i)\left(\dfrac{\partial^2}{\partial \eta \partial z} - \dfrac{\partial^2}{\partial \xi \partial z} \right) \end{bmatrix} \tag{D.34}$$

where assumption is made that $\dfrac{\partial^2}{\partial \eta \partial \xi} = \dfrac{\partial^2}{\partial \xi \partial \eta}$ for a smooth continuous function.

D.5.3 Partials of the Basis Function in the Cartesian Coordinates

The expressions of the higher-order partial derivatives are derived. The theory discussed here is based on the work by Cunningham [15]. The theory of complex conjugate rectifies the oversight made earlier when taking the partials. The overlook made is that a p-th order derivative of the associated Legendre function of order m yields an $(m-p)$-th order associated Legendre function, which is simply treated as zero when $m-p<0$. However, the resultant $(m-p)$-th order associated Legendre function is non-zero, as claimed by Cunningham, due to the property of the complex variables. Cunningham's method is described both for the exterior and interior gravity fields by Takahashi and Scheeres [69] and Takahashi et al. [70]; however, in this thesis, only the higher-order partials for the interior gravity field are derived.

First, the operators P and M are defined as

$$P = 2\frac{\partial}{\partial \eta} = \frac{\partial}{\partial x} + i\frac{\partial}{\partial y} \tag{D.35}$$

$$M = 2\frac{\partial}{\partial \xi} = \frac{\partial}{\partial x} - i\frac{\partial}{\partial y} \tag{D.36}$$

The important characteristics of P and M applied to the potential expression is that, when $PM = MP$ is applied, the expression reduces to the negative of the second-order partial with respect to z because of the Laplace's equation:

$$(PM)\,U = \left(\frac{\partial^2}{\partial x^2} + \frac{\partial^2}{\partial y^2}\right) U = -\left(\frac{\partial^2}{\partial z^2}\right) U \tag{D.37}$$

By leveraging the results by Werner [74], it can be shown that

$$P^s b^i_{nm} = \left(\frac{\partial}{\partial x} + i\frac{\partial}{\partial y}\right)^s b^i_{nm} = (-1)^s \left(\frac{1}{R^*}\right)^s b^i_{n-s,m+s} \tag{D.38}$$

$$M^q b^i_{nm} = \left(\frac{\partial}{\partial x} - i\frac{\partial}{\partial y}\right)^q b^i_{nm} = \frac{(n+m)!}{(n+m-2q)!}\left(\frac{1}{R^*}\right)^q b^i_{n-q,m-q} \tag{D.39}$$

$$\frac{\partial^\gamma b^i_{nm}}{\partial z^\gamma} = \frac{(n+m)!}{(n+m-\gamma)!}\left(\frac{1}{R^*}\right)^\gamma b^i_{n-\gamma,m} \tag{D.40}$$

where Equation D.39 is defined only when $m \geq q$. When $m < q$, Equation D.39 is rearranged to obtain

$$
\begin{aligned}
M^q b^i_{nm} &= \left(\frac{\partial}{\partial x} - i\frac{\partial}{\partial y}\right)^q b^i_{nm} \\
&= \left(\frac{\partial}{\partial x} - i\frac{\partial}{\partial y}\right)^{q-m} \left(\frac{\partial}{\partial x} - i\frac{\partial}{\partial y}\right)^m b^i_{nm} \qquad \text{(D.41)} \\
&= \left(\frac{\partial}{\partial x} - i\frac{\partial}{\partial y}\right)^{q-m} \frac{(n+m)!}{(n-m)!} \left(\frac{1}{R^*}\right)^m b^i_{n-m,0}
\end{aligned}
$$

Note that the zeroth-order of b^i contains only z and r^2, and successive applications of P and M for this type of function yield a conjugate pair g and $\tilde{g}$:

$$
\left(\frac{\partial}{\partial x} + i\frac{\partial}{\partial y}\right)^p f(z, r^2) = P^p f(z, r^2) = 2^p (x+iy)^p \frac{\partial^p f}{\partial (r^2)^p} = g \qquad \text{(D.42)}
$$

$$
\left(\frac{\partial}{\partial x} - i\frac{\partial}{\partial y}\right)^p f(z, r^2) = M^p f(z, r^2) = 2^p (x-iy)^p \frac{\partial^p f}{\partial (r^2)^p} = \tilde{g} \qquad \text{(D.43)}
$$

where the tilde denotes the complex conjugate. The power index of p appears due to the successive chain rule operations. For $m < q$, Equation D.41 and D.43 are used once the partial of the m-th order is related to the zeroth-order. Now, Equation D.38 is substituted with $s = q - m$, $n' = n - m$, and $m' = 0$ to get

$$
\left(\frac{\partial}{\partial x} + i\frac{\partial}{\partial y}\right)^s b^i_{n'm'} = \left(\frac{\partial}{\partial x} + i\frac{\partial}{\partial y}\right)^{q-m} b^i_{n-m,0} = (-1)^{q-m} \left(\frac{1}{R^*_i}\right)^{q-m} b^i_{n-q,q-m} \qquad \text{(D.44)}
$$

Thus, when $m < q$, the following expression is obtained by combining Equation D.41 and D.44:

$$
\left(\frac{\partial}{\partial x} - i\frac{\partial}{\partial y}\right)^q b^i_{nm} = (-1)^{q-m} \frac{(n+m)!}{(n-m)!} \left(\frac{1}{R^*_i}\right)^q \tilde{b}^i_{n-q,q-m} \qquad \text{(D.45)}
$$

For Equation D.39 to hold for any combination of m and q, Equation D.39 is equated with Equation D.45, with substitutions $n' = n + q$ and $m' = q - m$ as shown on the next page.

$$b^i_{n,-m} = (-1)^m \frac{(n-m)!}{(n+m)!} \tilde{b}^i_{n,m} \tag{D.46}$$

After rearranging Equation D.35 and D.36 to express the partial with respect to x and y, direct substitution yields the higher-order partials as

$$\begin{aligned} \frac{\partial^{\alpha+\beta+\gamma}}{\partial x^\alpha \partial y^\beta \partial z^\gamma} b^i_{nm} &= i^\beta \left(\frac{1}{R^*_i}\right)^{\alpha+\beta+\gamma} \\ &\quad \times \sum_{j=0}^{\alpha+\beta} \frac{(-1)^{\alpha-j}}{2^{\alpha+\beta}} \frac{(n+m)!}{(n+m-\gamma-2j)!} L_{\alpha,\beta,j} b^i_{n-\alpha-\beta-\gamma,m+\alpha+\beta-2j} \end{aligned} \tag{D.47}$$

where $L_{\alpha,\beta,j}$ is defined by Cunningham as

$$L_{\alpha,\beta,j} = \sum_{k=0}^{j} (-1)^k \binom{\alpha}{j-k} \binom{\beta}{k} \tag{D.48}$$

Equation D.47 is the final form of the partial of b^i_{nm}. Then, direct substitution yields the acceleration expressions in Equation 6.15 through 6.17. Explicit expressions for the dynamics matrix are listed in Section D.5.4.

D.5.4 Dynamics Matrix of the Interior Potential

The dynamics matrix as well as the partial derivatives of the acceleration with respect to the normalized interior spherical harmonic coefficients are presented in the next two sections. These parameters are required to compute the state transition matrix for OD purposes. Note that only five components are necessary to compute the second-order partial of the potential, as the Laplace's equation needs to be satisfied at all times.

D.5.4.1 Dynamics Matrix of the Unnormalized Interior Gravity Field

Using the results of Section D.5.3, the dynamics matrix of the unnormalized interior gravity field is given as follows.

$$
\begin{aligned}
\frac{\partial^2 U^i}{\partial x^2} &\overset{m\geq 1}{=} \frac{1}{4}\frac{GM^*}{(R_i^*)^3}\begin{bmatrix} C_{nm}^i \\ S_{nm}^i \end{bmatrix} \cdot \left[b_{n-2,m+2}^i - 2\frac{(n+m)!}{(n+m-2)!} b_{n-2,m}^i + \frac{(n+m)!}{(n+m-4)!} b_{n-2,m-2}^i \right] \\
&\overset{m=1}{=} \frac{1}{4}\frac{GM^*}{(R_i^*)^3}\begin{bmatrix} C_{n,1}^i \\ S_{n,1}^i \end{bmatrix} \cdot \left[b_{n-2,3}^i - \frac{(n+1)!}{(n-1)!}\begin{bmatrix} 3\Re\left\{b_{n-2,1}^i\right\} \\ \Im\left\{b_{n-2,1}^i\right\} \end{bmatrix} \right] \\
&\overset{m=0}{=} \frac{1}{2}\frac{GM^*}{(R_i^*)^3}\begin{bmatrix} C_{n,0}^i \\ S_{n,0}^i \end{bmatrix} \cdot \left[b_{n-2,2}^i - \frac{n!}{(n-2)!} b_{n-2,0}^i \right]
\end{aligned}
\tag{D.49}
$$

$$
\begin{aligned}
\frac{\partial^2 U^i}{\partial y \partial x} &\overset{m\geq 1}{=} \frac{1}{4}\frac{GM^*}{(R_i^*)^3}\begin{bmatrix} -S_{nm}^i \\ C_{nm}^i \end{bmatrix} \cdot \left[b_{n-2,m+2}^i - \frac{(n+m)!}{(n+m-4)!} \tilde{b}_{n-2,m-2}^i \right] \\
&\overset{m=1}{=} \frac{1}{4}\frac{GM^*}{(R_i^*)^3}\begin{bmatrix} -S_{n,1}^i \\ C_{n,1}^i \end{bmatrix} \cdot \left[b_{n-2,3}^i + \frac{(n+1)!}{(n-1)!}\begin{bmatrix} \Re\left\{b_{n-2,1}^i\right\} \\ -\Im\left\{b_{n-2,1}^i\right\} \end{bmatrix} \right] \\
&\overset{m=0}{=} \frac{1}{2}\frac{GM^*}{(R_i^*)^3}\begin{bmatrix} -S_{n,0}^i \\ C_{n,0}^i \end{bmatrix} \cdot \left[b_{n-2,2}^i \right]
\end{aligned}
\tag{D.50}
$$

$$
\begin{aligned}
\frac{\partial^2 U^i}{\partial y^2} &\overset{m\geq 1}{=} -\frac{1}{4}\frac{GM^*}{(R_i^*)^3}\begin{bmatrix} C_{nm}^i \\ S_{nm}^i \end{bmatrix} \cdot \left[b_{n-2,m+2}^i + 2\frac{(n+m)!}{(n+m-2)!} b_{n-2,m}^i + \frac{(n+m)!}{(n+m-4)!} b_{n-2,m-2}^i \right] \\
&\overset{m=1}{=} -\frac{1}{4}\frac{GM^*}{(R_i^*)^3}\begin{bmatrix} C_{n,1}^i \\ S_{n,1}^i \end{bmatrix} \cdot \left[b_{n-2,3}^i + \frac{(n+1)!}{(n-1)!}\begin{bmatrix} \Re\left\{b_{n-2,1}^i\right\} \\ 3\Im\left\{b_{n-2,1}^i\right\} \end{bmatrix} \right] \\
&\overset{m=0}{=} -\frac{1}{2}\frac{GM^*}{(R_i^*)^3}\begin{bmatrix} C_{n,0}^i \\ S_{n,0}^i \end{bmatrix} \cdot \left[b_{n-2,2}^i + \frac{n!}{(n-2)!} b_{n-2,0}^i \right]
\end{aligned}
\tag{D.51}
$$

$$\frac{\partial^2 U^i}{\partial x \partial z} \overset{m\geq 0}{=} \frac{1}{2}\frac{GM^*}{(R_i^*)^3}\begin{bmatrix} C_{nm}^i \\ S_{nm}^i \end{bmatrix} \cdot \left[-(n+m)b_{n-2,m+1}^i + \frac{(n+m)!}{(n+m-3)!}b_{n-2,m-1}^i\right]$$

$$\overset{m=0}{=} \frac{GM^*}{(R_i^*)^3}\begin{bmatrix} C_{n,0}^i \\ S_{n,0}^i \end{bmatrix} \cdot \left[-nb_{n-2,1}^i\right] \tag{D.52}$$

$$\frac{\partial^2 U^i}{\partial y \partial z} \overset{m\geq 0}{=} \frac{1}{2}\frac{GM^*}{(R_i^*)^3}\begin{bmatrix} -S_{nm}^i \\ C_{nm}^i \end{bmatrix} \cdot \left[-(n+m)b_{n-2,m+1}^i - \frac{(n+m)!}{(n+m-3)!}b_{n-2,m-1}^i\right]$$

$$\overset{m=0}{=} \frac{GM^*}{(R_i^*)^3}\begin{bmatrix} -S_{n,0}^i \\ C_{n,0}^i \end{bmatrix} \cdot \left[-nb_{n-2,1}^i\right] \tag{D.53}$$

$$\frac{\partial^2 U^i}{\partial z^2} = \frac{GM^*}{(R_i^*)^3}\begin{bmatrix} C_{nm}^i \\ S_{nm}^i \end{bmatrix} \cdot \left[\frac{(n+m)!}{(n+m-2)!}b_{n-2,m}^i\right] \tag{D.54}$$

Although the summation notation is omitted, contribution from each degree and order spherical harmonic coefficient must be summed in the above expressions. Also, note that some elements of the basis function do not exist. That is, one needs to ensure that the degree of the basis function is either larger or equal to the order of the basis function. For example, when $n = 2$ and $m = 1$, neither $b_{n-2,3}^i$ nor $b_{n-2,1}^i$ appears in Equation D.49.

D.5.4.2 Dynamics Matrix with respect to the Unnormalized Interior Spherical Harmonic Coefficients

The components that fill in the dynamics matrix for the spherical harmonic coefficients are obtained by taking the partial of the acceleration with respect to the spherical harmonic coefficients. That is, the acceleration expressions in Equation 6.15 through 6.17 are divided by the corresponding spherical harmonic coefficients.

$$\frac{\partial \ddot{x}}{\partial C_{nm}^i} = \frac{GM^*}{(R_i^*)^2}\left[-g_1^i(n,m)\Re\left\{b_{n-1,m+1}^i\right\} + g_2^i(n,m)\Re\left\{b_{n-1,m-1}^i\right\}\right] \tag{D.55}$$

$$\frac{\partial \ddot{x}}{\partial S_{nm}^i} = \frac{GM^*}{(R_i^*)^2}\left[-g_1^i(n,m)\Im\left\{b_{n-1,m+1}^i\right\} + g_2^i(n,m)\Im\left\{b_{n-1,m-1}^i\right\}\right] \tag{D.56}$$

$$\frac{\partial \ddot{y}}{\partial C_{nm}^i} = \frac{GM^*}{(R_i^*)^2}\left[-g_1^i(n,m)\Im\left\{b_{n-1,m+1}^i\right\} - g_2^i(n,m)\Im\left\{b_{n-1,m-1}^i\right\}\right] \tag{D.57}$$

$$\frac{\partial \ddot{y}}{\partial S_{nm}^i} = \frac{GM^*}{(R_i^*)^2}\left[g_1^i(n,m)\Re\left\{b_{n-1,m+1}^i\right\} + g_2^i(n,m)\Re\left\{b_{n-1,m-1}^i\right\}\right] \tag{D.58}$$

$$\frac{\partial \ddot{z}}{\partial C_{nm}^i} = \frac{GM^*}{(R_i^*)^2}\left[g_3^i(n,m)\Re\left\{b_{n-1,m+1}^i\right\}\right] \tag{D.59}$$

$$\frac{\partial \ddot{z}}{\partial S_{nm}^i} = \frac{GM^*}{(R_i^*)^2}\left[g_3^i(n,m)\Im\left\{b_{n-1,m+1}^i\right\}\right] \tag{D.60}$$

where $g_1^i(n,m)$, $g_2^i(n,m)$, and $g_3^i(n,m)$ are defined as

$$\begin{cases} g_1^i(n,m) = \dfrac{1}{2}(1+\delta_{0,m}) \\ g_2^i(n,m) = \dfrac{1}{2}\dfrac{(n+m)!}{(n+m-2)!} \\ g_3^i(n,m) = (n+m) \end{cases} \tag{D.61}$$

In contrast to the dynamics matrix expressions in Section D.5.4.1, it is unnecessary to sum over degree and order.

D.5.4.3 Dynamics Matrix of the Normalized Interior Gravity Field

The dynamics matrix of the normalized interior gravity field is given as

$$\begin{aligned}
\frac{\partial^2 U^i}{\partial x^2} \overset{m\geq 1}{=} & \frac{1}{4}\frac{GM^*}{(R_i^*)^3}\begin{bmatrix}\bar{C}^i_{nm}\\ \bar{S}^i_{nm}\end{bmatrix}\cdot\Bigg[\sqrt{\frac{(2n+1)}{(2n-3)}\frac{(n-m)!}{(n-m-4)!}}\bar{b}^i_{n-2,m+2} \\
& -2\sqrt{\frac{(2n+1)}{(2n-3)}\frac{(n+m)!}{(n+m-2)!}\frac{(n-m)!}{(n-m-2)!}}\bar{b}^i_{n-2,m} \\
& +\sqrt{\frac{2}{(2-\delta_{2,m})}\frac{(2n+1)}{(2n-3)}\frac{(n+m)!}{(n+m-4)!}}\bar{b}^i_{n-2,m-2}\Bigg] \\
\overset{m=1}{=} & \frac{1}{4}\frac{GM^*}{(R_i^*)^3}\begin{bmatrix}\bar{C}^i_{n,1}\\ \bar{S}^i_{n,1}\end{bmatrix}\cdot\left[\sqrt{\frac{(2n+1)}{(2n-3)}\frac{(n-1)!}{(n-5)!}}\bar{b}^i_{n-2,3}-\sqrt{\frac{(2n+1)}{(2n-3)}\frac{(n+1)!}{(n-3)!}}\begin{bmatrix}3\Re\left\{\bar{b}^i_{n-2,1}\right\}\\ \Im\left\{\bar{b}^i_{n-2,1}\right\}\end{bmatrix}\right] \\
\overset{m=0}{=} & \frac{1}{2}\frac{GM^*}{(R_i^*)^3}\begin{bmatrix}\bar{C}^i_{n,0}\\ \bar{S}^i_{n,0}\end{bmatrix}\cdot\left[\sqrt{\frac{1}{2}\frac{(2n+1)}{(2n-3)}\frac{n!}{(n-4)!}}\bar{b}^i_{n-2,2}-\frac{n!}{(n-2)!}\sqrt{\frac{(2n+1)}{(2n-3)}}\bar{b}^i_{n-2,0}\right]
\end{aligned} \tag{D.62}$$

$$\begin{aligned}
\frac{\partial^2 U^i}{\partial y \partial x} \overset{m\geq 1}{=} & \frac{1}{4}\frac{GM^*}{(R_i^*)^3}\begin{bmatrix}-\bar{S}^i_{nm}\\ \bar{C}^i_{nm}\end{bmatrix}\cdot\Bigg[\sqrt{\frac{(2n+1)}{(2n-3)}\frac{(n-m)!}{(n-m-4)!}}\bar{b}^i_{n-2,m+2} \\
& -\sqrt{\frac{2}{(2-\delta_{2,m})}\frac{(2n+1)}{(2n-3)}\frac{(n+m)!}{(n+m-4)!}}\bar{b}^i_{n-2,m-2}\Bigg] \\
\overset{m=1}{=} & \frac{1}{4}\frac{GM^*}{(R_i^*)^3}\begin{bmatrix}-\bar{S}^i_{n,1}\\ \bar{C}^i_{n,1}\end{bmatrix}\cdot\left[\sqrt{\frac{(2n+1)}{(2n-3)}\frac{(n-1)!}{(n-5)!}}\bar{b}^i_{n-2,3}+\sqrt{\frac{(2n+1)}{(2n-3)}\frac{(n+1)!}{(n-3)!}}\begin{bmatrix}\Re\left\{\bar{b}^i_{n-2,1}\right\}\\ -\Im\left\{\bar{b}^i_{n-2,1}\right\}\end{bmatrix}\right] \\
\overset{m=0}{=} & \frac{1}{2}\frac{GM^*}{(R_i^*)^3}\begin{bmatrix}-\bar{S}^i_{n,0}\\ \bar{C}^i_{n,0}\end{bmatrix}\cdot\left[\sqrt{\frac{1}{2}\frac{(2n+1)}{(2n-3)}\frac{n!}{(n-4)!}}\bar{b}^i_{n-2,2}\right]
\end{aligned} \tag{D.63}$$

$$\frac{\partial^2 U^i}{\partial y^2} \overset{m\geq 1}{=} -\frac{1}{4}\frac{GM^*}{(R_i^*)^3}\begin{bmatrix}\bar{C}^i_{nm}\\ \bar{S}^i_{nm}\end{bmatrix}\cdot\Bigg[\sqrt{\frac{(2n+1)}{(2n-3)}\frac{(n-m)!}{(n-m-4)!}}\bar{b}^i_{n-2,m+2}$$
$$+2\sqrt{\frac{(2n+1)}{(2n-3)}\frac{(n+m)!}{(n+m-2)!}\frac{(n-m)!}{(n-m-2)!}}\bar{b}^i_{n-2,m} \tag{D.64}$$
$$+\sqrt{\frac{2}{(2-\delta_{2,m})}\frac{(2n+1)}{(2n-3)}\frac{(n+m)!}{(n+m-4)!}}\bar{b}^i_{n-2,m-2}\Bigg]$$

$$\overset{m=1}{=} -\frac{1}{4}\frac{GM^*}{(R_i^*)^3}\begin{bmatrix}\bar{C}^i_{n,1}\\ \bar{S}^i_{n,1}\end{bmatrix}\cdot\left[\sqrt{\frac{(2n+1)}{(2n-3)}\frac{(n-1)!}{(n-5)!}}\bar{b}^i_{n-2,3}+\sqrt{\frac{(2n+1)}{(2n-3)}\frac{(n+1)!}{(n-3)!}}\begin{bmatrix}\Re\left\{\bar{b}^i_{n-2,1}\right\}\\ 3\Im\left\{\bar{b}^i_{n-2,1}\right\}\end{bmatrix}\right]$$

$$\overset{m=0}{=} -\frac{1}{2}\frac{GM^*}{(R_i^*)^3}\begin{bmatrix}\bar{C}^i_{n,0}\\ \bar{S}^i_{n,0}\end{bmatrix}\cdot\left[\sqrt{\frac{1}{2}\frac{(2n+1)}{(2n-3)}\frac{n!}{(n-4)!}}\bar{b}^i_{n-2,2}+\frac{n!}{(n-2)!}\sqrt{\frac{(2n+1)}{(2n-3)}}\bar{b}^i_{n-2,0}\right]$$

$$\frac{\partial^2 U^i}{\partial x\partial z} \overset{m\geq 0}{=} \frac{1}{2}\frac{GM^*}{(R_i^*)^3}\begin{bmatrix}\bar{C}^i_{nm}\\ \bar{S}^i_{nm}\end{bmatrix}\cdot\Bigg[-\sqrt{\frac{(2n+1)}{(2n-3)}\frac{(n-m)!}{(n-m-3)!}(n+m)}\bar{b}^i_{n-2,m+1}$$
$$+\sqrt{\frac{2}{(2-\delta_{1,m})}\frac{(2n+1)}{(2n-3)}\frac{(n+m)!}{(n+m-3)!}\frac{(n-m)!}{(n-m-1)!}}\bar{b}^i_{n-2,m-1}\Bigg] \tag{D.65}$$

$$\overset{m=0}{=} \frac{GM^*}{(R_i^*)^3}\begin{bmatrix}\bar{C}^i_{n,0}\\ \bar{S}^i_{n,0}\end{bmatrix}\cdot\left[-\sqrt{\frac{n}{2}\frac{(2n+1)}{(2n-3)}\frac{n!}{(n-3)!}}\bar{b}^i_{n-2,1}\right]$$

$$\frac{\partial^2 U^i}{\partial y\partial z} \overset{m\geq 0}{=} \frac{1}{2}\frac{GM^*}{(R_i^*)^3}\begin{bmatrix}-\bar{S}^i_{nm}\\ \bar{C}^i_{nm}\end{bmatrix}\cdot\Bigg[-\sqrt{\frac{(2n+1)}{(2n-3)}\frac{(n-m)!}{(n-m-3)!}(n+m)}\bar{b}^i_{n-2,m+1}$$
$$-\sqrt{\frac{2}{(2-\delta_{1,m})}\frac{(2n+1)}{(2n-3)}\frac{(n+m)!}{(n+m-3)!}\frac{(n-m)!}{(n-m-1)!}}\bar{b}^i_{n-2,m-1}\Bigg] \tag{D.66}$$

$$\overset{m=0}{=} \frac{GM^*}{(R_i^*)^3}\begin{bmatrix}-\bar{S}^i_{n,0}\\ \bar{C}^i_{n,0}\end{bmatrix}\cdot\left[-\sqrt{\frac{n}{2}\frac{(2n+1)}{(2n-3)}\frac{n!}{(n-3)!}}\bar{b}^i_{n-2,1}\right]$$

$$\frac{\partial^2 U^i}{\partial z^2} = \frac{GM^*}{(R_i^*)^3}\begin{bmatrix}\bar{C}^i_{nm}\\ \bar{S}^i_{nm}\end{bmatrix}\cdot\left[\sqrt{\frac{(2n+1)}{(2n-3)}\frac{(n+m)!}{(n+m-2)!}\frac{(n-m)!}{(n-m-2)!}}\bar{b}^i_{n-2,m}\right] \tag{D.67}$$

Again, summation over degree and order is necessary.

D.5.4.4 Dynamics Matrix with respect to the Normalized Interior Spherical Harmonic Coefficients

The partials of the acceleration with respect to the normalized interior spherical harmonic coefficients are given as

$$\frac{\partial \ddot{x}}{\partial \bar{C}^i_{nm}} = \frac{GM^*}{(R_i^*)^2}\left[-\bar{g}^i_1(n,m)\Re\left\{\bar{b}^i_{n-1,m+1}\right\} + \bar{g}^i_2(n,m)\Re\left\{\bar{b}^i_{n-1,m-1}\right\}\right] \tag{D.68}$$

$$\frac{\partial \ddot{x}}{\partial \bar{S}^i_{nm}} = \frac{GM^*}{(R_i^*)^2}\left[-\bar{g}^i_1(n,m)\Im\left\{\bar{b}^i_{n-1,m+1}\right\} + \bar{g}^i_2(n,m)\Im\left\{\bar{b}^i_{n-1,m-1}\right\}\right] \tag{D.69}$$

$$\frac{\partial \ddot{y}}{\partial \bar{C}^i_{nm}} = \frac{GM^*}{(R_i^*)^2}\left[-\bar{g}^i_1(n,m)\Im\left\{\bar{b}^i_{n-1,m+1}\right\} - \bar{g}^i_2(n,m)\Im\left\{\bar{b}^i_{n-1,m-1}\right\}\right] \tag{D.70}$$

$$\frac{\partial \ddot{y}}{\partial \bar{S}^i_{nm}} = \frac{GM^*}{(R_i^*)^2}\left[\bar{g}^i_1(n,m)\Re\left\{\bar{b}^i_{n-1,m+1}\right\} + \bar{g}^i_2(n,m)\Re\left\{\bar{b}^i_{n-1,m-1}\right\}\right] \tag{D.71}$$

$$\frac{\partial \ddot{z}}{\partial \bar{C}^i_{nm}} = \frac{GM^*}{(R_i^*)^2}\left[\bar{g}^i_3(n,m)\Re\left\{\bar{b}^i_{n-1,m+1}\right\}\right] \tag{D.72}$$

$$\frac{\partial \ddot{z}}{\partial \bar{S}^i_{nm}} = \frac{GM^*}{(R_i^*)^2}\left[\bar{g}^i_3(n,m)\Im\left\{\bar{b}^i_{n-1,m+1}\right\}\right] \tag{D.73}$$

where

$$\begin{cases} \bar{g}_1^i(n,m) &= \dfrac{1}{2}(1+\delta_{0,m})\sqrt{\dfrac{(2-\delta_{0,m})}{(2-\delta_{0,m+1})}\dfrac{(2n+1)}{(2n-1)}\dfrac{(n-m)!}{(n-m-2)!}} \\ \bar{g}_2^i(n,m) &= \dfrac{1}{2}\sqrt{\dfrac{(2-\delta_{0,m})}{(2-\delta_{1,m})}\dfrac{(2n+1)}{(2n-1)}\dfrac{(n+m)!}{(n+m-2)!}} \\ \bar{g}_3^i(n,m) &= \sqrt{\dfrac{(2n+1)}{(2n-1)}(n+m)(n-m)} \end{cases} \tag{D.74}$$

It is not necessary to sum over degree and order.

D.6 Two Bases in the First-order Partial Derivatives

We seek to express the field point acceleration by anchoring the summation to b_{nm} or c_{nm}. We derive these expressions for both the exterior and interior gravity fields.

D.6.1 Exterior Gravity Field

As mentioned earlier, the potential expression is in its complete form when the imaginary part is included, and 270° rotation of a vector occurs when taking the partial with respect to y. Now, let us simply follow the rules of the partial derivatives described so far to find the acceleration due to the exterior gravity field.

$$
\begin{aligned}
\frac{\partial U^e}{\partial x} &= \frac{GM^*}{R_e^*}\sum_{n=0}^{\infty}\sum_{m=0}^{n}\Re\left\{K_{nm}^e\frac{\partial b_{nm}^e}{\partial x}\right\} \\
&= \frac{GM^*}{R_e^*}\sum_{n=0}^{\infty}\sum_{m=0}^{n}\Re\left\{K_{nm}^e\left(\frac{\partial b_{nm}^e}{\partial \eta}+\frac{\partial b_{nm}^e}{\partial \xi}\right)\right\} \qquad \text{(D.75)} \\
&= \frac{GM^*}{R_e^*}\sum_{n=0}^{\infty}\sum_{m=0}^{n}\Re\left\{\left[C_{nm}^e\left(\frac{\partial\left[\Re\left\{b_{nm}^e\right\}\right]}{\partial \eta}+\frac{\partial\left[\Re\left\{b_{nm}^e\right\}\right]}{\partial \xi}\right)+S_{nm}^e\left(\frac{\partial\left[\Im\left\{b_{nm}^e\right\}\right]}{\partial \eta}+\frac{\partial\left[\Im\left\{b_{nm}^e\right\}\right]}{\partial \xi}\right)\right]\right. \\
&\quad \left.+i\left[-S_{nm}^e\left(\frac{\partial\left[\Re\left\{b_{nm}^e\right\}\right]}{\partial \eta}+\frac{\partial\left[\Re\left\{b_{nm}^e\right\}\right]}{\partial \xi}\right)+C_{nm}^e\left(\frac{\partial\left[\Im\left\{b_{nm}^e\right\}\right]}{\partial \eta}+\frac{\partial\left[\Im\left\{b_{nm}^e\right\}\right]}{\partial \xi}\right)\right]\right\} \\
&= \frac{GM^*}{R_e^*}\sum_{n=0}^{\infty}\sum_{m=0}^{n}\left[C_{nm}^e\left(\frac{\partial\left[\Re\left\{b_{nm}^e\right\}\right]}{\partial \eta}+\frac{\partial\left[\Re\left\{b_{nm}^e\right\}\right]}{\partial \xi}\right)+S_{nm}^e\left(\frac{\partial\left[\Im\left\{b_{nm}^e\right\}\right]}{\partial \eta}+\frac{\partial\left[\Im\left\{b_{nm}^e\right\}\right]}{\partial \xi}\right)\right] \\
&= \frac{GM^*}{R_e^*}\sum_{n=0}^{\infty}\sum_{m=0}^{n}\Re\left\{K_{nm}^e\left(\alpha_{n+1,m+1}^{e,x}b_{n+1,m+1}^e+\beta_{n+1,m-1}^{e,x}b_{n+1,m-1}^e\right)\right\} \\
&= \frac{GM^*}{R_e^*}\sum_{n=0+1}^{\infty+1}\sum_{m=0}^{n}\Re\left\{\left[K_{nm}^e\right]_x b_{nm}^e\right\}
\end{aligned}
$$

This seemingly ordinary equation contains a wealth of information about the structure of the field point acceleration. First, $\Re\{\}$ bracketing the whole expression in the double summation appears because we only consider the real part of the potential expression. Recall that K_{nm}^e is merely a constant, and we only need to take the partial of b_{nm}^e. Now we invoke Equation D.28 to take the partial of x via η and ξ. Then, the second line immediately falls out of the definition of the partials. We list its components individually in the third line, making it clear which term is included in the real part and which term is in the imaginary part. By applying the $\Re\{\}$ operator, we obtain the fourth line, and we see that the real part of b_{nm}^e is associated with C_{nm}, and the imaginary part of b_{nm}^e is associated with S_{nm}.

We realize that the second line is identical to the fifth line, due to the recursive formulae of the partial derivative of b_{nm}^e, where $\alpha_{n+1,m+1}^{e,x}$ and $\beta_{n+1,m+1}^{e,x}$ incorporate all the coefficients given by R_e^*, n, and m. A closer look at the fifth line reveals that K_{nm}^e serves as the basis of the double

summation. Alternatively, we can switch the point of view and set the basis to b^e_{nm} in the double summation. Note that, in the fifth line, b_{00} term does not appear, and the summation starts from $n = 1$, and $n_{max} + 1$ terms appear due to the recursion formula. In other words, we can switch the double summation from $n = 0 \rightarrow n_{max}$ to $n = 1 \rightarrow n_{max} + 1$ for each basis function b^e_{nm} and define the coefficient $[K^e_{nm}]_x$. We know $[K^e_{nm}]_x$ is a function of two interior spherical harmonic coefficients as b^e_{nm} appears precisely twice in the double summation when $(n', m') = (n-1, m-1)$ and $(n'', m'') = (n-1, m+1)$.

For the exterior harmonics, the data flows downward since the partial of the basis function of degree n depends on the that of degree $n+1$. This downward flow of the data is the source of $+1$ in the sixth line of the equation. As we will see, the cascade is in the opposite direction for the interior gravity field.

We can perform the same operation to the partial with respect to y and z to get

$$
\begin{aligned}
\frac{\partial U^e}{\partial y} &= \frac{GM^*}{R^*_e} \sum_{n=0}^{\infty} \sum_{m=0}^{n} \Re \left\{ K^e_{nm} \frac{\partial b^e_{nm}}{\partial y} \right\} \qquad \text{(D.76)} \\
&= \frac{GM^*}{R^*_e} \sum_{n=0}^{\infty} \sum_{m=0}^{n} \left[-S^e_{nm} \left(\frac{\partial \left[\Re \left\{ b^e_{nm} \right\} \right]}{\partial \eta} - \frac{\partial \left[\Re \left\{ b^e_{nm} \right\} \right]}{\partial \xi} \right) + C^e_{nm} \left(\frac{\partial \left[\Im \left\{ b^e_{nm} \right\} \right]}{\partial \eta} - \frac{\partial \left[\Im \left\{ b^e_{nm} \right\} \right]}{\partial \xi} \right) \right] \\
&= \frac{GM^*}{R^*_e} \sum_{n=0}^{\infty} \sum_{m=0}^{n} \Re \left\{ (-i) K^e_{nm} \left(\alpha^{e,y}_{n+1,m+1} b^e_{n+1,m+1} + \beta^{e,y}_{n+1,m-1} b^e_{n+1,m-1} \right) \right\} \\
&= \frac{GM^*}{R^*_e} \sum_{n=0+1}^{\infty+1} \sum_{m=0}^{n} \Re \left\{ \left[K^e_{nm} \right]_y b^e_{nm} \right\}
\end{aligned}
$$

$$\begin{aligned}
\frac{\partial U^e}{\partial z} &= \frac{GM^*}{R_e^*}\sum_{n=0}^{\infty}\sum_{m=0}^{n}\Re\left\{K_{nm}^e\frac{\partial b_{nm}^e}{\partial z}\right\} \\
&= \frac{GM^*}{R_e^*}\sum_{n=0}^{\infty}\sum_{m=0}^{n}\left[C_{nm}^e\left(\frac{\partial\left[\Re\left\{b_{nm}^e\right\}\right]}{\partial z}\right)+S_{nm}^e\left(\frac{\partial\left[\Im\left\{b_{nm}^e\right\}\right]}{\partial z}\right)\right] \qquad \text{(D.77)} \\
&= \frac{GM^*}{R_e^*}\sum_{n=0}^{\infty}\sum_{m=0}^{n}\Re\left\{K_{nm}^e\alpha_{n+1,m}^{e,z}b_{n+1,m}^e\right\} \\
&= \frac{GM^*}{R_e^*}\sum_{n=0+1}^{\infty+1}\sum_{m=0}^{n}\Re\left\{\left[K_{nm}^e\right]_z b_{nm}^e\right\}
\end{aligned}$$

Note that the partial with respect to z also requires $\Re\{\}$ because we are working only on the real part of the potential.

D.6.2 Interior Gravity Field

As with the exterior gravity field, we can perform the same operation for the interior gravity field to get

$$\begin{aligned}
\frac{\partial U^i}{\partial x} &= \frac{GM^*}{R_i^*}\sum_{n=0}^{\infty}\sum_{m=0}^{n}\Re\left\{K_{nm}^i\frac{\partial b_{nm}^i}{\partial x}\right\} \qquad \text{(D.78)} \\
&= \frac{GM^*}{R_i^*}\sum_{n=0}^{\infty}\sum_{m=0}^{n}\left[C_{nm}^i\left(\frac{\partial\left[\Re\left\{b_{nm}^i\right\}\right]}{\partial\eta}+\frac{\partial\left[\Re\left\{b_{nm}^i\right\}\right]}{\partial\xi}\right)+S_{nm}^i\left(\frac{\partial\left[\Im\left\{b_{nm}^i\right\}\right]}{\partial\eta}+\frac{\partial\left[\Im\left\{b_{nm}^i\right\}\right]}{\partial\xi}\right)\right] \\
&= \frac{GM^*}{R_i^*}\sum_{n=0}^{\infty}\sum_{m=0}^{n}\Re\left\{K_{nm}^i\left(\alpha_{n-1,m+1}^{i,x}b_{n-1,m+1}^i+\beta_{n-1,m-1}^{i,x}b_{n-1,m-1}^i\right)\right\} \\
&= \frac{GM^*}{R_i^*}\sum_{n=0-1}^{\infty-1}\sum_{m=0}^{n}\Re\left\{\left[K_{nm}^i\right]_x b_{nm}^i\right\}
\end{aligned}$$

For the interior gravity field, the data flows upward. That is, the partial of the basis function of degree n is a function of the basis function of degree $n-1$. Now, recall that the zeroth-degree

term corresponds to the bias term in the interior potential, thereby yielding no contribution to the acceleration. This is explicitly observed in the third line of the above equation, where C^i_{00} term has no data flow from $n = -1$. By anchoring the summation to b^i_{nm}, we obtain the fourth line, and we intentionally leave -1 in the summation index to remind ourselves that the data flows upward. Similarly, the partials with respect to y and z are given as

$$\begin{aligned}
\frac{\partial U^i}{\partial y} &= \frac{GM^*}{R^*_i}\sum_{n=0}^{\infty}\sum_{m=0}^{n}\Re\left\{K^i_{nm}\frac{\partial b^i_{nm}}{\partial y}\right\} \qquad \text{(D.79)}\\
&= \frac{GM^*}{R^*_i}\sum_{n=0}^{\infty}\sum_{m=0}^{n}\left[-S^i_{nm}\left(\frac{\partial\left[\Re\left\{b^i_{nm}\right\}\right]}{\partial\eta}-\frac{\partial\left[\Re\left\{b^i_{nm}\right\}\right]}{\partial\xi}\right)+C^i_{nm}\left(\frac{\partial\left[\Im\left\{b^i_{nm}\right\}\right]}{\partial\eta}-\frac{\partial\left[\Im\left\{b^i_{nm}\right\}\right]}{\partial\xi}\right)\right]\\
&= \frac{GM^*}{R^*_i}\sum_{n=0}^{\infty}\sum_{m=0}^{n}\Re\left\{(-i)K^i_{nm}\left(\alpha^{i,y}_{n-1,m+1}b^i_{n-1,m+1}+\beta^{i,y}_{n-1,m-1}b^i_{n-1,m-1}\right)\right\}\\
&= \frac{GM^*}{R^*_i}\sum_{n=0-1}^{\infty-1}\sum_{m=0}^{n}\Re\left\{\left[K^i_{nm}\right]_y b^i_{nm}\right\}
\end{aligned}$$

$$\begin{aligned}
\frac{\partial U^i}{\partial z} &= \frac{GM^*}{R^*_i}\sum_{n=0}^{\infty}\sum_{m=0}^{n}\Re\left\{K^i_{nm}\frac{\partial b^i_{nm}}{\partial z}\right\}\\
&= \frac{GM^*}{R^*_i}\sum_{n=0}^{\infty}\sum_{m=0}^{n}\left[C^i_{nm}\left(\frac{\partial\left[\Re\left\{b^i_{nm}\right\}\right]}{\partial z}\right)+S^i_{nm}\left(\frac{\partial\left[\Im\left\{b^i_{nm}\right\}\right]}{\partial z}\right)\right] \qquad \text{(D.80)}\\
&= \frac{GM^*}{R^*_i}\sum_{n=0}^{\infty}\sum_{m=0}^{n}\Re\left\{K^i_{nm}\alpha^{i,z}_{n-1,m}b^i_{n-1,m}\right\}\\
&= \frac{GM^*}{R^*_i}\sum_{n=0-1}^{\infty-1}\sum_{m=0}^{n}\Re\left\{\left[K^i_{nm}\right]_z b^i_{nm}\right\}
\end{aligned}$$

D.7 List of Interior Spherical Harmonic Coefficients

The values of the interior spherical harmonic coefficients used to propagate the spacecraft dynamics in Section 6.4.2 are listed. The TAG point coordinates are $[-0.344, -0.0677, 0.374]$ $[km]$, and the interior Brillouin radius is $R_i^* = 2.5$ $[km]$. For space purposes, we only provide 12×12 interior spherical harmonic coefficients. Note that the zeroth degree coefficient is the bias term plus the constant offset of the potential.

Table D.1: Numerically approximated normalized interior spherical harmonic coefficients (Section 6.3.1).

Degree (n)	Order (m)	$\bar{C}^i_{nm}$	$\bar{S}^i_{nm}$
0	0	$8.671933803 \times 10^{-1}$	-
1	0	$-4.294875615 \times 10^{-1}$	-
1	1	$8.120673749 \times 10^{-3}$	$2.303011756 \times 10^{-2}$
2	0	$2.822870503 \times 10^{-1}$	-
2	1	$-8.505578460 \times 10^{-3}$	$-2.640537399 \times 10^{-2}$
2	2	$2.978959177 \times 10^{-3}$	$4.621403642 \times 10^{-4}$
3	0	$-2.002014182 \times 10^{-1}$	-
3	1	$7.633131661 \times 10^{-3}$	$2.682639552 \times 10^{-2}$
3	2	$-4.791030429 \times 10^{-3}$	$-6.855587939 \times 10^{-4}$
3	3	$1.976597828 \times 10^{-4}$	$3.152131075 \times 10^{-4}$
4	0	$1.463890291 \times 10^{-1}$	-
4	1	$-6.164070060 \times 10^{-3}$	$-2.573112741 \times 10^{-2}$
4	2	$6.166920346 \times 10^{-3}$	$7.875589106 \times 10^{-4}$
4	3	$-3.842986975 \times 10^{-4}$	$-6.205334437 \times 10^{-4}$
4	4	$1.799867656 \times 10^{-5}$	$2.482523910 \times 10^{-5}$
5	0	$-1.084534526 \times 10^{-1}$	-
5	1	$4.475721057 \times 10^{-3}$	$2.384408182 \times 10^{-2}$
5	2	$-7.137395844 \times 10^{-3}$	$-7.884700939 \times 10^{-4}$
5	3	$5.764797719 \times 10^{-4}$	$9.438260136 \times 10^{-4}$
5	4	$-4.108005743 \times 10^{-5}$	$-5.554440367 \times 10^{-5}$
5	5	$1.399963431 \times 10^{-6}$	$3.876686886 \times 10^{-6}$
6	0	$8.065759741 \times 10^{-2}$	-
6	1	$-2.778109797 \times 10^{-3}$	$-2.154251881 \times 10^{-2}$
6	2	$7.728216842 \times 10^{-3}$	$7.050230573 \times 10^{-4}$
6	3	$-7.560742538 \times 10^{-4}$	$-1.257978980 \times 10^{-3}$
6	4	$7.064045621 \times 10^{-5}$	$9.373397010 \times 10^{-5}$
6	5	$-3.665028016 \times 10^{-6}$	$-9.917161087 \times 10^{-6}$
6	6	$1.455680816 \times 10^{-7}$	$5.919739848 \times 10^{-8}$
7	0	$-5.986895123 \times 10^{-2}$	-
7	1	$1.206156904 \times 10^{-3}$	$1.906778356 \times 10^{-2}$
7	2	$-7.982292450 \times 10^{-3}$	$-5.582844045 \times 10^{-4}$
7	3	$9.087880626 \times 10^{-4}$	$1.540648417 \times 10^{-3}$
7	4	$-1.046801009 \times 10^{-4}$	$-1.361711760 \times 10^{-4}$
7	5	$7.132110904 \times 10^{-6}$	$1.890116462 \times 10^{-5}$
7	6	$-4.145629549 \times 10^{-7}$	$-1.439414745 \times 10^{-7}$
7	7	$7.596460593 \times 10^{-8}$	$-2.624597318 \times 10^{-8}$
8	0	$4.416345142 \times 10^{-2}$	-
8	1	$1.581508784 \times 10^{-4}$	$-1.657915556 \times 10^{-2}$
8	2	$7.952533768 \times 10^{-3}$	$3.705958472 \times 10^{-4}$
8	3	$-1.025110855 \times 10^{-3}$	$-1.775797906 \times 10^{-3}$
8	4	$1.407914946 \times 10^{-4}$	$1.791918802 \times 10^{-4}$
8	5	$-1.184128517 \times 10^{-5}$	$-3.077016516 \times 10^{-5}$
8	6	$8.703025732 \times 10^{-7}$	$2.530582663 \times 10^{-7}$
8	7	$-2.376138812 \times 10^{-7}$	$8.275804341 \times 10^{-8}$
8	8	$2.117005569 \times 10^{-8}$	$-9.332515535 \times 10^{-9}$

9	0	$-3.225792014 \times 10^{-2}$	-
9	1	$-1.271867830 \times 10^{-3}$	$1.418174415 \times 10^{-2}$
9	2	$-7.695577352 \times 10^{-3}$	$-1.633165658 \times 10^{-4}$
9	3	$1.100139288 \times 10^{-3}$	$1.953592749 \times 10^{-3}$
9	4	$-1.765363753 \times 10^{-4}$	$-2.192685572 \times 10^{-4}$
9	5	$1.770490779 \times 10^{-5}$	$4.514350672 \times 10^{-5}$
9	6	$-1.548084248 \times 10^{-6}$	$-3.624746521 \times 10^{-7}$
9	7	$5.446892205 \times 10^{-7}$	$-1.899885367 \times 10^{-7}$
9	8	$-7.054343149 \times 10^{-8}$	$3.077786392 \times 10^{-8}$
9	9	$4.975995428 \times 10^{-9}$	$-1.218459955 \times 10^{-9}$
10	0	$2.324497166 \times 10^{-2}$	-
10	1	$2.121060961 \times 10^{-3}$	$-1.194283084 \times 10^{-2}$
10	2	$7.267136341 \times 10^{-3}$	$-4.472800026 \times 10^{-5}$
10	3	$-1.132979556 \times 10^{-3}$	$-2.069726597 \times 10^{-3}$
10	4	$2.097038823 \times 10^{-4}$	$2.533940670 \times 10^{-4}$
10	5	$-2.452390598 \times 10^{-5}$	$-6.139068974 \times 10^{-5}$
10	6	$2.465492310 \times 10^{-6}$	$4.331039107 \times 10^{-7}$
10	7	$-1.053248536 \times 10^{-6}$	$3.664098235 \times 10^{-7}$
10	8	$1.713980897 \times 10^{-7}$	$-7.381764148 \times 10^{-8}$
10	9	$-1.750956399 \times 10^{-8}$	$4.132145852 \times 10^{-9}$
10	10	$1.082713959 \times 10^{-9}$	$-2.413640574 \times 10^{-10}$
11	0	$-1.645588131 \times 10^{-2}$	-
11	1	$-2.712875788 \times 10^{-3}$	$9.902479418 \times 10^{-3}$
11	2	$-6.718838683 \times 10^{-3}$	$2.381798307 \times 10^{-4}$
11	3	$1.125955330 \times 10^{-3}$	$2.124488181 \times 10^{-3}$
11	4	$-2.384828312 \times 10^{-4}$	$-2.793209883 \times 10^{-4}$
11	5	$3.201091153 \times 10^{-5}$	$7.871412999 \times 10^{-5}$
11	6	$-3.619313657 \times 10^{-6}$	$-4.136860154 \times 10^{-7}$
11	7	$1.817275484 \times 10^{-6}$	$-6.288005179 \times 10^{-7}$
11	8	$-3.497832432 \times 10^{-7}$	$1.484583554 \times 10^{-7}$
11	9	$4.474171305 \times 10^{-8}$	$-1.010822146 \times 10^{-8}$
11	10	$-4.009463756 \times 10^{-9}$	$8.889006406 \times 10^{-10}$
11	11	$2.167735844 \times 10^{-10}$	$1.080851720 \times 10^{-11}$
12	0	$1.138360691 \times 10^{-2}$	-
12	1	$3.069022951 \times 10^{-3}$	$-8.080952360 \times 10^{-3}$
12	2	$6.096275269 \times 10^{-3}$	$-4.055727608 \times 10^{-4}$
12	3	$-1.083752789 \times 10^{-3}$	$-2.121733970 \times 10^{-3}$
12	4	$2.615576597 \times 10^{-4}$	$2.956734100 \times 10^{-4}$
12	5	$-3.981865171 \times 10^{-5}$	$-9.623630127 \times 10^{-5}$
12	6	$4.984555940 \times 10^{-6}$	$2.455715088 \times 10^{-7}$
12	7	$-2.882855944 \times 10^{-6}$	$9.901796706 \times 10^{-7}$
12	8	$6.346159500 \times 10^{-7}$	$-2.651647124 \times 10^{-7}$
12	9	$-9.568750359 \times 10^{-8}$	$2.056102757 \times 10^{-8}$
12	10	$1.074807295 \times 10^{-8}$	$-2.368158137 \times 10^{-9}$
12	11	$-8.437820575 \times 10^{-10}$	$-4.661563650 \times 10^{-11}$
12	12	$3.196038107 \times 10^{-11}$	$3.497625935 \times 10^{-12}$

Table D.2: Normalized interior spherical harmonic coefficients estimated from the 15×15 exterior gravity field (Section 6.3.2).

Degree (n)	Order (m)	$\bar{C}^i_{nm}$	$\bar{S}^i_{nm}$
0	0	$3.262227511 \times 10^{-8}$	-
1	0	$-4.295276525 \times 10^{-1}$	-
1	1	$8.133916332 \times 10^{-3}$	$2.304298826 \times 10^{-2}$
2	0	$2.823031966 \times 10^{-1}$	-
2	1	$-8.517833720 \times 10^{-3}$	$-2.641976974 \times 10^{-2}$
2	2	$2.980730570 \times 10^{-3}$	$4.644044024 \times 10^{-4}$
3	0	$-2.001687525 \times 10^{-1}$	-
3	1	$7.630316608 \times 10^{-3}$	$2.680233019 \times 10^{-2}$
3	2	$-4.779536997 \times 10^{-3}$	$-6.826332938 \times 10^{-4}$
3	3	$1.954535198 \times 10^{-4}$	$3.129178274 \times 10^{-4}$
4	0	$1.463823833 \times 10^{-1}$	-
4	1	$-6.171859018 \times 10^{-3}$	$-2.571864259 \times 10^{-2}$
4	2	$6.155362555 \times 10^{-3}$	$7.867954875 \times 10^{-4}$
4	3	$-3.816055679 \times 10^{-4}$	$-6.177141763 \times 10^{-4}$
4	4	$1.811164189 \times 10^{-5}$	$2.434616084 \times 10^{-5}$
5	0	$-1.084585323 \times 10^{-1}$	-
5	1	$4.489735490 \times 10^{-3}$	$2.383673904 \times 10^{-2}$
5	2	$-7.124625404 \times 10^{-3}$	$-7.893259036 \times 10^{-4}$
5	3	$5.731862254 \times 10^{-4}$	$9.403820765 \times 10^{-4}$
5	4	$-4.127605533 \times 10^{-5}$	$-5.475513972 \times 10^{-5}$
5	5	$1.416992372 \times 10^{-6}$	$3.813026936 \times 10^{-6}$
6	0	$8.067448807 \times 10^{-2}$	-
6	1	$-2.786283386 \times 10^{-3}$	$-2.153661054 \times 10^{-2}$
6	2	$7.715369492 \times 10^{-3}$	$7.064303166 \times 10^{-4}$
6	3	$-7.530488622 \times 10^{-4}$	$-1.251954541 \times 10^{-3}$
6	4	$6.525571939 \times 10^{-5}$	$9.206629662 \times 10^{-5}$
6	5	$-2.295087079 \times 10^{-6}$	$-1.240450274 \times 10^{-5}$
6	6	$7.306813577 \times 10^{-7}$	$6.003717228 \times 10^{-7}$
7	0	$-5.989321953 \times 10^{-2}$	-
7	1	$1.214431968 \times 10^{-3}$	$1.906400031 \times 10^{-2}$
7	2	$-7.968223768 \times 10^{-3}$	$-5.604948858 \times 10^{-4}$
7	3	$9.053954622 \times 10^{-4}$	$1.535239001 \times 10^{-3}$
7	4	$-9.859138349 \times 10^{-5}$	$-1.340356485 \times 10^{-4}$
7	5	$4.504660022 \times 10^{-6}$	$2.275050792 \times 10^{-5}$
7	6	$-1.639446709 \times 10^{-6}$	$-1.431346878 \times 10^{-6}$
7	7	$5.884640673 \times 10^{-7}$	$-5.118325982 \times 10^{-7}$
8	0	$4.419501234 \times 10^{-2}$	-
8	1	$1.471259584 \times 10^{-4}$	$-1.657691215 \times 10^{-2}$
8	2	$7.933573486 \times 10^{-3}$	$3.725645964 \times 10^{-4}$
8	3	$-1.019934418 \times 10^{-3}$	$-1.774377615 \times 10^{-3}$
8	4	$1.396778133 \times 10^{-4}$	$1.778102295 \times 10^{-4}$
8	5	$-1.000548902 \times 10^{-5}$	$-3.378783265 \times 10^{-5}$
8	6	$2.575157679 \times 10^{-6}$	$1.823561229 \times 10^{-6}$
8	7	$-1.136470169 \times 10^{-6}$	$9.731588269 \times 10^{-7}$
8	8	$-3.924191004 \times 10^{-7}$	$-2.384074886 \times 10^{-7}$

9	0	$-3.229609681 \times 10^{-2}$	-
9	1	$-1.261482661 \times 10^{-3}$	$1.418045034 \times 10^{-2}$
9	2	$-7.676183318 \times 10^{-3}$	$-1.652644898 \times 10^{-4}$
9	3	$1.093969487 \times 10^{-3}$	$1.954663858 \times 10^{-3}$
9	4	$-1.801612665 \times 10^{-4}$	$-2.186276453 \times 10^{-4}$
9	5	$1.633755926 \times 10^{-5}$	$4.667739106 \times 10^{-5}$
9	6	$-3.366525872 \times 10^{-6}$	$-2.145861211 \times 10^{-6}$
9	7	$2.196422496 \times 10^{-6}$	$-1.705872309 \times 10^{-6}$
9	8	$1.017450978 \times 10^{-6}$	$6.693896092 \times 10^{-7}$
9	9	$-3.780076797 \times 10^{-8}$	$1.947100598 \times 10^{-7}$
10	0	$2.328775529 \times 10^{-2}$	-
10	1	$2.109358759 \times 10^{-3}$	$-1.194192925 \times 10^{-2}$
10	2	$7.245238628 \times 10^{-3}$	$-4.388874489 \times 10^{-5}$
10	3	$-1.126401996 \times 10^{-3}$	$-2.074371643 \times 10^{-3}$
10	4	$2.230998140 \times 10^{-4}$	$2.542666932 \times 10^{-4}$
10	5	$-2.691756473 \times 10^{-5}$	$-5.582782064 \times 10^{-5}$
10	6	$1.977354342 \times 10^{-6}$	$-3.310917191 \times 10^{-7}$
10	7	$-1.390028813 \times 10^{-6}$	$8.402634449 \times 10^{-7}$
10	8	$-5.643112049 \times 10^{-7}$	$-4.884354509 \times 10^{-7}$
10	9	$-1.771631901 \times 10^{-8}$	$-2.503148682 \times 10^{-7}$
10	10	$5.990699288 \times 10^{-8}$	$9.304840707 \times 10^{-9}$
11	0	$-1.650341960 \times 10^{-2}$	-
11	1	$-2.702504383 \times 10^{-3}$	$9.901306481 \times 10^{-3}$
11	2	$-6.697245758 \times 10^{-3}$	$2.388046874 \times 10^{-4}$
11	3	$1.119083830 \times 10^{-3}$	$2.129593481 \times 10^{-3}$
11	4	$-2.549290349 \times 10^{-4}$	$-2.816186909 \times 10^{-4}$
11	5	$3.740124660 \times 10^{-5}$	$6.954442538 \times 10^{-5}$
11	6	$-1.714004239 \times 10^{-6}$	$2.105457192 \times 10^{-6}$
11	7	$1.309705467 \times 10^{-6}$	$-3.552479376 \times 10^{-7}$
11	8	$1.981256702 \times 10^{-7}$	$5.291431591 \times 10^{-7}$
11	9	$8.858245361 \times 10^{-9}$	$3.589334707 \times 10^{-7}$
11	10	$-5.970656322 \times 10^{-8}$	$-2.429011989 \times 10^{-8}$
11	11	$-2.162761552 \times 10^{-8}$	$-8.622099268 \times 10^{-9}$
12	0	$1.142887977 \times 10^{-2}$	-
12	1	$3.076500310 \times 10^{-3}$	$-8.079072543 \times 10^{-3}$
12	2	$6.094651166 \times 10^{-3}$	$-4.051119117 \times 10^{-4}$
12	3	$-1.083911556 \times 10^{-3}$	$-2.112932960 \times 10^{-3}$
12	4	$2.584692683 \times 10^{-4}$	$2.959363249 \times 10^{-4}$
12	5	$-4.185407992 \times 10^{-5}$	$-9.177477983 \times 10^{-5}$
12	6	$1.959365593 \times 10^{-6}$	$-3.044208107 \times 10^{-6}$
12	7	$-4.529223926 \times 10^{-7}$	$-9.372438109 \times 10^{-7}$
12	8	$2.143779817 \times 10^{-6}$	$5.074039052 \times 10^{-7}$
12	9	$-1.205517764 \times 10^{-7}$	$3.053313395 \times 10^{-7}$
12	10	$-5.302605439 \times 10^{-8}$	$-8.300234984 \times 10^{-9}$
12	11	$-3.039848283 \times 10^{-8}$	$-1.346668387 \times 10^{-9}$
12	12	$-5.271873554 \times 10^{-9}$	$7.959793365 \times 10^{-10}$

Table D.3: Normalized interior spherical harmonic coefficients estimated from the polyhedral gravity field (Section 6.3.2).

Degree (n)	Order (m)	$\bar{C}^i_{nm}$	$\bar{S}^i_{nm}$
0	0	$3.262227511 \times 10^{-8}$	-
1	0	$-4.295276523 \times 10^{-1}$	-
1	1	$8.133916130 \times 10^{-3}$	$2.304298876 \times 10^{-2}$
2	0	$2.823032001 \times 10^{-1}$	-
2	1	$-8.517830925 \times 10^{-3}$	$-2.641977190 \times 10^{-2}$
2	2	$2.980728492 \times 10^{-3}$	$4.644069596 \times 10^{-4}$
3	0	$-2.001687469 \times 10^{-1}$	-
3	1	$7.630337249 \times 10^{-3}$	$2.680231716 \times 10^{-2}$
3	2	$-4.779544531 \times 10^{-3}$	$-6.826309037 \times 10^{-4}$
3	3	$1.954530631 \times 10^{-4}$	$3.129206545 \times 10^{-4}$
4	0	$1.463823139 \times 10^{-1}$	-
4	1	$-6.171868809 \times 10^{-3}$	$-2.571859603 \times 10^{-2}$
4	2	$6.155363692 \times 10^{-3}$	$7.868146797 \times 10^{-4}$
4	3	$-3.816456349 \times 10^{-4}$	$-6.176835187 \times 10^{-4}$
4	4	$1.808186638 \times 10^{-5}$	$2.432030795 \times 10^{-5}$
5	0	$-1.084589316 \times 10^{-1}$	-
5	1	$4.489508935 \times 10^{-3}$	$2.383706103 \times 10^{-2}$
5	2	$-7.124394428 \times 10^{-3}$	$-7.893456211 \times 10^{-4}$
5	3	$5.732372694 \times 10^{-4}$	$9.405555932 \times 10^{-4}$
5	4	$-4.120963091 \times 10^{-5}$	$-5.480718148 \times 10^{-5}$
5	5	$1.310917923 \times 10^{-6}$	$4.003354465 \times 10^{-6}$
6	0	$8.067031564 \times 10^{-2}$	-
6	1	$-2.796884555 \times 10^{-3}$	$-2.153872960 \times 10^{-2}$
6	2	$7.714148348 \times 10^{-3}$	$7.074566449 \times 10^{-4}$
6	3	$-7.521832046 \times 10^{-4}$	$-1.253948492 \times 10^{-3}$
6	4	$7.092356546 \times 10^{-5}$	$9.267065104 \times 10^{-5}$
6	5	$-3.696245549 \times 10^{-6}$	$-9.789162836 \times 10^{-6}$
6	6	$1.477706163 \times 10^{-7}$	$3.574318797 \times 10^{-8}$
7	0	$-5.988717075 \times 10^{-2}$	-
7	1	$1.228684134 \times 10^{-3}$	$1.906686433 \times 10^{-2}$
7	2	$-7.967098970 \times 10^{-3}$	$-5.622833801 \times 10^{-4}$
7	3	$9.043780248 \times 10^{-4}$	$1.536096712 \times 10^{-3}$
7	4	$-1.050456259 \times 10^{-4}$	$-1.348665352 \times 10^{-4}$
7	5	$7.174184816 \times 10^{-6}$	$1.869701929 \times 10^{-5}$
7	6	$-4.210556566 \times 10^{-7}$	$-8.666475824 \times 10^{-8}$
7	7	$7.501501204 \times 10^{-8}$	$-3.167571903 \times 10^{-8}$
8	0	$4.418566591 \times 10^{-2}$	-
8	1	$1.328079611 \times 10^{-4}$	$-1.658068347 \times 10^{-2}$
8	2	$7.936491618 \times 10^{-3}$	$3.760896419 \times 10^{-4}$
8	3	$-1.020306930 \times 10^{-3}$	$-1.770811555 \times 10^{-3}$
8	4	$1.412248792 \times 10^{-4}$	$1.776916659 \times 10^{-4}$
8	5	$-1.188085381 \times 10^{-5}$	$-3.048423103 \times 10^{-5}$
8	6	$8.837932832 \times 10^{-7}$	$1.529122544 \times 10^{-7}$
8	7	$-2.388883156 \times 10^{-7}$	$9.666656019 \times 10^{-8}$
8	8	$2.344262810 \times 10^{-8}$	$-1.239501410 \times 10^{-8}$

9	0	$-3.228291589 \times 10^{-2}$	-
9	1	$-1.244609108 \times 10^{-3}$	$1.418537417 \times 10^{-2}$
9	2	$-7.678996568 \times 10^{-3}$	$-1.701665407 \times 10^{-4}$
9	3	$1.095080634 \times 10^{-3}$	$1.948302422 \times 10^{-3}$
9	4	$-1.770264655 \times 10^{-4}$	$-2.176701253 \times 10^{-4}$
9	5	$1.772792655 \times 10^{-5}$	$4.477974245 \times 10^{-5}$
9	6	$-1.570300391 \times 10^{-6}$	$-2.045906798 \times 10^{-7}$
9	7	$5.466295876 \times 10^{-7}$	$-2.166280757 \times 10^{-7}$
9	8	$-7.829275167 \times 10^{-8}$	$3.947883333 \times 10^{-8}$
9	9	$3.716727523 \times 10^{-9}$	$-3.339745095 \times 10^{-9}$
10	0	$2.327172832 \times 10^{-2}$	-
10	1	$2.092793584 \times 10^{-3}$	$-1.194825199 \times 10^{-2}$
10	2	$7.250339245 \times 10^{-3}$	$-3.673254198 \times 10^{-5}$
10	3	$-1.127831058 \times 10^{-3}$	$-2.064260104 \times 10^{-3}$
10	4	$2.102353929 \times 10^{-4}$	$2.517967763 \times 10^{-4}$
10	5	$-2.450631724 \times 10^{-5}$	$-6.095891365 \times 10^{-5}$
10	6	$2.504092661 \times 10^{-6}$	$2.218232160 \times 10^{-7}$
10	7	$-1.068553404 \times 10^{-6}$	$4.071250301 \times 10^{-7}$
10	8	$1.788641267 \times 10^{-7}$	$-8.426237680 \times 10^{-8}$
10	9	$-1.653418591 \times 10^{-8}$	$6.141564147 \times 10^{-9}$
10	10	$9.637349283 \times 10^{-10}$	$-6.103297248 \times 10^{-10}$
11	0	$-1.648350300 \times 10^{-2}$	-
11	1	$-2.684453131 \times 10^{-3}$	$9.909385231 \times 10^{-3}$
11	2	$-6.702123348 \times 10^{-3}$	$2.293043043 \times 10^{-4}$
11	3	$1.120879545 \times 10^{-3}$	$2.118969666 \times 10^{-3}$
11	4	$-2.390409253 \times 10^{-4}$	$-2.778507375 \times 10^{-4}$
11	5	$3.192657541 \times 10^{-5}$	$7.824206835 \times 10^{-5}$
11	6	$-3.670740955 \times 10^{-6}$	$-1.398435010 \times 10^{-7}$
11	7	$1.845017653 \times 10^{-6}$	$-6.892920657 \times 10^{-7}$
11	8	$-3.594269228 \times 10^{-7}$	$1.656190184 \times 10^{-7}$
11	9	$4.292511773 \times 10^{-8}$	$-1.415416702 \times 10^{-8}$
11	10	$-4.261135619 \times 10^{-9}$	$2.234416930 \times 10^{-9}$
11	11	$7.591475498 \times 10^{-10}$	$7.726753851 \times 10^{-10}$
12	0	$1.141139459 \times 10^{-2}$	-
12	1	$3.041186814 \times 10^{-3}$	$-8.089039226 \times 10^{-3}$
12	2	$6.079896763 \times 10^{-3}$	$-3.960988760 \times 10^{-4}$
12	3	$-1.078870168 \times 10^{-3}$	$-2.116372713 \times 10^{-3}$
12	4	$2.621534990 \times 10^{-4}$	$2.945323562 \times 10^{-4}$
12	5	$-3.965054075 \times 10^{-5}$	$-9.576117731 \times 10^{-5}$
12	6	$5.041807234 \times 10^{-6}$	$-1.008642024 \times 10^{-7}$
12	7	$-2.927618091 \times 10^{-6}$	$1.071676912 \times 10^{-6}$
12	8	$6.375467393 \times 10^{-7}$	$-2.812741758 \times 10^{-7}$
12	9	$-9.951140424 \times 10^{-8}$	$2.203114195 \times 10^{-8}$
12	10	$1.092352935 \times 10^{-8}$	$-3.093253338 \times 10^{-9}$
12	11	$-9.127961101 \times 10^{-10}$	$2.555268217 \times 10^{-10}$
12	12	$1.290763729 \times 10^{-10}$	$-2.382856911 \times 10^{-10}$

Appendix E

Interior and Exterior Spherical Bessel Gravity Fields

We provide some useful equations used to derive the interior spherical Bessel gravity field. In Appendix E.7, the exterior spherical Bessel gravity field is fully derived.

E.1 Partials of the Surface Spherical Harmonic Potential $\mathscr{H}_{nm}$

The partial derivatives of the surface spherical harmonic potential $\mathscr{H}_{nm}$ in the Cartesian coordinate frame is given as

$$\frac{\partial}{\partial x}\mathscr{H}_{nm} = -\frac{nx}{r^2}\mathscr{H}_{nm} + \frac{1}{2r}\left[-\mathscr{H}_{n-1,m+1} + (n+m)(n+m-1)\mathscr{H}_{n-1,m-1}\right] \tag{E.1}$$

$$\frac{\partial}{\partial y}\mathscr{H}_{nm} = -\frac{ny}{r^2}\mathscr{H}_{nm} + \frac{i}{2r}\left[\mathscr{H}_{n-1,m+1} + (n+m)(n+m-1)\mathscr{H}_{n-1,m-1}\right] \tag{E.2}$$

$$\frac{\partial}{\partial z}\mathscr{H}_{nm} = -n\frac{z}{r^2}\mathscr{H}_{nm} + (n+m)\frac{1}{r}\mathscr{H}_{n-1,m} \tag{E.3}$$

which is obtained via the chain rule operation of the exterior basis b^e_{nm} (Equation D.19) or the interior basis b^i_{nm} (Equation D.20). Then, another chain rule operation yields the acceleration expressions in Equation 7.65 through 7.67.

E.2 Recursive Formulae of the Associated Legendre Function

Equation 7.68 can be proven after tedious algebra. Two useful, inconspicuous properties of the associated Legendre function that are used during the process are provided below. From Werner [74], we have the North recursion formula for the associated Legendre function:

$$\begin{aligned} -(n+m-1)(n+m)\cos\phi P_{n-1,m-1}(\sin\phi) &= -2mP_{n,m}(\sin\phi) \\ &\quad + \cos\phi P_{n-1,m+1}(\sin\phi) \end{aligned} \tag{E.4}$$

Also, after substituting $n-1$ for n in the Southeast recursion, we get

$$-(n-m)P_{n,m}(\sin\phi) + (n+m)\sin\phi P_{n-1,m}(\sin\phi) - \cos\phi P_{n-1,m+1} = 0 \tag{E.5}$$

Then, consecutive applications of the recursion formula (Equation 7.42) yields Equation 7.68.

E.3 Orthogonality of Spherical Bessel/Spherical Neumann Functions

We prove the orthogonal properties of the spherical Bessel/Neumann functions used to obtain the interior/exterior spherical Bessel coefficients in Equation 7.32 and E.74.

E.3.1 Spherical Bessel's Equation

Spherical Bessel's equation in Equation 7.14 can be compactly expressed as

$$\frac{d}{dr}\left[r^2\frac{d}{dr}R_n(kr)\right] + \left[k^2r^2 - n(n+1)\right]R_n(kr) = 0 \tag{E.6}$$

for which $j_n(kr)$ and $\mathcal{Y}_n(kr)$ are the solutions.

E.3.2 Orthogonality of Spherical Bessel Function

First, we prove the orthogonality of spherical Bessel function. In Equation E.6, we substitute $R_n(kr) = j_n(\alpha_{\nu n}r/R^*)$ to get

$$\frac{d}{dr}\left[r^2\frac{d}{dr}j_n\left(\frac{\alpha_{\nu n}r}{R^*}\right)\right]+\left[\frac{\alpha_{\nu n}^2}{R^{*2}}r^2-n(n+1)\right]j_n\left(\frac{\alpha_{\nu n}r}{R^*}\right) = 0 \tag{E.7}$$

where $\alpha_{\nu n}$ is the ν-th eigenvalue of degree n that satisfy $j_{n-1}(\alpha_{\nu n})=0$ (i.e., boundary condition in Equation 7.46). We multiply Equation E.7 by $j_n(\alpha_{\mu n}r/R^*)$ to get

$$j_n\left(\frac{\alpha_{\mu n}r}{R^*}\right)\frac{d}{dr}\left[r^2\frac{d}{dr}j_n\left(\frac{\alpha_{\nu n}r}{R^*}\right)\right]+\left[\frac{\alpha_{\nu n}^2}{R^{*2}}r^2-n(n+1)\right]j_n\left(\frac{\alpha_{\mu n}r}{R^*}\right)j_n\left(\frac{\alpha_{\nu n}r}{R^*}\right) = 0 \tag{E.8}$$

where $\alpha_{\mu n}$ is the μ-th eigenvalue of degree n that satisfy $j_{n-1}(\alpha_{\mu n})=0$. Similarly, we substitute $R_n(kr)=j_n(\alpha_{\mu n}r/R^*)$ in Equation E.6 and multiply it by $j_n(\alpha_{\nu n}r/R^*)$ to get

$$j_n\left(\frac{\alpha_{\nu n}r}{R^*}\right)\frac{d}{dr}\left[r^2\frac{d}{dr}j_n\left(\frac{\alpha_{\mu n}r}{R^*}\right)\right]+\left[\frac{\alpha_{\mu n}^2}{R^{*2}}r^2-n(n+1)\right]j_n\left(\frac{\alpha_{\mu n}r}{R^*}\right)j_n\left(\frac{\alpha_{\nu n}r}{R^*}\right) = 0 \tag{E.9}$$

Then, we subtract Equation E.8 from Equation E.9 to get

$$\begin{aligned} &j_n\left(\frac{\alpha_{\nu n}r}{R^*}\right)\frac{d}{dr}\left[r^2\frac{d}{dr}j_n\left(\frac{\alpha_{\mu n}r}{R^*}\right)\right]-j_n\left(\frac{\alpha_{\mu n}r}{R^*}\right)\frac{d}{dr}\left[r^2\frac{d}{dr}j_n\left(\frac{\alpha_{\nu n}r}{R^*}\right)\right] \\ &\qquad=\frac{\alpha_{\nu n}^2-\alpha_{\mu n}^2}{R^{*2}}r^2j_n\left(\frac{\alpha_{\mu n}r}{R^*}\right)j_n\left(\frac{\alpha_{\nu n}r}{R^*}\right) \end{aligned} \tag{E.10}$$

By integrating both sides from $r=0$ to R^*, we get

$$\begin{aligned} &\int_0^{R^*}j_n\left(\frac{\alpha_{\nu n}r}{R^*}\right)\frac{d}{dr}\left[r^2\frac{d}{dr}j_n\left(\frac{\alpha_{\mu n}r}{R^*}\right)\right]dr-\int_0^{R^*}j_n\left(\frac{\alpha_{\mu n}r}{R^*}\right)\frac{d}{dr}\left[r^2\frac{d}{dr}j_n\left(\frac{\alpha_{\nu n}r}{R^*}\right)\right]dr \\ &\qquad=\frac{\alpha_{\nu n}^2-\alpha_{\mu n}^2}{R^{*2}}\int_0^{R^*}r^2j_n\left(\frac{\alpha_{\mu n}r}{R^*}\right)j_n\left(\frac{\alpha_{\nu n}r}{R^*}\right)dr \end{aligned} \tag{E.11}$$

Now, we look at the first term of the left-hand side of Equation E.11. By integration by parts and ignoring the limits of integration, it reduces to

$$\int j_n\left(\frac{\alpha_{\nu n}r}{R^*}\right)\frac{d}{dr}\left[r^2\frac{d}{dr}j_n\left(\frac{\alpha_{\mu n}r}{R^*}\right)\right]dr = = r^2 j_n\left(\frac{\alpha_{\nu n}r}{R^*}\right)\frac{d}{dr}\left[j_n\left(\frac{\alpha_{\mu n}r}{R^*}\right)\right] - r^2\frac{d}{dr}\left[j_n\left(\frac{\alpha_{\mu n}r}{R^*}\right)\right]\frac{d}{dr}\left[j_n\left(\frac{\alpha_{\nu n}r}{R^*}\right)\right] \quad \text{(E.12)}$$

A similar expression is obtained for the second term. Thus, the left-hand side of Equation E.11 becomes

$$\begin{aligned}
&\int_0^{R^*} j_n\left(\frac{\alpha_{\nu n}r}{R^*}\right)\frac{d}{dr}\left[r^2\frac{d}{dr}j_n\left(\frac{\alpha_{\mu n}r}{R^*}\right)\right]dr - \int_0^{R^*} j_n\left(\frac{\alpha_{\mu n}r}{R^*}\right)\frac{d}{dr}\left[r^2\frac{d}{dr}j_n\left(\frac{\alpha_{\nu n}r}{R^*}\right)\right]dr \\
&\quad r^2 j_n\left(\frac{\alpha_{\nu n}r}{R^*}\right)\frac{d}{dr}\left[j_n\left(\frac{\alpha_{\mu n}r}{R^*}\right)\right]\Big|_{r=0}^{r=R^*} - r^2 j_n\left(\frac{\alpha_{\mu n}r}{R^*}\right)\frac{d}{dr}\left[j_n\left(\frac{\alpha_{\nu n}r}{R^*}\right)\right]\Big|_{r=0}^{r=R^*} \\
&\quad = R^{*2} j_n(\alpha_{\nu n}) j_n'(\alpha_{\mu n})\frac{\alpha_{\mu n}}{R^*} - R^{*2} j_n(\alpha_{\mu n}) j_n'(\alpha_{\nu n})\frac{\alpha_{\nu n}}{R^*} \\
&\quad = \alpha_{\mu n} R^* j_n(\alpha_{\nu n}) j_n'(\alpha_{\mu n}) - \alpha_{\nu n} R^* j_n(\alpha_{\mu n}) j_n'(\alpha_{\nu n})
\end{aligned} \quad \text{(E.13)}$$

In Equation E.13, the lower limit yields zero as $j_n(0) = 0$ for $n \neq 0$ and $j_0\prime(0) = -j_1(0) = 0$ for $n = 0$. The upper limit is not necessarily zero, as the eigenvalues $\alpha_{\nu n}$ and $\alpha_{\mu n}$ only satisfy $j_{n-1}(\alpha_{\nu n}) = j_{n-1}(\alpha_{\mu n}) = 0$ (Equation 7.46), and neither $j_n(\alpha_{\nu n})$ nor $j_n(\alpha_{\mu n})$ is zero. By combining Equation 7.42 and 7.43, the partial of j_n is given as

$$j_n'(x) = j_{n-1}(x) - \frac{(n+1)}{x}j_n(x) \quad \text{(E.14)}$$

Thus, we get

$$j_n'(\alpha_{\nu n}) = j_{n-1}(\alpha_{\nu n}) - \frac{(n+1)}{\alpha_{\nu n}}j_n(\alpha_{\nu n}) = -\frac{(n+1)}{\alpha_{\nu n}}j_n(\alpha_{\nu n}) \quad \text{(E.15)}$$

$$j_n'(\alpha_{\mu n}) = -\frac{(n+1)}{\alpha_{\mu n}} j_n(\alpha_{\mu n}) \tag{E.16}$$

Then, substitution of Equation E.15 and E.16 into Equation E.13 yields the orthogonality relationship

$$\int_0^{R^*} r^2 j_n\left(\frac{\alpha_{\mu n} r}{R^*}\right) j_n\left(\frac{\alpha_{\nu n} r}{R^*}\right) dr = 0 \qquad \text{for } \mu \neq \nu \tag{E.17}$$

When $\mu = \nu$, we let $\alpha_{\nu n} = \alpha_{\mu n} + \epsilon$ where $j_{n-1}(\alpha_{\mu n}) = 0$ and take the limit as $\epsilon \to 0$. By Taylor series expansion, $\alpha_{\nu n}^2 - \alpha_{\mu n}^2$, $j_n(\alpha_{\nu n})$, and $j_n'(\alpha_{\nu n})$ are obtained as

$$\alpha_{\nu n}^2 - \alpha_{\mu n}^2 = (\alpha_{\mu n} + \epsilon)^2 - \alpha_{\mu n}^2 = 2\alpha_{\mu n}\epsilon + \epsilon^2 \approx 2\alpha_{\mu n}\epsilon \tag{E.18}$$

$$j_n(\alpha_{\nu n}) = j_n(\alpha_{\mu n} + \epsilon) \approx j_n(\alpha_{\mu n}) + \epsilon j_n'(\alpha_{\mu n}) \tag{E.19}$$

$$j_n'(\alpha_{\nu n}) = j_n'(\alpha_{\mu n} + \epsilon) \approx j_n'(\alpha_{\mu n}) + \epsilon j_n''(\alpha_{\mu n}) \tag{E.20}$$

Also, from Equation E.14, $j_n''(x)$ is obtained as

$$\begin{aligned} j_n''(x) &= j_{n-1}'(x) + \frac{(n+1)}{x^2} j_n(x) - \frac{(n+1)}{x} j_n'(x) \\ &= \frac{(n+1)(n+2)}{x^2} j_n(x) - \frac{2n+1}{x} j_{n-1}(x) + j_{n-2}(x) \end{aligned} \tag{E.21}$$

which yields

$$j_n''(\alpha_{\mu n}) = \frac{(n+1)(n+2)}{\alpha_{\mu n}^2} j_n(\alpha_{\mu n}) + j_{n-2}(\alpha_{\mu n})$$

Thus, Equation E.13 becomes

$$\alpha_{\mu n} R^* j_n(\alpha_{\nu n}) j_n'(\alpha_{\mu n}) - \alpha_{\nu n} R^* j_n(\alpha_{\mu n}) j_n'(\alpha_{\nu n})$$

$$= \alpha_{\mu n} R^* \left[j_n(\alpha_{\mu n}) + \epsilon j_n'(\alpha_{\mu n}) \right] j_n'(\alpha_{\mu n}) - (\alpha_{\mu n} + \epsilon) R^* j_n(\alpha_{\mu n}) \left[j_n'(\alpha_{\mu n}) + \epsilon j_n''(\alpha_{\mu n}) \right]$$

$$= \epsilon \alpha_{\mu n} R^* \left[j_n'(\alpha_{\mu n}) \right]^2 - \epsilon \alpha_{\mu n} R^* j_n(\alpha_{\mu n}) j_n''(\alpha_{\mu n}) - \epsilon R^* j_n(\alpha_{\mu n}) j_n'(\alpha_{\mu n}) \qquad \text{(E.22)}$$

$$= -\epsilon \alpha_{\mu n} R^* j_n(\alpha_{\mu n}) j_{n-2}(\alpha_{\mu n})$$

$$= \epsilon \alpha_{\mu n} R^* \left[j_n(\alpha_{\mu n}) \right]^2$$

where we used the recursion formula

$$j_n(\alpha_{\mu n}) \quad = \quad \frac{2n-1}{\alpha_{\mu n}} j_{n-1}(\alpha_{\mu n}) - j_{n-2}(\alpha_{\mu n}) \quad = \quad -j_{n-2}(\alpha_{\mu n}) \qquad \text{(E.23)}$$

Therefore, Equation E.11 becomes

$$\int_0^{R^*} r^2 \left[j_n \left(\frac{\alpha_{\mu n} r}{R^*} \right) \right]^2 dr \quad = \quad \frac{R^{*3}}{2} \left[j_n(\alpha_{\mu n}) \right]^2 \qquad \text{(E.24)}$$

E.3.3 Orthogonality of Spherical Neumann Function

We derive the orthogonality relationship of spherical Neumann function. As the partial differential equation of spherical Bessel/Neumann functions are the same, we start from Equation E.11 (with $\alpha_{\nu n}$ and $\alpha_{\mu n}$ interchanged) and replace $j_n(x)$ with $\mathcal{Y}_n(x)$.

$$= \frac{\alpha_{\nu n}^2 - \alpha_{\mu n}^2}{R^{*2}} \int_{R^*}^{\infty} r^2 \mathcal{Y}_n \left(\frac{\alpha_{\mu n} r}{R^*}\right) \mathcal{Y}_n \left(\frac{\alpha_{\nu n} r}{R^*}\right) dr$$

$$= r^2 \mathcal{Y}_n \left(\frac{\alpha_{\mu n} r}{R^*}\right) \frac{d}{dr} \left[\mathcal{Y}_n \left(\frac{\alpha_{\nu n} r}{R^*}\right)\right]\Bigg|_{r=R^*}^{r=\infty} - r^2 \mathcal{Y}_n \left(\frac{\alpha_{\nu n} r}{R^*}\right) \frac{d}{dr} \left[\mathcal{Y}_n \left(\frac{\alpha_{\mu n} r}{R^*}\right)\right]\Bigg|_{r=R^*}^{r=\infty} \tag{E.25}$$

$$= \alpha_{\mu n} R^* \mathcal{Y}_n(\alpha_{\nu n}) \mathcal{Y}_n'(\alpha_{\mu n}) - \alpha_{\nu n} R^* \mathcal{Y}_n(\alpha_{\mu n}) \mathcal{Y}_n'(\alpha_{\nu n})$$

Note that the limits of integration are now from $r = R^*$ to ∞ as the density is redistributed outside the interior Brillouin sphere for the exterior spherical Bessel gravity field. As the boundary condition satisfies Equation E.86, we seek for a partial expression containing $\mathcal{Y}_{n+1}(x)$. The recursion formula is given as

$$\mathcal{Y}_{n-1}(x) = -\mathcal{Y}_{n+1}(x) + \frac{2n+1}{x} \mathcal{Y}_n(x) \tag{E.26}$$

Thus, the partial of $\mathcal{Y}_n(x)$ can be written as

$$\mathcal{Y}_n'(x) = \frac{n}{2n+1} \mathcal{Y}_{n-1}(x) - \frac{n+1}{2n+1} \mathcal{Y}_{n+1}(x) = -\mathcal{Y}_{n+1}(x) + \frac{n}{x} \mathcal{Y}_n(x) \tag{E.27}$$

which yields

$$\mathcal{Y}_n'(\alpha_{\mu n}) = -\mathcal{Y}_{n+1}(\alpha_{\mu n}) + \frac{n}{\alpha_{\mu n}} \mathcal{Y}_n(\alpha_{\mu n}) = \frac{n}{\alpha_{\mu n}} \mathcal{Y}_n(\alpha_{\mu n}) \tag{E.28}$$

$$\mathcal{Y}_n'(\alpha_{\nu n}) = -\mathcal{Y}_{n+1}(\alpha_{\nu n}) + \frac{n}{\alpha_{\nu n}} \mathcal{Y}_n(\alpha_{\mu n}) = \frac{n}{\alpha_{\nu n}} \mathcal{Y}_n(\alpha_{\nu n}) \tag{E.29}$$

Thus, when $\mu \neq \nu$, Equation E.25 becomes

$$\int_{R^*}^{\infty} r^2 \mathcal{Y}_n \left(\frac{\alpha_{\mu n} r}{R^*}\right) \mathcal{Y}_n \left(\frac{\alpha_{\nu n} r}{R^*}\right) dr = 0 \qquad \text{for } \mu \neq \nu \tag{E.30}$$

When $\mu = \nu$, we use the Taylor series expansion again and take the limit as $\epsilon \to 0$. By applying the recursion formula, $\mathcal{Y}_n''(x)$ is obtained as

$$\begin{aligned}
\mathcal{Y}_n''(x) &= -\mathcal{Y}_{n+1}'(x) - \frac{n}{x^2}\mathcal{Y}_n(x) + \frac{n}{x}\mathcal{Y}_n'(x) \\
&= \mathcal{Y}_{n+2}(x) - \frac{2n+1}{x}\mathcal{Y}_{n+1}(x) + \frac{n(n-1)}{x^2}\mathcal{Y}_n(x) \qquad \text{(E.31)} \\
&= \frac{2}{x}\mathcal{Y}_{n+1}(x) + \left[\frac{n(n-1)}{x^2} - 1\right]\mathcal{Y}_n(x)
\end{aligned}$$

which yields

$$\mathcal{Y}_n''(\alpha_{\mu n}) = \frac{2}{x}\mathcal{Y}_{n+1}(\alpha_{\mu n}) + \left[\frac{n(n-1)}{\alpha_{\mu n}^2} - 1\right]\mathcal{Y}_n(\alpha_{\mu n}) = \left[\frac{n(n-1)}{\alpha_{\mu n}^2} - 1\right]\mathcal{Y}_n(\alpha_{\mu n}) \qquad \text{(E.32)}$$

Then, Equation E.25 becomes

$$\begin{aligned}
&\alpha_{\mu n}R^*\mathcal{Y}_n(\alpha_{\nu n})\mathcal{Y}_n'(\alpha_{\mu n}) - \alpha_{\nu n}R^*\mathcal{Y}_n(\alpha_{\mu n})\mathcal{Y}_n'(\alpha_{\nu n}) \\
&= \epsilon\alpha_{\mu n}R^*\left[\mathcal{Y}_n'(\alpha_{\mu n})\right]^2 - \epsilon\alpha_{\mu n}R^*\mathcal{Y}_n(\alpha_{\mu n})\mathcal{Y}_n''(\alpha_{\mu n}) - \epsilon R^*\mathcal{Y}_n(\alpha_{\mu n})\mathcal{Y}_n'(\alpha_{\mu n}) \qquad \text{(E.33)} \\
&= \epsilon\alpha_{\mu n}R^*\left[\mathcal{Y}_n(\alpha_{\mu n})\right]^2
\end{aligned}$$

Thus, we get

$$\int_{R^*}^{\infty} r^2\left[\mathcal{Y}_n\left(\frac{\alpha_{\mu n}r}{R^*}\right)\right]^2 dr = \frac{R^{*3}}{2}\left[\mathcal{Y}_n(\alpha_{\mu n})\right]^2 \qquad \text{(E.34)}$$

E.4 Eigenvalues of the Interior and Exterior Spherical Bessel Gravity Fields

Table E.1 lists the eigenvalues of the interior/exterior spherical Bessel gravity fields obtained by the boundary conditions Equation 7.46 and E.86.

Table E.1: Eigenvalues of the interior and exterior spherical Bessel gravity fields.

Degree (n)	Power (l)	α^i_{ln}	α^e_{ln}
0	0	1.5708	2.7984
0	1	4.7124	6.1213
0	2	7.854	9.3179
0	3	10.9956	12.4865
0	4	14.1372	15.6441
0	5	17.2788	18.7964
1	0	3.1416	3.9595
1	1	6.2832	7.4516
1	2	9.4248	10.7156
1	3	12.5664	13.9217
1	4	15.708	17.1034
1	5	18.8496	20.2724
2	0	0	5.0885
2	1	4.4934	8.7337
2	2	7.7253	12.0675
2	3	10.9041	15.3154
2	4	14.0662	18.5252
2	5	17.2208	21.7145
3	0	0	6.1978
3	1	5.7635	9.9825
3	2	9.095	13.3853
3	3	12.3229	16.6766
3	4	15.5146	19.9168
3	5	18.689	23.1286
4	0	0	7.2937
4	1	6.9879	11.2065
4	2	10.4171	14.6764
4	3	13.698	18.0116
4	4	16.9236	21.2832
4	5	20.1218	24.5189

5	0	0	8.3796
5	1	8.1826	12.4113
5	2	11.7049	15.946
5	3	15.0397	19.3248
5	4	18.3013	22.6284
5	5	21.5254	25.8887
6	0	0	9.4579
6	1	9.3558	13.6006
6	2	12.9665	17.1978
6	3	16.3547	20.6196
6	4	19.6532	23.9553
6	5	22.9046	27.2406
7	0	0	10.53
7	1	10.5128	14.7772
7	2	14.2074	18.4345
7	3	17.648	21.8986
7	4	20.9835	25.2661
7	5	24.2628	28.5767
8	0	0	11.597
8	1	11.657	15.9429
8	2	15.4313	19.6584
8	3	18.923	23.1637
8	4	22.2953	26.563
8	5	25.6029	29.8988
9	0	0	12.6598
9	1	12.7908	17.0995
9	2	16.641	20.871
9	3	20.1825	24.4167
9	4	23.5913	27.8472
9	5	26.927	31.2083
10	0	0	13.719
10	1	13.9158	18.248
10	2	17.8386	22.0737
10	3	21.4285	25.659
10	4	24.8732	29.1203
10	5	28.2371	32.5063

E.5 Properties of the Interior Spherical Bessel Gravity Field

Some useful properties of the interior spherical Bessel gravity field are presented here.

E.5.1 Lower-degree Spherical Bessel Functions

The analytical expressions of the lower-degree spherical Bessel functions are presented in this section. By Arfken [4] (Chapter 11.7), we have

$$j_n(x) = 2^n x^n \sum_{s=0}^{\infty} \frac{(-1)^s (s+n)!}{s!(2s+2n+1)!} x^{2s} \tag{E.35}$$

Abramowitz and Stegun [2] list the lower-order spherical Bessel functions:

$$\begin{aligned} j_{-1}(x) &= \frac{\cos x}{x} & j_2(x) &= \left(\frac{3}{x^3} - \frac{1}{x}\right)\sin x - \frac{3}{x^2}\cos x \\ j_0(x) &= \frac{\sin x}{x} & j_3(x) &= \left(\frac{15}{x^4} - \frac{6}{x^2}\right)\sin x - \frac{15}{x^3}\cos x + \frac{\cos x}{x} \\ j_1(x) &= \frac{\sin x}{x^2} - \frac{\cos x}{x} \end{aligned} \tag{E.36}$$

Then, the conditions to satisfy, for $j_{-1}(\alpha_{l0}^i)$, $j_0(\alpha_{l1}^i)$, and $j_1(\alpha_{l2}^i)$, are

$$j_{-1}(\alpha_{l0}^i) = \frac{\cos \alpha_{l0}^i}{\alpha_{l0}^i} = 0 \tag{E.37}$$

$$j_0(\alpha_{l1}^i) = \frac{\sin \alpha_{l1}^i}{\alpha_{l1}^i} = 0 \tag{E.38}$$

$$j_1(\alpha_{l2}^i) = \frac{\sin \alpha_{l2}^i - \alpha_{l2}^i \cos \alpha_{l2}^i}{\alpha_{l2}^{i2}} = 0 \tag{E.39}$$

Thus, we get

$$\begin{cases} \alpha^i_{l0} &= \left(l+\frac{1}{2}\right)\pi \\ \alpha^i_{l1} &= (l+1)\pi \\ \alpha^i_{l2} &= \tan\alpha^i_{l2} \end{cases} \qquad \begin{cases} j_0(\alpha^i_{l0}) &= \dfrac{2(-1)^l}{(2l+1)\pi} \\ j_1(\alpha^i_{l1}) &= \dfrac{(-1)^l}{(l+1)\pi} \\ j_2(\alpha^i_{l2}) &= \begin{cases} 0 & \text{for} \quad l=0 \\ \dfrac{(-1)^{l+1}}{\sqrt{1+\alpha^{i2}_{l2}}} & \text{for} \quad l\neq 0 \end{cases} \end{cases} \tag{E.40}$$

for $l = 0, 1, 2, \cdots$. Other useful quantities are $j_1(\alpha^i_{l0})$, $j_2(\alpha^i_{l1})$, $j_3(\alpha^i_{l2})$, $\alpha^{i2}_{l0}\left[j_1(\alpha^i_{l0})\right]^2$, $\alpha^{i2}_{l1}\left[j_2(\alpha^i_{l1})\right]^2$, and $\alpha^{i2}_{l2}\left[j_3(\alpha^i_{l2})\right]^2$. These values are easily obtained from Equation 7.42, with the term $j_{n-1}(\alpha^i_{ln})$ set to zero due to the boundary condition (Equation 7.46).

$$\begin{cases} j_1(\alpha^i_{l0}) &= \dfrac{4(-1)^l}{(2l+1)^2\pi^2} \\ j_2(\alpha^i_{l1}) &= \dfrac{3(-1)^l}{(l+1)^2\pi^2} \\ j_3(\alpha^i_{l2}) &= \begin{cases} 0 & \text{for} \quad l=0 \\ \dfrac{5(-1)^{l+1}}{\alpha^i_{l2}\sqrt{1+\alpha^{i2}_{l2}}} & \text{for} \quad l\neq 0 \end{cases} \end{cases} \qquad \begin{cases} \alpha^{i2}_{l0}\left[j_1(\alpha^i_{l0})\right]^2 &= \dfrac{4}{(2l+1)^2\pi^2} \\ \alpha^{i2}_{l1}\left[j_2(\alpha^i_{l1})\right]^2 &= \dfrac{9}{(l+1)^2\pi^2} \\ \alpha^{i2}_{l2}\left[j_3(\alpha^i_{l2})\right]^2 &= \begin{cases} 0 & \text{for} \quad l=0 \\ \dfrac{25}{1+\alpha^{i2}_{l2}} & \text{for} \quad l\neq 0 \end{cases} \end{cases} \tag{E.41}$$

E.5.2 Recursive Formulae of the Basis Functions of the Interior Spherical Bessel Gravity Field

It is of interest to find a recursive formulae for the basis functions β^i_{nm} and $\varkappa^i_{nm}$. β^i_{nm} is already defined in the main text. $\varkappa^i_{nm}$ is defined as

$$\begin{cases} \mathscr{K}^i_{lnm} = \mathscr{A}^i_{lnm} - i\mathscr{B}^i_{lnm} = \int \varkappa^i_{nm}(\alpha^i_{ln})dm \\ \varkappa^i_{nm}(\alpha^i_{ln}) = \dfrac{2(2-\delta_{0m})(2n+1)(n-m)!}{M^*\mathscr{E}^i_n(\alpha^i_{ln})(n+m)!}\beta^i_{nm}(\alpha^i_{ln}) \end{cases} \tag{E.42}$$

The motivation arises as both the exterior and interior gravity fields have similar recursive expressions due to the properties of the associated Legendre function and trigonometric functions. It seems natural to probe if this is the case for the interior spherical Bessel gravity field. To state the results first, the recursive formulae for the interior spherical Bessel gravity field is not as convenient as those for the exterior/interior gravity fields, and the direct computation is rather encouraged. Nonetheless, these formulae are provided below.

We will consider the two cases where $n = m$ and $n \neq m$. We first consider the diagonal recursion.

$$\begin{aligned} \beta^i_{nn}(\alpha^i_{ln}) &= j_n\left(\frac{\alpha^i_{ln}r}{R^*_e}\right)P_{nn}(\sin\phi)\begin{bmatrix}\cos n\lambda \\ \sin n\lambda\end{bmatrix} \\ &= (2n-1)\frac{j_n\left(\dfrac{\alpha^i_{ln}r}{R^*_e}\right)}{j_{n-1}\left(\dfrac{\alpha^i_{ln}r}{R^*_e}\right)}\begin{bmatrix}x/r & -y/r \\ y/r & x/r\end{bmatrix}\beta^i_{n-1,n-1}(\alpha^i_{ln}) \end{aligned} \tag{E.43}$$

$$\begin{aligned} \varkappa^i_{nn}(\alpha^i_{ln}) &= \frac{(2-\delta_{0n})(2n+1)\mathscr{E}^i_{n-1}(\alpha^i_{ln})}{(2-\delta_{1n})(2n)(2n-1)\mathscr{E}^i_n(\alpha^i_{ln})} \\ &\quad\times\frac{j_n\left(\dfrac{\alpha^i_{ln}r'}{R^*_e}\right)}{j_{n-1}\left(\dfrac{\alpha^i_{ln}r'}{R^*_e}\right)}\begin{bmatrix}x/r' & -y/r' \\ y/r' & x/r'\end{bmatrix}\varkappa^i_{n-1,n-1}(\alpha^i_{ln}) \end{aligned} \tag{E.44}$$

And the vertical recurrence formulae are given as

$$\begin{aligned}\beta^i_{nm}(\alpha^i_{ln}) &= j_n\left(\frac{\alpha^i_{ln}r}{R^*_e}\right)P_{nm}(\sin\phi)\begin{bmatrix}\cos m\lambda\\ \sin m\lambda\end{bmatrix} \\ &= \frac{(2n-1)}{(n-m)}\frac{z}{r}\frac{j_n\left(\frac{\alpha^i_{ln}r}{R^*_e}\right)}{j_{n-1}\left(\frac{\alpha^i_{ln}r}{R^*_e}\right)}\beta^i_{n-1,m}(\alpha^i_{ln}) - \frac{(n+m-1)}{(n-m)}\frac{j_n\left(\frac{\alpha^i_{ln}r}{R^*_e}\right)}{j_{n-2}\left(\frac{\alpha^i_{ln}r}{R^*_e}\right)}\beta^i_{n-2,m}(\alpha^i_{ln})\end{aligned} \tag{E.45}$$

$$\begin{aligned}\varkappa^i_{nm}(\alpha^i_{ln}) &= \frac{(2n+1)\mathscr{E}^i_{n-1}(\alpha^i_{ln})}{(n+m)\mathscr{E}^i_n(\alpha^i_{ln})}\frac{z}{r}\frac{j_n\left(\frac{\alpha^i_{ln}r'}{R^*_e}\right)}{j_{n-1}\left(\frac{\alpha^i_{ln}r'}{R^*_e}\right)}\varkappa^i_{n-1,m}(\alpha^i_{ln}) \\ &\quad -\frac{(2n+1)(n-m-1)\mathscr{E}^i_{n-2}(\alpha^i_{ln})}{(2n-3)(n+m)\mathscr{E}^i_n(\alpha^i_{ln})}\frac{j_n\left(\frac{\alpha^i_{ln}r'}{R^*_e}\right)}{j_{n-2}\left(\frac{\alpha^i_{ln}r'}{R^*_e}\right)}\varkappa^i_{n-2,m}(\alpha^i_{ln})\end{aligned} \tag{E.46}$$

Again, as mentioned above, the recursive formulae for β^i_{nm} and $\varkappa^i_{nm}$ are convoluted, and the direct computation is more convenient.

E.5.3 Second-order Partials of the Interior Spherical Bessel Gravity Field

For the sake of theoretical interest, the second-order partials of the interior spherical Bessel gravity field are provided in this section.

E.5.3.1 Unnormalized Interior Spherical Bessel Gravity Field

$$\begin{aligned}
\frac{\partial^2}{\partial x^2}\beta_{nm}^i(\alpha_{ln}^i) \overset{m\geq 1}{=} & \frac{\alpha_{ln}^{i2}x^2}{R_e^{*2}r^2}j_{n+2}\left(\frac{\alpha_{ln}^i r}{R_e^*}\right)\mathscr{H}_{nm} - \frac{\alpha_{ln}^i}{R_e^* r}j_{n+1}\left(\frac{\alpha_{ln}^i r}{R_e^*}\right)\mathscr{H}_{nm} \\
& + \frac{\alpha_{ln}^i x}{R_e^* r^2}j_{n+1}\left(\frac{\alpha_{ln}^i r}{R_e^*}\right)\mathscr{H}_{n-1,m+1} \\
& - (n+m)(n+m-1)\frac{\alpha_{ln}^i x}{R_e^* r^2}j_{n+1}\left(\frac{\alpha_{ln}^i r}{R_e^*}\right)\mathscr{H}_{n-1,m-1} \\
& - \frac{(n+m)(n+m-1)}{2}\frac{1}{r^2}j_n\left(\frac{\alpha_{ln}^i r}{R_e^*}\right)\mathscr{H}_{n-2,m} \\
& + \frac{1}{4}\frac{1}{r^2}j_n\left(\frac{\alpha_{ln}^i r}{R_e^*}\right)\mathscr{H}_{n-2,m+2} + \frac{(n+m)!}{4(n+m-4)!}\frac{1}{r^2}j_n\left(\frac{\alpha_{ln}^i r}{R_e^*}\right)\mathscr{H}_{n-2,m-2} \\
\overset{m=1}{=} & \frac{\alpha_{ln}^{i2}x^2}{R_e^{*2}r^2}j_{n+2}\left(\frac{\alpha_{ln}^i r}{R_e^*}\right)\mathscr{H}_{n1} - \frac{\alpha_{ln}^i}{R_e^* r}j_{n+1}\left(\frac{\alpha_{ln}^i r}{R_e^*}\right)\mathscr{H}_{n1} \\
& + \frac{\alpha_{ln}^i x}{R_e^* r^2}j_{n+1}\left(\frac{\alpha_{ln}^i r}{R_e^*}\right)\mathscr{H}_{n-1,2} - n(n+1)\frac{\alpha_{ln}^i x}{R_e^* r^2}j_{n+1}\left(\frac{\alpha_{ln}^i r}{R_e^*}\right)\mathscr{H}_{n-1,0} \\
& - \frac{1}{4}\frac{(n+1)!}{(n-1)!}\frac{1}{r^2}j_n\left(\frac{\alpha_{ln}^i r}{R_e^*}\right)P_{n-2,1}\begin{bmatrix}3\cos\lambda \\ \sin\lambda\end{bmatrix} + \frac{1}{4}\frac{1}{r^2}j_n\left(\frac{\alpha_{ln}^i r}{R_e^*}\right)\mathscr{H}_{n-2,3}
\end{aligned} \tag{E.47}$$

$$
\begin{aligned}
\overset{m=0}{=} \quad & \frac{\alpha_{ln}^{i2}x^2}{R_e^{*2}r^2} j_{n+2}\left(\frac{\alpha_{ln}^i r}{R_e^*}\right)\mathscr{H}_{n0} - \frac{\alpha_{ln}^i}{R_e^* r} j_{n+1}\left(\frac{\alpha_{ln}^i r}{R_e^*}\right)\mathscr{H}_{n0} \\
& +2\frac{\alpha_{ln}^i x}{R_e^* r^2} j_{n+1}\left(\frac{\alpha_{ln}^i r}{R_e^*}\right) P_{n-1,1}\begin{bmatrix}\cos\lambda \\ 0\end{bmatrix} \\
& -\frac{n(n-1)}{2}\frac{1}{r^2} j_n\left(\frac{\alpha_{ln}^i r}{R_e^*}\right)\mathscr{H}_{n-2,0} + \frac{1}{2}\frac{1}{r^2} j_n\left(\frac{\alpha_{ln}^i r}{R_e^*}\right) P_{n-2,2}\begin{bmatrix}\cos 2\lambda \\ 0\end{bmatrix}
\end{aligned}
$$

$$
\begin{aligned}
\frac{\partial^2}{\partial y^2}\beta_{nm}^i(\alpha_{ln}^i) \overset{m\geq 1}{=} \quad & \frac{\alpha_{ln}^{i2}y^2}{R_e^{*2}r^2} j_{n+2}\left(\frac{\alpha_{ln}^i r}{R_e^*}\right)\mathscr{H}_{nm} - \frac{\alpha_{ln}^i}{R_e^* r} j_{n+1}\left(\frac{\alpha_{ln}^i r}{R_e^*}\right)\mathscr{H}_{nm} \\
& -\frac{\alpha_{ln}^i y}{R_e^* r^2} j_{n+1}\left(\frac{\alpha_{ln}^i r}{R_e^*}\right) i\mathscr{H}_{n-1,m+1} \\
& -(n+m)(n+m-1)\frac{\alpha_{ln}^i y}{R_e^* r^2} j_{n+1}\left(\frac{\alpha_{ln}^i r}{R_e^*}\right) i\mathscr{H}_{n-1,m-1} \\
& -\frac{(n+m)(n+m-1)}{2}\frac{1}{r^2} j_n\left(\frac{\alpha_{ln}^i r}{R_e^*}\right)\mathscr{H}_{n-2,m} \\
& -\frac{1}{4}\frac{1}{r^2} j_n\left(\frac{\alpha_{ln}^i r}{R_e^*}\right)\mathscr{H}_{n-2,m+2} - \frac{(n+m)!}{4(n+m-4)!}\frac{1}{r^2} j_n\left(\frac{\alpha_{ln}^i r}{R_e^*}\right)\mathscr{H}_{n-2,m-2}
\end{aligned}
\tag{E.48}
$$

$$
\begin{aligned}
\overset{m=1}{=} \quad & \frac{\alpha_{ln}^{i2}y^2}{R_e^{*2}r^2} j_{n+2}\left(\frac{\alpha_{ln}^i r}{R_e^*}\right)\mathscr{H}_{n1} - \frac{\alpha_{ln}^i}{R_e^* r} j_{n+1}\left(\frac{\alpha_{ln}^i r}{R_e^*}\right)\mathscr{H}_{n1} \\
& -\frac{\alpha_{ln}^i y}{R_e^* r^2} j_{n+1}\left(\frac{\alpha_{ln}^i r}{R_e^*}\right) i\mathscr{H}_{n-1,2} - n(n+1)\frac{\alpha_{ln}^i y}{R_e^* r^2} j_{n+1}\left(\frac{\alpha_{ln}^i r}{R_e^*}\right) i\mathscr{H}_{n-1,0} \\
& -\frac{1}{4}\frac{(n+1)!}{(n-1)!}\frac{1}{r^2} j_n\left(\frac{\alpha_{ln}^i r}{R_e^*}\right) P_{n-2,1}\begin{bmatrix}\cos\lambda \\ 3\sin\lambda\end{bmatrix} - \frac{1}{4}\frac{1}{r^2} j_n\left(\frac{\alpha_{ln}^i r}{R_e^*}\right)\mathscr{H}_{n-2,3}
\end{aligned}
$$

$$\overset{m=0}{=} \quad \frac{\alpha_{ln}^{i2}y^2}{R_e^{*2}r^2}j_{n+2}\left(\frac{\alpha_{ln}^i r}{R_e^*}\right)\mathscr{H}_{n0} - \frac{\alpha_{ln}^i}{R_e^* r}j_{n+1}\left(\frac{\alpha_{ln}^i r}{R_e^*}\right)\mathscr{H}_{n0}$$

$$+2\frac{\alpha_{ln}^i y}{R_e^* r^2}j_{n+1}\left(\frac{\alpha_{ln}^i r}{R_e^*}\right)P_{n-1,1}\begin{bmatrix}\sin\lambda\\ \\ 0\end{bmatrix}$$

$$-\frac{1}{2}\frac{n!}{(n-2)!}\frac{1}{r^2}j_n\left(\frac{\alpha_{ln}^i r}{R_e^*}\right)\mathscr{H}_{n-2,0} - \frac{1}{2}\frac{1}{r^2}j_n\left(\frac{\alpha_{ln}^i r}{R_e^*}\right)P_{n-2,2}\begin{bmatrix}\cos 2\lambda\\ \\ 0\end{bmatrix}$$

$$\frac{\partial^2}{\partial z^2}\beta_{nm}^i(\alpha_{ln}^i) = \frac{\alpha_{ln}^{i2}z^2}{R_e^{*2}r^2}j_{n+2}\left(\frac{\alpha_{ln}^i r}{R_e^*}\right)\mathscr{H}_{nm} - \frac{\alpha_{ln}^i}{R_e^* r}j_{n+1}\left(\frac{\alpha_{ln}^i r}{R_e^*}\right)\mathscr{H}_{nm} \tag{E.49}$$

$$-2(n+m)\frac{\alpha_{ln}^i z}{R_e^* r^2}j_{n+1}\left(\frac{\alpha_{ln}^i r}{R_e^*}\right)\mathscr{H}_{n-1,m}$$

$$+(n+m)(n+m-1)\frac{1}{r^2}j_n\left(\frac{\alpha_{ln}^i r}{R_e^*}\right)\mathscr{H}_{n-2,m}$$

$$\frac{\partial^2}{\partial x \partial y}\beta^i_{nm}(\alpha^i_{ln}) \overset{m\geq 1}{=} \frac{\alpha^{i2}_{ln}xy}{R^{*2}_e r^2} j_{n+2}\left(\frac{\alpha^i_{ln}r}{R^*_e}\right)\mathscr{H}_{nm} \tag{E.50}$$

$$-\frac{\alpha^i_{ln}}{2R^*_e}\frac{\cos\phi}{r} j_{n+1}\left(\frac{\alpha^i_{ln}r}{R^*_e}\right) i\mathscr{H}_{n-1,m+1}e^{i\lambda}$$

$$-\frac{(n+m)(n+m-1)}{2}\frac{\alpha^i_{ln}}{R^*_e}\frac{\cos\phi}{r} j_{n+1}\left(\frac{\alpha^i_{ln}r}{R^*_e}\right) i\mathscr{H}_{n-1,m-1}e^{-i\lambda}$$

$$-\frac{1}{4}\frac{1}{r^2} j_n\left(\frac{\alpha^i_{ln}r}{R^*_e}\right) i\mathscr{H}_{n-2,m+2} + \frac{(n+m)!}{4(n+m-4)!}\frac{1}{r^2} j_n\left(\frac{\alpha^i_{ln}r}{R^*_e}\right) i\mathscr{H}_{n-2,m-2}$$

$$\overset{m=1}{=} \frac{\alpha^{i2}_{ln}xy}{R^{*2}_e r^2} j_{n+2}\left(\frac{\alpha^i_{ln}r}{R^*_e}\right)\mathscr{H}_{n1}$$

$$-\frac{\alpha^i_{ln}}{2R^*_e}\frac{\cos\phi}{r} j_{n+1}\left(\frac{\alpha^i_{ln}r}{R^*_e}\right) i\mathscr{H}_{n-1,2}e^{i\lambda}$$

$$-\frac{n(n+1)}{2}\frac{\alpha^i_{ln}}{R^*_e}\frac{\cos\phi}{r} j_{n+1}\left(\frac{\alpha^i_{ln}r}{R^*_e}\right) i\mathscr{H}_{n-1,0}e^{-i\lambda}$$

$$-\frac{1}{4}\frac{1}{r^2} j_n\left(\frac{\alpha^i_{ln}r}{R^*_e}\right) i\mathscr{H}_{n-2,3} - \frac{1}{4}\frac{(n+1)!}{(n-1)!}\frac{1}{r^2} j_n\left(\frac{\alpha^i_{ln}r}{R^*_e}\right) i\tilde{\mathscr{H}}_{n-2,1}$$

$$\overset{m=0}{=} \frac{\alpha^{i2}_{ln}xy}{R^{*2}_e r^2} j_{n+2}\left(\frac{\alpha^i_{ln}r}{R^*_e}\right)\mathscr{H}_{n0}$$

$$+\frac{\alpha^i_{ln}}{R^*_e}\frac{\cos\phi}{r} j_{n+1}\left(\frac{\alpha^i_{ln}r}{R^*_e}\right) P_{n-1,1}\begin{bmatrix}\sin 2\lambda \\ 0\end{bmatrix} + \frac{1}{2}\frac{1}{r^2} j_n\left(\frac{\alpha^i_{ln}r}{R^*_e}\right) P_{n-2,2}\begin{bmatrix}\sin 2\lambda \\ 0\end{bmatrix}$$

$$\frac{\partial^2}{\partial x \partial z}\beta^i_{nm}(\alpha^i_{ln}) \overset{m\geq 0}{=} \frac{\alpha^{i2}_{ln} xz}{R_e^{*2} r^2} j_{n+2}\left(\frac{\alpha^i_{ln} r}{R_e^*}\right) \mathscr{H}_{nm} - (n+m)\frac{\alpha^i_{ln} x}{R_e^* r^2} j_{n+1}\left(\frac{\alpha^i_{ln} r}{R_e^*}\right) \mathscr{H}_{n-1,m} \tag{E.51}$$

$$+\frac{\alpha^i_{ln} z}{2R_e^* r^2} j_{n+1}\left(\frac{\alpha^i_{ln} r}{R_e^*}\right) \mathscr{H}_{n-1,m+1}$$

$$-\frac{(n+m)(n+m-1)}{2}\frac{\alpha^i_{ln} z}{R_e^* r^2} j_{n+1}\left(\frac{\alpha^i_{ln} r}{R_e^*}\right) \mathscr{H}_{n-1,m-1}$$

$$-\frac{(n+m)}{2}\frac{1}{r^2} j_n\left(\frac{\alpha^i_{ln} r}{R_e^*}\right) \mathscr{H}_{n-2,m+1} + \frac{(n+m)!}{2(n+m-3)!}\frac{1}{r^2} j_n\left(\frac{\alpha^i_{ln} r}{R_e^*}\right) \mathscr{H}_{n-2,m-1}$$

$$\overset{m=0}{=} \frac{\alpha^{i2}_{ln} xz}{R_e^{*2} r^2} j_{n+2}\left(\frac{\alpha^i_{ln} r}{R_e^*}\right) \mathscr{H}_{n0} - n\frac{\alpha^i_{ln} x}{R_e^* r^2} j_{n+1}\left(\frac{\alpha^i_{ln} r}{R_e^*}\right) \mathscr{H}_{n-1,0}$$

$$+\frac{\alpha^i_{ln} z}{R_e^* r^2} j_{n+1}\left(\frac{\alpha^i_{ln} r}{R_e^*}\right) P_{n-1,1}\begin{bmatrix}\cos\lambda \\ \\ 0\end{bmatrix} - n\frac{1}{r^2} j_n\left(\frac{\alpha^i_{ln} r}{R_e^*}\right) P_{n-2,1}\begin{bmatrix}\cos\lambda \\ \\ 0\end{bmatrix}$$

$$\frac{\partial^2}{\partial y \partial z}\beta^i_{nm}(\alpha^i_{ln}) \overset{m\geq 0}{=} \frac{\alpha^{i2}_{ln} yz}{R_e^{*2} r^2} j_{n+2}\left(\frac{\alpha^i_{ln} r}{R^*_e}\right) \mathscr{H}_{nm} - (n+m)\frac{\alpha^i_{ln} y}{R^*_e r^2} j_{n+1}\left(\frac{\alpha^i_{ln} r}{R^*_e}\right) \mathscr{H}_{n-1,m} \quad \text{(E.52)}$$

$$-\frac{\alpha^i_{ln} z}{2R^*_e r^2} j_{n+1}\left(\frac{\alpha^i_{ln} r}{R^*_e}\right) i\mathscr{H}_{n-1,m+1}$$

$$-\frac{1}{2}\frac{(n+m)!}{(n+m-2)!}\frac{\alpha^i_{ln} z}{R^*_e r^2} j_{n+1}\left(\frac{\alpha^i_{ln} r}{R^*_e}\right) i\mathscr{H}_{n-1,m-1}$$

$$+\frac{(n+m)}{2}\frac{1}{r^2} j_n\left(\frac{\alpha^i_{ln} r}{R^*_e}\right) i\mathscr{H}_{n-2,m+1}$$

$$+\frac{(n+m)!}{2(n+m-3)!}\frac{1}{r^2} j_n\left(\frac{\alpha^i_{ln} r}{R^*_e}\right) i\mathscr{H}_{n-2,m-1}$$

$$\overset{m=0}{=} \frac{\alpha^{i2}_{ln} yz}{R_e^{*2} r^2} j_{n+2}\left(\frac{\alpha^i_{ln} r}{R^*_e}\right) \mathscr{H}_{n0} - n\frac{\alpha^i_{ln} y}{R^*_e r^2} j_{n+1}\left(\frac{\alpha^i_{ln} r}{R^*_e}\right) \mathscr{H}_{n-1,0}$$

$$+\frac{\alpha^i_{ln} z}{R^*_e r^2} j_{n+1}\left(\frac{\alpha^i_{ln} r}{R^*_e}\right) P_{n-1,1}\begin{bmatrix}\sin\lambda \\ \\ 0\end{bmatrix} - n\frac{1}{r^2} j_n\left(\frac{\alpha^i_{ln} r}{R^*_e}\right) P_{n-2,1}\begin{bmatrix}\sin\lambda \\ \\ 0\end{bmatrix}$$

E.5.3.2 Normalized Interior Spherical Bessel Gravity Field

$$\frac{\partial^2}{\partial x^2}\bar{\beta}^i_{nm}(\alpha^i_{ln}) \overset{m\geq 1}{=} \frac{\alpha^{i2}_{ln}x^2}{R^{*2}_e r^2} j_{n+2}\left(\frac{\alpha^i_{ln}r}{R^*_e}\right)\bar{\mathscr{H}}_{nm} - \frac{\alpha^i_{ln}}{R^*_e r} j_{n+1}\left(\frac{\alpha^i_{ln}r}{R^*_e}\right)\bar{\mathscr{H}}_{nm} \tag{E.53}$$

$$+\sqrt{\frac{(2-\delta_{0m})(2n+1)(n-m)!}{2(2n-1)(n-m-2)!}}\frac{\alpha^i_{ln}x}{R^*_e r^2} j_{n+1}\left(\frac{\alpha^i_{ln}r}{R^*_e}\right)\bar{\mathscr{H}}_{n-1,m+1}$$

$$-\sqrt{\frac{(2-\delta_{0m})(2n+1)(n+m)!}{(2-\delta_{1,m})(2n-1)(n+m-2)!}}\frac{\alpha^i_{ln}x}{R^*_e r^2} j_{n+1}\left(\frac{\alpha^i_{ln}r}{R^*_e}\right)\bar{\mathscr{H}}_{n-1,m-1}$$

$$-\frac{1}{2}\sqrt{\frac{(2n+1)(n+m)!(n-m)!}{(2n-3)(n+m-2)!(n-m-2)!}}\frac{1}{r^2} j_n\left(\frac{\alpha^i_{ln}r}{R^*_e}\right)\bar{\mathscr{H}}_{n-2,m}$$

$$+\frac{1}{4}\sqrt{\frac{(2-\delta_{0m})(2n+1)(n-m)!}{2(2n-3)(n-m-4)!}}\frac{1}{r^2} j_n\left(\frac{\alpha^i_{ln}r}{R^*_e}\right)\bar{\mathscr{H}}_{n-2,m+2}$$

$$+\frac{1}{4}\sqrt{\frac{(2-\delta_{0m})(2n+1)(n+m)!}{(2-\delta_{2,m})(2n-3)(n+m-4)!}}\frac{1}{r^2} j_n\left(\frac{\alpha^i_{ln}r}{R^*_e}\right)\bar{\mathscr{H}}_{n-2,m-2}$$

$$\overset{m=1}{=} \frac{\alpha^{i2}_{ln}x^2}{R^{*2}_e r^2} j_{n+2}\left(\frac{\alpha^i_{ln}r}{R^*_e}\right)\bar{\mathscr{H}}_{n1} - \frac{\alpha^i_{ln}}{R^*_e r} j_{n+1}\left(\frac{\alpha^i_{ln}r}{R^*_e}\right)\bar{\mathscr{H}}_{n1}$$

$$+\sqrt{\frac{(2n+1)(n-1)!}{(2n-1)(n-3)!}}\frac{\alpha^i_{ln}x}{R^*_e r^2} j_{n+1}\left(\frac{\alpha^i_{ln}r}{R^*_e}\right)\bar{\mathscr{H}}_{n-1,2}$$

$$-\sqrt{\frac{2(2n+1)(n+1)!}{(2n-1)(n-1)!}}\frac{\alpha^i_{ln}x}{R^*_e r^2} j_{n+1}\left(\frac{\alpha^i_{ln}r}{R^*_e}\right)\bar{\mathscr{H}}_{n-1,0}$$

$$-\frac{1}{4}\sqrt{\frac{(2n+1)(n+1)!}{(2n-3)(n-3)!}}\frac{1}{r^2} j_n\left(\frac{\alpha^i_{ln}r}{R^*_e}\right)\bar{P}_{n-2,1}\begin{bmatrix}3\cos\lambda\\ \sin\lambda\end{bmatrix}$$

$$+\frac{1}{4}\sqrt{\frac{(2n+1)(n-1)!}{(2n-3)(n-5)!}}\frac{1}{r^2} j_n\left(\frac{\alpha^i_{ln}r}{R^*_e}\right)\bar{\mathscr{H}}_{n-2,3}$$

$$\overset{m=0}{=} \quad \frac{\alpha_{ln}^{i2}x^2}{R_e^{*2}r^2}j_{n+2}\left(\frac{\alpha_{ln}^i r}{R_e^*}\right)\bar{\mathscr{H}}_{n0} - \frac{\alpha_{ln}^i}{R_e^* r}j_{n+1}\left(\frac{\alpha_{ln}^i r}{R_e^*}\right)\bar{\mathscr{H}}_{n0}$$

$$+2\sqrt{\frac{(2n+1)n!}{2(2n-1)(n-2)!}}\frac{\alpha_{ln}^i x}{R_e^* r^2}j_{n+1}\left(\frac{\alpha_{ln}^i r}{R_e^*}\right)\bar{P}_{n-1,1}\begin{bmatrix}\cos\lambda\\ 0\end{bmatrix}$$

$$-\frac{1}{2}\sqrt{\frac{(2n+1)}{(2n-3)}n^2(n-1)^2}\frac{1}{r^2}j_n\left(\frac{\alpha_{ln}^i r}{R_e^*}\right)\bar{\mathscr{H}}_{n-2,0}$$

$$+\frac{1}{2}\sqrt{\frac{(2n+1)n!}{2(2n-3)(n-4)!}}\frac{1}{r^2}j_n\left(\frac{\alpha_{ln}^i r}{R_e^*}\right)\bar{P}_{n-2,2}\begin{bmatrix}\cos 2\lambda\\ 0\end{bmatrix}$$

$$\frac{\partial^2}{\partial y^2}\bar{\beta}_{nm}^i(\alpha_{ln}^i) \quad \overset{m\geq 1}{=} \quad \frac{\alpha_{ln}^{i2}y^2}{R_e^{*2}r^2}j_{n+2}\left(\frac{\alpha_{ln}^i r}{R_e^*}\right)\bar{\mathscr{H}}_{nm} - \frac{\alpha_{ln}^i}{R_e^* r}j_{n+1}\left(\frac{\alpha_{ln}^i r}{R_e^*}\right)\bar{\mathscr{H}}_{nm} \tag{E.54}$$

$$-\sqrt{\frac{(2-\delta_{0m})(2n+1)(n-m)!}{2(2n-1)(n-m-2)!}}\frac{\alpha_{ln}^i y}{R_e^* r^2}j_{n+1}\left(\frac{\alpha_{ln}^i r}{R_e^*}\right)i\bar{\mathscr{H}}_{n-1,m+1}$$

$$-\sqrt{\frac{(2-\delta_{0m})(2n+1)(n+m)!}{(2-\delta_{1,m})(2n-1)(n+m-2)!}}\frac{\alpha_{ln}^i y}{R_e^* r^2}j_{n+1}\left(\frac{\alpha_{ln}^i r}{R_e^*}\right)i\bar{\mathscr{H}}_{n-1,m-1}$$

$$-\frac{1}{2}\sqrt{\frac{(2n+1)(n+m)!(n-m)!}{(2n-3)(n+m-2)!(n-m-2)!}}\frac{1}{r^2}j_n\left(\frac{\alpha_{ln}^i r}{R_e^*}\right)\bar{\mathscr{H}}_{n-2,m}$$

$$-\frac{1}{4}\sqrt{\frac{(2-\delta_{0m})(2n+1)(n-m)!}{2(2n-3)(n-m-4)!}}\frac{1}{r^2}j_n\left(\frac{\alpha_{ln}^i r}{R_e^*}\right)\bar{\mathscr{H}}_{n-2,m+2}$$

$$-\frac{1}{4}\sqrt{\frac{(2-\delta_{0m})(2n+1)(n+m)!}{(2-\delta_{2,m})(2n-3)(n+m-4)!}}\frac{1}{r^2}j_n\left(\frac{\alpha_{ln}^i r}{R_e^*}\right)\bar{\mathscr{H}}_{n-2,m-2}$$

$$\overset{m=1}{=} \quad \frac{\alpha_{ln}^{i2}y^2}{R_e^{*2}r^2}j_{n+2}\left(\frac{\alpha_{ln}^i r}{R_e^*}\right)\bar{\mathscr{H}}_{n1} - \frac{\alpha_{ln}^i}{R_e^* r}j_{n+1}\left(\frac{\alpha_{ln}^i r}{R_e^*}\right)\bar{\mathscr{H}}_{n1}$$

$$-\sqrt{\frac{(2n+1)(n-1)!}{(2n-1)(n-3)!}}\frac{\alpha_{ln}^i y}{R_e^* r^2}j_{n+1}\left(\frac{\alpha_{ln}^i r}{R_e^*}\right) i\bar{\mathscr{H}}_{n-1,2}$$

$$-\sqrt{\frac{2(2n+1)(n+1)!}{(2n-1)(n-1)!}}\frac{\alpha_{ln}^i y}{R_e^* r^2}j_{n+1}\left(\frac{\alpha_{ln}^i r}{R_e^*}\right) i\bar{\mathscr{H}}_{n-1,0}$$

$$-\frac{1}{4}\sqrt{\frac{(2n+1)(n+1)!}{(2n-3)(n-3)!}}\frac{1}{r^2}j_n\left(\frac{\alpha_{ln}^i r}{R_e^*}\right)\bar{P}_{n-2,1}\begin{bmatrix}\cos\lambda\\ \\ 3\sin\lambda\end{bmatrix}$$

$$-\frac{1}{4}\sqrt{\frac{(2n+1)(n-1)!}{(2n-3)(n-5)!}}\frac{1}{r^2}j_n\left(\frac{\alpha_{ln}^i r}{R_e^*}\right)\bar{\mathscr{H}}_{n-2,3}$$

$$\overset{m=0}{=} \quad \frac{\alpha_{ln}^{i2}y^2}{R_e^{*2}r^2}j_{n+2}\left(\frac{\alpha_{ln}^i r}{R_e^*}\right)\bar{\mathscr{H}}_{n0} - \frac{\alpha_{ln}^i}{R_e^* r}j_{n+1}\left(\frac{\alpha_{ln}^i r}{R_e^*}\right)\bar{\mathscr{H}}_{n0}$$

$$+2\sqrt{\frac{(2n+1)n!}{2(2n-1)(n-2)!}}\frac{\alpha_{ln}^i y}{R_e^* r^2}j_{n+1}\left(\frac{\alpha_{ln}^i r}{R_e^*}\right)\bar{P}_{n-1,1}\begin{bmatrix}\sin\lambda\\ \\ 0\end{bmatrix}$$

$$-\frac{1}{2}\sqrt{\frac{(2n+1)}{(2n-3)}n^2(n-1)^2}\frac{1}{r^2}j_n\left(\frac{\alpha_{ln}^i r}{R_e^*}\right)\bar{\mathscr{H}}_{n-2,0}$$

$$-\frac{1}{2}\sqrt{\frac{(2n+1)n!}{2(2n-3)(n-4)!}}\frac{1}{r^2}j_n\left(\frac{\alpha_{ln}^i r}{R_e^*}\right)\bar{P}_{n-2,2}\begin{bmatrix}\cos 2\lambda\\ \\ 0\end{bmatrix}$$

$$\frac{\partial^2}{\partial z^2}\bar{\beta}^i_{nm}(\alpha^i_{ln}) = \frac{\alpha^{i2}_{ln}z^2}{R^{*2}_e r^2} j_{n+2}\left(\frac{\alpha^i_{ln}r}{R^*_e}\right)\bar{\mathscr{H}}_{nm} - \frac{\alpha^i_{ln}}{R^*_e r} j_{n+1}\left(\frac{\alpha^i_{ln}r}{R^*_e}\right)\bar{\mathscr{H}}_{nm} \tag{E.55}$$

$$-2\sqrt{\frac{(2n+1)}{(2n-1)}(n+m)(n-m)}\frac{\alpha^i_{ln}z}{R^*_e r^2} j_{n+1}\left(\frac{\alpha^i_{ln}r}{R^*_e}\right)\bar{\mathscr{H}}_{n-1,m}$$

$$+\sqrt{\frac{(2n+1)(n+m)!(n-m)!}{(2n-3)(n+m-2)!(n-m-2)!}}\frac{1}{r^2} j_n\left(\frac{\alpha^i_{ln}r}{R^*_e}\right)\bar{\mathscr{H}}_{n-2,m}$$

$$\frac{\partial^2}{\partial x \partial y}\bar{\beta}^i_{nm}(\alpha^i_{ln}) \overset{m\geq 1}{=} \frac{\alpha^{i2}_{ln}xy}{R^{*2}_e r^2} j_{n+2}\left(\frac{\alpha^i_{ln}r}{R^*_e}\right)\bar{\mathscr{H}}_{nm} \tag{E.56}$$

$$-\frac{1}{2}\sqrt{\frac{(2-\delta_{0m})(2n+1)(n-m)!}{2(2n-1)(n-m-2)!}}\frac{\alpha^i_{ln}}{R^*_e}\frac{\cos\phi}{r} j_{n+1}\left(\frac{\alpha^i_{ln}r}{R^*_e}\right) i\bar{\mathscr{H}}_{n-1,m+1}e^{i\lambda}$$

$$-\frac{1}{2}\sqrt{\frac{(2-\delta_{0m})(2n+1)(n+m)!}{(2-\delta_{1,m})(2n-1)(n+m-2)!}}\frac{\alpha^i_{ln}}{R^*_e}\frac{\cos\phi}{r} j_{n+1}\left(\frac{\alpha^i_{ln}r}{R^*_e}\right) i\bar{\mathscr{H}}_{n-1,m-1}e^{-i\lambda}$$

$$-\frac{1}{4}\sqrt{\frac{(2-\delta_{0m})(2n+1)(n-m)!}{2(2n-3)(n-m-4)!}}\frac{1}{r^2} j_n\left(\frac{\alpha^i_{ln}r}{R^*_e}\right) i\bar{\mathscr{H}}_{n-2,m+2}$$

$$+\frac{1}{4}\sqrt{\frac{(2-\delta_{0m})(2n+1)(n+m)!}{(2-\delta_{2,m})(2n-3)(n+m-4)!}}\frac{1}{r^2} j_n\left(\frac{\alpha^i_{ln}r}{R^*_e}\right) i\bar{\mathscr{H}}_{n-2,m-2}$$

$$\overset{m=1}{=} \quad \frac{\alpha_{ln}^{i2} xy}{R_e^{*2} r^2} j_{n+2}\left(\frac{\alpha_{ln}^{i} r}{R_e^{*}}\right) \bar{\mathscr{H}}_{n1}$$

$$-\frac{1}{2}\sqrt{\frac{(2n+1)(n-1)!}{(2n-1)(n-3)!}}\frac{\alpha_{ln}^{i}}{R_e^{*}}\frac{\cos\phi}{r} j_{n+1}\left(\frac{\alpha_{ln}^{i} r}{R_e^{*}}\right) i\bar{\mathscr{H}}_{n-1,2} e^{i\lambda}$$

$$-\frac{1}{2}\sqrt{\frac{2(2n+1)(n+1)!}{(2n-1)(n-1)!}}\frac{\alpha_{ln}^{i}}{R_e^{*}}\frac{\cos\phi}{r} j_{n+1}\left(\frac{\alpha_{ln}^{i} r}{R_e^{*}}\right) i\bar{\mathscr{H}}_{n-1,0} e^{-i\lambda}$$

$$-\frac{1}{4}\sqrt{\frac{(2n+1)(n-1)!}{(2n-3)(n-5)!}}\frac{1}{r^2} j_{n}\left(\frac{\alpha_{ln}^{i} r}{R_e^{*}}\right) i\bar{\mathscr{H}}_{n-2,3}$$

$$-\frac{1}{4}\sqrt{\frac{(2n+1)(n+1)!}{(2n-3)(n-3)!}}\frac{1}{r^2} j_{n}\left(\frac{\alpha_{ln}^{i} r}{R_e^{*}}\right) i\tilde{\bar{\mathscr{H}}}_{n-2,1}$$

$$\overset{m=0}{=} \quad \frac{\alpha_{ln}^{i2} xy}{R_e^{*2} r^2} j_{n+2}\left(\frac{\alpha_{ln}^{i} r}{R_e^{*}}\right) \bar{\mathscr{H}}_{n0}$$

$$+\sqrt{\frac{(2n+1)n!}{2(2n-1)(n-2)!}}\frac{\alpha_{ln}^{i}}{R_e^{*}}\frac{\cos\phi}{r} j_{n+1}\left(\frac{\alpha_{ln}^{i} r}{R_e^{*}}\right) \bar{P}_{n-1,1}\begin{bmatrix}\sin 2\lambda \\ 0\end{bmatrix}$$

$$+\frac{1}{2}\sqrt{\frac{(2n+1)n!}{2(2n-3)(n-4)!}}\frac{1}{r^2} j_{n}\left(\frac{\alpha_{ln}^{i} r}{R_e^{*}}\right) \bar{P}_{n-2,2}\begin{bmatrix}\sin 2\lambda \\ 0\end{bmatrix}$$

$$\frac{\partial^2}{\partial x \partial z}\bar{\beta}^i_{nm}(\alpha^i_{ln}) \overset{m\geq 0}{=} \frac{\alpha^{i2}_{ln} xz}{R_e^{*2} r^2} j_{n+2}\left(\frac{\alpha^i_{ln} r}{R^*_e}\right)\bar{\mathscr{H}}_{nm} \tag{E.57}$$

$$-\sqrt{\frac{(2n+1)}{(2n-1)}(n+m)(n-m)}\frac{\alpha^i_{ln} x}{R^*_e r^2} j_{n+1}\left(\frac{\alpha^i_{ln} r}{R^*_e}\right)\bar{\mathscr{H}}_{n-1,m}$$

$$+\frac{1}{2}\sqrt{\frac{(2-\delta_{0m})(2n+1)(n-m)!}{2(2n-1)(n-m-2)!}}\frac{\alpha^i_{ln} z}{R^*_e r^2} j_{n+1}\left(\frac{\alpha^i_{ln} r}{R^*_e}\right)\bar{\mathscr{H}}_{n-1,m+1}$$

$$-\frac{1}{2}\sqrt{\frac{(2-\delta_{0m})(2n+1)(n+m)!}{(2-\delta_{1,m})(2n-1)(n+m-2)!}}\frac{\alpha^i_{ln} z}{R^*_e r^2} j_{n+1}\left(\frac{\alpha^i_{ln} r}{R^*_e}\right)\bar{\mathscr{H}}_{n-1,m-1}$$

$$-\frac{1}{2}\sqrt{\frac{(2-\delta_{0m})(2n+1)(n+m)(n-m)!}{2(2n-3)(n-m-3)!}}\frac{1}{r^2} j_{n}\left(\frac{\alpha^i_{ln} r}{R^*_e}\right)\bar{\mathscr{H}}_{n-2,m+1}$$

$$+\frac{1}{2}\sqrt{\frac{(2-\delta_{0m})(2n+1)(n-m)(n+m)!}{(2-\delta_{1,m})(2n-3)(n+m-3)!}}\frac{1}{r^2} j_{n}\left(\frac{\alpha^i_{ln} r}{R^*_e}\right)\bar{\mathscr{H}}_{n-2,m-1}$$

$$\overset{m=0}{=} \frac{\alpha^{i2}_{ln} xz}{R_e^{*2} r^2} j_{n+2}\left(\frac{\alpha^i_{ln} r}{R^*_e}\right)\bar{\mathscr{H}}_{n0} - \sqrt{\frac{n^2(2n+1)}{(2n-1)}}\frac{\alpha^i_{ln} x}{R^*_e r^2} j_{n+1}\left(\frac{\alpha^i_{ln} r}{R^*_e}\right)\bar{\mathscr{H}}_{n-1,0}$$

$$+\sqrt{\frac{(2n+1)n!}{2(2n-1)(n-2)!}}\frac{\alpha^i_{ln} z}{R^*_e r^2} j_{n+1}\left(\frac{\alpha^i_{ln} r}{R^*_e}\right)\bar{P}_{n-1,1}\begin{bmatrix}\cos\lambda \\ 0\end{bmatrix}$$

$$-\sqrt{\frac{(2n+1)n\cdot n!}{2(2n-3)(n-3)!}}\frac{1}{r^2} j_{n}\left(\frac{\alpha^i_{ln} r}{R^*_e}\right)\bar{P}_{n-2,1}\begin{bmatrix}\cos\lambda \\ 0\end{bmatrix}$$

$$\frac{\partial^2}{\partial y \partial z}\bar{\beta}^i_{nm}(\alpha^i_{ln}) \overset{m>0}{=} \frac{\alpha^{i2}_{ln} yz}{R_e^{*2} r^2} j_{n+2}\left(\frac{\alpha^i_{ln} r}{R^*_e}\right) \bar{\mathscr{H}}_{nm} \tag{E.58}$$

$$-\sqrt{\frac{(2n+1)}{(2n-1)}(n+m)(n-m)}\frac{\alpha^i_{ln} y}{R^*_e r^2} j_{n+1}\left(\frac{\alpha^i_{ln} r}{R^*_e}\right) \bar{\mathscr{H}}_{n-1,m}$$

$$-\frac{1}{2}\sqrt{\frac{(2-\delta_{0m})(2n+1)(n-m)!}{2(2n-1)(n-m-2)!}}\frac{\alpha^i_{ln} z}{R^*_e r^2} j_{n+1}\left(\frac{\alpha^i_{ln} r}{R^*_e}\right) i\bar{\mathscr{H}}_{n-1,m+1}$$

$$-\frac{1}{2}\sqrt{\frac{(2-\delta_{0m})(2n+1)(n+m)!}{(2-\delta_{1,m})(2n-1)(n+m-2)!}}\frac{\alpha^i_{ln} z}{R^*_e r^2} j_{n+1}\left(\frac{\alpha^i_{ln} r}{R^*_e}\right) i\bar{\mathscr{H}}_{n-1,m-1}$$

$$+\frac{1}{2}\sqrt{\frac{(2-\delta_{0m})(2n+1)(n+m)(n-m)!}{2(2n-3)(n-m-3)!}}\frac{1}{r^2} j_n\left(\frac{\alpha^i_{ln} r}{R^*_e}\right) i\bar{\mathscr{H}}_{n-2,m+1}$$

$$+\frac{1}{2}\sqrt{\frac{(2-\delta_{0m})(2n+1)(n-m)(n+m)!}{(2-\delta_{1,m})(2n-3)(n+m-3)!}}\frac{1}{r^2} j_n\left(\frac{\alpha^i_{ln} r}{R^*_e}\right) i\bar{\mathscr{H}}_{n-2,m-1}$$

$$\overset{m=0}{=} \frac{\alpha^{i2}_{ln} yz}{R_e^{*2} r^2} j_{n+2}\left(\frac{\alpha^i_{ln} r}{R^*_e}\right) \bar{\mathscr{H}}_{n0} - \sqrt{\frac{n^2(2n+1)}{(2n-1)}}\frac{\alpha^i_{ln} y}{R^*_e r^2} j_{n+1}\left(\frac{\alpha^i_{ln} r}{R^*_e}\right) \bar{\mathscr{H}}_{n-1,0}$$

$$+\sqrt{\frac{(2n+1)n!}{2(2n-1)(n-2)!}}\frac{\alpha^i_{ln} z}{R^*_e r^2} j_{n+1}\left(\frac{\alpha^i_{ln} r}{R^*_e}\right) \bar{P}_{n-1,1}\begin{bmatrix}\sin\lambda \\ \\ 0\end{bmatrix}$$

$$-\sqrt{\frac{(2n+1)n\cdot n!}{2(2n-3)(n-3)!}}\frac{1}{r^2} j_n\left(\frac{\alpha^i_{ln} r}{R^*_e}\right) \bar{P}_{n-2,1}\begin{bmatrix}\sin\lambda \\ \\ 0\end{bmatrix}$$

E.5.4 Partials of the Acceleration with respect to the Interior Spherical Bessel Coefficients

In this section, we present the partials of the acceleration with respect to the interior spherical Bessel coefficients that enter the matrix $[\mathscr{Q}^i_{lnm}]$ (Section 7.12.2.1). These partials are directly obtained by extracting the real part ($\Re()$ operator) and the imaginary part ($\Im()$ operator) of the field point acceleration.

E.5.4.1 Unnormalized Interior Spherical Bessel Coefficients

$$\frac{\partial \ddot{x}}{\partial \mathscr{A}^i_{lnm}} = \frac{GM^*}{R_e^*}\frac{\partial}{\partial \mathscr{A}^i_{lnm}\partial x}\left[\beta^i_{nm}(\alpha^i_{ln})\cdot\begin{bmatrix}\mathscr{A}^i_{lnm}\\ \mathscr{B}^i_{lnm}\end{bmatrix}\right] = \frac{GM^*}{R_e^*}\Re\left[\frac{\partial \beta^i_{nm}(\alpha^i_{ln})}{\partial x}\right] \tag{E.59}$$

$$\frac{\partial \ddot{x}}{\partial \mathscr{B}^i_{lnm}} = \frac{GM^*}{R_e^*}\frac{\partial}{\partial \mathscr{B}^i_{lnm}\partial x}\left[\beta^i_{nm}(\alpha^i_{ln})\cdot\begin{bmatrix}\mathscr{A}^i_{lnm}\\ \mathscr{B}^i_{lnm}\end{bmatrix}\right] \overset{m\geq 0}{=} \frac{GM^*}{R_e^*}\Im\left[\frac{\partial \beta^i_{nm}(\alpha^i_{ln})}{\partial x}\right] \tag{E.60}$$

$$\frac{\partial \ddot{y}}{\partial \mathscr{A}^i_{lnm}} = \frac{GM^*}{R_e^*}\frac{\partial}{\partial \mathscr{A}^i_{lnm}\partial y}\left[\beta^i_{nm}(\alpha^i_{ln})\cdot\begin{bmatrix}\mathscr{A}^i_{lnm}\\ \mathscr{B}^i_{lnm}\end{bmatrix}\right] = \frac{GM^*}{R_e^*}\Re\left[\frac{\partial \beta^i_{nm}(\alpha^i_{ln})}{\partial y}\right] \tag{E.61}$$

$$\frac{\partial \ddot{y}}{\partial \mathscr{B}^i_{lnm}} = \frac{GM^*}{R_e^*}\frac{\partial}{\partial \mathscr{B}^i_{lnm}\partial y}\left[\beta^i_{nm}(\alpha^i_{ln})\cdot\begin{bmatrix}\mathscr{A}^i_{lnm}\\ \mathscr{B}^i_{lnm}\end{bmatrix}\right] \overset{m\geq 0}{=} \frac{GM^*}{R_e^*}\Im\left[\frac{\partial \beta^i_{nm}(\alpha^i_{ln})}{\partial y}\right] \tag{E.62}$$

$$\frac{\partial \ddot{z}}{\partial \mathscr{A}^i_{lnm}} = \frac{GM^*}{R_e^*}\frac{\partial}{\partial \mathscr{A}^i_{lnm}\partial z}\left[\beta^i_{nm}(\alpha^i_{ln})\cdot\begin{bmatrix}\mathscr{A}^i_{lnm}\\ \mathscr{B}^i_{lnm}\end{bmatrix}\right] = \frac{GM^*}{R_e^*}\Re\left[\frac{\partial \beta^i_{nm}(\alpha^i_{ln})}{\partial z}\right] \tag{E.63}$$

$$\frac{\partial \ddot{z}}{\partial \mathscr{B}^i_{lnm}} = \frac{GM^*}{R_e^*}\frac{\partial}{\partial \mathscr{B}^i_{lnm}\partial z}\left[\beta^i_{nm}(\alpha^i_{ln})\cdot\begin{bmatrix}\mathscr{A}^i_{lnm}\\ \mathscr{B}^i_{lnm}\end{bmatrix}\right] \overset{m\geq 0}{=} \frac{GM^*}{R_e^*}\Im\left[\frac{\partial \beta^i_{nm}(\alpha^i_{ln})}{\partial z}\right] \tag{E.64}$$

E.5.5 Normalized Interior Spherical Bessel Coefficients

$$\frac{\partial \ddot{x}}{\partial \bar{\mathscr{A}}^i_{lnm}} = \frac{GM^*}{R_e^*}\frac{\partial}{\partial \bar{\mathscr{A}}^i_{lnm}\partial x}\left[\bar{\beta}^i_{nm}(\alpha^i_{ln})\cdot\begin{bmatrix}\bar{\mathscr{A}}^i_{lnm}\\ \bar{\mathscr{B}}^i_{lnm}\end{bmatrix}\right] = \frac{GM^*}{R_e^*}\Re\left[\frac{\partial \bar{\beta}^i_{nm}(\alpha^i_{ln})}{\partial x}\right] \tag{E.65}$$

$$\frac{\partial \ddot{x}}{\partial \bar{\mathscr{B}}^i_{lnm}} = \frac{GM^*}{R_e^*}\frac{\partial}{\partial \bar{\mathscr{B}}^i_{lnm}\partial x}\left[\bar{\beta}^i_{nm}(\alpha^i_{ln})\cdot\begin{bmatrix}\bar{\mathscr{A}}^i_{lnm}\\ \bar{\mathscr{B}}^i_{lnm}\end{bmatrix}\right] \overset{m\geq 0}{=} \frac{GM^*}{R_e^*}\Im\left[\frac{\partial \bar{\beta}^i_{nm}(\alpha^i_{ln})}{\partial x}\right] \tag{E.66}$$

$$\frac{\partial \ddot{y}}{\partial \bar{\mathscr{A}}^i_{lnm}} = \frac{GM^*}{R_e^*}\frac{\partial}{\partial \bar{\mathscr{A}}^i_{lnm}\partial y}\left[\bar{\beta}^i_{nm}(\alpha^i_{ln})\cdot\begin{bmatrix}\bar{\mathscr{A}}^i_{lnm}\\ \bar{\mathscr{B}}^i_{lnm}\end{bmatrix}\right] = \frac{GM^*}{R_e^*}\Re\left[\frac{\partial \bar{\beta}^i_{nm}(\alpha^i_{ln})}{\partial y}\right] \tag{E.67}$$

$$\frac{\partial \ddot{y}}{\partial \bar{\mathscr{B}}^i_{lnm}} = \frac{GM^*}{R_e^*}\frac{\partial}{\partial \bar{\mathscr{B}}^i_{lnm}\partial y}\left[\bar{\beta}^i_{nm}(\alpha^i_{ln})\cdot\begin{bmatrix}\bar{\mathscr{A}}^i_{lnm}\\ \bar{\mathscr{B}}^i_{lnm}\end{bmatrix}\right] \overset{m\geq 0}{=} \frac{GM^*}{R_e^*}\Im\left[\frac{\partial \bar{\beta}^i_{nm}(\alpha^i_{ln})}{\partial y}\right] \tag{E.68}$$

$$\frac{\partial \ddot{z}}{\partial \bar{\mathscr{A}}^i_{lnm}} = \frac{GM^*}{R_e^*}\frac{\partial}{\partial \bar{\mathscr{A}}^i_{lnm}\partial z}\left[\bar{\beta}^i_{nm}(\alpha^i_{ln})\cdot\begin{bmatrix}\bar{\mathscr{A}}^i_{lnm}\\ \bar{\mathscr{B}}^i_{lnm}\end{bmatrix}\right] = \frac{GM^*}{R_e^*}\Re\left[\frac{\partial \bar{\beta}^i_{nm}(\alpha^i_{ln})}{\partial z}\right] \tag{E.69}$$

$$\frac{\partial \ddot{z}}{\partial \bar{\mathscr{B}}^i_{lnm}} = \frac{GM^*}{R_e^*}\frac{\partial}{\partial \bar{\mathscr{B}}^i_{lnm}\partial z}\left[\bar{\beta}^i_{nm}(\alpha^i_{ln})\cdot\begin{bmatrix}\bar{\mathscr{A}}^i_{lnm}\\ \bar{\mathscr{B}}^i_{lnm}\end{bmatrix}\right] \overset{m\geq 0}{=} \frac{GM^*}{R_e^*}\Im\left[\frac{\partial \bar{\beta}^i_{nm}(\alpha^i_{ln})}{\partial z}\right] \tag{E.70}$$

E.6 List of the Interior Spherical Bessel Coefficients

We provide a few sets of the interior spherical Bessel coefficients used to analyze the surface gravity field of Bennu and Castalia in Section 7.12. For space purposes, we only list the coefficients up to the fourth degree and order and second power.

E.6.1 Analytically Converted Interior Spherical Bessel Coefficients

Table E.2 and E.3 list the normalized $10 \times 10 \times 2$ interior spherical Bessel coefficients for Bennu and Castalia (i.e., case 3 in Section 7.12.1).

Table E.2: Normalized $10 \times 10 \times 2$ interior spherical Bessel coefficients analytically converted from the exterior gravity field for Bennu (Section 7.12.1.1).

Power (l)	Degree (n)	Order (m)	$\bar{A}^i_{lnm}$	$\bar{B}^i_{lnm}$
0	0	0	1.767018160	-
0	1	0	$1.721498089 \times 10^{-12}$	-
0	1	1	$1.082761172 \times 10^{-11}$	$-8.376180398 \times 10^{-12}$
1	0	0	$5.884739409 \times 10^{-1}$	-
1	1	0	$8.600403931 \times 10^{-13}$	-
1	1	1	$5.409348694 \times 10^{-12}$	$-4.184642160 \times 10^{-12}$
1	2	0	$-7.886882936 \times 10^{-2}$	-
1	2	1	$-7.837730409 \times 10^{-12}$	$-9.623522903 \times 10^{-12}$
1	2	2	$2.749559802 \times 10^{-2}$	$-2.126849496 \times 10^{-12}$
1	3	0	$3.612297136 \times 10^{-2}$	-
1	3	1	$9.881388043 \times 10^{-3}$	$9.815953053 \times 10^{-3}$
1	3	2	$6.282743968 \times 10^{-4}$	$2.596874969 \times 10^{-4}$
1	3	3	$1.684543032 \times 10^{-2}$	$-6.074776663 \times 10^{-3}$
1	4	0	$7.392830546 \times 10^{-2}$	-
1	4	1	$3.291497157 \times 10^{-3}$	$1.363571937 \times 10^{-2}$
1	4	2	$-1.643627145 \times 10^{-2}$	$5.997970322 \times 10^{-3}$
1	4	3	$-8.552005760 \times 10^{-3}$	$5.536580618 \times 10^{-4}$
1	4	4	$1.481948423 \times 10^{-2}$	$2.238845343 \times 10^{-2}$
2	0	0	$-3.192675460 \times 10^{-4}$	-
2	1	0	$-4.724342979 \times 10^{-16}$	-
2	1	1	$-2.971443985 \times 10^{-15}$	$2.298692593 \times 10^{-15}$
2	2	0	$-4.515233378 \times 10^{-2}$	-
2	2	1	$-4.487093601 \times 10^{-12}$	$-5.509458195 \times 10^{-12}$
2	2	2	$1.574120510 \times 10^{-2}$	$-1.217619421 \times 10^{-12}$
2	3	0	$2.224746697 \times 10^{-2}$	-
2	3	1	$6.085763321 \times 10^{-3}$	$6.045463126 \times 10^{-3}$
2	3	2	$3.869425290 \times 10^{-4}$	$1.599367049 \times 10^{-4}$
2	3	3	$1.037478758 \times 10^{-2}$	$-3.741342090 \times 10^{-3}$
2	4	0	$4.772735353 \times 10^{-2}$	-
2	4	1	$2.124956706 \times 10^{-3}$	$8.803080161 \times 10^{-3}$
2	4	2	$-1.061108777 \times 10^{-2}$	$3.872227941 \times 10^{-3}$
2	4	3	$-5.521086948 \times 10^{-3}$	$3.574359494 \times 10^{-4}$
2	4	4	$9.567306579 \times 10^{-3}$	$1.445375523 \times 10^{-2}$

Table E.3: Normalized $10 \times 10 \times 2$ interior spherical Bessel coefficients analytically converted from the exterior gravity field for Castalia (Section 7.12.1.2).

Power (l)	Degree (n)	Order (m)	$\bar{A}^i_{lnm}$	$\bar{B}^i_{lnm}$
0	0	0	1.767018160	-
0	1	0	$2.531975434 \times 10^{-14}$	-
0	1	1	$-5.096811240 \times 10^{-12}$	$-2.016329719 \times 10^{-12}$
1	0	0	$5.884739409 \times 10^{-1}$	-
1	1	0	$1.264945434 \times 10^{-14}$	-
1	1	1	$-2.546307527 \times 10^{-12}$	$-1.007334841 \times 10^{-12}$
1	2	0	$-2.929085611 \times 10^{-1}$	-
1	2	1	$-1.214564071 \times 10^{-12}$	$-2.072938673 \times 10^{-12}$
1	2	2	$4.162083375 \times 10^{-1}$	$-1.515423215 \times 10^{-12}$
1	3	0	$-3.601785956 \times 10^{-2}$	-
1	3	1	$-9.048256852 \times 10^{-2}$	$2.865315795 \times 10^{-3}$
1	3	2	$1.509608721 \times 10^{-2}$	$1.509956025 \times 10^{-3}$
1	3	3	$4.914378012 \times 10^{-2}$	$-3.264398516 \times 10^{-2}$
1	4	0	$7.265010174 \times 10^{-2}$	-
1	4	1	$5.332276866 \times 10^{-3}$	$8.033845549 \times 10^{-4}$
1	4	2	$-1.018865468 \times 10^{-1}$	$7.837651231 \times 10^{-3}$
1	4	3	$1.216950294 \times 10^{-2}$	$-3.463287673 \times 10^{-3}$
1	4	4	$9.979797802 \times 10^{-2}$	$-1.359106269 \times 10^{-2}$
2	0	0	$-3.192675460 \times 10^{-4}$	-
2	1	0	$-6.948552801 \times 10^{-18}$	-
2	1	1	$1.398728500 \times 10^{-15}$	$5.533455550 \times 10^{-16}$
2	2	0	$-1.676898874 \times 10^{-1}$	-
2	2	1	$-6.953368372 \times 10^{-13}$	$-1.186755523 \times 10^{-12}$
2	2	2	$2.382788984 \times 10^{-1}$	$-8.675784260 \times 10^{-13}$
2	3	0	$-2.218273057 \times 10^{-2}$	-
2	3	1	$-5.572653298 \times 10^{-2}$	$1.764694766 \times 10^{-3}$
2	3	2	$9.297399662 \times 10^{-3}$	$9.299538644 \times 10^{-4}$
2	3	3	$3.026674119 \times 10^{-2}$	$-2.010482400 \times 10^{-2}$
2	4	0	$4.690215836 \times 10^{-2}$	-
2	4	1	$3.442463094 \times 10^{-3}$	$5.186568046 \times 10^{-4}$
2	4	2	$-6.577690660 \times 10^{-2}$	$5.059907012 \times 10^{-3}$
2	4	3	$7.856505917 \times 10^{-3}$	$-2.235862896 \times 10^{-3}$
2	4	4	$6.442854803 \times 10^{-2}$	$-8.774250269 \times 10^{-3}$

E.6.2 Optimal Interior Spherical Bessel Coefficients

Table E.4 and E.5 list the optimal interior spherical Bessel coefficients estimated from the polyhedral gravity field for Bennu and Castalia in Section 7.12.3.

Table E.4: Optimal normalized $20 \times 20 \times 2$ interior spherical Bessel coefficients estimated from the polyhedral gravity field for Bennu (Section 7.12.3.1).

Power (l)	Degree (n)	Order (m)	$\bar{A}^i_{lnm}$	$\bar{B}^i_{lnm}$
0	0	0	1.790976865	-
0	1	0	$-2.651078993 \times 10^{-3}$	-
0	1	1	$-4.805888264 \times 10^{-3}$	$7.709247087 \times 10^{-5}$
1	0	0	$6.994306871 \times 10^{-1}$	-
1	1	0	$-9.016453713 \times 10^{-3}$	-
1	1	1	$-1.574025759 \times 10^{-2}$	$-5.045468258 \times 10^{-4}$
1	2	0	$-7.565529404 \times 10^{-2}$	-
1	2	1	$-3.592248075 \times 10^{-4}$	$-2.485825790 \times 10^{-5}$
1	2	2	$2.516075663 \times 10^{-2}$	$5.983468509 \times 10^{-4}$
1	3	0	$3.611472617 \times 10^{-2}$	-
1	3	1	$1.012328059 \times 10^{-2}$	$9.139662929 \times 10^{-3}$
1	3	2	$1.007098716 \times 10^{-3}$	$-4.263927377 \times 10^{-5}$
1	3	3	$1.606993335 \times 10^{-2}$	$-5.528866691 \times 10^{-3}$
1	4	0	$7.347328771 \times 10^{-2}$	-
1	4	1	$3.542357030 \times 10^{-3}$	$1.401855535 \times 10^{-2}$
1	4	2	$-1.531634331 \times 10^{-2}$	$6.460046960 \times 10^{-3}$
1	4	3	$-8.595541871 \times 10^{-3}$	$4.356750039 \times 10^{-4}$
1	4	4	$1.326069183 \times 10^{-2}$	$1.964838782 \times 10^{-2}$
2	0	0	$5.923065732 \times 10^{-2}$	-
2	1	0	$-5.535986632 \times 10^{-3}$	-
2	1	1	$-9.601736657 \times 10^{-3}$	$-1.195352794 \times 10^{-3}$
2	2	0	$-3.909724987 \times 10^{-2}$	-
2	2	1	$-6.372758133 \times 10^{-4}$	$-3.583905335 \times 10^{-5}$
2	2	2	$1.157487960 \times 10^{-2}$	$1.310740820 \times 10^{-3}$
2	3	0	$2.204794098 \times 10^{-2}$	-
2	3	1	$6.331347479 \times 10^{-3}$	$4.848708356 \times 10^{-3}$
2	3	2	$1.171642377 \times 10^{-3}$	$-4.018932733 \times 10^{-4}$
2	3	3	$9.040525922 \times 10^{-3}$	$-3.000190246 \times 10^{-3}$
2	4	0	$4.740230904 \times 10^{-2}$	-
2	4	1	$2.468453051 \times 10^{-3}$	$9.319816073 \times 10^{-3}$
2	4	2	$-9.179642461 \times 10^{-3}$	$4.764194503 \times 10^{-3}$
2	4	3	$-5.512280007 \times 10^{-3}$	$1.945699382 \times 10^{-4}$
2	4	4	$7.424431260 \times 10^{-3}$	$1.026249824 \times 10^{-2}$

Table E.5: Optimal normalized $18 \times 18 \times 5$ interior spherical Bessel coefficients estimated from the polyhedral gravity field for Castalia (Section 7.12.3.2).

Power (l)	Degree (n)	Order (m)	$\bar{A}^i_{lnm}$	$\bar{B}^i_{lnm}$
0	0	0	1.802974690	-
0	1	0	$-1.735007668 \times 10^{-2}$	-
0	1	1	$-7.131813697 \times 10^{-2}$	$1.362482061 \times 10^{-4}$
1	0	0	$7.391186806 \times 10^{-1}$	-
1	1	0	$-6.119001962 \times 10^{-2}$	-
1	1	1	$-2.455384409 \times 10^{-1}$	$-1.169035081 \times 10^{-2}$
1	2	0	$-3.371599844 \times 10^{-1}$	-
1	2	1	$1.180985071 \times 10^{-2}$	$6.489313919 \times 10^{-3}$
1	2	2	$4.615366023 \times 10^{-1}$	$7.966833023 \times 10^{-3}$
1	3	0	$-2.479669965 \times 10^{-2}$	-
1	3	1	$-6.776972878 \times 10^{-2}$	$-2.154017728 \times 10^{-3}$
1	3	2	$-1.242368501 \times 10^{-2}$	$-1.469634423 \times 10^{-2}$
1	3	3	$1.646083195 \times 10^{-2}$	$-3.564784335 \times 10^{-2}$
1	4	0	$8.533444910 \times 10^{-2}$	-
1	4	1	$8.902368720 \times 10^{-3}$	$-3.112486340 \times 10^{-3}$
1	4	2	$-1.212298075 \times 10^{-1}$	$1.113145643 \times 10^{-2}$
1	4	3	$2.067640881 \times 10^{-2}$	$6.400094817 \times 10^{-3}$
1	4	4	$1.211059773 \times 10^{-1}$	$8.463361733 \times 10^{-3}$
2	0	0	$5.155596040 \times 10^{-2}$	-
2	1	0	$-4.271461929 \times 10^{-2}$	-
2	1	1	$-1.802760480 \times 10^{-1}$	$-3.275896829 \times 10^{-2}$
2	2	0	$-3.029474832 \times 10^{-1}$	-
2	2	1	$6.068636081 \times 10^{-2}$	$2.979474150 \times 10^{-2}$
2	2	2	$3.650090715 \times 10^{-1}$	$1.558292408 \times 10^{-2}$
2	3	0	$1.609467527 \times 10^{-2}$	-
2	3	1	$1.892772671 \times 10^{-2}$	$-1.133832717 \times 10^{-2}$
2	3	2	$-8.062631405 \times 10^{-2}$	$-7.173968387 \times 10^{-2}$
2	3	3	$-6.812518249 \times 10^{-2}$	$-5.601270273 \times 10^{-2}$
2	4	0	$8.246146486 \times 10^{-2}$	-
2	4	1	$-8.723520344 \times 10^{-3}$	$-1.831448635 \times 10^{-2}$
2	4	2	$-1.200619102 \times 10^{-1}$	$3.344907003 \times 10^{-2}$
2	4	3	$4.474184742 \times 10^{-2}$	$4.650009823 \times 10^{-2}$
2	4	4	$1.262690634 \times 10^{-1}$	$4.623192337 \times 10^{-2}$

E.7 Properties of the Exterior Spherical Bessel Gravity Field

We derive and provide some useful properties of the exterior spherical Bessel gravity field.

E.7.1 Structure of the Exterior Spherical Bessel Coefficients

The exterior spherical Bessel gravity field with the dimensional coefficients is given in Equation 7.26. We non-dimensionalize the exterior spherical Bessel coefficients and substitute the eigenvalue α_{ln}^e to get

$$V^e = \frac{GM^*}{R_i^*} \sum_{l=0}^{\infty} \sum_{n=0}^{\infty} \sum_{m=0}^{n} \mathcal{Y}_n \left(\frac{\alpha_{ln}^e r}{R_i^*} \right) P_{nm}(\sin\phi) \begin{bmatrix} \cos(m\lambda) \\ \sin(m\lambda) \end{bmatrix} \cdot \begin{bmatrix} \mathscr{A}_{lnm}^e \\ \mathscr{B}_{lnm}^e \end{bmatrix} \tag{E.71}$$

where

$$\alpha_{ln}^e = R_i^* k_{ln}^e \tag{E.72}$$

Equation E.71 reveals an interesting characteristic of the exterior spherical Bessel gravity field. Recall that the zeroth term of the interior potential in Equation 6.13 is only a bias and does not contribute to the field point acceleration. However, the zeroth term of the exterior spherical Bessel potential clearly shows the position dependency, and its partial is non-zero. Thus, when analytically converting the interior spherical harmonic coefficients into the exterior spherical Bessel coefficients, the bias term of the interior potential needs to be precisely determined. This behavior of the exterior spherical Bessel gravity field is contrary to one's intuition.

E.7.1.1 Density Distribution due to the Exterior Spherical Bessel Gravity Field

By direct substitution of Equation E.71 into Equation 7.9, the density distribution is obtained as

$$\rho_e = \frac{M^*}{4\pi R_i^{*3}} \sum_{l=0}^{\infty} \sum_{n=0}^{\infty} \sum_{m=0}^{n} \alpha_{ln}^{e2} \mathcal{Y}_n \left(\frac{\alpha_{ln}^e r}{R_i^*} \right) P_{nm} \begin{bmatrix} \cos(m\lambda) \\ \sin(m\lambda) \end{bmatrix} \cdot \begin{bmatrix} \mathscr{A}_{lnm}^e \\ \mathscr{B}_{lnm}^e \end{bmatrix} \tag{E.73}$$

E.7.1.2 Unnormalized Exterior Spherical Bessel Coefficients

As with the interior spherical Bessel gravity field, we leverage the orthogonal properties of spherical Neumann function and associated Legendre function to obtain the exterior spherical Bessel coefficients. Since the density is redistributed outside the interior Brillouin sphere, the limits of integration for the radial coordinate is between R_i^* and ∞.

$$\int_V \mathcal{Y}_n \left(\frac{\alpha_{ln}^e r'}{R_i^*} \right) P_{nm}(\sin\phi') \cos(m\lambda') \rho_e dv = \frac{\mathscr{A}_{lnm}^e M^* \mathscr{E}_n^e(\alpha_{ln}^e)(n+m)!}{2(2-\delta_{0m})(2n+1)(n-m)!} \tag{E.74}$$

where $\mathscr{E}_q^e(\alpha_{ln}^e) = \alpha_{ln}^{e2} \left[\mathcal{Y}_q(\alpha_{ln}^e)\right]^2$. We can perform similar operation for the sine term of the density to get

$$\begin{cases} \mathscr{A}_{lnm}^e = \dfrac{2(2-\delta_{0m})(2n+1)(n-m)!}{M^* \mathscr{E}_n^e(\alpha_{ln}^e)(n+m)!} \displaystyle\int_M \mathcal{Y}_n \left(\frac{\alpha_{ln}^e r'}{R_i^*} \right) P_{nm}(\sin\phi') \cos(m\lambda') dm' \\ \mathscr{B}_{lnm}^e \overset{m>0}{=} \dfrac{4(2n+1)(n-m)!}{M^* \mathscr{E}_n^e(\alpha_{ln}^e)(n+m)!} \displaystyle\int_M \mathcal{Y}_n \left(\frac{\alpha_{ln}^e r'}{R_i^*} \right) P_{nm}(\sin\phi') \sin(m\lambda') dm' \end{cases} \tag{E.75}$$

where $dm' = \rho_e dv$ is substituted. Notice the remarkable similarities between the exterior spherical Bessel coefficients and the interior spherical harmonic coefficients in Equation 6.11.

E.7.1.3 Normalized Exterior Spherical Bessel Coefficients

The normalized exterior spherical Bessel coefficients are given as

$$\begin{cases} \bar{\mathscr{A}}^e_{lnm} & = & \dfrac{2}{M^* \mathscr{E}^e_n(\alpha^e_{ln})} \sqrt{\dfrac{(2-\delta_{0m})(2n+1)(n-m)!}{(n+m)!}} \displaystyle\int_M \mathcal{Y}_n \left(\frac{\alpha^e_{ln} r'}{R^*_i} \right) P_{nm}(\sin\phi') \cos(m\lambda') dm' \\ \\ \bar{\mathscr{B}}^e_{lnm} & \overset{m>0}{=} & \dfrac{2}{M^* \mathscr{E}^e_n(\alpha^e_{ln})} \sqrt{\dfrac{2(2n+1)(n-m)!}{(n+m)!}} \displaystyle\int_M \mathcal{Y}_n \left(\frac{\alpha^e_{ln} r'}{R^*_i} \right) P_{nm}(\sin\phi') \sin(m\lambda') dm' \end{cases} \tag{E.76}$$

E.7.2 Interior Gravity Field Expressed via Spherical Neumann Function

The two potential expressions U^i and V^e cannot have discontinuity on the boundary of the interior Brillouin sphere. Therefore, we impose a constraint that the potentials given by U^i and V^e match on the boundary of the interior Brillouin sphere. The interior potential on the boundary of the interior Brillouin sphere is given as

$$U^i\big|_{r=R^*_i} = \frac{GM^*}{R^*_i} \sum_{n=0}^{\infty} \sum_{m=0}^{n} P_{nm}(\sin\phi) \begin{bmatrix} \cos(m\lambda) \\ \sin(m\lambda) \end{bmatrix} \cdot \begin{bmatrix} C^i_{nm} \\ S^i_{nm} \end{bmatrix} \tag{E.77}$$

Also, the exterior spherical Bessel potential on the boundary of the interior Brillouin sphere is given as

$$V^e\big|_{r=R^*_i} = \frac{GM^*}{R^*_i} \sum_{l=0}^{\infty} \sum_{n=0}^{\infty} \sum_{m=0}^{n} \mathcal{Y}_n\left(\alpha^e_{ln}\right) P_{nm}(\sin\phi) \begin{bmatrix} \cos(m\lambda) \\ \sin(m\lambda) \end{bmatrix} \cdot \begin{bmatrix} \mathscr{A}^e_{lnm} \\ \mathscr{B}^e_{lnm} \end{bmatrix} \tag{E.78}$$

As we must have the condition $U^i\big|_{r=R^*_i} = V^e\big|_{r=R^*_i}$, comparison of the two equations immediately yields

$$\begin{cases} C^i_{nm} & = & \displaystyle\sum_{l=0}^{\infty} \mathcal{Y}_n(\alpha^e_{ln}) \mathscr{A}^e_{lnm} \\ \\ S^i_{nm} & = & \displaystyle\sum_{l=0}^{\infty} \mathcal{Y}_n(\alpha^e_{ln}) \mathscr{B}^e_{lnm} \end{cases} \tag{E.79}$$

Thus, the interior potential is expressed via the exterior spherical Bessel coefficients as

$$U^i = \frac{GM^*}{R_i^*}\sum_{l=0}^{\infty}\sum_{n=0}^{\infty}\sum_{m=0}^{n}\mathcal{Y}_n(\alpha_{ln}^e)\left(\frac{r}{R_i^*}\right)^n P_{nm}(\sin\phi)\begin{bmatrix}\cos(m\lambda)\\ \sin(m\lambda)\end{bmatrix}\cdot\begin{bmatrix}\mathscr{A}_{lnm}^e\\ \mathscr{B}_{lnm}^e\end{bmatrix} \tag{E.80}$$

E.7.3 Boundary Conditions and Eigenvalues of the Exterior Spherical Bessel Gravity Field

We match the acceleration due to the interior gravity field and exterior spherical Bessel gravity field on the boundary of the interior Brillouin sphere. That is,

$$\begin{aligned}\ddot{\vec{r}}\Big|_{r=R_i^*} &= \frac{\partial U^i}{\partial r}\hat{r}+\frac{1}{r}\frac{\partial U^i}{\partial\phi}\hat{\phi}+\frac{1}{r\cos\phi}\frac{\partial U^i}{\partial\lambda}\hat{\lambda}\Big|_{r=R_i^*}\\ &= \frac{\partial V^e}{\partial r}\hat{r}+\frac{1}{r}\frac{\partial V^e}{\partial\phi}\hat{\phi}+\frac{1}{r\cos\phi}\frac{\partial V^e}{\partial\lambda}\hat{\lambda}\Big|_{r=R_i^*}\end{aligned} \tag{E.81}$$

Note that the interior potential can be expressed as $U_{lmm}^i = R_{ln}^i(r)\Phi_{nm}^i(\phi)\Lambda_m^i(\lambda)$, where the interior radial potential is given as

$$R_{ln}^i(r) = \frac{GM^*}{R_i^*}\mathcal{Y}_n(\alpha_{ln}^e)\left(\frac{r}{R_i^*}\right)^n \tag{E.82}$$

which yields

$$\ddot{r}_{lnm}|_{r=R_i^*} = \frac{\partial R_{ln}^i(r)}{\partial r}\Big|_{r=R_i^*} = n\frac{GM^*}{R_i^{*2}}\mathcal{Y}_n(\alpha_{ln}^e) \tag{E.83}$$

Next, we compute $\ddot{r}_{lnm}$ from V^e. As both the recursive formula and the partials of $\mathcal{Y}_n$ are identical to those of j_n (see Equation 7.42 and 7.43), we get

$$\ddot{r}_{lnm}|_{r=R_i^*} = \frac{GM^*\alpha_{ln}^e}{R_i^{*2}}\mathcal{Y}_{n-1}(\alpha_{ln}^e)-(n+1)\frac{GM^*}{R_i^{*2}}\mathcal{Y}_n(\alpha_{ln}^e) \tag{E.84}$$

Then, by equating Equation E.83 and E.84 and applying the recursive formula, we get

$$\frac{GM^*}{R_i^{*2}}\left[(2n+1)\mathcal{Y}_n\left(\alpha_{ln}^e\right)-\alpha_{ln}^e\mathcal{Y}_{n-1}(\alpha_{ln}^e)\right] \;=\; \frac{GM^*}{R_i^{*2}}\alpha_{ln}^e\mathcal{Y}_{n+1}(\alpha_{ln}^e) \;=\; 0 \tag{E.85}$$

As α_{ln}^e is not necessarily zero (i.e., $\alpha_{ln}^e = 0$ for $\forall l$, $\forall n$ is Laplace's equation), we get

$$\mathcal{Y}_{n+1}(\alpha_{ln}^e) \;=\; 0 \tag{E.86}$$

Unlike the eigenvalues of the interior spherical Bessel potential, α_{ln}^e is never zero and all coefficients $\mathscr{A}_{lnm}^e$ and $\mathscr{B}_{lnm}^e$ are non-zero. The lower-degree, lower-power eigenvalues α_{ln}^e are given in Appendix E.4.

E.7.4 Analytical Conversion between the Interior Spherical Harmonic Coefficients and Exterior Spherical Bessel Coefficients

We follow the same procedure as the interior spherical Bessel gravity field to convert the interior spherical harmonic coefficients into the exterior spherical Bessel coefficients. In order to make a smooth transition from Poisson's equation to Laplace's equation, the density distribution evaluated on the boundary of the interior Brillouin sphere has to reach the limit

$$\lim_{r\to R_i^*}\rho_e(r,\phi,\lambda) \;=\; 0 \text{ for } \forall\phi,\forall\lambda \tag{E.87}$$

which yields

$$\begin{cases} \displaystyle\sum_{l=0}^{\infty}\alpha_{ln}^{e2}\mathcal{Y}_n(\alpha_{ln}^e)\mathscr{A}_{lnm}^e \;=\; 0 \\ \\ \displaystyle\sum_{l=0}^{\infty}\alpha_{ln}^{e2}\mathcal{Y}_n(\alpha_{ln}^e)\mathscr{B}_{lnm}^e \;=\; 0 \end{cases} \tag{E.88}$$

For the exterior spherical Bessel gravity field, $l^* = 0$. Thus, we get

$$\begin{cases} \mathscr{A}^e_{lnm} &= \dfrac{\alpha^{e2}_{l^*n}}{(\alpha^{e2}_{l^*n} - \alpha^{e2}_{ln})\mathcal{Y}_n(\alpha^e_{ln})} \dfrac{g(l)}{\sum_{\gamma=1}^{\infty} g(\gamma)} C^i_{nm} \\ \mathscr{B}^e_{lnm} &= \dfrac{\alpha^{e2}_{l^*n}}{(\alpha^{e2}_{l^*n} - \alpha^{e2}_{ln})\mathcal{Y}_n(\alpha^e_{ln})} \dfrac{g(l)}{\sum_{\gamma=1}^{\infty} g(\gamma)} S^i_{nm} \end{cases} \tag{E.89}$$

for $l \geq l^* + 1$. Also, $A^e_{l^*nm}$ and $B^e_{l^*nm}$ are obtained as

$$\begin{cases} \mathscr{A}^e_{l^*nm} &= -\dfrac{1}{\alpha^{e2}_{l^*n}\mathcal{Y}_n(\alpha^e_{l^*n})} \sum_{l=l^*+1}^{\infty} \alpha^{e2}_{ln}\mathcal{Y}_n(\alpha^e_{ln})\mathscr{A}^e_{lnm} \\ \mathscr{B}^e_{l^*nm} &= -\dfrac{1}{\alpha^{e2}_{l^*n}\mathcal{Y}_n(\alpha^e_{l^*n})} \sum_{l=l^*+1}^{\infty} \alpha^{e2}_{ln}\mathcal{Y}_n(\alpha^e_{ln})\mathscr{B}^e_{lnm} \end{cases} \tag{E.90}$$

E.7.5 Acceleration and Dynamics Matrix due to the Exterior Spherical Bessel Gravity Field

As mentioned in Appendix E.7.3, both the recursive formula and the partials of $\mathcal{Y}_n$ are identical to those of j_n. Thus, the acceleration and the dynamics matrix expressions of the interior/exterior spherical Bessel gravity fields are identical. One only needs to define the exterior basis function $\beta^e_{nm}(\alpha^e_{ln})$ and express V^e as

$$\beta^e_{nm}(\alpha^e_{ln}) = \mathcal{Y}_n\left(\frac{\alpha^e_{ln} r}{R^*_i}\right)\mathscr{H}_{nm} \tag{E.91}$$

$$V^e = \frac{GM^*}{R^*_i}\sum_{l=0}^{\infty}\sum_{n=0}^{\infty}\sum_{m=0}^{n}\beta^e_{nm}(\alpha^e_{ln}) \cdot \begin{bmatrix} \mathscr{A}^e_{lnm} \\ \mathscr{B}^e_{lnm} \end{bmatrix} \tag{E.92}$$

and make appropriate substitutions in order to compute the partials of the exterior spherical Bessel gravity field.

E.7.6 Lower-degree Spherical Neumann Functions

By Arfken [4] (Chapter 11.7), $\mathcal{Y}_n(x)$ is given as

$$\mathcal{Y}_n(x) = \frac{(-1)^{n+1}}{2^n x^{n+1}} \sum_{s=0}^{\infty} \frac{(-1)^s (s-n)!}{s!(2s-2n)!} x^{2s} \tag{E.93}$$

Abramowitz and Stegun [2] list $\mathcal{Y}_0(x)$ through $\mathcal{Y}_2(x)$ as

$$\mathcal{Y}_0(x) = -j_{-1}(x) = -\frac{\cos x}{x} \tag{E.94}$$

$$\mathcal{Y}_1(x) = j_{-2}(x) = -\frac{\cos x}{x^2} - \frac{\sin x}{x} \tag{E.95}$$

$$\mathcal{Y}_2(x) = -j_{-3}(x) = \left(-\frac{3}{x^3} + \frac{1}{x}\right) \cos x - \frac{3}{x^2} \sin x \tag{E.96}$$

As shown above, it quickly becomes cumbersome to obtain an analytical solution to $\mathcal{Y}_n(x) = 0$. Therefore, we will only solve for α_{l0}^e. From Equation E.86, α_{l0}^e satisfies

$$\mathcal{Y}_1(\alpha_{l0}^e) = -\frac{\cos \alpha_{l0}^e}{\alpha_{l0}^{e2}} - \frac{\sin \alpha_{l0}^e}{\alpha_{l0}^e} = 0 \tag{E.97}$$

which yields

$$\alpha_{l0}^e = -\frac{1}{\tan \alpha_{l0}^e} \tag{E.98}$$

Thus, we get

$$\mathcal{Y}_0(\alpha_{l0}^e) = -\frac{\cos \alpha_{l0}^e}{\alpha_{l0}^e} = \sin \alpha_{l0}^e \tag{E.99}$$

$$\alpha_{l0}^{e2} \left[\mathcal{Y}_0(\alpha_{l0}^e)\right]^2 = \alpha_{l0}^{e2} \sin^2 \alpha_{l0}^e \tag{E.100}$$